Designing optically switchable multifunctional materials using photochromic spirooxazine ligands

by

Michelle Marie Paquette
B.Sc., University of Guelph, 2006

A Thesis Submitted in Partial Fulfillment
of the Requirements for the Degree of

DOCTOR OF PHILOSOPHY

in the Department of Chemistry

Supervisory Committee

Designing optically switchable multifunctional materials using photochromic spirooxazine ligands

by

Michelle Marie Paquette
B.Sc., University of Guelph, 2006

Supervisory Committee

Dr. Natia L. Frank (Department of Chemistry)
Supervisor

Dr. David J. Berg (Department of Chemistry)
Departmental Member

Dr. Cornelia Bohne (Department of Chemistry)
Departmental Member

Dr. Geoffrey M. Steeves (Department of Physics and Astronomy)
Outside Member

Abstract

Supervisory Committee

Dr. Natia L. Frank (Department of Chemistry)

Supervisor

Dr. David J. Berg (Department of Chemistry)

Departmental Member

Dr. Cornelia Bohne (Department of Chemistry)

Departmental Member

Dr. Geoffrey M. Steeves (Department of Physics and Astronomy)

Outside Member

Photoswitchable molecular materials are of interest for optical data storage, optically controlled electronics, and light-controlled molecular machines or ‘smart’ surfaces. A promising way to incorporate optical switchability into materials is by using organic photochromic molecules—which convert reversibly between two forms with light—as ligands in coordination complexes. This design allows for the intimate communication between ligand and metal such that light-induced photoisomerization may be used to modulate metal-based properties. Spirooxazines, photochromic systems that photochemically isomerize between nonconjugated ring-closed spirooxazine (SO) and highly conjugated ring-opened photomerocyanine (PMC) forms, were derivatized with a phenanthroline moiety to enable the binding of transition-metal ions. Two phenanthroline–spirooxazines, an indolyl derivative and an azahomoadamantyl derivative, were investigated in the context of chemical substitution and medium effects. The ring-opened PMC forms of the spirooxazines were characterized by solid- and/or solution-state methods to extract the relative contributions of the canonical quinoidal and zwitterionic resonance forms to their molecular structure. The PMC form of the azahomoadamantyl derivative was found to exhibit significant zwitterionic character, with demonstrated sensitivity to medium polarity. The pronounced zwitterionic character was correlated with the high stability of the PMC form, high photoresponsivity, and slow thermal relaxation rates in this class of spirooxazines. The relative ligand field strengths of the SO and PMC forms of the two phenanthroline–spirooxazines were analyzed using

the FT-IR and ^{13}C NMR carbonyl signals of their molybdenum–tetracarbonyl–spirooxazine complexes. Differences in metal–ligand bonding in the SO and PMC forms were also investigated by a density functional theory fragment molecular orbital analysis. The SO form was found to be a better π-acceptor both empirically and theoretically. Lastly, the spirooxazine ligands were incorporated into electronically bistable cobalt–dioxolene redox isomers, where the low-spin-Co^{III}/high-spin-Co^{II} equilibrium is sensitive to ligand field strength. Using solution-state spectroscopic methods, it was shown that the redox state of the cobalt centre could be modulated through photoisomerization of the spirooxazine ligand. As changes in cobalt redox state are associated with changes in magnetic spin state, this system forms the basis for a room-temperature photomagnetic material and highlights the powerful role of photochromic phenanthroline–spirooxazine ligands in developing photoswitchable multifunctional materials.

Table of Contents

List of Tables

List of Figures

List of Schemes

List of Numbered Compounds

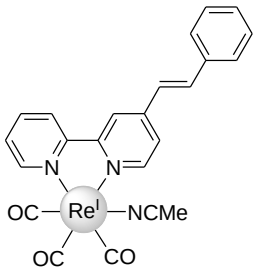

1

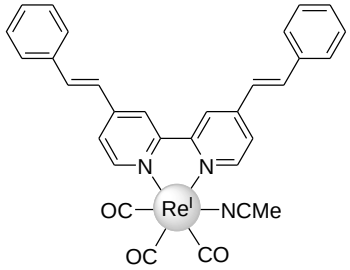

2

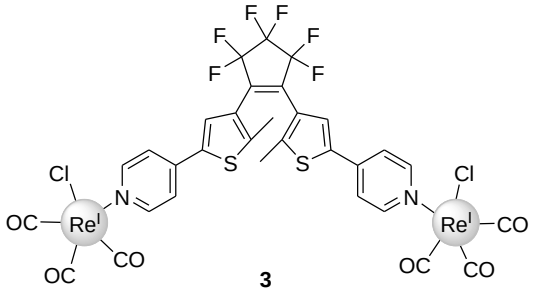

3

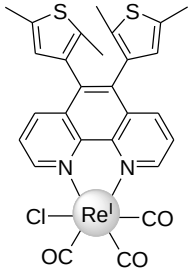

4

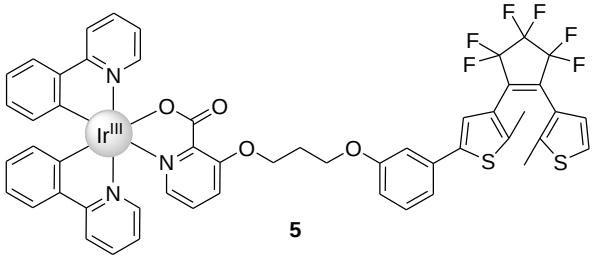

5

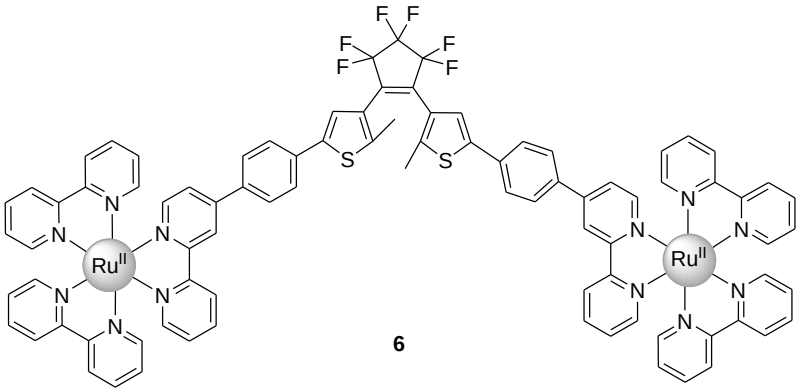

6

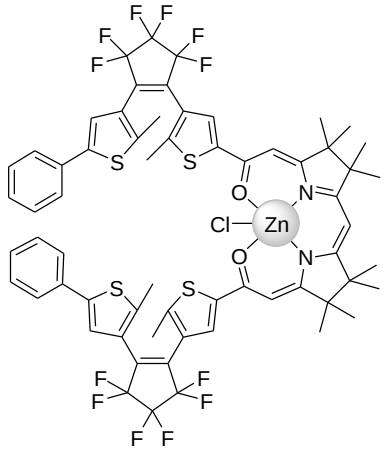

7

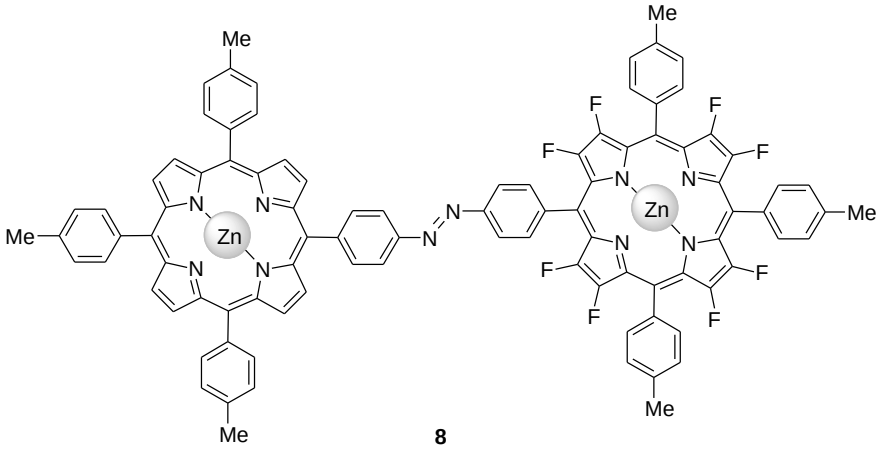

8

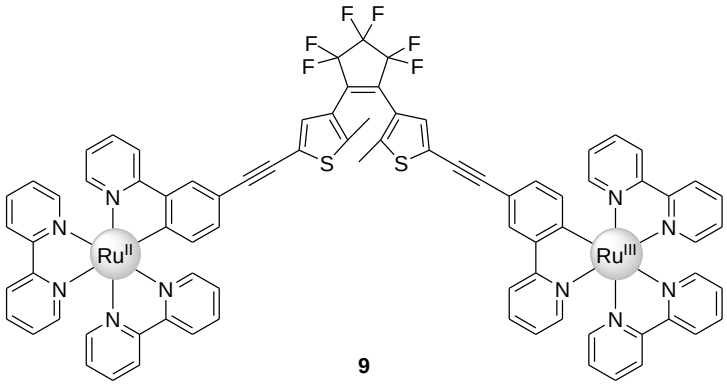

9

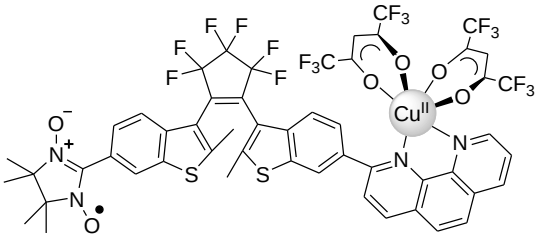

10

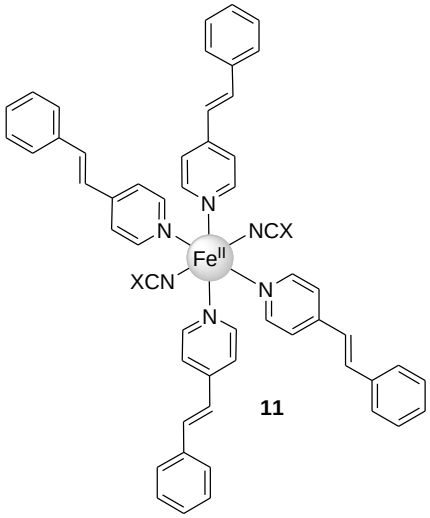

11

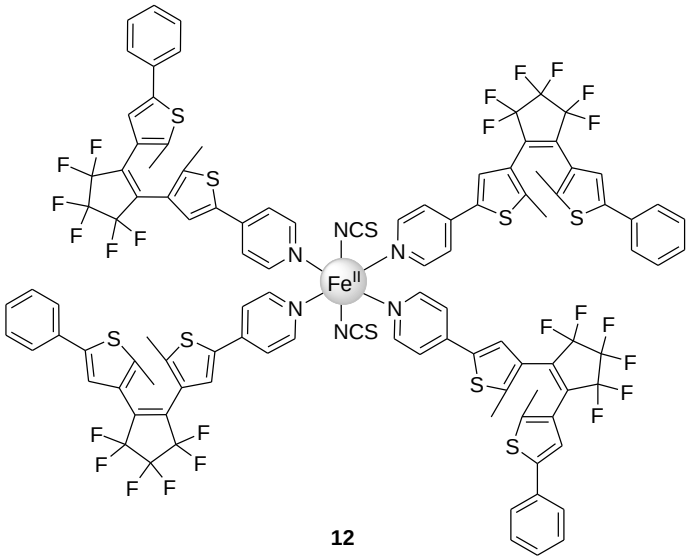

12

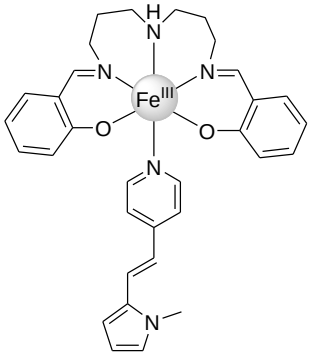

13

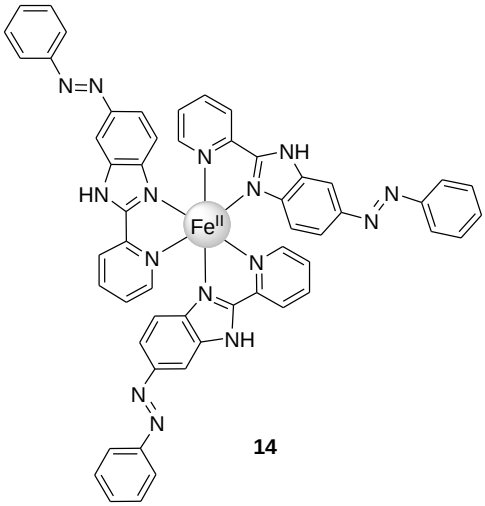

14

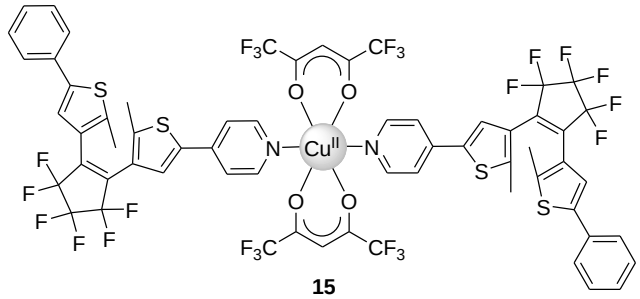

15

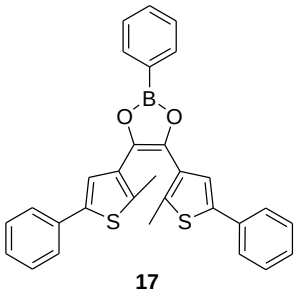

17

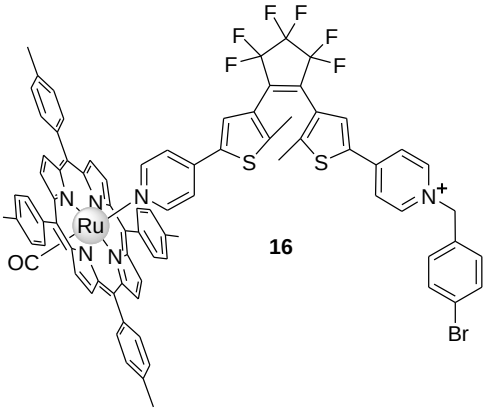

16

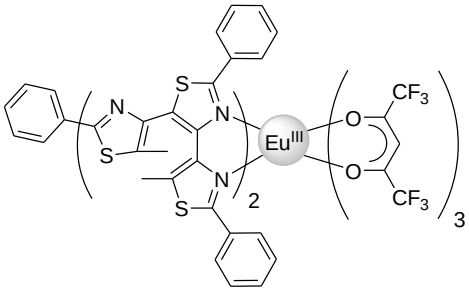

18

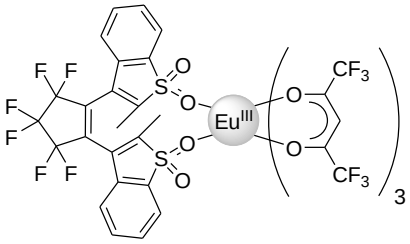

19

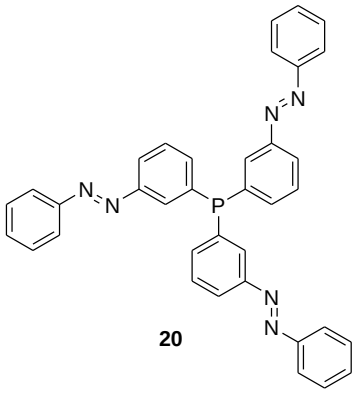

20

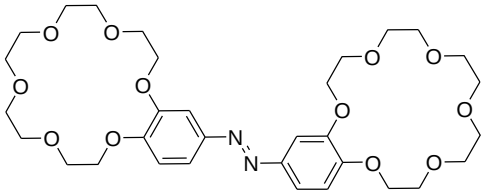

21

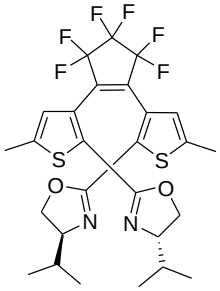

22

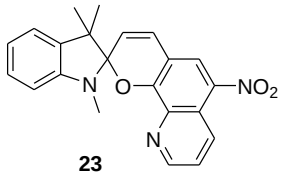

23

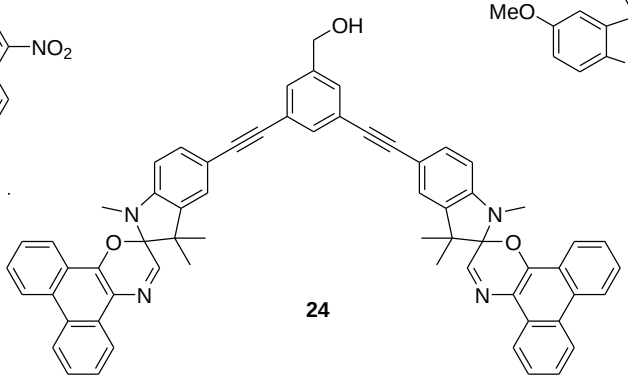

24

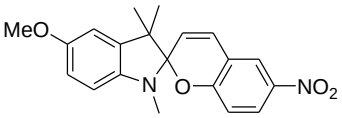

25

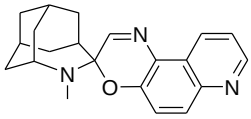

26

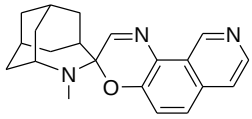

27

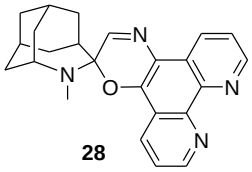

28

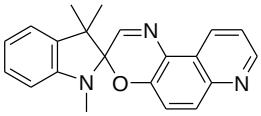

29

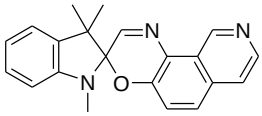

30

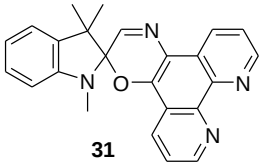

31

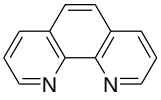

32

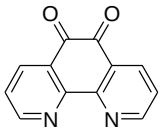

33

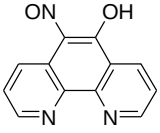

34

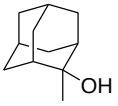

35

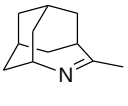

36

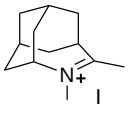

37

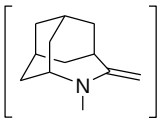

38

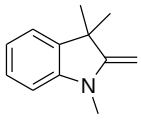

39

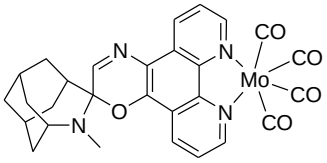

40

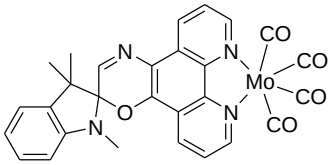

41

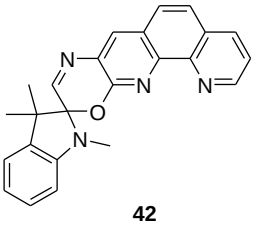

42

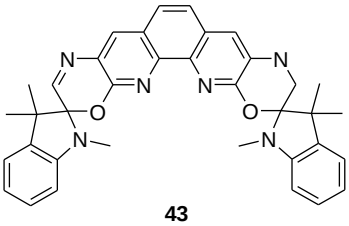

43

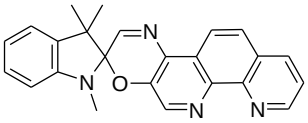

44

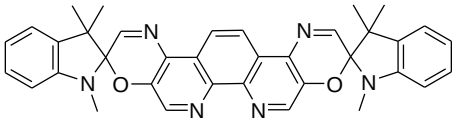

45

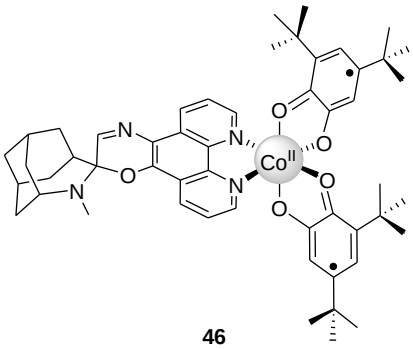

46

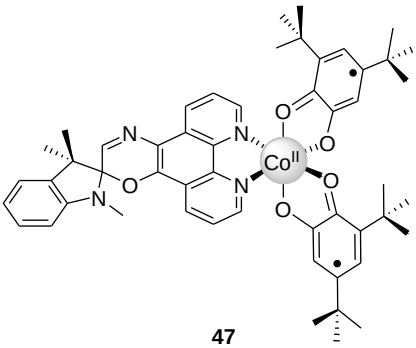

47

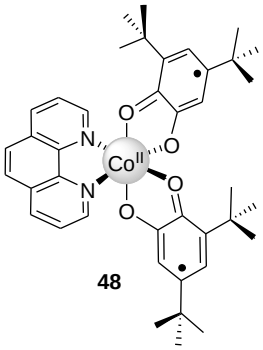

48

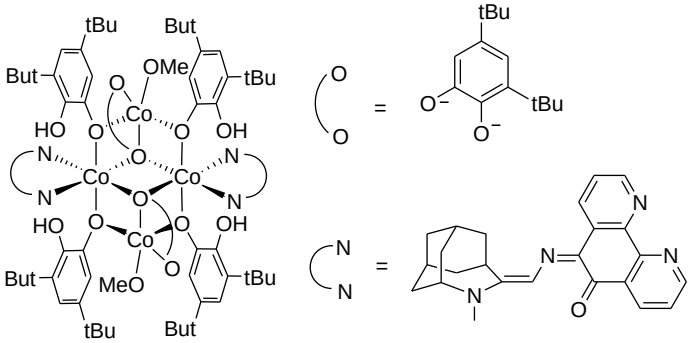

49

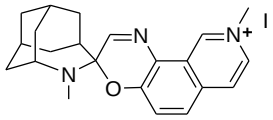

50

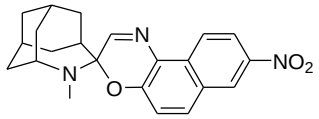

51

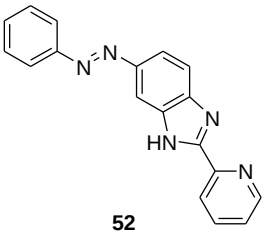

52

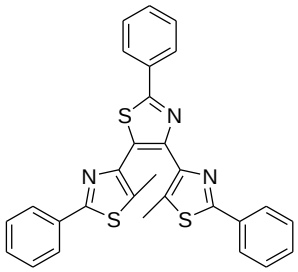

53

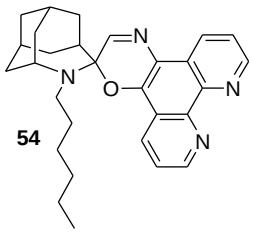

54

List of Abbreviations

^{1}H	proton
^{13}C	carbon-thirteen
1D	one-dimensional
2D	two-dimensional
6-31G(d,p)	split-valence basis set with polarization functions
6-31+G(d,p)	split-valence basis set with diffuse and polarization functions
6-311G(d,p)	triple split-valence basis set with polarization functions
6-311+G(d,p)	triple split-valence basis set with diffuse and polarization functions
a	crystallographic lattice constant
A	acceptor
A	absorbance
A_{inf}/A_{∞}	absorbance at photostationary state
A_o	initial absorbance
A_t	absorbance at time, *t*
a_o	calculated molecular volume
anal. calcd	analytically calculated
APSO	spiro[azahomoadamantane-phenanthrolinoxazine]
aq	aqueous
a. u.	arbitrary units
ax	axial
b	crystallographic lattice constant
B3LYP	Becke-style 3-parameter DFT with Lee-Yang-Parr correlation functional
BPh_4^-	tetraphenylborate
bpy	2,2′-bipyridine
BQ	benzoquinone
br	broad
bu	butyl
c	crystallographic lattice constant
Can. Micro.	Canadian Microanalytical Services

CAS	Columbia Analytical Services
CASSCF	complete active space multiconfiguration self-consistent field
CASSPT2	complete active space with second-order perturbation theory
Cat^{2-}	catecholate
CCC	*cis*-*cis*-*cis*
CCD	charge-coupled device
CCT	*cis*-*cis*-*trans*
CD	compact disk
cm	centimetre
cm^{-1}	wavenumber
COSY	correlation spectroscopy
CT	charge transfer
CTC	*cis*-*trans*-*cis*
CTT	*cis*-*trans*-*trans*
CV	cyclic voltammogram
Cy	cyclohexane
d	day, doublet
D	debye, donor
DA	Desert Analytics
deg	degree
DFT	density functional theory
diox	dioxolene
DMSO	dimethylsulfoxide
DNA	deoxyribonucleic acid
DTBBQ	di-*tert*-butyl-*ortho*-benzoquinone
DTBCat	di-*tert*-butyl-*ortho*-catecholate
DTBQ	di-*tert*-butyl-*ortho*-quinone
DTBSQ	di-*tert*-butyl-*ortho*-semiquinone
DTE	dithienylethene
DVD	digital versatile disk
e^-	electron

$E_{1/2}$	half-wave potential
E_a	activation energy
EA	elemental analysis
ED	electric dipole
EDG	electron-donating group
EI-MS	electron-impact mass spectrometry
emu	electromagnetic unit
E_{pa}	anodic peak potential
E_{pc}	cathodic peak potential
eq	equatorial
equiv.	equivalent(s)
EPR	electron paramagnetic resonance
e.s.d.	estimated standard deviation
ESI-MS	electrospray ionization mass spectrometry
$E_T/E_T(30)$	Dimroth–Reichardt solvent polarity scale
E_T^N	normalized Dimroth–Reichardt solvent polarity scale
Et_2O	diethyl ether
Et_3N	triethylamine
EtOAc	ethyl acetate
EtOH	ethanol
eV	electron–volt
EW	electron withdrawing
EWG	electron-withdrawing group
expt.	experimental
Fc	ferrocene
FT-IR	Fourier transform infrared
FW	formula weight
g	gaseous
g	gram, electron spin g-factor
GIAO	gauge invariant atomic orbital
h	hour

h	crystallographic index
H	HOMO
H_2salten	4-azaheptamethylene-1,7-bis(salicylideneiminate)
HD-DVD	high-definition digital versatile disk
hfac	hexafluoroacetylacetonate
HOMO	highest occupied molecular orbital
hs	high spin
hv	photon
Hz	hertz
i_a	anodic current
i_c	cathodic current
I_c	critical input parameter
IEFPCM	integral equation formalism polarized continuum model
IET	intramolecular electron transfer
IL	intraligand
^{1}IL	singlet intraligand
^{3}IL	triplet intraligand
IPSO	spiro[indoline-phenanthrolinoxazine]
IVCT	intervalence charge transfer
J	NMR coupling constant
k	crystallographic index, rate constant
K	Kelvin
k_1	rate constant for SO → PMC thermal isomerization
k_2	rate constant for PMC → SO thermal isomerization
k_{dis}	rate constant for PMC → SO thermal equilibration after dissolution
k_{obs}	observed rate constant for thermal relaxation
K_T	thermal equilibrium constant
K_{UV}	equilibrium constant at the UV-light-induced PSS
k_{UV}^{-1}	observed rate constant for thermal relaxation from UV-induced PSS
kV	kilovolt
K_{Vis}	equilibrium constant at the visible-light-induced PSS

k_{Vis}^{-1}	observed rate constant for thermal relaxation from Vis-light-induced PSS
l	crystallographic index
L	ligand, LUMO
LANL2DZ	double-zeta basis set with effective core potential
LD-LIRI	ligand-driven light-induced redox isomerism
LD-LISC	ligand-driven light-induced spin change
LF	ligand field
LIESST	light-induced excited-spin-state trapping
lit.	literature
LLCT	ligand-to-ligand charge transfer
Ln	lanthanide
ls	low spin
LUMO	lowest unoccupied molecular orbital
m	medium, multiplet
m	mass of paramagnetic solute in 1.00 mL solvent (Evan's method)
M	metal, molarity, molecular ion
mA	milliamp
MALDI	matrix-assisted laser desorption/ionization
max	maximum
MD	magnetic dipole
Me	methyl
MeCN	acetonitrile
MeO	methoxide
MeOH	methanol
Mepepy	1-(pyridin-4-yl)2-(N-methylpyrrol-2-yl)-ethene
mg	milligram
MHz	megahertz
min	minute
mL	milliliter
MLCT	metal-to-ligand charge transfer
^{1}MLCT	singlet metal-to-ligand charge transfer

^{3}MLCT	triplet metal-to-ligand charge transfer
mm	millimeter
mmol	mmol
MO	molecular orbital
mol	mole(s)
m.p.	melting point
mV	millivolt
mW	milliwatt
m/*z*	mass-to-charge ratio
NIR	near infrared
NLO	nonlinear optical
nm	nanometer
NMR	nuclear magnetic resonance
NN	diimine ligand
NN-NN	4,6-di-2′-pyridylpyrimidine ligand
No.	number
NOESY	nuclear overhauser effect spectroscopy
o	ortho
Oe	Oersted
Ox_1	first oxidation process
Ox_2	second oxidation process
P	Photochromic ligand
P	pressure
PES	potential energy surface
Ph	phenyl
phen	1,10-phenanthroline
phen-NN	1,10-phenanthroline-containing diimine ligand
pip	piperidine
PMC	photomerocyanine
PMMA	poly(methyl methacrylate)
ppb	parts per billion

ppm	parts per million
PSS	photostationary state
PXRD	powder X-ray diffraction
Q	reaction coordinate
R	enantiomer, R-factor
Red_1	first reduction process
Red_2	second reduction process
RNA	ribonucleic acid
r.t.	room temperature
s	second, singlet, strong
S	solvent
S	enantiomer
SCE	standard calomel electrode
SCO	spin-crossover
sh	shoulder
SO	spirooxazine
SOC	spin–orbit coupling
$SQ^{-\bullet}$	semiquinone
SQUID	superconducting quantum interference device
stpy	styrylpyridine
t	triplet
t	*tert*/tertiary, time
T	temperature, transmittance
TBA-TFB	tetrabutylammonium tetrafluoroborate
T_c	critical temperature
TCT	*trans-cis-trans*
TCC	*trans-cis-cis*
THF	tetrahydrofuran
TMS	tetramethylsilane
TTC	*trans-trans-cis*
TTT	*trans-trans-trans*

UBC	University of British Columbia
UV	ultraviolet
v	very
v	vibrational quantum number
V	volt
V	volume
Vis	visible
VT	variable temperature
w	weak
W	Watt
wR_2	weighted *R*-factor
x	cartesian axis
X	anion, atomic substituent
XRD	X-ray diffraction
y	cartesian axis
z	cartesian axis
Z	number of molecules per crystallographic unit cell
α	crystallographic lattice constant, torsional angle
β	crystallographic lattice constant, torsional angle
γ	crystallographic lattice constant, torsional angle
δ	chemical shift, partial charge
ε	dielectric constant, extinction coefficient
θ	theta (range for crystallographic data collection)
λ	wavelength
λ_{em}	emission wavelength
λ_{ex}	excitation wavelength
λ_{max}	maximum wavelength of absorption peak
μ	absorption coefficient
μM	micromolar
ν	operating frequency of NMR spectrometer
$\boldsymbol{\nu}$	wavenumber

ρ_{calc}	calculated density
ρ_0	density of pure solvent (Evan's method)
ρ	density of solvent-containing solute (Evan's method)
σ	estimated standard deviation
χ_{g0}	gram magnetic susceptibility of solvent (Evan's method)
χ_g	gram magnetic susceptibility of sample (Evan's method)
χT	magnetic moment
$\chi_M T$	molar magnetic moment
χ_M	molar susceptibility
χ_d	diamagnetic susceptibility
Δ	thermal energy, octahedral ligand-field splitting term
ΔE_p	peak-to-peak separation for forward and reverse peaks of redox process
ΔG^o	Gibbs free energy
ΔH^o	change in enthalpy
ΔK	photoresponsivity
ΔK_{UV}	photoresponsivity to UV light
ΔK_{Vis}	photoresponsivity to visible light
ΔS^o	change in entropy
$\Delta \nu$	resonance shift between solute-containing solvent and reference solvent
°	degree
°C	degree Celsius
Å	angstrom

Acknowledgments

The thesis template I am using informs me that I should keep the acknowledgments to less than a page, but I have so many people to thank that I suspect this will prove impossible. First I must thank my supervisor, Natia, for all of her support and patience. I don't believe I have ever met a more scientifically knowledgeable person, and I thank her for passing along a small fragment of this knowledge, and inspiring me to push myself to learn as much as humanly possible. Huge thank you's go out to all of my Frank group coworkers, past and present, but extra special thanks go to those who have been there from the beginning: thanks to Brynn, my partner in crime, for infusing the group with her charisma and for keeping me sane; thanks to Mark for staying laid back, for the chemistry help, for all of the great music, and for generally being there through better and worse—I forgive you for never doing your dishes; thanks to Nick for gracing me with his wit and always laughing at my jokes; and finally, thanks to Olga for all of the late-night lab companionship and meaning-of-life discussions—your passion is an inspiration.

The UVic Chemistry Department has been an amazing place to spend four and a half years and many, many people have contributed to the enjoyable atmosphere. I need to thank my committee members, Dave and Cornelia, for all of their advice and patience throughout the trials and tribulations of grad school. What doesn't kill you only makes you stronger. Thank you for allowing me to fail and discover my boundaries. Thank you to all of the professors for being such friendly and approachable people. I am absolutely indebted to the department staff members, who have been instrumental to my research success. From top to bottom floor: thank you to Rosemary and Carol for staying on top of things and for all of the free meals; thank you to Cathy for making me laugh during my visits to the office; thanks to Dave and Kelli for being amazing teaching role models—I truly admire your dedication; thank you to Bob for the printer help and to Mike for the computer hookups; thanks to Terry, Mario, and Shubha for all of the instrument help and expertise; thank you to the Science Stores crew—Glenda, Derek, Rob, James, Mike, Karen, and others—I never had a request that was not fulfilled with a smile, even the emergency 4:15 PM cylinder swaps; gigantic thanks to Chris who has bent over

backwards to help me with NMR experiments; and finally, thank you to J.-P., Doug, and Sean in the basement who have all crafted some beautiful equipment.

It is my pleasure to acknowledge my external scientific collaborators. I have thoroughly enjoyed working with Brian Patrick (UBC), Michael Ferguson (U of A), and Werner Kaminsky (UW) on X-ray structure determinations. I am also grateful to Yun Ling (UBC) for all of the prompt analytical work.

I need to thank all of my fellow students. I count myself extremely lucky to have been part of such a collegial department. I apologize in advance for not being able to thank everyone individually, but a few shout outs go to Joe for being a great role model and all of the science advice, to Steve M.—my cubicle buddy—for the chemistry discussions, to Tyler for being a good friend and ranting partner, to Kander for the antics, to Steve H. for the poker nights, and to Dean for never failing to make me smile with a new cheesy pickup line. Also, I must absolutely thank the B team: Keith, Simon B., Marie, Aaron, Keri, Simon O., Rob, Emmanuel, and Krista—we shared many great memories.

My last round of thanks goes to all those who have been a source of support and inspiration, without whom I might be a very different person today. Thanks to Anthony for all of the science discussions and for teaching me to internalize science, but especially for encouraging me to follow my most ambitious dreams when no one else would; saying thank you is really not enough to articulate my appreciation, so I will do my best to follow your lead and lead by example. I feel obliged to express my gratitude to the scientific role models who have truly inspired me. Thank you to Richard Hamming for inspiring me to be a great scientist, work on grand challenges, and change the world. Thank you to Roald Hoffmann for sharing his joy of chemistry and teaching me that not only is it possible for scientific prose to be beautiful, but that it should be encouraged. Thanks to Richard Feynman for making science as engrossing as a good novel and for rekindling some of my scientific excitement that got lost along the way. Thanks to Eliezer Yudkowsky for teaching me to realize when I am confused and to not settle on incomplete answers. Finally, thank you to my parents for teaching me to work hard and play hard, for helping mold me into the person I am, and for supporting me every step of the way. And last, thank you to my siblings—three of my favourite people in the world—for loving their eldest sister no matter how much of a weirdo or workaholic she may be.

Chapter 1. Photochromic Photoswitchable Multifunctional Molecular Materials: Motivation and Background

Photoswitchable molecular materials are of interest for technologies ranging from optically controlled electronics and data storage to functional coatings and intricate molecular machinery. A photoswitchable material interconverts between two or more forms with optical stimuli.[1] This conversion is accompanied by physicochemical changes, and the state of such a photolabile material may be probed through the readout of a signal associated with one or more of the optically perturbed properties—for example, the material's fluorescence, optical rotation, magnetic state, or electrical conductivity. Figure 1.1 illustrates a schematic wherein a system in an initial form 'A' converts to a second form 'B' when exposed to optical input A (process 1). This optically actuated change is reversible upon application of optical input B (process 2). For more complex applications, molecular systems could be designed in which three or more forms are accessible via multiple optical inputs, possibly in combination with other external stimuli.

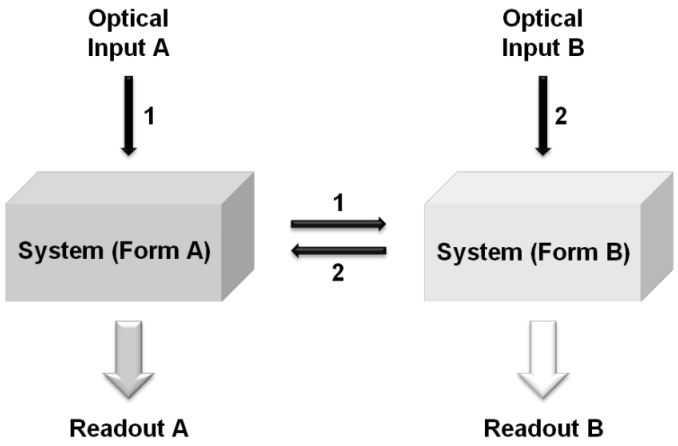

Figure 1.1. Schematic illustration of a bistable photoswitchable material.

This thesis describes the design of novel multifunctional molecular materials that incorporate photochromic spirooxazine ligands as optically switchable building blocks.

Before spirooxazine ligands are discussed in detail, however, the following will explore the motivation for designing such materials and some of the approaches that have so far been investigated toward this goal.

1.1. Applied Motivation

For the last half century, most devices have been constructed as heterostructures from bulk inorganic solids. Inorganic material components are only available in a limited number of 'flavours,' and obtaining new variants often requires a synthetic exploration of parameter space—semi-methodical at best—where outcomes are notoriously difficult to predict a priori and not uncommonly lacking in reproducibility. The properties of the heterostructure components, their surfaces and interfaces, and the resulting devices, are typically controlled by 'top-down' processing methods such as heat/chemical treatments, thin-film deposition methods, and lithographic techniques. This approach has worked well historically, and continues to work well in the fabrication of contemporary devices, but may fall short in meeting the requirements of next-generation devices where sophisticated functionality and very precise control over local and long-range properties is necessary.

There is an enormous thrust in the chemical community toward harnessing the powers of synthetic chemistry—increasingly refined over the last several decades—in the exacting 'bond-by-bond' design of functional materials. Although synthetic costs can be high and our understanding of large-scale processing and device-level properties (e.g., surface interface behaviour, solid-state interactions) of many molecular materials is still at an immature stage, the options afforded by the synthetic flexibility achievable at the molecular level are virtually limitless. At this level, one may incorporate multiple functions into one molecular unit, which may then be tuned very precisely with small changes to chemical structure. In contrast, bulk inorganic solids and nanostructures would likely require many layers to derive the same functionality, if this is achievable at all. Heterostructure devices incorporating molecule-based materials may benefit from advantages associated with requiring fewer layers (e.g., less processing, less surface compatibility issues) or may benefit from avoiding undesirable effects arising due to surface segregation and reconstruction effects.[2] In typical inorganic materials, surface

segregration and reconstruction often occur in order to decrease differences in free energy between the bulk and the surface, whereas in molecular materials, these differences in free energy are expected to be much smaller. Processing methods applicable to molecular materials may prove flexible, robust, and/or cost effective in comparison with those traditionally used with bulk inorganic materials. Molecule-based materials may also offer a unique size advantage, particularly if we achieve the elusive goal of control over matter at the single-molecule or molecular cluster level. In essence, the ability to construct molecules from the 'bottom up'[3] allows for unique control over single-molecule and long-range material properties, and these molecules may then be incorporated—from the top or bottom—into materials and devices to achieve new and precise functionality.

Light may play an increasingly important role as a means of energy manipulation in device technologies. Scientists continue to refine our ability to manipulate light with advances in nanophotonics,[4, 5] such as photonic crystals[6] and plasmonics.[7-9] Interest persists in moving toward the use of photonics (i.e., the manipulation of light) as a complement to electronics (i.e., the manipulation of charge), ubiquitous in logical circuitry.[10-12] Light possesses multiple unique properties that may be exploited either independently or in combination including energy, phase, amplitude, and polarization. Additionally, light-based interactions may offer unique parallel processing opportunities as multiple beams can be transmitted coherently without interference.[11]

With these points in mind, the following sections will explore a few of the next-generation technologies for which novel photoswitchable materials may be of interest.

1.1.1. Optically Controlled Electronics and Photonics

Despite adhering to Moore's Law[13, 14] for decades, the progress of silicon-based integrated circuit technology is facing a growing number of fundamental physical limitations.[15] The demand for smaller, more powerful computers, however, has not abated. Scientists have proposed for some time that molecular materials may play a key role in next-generation computing technologies.[16-19] This may happen in two ways: (1) molecular materials with precise and unique functions will be integrated into current silicon-based and other well-developed devices; or (2) novel computing circuitry will be developed using molecule-based components and processes.

As switches currently lie at the heart of computing, enabling the processing of digital logic operations, it is not unreasonable to expect that molecular materials capable of switching functions may prove especially useful in future technologies.[20-23] According to Carroll and Gorman,[15] "*The development of a molecular switch is perhaps the single most important element in developing molecular replacements for conventional integrated circuits*." The near-term will likely see integration of photoswitchable materials into traditional device components in the form of, for example, optically switchable organic light-emitting diodes[24] organic thin-film transistors,[25] and electrode surfaces.[26] The development of molecular electronic/photonic circuitry on the scale of single molecules or small groups of molecules is, however, a more ambitious and simultaneously more elusive long-term prospect. Along these lines, photoswitchable molecules may find their way into key components such as switchable molecular junctions[17, 27] and complex logic circuits.[28-30]

While scientists have made significant progress in designing new functional photoswitchable molecules and understanding their properties, many roadblocks remain before their potential may be harnessed in molecular electronic/photonic applications.[31-33] Challenges arise in optimally exploiting light-based processing at a molecular level given our current inability to manipulate light on an adequately small scale, although parallel progress in photonic technologies illuminates future prospects.[4-9] Challenges associated with fabricating circuits based on individual or small groups of molecules are substantial. Arranging molecules in an orderly fashion and ensuring the subsequent stability of these arrangements presents an initial obstacle. Additional hurdles include successfully contacting individual molecules,[34] unambiguously detecting signals from these molecules, dealing with stochastic effects, and managing heat dissipation.[33] None of these challenges are insurmountable,[33] although rising above them might require a divergence from traditional computing paradigms—altogether possible, if not necessarily plausible, when dealing with matter at the molecular level.

1.1.2. Optical Data Storage

Photoswitchable molecular materials are often heralded as candidates for optical data storage. As they can be switched between two or more states with different readout

properties (Figure 1.1), they can be used to store bits of information—their application to data storage appears an obvious goal. The near future of optical storage technologies, however, may rely more on improvements to device infrastructure than to available materials. Optical data storage has been popular since the commercialization of the compact disk (CD) in the mid-1990's, and subsequent commercialization of the digital versatile disk (DVD), high-definition digital versatile disk (HD-DVD), and blu-ray disk in the 2000's.[35] The primary limitation to improving these technologies currently lies in the available optical beam spot size, fundamentally limited by diffraction. Some scaling may be possible with improvements in near-field recording, yet this poses significant engineering challenges and device limitations.[36] Proposed future directions to circumvent these issues are the development of three-dimensional optical data storage based on two-photon processes[37-39] or holographic storage,[40, 41] with the latter typically considered unsuitable for large-scale distribution due to cost and complexity.[36] Another viable alternative is the development of higher-density two-dimensional (possibly layered) storage based on light multiplexing, where it would be possible to store more than one bit of data per memory element by taking advantage of the different properties of light (wavelength, phase, amplitude, polarization).[36] Novel molecule-based photoswitchable materials, which can be designed to exhibit a complex variety of responses and which may be amenable to incorporation into hybrid layered systems, may find applications in this area.[42-47]

In terms of device engineering, it is likely that disc-based storage designs—the current format of optical storage systems—will become outmoded as a result of excessive power consumption, slow data transfer, and lack of robustness, and that solid-state memory designs will become dominant for many near-term data storage and memory needs.[48] Again, owing to current limitations in optical technologies, electronic and magnetic memory will likely play a more prominent role in such devices, although optical memory may find a role in niche applications (e.g., on the basis of power consumption, material flexibility, parallel processing functionality, or cost). However, when/if available optical technologies become competitive in the context of optical storage applications, it will be critical to have on hand a catalogue of photoswitchable materials with excellent figures of merit in terms of stability, response time, signal strength, and device integrability.

1.1.3. Molecular Machines and Functional Molecular Systems

Within the ongoing theme of harnessing the functionality of molecules toward next-generation applications, one might consider the possibility of creating functional molecular machines. Most famously credited to Feynman[49] for suggesting the idea, but perhaps more accurately attributed to Drexler[50-52] for coining the term 'molecular nanotechnology' and expounding on the theoretical details and societal impacts, the notion of controlling matter at the molecular level to accomplish useful tasks—including the manipulation of more matter at the molecular level—could have dramatic implications.[52-54] While Feynman and Drexler proposed what has been termed a 'hard' chemical approach to the development of molecular machines (i.e., 'mechanosynthesis' or mechanically guided chemical synthesis based on mechanical engineering principles extended to the nanoscale), others such as Feringa,[55, 56] Balzani et al.,[57] Jones,[54] and Kay et al.[58] have championed the development of molecular machines from a 'soft' chemical approach (i.e., one that applies principles from molecular biochemistry and synthetic chemistry in a predominantly solution-phase environment in which Brownian motion is a central force). Although the development of functional molecular machines might seem an unattainable goal, the proof of principle lies in nature, wherein an abundance of complex biochemical pathways take place on the molecular scale, such as photosynthesis and RNA transcription. In nature, complex molecular systems have evolved through innumerable accidental optimizations and, while humans have not yet succeeded at artificially reproducing a similar level of complexity, they have been working at the optimization task for a mere fraction of the time—presumably the element of intelligent design will vastly accelerate the process.

In order to make molecular systems do mechanical work, energy must be transduced. This energy may take the form of chemical energy, electrical energy, or light.[59, 60] As light is a particularly convenient source of energy and means of external control, molecular photoswitchable components are poised to play an important role in larger, more complex systems in which they can function as power sources or on/off switches.[58] In this vein, numerous molecular systems have been reported, including light-activated 'molecular scissors,'[61] 'molecular hinges,'[62] 'molecular rotors,'[55] 'molecular shuttles,'[63] or 'DNA nanomachines' for RNA digestion.[64] There has also been much interest in the

use of light to toggle molecular-level activities such as catalysis,[65-67] drug delivery,[68] molecular imaging and cell biology,[69] artificial photosynthesis,[70] and sensing.[71] At this stage, the field of molecular nanotechnology is still in its infancy; most of the work accomplished so far represents merely primitive models and initial steps toward the end goal. Nevertheless, despite the challenges inherent in achieving precise control over function at the molecular scale, the rapid and ongoing progress in synthetic chemistry, computational modeling, and our understanding of complex chemical and biochemical pathways promises important developments in the field in the years ahead.

1.1.4. Functional Coatings

In addition to their use in thin films for information processing or storage devices as described in Sections 1.1.1 and 1.1.2, photoswitchable molecular materials may also be suitable for incorporation into many different functional coatings or 'smart surfaces.'[31] These might include filters,[72] protective coatings,[73] decorative coatings,[74] or 'paper' for light-based ink/erasers.[75] If the concept of functional surfaces is extended to functional membranes, photoswitchable molecules may be used to fabricate membranes encapsulating such functional elements as light-controlled ion channels[76] or nanovalves.[77] Photoswitchable materials may be useful in a surface engineering role to optically control surface patterns,[78, 79] metal deposition,[80] magnetic nanopatterns,[81] surface wettability,[82] and so on. Smart photoresponsive surfaces could also be valuable in lab-on-a-chip[83] applications. For example, a photoresponsive surface was fabricated upon which a microlitre droplet of liquid could be powered up a twelve-degree incline using light alone;[84] such a mechanism could be useful for transporting analytes or reagents across microscale surfaces. As one might surmise, the immobilization of photoswitchable molecules onto surfaces presents several challenges, including the quenching of electronically excited states and hindered photoisomerization in constrained environments;[85, 86] however, for cases in which the kinks in surface fabrication are ironed out, photoswitchable coatings show great promise for diverse and versatile applications.

1.2. Strategies for Integrating Photochromic Molecules into Multifunctional Materials: Photochromic Coordination Complexes

One of the most promising methods for designing optically switchable materials is through the use of organic photochromic molecules as building blocks.[87-93] Photochromic molecules can interconvert between two states having different optical absorption spectra, with this interconversion being effected in one or both directions by light.[94-96] The change in optical absorption is accompanied by changes in numerous interdependent physicochemical properties such as molecular volume or conformation,[75] degree of conjugation,[97] electrical conductivity,[98, 99] electric dipole,[100] refractive index,[100, 101] or optical rotation.[87, 102] The most common classes of photochromic compounds demonstrate either photoinduced *cis–trans* isomerization, as in the case of stilbenes and azobenzenes[103-105] [Scheme 1.1, (1)], or photocyclization chemistry, as in the case of dithienylethenes (DTEs)[92, 106] (commonly functionalized with perfluorocyclopentene)[107-109] [Scheme 1.1, (2)], or spiropyrans and spirooxazines[93, 110] [Scheme 1.1, (3)].

Scheme 1.1. Common classes of photochromic molecules: (1) stilbenes (X = CH) and azobenzenes (X = N), (2) dithienylethenes (X = S), and (3) spiropyrans (X = CH) and spirooxazines (X = N).

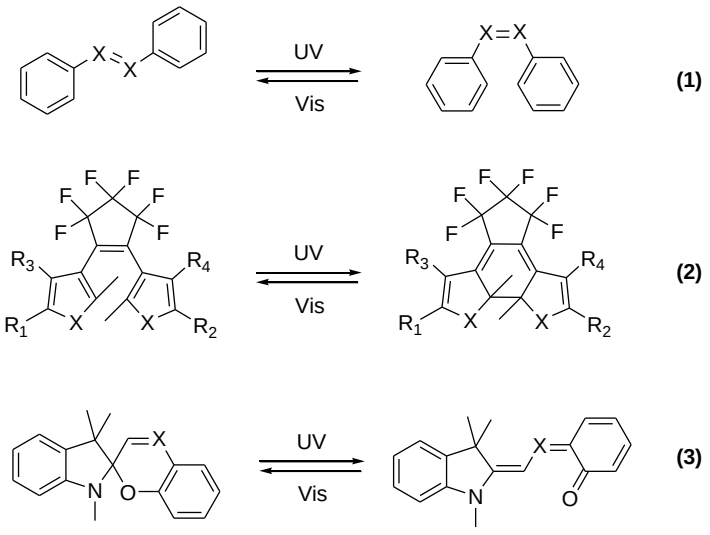

Photochromic molecules are useful as materials in their own right, and they may prove even more useful when integrated into more complex hybrid systems. Such hybrid

materials may take on the properties of their components in either additive or, preferably, synergistic fashions. While it may be desirable to have a material in which photochromism coexists with the properties of the nonphotochromic component(s), it is more desirable to have a material in which photoisomerization of the photochromic component interacts synergistically with the properties of the nonphotochromic component(s). This sets up a design strategy whereby photochromic molecules can be used to modulate additional properties or functions. The last couple of decades have seen an explosion in reports of molecular materials incorporating photochromic compounds. In general, three types of photochromic materials may be delineated: (1) noncovalent hybrid materials, (2) covalent hybrid materials, and (3) metal–ligand coordination complexes. In each case, photoisomerization can have many possible effects on material properties—sometimes unexpected—as a result of steric and/or electronic interactions between components.

In the first category, photochromic molecules are integrated into hybrid materials in a noncovalently bound fashion.[111] Photochromic molecules have been frequently incorporated into bulk polymer matrices[112, 113] or liquid-crystalline materials.[87, 114] For example, Ichimura[114] has done much work on the surface-assisted photoalignment of liquid crystals. Figure 1.2(a) shows a schematic of an azobenzene-functionalized surface on which liquid crystal molecules may be photoaligned from a homeotropic orientation (left) to a homogeneous planar orientation (right) upon *trans* → *cis* photoisomerization of the azobenzene layer with linearly polarized UV light. Here the interaction between photochromic and nonphotochromic components is predominantly based on the photoinduced reorientation of molecular geometry. The azobenzene-functionalized surfaces have been termed ‘command surfaces’ as each photochromic molecule is able to control the orientation of thousands of liquid crystal molecules, which highlights the potentially powerful influence of photoswitchable components in appropriate environments. Photochromic molecules have also been incorporated into hybrid organic–inorganic nanocomposites via methods such as the sol-gel process,[115] hydro- or solvothermal methods, intercalation chemistry,[116-118] or the reverse micelle techniques.[119] Figure 1.2(b) shows a representation of an organic–inorganic cobalt layered double hydroxide with intercalated DTE anions.[118, 120] Here, the Curie temperature of the

material is increased from 9 to 20 K upon photoisomerization of the DTE units from the open to the closed form. As the overall geometry of the material does not change significantly upon photochemical conversion, the effect is proposed to be predominantly electronic, where the delocalized π-system of the closed form mediates the magnetic exchange between cobalt layers to increases the Curie temperature of the material.

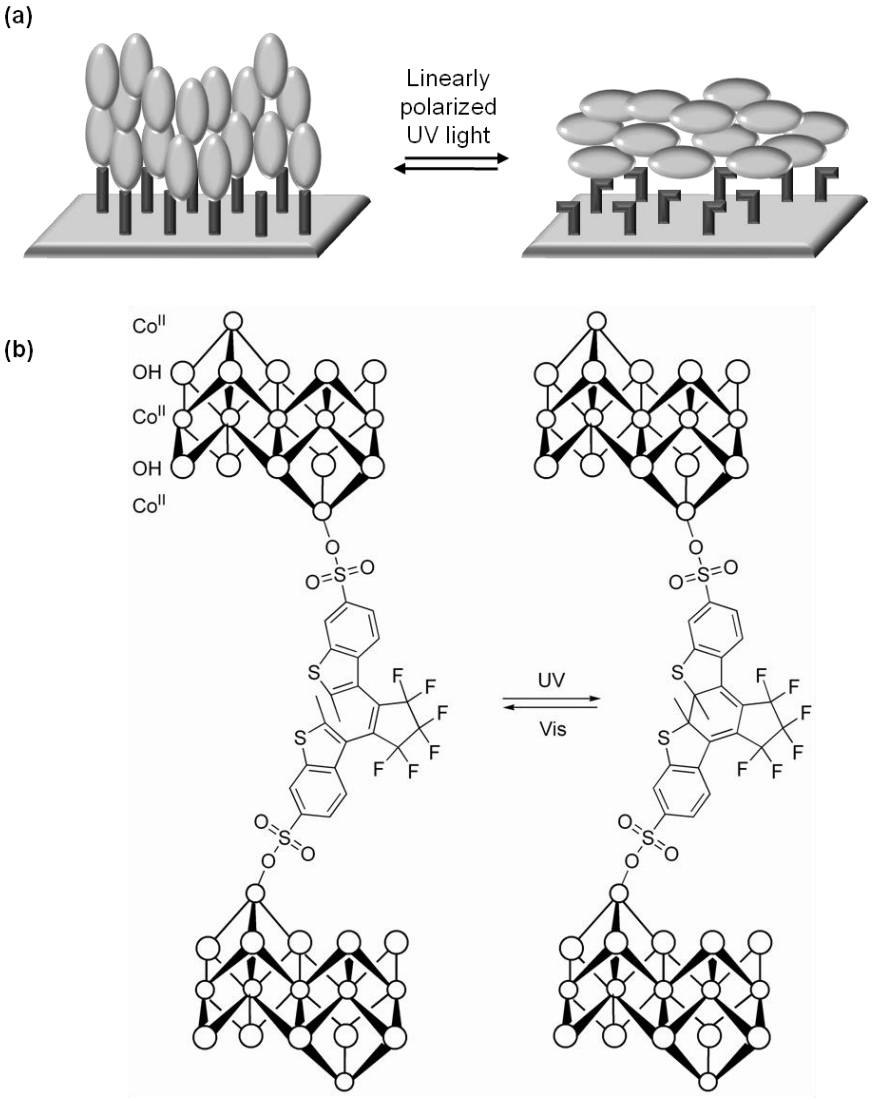

Figure 1.2. (a) Schematic representation of an azobenzene-functionalized 'command surface' on which liquid crystal molecules may be photoaligned from a homeotropic orientation (left) to a homogeneous planar orientation (right) upon *trans* → *cis* isomerization with linearly polarized UV light. (b) Schematic representation of cobalt layered double hydroxide intercalated with DTE ions, in which photoisomerization of the DTEs alters the magnetic exchange interactions between inorganic layers. (Adapted with permission from ref[118]. Copyright 2007 Elsevier.)

In the second category, many examples of covalently bound photochromic molecular materials have been reported.[88, 90] This design may allow for more direct control over the interaction between photochromic and nonphotochromic components. Photochromic functionalities have been bound to DNA or other biological molecules,[121, 122] tethered to nanoparticles,[123-127] attached to polymer backbones,[128] or bound to a host of other functionalities such as organogelators,[129] fluorescent naphthalimides,[130] or fluorescent porphyrins.[131]

In the third category, a slight variation on the fabrication of covalent hybrid photochromic materials is the fabrication of photochromic ligand–metal coordination complexes—an approach that has become widespread only recently.[132-135] The intimate relationship between metal and ligand in these complexes provides a unique opportunity for tuning material properties. In the study of coordination complexes containing photochromic ligands, two fundamental questions arise. The first inquires as to how metal coordination affects the properties of the photochromic ligand. Metal coordination may have drastic effects: the metal functionality may sensitize a photochemical process, completely deactivate a photochemical pathway, or dramatically alter the thermodynamics and kinetics of the system, altering such properties as quantum yield, thermal stability, and fatigue resistance. Such effects of metal coordination may be exploited to tune photochromic properties, perhaps more powerfully than by standard functional group derivatization.[132, 135] The second question seeks to understand how photoisomerization of the photochromic ligand affects the properties of the coordinated metal and how one might harness such effects to gain optical control over the overall properties of the material.

Although a thorough investigation of the first question is critical to advancing the design of photochromic materials, this thesis focuses predominantly on the second question. The following section explores a series of mechanisms by which the properties of a metal centre may be influenced by the photoisomerization of a coordinated photochromic ligand. These mechanisms are not mutually exclusive, and two or more may act simultaneously in a given material. However, specific examples will be highlighted for each mechanism to illustrate the various strategies that may be employed in the design of novel photoswitchable materials.

1.2.1. Modulation of Excited-State Photochemical and Photophysical Processes

As soon as an organic photochromic unit is connected to a transition-metal unit, new excited-state photochemical and photophysical pathways become accessible. The activation of new pathways can have implications on the native properties and functions of the photochromic component and/or the transition-metal component. Although such phenomena should be considered in the design and study of *any* metal complex containing a photochromic ligand, this section will be concerned with the deliberate use of this mechanism as a means to control the properties of the coordinated transition-metal centre with light.

The modulation of excited-state photochemical and photophysical processes in metal complexes containing photochromic ligands has predominantly been investigated toward the development of photoswitchable memory elements. Photochromic molecules are obvious candidates for binary or higher order information storage as they can be optically switched between two or more states—denoted here as states A and B for a two-state system. While the writing of information in a photochromic system is straightforward as photochromic molecules can be switched reversibly between two states with two distinct wavelengths of light, said system is only useful in a memory context if its state may also be detected, a feat which could require some ingenuity. Many physical and chemical properties are subject to detection, but a detection method based on optical transduction is appealing. To detect the optical properties of a system, one must optically probe the system without disturbing its state. Herein lies the challenge in achieving nondestructive optical readout. In a simple photochromic system, if one seeks to read out the state of the system through the detection of its optical absorbance, one would need to probe the system with light at the wavelength of interest, effectively perturbing the system by inducing photochemical conversion to the second state. To achieve nondestructive optical readout, three different light sources must be able to act on the system independently: one to switch the system from state A to state B, one to switch the system from state B to state A, and one to probe the state of the system. Enter photochromic coordination complexes. In these hybrid systems, the state of the photochromic ligand can influence the properties of a coordinated metal, which can be probed independently of the photochromic component. When considering the use of photochromic ligands to

modulate photoexcited-state processes in coordination complexes, the obvious application of such a mechanism is to design a system in which only one form of the photochromic ligand selectively quenches a metal-based emission process, such that the state of the system can be detected via a change in luminescence readout.

Complexes composed of a photochromic unit (P) tethered to a metal-based luminescent chromophore (M) are—in principle—capable of achieving nondestructive luminescence readout.[136] Many chromophores, such as the well-known Ru–polypyridyls or Re–tricarbonyls, exhibit excitation to a singlet metal-to-ligand charge transfer (^{1}MLCT) state, followed by nonradiative relaxation to a triplet metal-to-ligand charge transfer (^{3}MLCT) state, and subsequent radiative decay (i.e., luminescence) to the ground state.[137] The goal is to design a system in which photoisomerization of the photochromic unit in both the A → B and B → A directions, in addition to excitation of the metal unit to the ^{1}MLCT state, may be selectively addressed, and in which the ^{3}MLCT state is quenched by one form of the photochromic ligand but not the other. At first glance, achieving this goal seems reasonably straightforward; however, the catch lies in the requirement that, for each of these processes, subsequent undesirable photochemistry must not ensue.

To illustrate the principle, a simplified schematic for a model photochromic ligand–metal (P–M) system is shown in Scheme 1.2. On the left is the P–M system in photochromic state A, and on the right is the P–M system in photochromic state B. Photoisomerization is achieved by excitation of form A or form B of the photochromic component to a singlet intraligand (^{1}IL) state (processes 1A and 1B), followed by photochemical conversion to the second form of the photochromic component from the singlet and/or triplet manifold (not shown). In the model system, a judicious choice of components with complimentary excited-state energy levels allows for excitation of the photochromic ligand in form A to the ^{1}IL state (process 1A) with low-energy (typically visible) light, of the metal to the ^{1}MLCT state in either form A or B (process 2A/2B) with moderate-energy light, and of the photochromic ligand in form B to the ^{1}IL state (process 1B) with high-energy (typically UV) light. After photoexcitation of the metal component to the ^{1}MLCT state and relaxation to the ^{3}MLCT state (process 3A/3B), the latter can be quenched by a slightly less energetic ^{3}IL state (process 5) when the photochromic ligand

is in form A, but not when it is in form B. This quenching process thus competes with—and ideally inhibits—emission from the ^{3}MLCT state (process 4A/4B).

Scheme 1.2. Simplified schematic of photochemical and photophysical pathways in a molecular system composed of a photochromic unit (P) attached to a metal-based chromophore (M) that can interconvert between forms A and B. Selected radiative processes are shown as solid blue lines, desirable nonradiative processes as dashed green lines, and nondesirable nonradiative processes as dotted red lines. The ground state of form B is arbitrarily chosen to be of higher energy than that of form A.

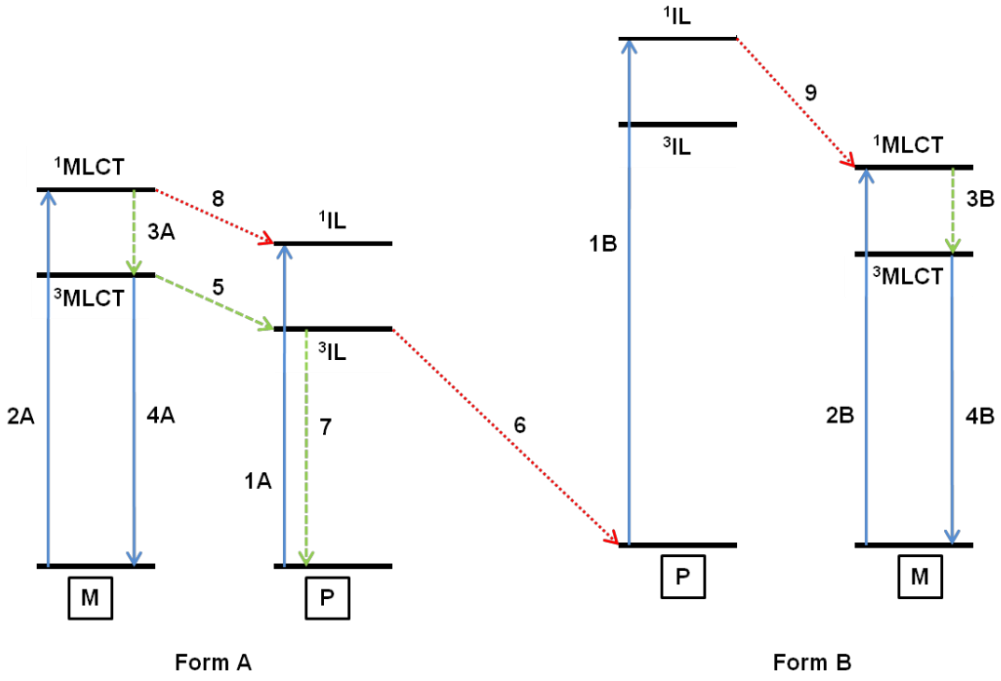

Scheme 1.2 also exemplifies potential pitfalls in the design of photochromic ligand–metal complexes for optical memory with nondestructive optical readout capabilities. In the model system, several undesirable photophysical/photochemical pathways can be pinpointed. For example: (1) In form A, after quenching of the ^{3}MLCT state by the ^{3}IL state (process 5), photochemical conversion to form B may occur (process 6) rather than nonradiative decay to the ground state of form A (process 7). This would imply that probing the state of the system would initiate photoisomerization and eliminate the potential for nondestructive readout. (2) In form A, the ^{1}MLCT state could be quenched

by the ^{1}IL state (process 8) instead of undergoing intersystem crossing to the ^{3}MLCT state (process 3A). This again would imply that probing the state of the system would initiate photoisomerization. (3) In form B, after excitation of the photochromic ligand to the ^{1}IL state, energy transfer to the ^{1}MLCT state of the metal component could occur (process 9), rather than photochemical conversion to form A. This would imply that the B $\rightarrow$ A photoisomerization pathway is deactivated and that excitation of the photochromic ligand in form B would instead lead to metal-based luminescence.

In summary, to design a photochromic ligand–metal complex capable of nondestructive readout, a stringent set of requirements must be met in terms of relative energy levels and kinetics of competitive photochemical and photophysical processes. One possible design is schematized in Scheme 1.2, wherein the ^{1}IL state of one form of the photochromic component lies below the ^{1}MLCT state of the metal component, while the ^{1}IL state of the second form of the photochromic component lies above it. The corresponding IL and MLCT triplet states show the same relative ordering. Presuming a triplet quenching mechanism, if the ^{3}IL states for both forms A and B were above the ^{3}MLCT state, no quenching of luminescence would be possible. If the ^{3}IL states for both forms were below it, selective quenching would be difficult. The scenario provided by Scheme 1.2 illustrates, however, that even if an ideal system is designed on paper in terms of relative energy levels, many competitive undesirable processes are liable to come into play. Therefore, the goal is to design a system which exhibits a delicate interplay of rates in which desirable processes outcompete undesirable ones.

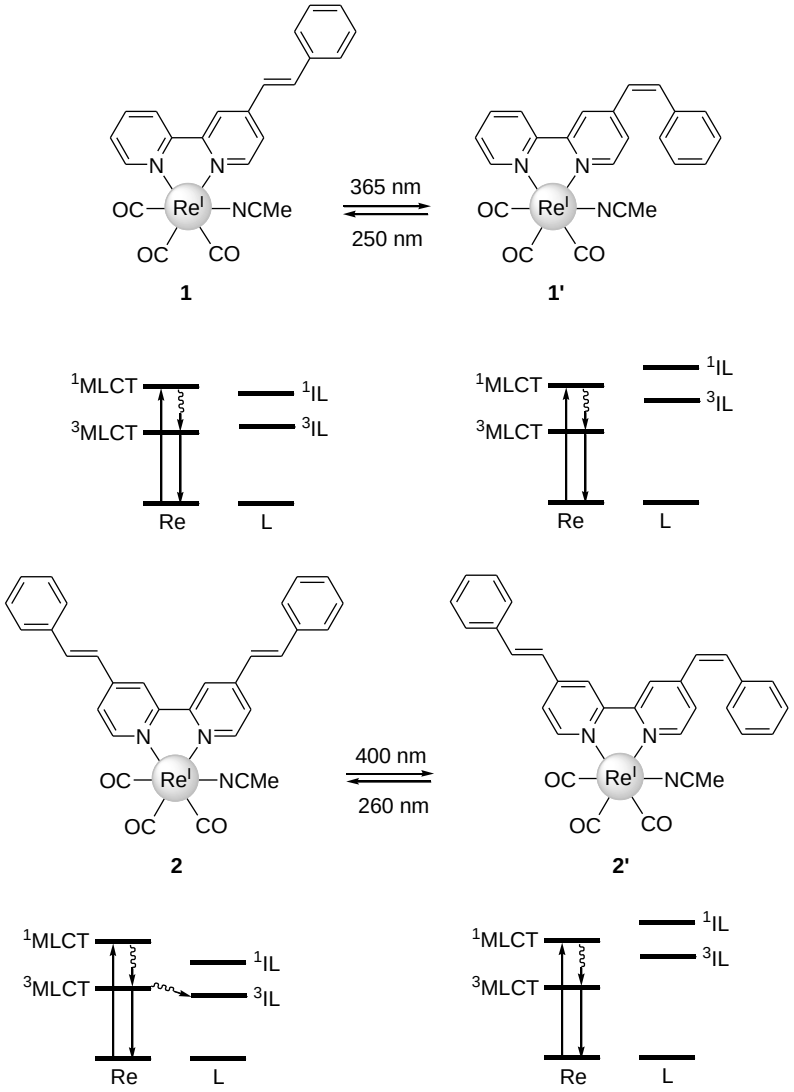

Figure 1.3. Photochromic ligand–metal complexes based on the Re^I–tricarbonyl chromophore with stilbene-substituted ligands, and proposed energy level schemes.

Researchers have pursued the study of luminescent photochromic ligand–metal complexes based on Re^I–tricarbonyls from both fundamental and applied perspectives.[138-142] Re^I–tricarbonyl complexes with nitrogen heterocycle ligands display a M(*d*)–L(π*) MLCT band at ~350–400 nm. The excitation energy for this band falls between those for the two forms of most photochromic ligands, where one form typically absorbs at higher energy in the UV region and one form typically absorbs at lower energy in the visible region. Thus, photochromic Re^I–tricarbonyl complexes should meet the base requirements for a photoswitchable luminescent system in which the ^{1}IL state of the

photochromic ligand in form A [^{1}IL(A)], the ^{1}IL state of the photochromic ligand in form B [^{1}IL(B)] and the ^{1}MLCT of the metal can be selectively excited. Ideally, selective luminescence quenching could then be achieved. In the case of azobenzenes and stilbenes, the photoisomerization energies for the forward and reverse isomerization processes lie fairly close together and fairly close to the energy of the ^{1}MLCT state. Achieving selective quenching with these particular photochromic ligands could therefore prove challenging. For example, the luminescence photoswitching properties of the mono- and bis-styryl-substituted Re^I–bipyridine complexes (**1** and **2**) reported by Wenger et al.[139] are very different despite the similarity of the systems (Figure 1.3). In the mono-styryl-substituted derivative (**1**), *trans* → *cis* isomerization is induced by 365-nm irradiation, while *cis* → *trans* isomerization can be induced by 250-nm irradiation. No difference in metal-based luminescence is observed for the two isomers, presumably because the IL states of both forms are higher in energy than the MLCT state. For the bis-styryl-substituted derivative (**2**), however, *trans* → *cis* isomerization is induced by 400-nm irradiation and *cis* → *trans* irradiation is induced by 260-nm irradiation. This slight shift of energy levels results in a two-fold increase in luminescence when the sample is converted to the *cis*-dominant photostationary state (PSS), which may occur because the lower energy of the IL states allows for ligand quenching of metal-based emission to become competitive with the emission process. One major pitfall in this particular system, however, is that gradual decomposition occurs upon UV irradiation, and therefore the material is not photostable enough for many applications.

Re^I–tricarbonyls incorporating dithienylethenes or spiropyrans/spirooxazines can show greater differences between ^{1}IL(A), ^{1}IL(B), and ^{1}MLCT excitation energies. In the pyridyl-substituted Re^I–tricarbonyl–DTE complex **3**, also reported by Wenger et al.,[139] photoisomerization of the closed to the open form can be effected with 620-nm light and photoisomerization of the open to the closed form can be effected with 350-nm light. A comparison of the emission spectra for both forms revealed that the metal-based luminescence in the open form is much greater than that in the closed form, and the toggling of luminescence intensity with photoisomerization was demonstrated. The authors postulated that the closed form has low-lying IL states able to quench the Re-based luminescence, although they did not rigorously investigate the photophysics of

the system. In the phen-substituted Re^{I}–tricarbonyl–DTE complex **4**, reported by Yam et al.,[140] the open form absorbs at ~300 nm and the closed form at 386, 546, and 580 nm. Through transient absorption experiments, the authors showed that energy transfer to the ^{3}IL state of the open form competes with ^{3}MLCT emission. In addition, this ^{3}MLCT quenching process leads to photochemical conversion to the closed form. This system demonstrates that (a) possible ^{3}MLCT quenching mechanisms are difficult to predict a priori; in this system many IL states were accessible in both forms of the ligand, and the observed photomodulation behaviour appears at odds with that observed for **3**, and (b) additional photochemistry is possible upon ^{3}MLCT quenching, so that ^{3}MLCT excitation becomes useful to sensitize photocyclization, but not necessarily as a means to nondestructive readout.

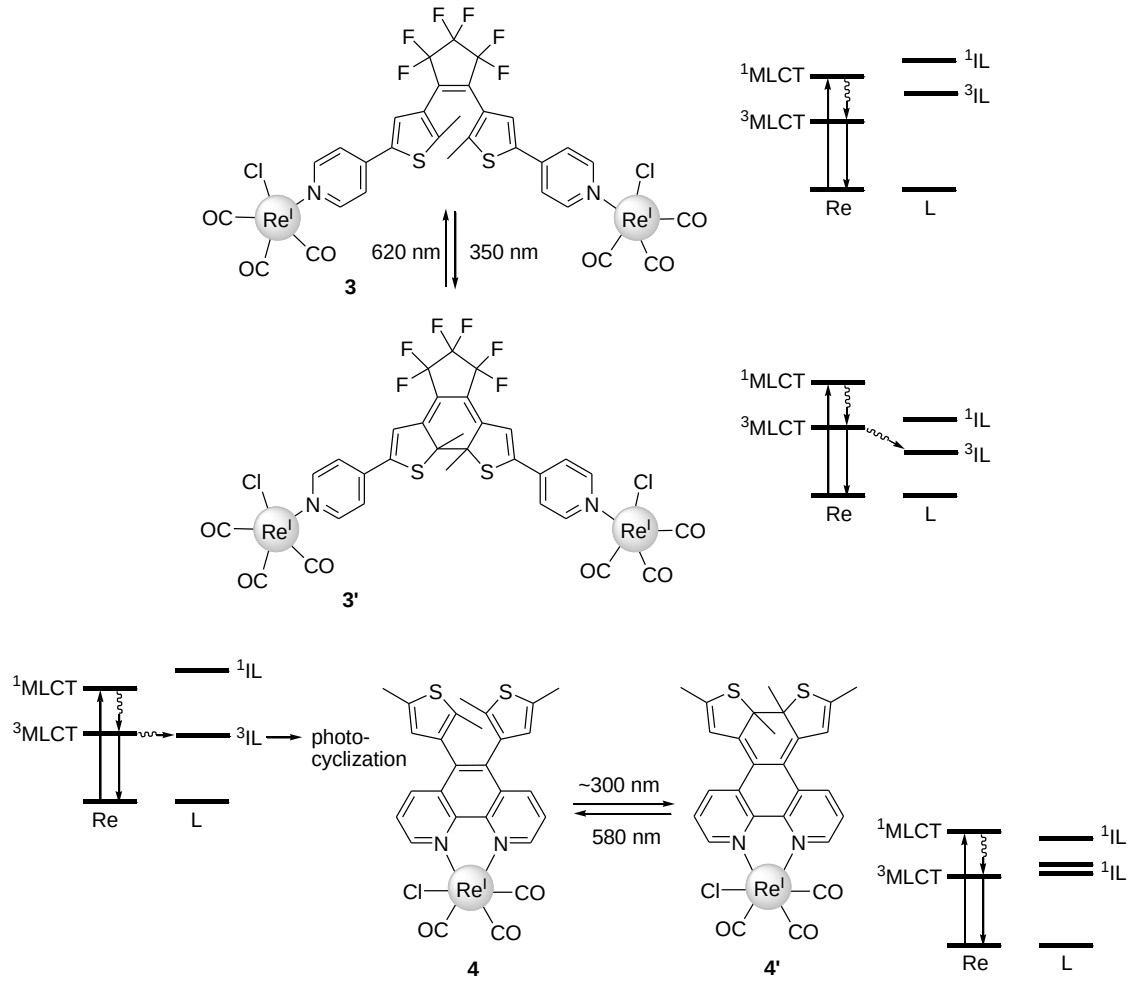

Figure 1.4. Photochromic ligand–metal complexes based on the Re^{I}–tricarbonyl chromophore with dithienylethene-based ligands, and proposed energy level schemes.

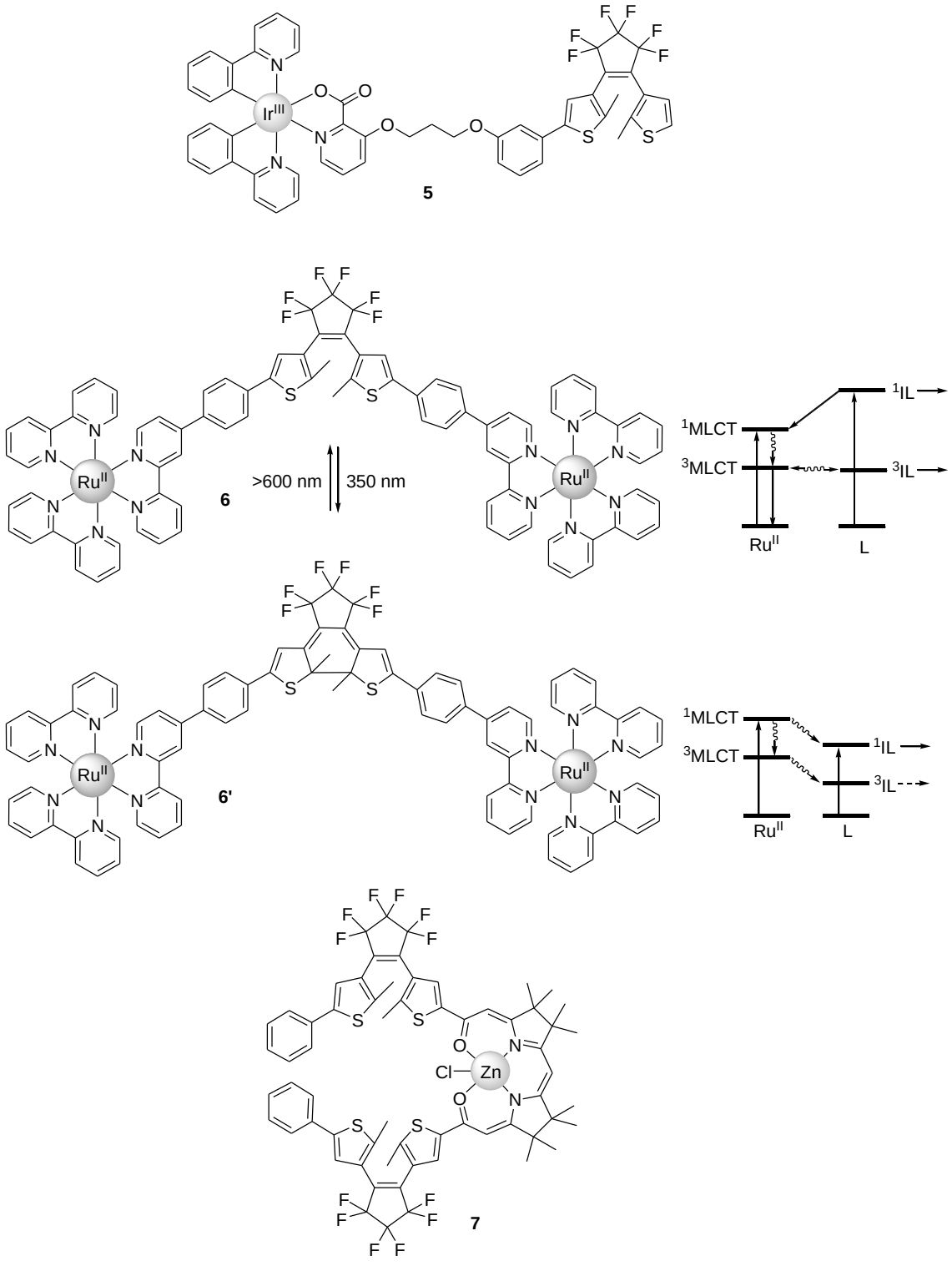

Figure 1.5. Photochromic ligand–metal complexes based on Ru/Ir polypyridyl or porphyrin chromophores, and proposed energy level schemes.

In addition to the Re^{I}–tricarbonyl systems, other luminescent photochromic metal complexes have been designed, notably those based on porphyrin or Ru/Os/Ir polypyridyl-type chromophores (Figure 1.5). Similarly to the Re^{I} chromophores, these systems can be excited to a ^{1}MLCT state with 350–500 nm light,[143] and can therefore be used in the design of photochromic complexes in which the two forms of the photochromic ligand absorb at higher and lower energies than the metal-based ^{1}MLCT excitation. Indeed, in the Ir^{III}–polypyridyl–DTE complex (**5**), a four-fold reduction in emission intensity occurs in the closed-form-dominant PSS, which has lower-energy IL states available for quenching.[144] The authors did not rigorously study the photophysical mechanisms or cycling/readout stability for this system, however. The binuclear Ru^{II}–polypyridine complex bridged by a DTE photoswitch (**6**) exhibits quenching of the ^{3}MLCT-based emission when in the ring-closed form but not in the ring-opened form.[145] For this system, the authors did conduct fairly rigorous photophysical studies and proposed the energy level schemes shown in Figure 1.5. Here, the ^{3}IL state of the closed form is lower in energy than the ^{3}MLCT state and can quench the metal-based emission. In the open form, however, the ^{3}IL state is of comparable energy to the ^{3}MLCT state, and energy transfer followed by photocyclization from the triplet manifold is competitive with the ^{3}MLCT emission process. Thus it is evident that even though the emission process can be toggled in the open and closed forms, nondestructive readout would not be possible in this system. This work also gives insight into some of the possible photoprocesses occurring in the DTE-based systems which were not studied in greater depth (e.g., in complexes **3** and **5**). Finally, the bis-DTE Zn–porphyrin complex **7** exhibits fluorescence quenching in the ring-closed form but not the ring-opened counterpart.[146] Although the authors admitted that excitation of the porphyrin does induce a small amount of photoconversion, and therefore readout is not completely nondestructive, the design is fairly robust and shows a high fluorescence contrast ratio of nearly 100:1 for the two forms of the photochromic ligand.

The luminescent photochromic ligand–metal complexes **1**–**7** represent a handful of those that have been reported in the literature. The above discussion highlights the possible photoexcited state pathways that are accessible in photochromic ligand–metal complexes and demonstrates how these may be photomodulated. The discussion also

brings up some of the complications involved in designing systems for nondestructive luminescence readout. Many of the systems reported in the literature do show some degree of luminescence photomodulation; however, most have not been studied in enough detail to elucidate the finer details of the photophysics nor to quantify their photocycling/readout stability. Those systems which have been studied in more depth point to the likelihood of multiple competitive pathways that will ultimately obstruct the design of systems for true nondestructive readout. It may therefore prove worthwhile to emphasize other types of systems[147] or mechanisms (vide infra) for such applications. Even if practical applications for optical data storage involving the photochromic ligand–metal interaction mechanism described in this section are not attained, the fundamental study of photophysical and photochemical processes occurring in photochromic ligand–metal complexes from a fundamental perspective is critical to advancing their integration into multifunctional materials.

1.2.2. Modulation of Communication Between Metal Centres with Bridging Photochromic Ligands

The use of photochromic bridges to optically toggle the communication between metal centres is a mechanism of interest in the development of multifunctional molecular materials, particularly molecular electronics. In principle, a photochromic bridge can behave as a molecular wire that can be switched on or off with light. A molecular wire can be described as a molecular system able to mediate the transfer of charge or energy between two ends.[148] At a molecular level, wire properties can be studied by sandwiching a bridge (the wire) between donor (D) and acceptor (A) components. If the donor is a chromophore, it may be photoexcited, thereby creating an initial excited state from which electron or energy transfer can occur. The rate of electron/energy transfer is a function of the coupling between the donor and acceptor components, which is in turn a function of factors such as the distance between the two and the relative orbital energy levels of the donor, acceptor, and bridging components.[149] Thus, a photochromic bridge can serve to mediate the transfer processes by modifying the D–A distance or orbital energy levels of the bridge upon photoisomerization.

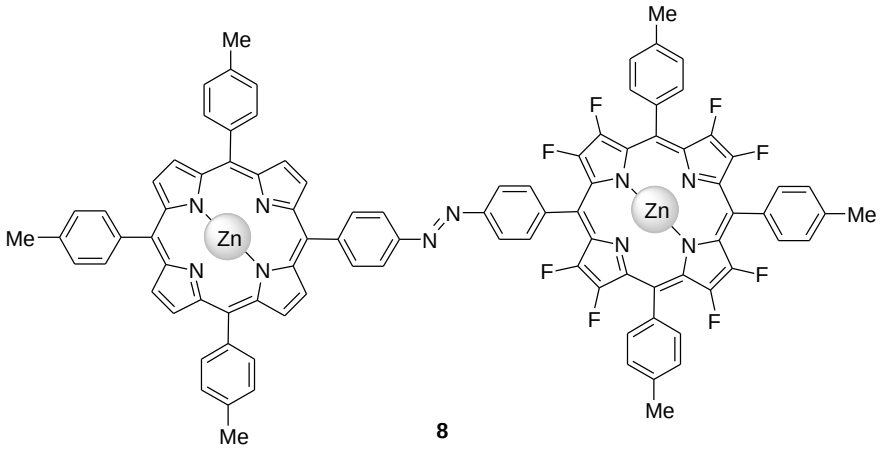

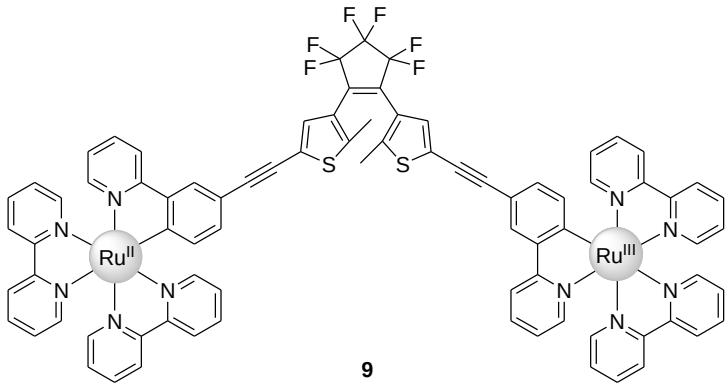

Figure 1.6. Molecular systems in which electron or energy transfer is mediated by a photoswitchable bridging unit.

The optical modulation of electron or energy transfer processes has been reported in complexes of metalloporphyrin and Ru–polypyridyl dimers bridged by photochromic ligands (Figure 1.6). Tsuchiya[150] reported a molecular system comprised of an electron-rich Zn–porphyrin moiety (the donor) bridged via an azobenzene group to an electron-deficient fluorinated Zn–porphyrin moiety (the acceptor) (**8**). The luminescence intensity was found to be lower in the *cis* isomer than in the *trans* isomer. In the porphyrin dimer, intramolecular electron transfer upon photoexcitation of the donor porphyrin is expected to lead to luminescence quenching. Thus, the difference in luminescence intensity found for the two azobenzene isomers was rationalized by greater electron transfer between donor and acceptor units in the *cis* isomer, which could be a function of distance and/or electronic effects. Launay et al.[151] reported a system containing two Ru^{II}–polypyridyl

chromophores bridged by a DTE photochromic ligand (**9**). The authors were able to observe an intervalence charge transfer band, characteristic of electron transfer,[152] upon oxidation to the Ru^{II}–Ru^{III} species in the ring-closed form, but not in the ring-opened form. As the closed and open forms of the DTE are expected to have the same approximate length, this is consistent with greater electronic coupling between metal centres when bridged with the more conjugated ring-closed DTE. The above systems clearly demonstrate potential as photoswitchable components for molecular electronic or photonic circuits. Interestingly, the porphyrin dimer design also fulfills the requirements for optical memory elements with nondestructive readout capabilities, as described in Section 1.2.1. Here, the luminescence quenching mechanism does not rely on sensitization by the photochromic linker, inevitably leading to complications, but rather sensitization occurs via electron or energy transfer to a second metal centre and is simply *mediated* by the photochromic linker.

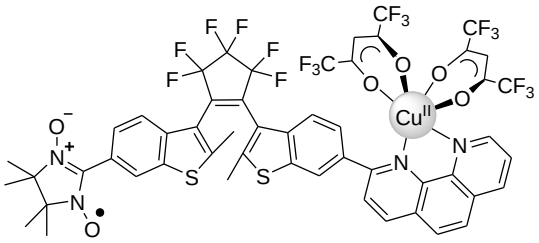

10

Another way in which a photoswitchable bridging ligand might be used to modulate communication between metal centres is by mediating the magnetic exchange between spin centres. Such an approach has been applied to several organic radical systems,[153] but only one metal complex that the author is aware of. Irie et al.[154] reported a molecular system in which a nitronyl nitroxide radical and a $Cu^{II}(hfac)_2(phen)$ (hfac = hexafluoroacetylacetonate, phen = 1,10-phenanthroline) moiety are bridged by a DTE photochromic unit (**10**). The authors found that the magnetic exchange between the Cu^{II} centre and nitronyl nitroxide radical was over 160 times greater in the π-conjugated ring-closed form than in the ring-opened form ($J_{closed} > 2.3 \times 10^{-2}$ cm^{-1} vs $J_{open} < 1.4 \times 10^{-4}$ cm^{-1}). Such effects may be of interest for optical data storage materials in which the recorded state of the system is read magnetically.

1.2.3. Exploiting Changes in Ligand Field Strength of Photochromic Ligands

A promising approach to modulating the properties of a coordinated metal is by using photoisomerizable ligands that exhibit light-induced changes in ligand field strength. Upon ligand photoisomerization, the metal functionality might display a gradual change in properties with changing ligand field strength (e.g., a change in MLCT absorption wavelength or redox potential), or, more interestingly, if the metal functionality exists in a bistable regime in which the electronic state of the system is highly sensitive to ligand field perturbations, a more dramatic change in properties could be effected by ligand photoisomerization.

This approach has most successfully been demonstrated via the ligand-driven light-induced spin change (LD-LISC) phenomenon,[155] first proposed for Fe spin-crossover (SCO) complexes coordinated to photochromic styrylpyridine (stpy) ligands.[156, 157] Fe SCO systems have been heavily investigated for their potential as switchable multifunctional materials, and are well-known for undergoing a low-spin (ls) to high-spin (hs) transition upon external perturbation (*T*, *P*, *hν*), with the two spin states displaying significantly different magnetic and optical properties.[158-161] When the ls → hs transition is cooperative, the transition can be quite abrupt, and it is often monitored as a function of temperature, where the temperature at which the transition takes place is defined as the critical temperature, T_c. Fe SCO complexes have been of interest for the development of photomagnetic materials as many exhibit light-induced excited-spin-state trapping (LIESST), an effect whereby photoexcitation of the ls state induces formation of an excited state, with subsequent relaxation to and trapping of the hs state.[162-166] This effect, however, becomes thermally reversible at relatively low temperatures (typically <50 K, with a few examples between 100–150 K), and is thus limited in utility for practical purposes. The LD-LISC effect, in contrast, takes advantage of the sensitivity of the ls/hs equilibrium to the ligand field of the coordination sphere (which influences T_c). In the case of coordination to stpy ligands, capable of *cis–trans* photoisomerization [Scheme 1.1, (1)], the *trans* form is expected to be a stronger π-acceptor on the basis of spectroscopic and electrochemical data.[156, 167] Such photochromic Fe SCO complexes should therefore be capable of light-induced changes in spin state at higher temperatures, including room temperature, provided the metal complex demonstrates bistability in the

appropriate temperature range. These materials would then be of use for data storage applications wherein the state of the system could be written with light and read magnetically.

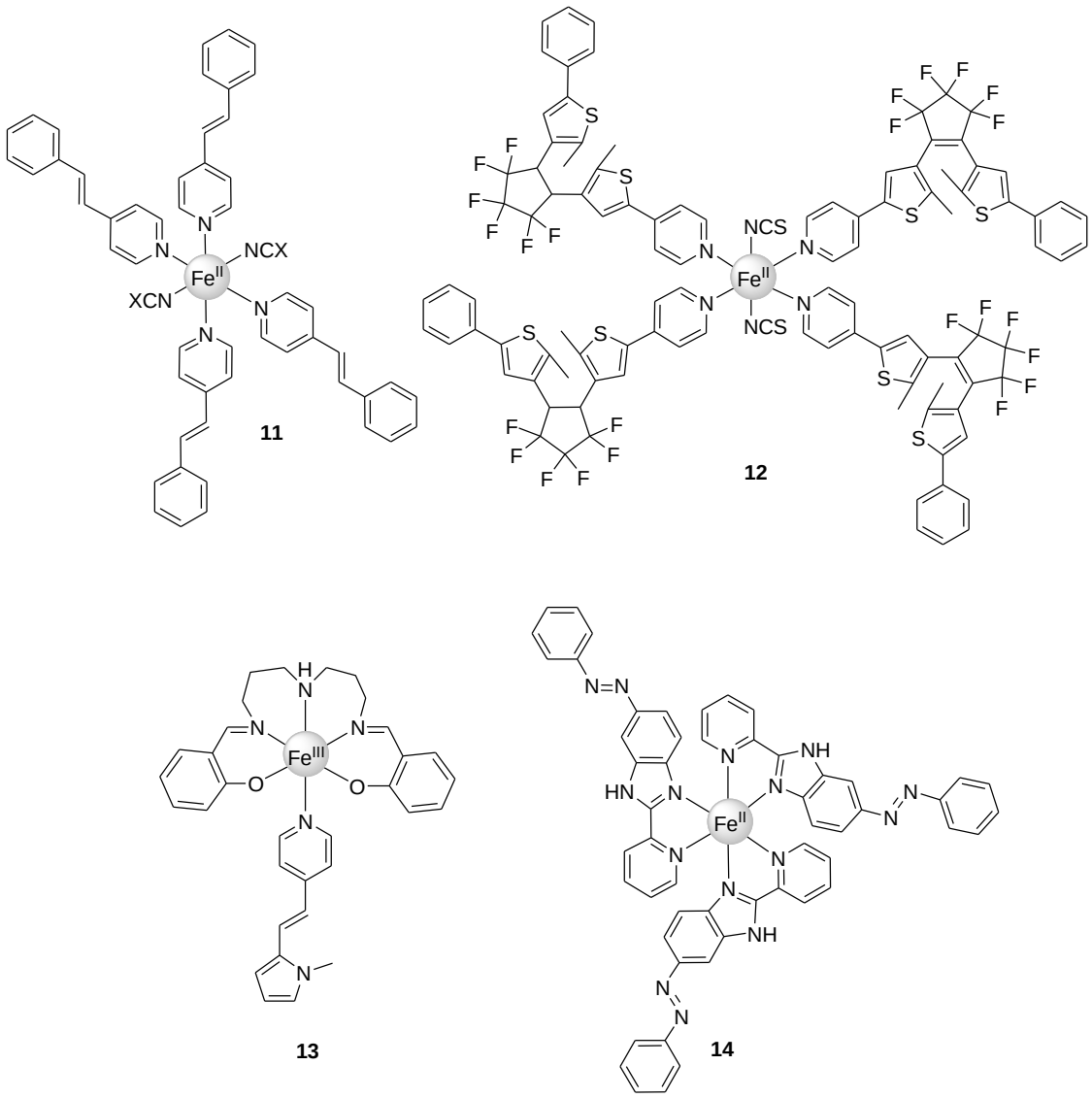

Figure 1.7. Several generations of Fe spin-crossover complexes designed to show ligand-driven light-induced spin change (LD-LISC) effects.

Several generations of photochromic Fe SCO complexes have been reported,[155-157, 167-173] and representative examples are compiled in Figure 1.7. Pioneering systems included $Fe^{II}(stpy)_4(NCX)_2$ complexes (**11**, NCX = NCS^-,[156] $NCBPh_3^-$, and $NCBH_3^-$),[157] where the latter two complexes display higher T_c values than the first. The LD-LISC effect was

demonstrated for the first time in thin films of $Fe(stpy)_4(NCBPh_3)_2$ in cellulose acetate at 140 K by electronic absorption spectroscopy.[157] An Fe^{II}–monopyridyl–DTE SCO complex (**12**) was shown to undergo changes in magnetization in the crystalline state upon UV irradiation,[171] where the major benefit of such a design may lie in the potential of DTEs for solid-state photochromism.[174, 175] An $[Fe^{III}(salten)(Mepepy)][BPh_4]$ complex[169] [**13**, H_2salten = 4-azaheptamethylene-1,7-bis(salicylideneiminate), Mepepy = 1-(pyridin-4-yl)2-(N-methylpyrrol-2-yl)-ethene] was also shown to exhibit the LD-LISC effect in acetonitrile solutions by Evan's method between 243 and 333 K. Another $Fe^{II}(stpy)_4(NCX)_2$ complex[172, 173] (**11**, NCX = $NCSe^-$) was shown to undergo changes in magnetization by SQUID magnetometry in a poly(methyl methacrylate) (PMMA) film at 130 K upon UV irradiation.[172] Recently,[167] reversible light-induced changes in magnetic susceptibility were demonstrated in the solution state at room temperature in an Fe^{II} complex coordinated to three 2-(2′-pyridyl)benzimidazole ligands derivatized with π-conjugated photochromic azobenzene units (**14**), using both UV and visible irradiation, through electronic absorption spectroscopy and Evan's method. It is clear from the numerous demonstrations of LD-LISC that the effect is a promising one for developing a range of materials in which properties may be reversibly and efficiently controlled by light in a variety of media and at useful temperatures.

The ligand field properties of pyridyl-substituted DTEs have been studied in a few systems (Figure 1.8). Irie et al. synthesized mononuclear (**15**) and multinuclear 1D-chain $Cu^{II}(hfac)_2$(DTE) complexes.[176] The authors observed differences in both the crystal structures and EPR spectra for the ring-closed and ring-opened isomers. They ascribed the differences in the multinuclear complex to the better π-acceptor properties of the ring-opened isomer. However—although there is no doubt that significant changes were observed in both mononuclear and multinuclear complexes—the assignment of these changes is ambiguous, particularly because the two types of complexes displayed opposite changes in Cu–O bond lengths for the closed and open forms. On the basis of decreasing Cu–N bond lengths in the ring-closed isomer for both complexes, an argument could instead be made for the better π-acceptor ability of the ring-closed isomer. Branda et al. studied the Lewis basicity of a pyridyl–DTE ligand functionalized with an electron-withdrawing (EW) pyridinium group (**16**) by monitoring coordination to a ruthenium

porphyrin[177] and an alkylation reaction.[178] In both cases they found that the ring-opened isomer was a better nucleophilic ligand, and attributed this to the greater availability of the lone pair on the N atom of the pyridine group as a result of a decrease in conjugation to the pyridinium group. They also looked at the π-acceptor abilities of the pyridine group by monitoring the C–O stretch in the Ru complex and determined that the ring-closed form was the better π-acceptor, at odds with the claim by Irie et al. that the ring-opened isomer was the better π-acceptor.

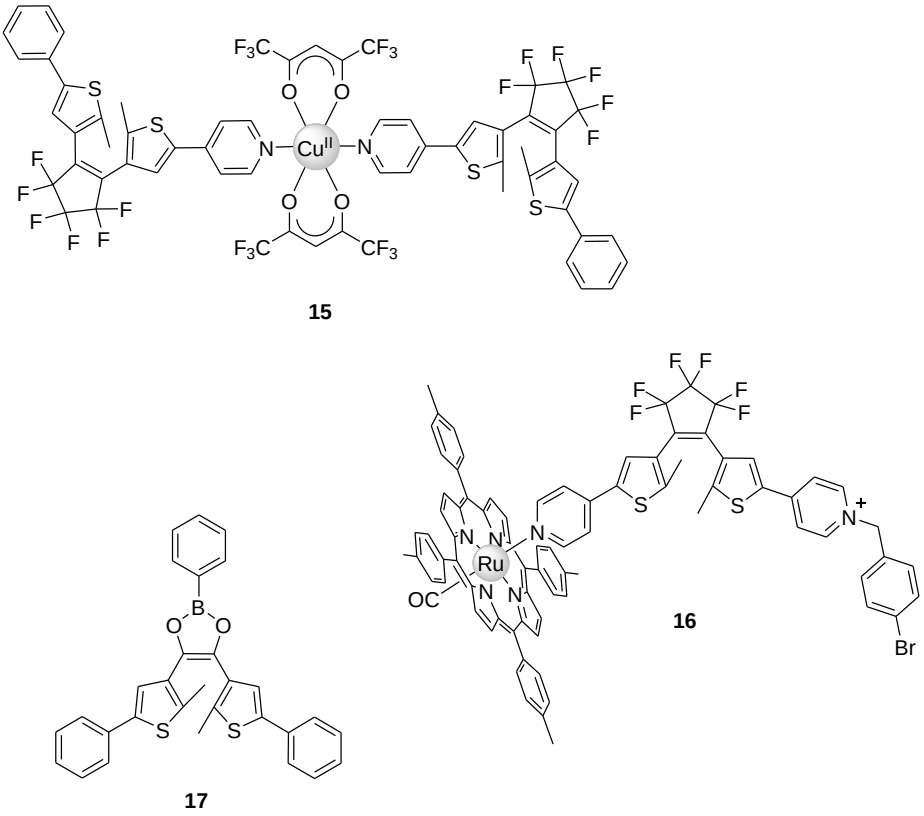

Figure 1.8. Dithienylethene-based ligands demonstrating changes in ligand field strength.

Another example of a ligand in which bonding properties may be controlled by photoisomerization is DTE **17**, in which the Lewis acidity of the boron atom was found to be stronger in the ring-closed form.[179] Finally, an example of a photochromic ligand in which the ligand field was explicitly reported to *not* change upon photoisomerization is the phenanthroline-functionalized DTE synthesized and studied by Yam et al. (**4**), discussed in the context of metal–ligand sensitization processes in Section 1.2.1. Here,

electrochemical experiments suggested insignificant changes to the π-acceptor ability of the phenanthroline functionality between the ring-closed and ring-opened isomers.[140, 180, 181]

In summary, evidence of changes in ligand field strength between photoisomers in both pyridyl-substituted DTEs and stilbenes or azobenzenes have been demonstrated, and in some cases nicely applied to the modulation of metal-based properties or functions. This approach, however, remains largely unexplored.

1.2.4. Exploiting Changes in Ligand Field Symmetry of Photochromic Ligands

Another approach to controlling metal-based properties via a coordinated photochromic ligand is to exploit changes in ligand field symmetry, where ligand photoisomerization can lead to changes in local molecular orbital symmetry at the coordination site. The photochromic ligand–metal interaction mechanism involved here is closely related to that based on changes in ligand field strength (Section 1.2.3), as in both cases effects are intimately tied to the characteristics of the metal coordination sphere. Certain metal-based properties can be strongly influenced by ligand field symmetry, in particular the spectroscopic (i.e., intensity of electronic absorption/emission) and magnetic (i.e., spin–orbit coupling) properties. The coordination of a photochromic ligand exhibiting changes in ligand field symmetry may therefore be a promising way to gain optical control over these properties.

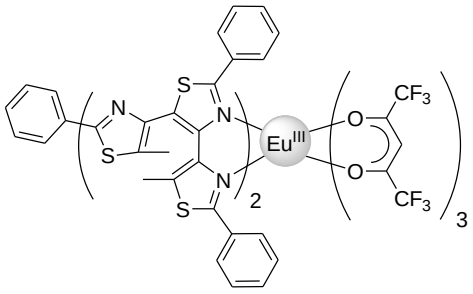

18

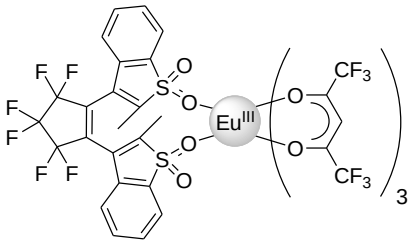

19

The modulation of metal-based properties through photoinduced changes in ligand field symmetry has been nicely demonstrated in a photochromic Eu^{III}–terthiazole complex (**18**)[182, 183] as well as a Eu^{III}–DTE complex (**19**).[184] Ln^{III} ions are well-known for

their favourable luminescent properties (i.e., long radiative lifetimes and sharp emission bands) arising from multiple 4*f*–4*f* transitions, and have been of much interest for displays, lighting, imaging, and other optical applications.[185, 186] The absorption and emission spectra of Ln^{III} ions result from both magnetic dipole (MD) and electric dipole (ED) transitions. The latter are dominant in Ln^{III} coordination complexes but are formally Laporte-forbidden by quantum mechanical selection rules. These selection rules may be relaxed through coupling with molecular vibrations or mixing of the 4*f* orbitals with orbitals of opposite parity such as ligand 5*d* orbitals. The result is that the intensity and lifetime of radiative ED transitions, unlike those of MD transitions, are strongly influenced by the ligand field, particularly its symmetry. Different transitions differ in ligand-field sensitivity, with some being exceptionally sensitive.[187, 188] In the Eu^{III} complex **18**, the authors compared the effect of ligand photoisomerization on the emission intensity of two different transitions, the $^5D_0$–$^7F_1$ MD transition, insensitive to ligand field, and the $^5D_0$–$^7F_2$ ED transition, hypersensitive to it.[183] As the latter transition displayed a significantly greater change in intensity upon ligand photoisomerization, the authors concluded that, in addition to the expected effects of Eu^{III}–ligand energy transfer, changes in the odd parity of the ligand upon photoisomerization were a contributing factor to the observed changes in luminescence intensity.

The photochromic ligand–metal interaction mechanism based on changes in ligand field symmetry demonstrated for complexes **18** and **19** shows promise for optical data storage applications with nondestructive readout capabilities. In Section 1.2.1, the key requirements for nondestructive luminescence readout in photochromic systems were outlined: (1) conversion of the photochromic ligand from form A to form B, conversion of the photochromic ligand from form B to form A, and excitation of the luminescent functionality must be achievable independently with distinct excitation wavelengths; and (2) quenching of the luminescent state via energy transfer to an excited state localized on the photochromic ligand must occur in one form of the ligand but not the other, *and* this quenching must not lead to subsequent photochemistry (i.e., leading to a change in the state of the system upon detection of its state). The latter requirement is particularly difficult to achieve via an excited-state energy-transfer mechanism; however, for the mechanism described here based on changes in ligand field symmetry, the requirements

are more easily met, particularly because photochemical conversion upon quenching of the luminescent state is no longer an issue. For complex **19**, the authors demonstrate clear differences in luminescence intensity at λ_{em} = 615 nm (originating from the hypersensitive $^5D_0$–$^7F_2$ transition) for the closed and open forms which do not change upon continuous irradiation at λ_{ex} = 526 nm ($^7F_0$–$^5D_1$ transition).[184] This experiment therefore convincingly demonstrates that the state of this system can be read out repeatedly from the detected luminescence intensity without perturbing the state of the system.

This mechanism could also be applied to memory applications based on magnetic readout. Here, distortion of the ligand field symmetry upon photoisomerization of a photochromic ligand–metal complex would affect the relative quenching of the orbital angular momentum of the metal ion and overall magnetization of the complex. The application of such a mechanism in photoswitchable materials was alluded to by Kopelman et al.[189] for photochromic phenanthroline–spirooxazine complexes. A similar mechanism was demonstrated recently by Juhász et al.,[190] who took advantage of the different possible coordination modes of a nonphotochromic nitrate ligand to perturb the ligand field symmetry in a hs-[$Co^{II}(NO_3)_2(L)$] complex [L = 2,6-di(pyrazol-1-yl)pyrazine]. Here, changes in the structural conformation of the coordinated nitrate ligands occurring during a temperature-induced phase change were correlated with changes in magnetization, attributed to changes in orbital angular momentum quenching. This result demonstrates the feasibility of a mechanism whereby the degree of orbital quenching is controlled through changes in ligand field symmetry. It would be anticipated that the use of photochromic ligands, whose coordination site properties are controlled by light, in lieu of nitrate ligands, whose coordination site properties are controlled by temperature-induced phase changes, would be conducive to more versatile applications. Overall, the exploitation of changes in ligand field symmetry in photochromic ligand–metal complexes is a promising, yet so far largely unexplored, mechanism for gaining optical control over transition metal or rare earth properties.

1.2.5. Exploiting Changes in Conformation of Photochromic Ligands

A mechanism that has perhaps been more frequently applied in purely organic photochromic materials[65, 105, 117, 191] than in photochromic ligand–metal complexes is the exploitation of changes in the molecular volume or conformation of the photochromic ligand upon photoisomerization to modulate the properties of hybrid photochromic materials. If the successes achieved for organic photochromic compounds are any indication, this strategy could prove extremely versatile in the design of functional photochromic ligand–metal systems. The majority of photochromic ligands that have been studied in the context of molecular conformation are based on ligands able to weakly bind metal ions. As such, this particular mechanism has to date predominantly been of interest for catalysis-oriented applications,[67, 192, 193] where a change in conformation of a photochromic ligand is expected to induce changes in catalytic function. Applications in light-controlled ion sensing,[194-196] ion extraction,[71] ion transport,[71] and chemionics[16, 60] have also been proposed.

Several photochromic ligand systems of interest in the context of catalysis are shown in Figure 1.9. A first example involves the common triarylphosphane ligand (**20**), which was derivatized with azobenzene groups in an attempt to gain optical control over the steric bulkiness of the ligand.[193] Molecular modelling results suggested a significant change in sterics for the *trans-trans-trans* vs *cis-cis-cis* azobenzene conformations; however, preliminary catalytic experiments showed only a slight influence of photoisomerization on reactivity. A second example is given by the bis-barium complex of the azobis(benzo-18-crown-6) ligand **21**, where the *cis* form is shown to be a significantly better catalyst than the *trans* form as it is able to bring the barium centres into closer proximity and better relative positions to catalyze a basic ethanolysis reaction.[192] Finally, in complex **22**, photoisomerization of the DTE moiety is expected to lead to changes in the binding ability of a chiral bis(oxaline) chelating group, which is expected to bind in the open form but not the closed form.[67] Indeed, the use of **22** in a copper-catalyzed olefin cyclopropanantion reaction showed higher enantiomeric selectivities for the open form than for the closed form.

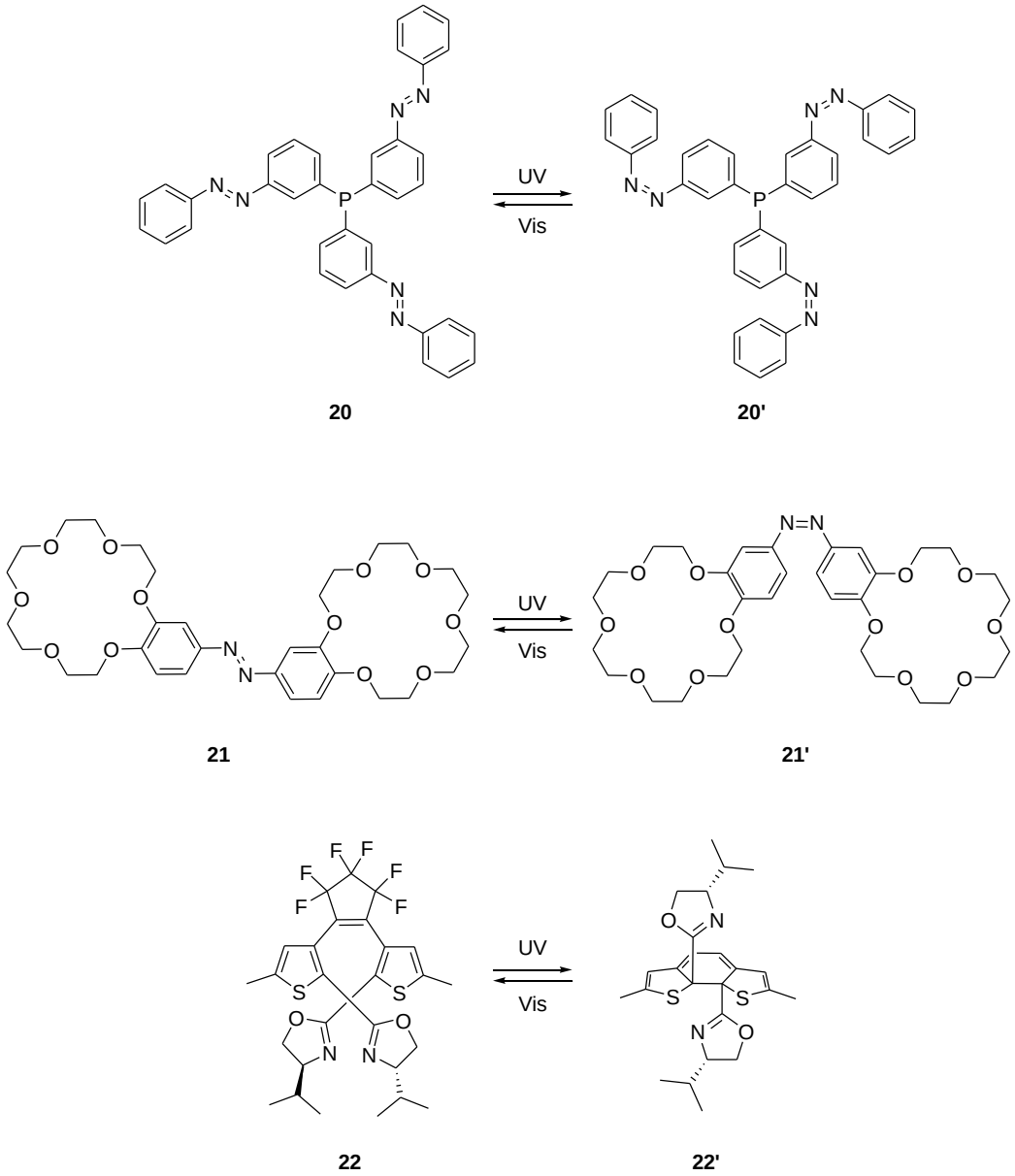

Figure 1.9. Photochromic ligands exhibiting significant changes in molecular conformation upon photoisomerization designed for the light-induced control of catalysis (note: the perfluorinated cyclopentene group is omitted in the ring-closed isomer of **22** for clarity)

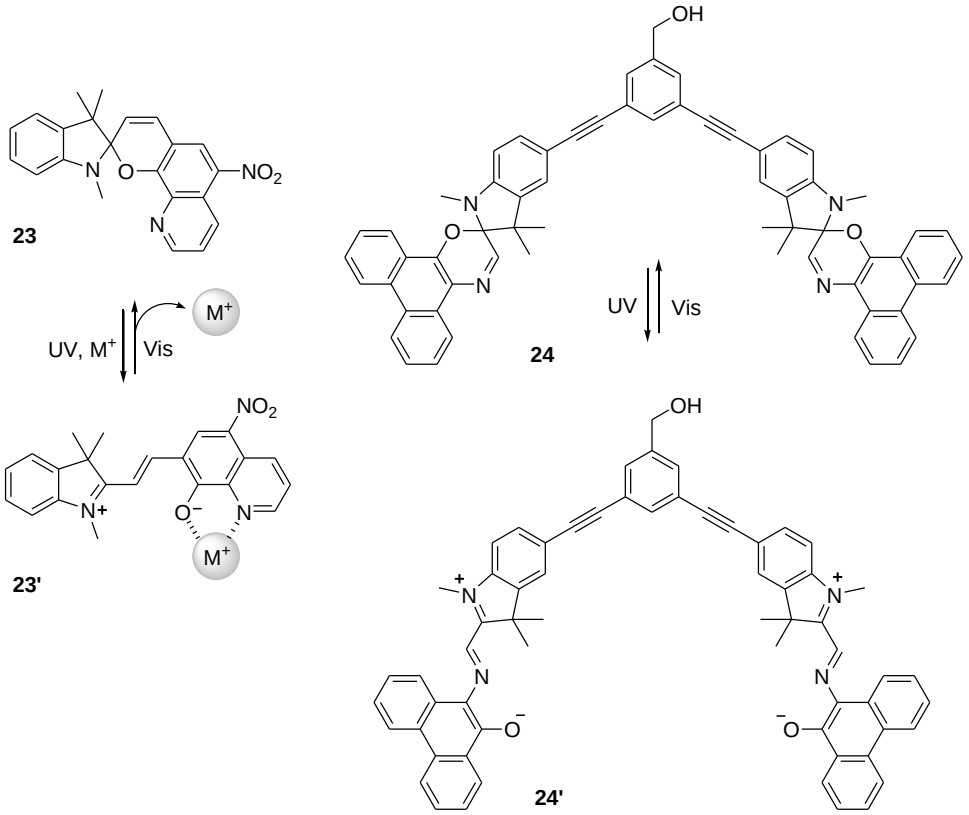

Figure 1.10. Different metal-ion binding capabilities for the ring-closed and ring-opened forms of spiropyrans and spirooxazines.

Spiropyrans and spirooxazines are known to bind metal ions in their open photomerocyanine form through their phenolate oxygen atom, and as such have been investigated for photomodulated metal-ion binding applications. Many examples of spiropyrans and spirooxazines that make use of this binding mechanism have been reported,[197-201] and a selection of examples are shown in Figure 1.10 and Scheme 1.3. One approach involves incorporation of a proximal chelating group to improve binding in the ring-opened form. Compound **23** demonstrates sensitivity for metal ions in the parts-per-billion (ppb) range that can be photochemically toggled.[195] Compound **24** is an example of a spirooxazine dimer which exhibits preferential binding to Pd in the ring-opened form.[202, 203] The methoxy-nitro-benzospiropyran derivative **25** (Scheme 1.3) may be switched reversibly between four possible states using a combination of optical (UV/Vis light) and chemical (Fe^{3+} ions/2,2′-bipyridine) stimuli and has been proposed as a molecular system capable of performing molecular logic functions as a half-adder.[204]

Overall, this mechanism has remained largely unexplored in photochromic ligand–metal complexes, though should present many opportunities for achieving optical control, not only over catalysis and metal ion binding, but over other material properties.

Scheme 1.3. Nitro-substituted benzospiropyran proposed as a molecular half-adder.

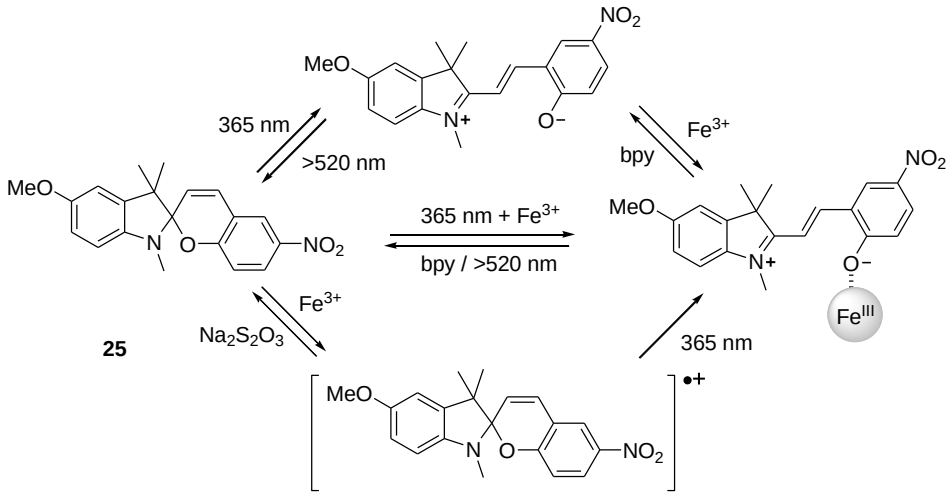

1.3. Photochromic Phenanthroline–Spirooxazine Coordination Complexes

Of the mechanisms outlined in Section 1.2, the majority of the studies pertaining to photochromic ligand–metal complexes have focused on excited-state energy transfer processes, whereby the sensitization of photochemical conversion pathways via excitation of the metal component or the quenching of metal-based luminescence by the photochromic component have been observed in a wide array of systems. The existence of multiple photophysical and photochemical pathways in photochromic ligand–metal complexes makes it difficult to design complexes in which photoisomerization may be used to control metal-based properties through selective excited-state quenching processes in a predictable and useful manner. It is, however, important to keep in mind that such excited-state processes could play an important role in the behaviour of any photochromic ligand–metal complex. Fewer studies have explored photochromic ligand–metal interaction mechanisms based on changes in ligand field strength or symmetry. The implementation of such mechanisms may provide a versatile way to control metal-based properties, and may provide a more straightforward design for photochromic ligand–

metal systems that behave in a predictable fashion. The work presented in this thesis focuses predominantly on the design and study of photochromic coordination complexes in which the effect of photoinduced changes in ligand field strength (Section 1.2.3) are exploited, though of course not at the exclusion of other possible photochromic ligand–metal interaction mechanisms.

The molecular systems studied here have been designed around photochromic ligands of the spirooxazine class. Spiropyrans [Scheme 1.1, (3)] have been studied since the 1950's with the early work of Hirshberg and Fisher,[205] while the closely related spirooxazines garnered much attention in subsequent years due to their greatly improved fatigue resistance.[93, 110] Spirooxazines undergo UV-light-induced cleavage of a spirocyclic C–O bond, which leads to a ring-opening reaction and the formation of a predominantly planar, highly conjugated, and highly coloured photomerocyanine (PMC) form. The reverse photoinduced cyclization process leading to the closed-ring spirooxazine (SO) form can be induced with visible light. Both the forward and reverse isomerization processes can also occur thermally along the ground-state potential energy surface.[93, 110]

Spirooxazines have only been recently explored as ligands. Early studies looked at the transient binding of metal ions through the phenolate oxygen atom of the PMC form[195, 198-201] or through tethered porphyrin[206] or crown ether groups.[207-210] In the late 1990's and early 2000's, a small handful of permanently bound spirooxazine coordination complexes were reported.[211-213] The Frank group has investigated a series of quinoline-, isoquinoline-, and phenanthroline-functionalized spirooxazine ligands capable of permanently binding transition metals (**26**–**31**).[214, 215] Previous studies in the group focused primarily on the effects of metal coordination on the photochemistry of the spirooxazine ligands. Several series of complexes of the two phenanthroline–spirooxazine ligands, $[M^{n+}(L)_3][X]_n$ (n = 2 or 3; M = Mn, Fe, Co, Ni, Cu, or Zn; L = **28** or **31**; X = BPh_4^-, PF_6^-, or ClO_4^-),were synthesized and characterized. It was shown that for the complexes of **31**, the photochromic properties were significantly affected by metal coordination, with the thermodynamics, kinetics of thermally induced and photochemically induced isomerization, absorption wavelength, and photoresponsivity all being metal-dependent.[189, 215, 216] For the complexes of **28**, in contrast, only a slight

perturbation of the photochromic properties was observed upon metal coordination.[214] A series of $M^{II}(L)_2(hfac)_2$ (M = Mn, Co, Ni, Cu) complexes was also synthesized with L = **29** and **30**, where it was noted that little perturbation to the photochromic properties occurred upon metal coordination, in contrast to the complexes of **31**.[215]

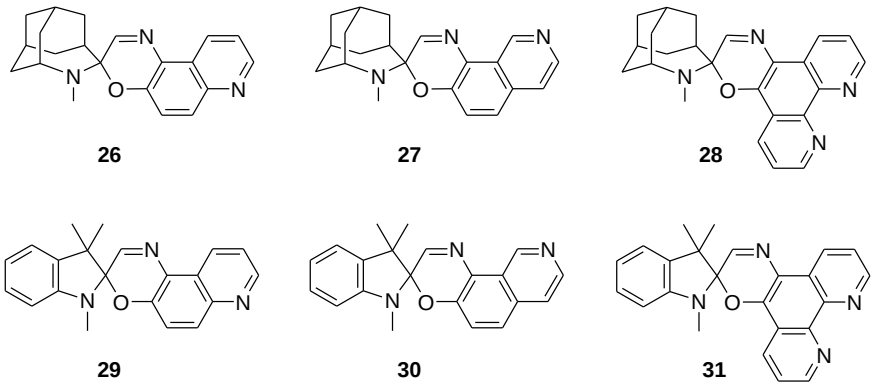

26 **27** **28**

29 **30** **31**

Each of the common classes of photochromic molecules (Scheme 1.1) has a unique set of features. Dithienylethenes have become extremely popular due to their thermal irreversibility, fatigue resistance, and solid-state photochromism.[92] Spirooxazines are also highly fatigue resistant, though their greatest downfall is arguably their thermal reversibility. This feature, however, may be advantageous for specific applications requiring fast thermal relaxation rates. In addition, while it has been known for some time that the properties of spirooxazines are highly tunable, more recent studies have shown that: (a) metal coordination can significantly alter the thermodynamics and kinetics of these systems, potentially leading to vastly different photochromic properties; and (b) light-induced photochromism in constrained media may be quite effective, while thermal processes may be ineffective in such environments.[217] Such observations are promising for future device applications, but neither of these areas has so far been sufficiently explored.

For our goal of designing photochromic ligands that exhibit changes in ligand field upon photoisomerization, one of the key advantages of the spirooxazine class is its synthetic versatility. In Section 1.2.3., it was made apparent that few photochromic ligand–metal systems have been explored with the goal of capitalizing on photoinduced changes in ligand field strength, and of these few systems, the majority are based on

pyridine ligands that may not demonstrate particularly strong electronic communication with the metal functionality. In spirooxazines, the ligand functionality (e.g., a heterocyclic nitrogen ligand) can be incorporated directly into the oxazine moiety such that the ligation site is expected to undergo a substantial change in electronic structure upon SO/PMC isomerization as a result of the large changes in conjugation occurring in the molecule. These heterocyclic spirooxazine ligands are therefore predicted to show considerable differences in ligand field between the two photoisomers. Incorporation of these spirooxazine ligands into metal complexes sensitive to ligand field thereby creates a useful framework for the design of new photoswitchable multifunctional materials.

1.4. Scope of Thesis

This thesis describes the design of photoswitchable materials based on coordination complexes of phenanthroline–spirooxazine ligands **28** and **31**. Chapter 2 presents an analysis of crystallographic and spectroscopic studies to elucidate the effects of substitution and medium on the molecular structure of the PMC form of spirooxazines **28** and **31**. These effects are then correlated with photochromic properties. Providing insight into a long-debated and controversial topic, the conclusions from this analysis are highly relevant to the development of spirooxazine-based systems for functional materials, with or without metal coordination, wherein the optimization of photochromic properties and the understanding of medium effects become critical. The studies presented in Chapter 3 were undertaken to elucidate the effect of ligand isomerization on the ligand field strength and metal–ligand bonding in phenanthroline–spirooxazine metal complexes. Empirical FT-IR and ^{13}C NMR spectroscopic measurements on molybdenum–tetracarbonyl–spirooxazine complexes demonstrate a change in ligand field strength between SO and PMC forms and allow for quantification of the direction and magnitude of this change. A theoretical fragment molecular orbital (MO) analysis using density functional theory (DFT) calculations clarifies the nature of the bonding interactions in these complexes, providing valuable information for the design and study of functional photochromic coordination complexes and next-generation photochromic spirooxazine ligands. Chapter 4 describes the integration of optically bistable phenanthroline–spirooxazine ligands into magnetically bistable cobalt–dioxolene redox isomeric

complexes with the goal of designing a molecular system which displays photoinduced changes in magnetization at room temperature. These cobalt–dioxolene–spirooxazine complexes are shown to exhibit both photochromic and redox isomeric bistability as a function of irradiation and temperature, respectively. Spectroscopic studies reveal a correlation between photochromic state and redox state (i.e., spin state), which provides a proof-of-principle that the spin state of a coordinated metal centre may be controlled via photoinduced ligand field changes of a photochromic spirooxazine ligand. Finally, Chapter 5 summarizes the work and outlines several avenues for further exploration of spirooxazine-based photoswitchable materials.

Chapter 2. Substituent and Medium Effects on Spirooxazine Properties

(This chapter reproduced in part with permission from ref[218]. Copyright 2010 American Chemical Society.)

2.1. Introduction and Background

The properties of spirooxazines are extremely sensitive to their chemical structure and external medium (e.g., solvent, polymer matrix, poly- or single-crystalline matrix). An understanding of these influences is critical to the efficient design and optimization of spirooxazines for incorporation into materials and devices, either as sole components or as part of a more complex hybrid multifunctional material. A key feature of spirooxazines that depends considerably on chemical structure and medium is the degree of charge separation of the photomerocyanine (PMC) form, often described in terms of the relative contributions of the canonical quinoidal (**A**, Scheme 2.1) or zwitterionic (**B**, Scheme 2.1) resonance forms to the ground- and excited-state molecular structures. As the relative quinoidal/zwitterionic structure of PMCs may be inferred experimentally and theoretically, an analysis of PMC charge separation provides a handle for elucidating how spirooxazines respond to substituent or medium effects on a structural level. This structural information can then be correlated to key spirooxazine properties, such as the thermodynamics of the SO/PMC equilibrium and the photo- and thermal isomerization rates, or can be used to glean insight into the effect of spirooxazine photoisomerization on nonphotochromic components in hybrid systems.

Scheme 2.1. Isomerization of spiro[indoline-benzoxazine] between spirooxazine (SO) and photomerocyanine (PMC) forms, illustrating canonical quinoidal (**A**) and zwitterionic (**B**) resonance forms of the latter.

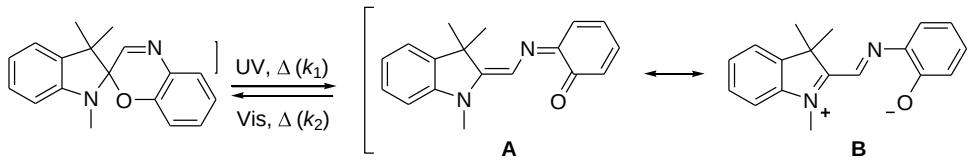

This chapter presents a thorough study of medium effects, interpreted in the context of the degree of PMC charge separation, in both the solution and single-crystalline states for two spirooxazine derivatives: a relatively novel and little studied bicyclic azahomoadamantyl derivative, spiro[azahomoadamantane-phenanthrolinoxazine] (APSO, **28**), and a more common and highly studied indolyl derivative, spiro[indoline-phenanthrolinoxazine] (IPSO, **31**). Azahomoadamantyl-substituted spirooxazines exhibit attractive properties such as crystalline-state photochromism, high photoresponsivities, slow thermal relaxation rates, and an exceptional stability of the PMC form relative to their indolyl counterparts.[214, 217, 219] While substituent effects have been fairly thoroughly investigated for indolyl-based spiropyrans and spirooxazines, few reports of the influence of azahomoadamantyl substitution exist.[214, 217, 219, 220] The comparison of these two phenanthroline–spirooxazine derivatives provides an enlightening look at the influence of the amine functionality on spirooxazine properties.

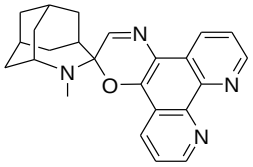

28

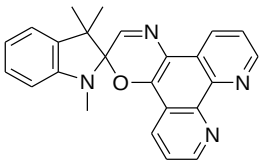

31

Solution-state medium effects are probed by indirect methods: the molecular structures of the PMC forms of APSO and IPSO are inferred from the solvatochromic behaviour and vibrational structure of the PMC-based π–π^* charge transfer (CT) band in a wide range of solvents. Solvent-dependent ^{1}H and ^{13}C NMR analyses are also performed to ascertain their usefulness in elucidating the effect of solvent polarity on molecular structure. The crystallization of not only one, but two crystalline pseudopolymorphs of APSO, the first crystal structures of the PMC form of a metastable spirooxazine, provided the fortuitous opportunity to investigate the PMC molecular structure in the solid state. The molecular geometries of the two pseudopolymorphs are compared to analyze the effect of the crystalline environment on PMC structure. The solid-state structures are also compared to the inferred solution-state structures. Density functional

theory (DFT) calculations are evaluated for their efficacy in predicting molecular structure, and—by extension— structure–property and medium–property relationships in PMCs. Finally, the degree of charge separation—or the degree of quinoidal or zwitterionic character—is shown to be correlated with a number of spirooxazine properties, highlighting the usefulness of this feature in determining both structure–property relationships and the effect of the environment on spirooxazine properties. The attractive photochromic properties of the azahomoadamantyl derivative are correlated with a high contribution of the zwitterionic resonance form to the PMC structure. An explanation of this effect in terms of chemical substituent and medium effects gives insight into how to optimize photochromic figures of merit for optical applications.

2.1.1. Molecular Structure of Photomerocyanines in Terms of Quinoidal and Zwitterionic Resonance Contributions: A Controversy

The degree of quinoidal or zwitterionic character of the PMC form of spiropyrans and spirooxazines has remained a topic of controversy. This has been due in part to the ignorance of a segment of the community regarding the structure of merocyanines and in part to a lack of comprehensive structure elucidation studies. Because the transient PMC form is difficult to crystallize[110, 221] and tends to form aggregates upon irradiation,[222, 223] the molecular structure of the PMC form has been typically inferred from indirect methods such as the analysis of the energy or vibrational structure of the π–π^* CT band as a function of solvent polarity, solution-state NMR studies, or computational analysis. These studies fall short due to a lack of concrete structural determination studies as well as the limited range of media polarity and derivatives investigated.

To date, the only metastable (i.e., photochromic or semipermanent) photomerocyanines that have been structurally characterized are a handful of nitro- and pyridinium-substituted spiropyran or spirothiopyran derivatives, which were all shown to exhibit a predominantly zwitterionic structure in the crystalline state.[224-229] These molecules also display negative solvatochromism, which corroborates their zwitterionic structure in solution.[229-231] Only a few permanent (i.e., nonphotochromic) spirooxazine-based PMCs have been characterized, and these have been described as predominantly quinoidal in character, in some cases on the basis of the C–O bond length alone.[232, 233] Solvatochromic studies of spirooxazine-based PMCs have indicated that these exhibit positive

solvatochromic behaviour, and it was therefore concluded that they possess a predominantly quinoidal structure.[110, 234-236] Early computational studies predicted a quinoidal structure for spirooxazine-based PMCs.[237] Malatesta et al. proposed a zwitterionic structure for these molecules on the basis of nucleophilic trapping studies.[238] The interpretation of these observations—limited to specific derivatives and conditions—led to ambiguity regarding the nature of the molecular structure of spiropyrans and spirooxazines and,[238, 239] in some instances, to the belief that spirooxazines as a class are quinoidal while spiropyrans are zwitterionic.[110] Recently several authors have emphasized that the degree of quinoidal or zwitterionic character in these photochromic photomerocyanines is highly dependent on chemical structure and medium.[240] Computational and solvatochromism studies on spirooxazines have predicted zwitterionic character in derivatives with electron-withdrawing groups (EWGs) on the oxazine moiety and a dependence of the degree of zwitterionic character on medium polarity.[241] Thus, when it comes to understanding molecular structure of spirooxazines, general misconceptions have resulted from both the misinterpretation of available data as well as the misguided generalization of results for specific derivatives in specific conditions to spirooxazines as a whole.

For a better understanding of the issue, we may turn to the more general class of merocyanines or, even more broadly, the class of conjugated donor–acceptor molecules, in which the observed solvatochromism phenomenon—or the effect of solvent polarity on molecular structure—has been scrutinized in depth. These molecules are well-known for their large hyperpolarizabilities, and have garnered much attention in the context of electro-optical applications. Toward this end, there has been much interest in understanding the effects of chemical structure and medium on these materials. As in the study of spirooxazines, this field, too, has remained plagued with controversy.[242] Key points of contention have been the concrete relationship between solvatochromic behaviour and molecular structure, the origin of the vibrational structure of the CT band, as well as the source of the experimentally observed phenomenon of ‘inverted solvatochromism,’ where a reversal in solvatochromic behaviour is observed with a change in solvent polarity.[243-245] The studies presented here, specific to spirooxazine-based photomerocyanines, shed light on these general issues.

2.2. Results and Discussion

2.2.1. Synthesis of Phenanthroline–Spirooxazines

The general methodology for the synthesis of spirooxazines involves the condensation of an enamine with an *o*-hydroxy-nitroso arene under dehydrating conditions.[110, 219, 246] The *o*-hydroxy-nitroso-phenanthroline derivative (**34**) required for the preparation of IPSO and APSO was obtained from 1,10-phenanthroline-5,6-dione (**33**),[247] prepared by the oxidation of 1,10-phenanthroline (**32**) with potassium bromide under acidic conditions to give **33** as yellow needles in 50–60% yield after recrystallization of the crude reaction product from EtOH. The base-catalyzed condensation of **33** with hydroxylamine hydrochloride gave 5-hydroxy-6-nitroso-1,10-phenanthroline (**34**) as a pure yellow powder in quantitative yields (Scheme 2.2).[248]

Scheme 2.2. Synthesis of *o*-hydroxy-nitroso-phenanthroline.

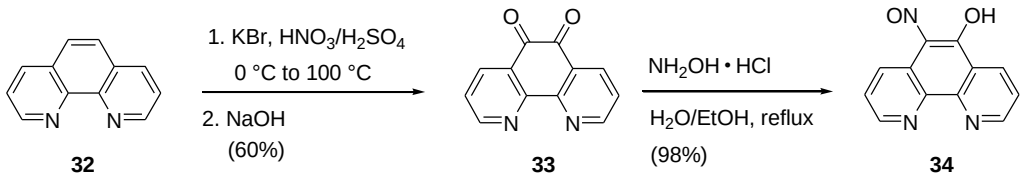

Scheme 2.3. Synthesis of APSO.

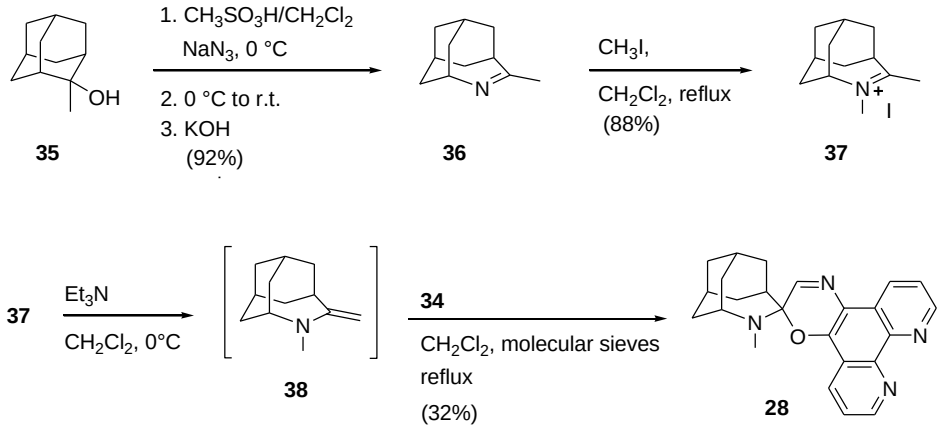

Scheme 2.4. Synthesis of IPSO.

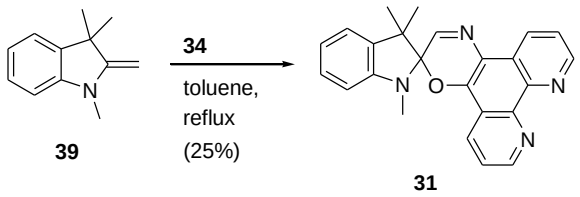

APSO (**28**) was synthesized by the condensation of the *o*-hydroxy-nitroso-phenanthroline (**34**) with 4-methyl-5-methylene-4-azahomoadamantane (**38**), generated in situ by the reaction of 4,5-dimethyl-4-azahomoadamant-4-enium iodide (**37**) with triethylamine at low temperature (Scheme 2.3).[219] The required azahomoadamantyl iodide **37** was synthesized by the ring expansion of 2-methyladamant-2-ol (**35**) with sodium azide to give **36** as a pale yellow oil in 92% yield, followed by treatment with methyl iodide to afford **37** as a white powder in 88% yield.[249] The condensation of *o*-hydroxy-nitroso derivative **34** with enamine **38** in dichloromethane under dehydrating conditions gave **28** as a purple crystalline solid with an iridescent green sheen in 32% yield after several purification steps. IPSO (**31**) was prepared by the condensation of commercially available 1,3,3-trimethyl-2-methyleneindole (**39**) with 5-hydroxy-6-nitroso-1,10-phenanthroline (**34**) in toluene to give **31** as yellow crystals in 25% yield, again after several purification steps (Scheme 2.4).[250]

2.2.2. Solution-State Thermodynamics and Kinetics of Isomerization

Spirooxazines in the SO form undergo a photochemically induced ring-opening reaction with UV light to generate a PMC form, and this process may be reversed with visible (Vis) light (Scheme 2.1). The PMC form, which may be represented by both canonical quinoidal and zwitterionic resonance forms, can additionally exist as eight possible isomers depending on the relative *transoid* or *cisoid* configuration about each of the three central bonds of the conjugated bridge (i.e., TTT, TTC, TCC, TCT, CTT, CTC, CCC, CCT, where ‘TTT’ represents the *trans–trans–trans* isomer, and so on). Not only do spirooxazines undergo photochemical isomerization, but they can undergo reversible thermal isomerization between SO and PMC forms along the ground-state potential energy surface (PES). As such, they can exist as a mixture of SO and PMC forms, for

which the equilibirum position is defined by the relative stabilities of the two isomers as well as the activation energy (E_a) barrier between the two, both of which are sensitive to chemical structure and external medium. The system may be defined thermodynamically by the equilibrium constant (K_T = [PMC]/[SO]) or kinetically by the rate constants for thermal isomerization from SO to PMC (k_1) or PMC to SO (k_2) (Scheme 2.1). The thermodynamic and kinetic constants may be related by $K_T = k_1/k_2$.[251]

The thermal equilibrium constants, K_T, of spirooxazines that exist as a mixture of SO and PMC forms may be extracted from their ^{1}H NMR spectra. This was done for APSO and IPSO in a series of solvents at ~300 K by calculating the ratio of the peak areas for the azomethine proton resonance of the PMC ($\delta \approx 10$ ppm) and SO ($\delta \approx 8$ ppm) forms. The K_T values are tabulated in Table 2.1. It is evident that the thermal equilibrium constants are significantly higher for APSO, in which they range from 1.2 (55% PMC form) in toluene to 25 (96% PMC form) in MeOH, than in IPSO, in which they range from only 0.02 (2% PMC form) in toluene to 0.13 (12% PMC form in DMSO). It is also evident that, in general, the PMC form is stabilized in higher polarity solvents.

Table 2.1. Thermal equilibrium constants (K_T), %PMC values, and thermal isomerization rate constants (k, s^{-1}) of APSO and IPSO in different solvents at ~300 K.[a,b,c]

		APSO					IPSO			
	E_T^N	K_T (%PMC)	k_{Vis}^{-1}	k_{UV}^{-1}	k_1	k_2	K_T (%PMC)	k_{UV}^{-1}	k_1	k_2
Toluene	0.099	1.2 (55)	2×10^{-1}	2×10^{-1}	1×10^{-1}	9×10^{-2}	0.02 (2)	2×10^{-1}	5×10^{-3}	2×10^{-1}
CH_2Cl_2	0.309	11 (92)	6×10^{-2}	N/A	5×10^{-2}	5×10^{-3}	0.06 (5)	7×10^{-1}	4×10^{-2}	7×10^{-1}
Acetone	0.355	8.3 (91)	5×10^{-2}	N/A	4×10^{-2}	5×10^{-3}	0.02 (2)	7×10^{-1}	1×10^{-2}	6×10^{-1}
DMSO	0.444	20 (95)	8×10^{-2}	N/A	7×10^{-2}	4×10^{-3}	0.13 (12)	7×10^{-1}	8×10^{-2}	6×10^{-1}
CH_3CN[d]	0.460	20 (95)	2×10^{-2}	N/A	2×10^{-2}	1×10^{-3}	0.07 (6)	2×10^{-1}	1×10^{-2}	2×10^{-1}
MeOH[d]	0.762	25 (96)	9×10^{-3}	N/A	9×10^{-3}	3×10^{-4}	0.07 (7)	1×10^{-1}	7×10^{-3}	9×10^{-2}

[a] K_T = [PMC]/[SO], k_{Vis}^{-1} = observed rate constant for SO → PMC thermal return from a visible-light-induced PSS, k_{UV}^{-1} = observed rate constant for PMC → SO thermal return from a UV-light-induced PSS, k_1 = rate constant for SO → PMC isomerization, k_2 = rate constant for PMC → SO isomerization, K_T values determined by ^{1}H NMR spectroscopy, k values determined by UV/Vis electronic absorption spectroscopy. [b] Experimental error for rate constant determination is on the order of 5–20%. [c] See Appendix A for ^{1}H NMR spectra and Appendix C for plots of kinetic fits. [d] See ref[214].

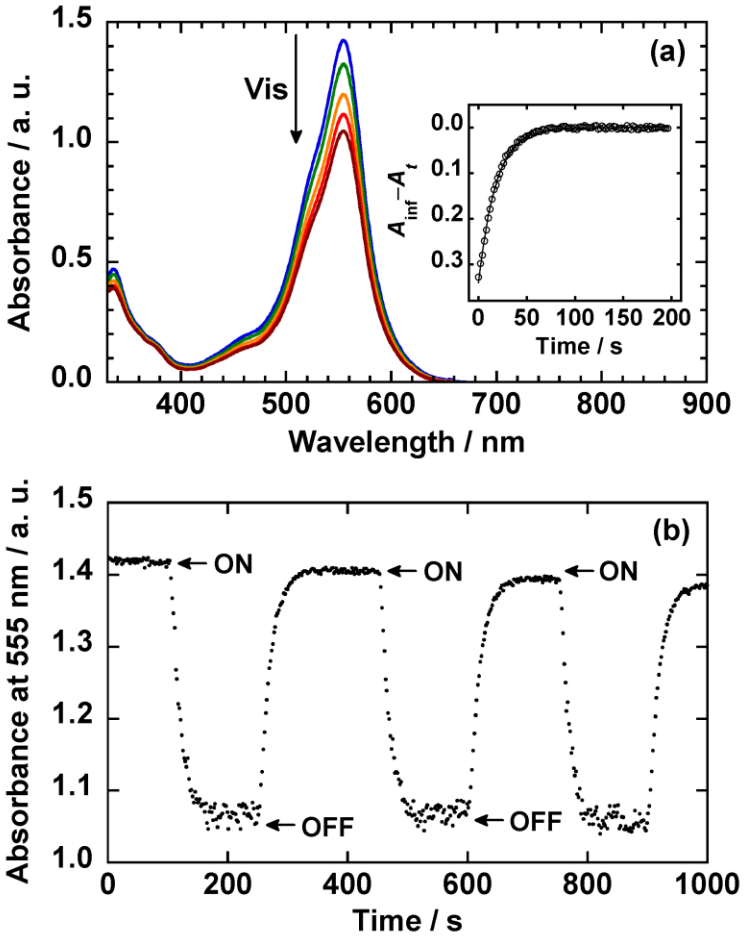

Figure 2.1. (a) UV/Vis electronic absorption spectrum of a CH_2Cl_2 solution (3×10^{-5} M) of APSO at ~300 K upon visible irradiation (λ_{ex} = 568 nm) (inset: first-order monoexponential fit of thermal relaxation kineticsat 555 nm in the absence of light); and (b) kinetic profile of the absorbance intensity of the PMC π–π* CT band at 555 nm over three irradiation cycles in the presence (ON) and absence (OFF) of light.

Upon irradiation of a spirooxazine solution with UV or visible light, the SO/PMC equilibrium is displaced from the thermal equilibrium, defined by K_T, to a photostationary state (PSS) defined by a new equilibrium constant, K_{UV} or K_{Vis}. The overall photochemical conversion is a function of the photoresponsivity ($\Delta K_{UV} = K_{UV} - K_T$ or $\Delta K_{Vis} = K_{Vis} - K_T$) of the sample in a given set of conditions, which depends on the quantum yield of photochemical conversion and rate of thermal relaxation. In the absence of light, the system returns thermally to the original equilibrium. The photochemical and thermal isomerization processeses may be monitored by following the absorbance of the

PMC π–π^* CT band—proportional to the PMC concentration—over time (Figure 2.1). As the rate of thermal relaxation does not depend on precise experimental irradiation conditions (e.g., solution concentration, irradiation intensity), the observed rate constant, k_{obs}, for this process, is most readily compared between compounds and experimental conditions. Here, the observed rate constant determined after generation of a UV-light-induced PSS is defined as k_{UV}^{-1}, while that determined after generation of a visible-light-induced PSS is defined as k_{Vis}^{-1}. The thermal isomerization rate constants, k_1 and k_2, may be obtained from the experimental data using the relationships $k_{obs} = k_1 + k_2$ and $K_T = k_1/k_2$.[96, 201, 235, 252] These constants can then be analyzed to gain mechanistic insight into the system.

Both APSO and IPSO are photoresponsive to visible light, whereupon PMC → SO photochemical isomerization occurs. In the case of IPSO, however, the equilibrium is already shifted far toward the SO isomer, and minimal PMC → SO conversion is possible. IPSO is also photoresponsive to UV light, in which case a more pronounced shift in the SO/PMC equilibrium occurs. APSO, however, typically exhibits photoinduced decomposition under UV irradiation conditions in all but a few solvents (e.g., toluene). This behaviour is not characteristic of all azahomoadamantyl spirooxazines,[218] but is specific to the phenanthroline derivative. Thermal rate constants, k_1 and k_2, for APSO and IPSO were calculated from the experimentally determined k_{Vis}^{-1} and k_{UV}^{-1} rate constants and are summarized in Table 2.1. Several trends may be noted. For APSO, $k_1 \approx k_2$ in toluene, but in more polar solvents $k_1 > k_2$ by an order of magnitude. The value of k_1 decreases slightly with solvent polarity, ranging from 1×10^{-1} s^{-1} in toluene to 9×10^{-3} s^{-1} in MeOH. The value of k_2 also shows a decrease with solvent polarity, shifting from 9×10^{-2} s^{-1} in toluene to 3×10^{-4} s^{-1} in MeOH. In general, the opposite trends are observed for IPSO. In this case, k_2 is between one and two orders of magnitude larger than k_1. Further, both k_1 and k_2 initially increase with increasing solvent polarity, as exemplified by increases in the rate constants on going from toluene to CH_2Cl_2, acetone, or DMSO, before decreasing again in more polar CH_3CN and MeOH. The different trends observed for the thermodynamic and kinetic constants for APSO and IPSO as a function of solvent polarity provide valuable mechanistic insight and will be discussed in the context of molecular structure in Section 2.2.7.

2.2.3. X-Ray Crystallographic Analysis of the PMC form of APSO

Dark purple single crystals of APSO-PMC were obtained from the slow evaporation of ethyl acetate solutions (in which the PMC form is expected to dominate the SO/PMC thermal equilibrium) in the absence of light as two pseudopolymorphs: an ordered lattice without solvent inclusion (APSO-PMC-I) and a disordered trihydrate of the PMC form (APSO-PMC-II). Here, the term 'pseudopolymorph' is taken to refer to different crystalline phases of a compound containing different amounts or types of solvent molecules.[253] The first pseudopolymorph, APSO-PMC-I, crystallized in the monoclinic *C*2/*c* space group with eight molecules in the unit cell (Figure 2.2). The molecules pack as slipped head-to-tail dimeric units with large intermolecular mean plane separations of 4.64 Å [Figure 2.2(b)]. These dimeric units assemble into chains running along the *c* axis in which each dimeric unit is tilted with respect to the last. The second pseudopolymorph, APSO-PMC-II, crystallized in the $P2_1/n$ space group (Figure 2.3). The X-ray data required fitting of residual electron density to disordered solvent in the lattice, where the most intense peaks in the difference map were 2.6–2.7 Å apart. The data could not be fit successfully to EtOAc solvent molecules from the crystallization solvent as the void was too small. However, by attributing the residual electron density to water, where a distance of 2.6–2.7 Å is a good estimate for the distance between oxygen atoms of hydrogen-bonded water molecules, the data could be fit quite reasonably to a trihydrate model. Overall, the quality of the data for this structure is high [$R_{(int)}$ = 0.0661 on 4020 reflections], although the solvent-induced disorder contributes to high *R* indices [R_1 = 0.0906, wR_2 = 0.2565]. The unit cell contains four molecules that are oriented about six water molecules to give a water cavity in the *b*/*c* plane. Strong hydrogen bonds exist between the heterocyclic ring oxygen, O(1), and closest H_2O molecule, O(1S), [H(1S)···O(1) = 1.880 Å] [Figure 2.3(b)] with additional hydrogen bonding (H···O = 1.900 Å) between remaining water molecules. The water molecules form a hydrogen-bonded chain along the *a* axis, leading to a water channel as a result of cooperative hydrogen bonding [Figure 2.3(c)].

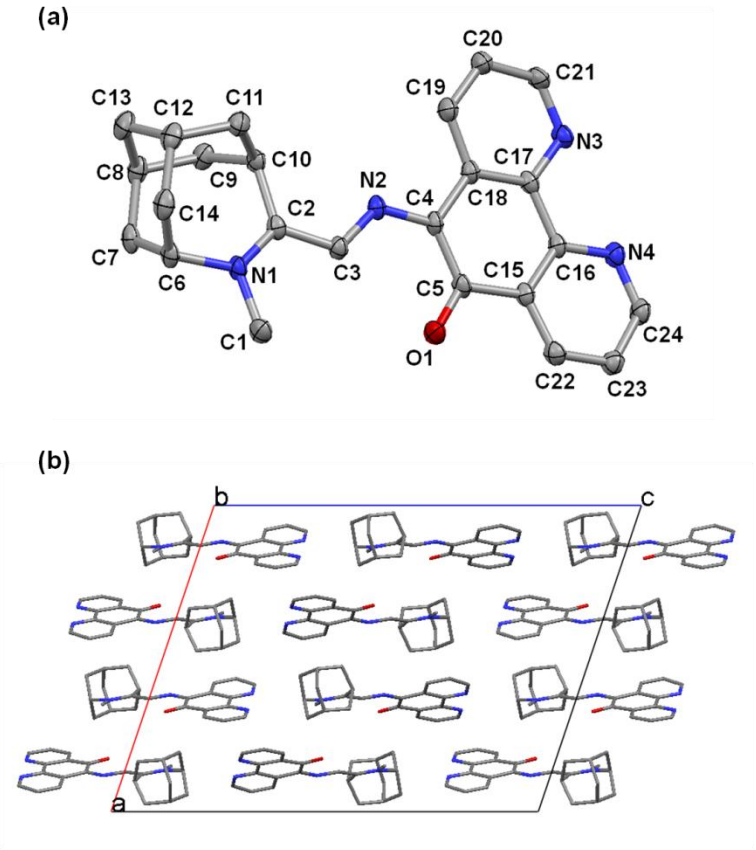

Figure 2.2. Molecular structure of APSO-PMC-I with thermal ellipsoids shown at the 50% probability level (a) and crystal packing viewed along the *b* axis (b).

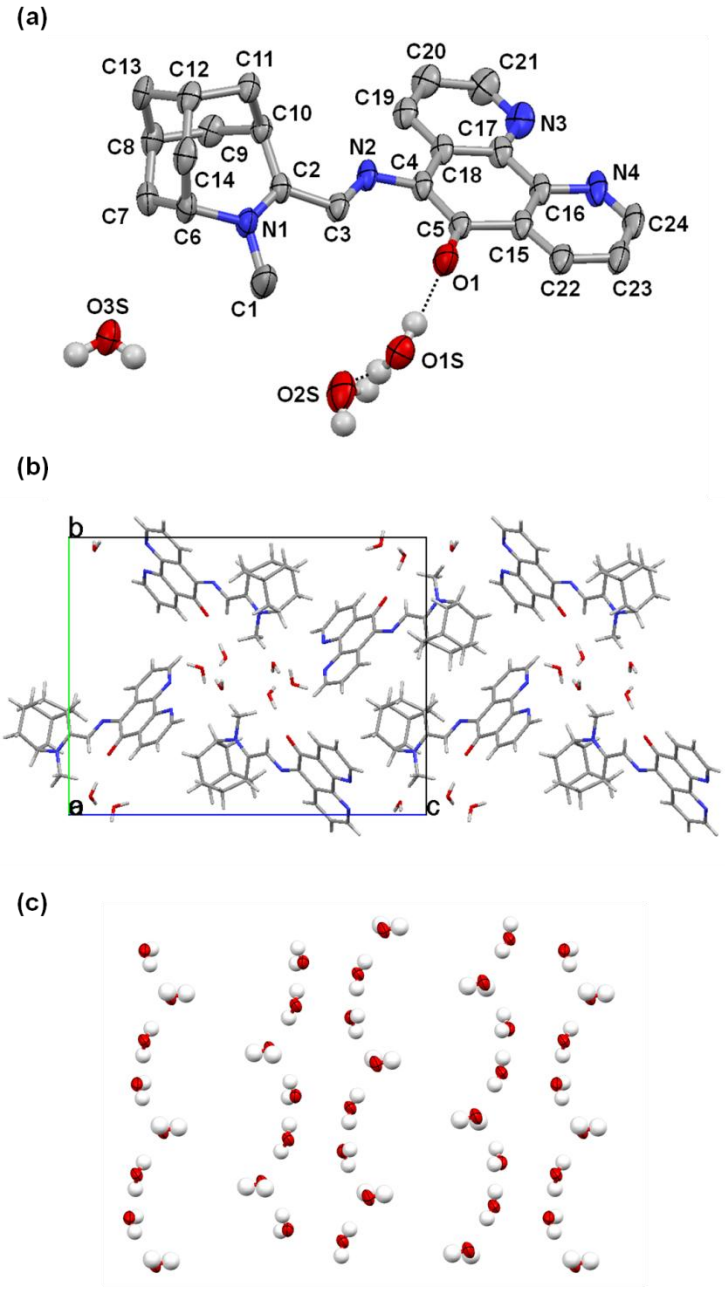

Figure 2.3. Molecular structure of APSO-PMC-II with thermal ellipsoids shown at the 50% probability level (a), crystal packing viewed along the *a* axis (b), and crystal packing of solvent molecules viewed along the *b* axis illustrating water channels (c).

Table 2.2. Selected bond lengths [Å] and angles [°] for APSO-PMC (I and II), and corresponding predicted bond lengths for the limiting quinoidal (A) and zwitterionic (B) resonance forms.[c]

	APSO-PMC-I[a]	**APSO-PMC-II**[b]	**A**[c]	**B**[c]
C(1)–N(1)	1.478(5)	1.473(6)	1.469(14)	1.485(9)
N(1)–C(2)	1.327(2)	1.313(5)	1.355(14)	1.316(9)
C(2)–C(3)	1.427(2)	1.448(5)	1.360(20)	1.460(15)
C(3)–N(2)	1.326(2)	1.315(5)	1.376(11)	1.279(8)
N(2)–C(4)	1.346(2)	1.359(5)	1.279(8)	1.376(11)
C(4)–C(5)	1.442(2)	1.423(6)	1.478(11)	1.364(14)
C(5)–O(1)	1.249(2)	1.245(5)	1.222(13)	1.362(15)
N(1)–C(2)–C(3)–N(2) [α]	179.2	170.8(4)		
C(2)–C(3)–N(2)–C(4) [β]	–174.9	176.4(3)		
C(3)–N(2)–C(4)–C(5) [γ]	1.5	–13.3(6)		

[a]Formula: $C_{24}H_{24}N_4O$; FW: 384.47 g mol^{-1}; Crystal system: monoclinic; Space group: *C*2/*c*; *a*: 18.7530(18) Å; *b*: 8.7476(8) Å; *c*: 24.797(3) Å; β: 108.605(5)°; *V*: 3855.3(7) Å^3; *Z*: 8; ρ_{calc}: 1.325 mg mm^{-3}; μ: 0.083 mm^{-1}; *T*: 110(2) K; λ: 0.71073 Å; R_1: 0.0469; wR_2: 0.1174; $R_1 = \Sigma||F_o| - |F_c||/\Sigma|F_o|$; $wR_2 = [\Sigma w(F_o^2 - F_c^2)^2/\Sigma w(F_o^2)]^{1/2}$; $w = [\sigma^2(F_o^2) + (0.0735P)^2 + 2.1923P]^{-1}$ where $P = [F_o^2 + 2F_c^2]/3$). [b]Formula: $C_{24}H_{24}N_4O{\cdot}3H_2O$; FW: 438.52 g mol^{-1}; Crystal system: monoclinic; Space group: $P2_1/n$ (an alternate setting of $P2_1/c$); *a*: 6.6536(12) Å; *b*: 16.165(3) Å; *c*: 20.809(4) Å; β: 93.277(2)°; *V*: 2234.4(7) Å^3; *Z*: 4; ρ_{calc}: 1.304 mg mm^{-3}; μ: 0.090 mm^{-1}; *T*: 193 K; λ: 0.71073 Å; R_1: 0.0906; wR_2: 0.2565; $R_1 = \Sigma||F_o| - |F_c||/\Sigma|F_o|$; $wR_2 = [\Sigma w(F_o^2 - F_c^2)^2/\Sigma w(F_o^4)]^{1/2}$; $w = [\sigma^2(F_o^2) + (0.1002P)^2 + 4.1726P]^{-1}$ where $P = [\mathrm{Max}(F_o^2, 0) + 2F_c^2]/3$). [c]Predicted bond lengths reported as average bond lengths for analogous bonds in organic compounds as compiled from the Cambridge Crystallographic Database by Allen et al.; see ref[254].

The experimental bond lengths and angles defining the central conjugated azomethine bridge for APSO-PMC are tabulated in Table 2.2, along with the corresponding bond lengths predicted for the limiting canonical quinoidal (Scheme 1, **A**) and zwitterionic (Scheme 1, **B**) resonance forms (reported as average bond lengths for analogous bonds in organic compounds as compiled from the Cambridge Crystallographic Database by Allen et al.[254]). A comparison of the two pseudopolymorphs of APSO-PMC provides insight into the effects of packing environment on the structure of the PMC form. Although the refined structure for APSO-PMC-II has a high degree of disorder and lower quality refinement parameters (R_1 = 0.0906, wR_2 = 0.2565) relative to that for APSO-PMC-I (R_1 = 0.0469, wR_2 = 0.1174), differences between the bond lengths throughout the

conjugated bridge for the two structures are greater than twice the estimated standard deviation (e.s.d., σ), which suggests that they are crystallographically significant. If two measurements differ from one another by twice the e.s.d., the probability is about 5% that the difference between them represents a random fluctuation; if they differ by 2.7 e.s.d. units, this probability is only about 1%. While some accept that a difference of 2 e.s.d. units (95% confidence level) between bond lengths implies that this difference is crystallographically 'significant,' those who are more conservative prefer to only assign significance to differences of 2.7 e.s.d units (99% confidence level) or greater. Here, the differences between bond lengths are such that the significance of the change in the C(3)–N(2) bond (0.011 Å) falls into the 95% confidence interval, while the significance of the changes in the N(1)–C(2), C(2)–C(3), N(2)–C(4), and C(4)–C(5) bonds (0.013–0.021 Å) all fall into the 99% confidence interval. In APSO-PMC-I, the bond lengths along the bridge [C(2)–C(3) = 1.427(2) Å, C(3)–N(2) = 1.326(2) Å, and N(2)–C(4) = 1.346(2) Å] fall between those expected for a quinoidal form (**A**) and a zwitterionic form (**B**), though lean closer to those expected for the zwitterionic form. In contrast, the corresponding bond lengths in APSO-PMC-II [C(2)–C(3) = 1.448(5) Å, C(3)–N(2) = 1.315(5) Å, and N(2)–C(4) = 1.359(5) Å] exhibit the same bond-length alternation pattern, but with a shifting of bond lengths toward those expected for the zwitterionic resonance form by 0.011–0.021 Å, which suggests that APSO-PMC-II has more zwitterionic character. Additionally, a decrease in length of the adjacent C(4)–C(5) bond by 0.019 Å is observed in APSO-PMC-II relative to APSO-PMC-I, as expected with a shift to a more zwitterionic structure. In both molecules, the C(5)–O(1) bond length [1.249(2) Å for APSO-PMC-I and 1.245(5) Å for APSO-PMC-II] falls between those expected for a quinoidal C=O bond [1.222(13) Å][254] and a zwitterionic phenoxyl C–O bond [1.362(15) Å],[254] although it lies closer to that expected for the quinoidal bond. The short C(5)–O(1) bond length and the relatively long C(4)–C(5) bond length observed in APSO-PMC-I and APSO-PMC-II suggest that they possess contributions from the zwitterionic resonance form **C** in addition to **B**, in which a portion of the negative charge on the oxygen atom is delocalized onto the conjugated bridge and the C–O bond takes on greater quinoidal character (Scheme 2.5). This delocalization pattern has been noted in

several structurally characterized zwitterionic photomerocyanines[224, 227] and has been corroborated by theoretical predictions of electrostatic charge distributions.[226]

Scheme 2.5. Proposed resonance forms of APSO-PMC.

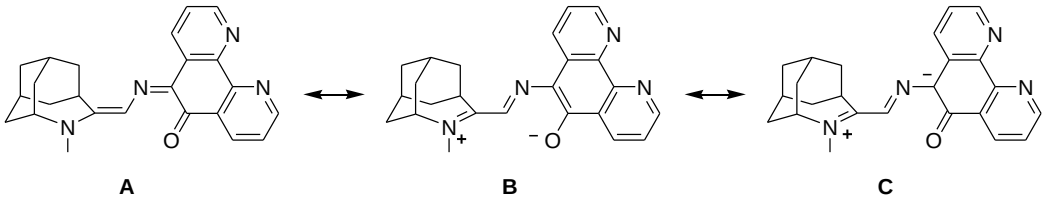

The torsional angles α, β, and γ [α = N(1)–C(2)–C(3)–N(2), β = C(2)–C(3)–N(2)–C(4), and γ = C(3)–N(2)–C(4)–C(5); Figure 2.4] relevant to the *cisoid* or *transoid* character about the azomethine bridge are tabulated in Table 2.2 for the APSO-PMC structures. These angles deviate slightly from those expected for a fully planar *trans-trans-cis* (or 'TTC') configuration (180°, 180°, and 0°), which suggests that this isomer is the most stable in the solid state, consistent with results observed for similar molecules.[227, 232, 233] The total deviation from planarity, as determined by the sum of the deviation from 0º or 180° for each of the three angles, differs considerably between pseudopolymorphs I and II, which exhibit total deviations of 7.35°, and 26.03°, respectively.

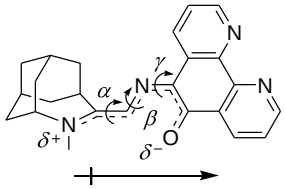

Figure 2.4. Torsional angles α, β, and γ about the azomethine bridge, as well as partial charges and total dipole moment, illustrated for APSO-PMC.

A comparison of the two pseudopolymorphs of APSO-PMC suggests that APSO-PMC-I has a greater contribution from the quinoidal resonance form **A** than does APSO-PMC-II, though both structures have more zwitterionic than quinoidal character overall. The differences between the pseudopolymorphs can be rationalized by a combination of intermolecular interactions and electronic effects. There is a correlation between the degree of twisting about the three partial double bonds of the central

azomethine bridge and the degree of charge separation in the solid-state PMC structures: APSO-PMC-II displays a greater deviation from planarity and a correspondingly greater degree of zwitterionic-like bond-length alternation than does APSO-PMC-I. Whether this twisting is sterically or electronically imposed is not clear, though hydrogen bonding to water solvate molecules in APSO-PMC-II may induce twisting about the central bridge. As regards possible electronic effects, each photomerocyanine has a large dipole moment directed along the long axis of the molecule (Figure 2.4), and the crystalline lattice itself can effectively act as a strong dielectric medium. The orientation of molecules in the highly ordered and unsolvated crystal of APSO-PMC-I facilitates charge compensation, a behaviour similar to that of typical merocyanine aggregates. The packing is such that the molecular dipole moments in relatively closely assembled head-to-tail dimeric PMC units compensate for one another, while relatively short interchain $N^{\delta+}\cdots O^{\delta-}$ contacts (4.49 Å) help to maintain additional local electrostatic neutrality. By contrast, in the crystalline lattice of APSO-PMC-II, the molecules are more disordered and more loosely packed (the unit cell volume for APSO-PMC-II is greater than that for APSO-PMC-I). It is therefore plausible that the crystalline lattice behaves as a stronger dielectric medium in APSO-PMC-II than in APSO-PMC-I. The presence of polar water molecules may also contribute to an increase in the effective dielectric of the lattice in APSO-PMC-II. The observation of different charge-separated character in the two pseudopolymorphs of APSO is a significant result, as it provides direct structural evidence for the shift in charge-separated character associated with environment in the crystalline state.

2.2.4. Solvatochromism and Vibrational Structure of the PMC π–π^* CT Band

The molecular structure of merocyanines can be probed indirectly by electronic absorption spectroscopy as a function of solvent polarity by analyzing either: (a) the relative geometries of the ground and excited states inferred from the relative intensities of the vibrational bands of the π–π^* CT electronic transition,[255, 256] or (b) the solvent-induced stabilization of the ground and excited states inferred from the shift in energy of the absorption band, i.e., its solvatochromism.[244] The inferred structural changes may be interpreted in the context of the relative contributions of the canonical quinoidal (**A**) and zwitterionic (**B**) resonance forms to the ground-state molecular structure (Scheme 2.1).[255]

Vibronic progressions are commonly observed in the π–π^* CT bands of merocyanines, where in addition to a $v = 0 \rightarrow v' = 0$ transition between the lowest vibrational levels of each electronic state, higher energy ($v = 0 \rightarrow v' = 1$, $v = 0 \rightarrow v' = 2$, etc.) transitions are evident as coarse band structure.[256-258] The major vibrational mode associated with the electronic transition in typical merocyanines is a C=C symmetric stretch, in which the C=C bonds are expected to lengthen in the excited state.[256] The spirooxazine-based photomerocyanines display an analogous vibronic progression in their electronic absorption spectra,[234, 259] presumably associated with similar symmetric modes involving the conjugated bridge. For a fully delocalized conjugated structure resulting from equal contributions of resonance forms **A** and **B**, small changes in geometry would be expected between ground and excited states, and the Franck–Condon overlap model dictates that the $v = 0 \rightarrow v' = 0$ transition should dominate the charge transfer band. For predominantly quinoidal (**A**) or zwitterionic (**B**) structures with localized bond alternation throughout the conjugated bridge, more significant differences in geometry are expected between the ground and excited states, and transitions to higher v' vibrational states should intensify relative to the $v = 0 \rightarrow v' = 0$ transition.

Because the π–π^* electronic transition in merocyanines displays charge transfer character, three types of solvatochromic behaviour can be delineated for a typical merocyanine dye:[260] (1) A merocyanine with a quinoidal (**A**) ground state should have a more dipolar excited state that displays greater stabilization in polar solvents; here, increasing solvent polarity is expected to lead to a bathochromic shift in λ_{max} (i.e., positive solvatochromism). (2) A merocyanine with a zwitterionic (**B**) ground state should have a more quinoidal excited state structure; here, the more dipolar ground state should exhibit greater stabilization in polar solvents, and increasing solvent polarity is expected to lead to a hypsochromic shift in λ_{max} (i.e., negative solvatochromism). (3) In a merocyanine with a hybrid ground-state structure possessing equal contributions from quinoidal and zwitterionic resonance forms **A** and **B**, the moderately dipolar ground and excited states should exhibit roughly equal stabilization in polar solvents, and no significant solvatochromism shift is expected with increasing solvent polarity.[244]

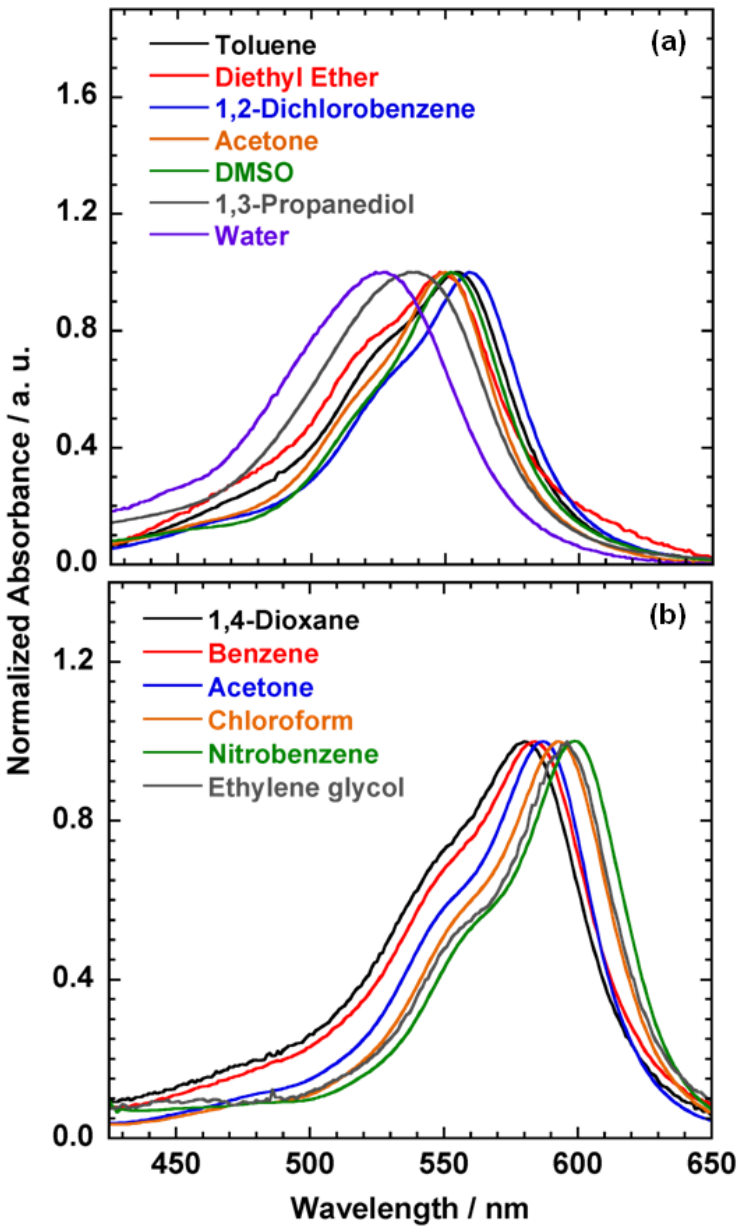

Figure 2.5. PMC π–π* absorption band shape at ~300 K for APSO (a) and IPSO (b) in a representative selection of solvents illustrating shifts in λ_{max} and changes in band structure with solvent.

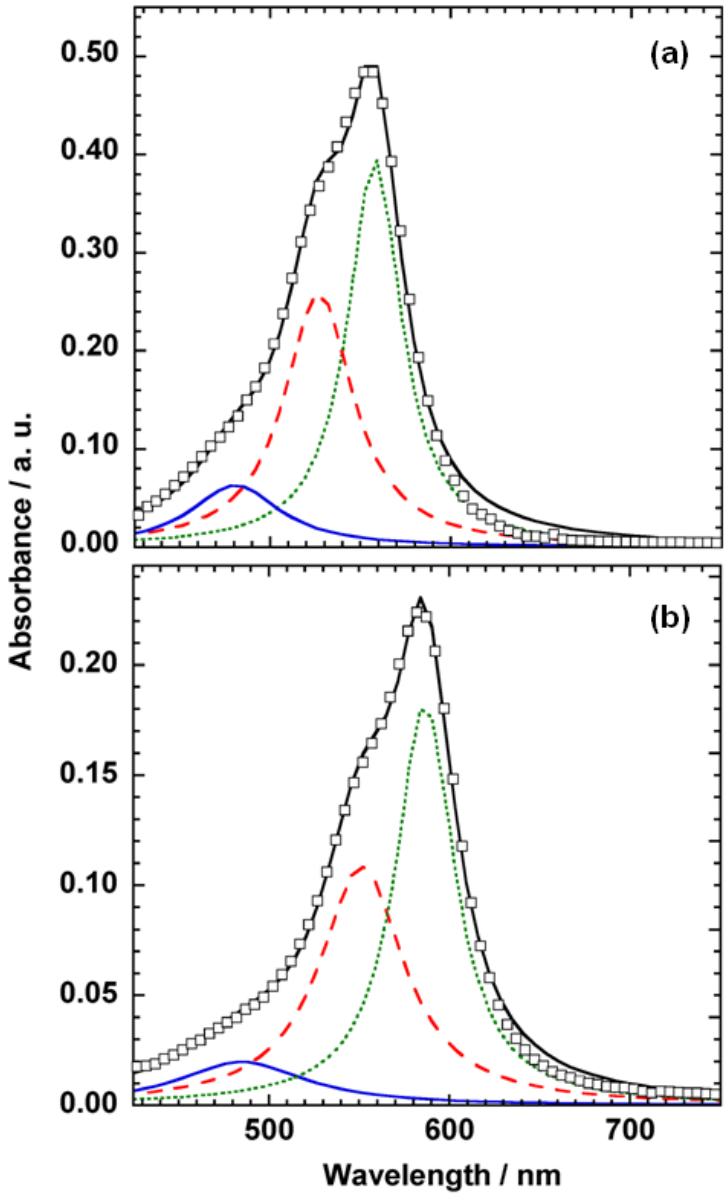

Figure 2.6. Lorentzian deconvolution [$\nu(1)$ ▪▪▪▪, $\nu(2)$ — —, $\nu(3)$ —] and sum of the deconvoluted peaks [—] of the raw PMC π–π* electronic absorption band [□] of APSO in toluene (a) and IPSO in benzene (b) at ~300 K.

Table 2.3. λ_{max} values and % peak areas for each of the three peaks obtained after Lorentzian deconvolution of the PMC π–π* electronic absorption band for APSO in a range of solvents.

Solvent	E_T^N	Expt. Peak	$\nu(1)$		$\nu(2)$		$\nu(3)$		R^2
		λ_{max} (nm)	λ_{max} (nm)	%Peak Area[a]	λ_{max} (nm)	%Peak Area[a]	λ_{max} (nm)	%Peak Area[a]	
Pentane	0.009	543							
Toluene	0.099	554	558	47	527	40	481	13	0.996
Et_2O	0.117	548	552	56	519	33	476	11	0.994
1,4-Dioxane	0.164	551	555	47	524	39	472	14	0.998
THF	0.207	553	555	53	524	37	476	10	0.994
1,2-Dichlorobenzene	0.225	559	562	55	530	38	472	7	0.995
EtOAc	0.228	550	553	54	522	37	477	9	0.993
CH_2Cl_2	0.309	554	557	53	526	39	456	8	0.997
Nitrobenzene	0.324	559	562	52	530	36	449	12	0.992
Acetone	0.355	550	552	57	521	36	461	7	0.994
DMSO	0.444	552	555	61	524	31	442	8	0.996
CH_3CN	0.460	547	549	58	519	35	447	7	0.996
Isopentyl Alcohol	0.565	553	554	64	523	31	441	5	0.994
1-Butanol	0.586	553	555	60	524	36	440	4	0.995
EtOH	0.654	550	552	59	522	35	437	6	0.994
1,3-Propanediol	0.747	537	547	40	517	48	449	12	0.994
MeOH	0.762	544	547	48	518	37	418	15	0.997
Ethylene glycol	0.790	543	547	53	518	42	426	5	0.992
H_2O	1	527	535	40	505	45	438	15	0.991

[a]Percent of total peak area of full experimental absorption band.

Table 2.4. λ_{max} values and % peak areas for each of the three peaks obtained after Lorentzian deconvolution of the PMC π–π* electronic absorption band for IPSO in a range of solvents.

Solvent	E_T^N	Expt. Peak	$\nu(1)$		$\nu(2)$		$\nu(3)$		R^2
		λ_{max} (nm)	λ_{max} (nm)	%Peak Area[a]	λ_{max} (nm)	%Peak Area[a]	λ_{max} (nm)	%Peak Area[a]	
Pentane	0.009	565							
Toluene	0.099	583	585	53	552	38	508	9	0.993
Benzene	0.111	584	586	48	551	41	485	11	0.998
Et_2O	0.117	575	578	35	545	35	458	30	0.995
1,4-Dioxane	0.164	580	583	45	548	42	479	13	0.995
THF	0.207	586	587	51	553	41	491	8	0.993
1,2-dichlorobenzene	0.225	593	595	55	559	40	490	5	0.990
EtOAc	0.228	582	584	55	549	38	490	7	0.989
$CHCl_3$	0.259	593	594	58	559	39	472	3	0.991
CH_2Cl_2	0.309	591	592	55	557	40	473	5	0.995
Nitrobenzene	0.324	599	600	58	563	36	453	6	0.988
Acetone	0.355	587	588	54	553	40	487	6	0.992
DMSO	0.444	597	598	61	561	37	473	2	0.990
Isopentyl Alcohol	0.565	596	597	60	561	39	463	1	0.986
1-Butanol	0.586	596	596	59	561	39	463	2	0.991
EtOH	0.654	593	594	60	559	37	458	3	0.989
1,3-Propanediol	0.747	597	598	59	561	37	432	4	0.986
MeOH	0.762	594	592	60	556	38	457	2	0.991
Ethylene glycol	0.790	596	596	56	559	35	443	9	0.997

[a]Percent of total peak area of full experimental absorption band.

The vibrational structure and solvatochromism of the PMC π–π^* CT band of APSO and IPSO were examined in a series of 22 solvents. The features of the absorption bands were correlated with the Dimroth–Reichardt $E_T(30)$ solvent polarity scale,[261] based on the negative solvatochromism of a pyridinium *N*-phenolate betaine dye, which takes into account solvation effects arising from both nonspecific (e.g., dipole–dipole, induced dipole–induced dipole, etc.) and specific (e.g., hydrogen bonding) interactions. This scale has been used often to study the solvatochromism of photomerocyanines and has been found to show reasonable correlations.[230, 243] The Dimroth–Reichardt scale can be conveniently applied using the normalized E_T^N scale, which sets the extreme polarity limits based on tetramethylsilane at 0.000 and H_2O to 1.000.

PMC π–π^* absorption bands are shown in a selection of solvents in Figure 2.5. All of the derivatives display a shoulder on the high-energy side of the absorption band as well as a third less prominent feature at even higher energies. Changes in both band shape (i.e., vibrational structure) and energy are evident as a function of solvent polarity. To more accurately analyze these changes, the absorption bands were deconvoluted into three peaks using Lorentzian functions (Figure 2.6, Table 2.3, Table 2.4). In accordance with the spectroscopic features of typical merocyanines, the low-energy band, $\nu(1)$, can be assigned to the $\nu = 0 \rightarrow \nu' = 0$ transition, the mid-energy band, $\nu(2)$, can be assigned to the $\nu = 0 \rightarrow \nu' = 1$ transition, and the high-energy band, $\nu(3)$, can be assigned to the $\nu = 0 \rightarrow \nu' = 2$ transition. Trends are evident in both the relative peak areas and λ_{max} values for the three peaks as a function of solvent, despite a fairly high degree of scattering arising from the complex solute–solvent interactions.

The relative peak areas of $\nu(1)$, $\nu(2)$, and $\nu(3)$ for APSO and IPSO are compared in Figure 2.7 as a function of solvent. The data were fit by locally weighted least-squares regression methods to highlight trends.[262] It is evident that for APSO, the relative peak area of $\nu(1)$ increases as a function of solvent polarity until $E_T^N \approx 0.5$ before decreasing in higher polarity solvents, while the relative peak areas for $\nu(2)$ and $\nu(3)$ exhibit the opposite behaviour [Figure 2.7(a)]. This is consistent with the ground- and excited-state molecular structures being most similar in moderate polarity solvents when the $\nu = 0 \rightarrow \nu' = 0$ transition has the highest intensity. A more quinoidal structure is expected in lower polarity solvents, and a more zwitterionic structure is expected in higher polarity

solvents. In contrast, for IPSO, the relative peak area of $\nu(1)$ increases as a function of solvent until $E_T^N \approx 0.5$ before essentially leveling off, with $\nu(2)$ and $\nu(3)$ again exhibiting the opposite behaviour [Figure 2.7(b)]. This is consistent with the existence of a quinoidal structure in low polarity solvents, and a hybrid **A**/**B** structure in moderate- to high-polarity solvents.

The λ_{max} values of $\nu(1)$, $\nu(2)$, and $\nu(3)$ for APSO and IPSO are compared in Figure 2.8 as a function of solvent, with the data again fit by locally weighted least-squares regression methods.[262] For both the $\nu(1)$ and $\nu(2)$ bands, APSO exhibits weakly positive solvatochromism at low (<0.3) E_T^N values and negative solvatochromism at higher (>0.3) E_T^N values [Figure 2.8(a)], which suggests that its ground-state structure progresses from quinoidal to zwitterionic in character. In contrast, IPSO exhibits more pronounced positive solvatochromism in solvents with low (<0.4) E_T^N values and relatively weak or no solvatochromism in solvents with higher (>0.4) E_T^N values [Figure 2.8(b)]. This behaviour suggests that the ground-state structure of IPSO progresses from predominantly quinoidal in character to a hybrid **A**/**B** form with increasing solvent polarity. The positive solvatochromism observed for IPSO in solvents with low to moderate E_T^N values is consistent with the observations previously reported by Pozzo et al.,[236] although the authors did not previously highlight the absence of a solvatochromic shift at higher E_T^N values. For both APSO and IPSO, the solvatochromism of the experimental PMC π–π^* absorption band mirrors that of both the deconvoluted $\nu(1)$ and $\nu(2)$ bands; however, the deconvoluted $\nu(3)$ band exhibits negative solvatochromism over the full range of solvent polarities. This observation can be rationalized by the possibility of different solvatochromic responses for different vibrational bands, as has been experimentally demonstrated by Würthner et al., who associated the effect with a change in molecular dipole of a given vibrational level in the excited state.[258] However, if this interpretation is correct, it begs the question of how the behaviour of each vibrational band ultimately corresponds to the molecular structure of the merocyanine.

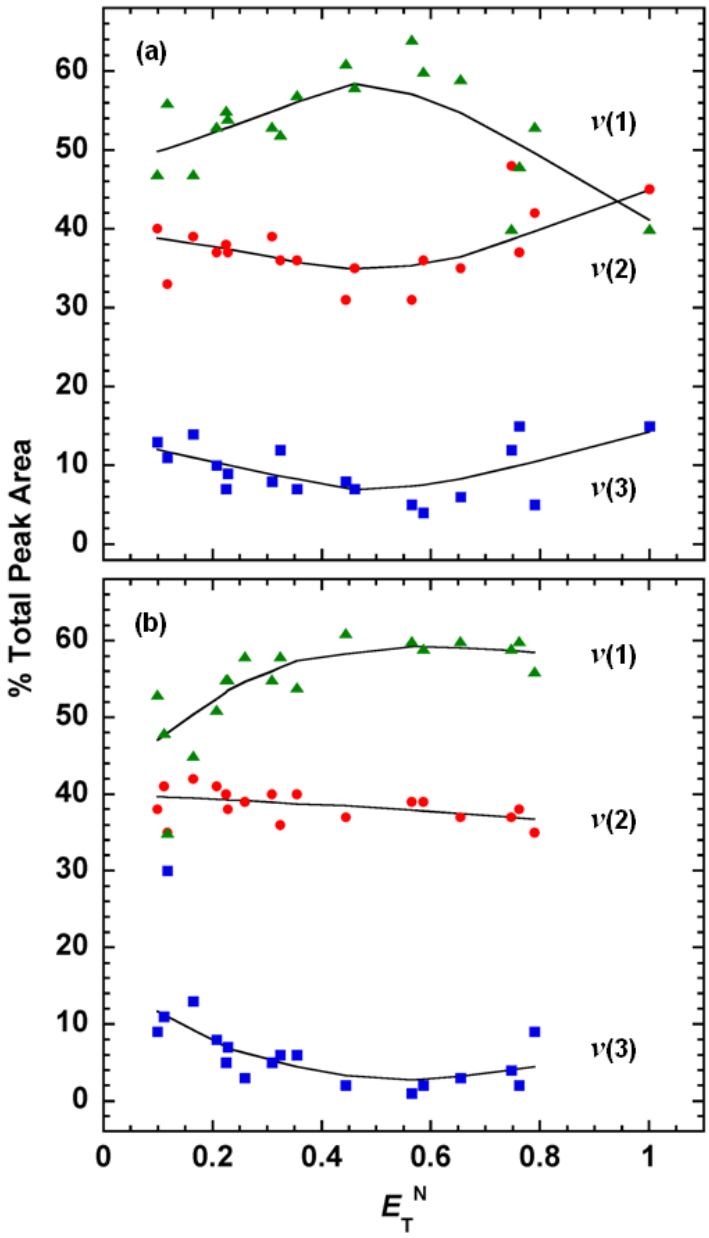

Figure 2.7. Relative peak areas of the three Lorentzian deconvolution peaks of the PMC π–π^* absorption band, $\nu(1)$, $\nu(2)$, and $\nu(3)$, for APSO (a) and IPSO (b) as a function of the Dimroth–Reichardt E_T^N solvent polarity scale at ~300 K (shown as the percent of the total peak area of the sum of the deconvoluted peaks and fit with locally weighted least-squares regression methods to highlight trends).

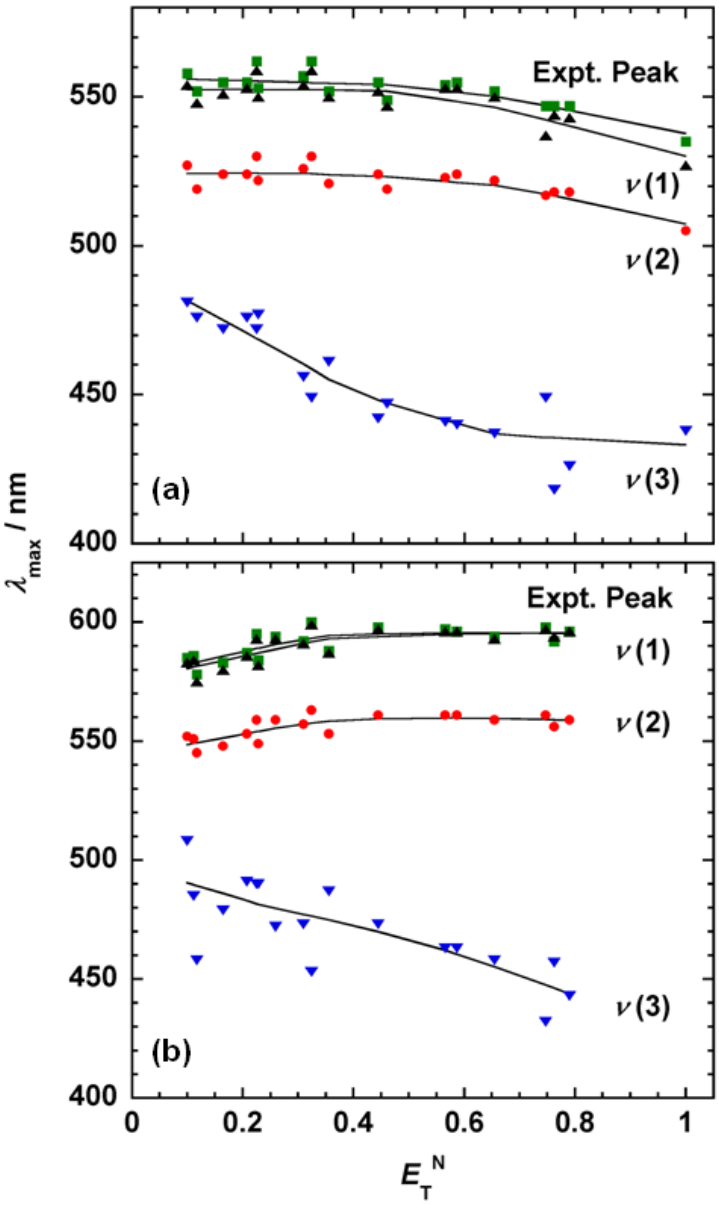

Figure 2.8. λ_{max} values of the experimental PMC π–π^* absorption band and Lorentzian deconvolution peaks, $\nu(1)$, $\nu(2)$, and $\nu(3)$, of APSO (a) and IPSO (b) as a function of the Dimroth–Reichardt E_T^N solvent polarity scale at ~300 K (fit with locally weighted least-squares regression methods to highlight trends).

It is of interest that the qualitative reversal in behaviour of the vibrational band intensity profile and solvatochromism as a function of solvent occurs at different solvent polarities, where the former is observed at slightly higher polarities. This observation is consistent with studies by Hiramatsu et al., who observed a similar effect and posited that the reversal of the vibrational band intensity profile behaviour may be a more accurate indicator of the polarity at which the limiting structure possessing equal contributions of quinoidal and zwitterionic resonance character exists.[255] However, in their case, negative solvatochromism was not observed even in high polarity solvents as it was for the molecules described here, and our data may underscore the fact that molecular structure may still be inferred from solvatochromic behaviour, with the caveat that the limiting **A**/**B** form exists at slightly higher polarities than predicted by the solvatochromic reversal. This is supported by theoretical work by Botrel et al., who showed that the limiting **A**/**B** form exists at slightly higher polarities than indicated by the solvatochromic data.[260]

Debate has arisen in the literature with regard to the correlation of solvatochromism or vibrational band structure with molecular structure. Several authors have proposed alternative explanations for the experimentally observed solvatochromic behaviours of merocyanines, including interactions between permanent solute dipoles and induced solvent dipoles,[255] as well as solvent-induced changes in molecular aggregation,[263] vibrational structure,[257] or distribution of *cis*/*trans* isomers in solution.[264] Theoretical studies, however, have correlated the experimentally observed solvatochromic effects with molecular structure. Calculations at various levels of theory predict significant changes in molecular structure and dipole moment upon increasing the dielectric constant of the surrounding medium, which indicates a clear transition from greater quinoidal character in the gas phase or nonpolar solvents to greater charge-separated zwitterionic character in polar solvents.[245, 260, 265-268] Recent electro-optical absorption studies have confirmed that such structural changes in polar solvents are indeed caused by solvent-induced polarization effects.[258]

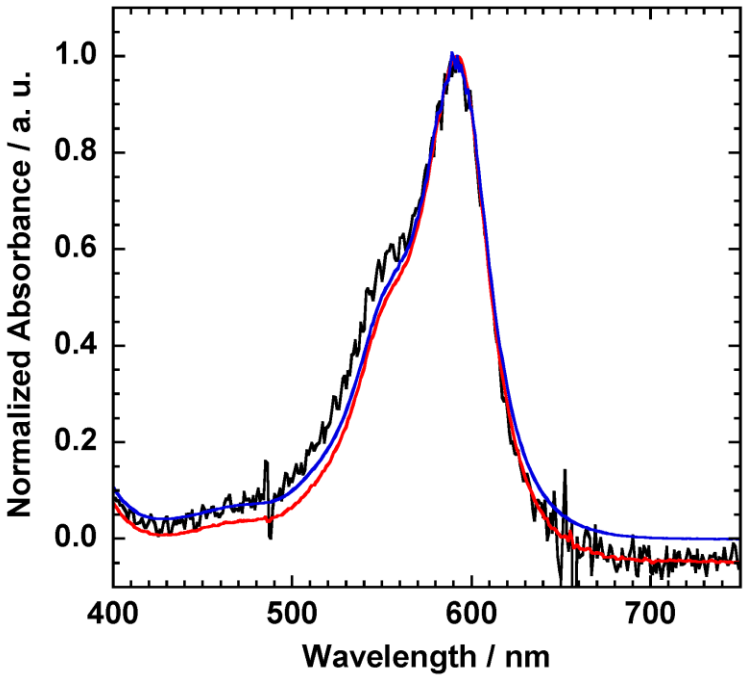

Figure 2.9. Shape and energy of the PMC CT band of IPSO in MeOH at ~300 K in solution concentrations spanning three orders of magnitude [4×10^{-6} M (—), 5×10^{-5} M (—), and 5×10^{-4} M (—)].

It is unlikely that aggregation effects play a role in the observed spectral shifts of IPSO and APSO as their π–π* transitions obey the Beer-Lambert law in both nonpolar and polar solvents, and no change in the appearance of their absorption bands is observed over a concentration range spanning several orders of magnitude (e.g., Figure 2.9). The occurrence of solute–solvent hydrogen bonding interactions in APSO in strong hydrogen-bond donating solvents is possible. We did not attempt to quantify the contributions of specific and non-specific interactions to PMC solvation, though we expect that both polarization and H-bonding effects play comparable solvating roles in the high-E_T^N-value solvents, as has been found for similar systems.[243, 261, 267, 269] Because there is no obvious steric reason for which the indolyl derivatives would not exhibit the same H-bonding effects as the azahomoadamantyl derivatives, this may suggest that solvation through H-bonding serves to stabilize the charge-separated character of molecules which have an intrinsically more stable zwitterionic structure rather than inducing a more zwitterionic structure through H-bonding interactions alone.

In summary, the degree of quinoidal or zwitterionic character of the PMC isomers in solution was found to dominate the observed behaviour of the PMC π–π* CT band with solvent polarity for the investigated spiroooxazines. The azahomoadamantyl derivative, APSO, clearly exhibits a reversal of the vibrational band intensity profile and a transition to negative solvatochromism in high polarity solvents, features that are absent in the analogous indolyl derivative, IPSO. This suggests that the two families of spirooxazines possess fundamentally different ground-state molecular structures with different relative degrees of quinoidal or zwitterionic character in a given medium. While APSO progresses from slightly quinoidal to zwitterionic in character with increasing solvent polarity, IPSO progresses from quinoidal in character to a hybrid **A**/**B** form. Each spirooxazine therefore possesses a unique solvent-dependent range of accessible charge-separated structures.

2.2.5. Experimental and Computational ^{1}H and ^{13}C NMR Studies

^{1}H and ^{13}C NMR studies were performed on APSO and IPSO to obtain additional spectroscopic insight into the PMC molecular structure with regard to both the relative changes in PMC structure as a function of solvent polarity and the absolute structures of APSO and IPSO [i.e., whether they exhibit more quinoidal (**A**) or zwitterionic (**B**) character]. To address the first point, NMR spectra of the spirooxazines were obtained in a range of solvents of different polarities. Solvent-dependent NMR studies on IPSO have been previously reported by Pozzo et al.,[236] although here the authors used a more limited series of solvents. Limited success has been achieved in unambiguously correlating ^{1}H or ^{13}C NMR shifts to solvent-induced structural changes of merocyanines.[236, 260, 267] Difficulties arise in distinguishing changes in chemical shifts originating from solvent-induced changes to electronic structure from specific solvent contributions to NMR shifts. Typical studies of merocyanines have demonstrated small changes in NMR shifts as a function of solvent that are not clearly correlated with solvent polarity.[236, 260, 267] Better success has been achieved in correlating solvent-dependent structural trends with chemical shifts and especially J_{HH} coupling constants for merocyanines with extended polymethine chains.[256, 270] Unfortunately, these J_{HH} coupling constants cannot be measured for spirooxazine-based PMCs as they lack adjacent CH groups in the

conjugated bridge. Because of the potentially ambiguous interpretations of the NMR chemical shifts, two approaches were taken to investigate potential changes in molecular structure with solvent polarity. First, the solvent-induced shifts for specific proton resonances of the PMC form were compared to the shifts observed for the same resonances in the SO form. As the structure of the SO form does not contain contributions from multiple resonance forms, its chemical shifts should roughly approximate specific solvent effects, although these are still expected to vary as a function of structure. Second, experimental NMR shifts were compared to theoretical shifts, calculated for model quinoidal (**A**) and zwitterionic (**B**) geometries of the PMCs as a function of solvent, in order to more accurately predict chemical shifts of the canonical resonance forms at their structural limits. The comparison of the experimental and theoretical shifts was also expected to be useful in determining the absolute structures of the photomerocyanines in solution.

Table 2.5. Theoretical ^{1}H and ^{13}C NMR shifts of model canonical quinoidal (**A**) and zwitterionic (**B**) forms of APSO-PMC and IPSO-PMC in toluene, $CHCl_3$, and DMSO calculated using the GIAO method at the DFT/B3LYP/6-31G(d,p) level of theory with the IEFPCM solvation model as implemented in Gaussian 03.[a]

APSO-PMC											
		H-1		**H-3**		**C-2**		**C-3**		**C-5**	
Solvent	E_T^N	**A**	**B**	**A**	**B**	**A**	**B**	**A**	**B**	**A**	**B**
Toluene	0.099	2.79	3.04	9.31	10.87	162.1	177.0	114.3	124.6	169.4	185.3
$CHCl_3$	0.259	2.97	3.27	9.50	11.08	166.4	181.4	117.6	128.5	172.0	186.6
DMSO	0.444	2.94	3.26	9.46	11.04	167.9	182.7	118.0	129.6	171.7	184.6
IPSO-PMC											
		H-1		**H-3**		**C-2**		**C-3**		**C-5**	
Solvent	E_T^N	**A**	**B**	**A**	**B**	**A**	**B**	**A**	**B**	**A**	**B**
Toluene	0.099	2.91	3.22	9.90	11.34	162.0	176.1	114.3	125.2	170.5	184.4
$CHCl_3$	0.259	3.14	3.47	10.09	11.55	165.8	179.9	117.4	128.8	173.3	185.6
DMSO	0.444	3.13	3.49	10.04	11.50	166.8	180.6	117.7	129.6	173.0	183.4

[a]See Scheme 2.6 for atom numbering; protons are numbered according to the carbon atoms to which they are attached.

Scheme 2.6. Atom numbering scheme for APSO.

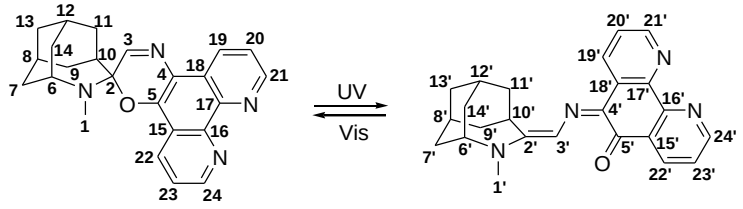

28 **28'**

Calculated NMR shifts have been known to reproduce experimental shifts with high accuracies.[271] Theoretical NMR shifts of model quinoidal and zwitterionic geometries of IPSO-PMC and APSO-PMC were calculated using the GIAO method at the DFT/B3LYP level of theory with the 6-31G(d,p) basis set and the IEFPCM solvation model in toluene, $CHCl_3$, and DMSO as implemented in Gaussian 03 (see Experimental Section for details). Data for the ^1H and ^{13}C signals which exhibit the greatest differences in chemical shift between theoretical limiting resonance forms are tabulated in Table 2.5. When going from a model quinoidal to a model zwitterionic form, significant downfield shifts of ~0.3 and ~1.5 ppm are predicted for the *N*-methyl (H-1) and azomethine (H-3) proton resonances, respectively, and significant downfield shifts of 10–15 ppm are predicted for the C-2, C-3, and C-5 ^{13}C resonances (see Scheme 2.6 for atom numbering; protons are numbered according to the carbon atoms to which they are attached). Slight downfield shifts (0.2–0.3 ppm for ^1H shifts, 1–4 ppm for ^{13}C shifts) are also predicted for each resonance form upon going from toluene to $CHCl_3$, while negligible or very slightly upfield shifts are predicted upon going from $CHCl_3$ to DMSO.

Experimental ^1H NMR spectra were obtained for APSO and IPSO in eight solvents ranging in polarity from toluene-*d*8 to CD_3OD, and ^{13}C NMR spectra were obtained in toluene-*d*8, THF-*d*8, $CDCl_3$, and DMSO-*d*6, although not all of the peaks of interest could be identified in each case. The experimental chemical shifts for the H-1 and H-3 signals of the SO forms and the H-1, H-3, C-2, C-3, and C-5 signals for the PMC forms are tabulated in Table 2.6. Changes in chemical shifts intrinsic to specific solvation effects are evident from the shifts of the H-1 and H-3 signals for the SO forms, which are not expected to exhibit significant resonance-based structural changes as a function of solvent polarity. These changes of 0.2–0.4 ppm are on the order of those predicted

computationally for the SO forms. For the 1-H resonance of both APSO-PMC and IPSO-PMC, a significant downfield shift from ~2.7 ppm in toluene-d_8/benzene-d_6 ($E_T^N \approx$ 0.1) to ~3.6 ppm in solvents ranging from THF-d_8 to methanol-d_4 ($E_T^N \approx$ 0.2–0.8) is observed. As this shift is greater than that expected due to solvent effects alone (0.3–0.4 ppm for the SO forms), this may indicate a change in molecular structure upon going from very low to moderate/high polarity solvents. However, because the shifts do not show a clear correlation with solvent polarity (i.e., after a large jump in chemical shift from toluene-d_8 to THF-d_8, the shift does not change over the polarity range spanning THF-d_8 through CD_3OD), this might instead be explained by specific solvation effects (or lack thereof) in aromatic hydrocarbons. In contrast, the H-3 signal does not shift significantly with solvent polarity for the PMC form of either APSO or IPSO, even though a large change is predicted computationally. As for the ^{13}C shifts, the C-3 and C-5 resonances shift downfield by ~4 ppm when going from toluene-d_8 to DMSO-d_6; however, the C-2 resonances shift upfield by ~4 ppm. The C-3 and C-5 shifts could be indicative of a shift to more zwitterionic character, as supported computationally, but the C-2 shift would indicate the opposite effect.

The comparison of experimental shifts to theoretical shifts may be useful in estimating absolute structures of APSO-PMC and IPSO-PMC in solution. In both compounds, the H-1 ^1H NMR resonance is more upfield than that predicted for the quinoidal form (**A**) in low polarity solvents (toluene/benzene) and more downfield than that predicted for the zwitterionic form (**B**) in high polarity solvents (>THF). This may corroborate the evolution of the PMCs from quinoidal to zwitterionic structures with increasing solvent polarity. A comparison of the experimental and calculated H-3 shifts for APSO-PMC suggests that its structure can be approximated by nearly equal contributions of resonance forms **A** and **B**, while this same comparison for IPSO-PMC suggests that its structure lies closer to that of the quinoidal form **A**. A comparison of the experimental and calculated shifts for C-3 and C-5 predict that the structures for APSO-PMC and IPSO-PMC fall between those of the limiting forms **A** and **B**, with slightly more zwitterionic character overall and more zwitterionic character for APSO-PMC. The C-2 shift predicts a significantly zwitterionic structure for both molecules. Caution in the interpretation of the absolute theoretical chemical shifts is necessary as the geometries used for the

calculations were not optimized and may not be minima on the potential energy surface. Additionally, structural effects such as the free rotation of methyl groups and specific solvent effects are not accounted for by the computations.

Table 2.6. ^{1}H and ^{13}C NMR shifts of the SO and PMC forms of APSO and IPSO in a selection of solvents at ~300 K[a]

		APSO-SO		APSO-PMC				
Solvent	E_T^N	**H-1**	**H-3**	**H-1**	**H-3**	**C-2**	**C-3**	**C-5**
Toluene-d_8	0.099	2.21	7.53	2.69	10.07	176.1	123.5	176.9
Benzene-d_6	0.111	2.20	7.59	2.61	10.20			
THF-d_8	0.207	2.49	7.75	3.5	10.03	175.4	125.8	179.3
$CDCl_3$	0.259	2.48	7.71	3.51	9.98	174.6	126.2	179.8
CD_2Cl_2	0.309	2.48	7.73	3.52	10.03			
Acetone-d_6	0.355	2.50	7.81	3.58	10.11			
DMSO-d_6	0.444	2.40	7.85	3.54	10.14	172.0	127.3	180.3
CD_3CN	0.460	2.44	7.75	3.51	10.12			
CD_3OD	0.762	2.45	7.75	3.62	10.16			
		IPSO-SO		**IPSO-PMC**				
Solvent	E_T^N	**H-1**	**H-3**	**H-1**	**H-3**	**C-2**	**C-3**	**C-5**
Toluene-d_8	0.099	2.40	7.57	2.74	10.03			
Benzene-d_6	0.111	2.38	7.60	2.62	10.10			
THF-d_8	0.207	2.78	7.93	3.66	10.05	174.6		177.8
$CDCl_3$	0.259	2.76	7.83	3.65	10.01	174.5	122.5	177.4
CD_2Cl_2	0.309	2.78	7.87	3.70	10.06			
Acetone-d_6	0.355	2.80	7.99	3.75	10.10			
DMSO-d_6	0.444	2.71	8.03	3.72	10.08		122.3	
CD_3CN	0.460	2.74	7.91	3.64	10.06			
CD_3OD	0.762	2.76	7.95	3.80	10.14			

[a]See Scheme 2.6 for atom numbering; protons are numbered according to the carbon atoms to which they are attached.

In summary, the NMR results do not emphatically support the change in molecular structure with solvent polarity suggested by the solvent-dependent UV/Vis electronic absorption spectroscopy studies. This is not surprising considering the lack of success for

similar studies reported in the literature.[236, 260, 267] However, the results do provide some evidence that the absolute structure of APSO-PMC is more zwitterionic than that of IPSO-PMC, as inferred from the UV/Vis spectroscopic studies. Barring the misinterpretation of the electronic absorption spectroscopy as it relates to the ground-state molecular structure of merocyanines, the discrepancies between the results may be attributed to strong specific solvation effects contributing to NMR shifts that cannot easily be deconvoluted from effects contributing to changes in molecular geometry.

2.2.6. DFT Geometry Optimization Calculations

Geometry optimization calculations for the PMC forms of APSO and IPSO were performed at the DFT/B3LYP level of theory with the 6-31G(d,p) basis set using the Gaussian 03 suite of software,[272] and selected geometric parameters are summarized in Table 2.7. The DFT/B3LYP level of theory has been found to reproduce the experimental geometries of many organic molecules with reasonable accuracies while using a practical level of computational resources,[273, 274] and this treatment has been used by several authors in the study of spiropyran and spirooxazine systems.[240, 275, 276] Additional calculations with the 6-31+G(d,p), 6-311G(d,p), and 6-311+G(d,p) basis sets were performed on APSO-PMC (Table 2.8); however, larger basis sets did not significantly affect the optimized geometries (variations in bond lengths were ≤0.005 Å), which is consistent with previous computational studies.[240, 275] For the PMC forms of APSO and IPSO, geometry optimizations were also performed in toluene (ε = 2.379), DMSO (ε = 46.7), and water (ε = 78.39) using the Onsager model, a treatment which places the molecule of interest within a spherical solvent cavity, where the solvent is treated as a uniform dielectric material. The results obtained in water were nearly identical to those obtained in DMSO, and therefore only the results obtained for DMSO are tabulated.

For APSO, the optimized bond lengths in the bridge [C(2)–C(3), C(3)–N(2), and N(2)–C(4)] lie nearly exactly between those expected for resonance forms **A** and **B**, which would indicate approximately equal contributions from the two forms. This result is consistent with previous calculations on spirooxazines.[275] The optimized bond lengths for the C(1)–N(1), N(1)–C(2), and C(4)–C(5) bonds are within 0.005 Å of those expected for the quinoidal resonance form **A** (Table 2.2). The predicted C(5)–O(1) bond length of

1.241 Å is only slightly longer than a quinoidal C=O double bond (1.221 Å),[254] but is significantly shorter than a C–O single bond (1.362 Å).[254] For IPSO, the C(1)–N(1) and N(1)–C(2) bond lengths are predicted to be shorter and longer, respectively, than those expected for resonance form **A**. Of the remaining bond lengths, all are within 0.005 Å of those obtained for APSO-PMC except for the C(2)–C(3) bond length, which is 0.018 Å shorter. This result indicates that the DFT-optimized geometries are quite similar for both the indolyl and azahomoadamantyl derivatives as regards the structure of the central bridge. However, the deviations observed—particularly for the C(2)–C(3) bond—suggest that the structure for IPSO has a slightly greater contribution from the quinoidal resonance form **A**. For all of the molecules, the optimized dihedral angles α, β, and γ are very close to 180º, 180º, and 0º, respectively, with the total deviation from planarity for the three angles not exceeding 2º. DFT calculations thus predict a highly planar structure relative to the experimental structures, consistent with the tendency of DFT to favour delocalized geometries and its inability to take into account possible intermolecular packing interactions.

Optimization of the geometries in solvents with varying dielectric constants using the Onsager model has a significant effect on the resulting structure. In both APSO and IPSO, the N(1)–C(2), C(2)–C(3), C(3)–N(2), N(2)–C(4), and C(4)–C(5) bond lengths change by 0.002–0.006 Å in toluene and 0.010–0.020 Å in DMSO relative to those predicted in the gas phase, in each case becoming closer to those expected for the zwitterionic resonance form **A**. The calculated C(5)–O(1) bond length, however, was found to be only 0.001 and 0.003 Å longer in toluene and DMSO, respectively.

The calculations predict large dipole moments along the long axis of the molecule for the PMC forms. The total dipole moments were calculated to be 9.20 and 7.15 D for APSO and IPSO, respectively, with the major contribution being along the *x* axis (long axis). The predicted dipole moment increases significantly for calculations performed in higher dielectric media: for APSO, the calculated total dipole moment increases to 11.71 and 16.35 D in toluene and DMSO, respectively, and for IPSO, it similarly increases to 10.14 and 18.37 D in toluene and DMSO, respectively. The calculations therefore suggest an increase in charge-separated character with increasing medium polarity.

Table 2.7. Selected geometric parameters (bond lengths [Å] and angles [°]) and dipole moments [D] calculated at the DFT/B3LYP level with the 6-31G(d,p) basis set for APSO-PMC and IPSO-PMC without solvation and with solvation using the Onsager model.

	APSO-PMC				IPSO-PMC		
	Gas	**Toluene**	**DMSO**	**Expt.**[a]	**Gas**	**Toluene**	**DMSO**
ε	0	2.379	46.7	-	0	2.379	46.7
C(1)–N(1)	1.467	1.469	1.472	1.478(5)	1.454	1.455	1.460
N(1)–C(2)	1.358	1.353	1.343	1.327(2)	1.369	1.363	1.348
C(2)–C(3)	1.403	1.409	1.422	1.427(2)	1.385	1.391	1.409
C(3)–N(2)	1.346	1.341	1.331	1.326(2)	1.351	1.345	1.331
N(2)–C(4)	1.322	1.326	1.335	1.346(2)	1.320	1.324	1.339
C(4)–C(5)	1.480	1.474	1.464	1.442(2)	1.484	1.478	1.462
C(5)–O(1)	1.241	1.242	1.244	1.249(2)	1.239	1.240	1.245
α	–179.20	–179.16	–179.04	179.2	–179.97	–179.98	–179.98
β	–179.19	–179.30	–179.53	–174.9	179.99	179.99	179.99
γ	0.18	0.14	0	–1.5	–0.01	0.01	–0.00
Dipole (*x*)	9.0405	11.5458	16.1694		7.00	10.0077	18.2626
Dipole (*y*)	1.68	1.98	2.44		1.43	1.66	2.01
Dipole (*z*)	0.0062	0.019	0.041		0.0008	0.0009	0.0009

[a]The experimental geometry for APSO-PMC-I was arbitrarily chosen for comparison.

Calculated and experimental bond lengths differ significantly for APSO-PMC. Calculated bond lengths in the conjugated azomethine bridge deviate by 0.03–0.05 Å from experiment, whereas those in the azahomoadamantyl and phenanthroline groups deviate by 0.01–0.02 Å. The differences between the calculated and experimental bond lengths for the azomethine bridge are greater than the experimental error for crystallographic analysis (the e.s.d.'s for the XRD measurements range from 0.002 to 0.007 Å). Deviations of 0.03–0.05 Å are quite significant when one considers that the canonical quinoidal and zwitterionic resonance forms differ only by bond lengths on the order of 0.05–0.10 Å. Importantly, the calculations consistently underestimate the contribution from the zwitterionic resonance form. Furthermore, the DFT-optimized structures possess nearly completely planar bridges (i.e., the α, β, and, γ dihedral angles are $\approx$ 0 or 180°), which does not accurately reflect the slight twisting observed in the

crystal structures. From the calculations alone, one would predict a higher contribution from the quinoidal resonance form relative to the zwitterionic form for APSO, which would be misleading in light of the crystallographic data.

Table 2.8. Selected geometric parameters (bond lengths [Å] and angles [°]) and dipole moments [D] calculated at the DFT/B3LYP level of theory with different basis sets for APSO-PMC.

	6-31G(d,p)	**6-31+G(d,p)**	**6-311G(d,p)**	**6-311+G(d,p)**
C(1)–N(1)	1.467	1.469	1.467	1.468
N(1)–C(2)	1.358	1.356	1.355	1.354
C(2)–C(3)	1.403	1.408	1.403	1.405
C(3)–N(2)	1.346	1.344	1.343	1.342
N(2)–C(4)	1.322	1.324	1.318	1.320
C(4)–C(5)	1.480	1.477	1.479	1.477
C(5)–O(1)	1.241	1.244	1.234	1.237
α	–179.20	–179.25	–179.34	–179.29
β	–179.19	–179.17	–179.00	–178.93
γ	0.18	0.24	0.31	0.39
Total dipole	9.1956	9.8986	9.3123	9.8140

Although we cannot compare the calculated geometry for IPSO with experimental structural data, we can analyze the computational results in the context of the solution-state electronic absorption spectroscopy studies of the PMC π–π* CT band. The relative behaviours of APSO and IPSO suggest that they possess fundamentally different electronic structures, and that the zwitterionic resonance contribution is more substantial in the azahomoadamantyl derivative. The DFT-optimized geometries for APSO and IPSO are, however, nearly the same in both the gas phase and more polar media, and therefore do not accurately reflect the differences in electronic structure suggested by the solvatochromism studies.

Both solid- and solution-state experiments suggest that the DFT/B3LYP level of theory does not accurately predict the geometries of metastable photomerocyanines. The deviation of the computational geometries from the experimental geometries can be understood on one hand within the context of the effects of molecular environments on

molecular geometries. The effect of solvents on solute molecules may be categorized into specific and nonspecific classes, in which nonspecific interactions arise from dispersion and electrostatic interactions between the charge distribution of the solute and solvent molecules. While electrostatic interactions between solute and solvent can be described by a dielectric continuum model such as that described by Onsager reaction field theory, the use of this model in the calculations, even in high dielectric solvents such as DMSO and H_2O, was not found to be sufficient to reproduce the experimental geometries of the PMC forms, most likely because of specific and nonspecific intermolecular interactions in the solid state. It is well-known that intermolecular interactions may cause the molecular geometries in the crystalline state to be quite different from those of the free molecules.[277, 278] On the other hand, inconsistencies between calculated and experimental geometries are not unexpected given the difficulties in reproducing ground states, excited states, charge-separated states, and donor–acceptor excitations of fully delocalized organic molecules by DFT methods.[279, 280] It is clear from the above discussion that DFT displays serious shortcomings in predicting absolute PMC structures as a function of substitution and medium. Discrepancies between calculated and experimental geometries are highly relevant to deriving structure–property relationships in PMCs, because even small changes in electronic structure—as manifested by small changes in molecular geometries—can have significant consequences on the photochromic properties of these materials.

2.2.7. Discussion of Substituent and Medium Effects on Spirooxazine Properties

Trends in the properties of spiropyrans and spirooxazines can be evaluated in terms of the substituents on the amine and oxazine functionalities.[110] Authors have discussed these trends in the context of ‘donor–acceptor’ effects, [240] ‘push–pull’ interactions,[241] or chemical hardness.[281] One of the trends that can be understood in this way is the relative contribution of the charge-separated zwitterionic resonance form to the PMC molecular structure. Because charge separation results in a greater distribution of positive charge at the amine moiety and of negative charge at the oxazine moiety, the presence of electron-withdrawing groups (EWGs) on the amine would be expected to destabilize the zwitterionic form, while their presence on the oxazine moiety would be expected to

stabilize it.[110, 240] Likewise, the chemical softness of a functional group might be expected to contribute to the ability of the PMCs to stabilize charge.[281] To date, all of the spiropyran or spirooxazine systems that have been found to exhibit zwitterionic character—as determined by XRD, spectroscopic, or computational studies—are indolyl-based and possess strong EWGs on the oxazine functionality. The substitution of EDGs on the amine does not have a strong enough effect to significantly stabilize the zwitterionic resonance form, at least as predicted by spectroscopic or computational studies (no such PMC derivatives have been structurally characterized).[110] The changes in the electronic structure of the PMC form resulting from the incorporation of the azahomoadamantyl group are apparently much more significant than those resulting from the substitution of EDGs on the amine moiety for typical indolyl derivatives. Whereas the stabilization of the zwitterionic resonance form is typically explained by the delocalization of negative charge onto an electron-withdrawing nitro or pyridinium substituent on the oxazine functionality, this is clearly not the case in the azahomoadamantyl derivatives, in which the zwitterionic form appears to be favoured through the stabilization of positive charge by the strongly electron-donating azahomoadamantyl group.

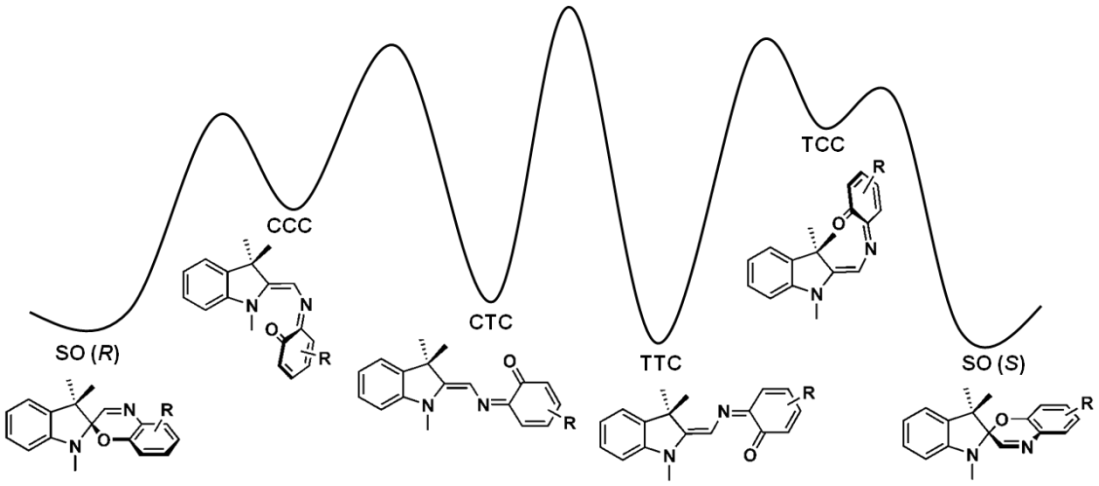

Figure 2.10. Representative ground-state potential energy surface for ring-opening and ring-closing SO/PMC thermal isomerization processes of spiro[indoline-benzoxazine] derivatives.

The mechanisms and rates of the photochemical and thermal isomerization processes in spirooxazines can be interpreted in the context of their chemical structure and

surrounding medium. An understanding of the ground-state potential energy surface (PES) is important for determining the rates of thermal isomerization that play a crucial role in determining the photochromic properties of spirooxazines.. The general consensus from recent computational work,[110, 240, 275, 276, 282] supported by experimental studies, is that SO → PMC isomerization proceeds via two steps: C–O bond cleavage to form a *cis* intermediate, followed by *cis*-to-*trans* isomerization to form a stable *trans* PMC isomer. Because the SO form may exist as two possible conformers (i.e., *R* and *S* enantiomers) and the PMC form can exist as four possible higher-energy *cis* isomers (i.e., CCC, CCT, TCT, and TCC isomers) and four possible lower-energy *trans* isomers (i.e., TTT, TTC, CTC, and CTT isomers), several SO → PMC or PMC → SO conversion pathways are accessible. Two of the more likely pathways are illustrated in Figure 2.10, where conversion from the *R* enantiomer of the SO form proceeds via a CCC intermediate to the stable CTC PMC isomer, and conversion from the *S* enantiomer of the SO form proceeds via a TCC intermediate to the stable TTC PMC isomer. Conversion between *trans* isomers is possible, although the activation energies for these processes are predicted to be higher than those for conversion to the appropriate *cis* isomers (by 5–10 kcal/mol).[240, 275]

Despite this being somewhat of a simplification, it is valuable to model photochromic trends in spirooxazines using this generalized two-step mechanism. The relative energies of the stable intermediates and activation energies for the thermal SO/PMC conversion depend on both chemical structure and medium. These effects have been described particularly well by Sheng et al.,[240] who underscore the two major geometric parameters that come into play. For the *cis*/*trans* isomerization step, the activation energy (E_a) barrier can be correlated to the bond order of the central C(3)–N(2) bond in the conjugated bridge (though it could also be a function of steric hindrance in the case of bulkier molecules).[231, 240, 275] Thus, a more zwitterionic structure with more double-bond character for the central bond would be expected to show more hindered bond rotation. The E_a for the C–O bond cleavage/formation step should be predominantly a function of the C_{spiro}–O bond length of the SO form.[240, 282] Interestingly, spirooxazines which have a more zwitterionic PMC form also tend to have longer C–O bond lengths,[218, 227] which suggests that these geometric parameters are interrelated and are both intimately tied to

chemical structure and medium. Ultimately, this PES model predicts that with stronger electron-donating or withdrawing substituents, or in higher polarity media, the E_a barrier for C–O bond cleavage decreases, while that for *cis*/*trans* isomerization increases. Sheng et al.[240] note that, for thermal SO → PMC isomerization, a switch in the rate-limiting step from the bond cleavage/formation step to the isomerization step can occur, which can lead to challenges in correlating trends in observed thermal isomerization rates to chemical substituents or solvent polarity.

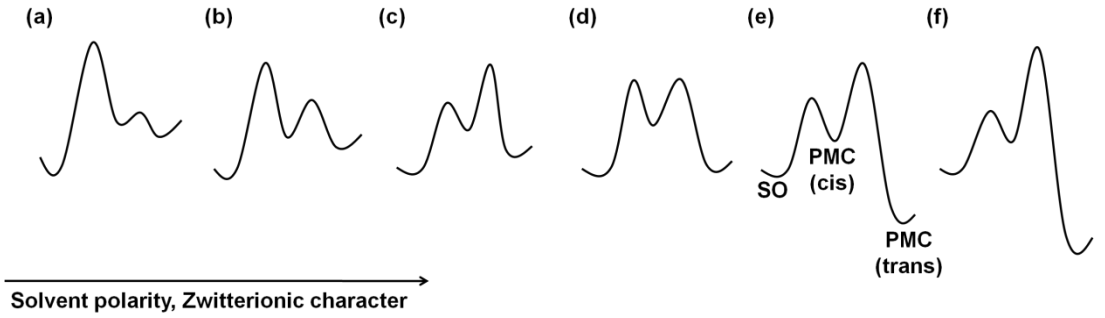

Figure 2.11. Proposed changes in ground-state potential energy surface for SO/PMC isomerization with chemical substitution or solvent polarity (changes are not necessarily to scale).

Insights into the ground-state PESs of IPSO and APSO, based on the two-step SO/PMC isomerization mechanism described above, can be extracted from the experimentally determined solvent-dependent thermal equilibrium constants and isomerization rate constants (Table 2.1). From XRD and electronic absorption studies, it was concluded that APSO and IPSO possess fundamentally different electronic structures, where APSO has more zwitterionic character overall. For both spirooxazines, increasing solvent polarity should increase the degree of zwitterionic character, which should have three main effects on the ground-state PES: (1) a thermodynamic stabilization of the PMC form; (2) an increase in E_a for the *cis*/*trans* isomerization step; and (3) a decrease in E_a for the C–O bond cleavage/formation step. The trends observed for IPSO correlate quite well to the behaviour predicted computationally for indolyl spirooxazine derivatives, where a reversal in the behaviour of both k_1 and k_2 is expected with increasing solvent polarity. This behaviour can be represented by the series of PESs (a)–(c) shown in Figure 2.11, where in (a) the C–O bond cleavage step is the rate-limiting

step and in (c) the isomerization step becomes the rate-limiting step. Therefore, an increase in solvent polarity (with corresponding structural changes) leads to an increase and then decrease in both the SO → PMC and PMC → SO isomerization rates, with the PMC → SO isomerization being much faster overall due to the thermodynamic destabilization of the PMC form relative to the SO form. APSO, on the other hand, behaves differently than the indolyl derivatives as the PMC form is thermodynamically stabilized relative to the SO form. For APSO in toluene, $K_T \approx 1$ and $k_1 \approx k_2$, which suggests that both SO and PMC forms have similar energies and both forward and reverse isomerization processes have similar E_a barriers. Such a scenario can be represented by PES (d) in Figure 2.11. In APSO, both k_1 and k_2 consistently decrease with increasing solvent polarity, with the decrease in k_2 being slightly more significant. This behaviour can be rationalized by considering PESs (e) and (f). Here, a slight decrease in the E_a for the C–O bond cleavage/formation step has minimal effect on the observed rate of the process. A slight increase in E_a for the *cis*/*trans* isomerization step will lead to slightly slower SO → PMC and PMC → SO isomerization rates, and the stabilization of the PMC isomer additionally contributes to even slower PMC → SO isomerization rates. In summary, the significant differences in molecular structure observed for IPSO and APSO correlate with the observed solvent-dependent trends in their thermodynamic and kinetic thermal isomerization parameters. The reversal in trend for changes in both k_1 and k_2 rate constants with solvent polarity for IPSO can be explained by a change in the rate-limiting step for thermal isomerization from C–O bond cleavage/formation in low-polarity solvents to *cis*/*trans* isomerization in high-polarity solvents. The small rate constants for PMC → SO isomerization (k_2) for APSO compared to IPSO can be explained by a higher E_a barrier for *cis*/*trans* isomerization. The steady decrease in both k_1 and k_2 with increasing solvent polarity for APSO can be rationalized by the more hindered *cis*/*trans* isomerization that results from increasing zwitterionic character and the greater thermodynamic stabilization of the zwitterionic PMC form by polar solvents.

2.3. Summary and Conclusions

Structural studies of the PMC form of spiropyrans and spirooxazines have been limited. In general, all of the spiropyrans that have been structurally characterized demonstrate predominantly zwitterionic character. All of these spiropyrans are also functionalized with strong EWGs on the oxazine moiety. On the other hand, structural characterizations of nonphotochromic spirooxazine-based PMCs—in combination with solvatochromism, NMR, and computational studies—have predicted quinoidal PMC character. These particular spirooxazine derivatives were not functionalized with strong EWGs on the oxazine moiety. Overall, the existing structure elucidation studies for the PMC form of spiropyrans and spirooxazines are inadequate and have not been completed for enough derivatives in enough conditions to properly extract the effect of chemical structure and medium on the molecular structure. This information is important as an understanding of the PMC molecular structure provides valuable insight into the specific photochromic properties of a given spirooxazine in a given set of conditions.

Here we have structurally characterized a photochromic spirooxazine-based PMC for the first time, and it was shown to exhibit predominantly zwitterionic character. Interestingly, this spirooxazine was not derivatized with an EWG on the oxazine moiety, but rather an EDG, in the form of a bicyclic azahomoadamantyl amine group, on the donor end of the molecule. We showed evidence that the PMC molecular structure displays a range of relative quinoidal and zwitterionic resonance contributions as a function of medium, with increasing zwitterionic character in more polar media. In the solution state, this was evidenced through an analysis of the solvatochromism and solvent-dependent vibrational structure of the PMC π–π^* CT band. The zwitterionic character in the solid state was corroborated by crystallographic data for two pseudopolymorphs through an analysis of bond length alternation in the conjugated bridge. This study revealed two interesting findings: (1) The fact that the solution-state spectroscopic analysis supported a quinoidal form in low-polarity solvents, yet the solid-state crystallographic analysis supported a zwitterionic structure, may indicate that the crystal lattice behaves as a fairly strong dielectric. (2) The fact that the degree of zwitterionic character is different for the two pseudopolymorphs reveals the strong

influence of intermolecular and electrostatic effects in the crystalline lattice on PMC molecular structure.

While, the analysis of APSO highlighted the effects of medium on PMC structure in both the solution and solid states, the comparison of solution-state solvent-dependent electronic absorption spectroscopy data for the indolyl and azahomoadamantyl derivatives, IPSO and APSO, emphasized the effects of chemical structure. These data suggested that IPSO is more quinoidal overall but that it, too, progresses toward greater zwitterionic character with increasing solvent polarity. Thus the PMC forms of both derivatives exist as a continuum of hybrid quinoidal/zwitterionic resonance structures with different accessible limits.

Solvent-dependent ^{1}H and ^{13}C NMR analyses and DFT computational studies, both in the gas phase and using the Onsager model, fell short in accurately predicting the PMC molecular structure expected on the basis of XRD and electronic absorption analyses.

Finally, the inferred solution-state molecular structures for the two types of spirooxazines were correlated with solvent-dependent trends in thermodynamic equilibrium constants and kinetic rate constants for thermal SO/PMC isomerization. The attractive photochromic properties of APSO such as high photoresponsivity, stability of the PMC form, and slow thermal relaxation, were correlated with the dominant zwitterionic PMC structure and rationalized in terms of the electron-donating power of the bicyclic amine group. This study underscores the specific effects that a zwitterionic vs quinoidal structure has on spirooxazine properties and highlights azahomoadamantyl derivatization as a promising approach to optimizing photochromic figures of merit in spirooxazines for photoswitching applications, whether these involve spirooxazines alone, or hybrid spirooxazine materials such as photochromic ligand–metal coordination complexes.

2.4. Experimental

2.4.1. Synthesis

All reagents were purchased from commercial sources and used without further purification unless otherwise specified. Spectroscopic-grade, dry, and deoxygenated CH_2Cl_2 and toluene were acquired from an MBraun solvent purification system. Et_3N

was dried over and distilled from KOH. ^{1}H NMR spectra were acquired with Bruker AC300, AVANCE360, or AVANCE500 spectrometers, and spectra were calibrated to the solvent residual peaks.[283] FT-IR spectra were acquired as KBr pellets with a Perkin Elmer Spectrum One spectrometer. Elemental analyses were performed by Desert Analytics and Canadian Microanalytical Services. The mass spectrum of IPSO was acquired with a Q-Tof2 ESI hybrid quadrupole time-of-flight mass spectrometer with the following settings: MCP voltage – 2800 V, capillary voltage – 3 kV, cone voltage – 20 V, source *T* – 80 °C, desolvation *T* – 250 °C. The sample was dissolved in CH_2Cl_2 and diluted with CH_3OH. The EI mass spectrum of APSO was obtained using a double-focusing Kratos MS-50 mass spectrometer coupled with a MASPEC data system. The sample was introduced using a direct insertion probe. Operation conditions: source *T* – 150 °C, ionization energy – 70 eV. Compounds **33**,[247] **34**,[248] **36**,[249] and **37**[249] were prepared according to previously reported procedures and characterized by ^{1}H NMR spectroscopy and/or melting points. The ^{1}H NMR spectrum of **28** was assigned with COSY and NOESY spectroscopy (see Scheme 2.6 for atom numbering; protons are numbered according to the carbon atoms to which they are attached).

1,10-Phenanthroline-5,6-dione (33).[247] M.p. 246–247 °C (lit m.p. 258 °C[284]). ^{1}H NMR (300 MHz, $CDCl_3$):[284] δ 9.09 (dd, *J* = 4.4, 1.4 Hz, 2H), 8.48 (dd, *J* = 7.3, 1.5 Hz, 2H), 7.57 (dd, *J* = 7.3, 4.4 Hz, 2H) ppm.

5-Hydroxy-6-nitroso-1,10-phenanthroline (34).[248] Isolation of the yellow powder precipitated from EtOH typically results in quantitative yields. M.p. 218–219 °C (lit m.p. 218–220 °C[248]). ^{1}H NMR (300 MHz, DMSO-d_6):[236] δ 9.58 (dd, *J* = 8.6, 1.4 Hz, 1H), 9.13 (dd, *J* = 5.1, 1.5 Hz, 1H), 8.94 (dd, *J* = 5.1, 1.3 Hz, 1H), 8.68 (dd, *J* = 8.1, 1.3 Hz, 1H), 7.93–8.00 (m, 2H) ppm.

5-Methyl-4-azahomoadamant-4-ene (36).[249] ^{1}H NMR (300 MHz, $CDCl_3$): δ 3.94 (quintet, *J* = 3.2 Hz, 1H), 2.53 (br septet, *J* = 2.4 Hz, 1H), 2.03 (br quintet, *J* = 3.2 Hz, 2H), 1.95 (s, 3H), 1.75–1.66 (m, 6H), 1.65–1.59 (m, 4H) ppm.

5-Methyl-4-azahomoadamant-4-enium Iodide (37).[249] ^{1}H NMR (300 MHz, $CDCl_3$): δ 4.19 (tt, *J* = 5.4, 1.7 Hz, 1H), 3.88 (s, 3H), 3.14 (br t, *J* = 6.1 Hz, 1H), 2.84 (s, 3H), 2.45 (t, *J* = 1.6 Hz, 1H), 2.40 (t, *J* = 1.4 Hz, 1H), 2.31 (br s, 1H), 2.26 (t, *J* = 1.4 Hz, 1H), 2.20 (br quintet, *J* = 3.0 Hz, 2H), 1.98–1.75 (m, 6H) ppm.

Spiro[azahomoadamantane-phenanthrolinoxazine] (APSO) (28). Et_3N (1.60 mL, 11.5 mmol) was added to a stirring solution of 4,5-dimethyl-4-azahomoadamant-4-enium iodide (**37**) (1.72 g, 5.62 mmol) in CH_2Cl_2 (150 mL) at 0 ºC. After 30 min, 4 Å molecular sieves (~3 g) and 5-hydroxy-6-nitroso-1,10-phenanthroline (**34**) (1.27 g, 5.63 mmol) were added to the mixture, and the solution was slowly warmed to r.t. and then heated at reflux for 3 h. The solution was filtered, washed with $NaHCO_3$, H_2O, and brine, and then dried over $MgSO_4$, before removal of the solvent by rotary evaporation to yield a dark purple solid (1.4 g, 65% yield) of reasonable purity. The material was further purified by column chromatography on silica gel with CH_2Cl_2/CH_3OH (90:10) followed by recrystallization from EtOAc to yield dark purple crystals with an iridescent green sheen (0.69 g, 32% yield). Anal. Calcd for $C_{24}H_{24}ON_4$: C, 74.98; H, 6.29; N, 14.57. Found: C, 74.71; H, 6.17, N, 14.36. M.p. 200–201 °C. EI-MS: *m*/*z* (%) 384 (91) $[M]^+$, 163 (100). ^{1}H NMR (300 MHz, $CDCl_3$) PMC form: δ 9.97 (s, 1H, H-3′), 9.03 (dd, *J* = 4.5, 1.7 Hz, 1H, H-24′), 8.75 (dd, *J* = 7.9, 1.7 Hz, 1H, H-22′), 8.74 (dd, *J* = 4.4, 2.1 Hz, 1H, H-21′), 8.64 (dd, *J* = 8.1, 2.2 Hz, 1H, H-19′), 7.48 (dd, *J* = 8.1, 4.4 Hz, 1H, H-23′), 7.39 (dd, *J* = 8.0, 4.4 Hz, 1H, H-20′), 5.11 (tt, *J* = 5.9, 1.9 Hz, 1H, H-10′), 3.74 (septet, *J* = 2.1 Hz, 1H, H-6′), 3.51 (s, 3H, H-1′), 2.20–1.75 (m, 12H); SO form: δ 9.14 (dd, *J* = 4.5, 2.1 Hz, 1H, H-24), 8.86 (dd, *J* = 8.1, 1.4 Hz, 1H, H-19), 7.63 (dd, *J* = 8.1, 4.4 Hz, 1H, H-23), 7.61 (dd, *J* = 8.1, 4.4 Hz, 1H, H-20), 7.70 (s, 1H, H-3), 2.47 (s, 3H, H-1), 2.20–1.75 (m, 12H) ppm (the remaining signals for the SO form are not distinguishable from those of the PMC form). ^{13}C NMR (125 MHz, $CDCl_3$) PMC and SO forms (not distinguished): δ 179.5 (C), 174.5 (C), 157.36 (CH), 152.6 (CH), 151.2 (C), 150.4 (CH), 147.8 (CH), 146.8 (CH), 146.4 (C), 143.5 (C), 140.1 (C), 135.2 (CH), 133.1 (C), 130.9 (CH), 130.4 (CH), 129.9 (CH), 129.7 (C), 127.8 (C), 127.1 (C), 125.9 (CH), 123.5 (CH), 123.3 (CH), 122.9 (CH), 122.7 (CH), 122.1 (C), 119.4 (C), 95.2 (C), 77.2 (C/CH), 64.5 (CH), 58.9 (CH), 42.9 (CH), 39.8 (CH_2), 39.7 (CH_2), 39.4 (CH_2), 38.4 (CH_2), 36.0 (CH_2), 34.0 (CH_2), 33.9 (CH_2), 33.6 (CH_2), 32.3 (CH_2), 30.2 (CH_2), 30.0 (CH_2), 29.3 (CH/CH_3), 26.7 (CH/CH_3), 26.7 (CH/CH_3), 26.2 (CH/CH_3) ppm. FT-IR (KBr): ν 2912 (m), 2901 (m), 2843 (w), 1594 (m), 1581 (s), 1564 (s), 1541 (m), 1475 (m), 1448 (s), 1408 (s), 1356 (s), 1347 (s), 1317 (s), 1303 (m), 1286 (vw, sh), 1253 (s), 1223 (vs), 1179 (w), 1130 (vs), 1101 (vs), 1079 (m),

1064 (s), 1037 (m), 1025 (m), 1012 (m), 999 (m), 948 (m), 884 (m), 837 (w), 810 (w), 802 (w), 777 (vw), 747 (w), 736 (w), 631 (w), 616 (w) cm^{-1}.

Spiro[indoline-phenanthrolinoxazine] (IPSO) (31): 2-methylene-1,3,3-trimethylindoline (**39**) (2.6 mL, 15 mmol, 1.0 equiv.) was added to a refluxing solution of 5-hydroxy-6-nitroso-1,10-phenanthroline (**34**) (3.3 g, 15 mmol, 1.0 equiv.) in dry toluene (300 mL). The solution was heated at reflux with a Dean–Stark apparatus in the dark for 16 h before the reaction mixture was filtered and the solvent was removed. The crude product was purified twice using column chromatography on silica gel (1. CH_2Cl_2/CH_3OH 90%:10%; 2. EtOAc/CH_3OH 90%:10%) to give a glassy blue solid, which was recrystallized from EtOAc to afford yellow crystals (1.4 g, 25% yield). Anal. Calcd for $C_{24}H_{20}N_4O$: C, 75.77; H, 5.30; N, 14.73. Found: C, 75.58; H, 5.13, N, 14.76. M.p. 199–200 °C. ESI-MS: *m*/*z* (%) 1164 (81) $[3IPSO + Na]^+$, 783 (100) $[2IPSO + Na]^+$, 403 (95) $[IPSO + Na]^+$, 381 (4) $[IPSO + H]^+$. ^1H NMR (SO form only) (300 MHz, $CDCl_3$): δ 9.12 (dd, *J* = 4.5, 1.4 Hz, 1H), 9.07 (dd, *J* = 4.4, 1.5 Hz, 1H), 8.96 (dd, *J* = 8.0, 2.3 Hz, 1H), 8.40 (dd, *J* = 8.1, 1.4 Hz, 1H), 7.83 (s, 1H), 7.67 (dd, *J* = 8.6, 4.4 Hz, 1H), 7.51 (dd, *J* = 8.2, 4.4 Hz, 1H), 7.23 (td, *J* = 7.4, 1.5 Hz, 1H), 7.10 (d, *J* = 7.0 Hz, 1H), 6.92 (t, *J* = 7.3 Hz, 1H), 6.59 (d, *J* = 7.8 Hz, 1H), 2.76 (s, 3H), 1.39 (s, 3H), 1.36 (s, 3H) ppm. FT-IR (KBr): ***ν*** 3050 (w), 3029 (w), 2992 (w), 2976 (w), 2961 (m), 2925 (w), 2904 (w), 2865 (w), 1600 (s), 1583 (s), 1559 (m), 1499 (m), 1484 (s), 1471 (s), 1455 (s), 1447 (s), 1432 (s), 1407 (m), 1383 (m), 1357 (s), 1342 (m), 1319 (s), 1300 (s), 1275 (m), 1238 (m), 1222 (w), 1193 (w), 1173 (m), 1162 (m), 1156 (sh), 1139 (w), 1117 (s), 1109 (s), 1105 (s), 1075 (m), 1068 (m), 1049 (w), 1019 (s), 1002 (s), 973 (s), 930 (s), 914 (m), 887 (m), 847 (w), 831 (m), 822 (m), 809 (m), 804 (m), 795 (m), 772 (m), 755 (m), 742 (s), 739 (s), 708 (w), 681 (m), 665 (m), 635 (w), 618 (m), 590 (w), 573 (w), 566 (w), 550 (m), 513 (m), 493 (m), 468 (m) cm^{-1}.

2.4.2. X-Ray Crystallographic Analysis

APSO-PMC-I. A dark red prism, measuring 0.22 × 0.15 × 0.12 mm^3, was mounted on a glass capillary with oil. Data were collected at 110 K with a Bruker APEX II single crystal X-ray diffractometer (Mo radiation). Crystal-to-detector distance was 40 mm and exposure time was 20 seconds per degree for all sets. The scan width was 0.5^o. Data

collection was 98.7% complete to 25° in θ. A total of 37730 (merged) reflections were collected covering the indices h = –22 to 23, k = –10 to 10, and l = –30 to 30. 3877 reflections were symmetry independent and the R_{int} = 0.0977 indicated that the data was about average quality (0.07). Indexing and unit cell refinement indicated a *C*-centered monoclinic lattice. The space group was found to be *C*2/*c* (No.15). The data were integrated and scaled using SAINT, SADABS within the APEX2 software package by Bruker.[285] Solution by direct methods (SHELXS, SIR97[286]) produced a complete heavy-atom phasing model consistent with the proposed structure. The structure was completed by difference Fourier synthesis with SHELXL97.[287, 288] Scattering factors are from Waasmair and Kirfel.[289] Hydrogen atoms were placed in geometrically idealized positions and constrained to ride on their parent atoms with C–H distances in the range of 0.95–1.00 Å. Isotropic thermal parameters U_{eq} were fixed such that they were 1.2U_{eq} of their parent atom U_{eq}'s for CH's and 1.5U_{eq} of their parent atom U_{eq}'s in the case of the methyl groups. All non-hydrogen atoms were refined anisotropically by full-matrix least-squares methods.

APSO-PMC-II. A purple block, measuring 0.53 × 0.22 × 0.17 mm^3, was mounted on a glass fiber with oil. Data were collected at 193 K with a Bruker SMART 1000 CCD detector/PLATFORM diffractometer equipped with Mo Kα radiation, using ω scans (0.3° scan width, 45 s exposures per frame). Total data collected was 23144 ($-7 \le h \le 7$, $-19 \le k \le 19$, $-24 \le l \le 24$), complete to 99.9% to 25.25° in θ; total independent reflections was 4020 (R_{int} = 0.0661). The data were corrected for absorption through use of a multi-scan model (SADABS). Structures were solved using the direct methods program SHELXL-97.[290] Refinements were completed using the program SHELXL-97.[290] Hydrogen atoms were assigned positions based on the geometries of their attached carbon atoms, and were given thermal parameters 20% greater than those of the attached carbons. Likely positions of the hydrogen atoms of the solvent water molecules were identified from the difference Fourier map and were given thermal parameters 20% greater than those of the attached oxygen atoms. The O–H and H···H distances of the solvent water molecules were restrained to be 0.850(4) and 1.390(8) Å, respectively.

2.4.3. Computational Methods

Geometries. Geometry optimization calculations were performed using density functional theory (DFT) with the hybrid Becke-style three-parameter exchange functional[291] and the Lee-Yang-Parr correlation functional[292] (B3LYP) with the Gaussian 03 software package.[272] Solvent effects were modeled in toluene (ε = 2.379), DMSO (ε = 46.7), and H_2O (ε = 78.39) using the Onsager model with a_o values of 5.64 Å for APSO-PMC and 5.95 Å for IPSO-PMC, as determined by a volume calculation in Gaussian. Stability calculations were performed on all optimized geometries obtained from gas-phase calculations, and structures were found to be minima on the potential energy surfaces.

NMR Shifts. Theoretical NMR shifts were calculated using the GIAO method at the DFT/B3LYP level of theory with the 6-31G(d,p) basis set and the IEFPCM solvation model as implemented in Gaussian 03, with OFAC=0.8 and RMIN=0.5 as modified parameters. Theoretical NMR shifts were first calculated for IPSO-SO as a control compound, for which it is known that the DFT-optimized geometry [gas phase, B3LYP/6-31G(d,p), (*R*) enantiomer] corresponds quite well with the experimental geometry determined from X-ray structural analysis. The gas-phase optimized geometry was used for the NMR calculations, which were performed in solvent using the IEFPCM model in toluene, $CHCl_3$ and DMSO. The calculated shifts were then corrected with the calculated shift for TMS obtained using an identical methodology. These corrected shifts were then compared to the experimental ^1H and ^{13}C NMR shifts in toluene-*d*8, $CDCl_3$, and DMSO-d_6 (Appendix E). (Experimental ^1H NMR shifts for IPSO-SO were assigned on the basis of coupling constants and 2D correlation spectroscopy. Experimental ^{13}C NMR shifts for IPSO-SO were assigned on the basis of ^1H–^{13}C correlation spectroscopy for all CH, CH_2, and CH_3 signals, but were assigned on the basis of the calculations for the quaternary signals.) Shifts for the methyl peaks were excluded from the ^1H NMR correlation as these were expected to deviate more significantly than the other shifts owing to free rotation in solution unaccounted for in the calculations. Correlations were very good, although in some cases systematic error was observed. In such cases, an additional correction factor was introduced based on the average deviation of experimental shifts from calculated shifts. After this correction was included, calculated

^{1}H NMR shifts had an average deviation from experimental shifts of 0.15 ppm in toluene, 0.05 ppm in $CHCl_3$ and 0.08 ppm in DMSO, and calculated ^{13}C NMR shifts had an average deviation from experimental shifts of 2.1 ppm in $CHCl_3$ and 2.2 ppm in DMSO. For the ^{13}C NMR shifts, the most significant error was observed for the methyl groups and the signals associated with the spiro-C functionality (C-2, C-3, and C-6), which may have to do with having a mixture of (*R*) and (*S*) enantiomers in solution and the lability of the C_{spiro}–O bond. The optimized geometries of the PMC forms [DFT/B3LYP/6-31G(d,p), TTC isomer] were then used as starting points for approximating the canonical quinoidal (**A**) and zwitterionic (**B**) resonance forms. New coordinates were obtained by modifying the lengths of the N(1)–C(2), C(2)–C(3), C(3)–N(2), N(2)–C(4), C(4)–C(5), and C(5)–O(1) bonds to those expected for the canonical resonance forms (Table 2.2). The remaining geometrical parameters were not reoptimized.

2.4.4. Spectroscopic Methods

Electronic Absorption Spectroscopy. Electronic absorption spectroscopy was performed with an Agilent 8453 spectrometer at ~300 K on solutions prepared at concentrations of 10^{-5}–10^{-6} M. For the determination of thermal isomerization kinetic parameters, sample solutions prepared in spectroscopy grade solvents were transferred to 1 cm × 1 cm cuvettes, subjected to rapid uniform stirring, and exposed to steady-state multiline UV irradiation (λ_{ex} = 333.6–363.8 nm) or single-line visible irradiation (λ_{ex} = 514, 532, or 568 nm) of 30–150 mW of power generated with a Spectra-Physics Stabilite 2018 mixed-gas Ar–Kr ion laser and directed through the sample cuvette perpendicularly to the sampling beam with a liquid light guide. A cuvette of acetone was placed between the sample and sampling beam to block irradiation from the spectrometer in the near-UV region (<300 nm). The rates of thermal return were determined in the absence of light after generating a photostationary state by following the absorbance kinetics at the PMC π–π^* λ_{max} and fitting A_∞–A_t or A_t–A_∞ (where A_t represents the absorbance at a given time, t, and A_∞ represents the absorbance at the photostationary state, or a close approximation thereof) to a first-order monoexponential rate function ($A = A_o e^{kt}$, where A_o is the initial absorbance) by linear least-squares methods. The

observed rate constants, k_{obs}, were then taken as the negative of the resulting value for k. The choice of kinetic model was assessed visually by the accuracy of the fits and by the appropriateness of the residuals, R, for the particular data set, and in all cases was deemed appropriate. See Appendix C for rate fitting plots.

^{1}H NMR. ^{1}H NMR spectra of APSO and IPSO were obtained in eight solvents ranging in polarity from toluene-d_8 (E_T^N of nondeuterated solvent = 0.099) to CD_3OD (E_T^N of nondeuterated solvent = 0.762), and ^{13}C NMR spectra of the compounds were obtained in toluene-d_8, THF-d_8, $CDCl_3$, and DMSO-d_6, although not all of the peaks of interest could be identified in all solvents. Chemicals shifts were referenced to solvent residual peaks, as per the Cambridge Isotope Labs NMR Solvent Data Chart[283] (toluene-d_8: δ ^{1}H = 2.09 ppm, δ ^{13}C = 20.4 ppm; benzene-d_6: δ ^{1}H = 7.16 ppm; THF-d_8: δ ^{1}H = 1.73 ppm, δ ^{13}C = 25.37 ppm; $CDCl_3$: δ ^{1}H = 7.24 ppm, δ ^{13}C = 77.23 ppm; CD_2Cl_2: δ ^{1}H = 5.32 ppm; acetone-d_8: δ ^{1}H = 2.05 ppm; DMSO-d_8: δ ^{1}H = 2.50 ppm, δ ^{13}C = 39.51 ppm; CD_3CN: δ ^{1}H = 1.94 ppm; CD_3OD: δ ^{1}H = 3.31 ppm).

Chapter 3. Analysis of Ligand Field Strength in Phenanthroline–Spirooxazine Ligands using $Mo(CO)_4(NN)$ Complexes

3.1. Introduction

To evaluate the utility of photochromic ligands for the photomodulation of metal-based properties in coordination complexes, a generalized method for determining the differences in ligand field strength between the photochromic forms is necessary. The analysis of UV/Vis spectral features, such as the energies of *d–d* or MLCT transitions is not useful for this purpose because the relevant features are obscured by the intense PMC π–π* CT band of the photochromic ligand. The computational analysis of frontier molecular orbitals or the electrochemical analysis of redox potentials can provide information about ligand bonding properties; however, information gained in this way is indirect. To obtain quantitative empirical evidence for changes in ligand field strength between the SO and PMC forms of phenanthroline–spirooxazines, we incorporated these ligands into molybdenum–tetracarbonyl complexes that could be used as spectroscopic probes of ligand field strength.

Metal–carbonyl complexes are one of the most highly studied classes of transition-metal complexes, and have historically been applied to many metal–ligand bonding problems.[293-296] As such, they are extremely well understood and provide a good model system with which to study the bonding properties of the phenanthroline–spirooxazine ligands. Metal–carbonyl bonding can be qualitatively described by a synergistic bonding model whereby the CO group transfers electron density to the metal through σ-donation, and the metal transfers electron density to the carbonyl group through π-backbonding.[297] Ancillary ligands will compete with the CO groups in the transfer of electron density to and from the metal centre as a function of their σ-donor or π-acceptor abilities. This competition will influence the electronic properties of the carbonyl groups, which can then be probed spectroscopically to gain information about the ancillary ligand bonding capabilities.

Scheme 3.1. Photo- and thermal isomerization of molybdenum–tetracarbonyl–spirooxazine complexes $Mo(CO)_4$(APSO) (**40**) and $Mo(CO)_4$(IPSO) (**41**) between spirooxazine (SO) and photomerocyanine (PMC) forms.

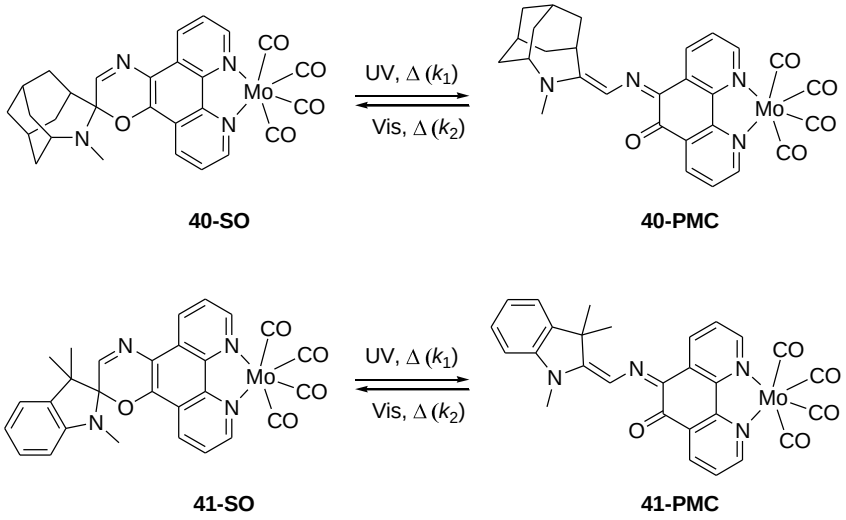

This chapter presents the synthesis, characterization, and analysis of the molybdenum–tetracarbonyl complexes of APSO (**28**) and IPSO (**31**): $Mo(CO)_4$(APSO) (**40**) and $Mo(CO)_4$(IPSO) (**41**) (Scheme 3.1). The solution-state behaviour, spectroscopic features, and photochromic properties of the complexes are first examined to set the stage for subsequent studies. The ligand field strength of the SO and PMC forms are then investigated empirically with FT-IR and ^{13}C NMR spectroscopies through an analysis of carbonyl IR stretching frequencies and ^{13}C chemical shifts. Finally, a density functional theory (DFT) fragment molecular orbital (MO) analysis corroborated by electrochemical studies is used to interpret the metal–ligand bonding interactions in these systems as a function of SO/PMC isomerization. Insights from the MO analysis lead to the proposition of novel phenanthroline–spirooxazine derivatives as synthetic targets which may exhibit different and potentially greater changes in ligand field strength upon photoisomerization.

3.2. Results and Discussion

3.2.1. Synthesis

The molybdenum–tetracarbonyl–spirooxazine complexes, $Mo(CO)_4$(APSO) and $Mo(CO)_4$(IPSO), were synthesized by complexation of the respective diimine ligand with

cis-$Mo(CO)_4(pip)_2$[298] (pip = piperidine) in toluene in the absence of light at ~300 K. In each case, a microcrystalline precipitate formed, and was subsequently filtered, washed with toluene and pentane, and collected in high yield. Spectroscopic characterization of the compounds confirmed complexation. The expected molecular ion peaks are observed by mass spectrometry. In the ^{1}H NMR spectra, chemical shifts for the proton resonances of the complexed ligands—most notably those of the phenanthroline moiety—are shifted downfield from those of the parent ligands, as expected for complexation to an electropositive metal centre. Sets of both axial and equatorial carbonyl resonances are observed in the ^{13}C NMR spectra. An intense four-band pattern is observed in the carbonyl region of the FT-IR spectra, as expected for *cis*-molybdenum–tetracarbonyl complexes.[299] Finally, a MLCT band characteristic of the Mo(*d*)–phen(π^*) transition typically observed in molybdenum–carbonyl–diimine complexes[300] is observed in the electronic absorption spectra.

3.2.2. Structural Analysis of $Mo(CO)_4$(APSO-PMC)

Purple prismatic crystals of $Mo(CO)_4$(APSO-PMC)·$C_6H_5CH_3$ suitable for X-ray diffraction analysis were isolated from the toluene mother liquor from the synthesis of $Mo(CO)_4$(APSO) in the absence of light; solutions of $Mo(CO)_4$(IPSO) repeatedly yielded clusters of tiny needles unsuitable for X-ray analysis. The APSO complex crystallized in the triclinic *P*-1 (No. 2) space group with one disordered toluene solvate molecule per metal complex and two equivalent molecules per unit cell (Z = 2). The molecular structure of $Mo(CO)_4$(APSO-PMC)·$C_6H_5CH_3$ is shown in Figure 3.1, and selected bond lengths and angles are tabulated in Table 3.1. The geometrical parameters of the complexed APSO ligand are equivalent, within 0.02–0.03 Å, to those of the parent APSO ligand.[218] The torsional angles N(4)–C(14)–C(13)–N(3), C(14)–C(13)–N(3)–C(6), and C(13)–N(3)–C(6)–C(5) of the complexed ligand are 174.7(2)°, 171.8(2)°, and –5.4(4)°, respectively, which indicates a nearly planar *trans-trans-cis* (TTC) conformation about the central conjugated azomethine bridge. This suggests that the TTC isomer is the most stable form in the solid state, as was found for the free ligand.[218] The bond lengths for the three bonds in the azomethine bridge, C(14)–C(13) [1.430(3) Å], C(13)–N(3) [1.315(3) Å], and N(3)–C(6) [1.344(3) Å], demonstrate predominantly single-bond,

double-bond, and single-bond character, respectively, when compared to average single and double bond lengths extracted from the Cambridge Crystallographic Database [C–C = 1.460(15) Å, C=C = 1.360(20) Å; C–N = 1.376(11) Å, C=N = 1.279(8) Å; N–C = 1.376(11) Å, N=C = 1.279(8) Å].[254] This bond-length alternation pattern indicates that in the Mo complex, as in the free ligand, the zwitterionic resonance form contributes more significantly to the PMC structure than does the quinoidal form.

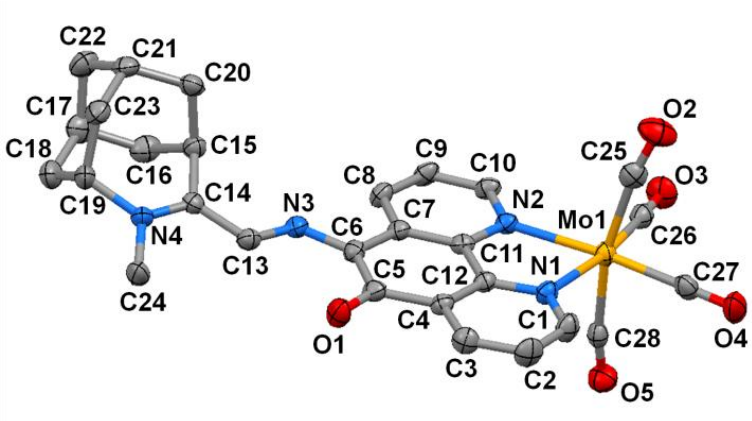

Figure 3.1. Molecular structure of $Mo(CO)_4$(APSO-PMC)·$C_6H_5CH_3$. Thermal ellipsoids are shown at the 50% probability level, and hydrogen atoms and toluene solvate molecules are omitted for clarity.

Crystallographic features relevant to the Mo core of the complex are similar to those observed in $Mo(CO)_4$(phen),[301] and these features have been analyzed in detail in the context of metal–carbonyl–diimine bonding for $W(CO)_4$(diimine) complexes.[302] $Mo(CO)_4$(APSO-PMC) has a distorted pseudo-octahedral geometry around the Mo centre. The N(1)–Mo(1)–N(2) angle is considerably less than 90° at 72.90(7)°, and the axial CO (CO_{ax}) groups bend away from the diimine ligand to give a C(25)–Mo(1)–C(28) angle of 166.82(10)°. The Mo–C and C–O bond lengths associated with the CO_{ax} groups are, respectively, longer and shorter than those of the equatorial CO groups (CO_{eq}). However, the Mo–C and C–O bond lengths associated with the CO_{eq} groups *trans* to the diimine ligand are, respectively, slightly shorter [1.946(2)/1.944(3) Å] and slightly longer [1.166(3)/1.167(3) Å] than those reported for $Mo(CO)_4$(phen) [Mo–C_{eq} = 1.958(3) Å, C_{eq}–O_{eq} = 1.155(3)Å]. This is consistent with the PMC form of APSO being a weaker π-acceptor than phen,[301] as expected on the basis of DFT MO analysis (vide infra, Sections

3.2.7–3.2.9). Additionally, the Mo–C and C–O bond lengths differ between the two CO_{ax} groups: one of the groups has a Mo(1)–C(25) bond length of 2.017(3) Å and a C(25)–O(2) bond length of 1.153(3) Å, and the other has a Mo(1)–C(28) bond length of 2.050(3) Å and a C(28)–O(5) bond length of 1.140(3) Å (in contrast to the equivalent M–C and C–O bond lengths associated with the equatorial CO groups).

Table 3.1. Selected bond lengths [Å] and angles [°] for $Mo(CO)_4$(APSO-PMC).[a]

Bond lengths		**Bond angles**	
N(4)–C(14)	1.324(3)	N(1)–Mo(1)–C(25)	97.08(9)
C(14)–C(13)	1.430(3)	N(1)–Mo(1)–C(28)	92.63(8)
C(13)–N(3)	1.315(3)	N(1)–Mo(1)–C(26)	169.74(8)
N(3)–C(6)	1.344(3)	N(1)–Mo(1)–C(27)	99.75(9)
C(6)–C(5)	1.445(3)	N(2)–Mo(1)–C(25)	96.65(9)
C(5)–O(1)	1.236(3)	N(2)–Mo(1)–C(28)	94.71(8)
C(1)–N(1)	1.337(3)	N(2)–Mo(1)–C(26)	96.91(8)
C(10)–N(2)	1.333(3)	N(2)–Mo(1)–C(27)	172.58(8)
N(1)–Mo(1)	2.2450(19)	N(1)–Mo(1)–N(2)	72.90(7)
N(2)–Mo(1)	2.2412(19)	C(25)–Mo(1)–C(28)	166.82(10)
Mo(1)–C(25)	2.017(3)	C(26)–Mo(1)–C(27)	90.41(10)
Mo(1)–C(28)	2.050(3)	Mo(1)–C(25)–O(2)	170.2(2)
Mo(1)–C(26)	1.946(2)	Mo(1)–C(28)–O(5)	169.8(2)
Mo(1)–C(27)	1.944(3)	Mo(1)–C(26)–O(3)	177.8(2)
C(25)–O(2)	1.153(3)	Mo(1)–C(27)–O(4)	179.2(2)
C(28)–O(5)	1.140(3)	N(4)–C(14)–C(13)–N(3)	174.7(2)
C(26)–O(3)	1.166(3)	C(14)–C(13)–N(3)–C(6)	171.8(2)
C(27)–O(4)	1.167(3)	C(13)–N(3)–C(6)–C(5)	–5.4(4)

[a]Formula: $C_{28}H_{28}MoN_4O_5 \cdot C_6H_5CH_3$. FW: 684.59 g mol^{-1}. Crystal system: triclinic. Space group: *P*–1 (No. 2). *a*: 7.8137(8) Å. *b*: 9.9057(11) Å. *c*: 14.0837(16) Å. α: 84.895(5)°. β: 77.368(5)°. γ: 81.828(5)°. *V*: 3178.6(2) $Å^3$. *Z* = 2. ρ_{calc} = 1.482 g cm^{-3}. *T*: 173 ± 0.1 K. λ: 0.71073 Å. μ: 4.78 cm^{-1}. $R_1(F^2)$: 0.031. $wR_2(F^2)$: 0.069. $R_1 = \Sigma||F_o| - |F_c|| / \Sigma|F_o|$. $wR_2 = [\Sigma(w(F_o^2 - F_c^2)^2) / \Sigma w(F_o^2)^2]^{1/2}$; $w = 1/[\sigma^2(F_o)^2 + (0.0334P)^2 + 0.5260P]$.

An examination of the crystal packing of $Mo(CO)_4$(APSO-PMC) reveals that the molecules pack head-to-tail throughout the lattice, and a network of short intermolecular O···H contacts between the carbonyl oxygen atoms and adjacent hydrogen atoms (O···H ≈ 2.5 Å) as well as the phenolate oxygen atom and adjacent hydrogen atoms [O(1)···H(C24) ≈ 2.7 Å] is evident (Figure 3.2). Both CO_{eq} groups take part in intermolecular O···H interactions with neighbouring PMC molecules [O(3)···H(C9) = 2.48 Å; O(4)···H(C19) = 2.56; O(4)···H(C24) = 2.52], whereas the axial C(25)–O(2) group with the longer C–O bond length of 1.153(3) Å forms a short O···H contact to a nearby PMC hydrogen atom [O(2)···H(C2) = 2.60 Å] while the second axial CO group does not. This suggests that the bond-length asymmetry observed for the CO_{ax} groups may be due to solid-state intermolecular interactions rather than intrinsic electronic effects.

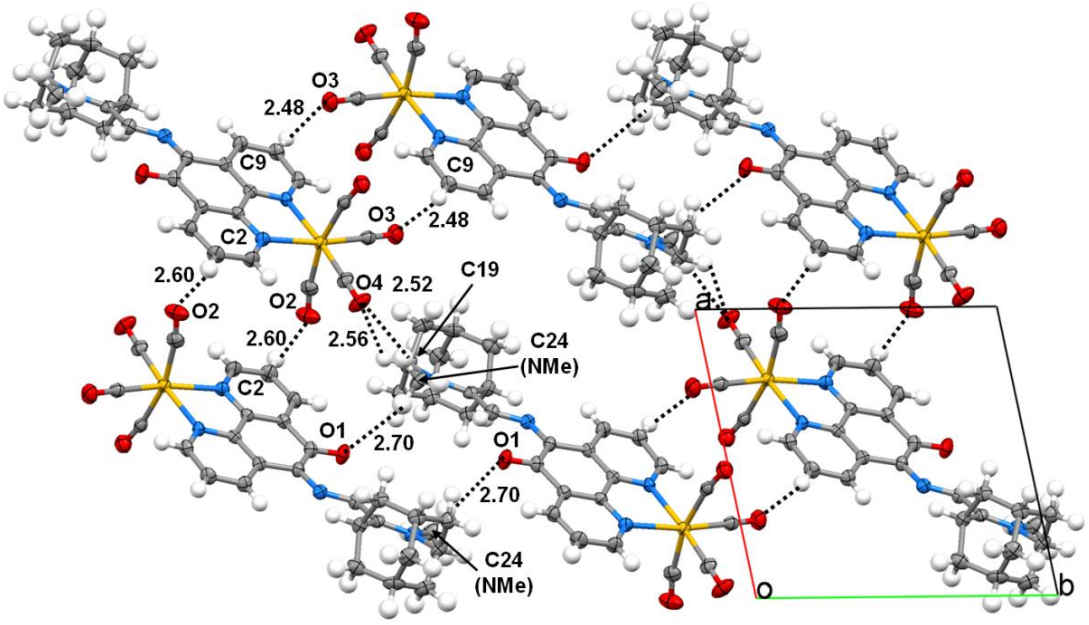

Figure 3.2. Molecular packing of $Mo(CO)_4$(APSO-PMC)·$C_6H_5CH_3$ shown along the *c* axis illustrating short intermolecular O···H contacts. Toluene solvate molecules are omitted for clarity.

3.2.3. Solution-State Behaviour and Photochromism

Key solution-state properties of the two Mo–CO spirooxazine complexes were studied to probe the effects of metal complexation on the spirooxazines and to lay the groundwork for subsequent solution-state spectroscopic studies.

The thermal equilibrium constants, K_T, for $Mo(CO)_4$(APSO) and $Mo(CO)_4$(IPSO) were determined in toluene and CH_2Cl_2 at ~300 K by ^{1}H NMR spectroscopy using the same methodology as for the free ligands. The results are tabulated along with those for APSO and IPSO in Table 3.2. As in the free ligands, the SO form is predominantly stabilized in the IPSO complex and the PMC form is predominantly stabilized in the APSO complex. For both the azahomoadamantyl and indolyl spirooxazine complexes, the PMC form is significantly stabilized upon metal complexation, consistent with previous studies involving metal complexation of IPSO.[189, 216] In addition, as is the case for the free ligands, the PMC form is further stabilized in polar solvents.

Evidence for the existence of multiple PMC isomers was observed in the ^{1}H NMR spectrum of $Mo(CO)_4$(APSO) in DMSO-d_6 at ~300 K. The presence of many weak signals along with one intense signal in the spectral regions for the azomethine protons (10.0–10.5 ppm) [Figure 3.3(a)] and the *N*-methyl protons (3–4 ppm) [Figure 3.3(b)] suggests the presence of low concentrations of up to seven PMC isomers (CTC, TTT, CTT, CCC, CCT, TCT, TCC) in solution, in addition to the TTC isomer, which is expected to be the most stable. The ^{1}H NMR spectrum for $Mo(CO)_4$(APSO) in DMSO-d_6 was monitored over time, and changes in the relative intensities of these signals were observed, consistent with a gradual equilibration of PMC isomers. The fact that several of the weaker signals decrease in intensity over time is evidence that these signals do in fact originate from isomers rather than decomposition products, in which case they would be expected to increase. Only one intense signal is observed in the azomethine and *N*-methyl regions for the ^{1}H NMR spectra of $Mo(CO)_4$(APSO) in several other solvents (e.g., toluene, CD_2Cl_2). It is possible that strong intermolecular interactions in DMSO hinder free rotation about the central C–N bond, which would lead to *cis–trans* isomerization being slow on the NMR timescale and the resolution of isomers. Evidence for more than one PMC isomer has been observed for spirooxazines in a few cases by ^{1}H NMR, but typically only the two most stable isomers (TTC and either CTC or TTT) are

observed,[303, 304] and no more than the four *trans* isomers (TTC, CTC, CTT, TTT),[305] predicted to be significantly more stable than the four *cis* isomers,[237] have been experimentally observed. This result is significant as it experimentally demonstrates the existence of 7–8 stable PMC isomers in solution.

Table 3.2. Absorption wavelengths [λ_{max}, nm], extinction coefficients [ε, $M^{-1}\cdot cm^{-1}$], thermal equilibrium constants [K_T], %PMC values, and thermal isomerization rate constants [k, s^{-1}] of APSO, IPSO, $Mo(CO)_4$(APSO), and $Mo(CO)_4$(IPSO) in toluene and CH_2Cl_2 at ~300 K.[a,b]

Toluene						
	λ_{max} (ε)	K_T (%PMC)	k_{Vis}^{-1}	k_{UV}^{-1} (k_{dis})	k_1	k_2
APSO[d]	555 (24000)	1.2 (55)	2×10^{-1}	2×10^{-1}	1×10^{-1}	9×10^{-2}
IPSO[d]	581 (1400)	0.02 (2)	N/A	2×10^{-1}	5×10^{-3}	2×10^{-1}
$Mo(CO)_4$(APSO)	465 (7400), 546 (18000)	>20 (>95)[e]	4×10^{-3}[f]	N/A	4×10^{-3}[g]	$k_2 << k_1$
$Mo(CO)_4$(IPSO)	511 (6900), 585 (5300)	0.06 (6)	3×10^{-2}	(2×10^{-2})[h]	1×10^{-3}	2×10^{-2}
CH_2Cl_2						
	λ_{max} (ε)	K_T (%PMC)	k_{Vis}^{-1}	k_{UV}^{-1} (k_{dis})	k_1	k_2
APSO[d]	555 (56000)	11 (92)	6×10^{-2}	N/A	5×10^{-2}	5×10^{-3}
IPSO[d]	591 (4000)	0.06 (5)	N/A	7×10^{-1}	4×10^{-2}	7×10^{-1}
$Mo(CO)_4$(APSO)	465 (1500), 557 (6600)	50 (98)	3×10^{-3}	N/A	3×10^{-3}	7×10^{-5}
$Mo(CO)_4$(IPSO)	476 (6600), 605 (8700)	0.14 (12)	2×10^{-2}	(1×10^{-2})[h]	2×10^{-3}	1×10^{-2}

[a] K_T = [PMC]/[SO], k_{Vis}^{-1} = observed rate constant for SO → PMC thermal return from a visible-light-induced PSS, k_{UV}^{-1} = observed rate constant for PMC → SO thermal return from a UV-light-induced PSS, k_{dis} = observed rate constant for PMC → SO thermal isomerization after initial dissolution of a solid sample, k_1 = rate constant for SO → PMC isomerization, k_2 = rate constant for PMC → SO isomerization, K_T values determined by ^{1}H NMR spectroscopy, k values determined by UV/Vis electronic absorption spectroscopy. [b] Experimental error for rate constant determination is on the order of 5–20%. [c] See Appendix A for ^{1}H NMR spectra and Appendix C for plots of kinetic fits. [d] Values from Chapter 2. [e] $Mo(CO)_4$(APSO) is minimally soluble in toluene and the amount of SO form in solution, if any, cannot be determined within the ^{1}H NMR detection limits. [f] Slightly better fits are obtained with a first-order biexponential kinetic model to give two components to the observed rate with k_{obs} = 6×10^{-3} s^{-1} (60%) and 3×10^{-3} s^{-1} (40%). [g] Assuming $k_1 >> k_2$. [h] Used k_{dis} for the calculation of k_1 and k_2.

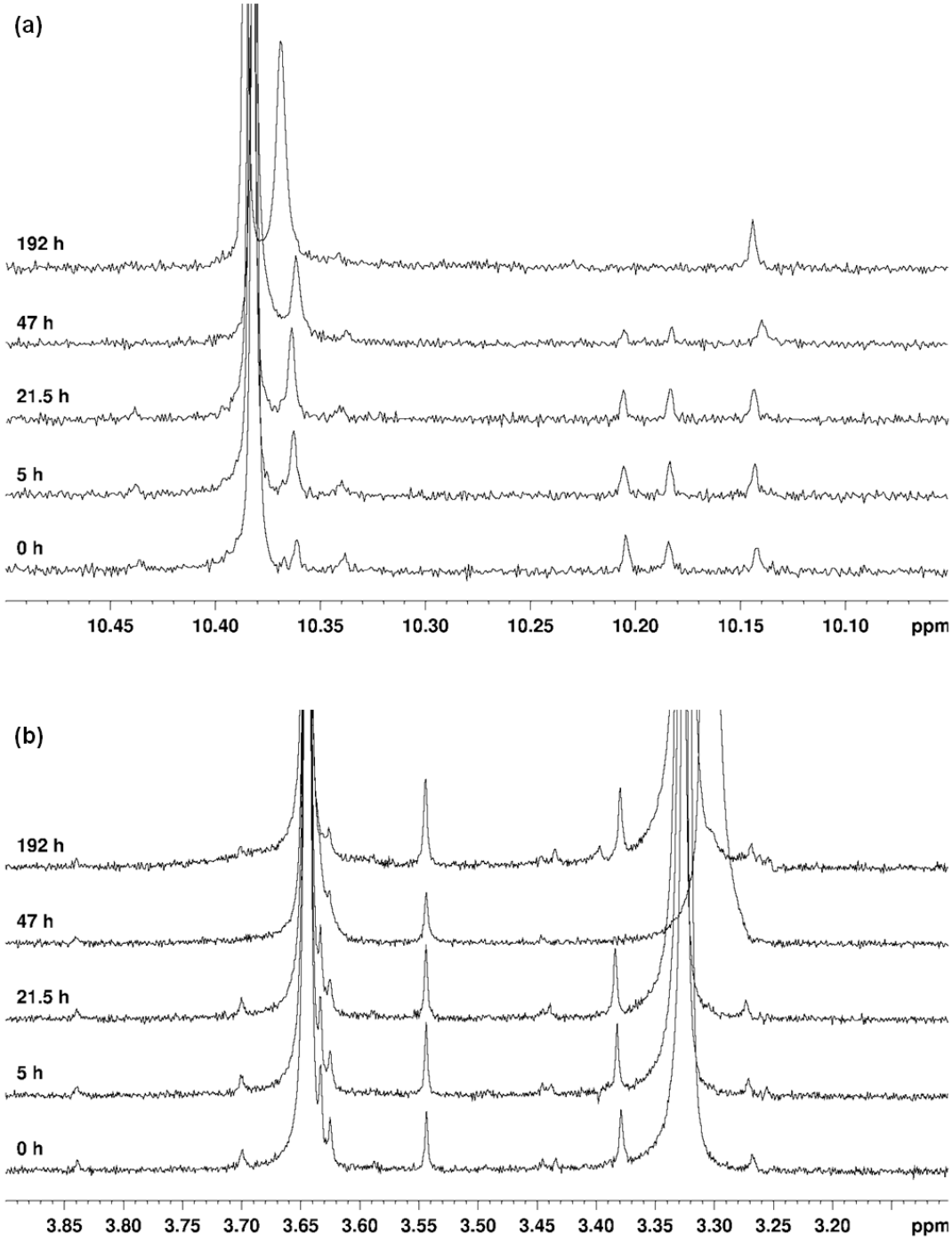

Figure 3.3. Expansions of the azomethine proton region (a) and *N*-methyl proton region (b) of the ^{1}H NMR spectrum (360 MHz) of $Mo(CO)_4$(APSO) in DMSO-d_6 at ~300 K.

Two dominant transitions are observed in the visible region of the electronic absorption spectra for the Mo–spirooxazine complexes: intense bands at ~550 nm for $Mo(CO)_4$(APSO) and ~600 nm for $Mo(CO)_4$(IPSO) are assigned to PMC-based π–π^* CT transitions, and broad, less intense bands at ~450 nm for the APSO complex and ~500 nm for the IPSO complex are assigned to Mo(*d*)–diimine(π^*) MLCT transitions. The absorption wavelengths (λ_{max}) and extinction coefficients (ε) for these bands are summarized in Table 3.2 for toluene and CH_2Cl_2 solutions at ~300 K. The MLCT bands were assigned by analogy with the $Mo(CO)_4$(phen) complex, which displays a MLCT band of similar energy and extinction coefficient (490 nm, 6160 $M^{-1}\cdot cm^{-1}$ in benzene).[306] It should be noted that the extinction coefficients are reported for solutions containing both SO and PMC isomers. Thus, to determine the extinction coefficients for the PMC π–π^* transition for the PMC form alone (ε_{PMC}), the observed values must be corrected for the actual PMC concentration. This concentration may be approximated from the K_T values determined by ^{1}H NMR spectroscopy, if it is assumed that the relative SO/PMC concentrations remain the same across ^{1}H NMR and electronic absorption spectroscopy concentration ranges. The ε_{PMC} values are solvent dependent [ε_{PMC} for $Mo(CO)_4$(APSO) in toluene = 18000 $M^{-1}\cdot cm^{-1}$ and in CH_2Cl_2 = 6700 $M^{-1}\cdot cm^{-1}$; ε_{PMC} for $Mo(CO)_4$(IPSO) in toluene = 88000 $M^{-1}\cdot cm^{-1}$ and in CH_2Cl_2 = 62000 $M^{-1}\cdot cm^{-1}$]. For the IPSO complex, ε_{PMC} is of the same order of magnitude as for the free ligand (60000–90000 $M^{-1}\cdot cm^{-1}$), whereas for the APSO complex, ε_{PMC} is significantly lower than for the free ligand (18000 vs 43000 $M^{-1}\cdot cm^{-1}$ in toluene and 6700 vs 60000 $M^{-1}\cdot cm^{-1}$ in CH_2Cl_2).

To investigate the solvatochromism of the complexes, spectra were acquired in the same series of solvents used for the studies of APSO and IPSO in Chapter 2, and λ_{max} values are plotted as a function of solvent polarity (E_T^N) in Figure 3.4. For $Mo(CO)_4$(APSO), only slight differences in λ_{max} are observed between the Mo complex and the free ligand, and the solvatochromism of the complex parallels that of the free ligand quite closely. For $Mo(CO)_4$(IPSO), in contrast, the PMC π–π^* λ_{max} is consistently bathochromically shifted from that of the ligand, with this shift being up to nearly 20 nm in moderately polar solvents (E_T^N = 0.2–0.3). The solvatochromism of the complex roughly parallels that of the free ligand, although in low polarity solvents, the complex exhibits more pronounced positive solvatochromism, and in high polarity solvents, the

complex exhibits evidence of negative solvatochromism, whereas this is very weak or absent for the free ligand. These results are consistent with previous metal complexation studies in which metal complexation to APSO had little effect[214] while metal complexation to IPSO had a significant effect on photochromic properties.[189, 216]

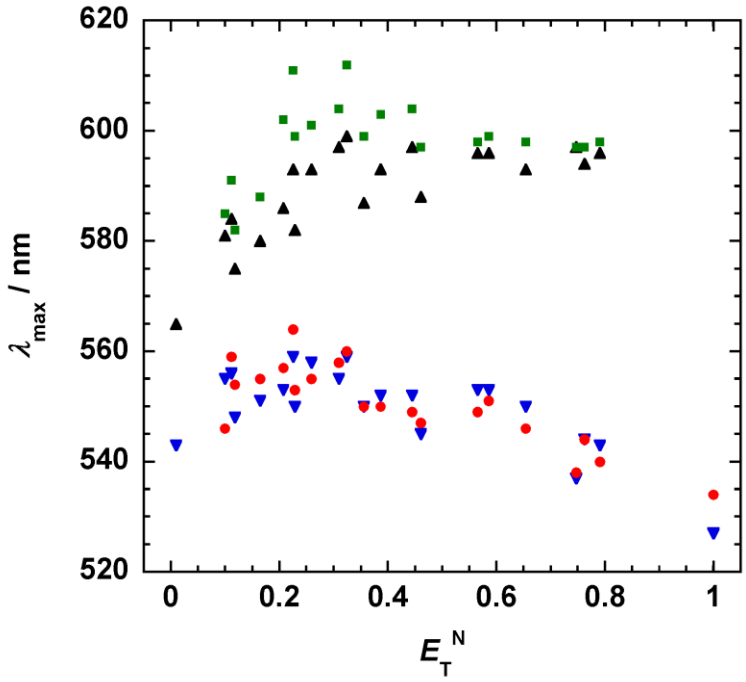

Figure 3.4. PMC π–π* λ_{max} as a function of solvent polarity (Dimroth–Reichardt E_T^N scale) for APSO (▼), $Mo(CO)_4$(APSO) (●), IPSO (▲), and $Mo(CO)_4$(IPSO) (■) at ~300 K.

Freshly prepared solutions of $Mo(CO)_4$(IPSO) exhibit a decrease in the PMC π–π* absorption band with time [shown for a toluene solution in Figure 3.5(a)], which suggests that the photochromic equilibrium is shifted more toward the PMC form in the solid state than in solution, and that once dissolved the solution equilibrates to a lower PMC concentration. From the absorbance intensities of a CH_2Cl_2 solution of $Mo(CO)_4$(IPSO) measured very shortly after dissolution and again at thermal equilibrium at ~300 K, it was estimated that ≥50% of the complex was in the PMC form in the original solid sample. The system then equilibrates to 6% PMC form in toluene and 12% PMC form in CH_2Cl_2 over time (~10 min) once dissolved. No analogous SO/PMC equilibration is observed for $Mo(CO)_4$(APSO), and, because the thermal equilibrium for the APSO

derivative is shifted to >95% PMC form in solution (toluene, CH_2Cl_2), this suggests that the complex exists entirely, or almost entirely, in the PMC form in the solid sample.

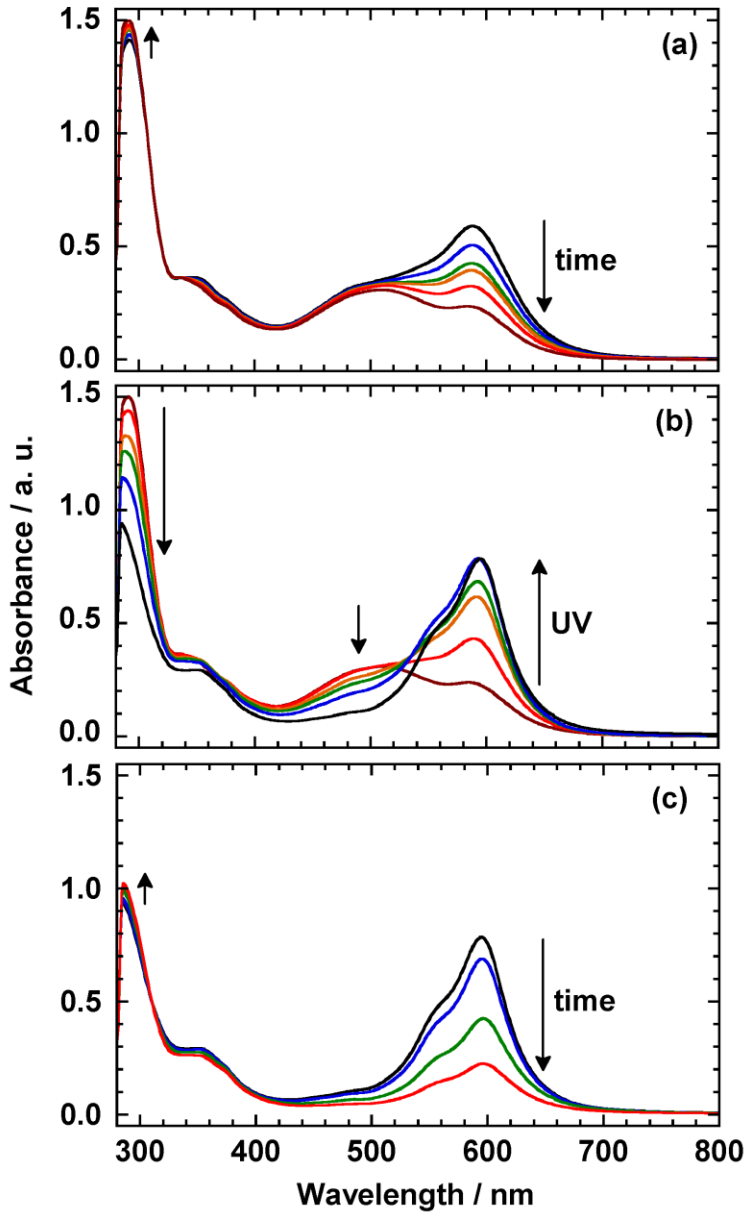

Figure 3.5. UV/Vis electronic absorption spectrum of a toluene solution (5×10^{-5} M) of $Mo(CO)_4$(IPSO) at ~300 K over time after dissolution of a solid sample in the absence of light (~10 min) (a), upon steady-state UV irradiation (~10 min) (b), and again over time in the absence of light (~3 min) (c).

Steady-state UV irradiation of solutions of $Mo(CO)_4$(IPSO) leads to an increase in the intensity of the PMC π–π* band [Figure 3.5(b)]—consistent with photoinduced ring opening to the PMC form—and a simultaneous decrease in the intensity of the MLCT band. In the absence of light, the PMC band decreases to its original intensity, but changes in the MLCT band are not reversible [Figure 3.5(c)]. This is evidence for the UV-induced decomplexation of the spirooxazine ligand, which is corroborated by both a permanent shift of the PMC π–π* λ_{max} to a lower wavelength after one irradiation/thermal relaxation cycle as well as the appearance of free ligand signals in the ^{1}H NMR spectrum of a sample irradiated with UV light. With subsequent UV irradiation cycles, the intensity of the π–π* band increases and decreases repeatedly without loss of intensity, which suggests that the spirooxazine ligand remains intact and photochromic after decomplexation. This behaviour is observed in a range of solvents including toluene, acetone, MeOH, and CH_3CN. In CH_2Cl_2, however, the spirooxazine ligand appears to undergo both decomplexation and decompositition, as evidenced by the disappearance of the MLCT band with UV irradiation and a gradual decrease in the maximum absorbance intensity of the PMC band reached upon thermal relaxation after each irradiation cycle.

The Mo–APSO complex appears to be even more sensitive to UV light than the Mo–IPSO complex. Steady-state UV irradiation of solutions of $Mo(CO)_4$(APSO) leads to a decrease in the intensity of the MLCT band, indicating decomplexation, as well as a decrease in the maximum intensity of the PMC band with cycling, indicating ligand decomposition. Solutions of $Mo(CO)_4$(APSO) also exhibit relatively rapid decomposition processes while exposed to the UV irradiation from ambient light or the incident beam from the spectrometer. All of the molybdenum complexes were therefore handled in the absence of light, and incident irradiation from the spectrometer of <300 nm was filtered during electronic absorption spectroscopy experiments. Solutions of the APSO free ligand alone also exhibit UV-induced decomposition processes in a range of solvents including CH_3CN, CH_2Cl_2, CH_3OH, and acetone, though are stable in toluene. The observed photoinduced decomposition process in the $Mo(CO)_4$(APSO) complex may therefore be the result of either ligand-based processes or a combination of metal- and ligand-based processes.

Upon steady-state visible irradiation (λ_{ex} = 568 nm), solutions of $Mo(CO)_4$(APSO) and $Mo(CO)_4$(IPSO) exhibit a decrease in the intensity of the PMC π–π* absorption band, consistent with PMC → SO conversion. The π–π* band returns gradually to its original intensity in the absence of light. This behaviour can be repeated over sequential irradiation/thermal reversion cycles with little change in the limiting absorbance intensities [shown for $Mo(CO)_4$(APSO) in CH_2Cl_2 in Figure 3.6], which indicates that the complexes are photoresponsive to visible irradiation without undergoing significant photodegradation.

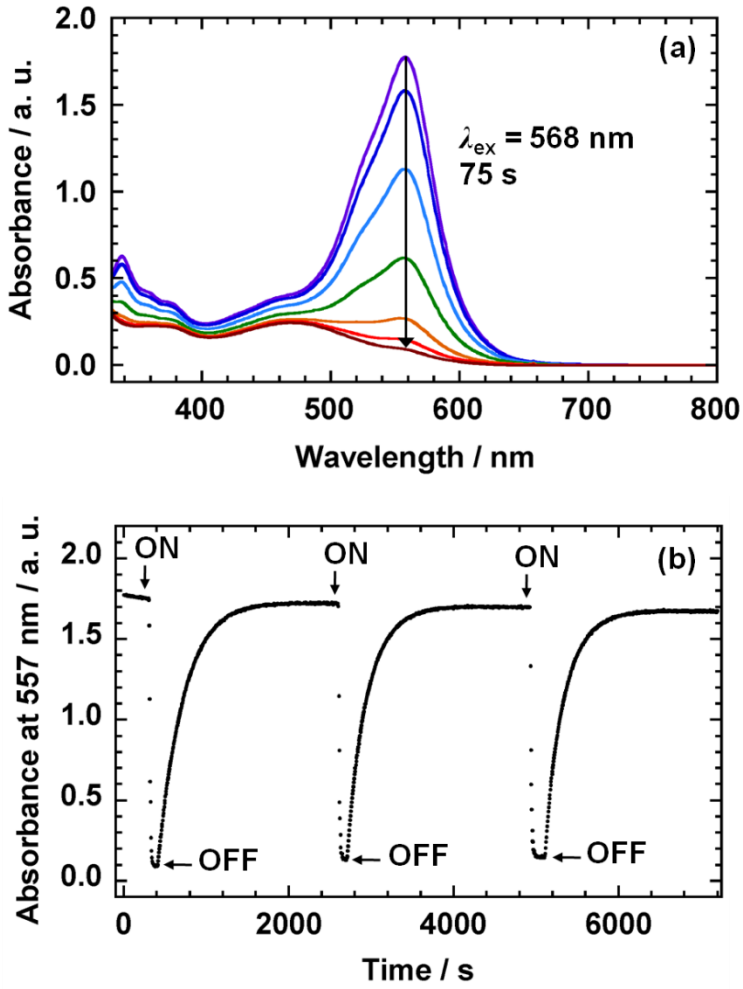

Figure 3.6. Electronic absorption spectrum of a CH_2Cl_2 solution (3×10^{-4} M) of $Mo(CO)_4$(APSO) at ~300 K upon steady-state visible irradiation at λ_{ex} = 568 nm (a), and kinetic profile of the absorbance intensity at the PMC π–π* λ_{max} value of 557 nm over three irradiation cycles in the presence (ON) and absence (OFF) of light (b).

The thermal SO → PMC and PMC → SO isomerization rate constants (k_1 and k_2, respectively), were determined from the k_{obs} and K_T values determined for the Mo complexes in the same way as for the free ligands. For the complexes, k_{obs} was determined by monitoring the time-dependence of the absorbance intensity of the PMC π–π* transition at λ_{max} under one or more of three possible conditions: (1) during thermal equilibration toward the SO form after establishing a photostationary state (PSS) with UV irradiation (k_{UV}^{-1}); (2) during thermal equilibration toward the PMC form after establishing a PSS with visible irradiation (k_{Vis}^{-1}); and (3) during thermal equilibration toward the SO form upon initial dissolution of a solid sample (k_{dis}). The kinetic traces were then fit to first-order monoexponential rate equations, with adequate fits in all cases except for the $Mo(CO)_4$(APSO) complex in toluene, in which case the kinetic data was better fit with a first-order biexponential rate equation to give two components of nearly equal contributions with rate constants on the same order of magnitude as that determined using a monoexponential fit. The observation of different components for the thermal relaxation rate of $Mo(CO)_4$(APSO) in toluene may support the existence of multiple stable *cis*/*trans* isomers in solution for the Mo complexes. The values of k_1 and k_2 were then calculated from K_T = [PMC]/[SO] = k_1/k_2 and $k_{obs} = k_1 + k_2$. In cases where more than one of k_{UV}^{-1}, k_{Vis}^{-1}, and k_{dis} were determined for a given compound in a given solvent, the k_{UV}^{-1} or k_{dis} values were used to calculate k_1 and k_2. The obtained kinetic parameters are summarized in Table 3.2. Both k_1 and k_2 are lower in the Mo complexes than in the free ligands. For the IPSO complex, both rate constants are about an order of magnitude smaller than those of the free ligands, and for the APSO complex, k_1 is an order of magnitude smaller and k_2 is two or more orders of magnitude smaller than the corresponding rate constants for the free ligands. The pronounced decrease in rate constants for both SO → PMC and PMC → SO isomerization upon molybdenum complexation may be due to hindered *cis*/*trans* rotation—required for thermal ring-opening or ring-closing—in the bulkier metal complexes. Additionally, the particularly significant decrease in k_2 for APSO upon complexation may be due to the exceptional stabilization of the PMC form in this derivative.

To summarize, $Mo(CO)_4$(IPSO) exists as ≥50% PMC and $Mo(CO)_4$(APSO) as ~100% PMC in the solid-state samples, while in solution, the IPSO complex exists

predominantly in the SO form and the APSO complex in the PMC form. Both of the Mo complexes appear to be sensitive to decomplexation by UV light, but are photoresponsive and photochemically stable upon irradiation with visible light. In the study of these systems, we can therefore efficiently experimentally monitor either: (a) the thermal SO → PMC equilibration of $Mo(CO)_4$(APSO) after a PSS is established with visible irradiation (where this PSS is nearly 100% SO form, and the system can be monitored from ~100% SO form to ~100% PMC form) or (b) the thermal PMC → SO equilibration of $Mo(CO)_4$(IPSO) immediately following dissolution (where ~50% PMC form is converted to ~10% PMC form over time).

3.2.4. FT-IR Spectroscopy of Molybdenum Complexes

The FT-IR spectrum of a sample of $Mo(CO)_4$(APSO) was acquired in CH_2Cl_2 at ~300 K before and immediately after 5 min of irradiation with visible light (λ_{ex} = 568 nm) to monitor the spectral changes occurring upon PMC → SO photoisomerization, and again 17 min after the light was removed to monitor the spectral changes upon return to the PMC form after SO → PMC thermal isomerization (Figure 3.7). Upon PMC → SO photoisomerizaton, large spectral changes occur in the fingerprint region [Figure 3.7(a)], while the peaks in the CO stretching region shift to higher energies by 1–4 cm^{-1} [Figure 3.7(b)]. These spectral changes are reversible following SO → PMC thermal isomerization, as evident from the return of the FT-IR spectrum to its original appearance after >15 min in the absence of light. Because $Mo(CO)_4$(APSO) initially exists as 98% PMC form in CD_2Cl_2 at ~300 K (Table 3.2), and the solution becomes essentially colorless after visible irradiation (Figure 3.8), it may be concluded that the complex converts from ~100% PMC form to ~100% SO form upon visible irradiation in CH_2Cl_2. The energies of the CO stretching vibrational modes determined before and after irradiation may therefore be assigned to the PMC or SO forms of the complex, respectively, as summarized in Table 3.3.

The FT-IR spectrum of a sample of $Mo(CO)_4$(IPSO) in CH_2Cl_2 at ~300 K was monitored over time shortly after dissolution of the solid sample to observe the spectral changes occurring upon PMC → SO thermal isomerization (Figure 3.9). The observed changes are similar to those described above for the APSO complex: the majority of the

peaks in the fingerprint region decrease in intensity with some shifting [Figure 3.9(a)], while the peaks in the CO stretching region shift to higher energies by up to 2 cm^{-1} [Figure 3.9(b)]. Although the direction of the experimental shifts for the CO peaks is the same for both complexes upon PMC → SO isomerization, the magnitude of these shifts is approximately half in the case of $Mo(CO)_4$(IPSO). Because the IPSO complex converts from ~50% PMC form to ~10% PMC form over the course of the experiment, whereas the APSO complex converts from ~100% to ~0% PMC form, the relative magnitudes of the shifts may be indicative of similar ligand field changes in both complexes if it is assumed that their C–O stretching force constants are equivalent.

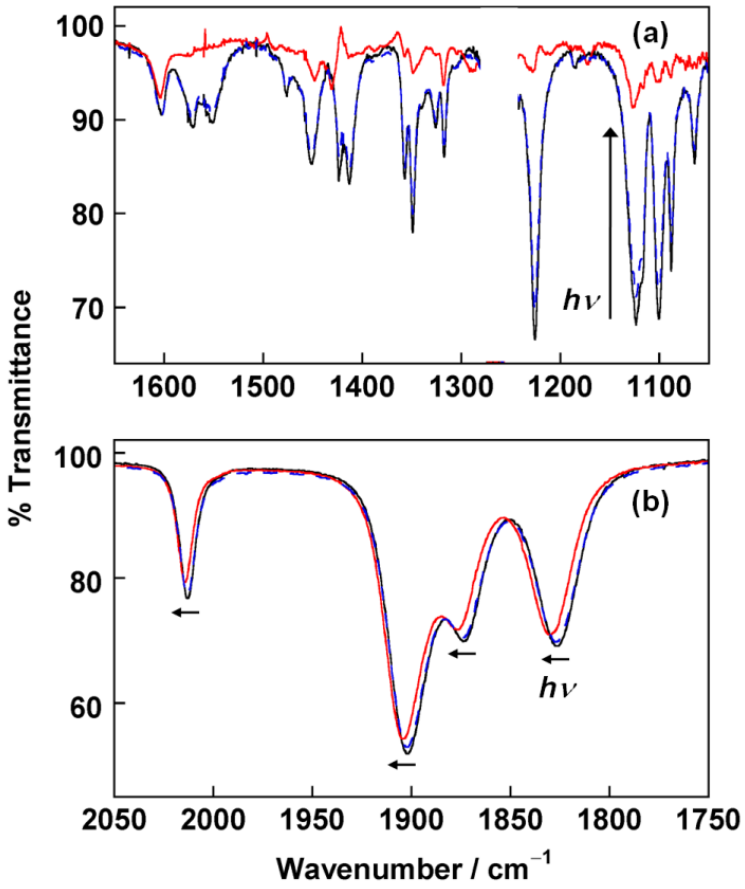

Figure 3.7. FT-IR spectrum of $Mo(CO)_4$(APSO) in CH_2Cl_2 at ~300 K illustrating spectral features in the fingerprint (a) and carbonyl stretching (b) regions before irradiation (—), immediately after 5 min of steady-state visible irradiation (λ_{ex} = 568 nm) (—), and after 17 min in the absence of light (— —). The gap at ~ 1275 cm^{-1} is due to a solvent background correction.

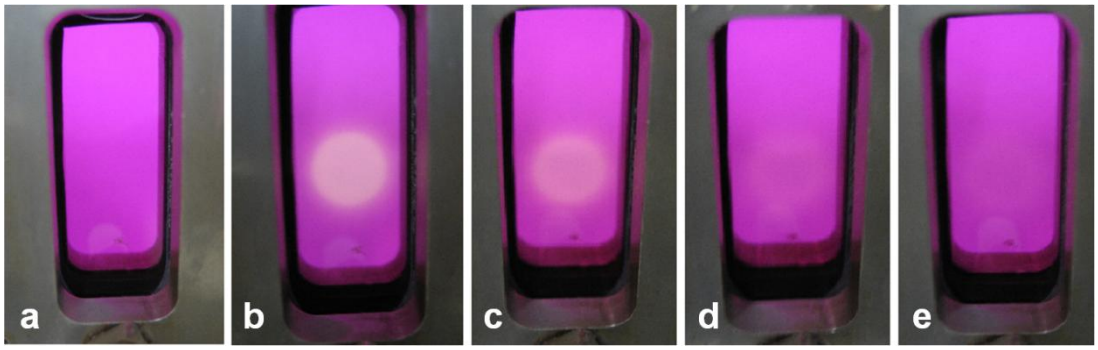

Figure 3.8. CH_2Cl_2 solution of $Mo(CO)_4$(APSO) in the FT-IR solution cell before irradiation (a), shortly after 5 min of steady-state visible irradiation (λ_{ex} = 568 nm) (b), and over the next few minutes in the absence of light (c)–(e).

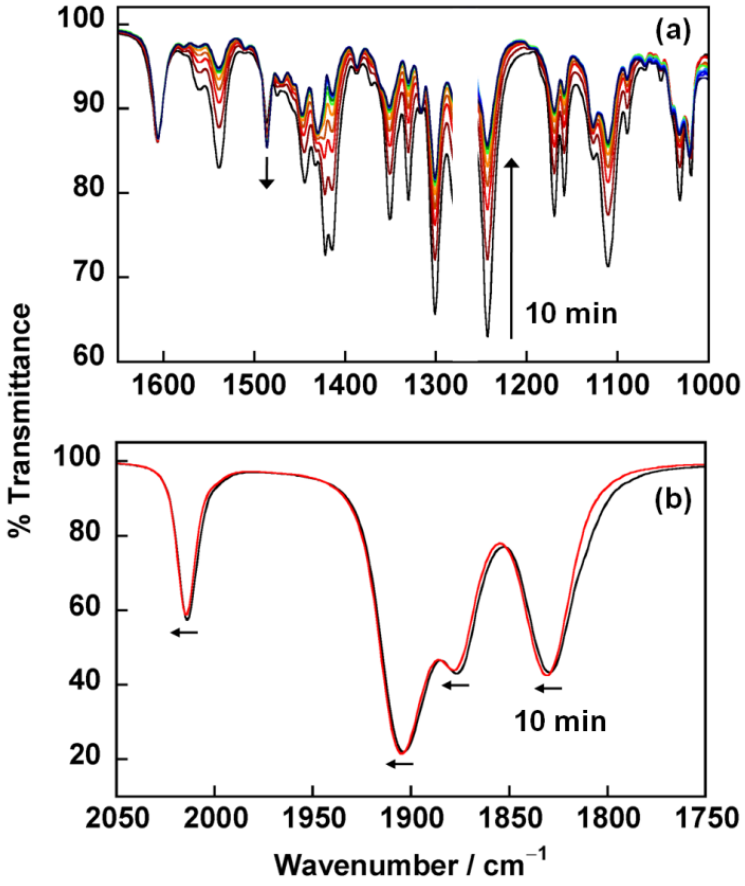

Figure 3.9. FT-IR spectrum of a freshly dissolved sample of $Mo(CO)_4$(IPSO) in CH_2Cl_2 at ~300 K over the course of 10 min illustrating spectral changes in the fingerprint (a) and carbonyl stretching (b) regions upon PMC → SO thermal isomerization. The gap at ~1275 cm^{-1} is due to a solvent background correction.

Table 3.3. Energies [cm^{-1}] of CO stretching vibrations of $Mo(CO)_4$(phen), $Mo(CO)_4$(APSO) and $Mo(CO)_4$(IPSO) in CH_2Cl_2 at ~300 K.[a]

		B_2	A_1^1	B_1	A_1^2
$Mo(CO)_4$(phen)		1831	1878	1905	2015
$Mo(CO)_4$(APSO)	SO	1830	1877	1904	2014
	PMC	1827	1873	1902	2013
	$\Delta\nu_{SO-PMC}$	3	4	2	1
$Mo(CO)_4$(IPSO)	SO	1832	1879	1905	2015
	PMC	1830	1877	1904	2015
	$\Delta\nu_{SO-PMC}$	2	2	1	0

[a]Vibrational modes were assigned assuming pseudo-C_{2v} symmetry; see ref[299].

In the FT-IR spectroscopy of metal–carbonyl complexes, higher-energy CO stretching vibrations are associated with higher CO bond orders. The Cotton–Kraihanzel force constants, which can be calculated from the energies of the CO vibrational modes, most accurately parallel CO bond orders as they take into account the interactions between carbonyl groups, and thus most accurately reflect the CO(σ)–M(d) and M(d)–CO(π*) interactions.[299, 307, 308] However, the direct CO stretching vibration energies still yield useful semiquantitative bonding information, particularly in the comparison of compounds of the same structure [e.g., only *cis*-$M(CO)_4$(LL) complexes] and the same ligand type (e.g, only diimine ligands). In the Mo–spiroxazine complexes, four CO stretching modes are observed, as expected for six-coordinate, *cis*-tetracarbonyl complexes.[299] The CO stretching energies are slightly higher (by 1–2 cm^{-1}) for $Mo(CO)_4$(IPSO) than $Mo(CO)_4$(APSO), and these same stretching energies are essentially the same for the SO form of $Mo(CO)_4$(IPSO) and $Mo(CO)_4$(phen) under the same experimental conditions (Table 3.3). Each of the CO stretching peaks is shifted to higher energy in the SO form of the spirooxazine ligand relative to the PMC form. The values of $\Delta\nu_{SO-PMC}$ are small, but are on the same order of magnitude as typically observed between $M(CO)_4$(NN) (M = Cr, Mo, W) complexes with different diimine ligands[300, 306, 309-312] [e.g., $Mo(CO)_4$(bpy) and $Mo(CO)_4$(phen) in CH_2Cl_2 or $CHCl_3$ show energy differences of 0–3 cm^{-1} for the four carbonyl stretching modes].[310, 312] Higher energy vibrational modes imply higher C–O bond orders, which imply less M(d)–CO(π*) backbonding, which in turn reveal greater M(d)–phen(π*) backbonding. Therefore, the

FT-IR results indicate that phen and IPSO-SO have similar π-acceptor strengths, that APSO is a weaker π-acceptor than IPSO, and—most importantly—that the SO form behaves as a stronger π-acceptor than the PMC form for both APSO and IPSO.

3.2.5. ^{13}C NMR Spectroscopy of Molybdenum Complexes

The ^{13}C NMR spectra of $Mo(CO)_4$(IPSO) and $Mo(CO)_4$(APSO) were acquired in CD_2Cl_2 at ~300 K, and the chemical shifts for the carbonyl groups are tabulated in Table 3.4. In both complexes, two sets of carbonyl resonances are observed: a first set at ~223 ppm is assigned to the CO_{eq} groups and a second set at ~205 ppm is assigned to the CO_{ax} groups. In the set of CO_{eq} resonances for $Mo(CO)_4$(IPSO), two intense peaks at 223.14 and 223.26 ppm and a less intense peak at 223.34 ppm are observed. The more intense peaks can be assigned to the SO form and the less intense one to the PMC form (as the IPSO complex exists as 12% PMC form from ^{1}H NMR data, Table 3.2). It is plausible that a second less intense peak is masked by the peak at 223.26 ppm and represents a second PMC-based CO_{eq} signal. The PMC-based resonances are more downfield than the SO-based resonances, and the differences between the chemical shifts of the two sets of signals, $\Delta\delta_{PMC-SO}$, are 15 Hz (223.26 – 223.14 ppm) and 10 Hz (223.34 – 223.26 ppm). In the set of CO_{ax} resonances for $Mo(CO)_4$(IPSO), only one intense and one weak peak are observed at 205.44 and 205.59 ppm, respectively. Both of these peaks are more intense than those of the CO_{eq} groups, as each comprises two overlapping ^{13}C resonances from two axial carbonyl groups, consistent with pseudo-C_{2v} symmetry of the complex. The value of $\Delta\delta_{PMC-SO}$ is 19 Hz for the axial carbonyl groups, with the signal attributed to the PMC form again further downfield. Although a ^{13}C NMR spectrum was also acquired for $Mo(CO)_4$(APSO), it was not useful for comparing chemical shifts between SO and PMC species since this complex exists as 98% PMC form in CD_2Cl_2 (Table 3.2) and the SO form cannot be clearly observed. However, in comparing the relative shifts of $Mo(CO)_4$(phen), $Mo(CO)_4$(IPSO), and $Mo(CO)_4$(APSO), we find that the shifts for the first two are nearly identical, while those for the latter are slightly more downfield.

Table 3.4. ^{13}C NMR chemical shifts [ppm] for the carbonyl groups of $Mo(CO)_4$(APSO) and $Mo(CO)_4$(IPSO) in CD_2Cl_2 at ~300 K.

		$\delta_{CO(ax)}$	$\delta_{CO(eq)}$	
$Mo(CO)_4$(phen)[a]		205.45	223.21	
$Mo(CO)_4$(IPSO)[b]	SO	205.44[c]	223.14	223.26
	PMC	205.59[c]	223.26[d]	223.34
	$\Delta\delta_{PMC-SO}$ [Hz]	19	15	10
$Mo(CO)_4$(APSO)[a]	SO	–	–	–
	PMC	205.73[c]	223.29	223.41

[a]Acquired at 90 MHz. [b]Acquired at 125 MHz. [c]Peak slightly broad; two peaks unresolved. [d]Assigned based on the assumption that a second PMC peak is masked by the SO peak at 223.26 ppm.

In the ^{13}C NMR experiment, there is a relationship between the chemical shifts of the carbonyl groups and the Cotton–Kraihanzel CO stretching force constants, and a linear correlation between the two variables has been documented for a number of systems.[313, 314] Precisely, a more upfield chemical shift can be correlated with higher force constants and, by extension, with higher-energy CO vibrational modes and bond orders. In the Mo–tetracarbonyl–spirooxazine complexes, the carbonyl chemical shifts are found more upfield in the SO form than in the PMC form. Again, the $\Delta\delta_{PMC-SO}$ values are small but are on the same order of magnitude expected for $M(CO)_x(L)_y$ complexes with different ligands, L.[314] Thus the ^{13}C NMR results reveal that the SO form is a stronger π-acceptor than the PMC form, consistent with the FT-IR results. Additionally, on the basis of relative carbonyl ^{13}C NMR shifts, phen and IPSO-SO are again predicted to have similar π-acceptor strengths, whereas APSO is predicted to be a slightly weaker π-acceptor.

3.2.6. Cyclic Voltammetry

The electrochemical behaviour of the spirooxazine ligands was investigated by cyclic voltammetry to establish redox potentials and correlate these to the calculated energies of the frontier molecular orbitals via Koopman's theorem. Cyclic voltammograms (CVs) for solutions of APSO and IPSO (5×10^{-4} – 1×10^{-3} M) were acquired in deoxygenated 0.1 M tetrabutylammonium tetrafluoroborate (TBA-TFB) CH_2Cl_2 and CH_3CN solutions at ~300 K and scan rates of 50 mV/s. All potentials were referenced to the Fc^+/Fc redox

couple and reported vs SCE. The relevant electrochemical data are summarized in Table 3.5, and representative CVs of APSO and IPSO in CH_3CN and $CH_2Cl_2$are shown in Figure 3.10 and Figure 3.11.

Table 3.5. Redox potentials [V vs SCE] for APSO, IPSO, $Mo(CO)_4$(APSO), and $Mo(CO)_4$(IPSO) in CH_2Cl_2 and CH_3CN at ~300 K.[a]

	CH_2Cl_2						
	Red_2		**Red_1**			**Ox_1**	**Ox_2**
	E_{pc}	E_{pc}	$E_{1/2}$	ΔE_p	i_a/i_c	E_{pa}	E_{pa}
APSO	–1.63	–1.15	–1.10	0.080[b]	0.70[b]	0.79	1.08
IPSO	–1.64	–0.84	–0.82	0.120	0.85	[c]	[c]
$Mo(CO)_4$(APSO)[d]	–1.42	–1.04	–1.01	0.085[e]	0.80[e]	0.89	
$Mo(CO)_4$(IPSO)[d]	–1.44	–0.87 (–0.78)[f]	–0.82 (–0.75)[f]	0.105 (0.056)[f]	0.76 (0.50)[f]	0.83	
	CH_3CN						
	Red_2		**Red_1**			**Ox_1**	**Ox_2**
	E_{pc}	E_{pc}	$E_{1/2}$	ΔE_p	i_a/i_c	E_{pa}	E_{pa}
APSO	–1.70	–1.26	–1.22	0.080	0.65	0.59	0.86
IPSO	–1.71	–1.02	–0.99	0.060	2.60	0.86	1.07

[a]Experimental conditions – solute concentration: 5×10^{-4} to 1×10^{-3} M; electrolyte: 0.1 M TBA-TFB in deoxygenated CH_2Cl_2 or CH_3CN solutions; scan rate: 50 mV/s; electrode configuration: glassy carbon working electrode, silver pseudo-reference electrode, platinum counter electrode; referenced to the Fc^+/Fc redox couple and reported vs SCE. [b]If the first reduction wave is isolated, these values are ΔE_p = 0.160 V, i_a/i_c = 1.0. [c]The oxidation processes for IPSO in CH_2Cl_2 are not distinguishable. [d]The Mo complexes are sparingly soluble in CH_3CN, and CVs were only acquired in CH_2Cl_2. [e]If the first reduction wave is isolated, these values are ΔE_p = 0.059 V, i_a/i_c = 1.0. [f]The first value listed is for the first time trace; the value in parentheses is for the last time trace.

The electrochemical processes observed in CH_2Cl_2 and CH_3CN are similar, and representative data are described. Two irreversible oxidation processes (Ox_1 and Ox_2) are observed for each of the ligands [except in the case of IPSO in CH_2Cl_2] with anodic peak potentials, E_{pa}, recorded between 0.6 and 1.1 V. Two notable reduction processes are also observed for each of the ligands. For APSO in CH_2Cl_2, a major quasireversible reduction wave (Red_1) is observed with a half-wave potential, $E_{1/2}$, of –1.10 V (ΔE_p = 0.080 V, i_a/i_c

= 0.70), and a second minor irreversible process (Red_2) is observed with a cathodic peak potential, E_{pc}, of –1.63 V. For IPSO in CH_2Cl_2, a minor quasireversible reduction process (Red_1) is observed with an $E_{1/2}$ value of –0.82 V (ΔE_p = 0.120 V, i_a/i_c = 0.85), and a major irreversible process (Red_2) is observed with an E_{pc} value of –1.64 V. Two additional peaks are observed between 0 and –1.0 V for both spirooxazine ligands: a small peak is observed during the anodic sweep, but only after cycling through the second reduction process at negative potentials, and a small peak is observed during the cathodic sweep after cycling through the oxidation processes at positive potentials.

For electrochemically reversible processes, the peak current is proportional to the concentration of electrochemically active species in solution.[315] Even though the reduction processes for APSO and IPSO are quasireversible or irreversible, we have tentatively assigned them to SO- or PMC-based processes on the basis of the relative concentrations of these species in solution. From ^{1}H NMR spectroscopy, it was determined that the majority (95 and 92% in CD_3CN and CD_2Cl_2, respectively) of APSO exists in the PMC form and the majority (94 and 95%, in CD_3CN and CD_2Cl_2, respectively) of IPSO exists in the SO form (^{1}H NMR spectra of APSO in CD_3CN and CD_2Cl_2 with 0.1 M TBA-TFB confirmed that the presence of the electrolyte did not shift the SO/PMC equilibrium). We can therefore reasonably assign the major reduction process (Red_1) for APSO to a PMC-based process and the major reduction process for IPSO (Red_2) to a SO-based process. We may also more tentatively assign the minor reduction process (Red_1) for IPSO to a PMC-based process. This assignment is consistent with the PMC species being present in ~5% in solutions of IPSO and with the observation of an analogous reduction process in solutions of APSO, in which the PMC form is the major species in solution. Following similar reasoning for APSO and assigning the second reduction process (Red_2) to a SO-based process may not be appropriate since the peak current for this process is fairly high relative to that of Red_1, and this may not be consistent with the SO species being present in only 5–8% in solution. This peak may in fact be due to a second reduction of the PMC species, which would be in agreement with the lower i_a/i_c observed for the first reduction process after cycling through the second reduction process at more negative potentials.

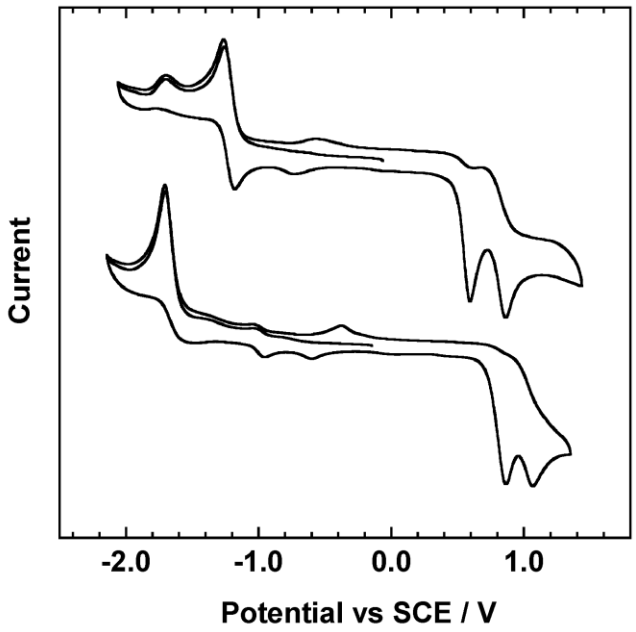

Figure 3.10. CVs of solutions (5×10^{-4} – 1×10^{-3} M) of APSO (top) and IPSO (bottom) in deoxygenated 0.1 M TBA-TFB CH_3CN at ~300 K (electrode configuration: glassy carbon working electrode, silver pseudo-reference electrode, platinum counter electrode; scan rate: 50 mV/s; referenced to the Fc^+/Fc redox couple and reported vs SCE).

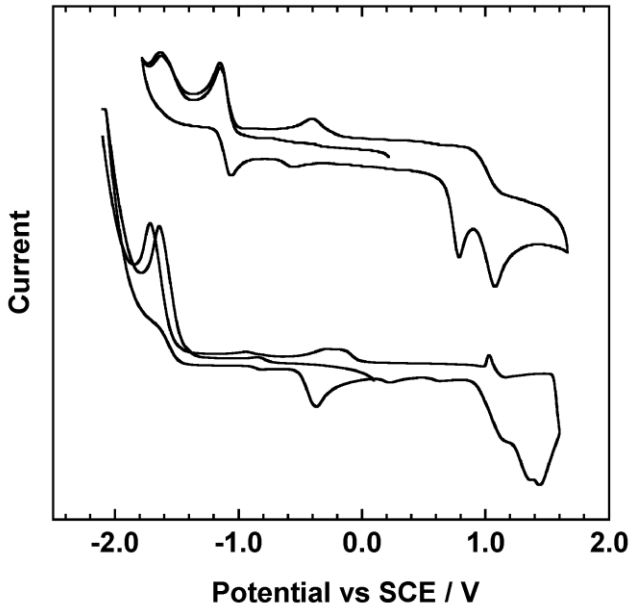

Figure 3.11. CVs of solutions (5×10^{-4} – 1×10^{-3} M) of APSO (top) and IPSO (bottom) in deoxygenated 0.1 M TBA-TFB CH_2Cl_2 at ~300 K (electrode configuration: glassy carbon working electrode, silver pseudo-reference electrode, platinum counter electrode; scan rate: 50 mV/s; referenced to the Fc^+/Fc redox couple and reported vs SCE).

The electrochemical behaviour of the Mo–tetracarbonyl–spirooxazine complexes was also studied by cyclic voltammetry, and data are summarized in Table 3.5. The Mo complexes are sparingly soluble in CH_3CN, and their CVs were therefore only acquired in solutions of CH_2Cl_2 with 0.1 M TBA-TFB (Figure 3.12 and Figure 3.13). The electrochemical behaviour of the complexes is analogous to that of the free ligands, with some of the reduction peaks being shifted to slightly more positive potentials and the first reduction process (Red_1) exhibiting greater reversibility. Again the electrochemical features can be tentatively assigned to SO- or PMC-based processes. The ^1H NMR spectra of the complexes indicate that upon thermal equilibration in CD_2Cl_2 at ~300 K, $Mo(CO)_4$(APSO) exists as 98% PMC form and $Mo(CO)_4$(IPSO) exists as 12% PMC form. Thus it is reasonable to assign the major reduction process observed in solutions of $Mo(CO)_4$(APSO) at an $E_{1/2}$ value of –1.01 V to a PMC species. In solutions of $Mo(CO)_4$(IPSO), the system slowly equilibrates from the PMC form (≥50%) to the SO form (12%) form over time (vide supra, Section 3.2.3), and the changes observed in the CV of a freshly dissolved sample over time, shown in Figure 3.13, are informative in assigning the reduction processes. Here, the forward peak current for the first reduction process decreases over time, and E_{pc} shifts from –0.87 to –0.77 V, while a peak at a more positive potential of –0.65 V grows in with what appears to be an isosbestic point. The reverse peak current for this same reduction process also decreases over time, but the peak position shifts only a small amount from –0.76 to –0.73 V. The ΔE_p for the process therefore decreases from 0.105 to 0.056 V over time. The peak current for the second reduction process at E_{pc} = –1.44 V increases over time with no associated shift in peak position. The changes in the relative peak currents for the two main reduction processes support the assignment of the first and second reduction processes to PMC- and SO-based processes, respectively, since the direction of change for the peak intensities corresponds with the expected PMC → SO isomerization upon dissolution. By extension, these observations also support the analogous peak assignments made above for the free ligands. The shift in E_{pc} and isosbestic behaviour for what is assigned as a PMC-based reduction process suggests the formation of different electrochemically active species in solution over time and may be due to changes in aggregation or H-bonding of the PMC species, or thermal isomerization to a different population of PMC *trans*/*cis* isomers.

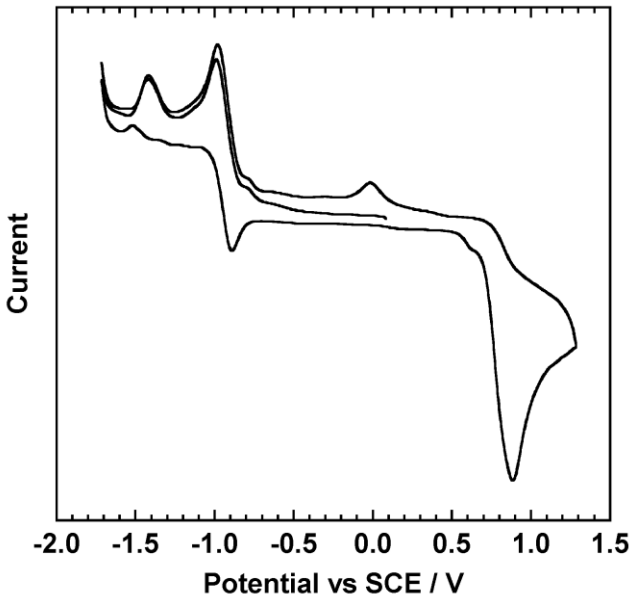

Figure 3.12. CV of a solution (10^{-4} M) of $Mo(CO)_4$(APSO) in deoxygenated 0.1 M TBA-TFB CH_2Cl_2 at ~300 K (electrode configuration: glassy carbon working electrode, silver pseudo-reference electrode, platinum counter electrode; scan rate: 50 mV/s; referenced to the Fc^+/Fc redox couple and reported vs SCE).

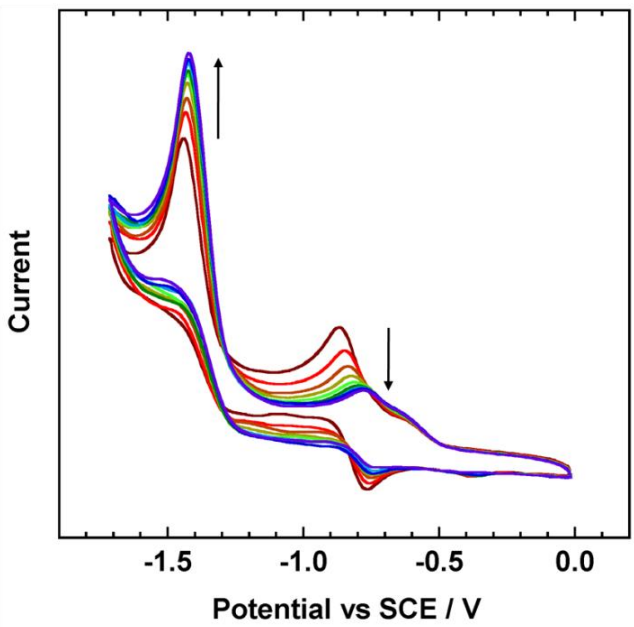

Figure 3.13. CV of a solution (10^{-4} M) of $Mo(CO)_4$(IPSO) in deoxygenated 0.1 M TBA-TFB CH_2Cl_2 at ~300 K over time (electrode configuration: glassy carbon working electrode, silver pseudo-reference electrode, platinum counter electrode; scan rate: 50 mV/s; referenced to the Fc^+/Fc redox couple and reported vs SCE).

3.2.7. DFT Molecular Orbital Analysis of APSO and IPSO

The molecular geometries of stationary points on the ground-state potential energy surfaces of APSO and IPSO were optimized at the DFT/B3LYP level of theory[273, 291, 292] using the Gaussian 03 software package.[272] In the SO form of the spirooxazines, the chirality of the spiro carbon leads to two possible enantiomers, and in this work the (*R*) enantiomer was arbitrarily calculated for all of the molecules. In the PMC form of the spirooxazines, for which eight *cis*/*trans* isomers are possible, geometry optimizations were only performed on the *trans*-*trans*-*cis* (TTC) isomer since it is known to be the most thermodynamically stable in nearly all spirooxazine-based PMCs,[227, 232, 233, 237, 316] and both APSO and $Mo(CO)_4$(APSO) have been found to crystallize in this form.[218] Ligand geometries were optimized using the 6-31G(d,p) basis set. The B3LYP/6-31G(d) level of theory has successfully reproduced experimental geometries of the SO form of spirooxazines—except in some cases for the C_{spiro}–O bond length.[218, 275, 276] DFT, however, is known to systematically underestimate the degree of bond-length alternation in conjugated molecules,[280] including photomerocyanines.[218, 276] Nevertheless, experimentally consistent energies and molecular orbital descriptions for the ground states of spirooxazines and photomerocyanines have been obtained using DFT.[276, 282] Larger basis sets have not been found to significantly improve the optimized geometries[218, 240, 275] nor, as verified here, to give frontier MOs significantly different from those obtained with the 6-31G(d,p) basis set.

High-lying occupied MOs and low-lying unoccupied MOs for both the SO and PMC forms of APSO and IPSO are shown in Figure 3.14 and Figure 3.15, respectively. It is immediately evident that the MOs of APSO and IPSO are nearly identical, although the MOs of IPSO are slightly lower in energy and exhibit in some cases a greater delocalization of electron density onto the indolyl moiety. The MOs for the SO and PMC forms of the ligands are, however, significantly different from each other, which at first glance suggests that the two forms will exhibit different bonding properties. In order to analyze the π-acceptor properties of the phen-based ligands, we have focused on the low-lying unoccupied frontier MOs of the ligands capable of π-backbonding throughout the following analysis. Low-lying unoccupied MOs of π^* symmetry for the SO and PMC forms of APSO and IPSO are shown in Figure 3.15, alongside corresponding unoccupied

orbitals for phen. The two lowest-lying π^* MOs for phen have b_1 and a_2 symmetries and are extremely close in energy.[317] In both SO and PMC forms of the spirooxazine ligands, the LUMO + 1 is essentially phen-based and, by analogy with phen, can be assigned pseudo-b_1 symmetry assuming pseudo-C_{2v} symmetry for the complex. This MO is 0.27 eV higher in energy in the PMC form than in the SO form for APSO, and 0.20 eV higher in energy for IPSO. In the SO form of the ligands, the LUMO and LUMO + 2 appear to be mixtures of phen(a_2)- and spirooxazine-based MOs.[282, 316] In the PMC form of the ligand, however, these two MOs are quite different: the LUMO has predominantly spirooxazine character, and the LUMO + 2 has predominantly phen(a_2) character. The LUMO is 0.60 eV lower in energy in the PMC form than in the SO form for APSO and 0.71 eV lower in energy for IPSO.

The character of the frontier unoccupied MOs can be understood by considering the interaction between the phenanthroline and remaining spirooxazine fragments.[318] In the phen fragment, the a_2 MO has large orbital coefficients at the 5- and 6-positions, whereas the b_1 MO has much smaller coefficients. Thus, attaching the spirooxazine fragment at these positions would be expected to lead to greater mixing with the phen(a_2) MO fragment relative to the phen(b_1) MO fragment, as is observed here.

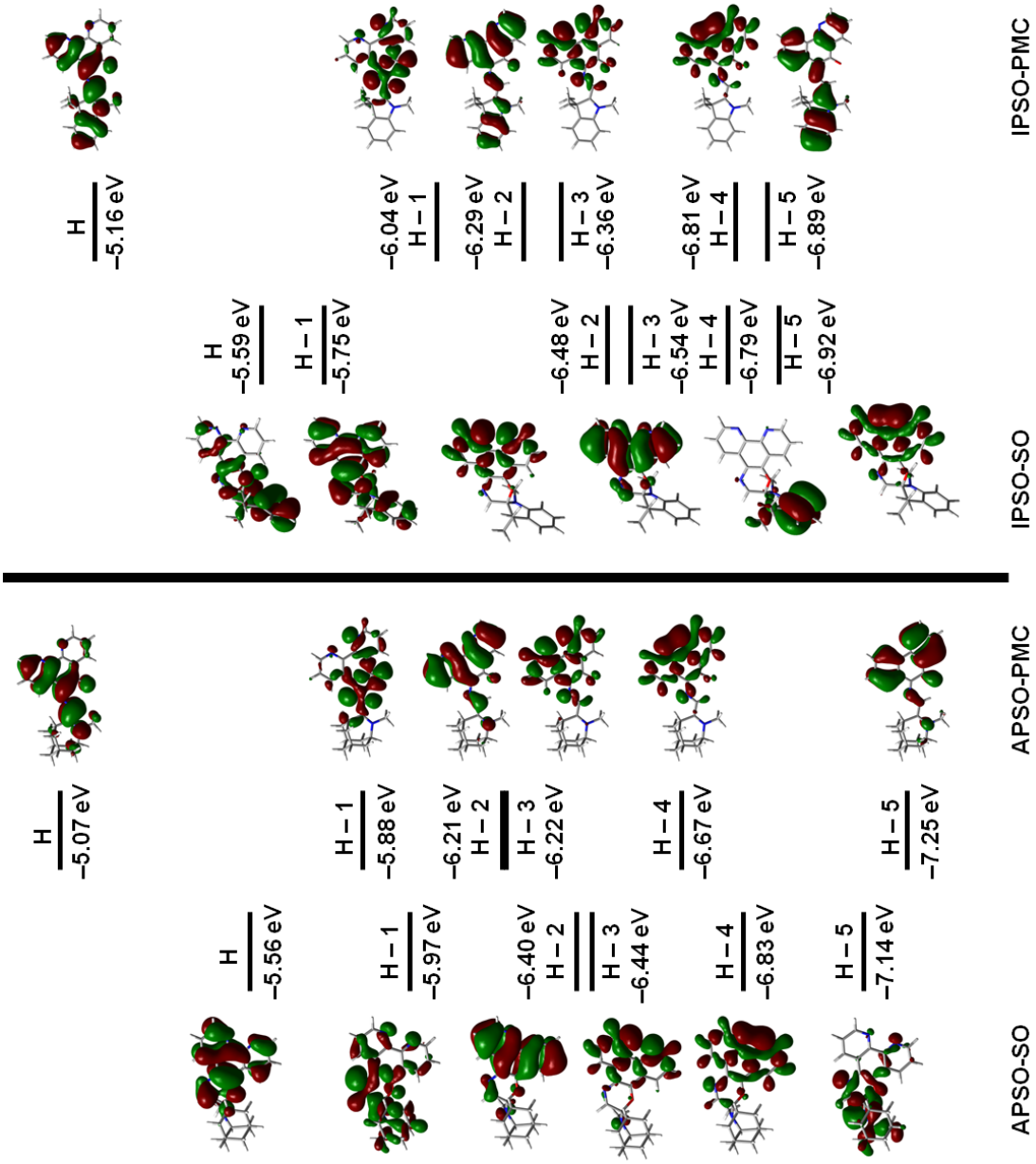

Figure 3.14. Highest-lying occupied molecular orbitals of the SO and PMC forms of APSO (left) and IPSO (right) calculated using DFT at the B3LYP/6-31G(d,p) level of theory (isovalue: MO = 0.02, density = 0.0004).

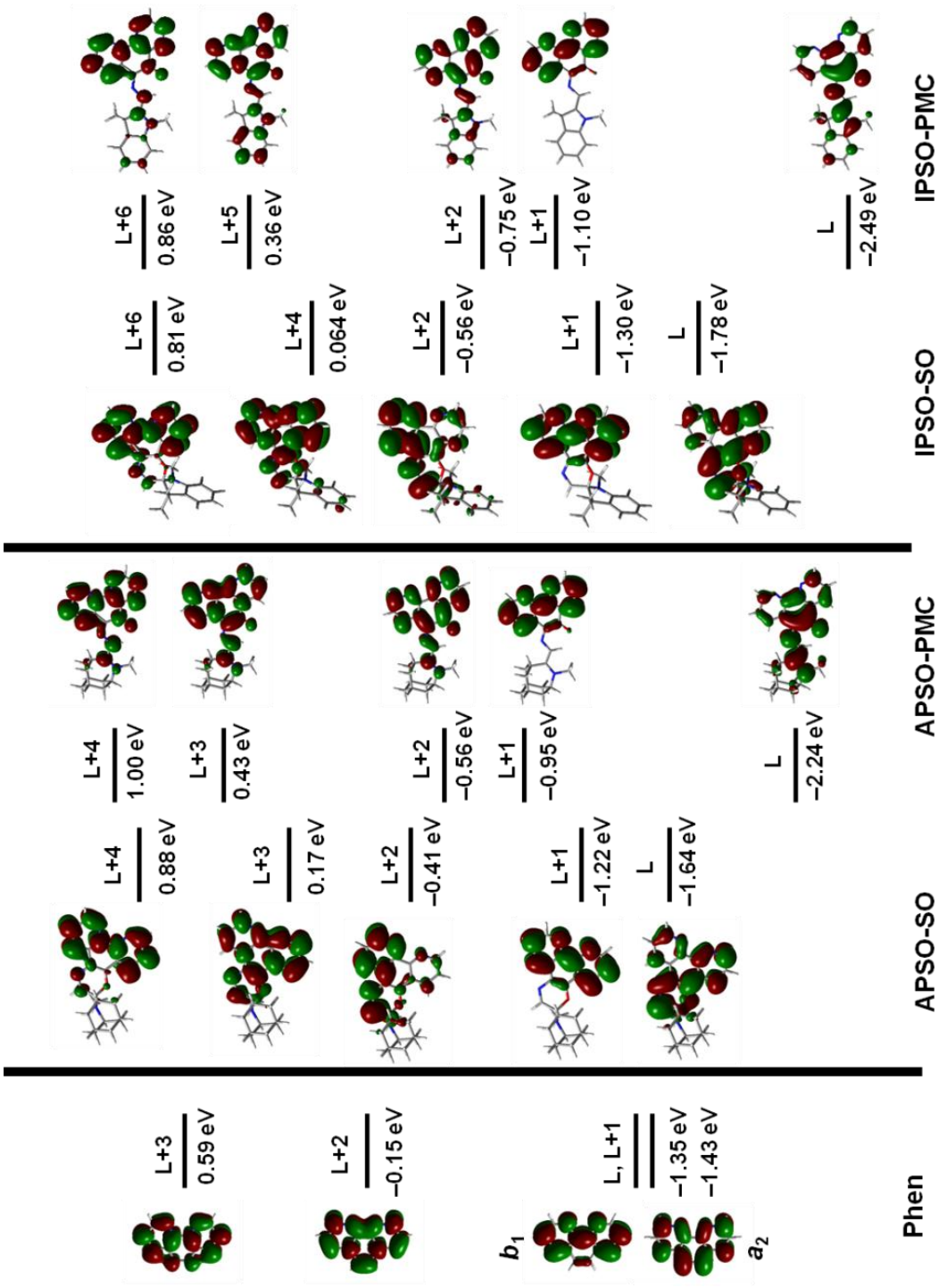

Figure 3.15. Lowest-lying unoccupied molecular orbitals of phen (left) and the SO and PMC forms of APSO (centre) and IPSO (right) calculated using DFT at the B3LYP/6-31G(d,p) level of theory (isovalue: MO = 0.02, density = 0.0004).

3.2.8. Comparison of Redox Potentials and MO Energies

The relative energies of the SO and PMC LUMOs for both APSO and IPSO correlate well with their relative reduction potentials, even though these values are derived from gas-phase and solution-phase data, respectively. The energy difference between the reduction processes assigned for APSO-PMC and IPSO-SO [$E_{pc(Red1,\ APSO)} - E_{pc(Red2,\ IPSO)}$ = 0.44 V in CH_3CN and 0.49 V in CH_2Cl_2] correlates remarkably well with the energy difference between the corresponding LUMOs [$E_{LUMO(IPSO\text{-}SO)} - E_{LUMO(APSO\text{-}PMC)}$ = 0.46 eV]. The difference between the first and second cathodic peak potentials for IPSO, assigned tentatively to the PMC and SO forms respectively [$E_{pc(Red1,\ IPSO)} - E_{pc(Red2,\ IPSO)}$ = 0.69 V in CH_3CN and 0.80 V in CH_2Cl_2], also correlates well with the energy difference between the corresponding LUMOs [$E_{LUMO(IPSO\text{-}SO)} - E_{LUMO(IPSO\text{-}PMC)}$ = 0.71 eV]. The consistency between the relative reduction potentials and the relative LUMO energies supports the accuracy of the DFT calculations as well as the correct assignment of the SO/PMC reduction processes.

3.2.9. Fragment MO Bonding Analysis of $Mo(CO)_4$(phen)

We will consider the bonding in the well-understood $Mo(CO)_4$(phen) complex from a fragment molecular orbital perspective prior to looking at bonding interactions in the analogous spirooxazine complexes. In $Mo(CO)_4$(phen), the $Mo(CO)_4$ fragment, under C_{2v} symmetry constraints [where the z axis is defined along the C_2 axis, Figure 3.16(a)], has three filled frontier MOs of b_1, a_2, and a_1 symmetries, which possess a mixture of CO π^* character and metal d_{xz}, d_{xy}, and $d_{z^2}/d_{x^2-y^2}$ characters, respectively, and two unoccupied frontier MOs of b_2 and a_1 symmetries.[319] Phenanthroline possesses two low-lying unoccupied π^* orbitals of b_1 and a_2 symmetries with nearly equal energies (Figure 3.15). These orbitals are of the correct symmetry to mix with the filled $Mo(CO)_4$ group orbitals of b_1 symmetry (with predominantly d_{xz} character) and a_2 symmetry (with predominantly d_{xy} character) [Figure 3.16(b)]. However, the mixing between the ligand- and metal-based MOs of b_1 symmetry is expected to be greater than that between the MOs of a_2 symmetry for two reasons: (1) the overlap between the phen(b_1, π^*) and $Mo(CO)_4$(b_1, d_{xz}) MOs should be greater than the overlap between the phen(a_2, π^*) and $Mo(CO)_4$(a_2, d_{xy}) MOs, as dictated by angular overlap arguments;[320] and (2) the MO coefficients at the

coordinating N atoms are larger on the phen(b_1, π^*) MO than on the phen(a_2, π^*) MO[317] [Figure 3.16(c)].

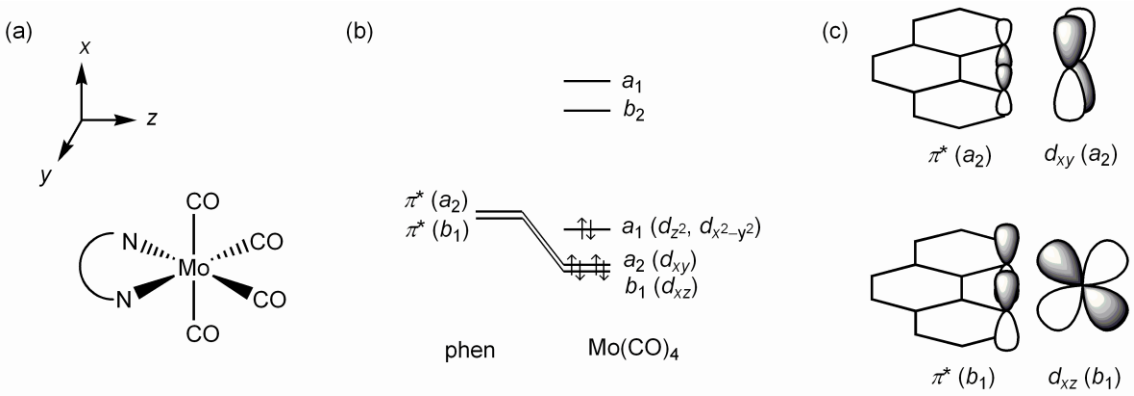

Figure 3.16. (a) Axis orientation for the $Mo(CO)_4(NN)$ complexes; (b) schematic of phen and $Mo(CO)_4$ MOs involved in Mo(d)–phen(π^*) backbonding; and (c) simplified illustration of metal–ligand bonding for a_2- and b_1-symmetry orbital combinations.

The predicted orbital mixing is corroborated by MO calculations of $M(CO)_4$(phen) complexes (M = Cr, Mo, W),[302, 321, 322] where the extent of mixing between the ligand and metal fragments is evident from the character of the frontier MOs (see Figure 3.17 for a qualitative MO scheme). From these calculations, the three highest-energy occupied MOs were found to have predominantly Mo(d) character: the HOMO (a_1) has ~60% Mo(d) character, ~40% $CO_{eq}(\pi^*)$ character, and a negligible amount of phen(π^*) character, the HOMO – 1 (a_2) has ~55% Mo(d_{xy}) character, ~25% $CO_{ax}(\pi^*)$ character, ~15% $CO_{eq}(\pi^*)$ character, and ~5% phen(π^*) character, and the HOMO – 2 (b_1) has ~55% Mo(d_{xz}) character, ~20% $CO_{ax}(\pi^*)$ character, ~10% $CO_{eq}(\pi^*)$ character, and ~15% phen(π^*) character. The two lowest-energy unoccupied MOs are phen-based: the LUMO has ~4% Mo(d_{xz}) character, ~3% each $CO_{eq}(\pi^*)$ and $CO_{ax}(\pi^*)$ characters, and ~90% phen(π^*) character, and the LUMO + 1 has ~99% phen(π^*) character. Greater mixing between the $Mo(CO)_4$(b_1, d_{xz}) and phen(b_1, π^*) MOs relative to the $Mo(CO)_4$(a_2, d_{xy}) and phen(a_2, π^*) MOs is thus evident. The former interaction represents the primary pathway for the Mo(d)–phen(π^*) backbonding mechanism whereby the phen ligand competes with the carbonyl ligands for electron density.

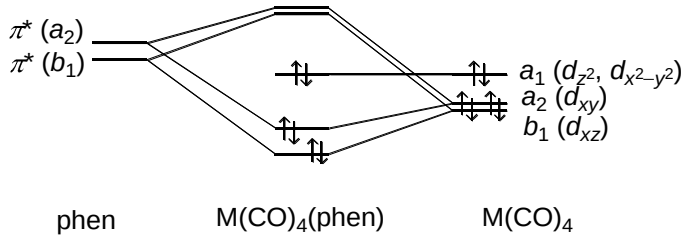

Figure 3.17. Qualitative MO bonding scheme for $M(CO)_4$(phen) complexes (M = Cr, Mo, W).

3.2.10. Fragment MO Bonding Analysis of $Mo(CO)_4$(IPSO)

The above analysis can be extended to the SO and PMC forms of the Mo–tetracarbonyl–spirooxazine complexes. Molecular geometries of $Mo(CO)_4$(APSO) and $Mo(CO)_4$(IPSO) were optimized at the DFT/B3LYP level of theory[273, 291, 292] using the Gaussian 03 software package.[272] As for the free ligand, only geometries of the (*R*) enantiomers for the SO forms and TTC isomers for the PMC form of the complexes were calculated. Geometry optimizations were performed using the double-ζ effective core potential LANL2DZ basis set.[323-325] The B3LYP/LANL2DZ level of theory has been used successfully in the analysis of frontier MO schemes for $M(CO)_4$(NN) (M = Cr, Mo, W; NN = diimine) complexes.[302, 321] The optimized geometry of $Mo(CO)_4$(APSO-PMC) is in satisfactory agreement with the crystal structure of this complex, with bond lengths deviating by up to 0.04 Å between the two. Molecular orbitals obtained from a single-point energy calculation using the optimized geometry and the experimental geometry for $Mo(CO)_4$(APSO-PMC) were very similar, with the only obvious inconsistency being a reversal in the ordering of the very close-lying HOMO – 2 and HOMO – 1, which is inconsequential at the level of analysis needed for this study. For $Mo(CO)_4$(APSO-SO), we were unable to obtain a minimized geometry in which the C_{spiro}–O bond remained intact. The instability of this bond is consistent with the long C_{spiro}–O bond lengths typically found in spiropyrans and spirooxazines[227, 326] and the exceptional stability of the PMC form of this particular compound. The MO schemes obtained for the SO and PMC forms of $Mo(CO)_4$(IPSO) were therefore used for the bonding analysis.

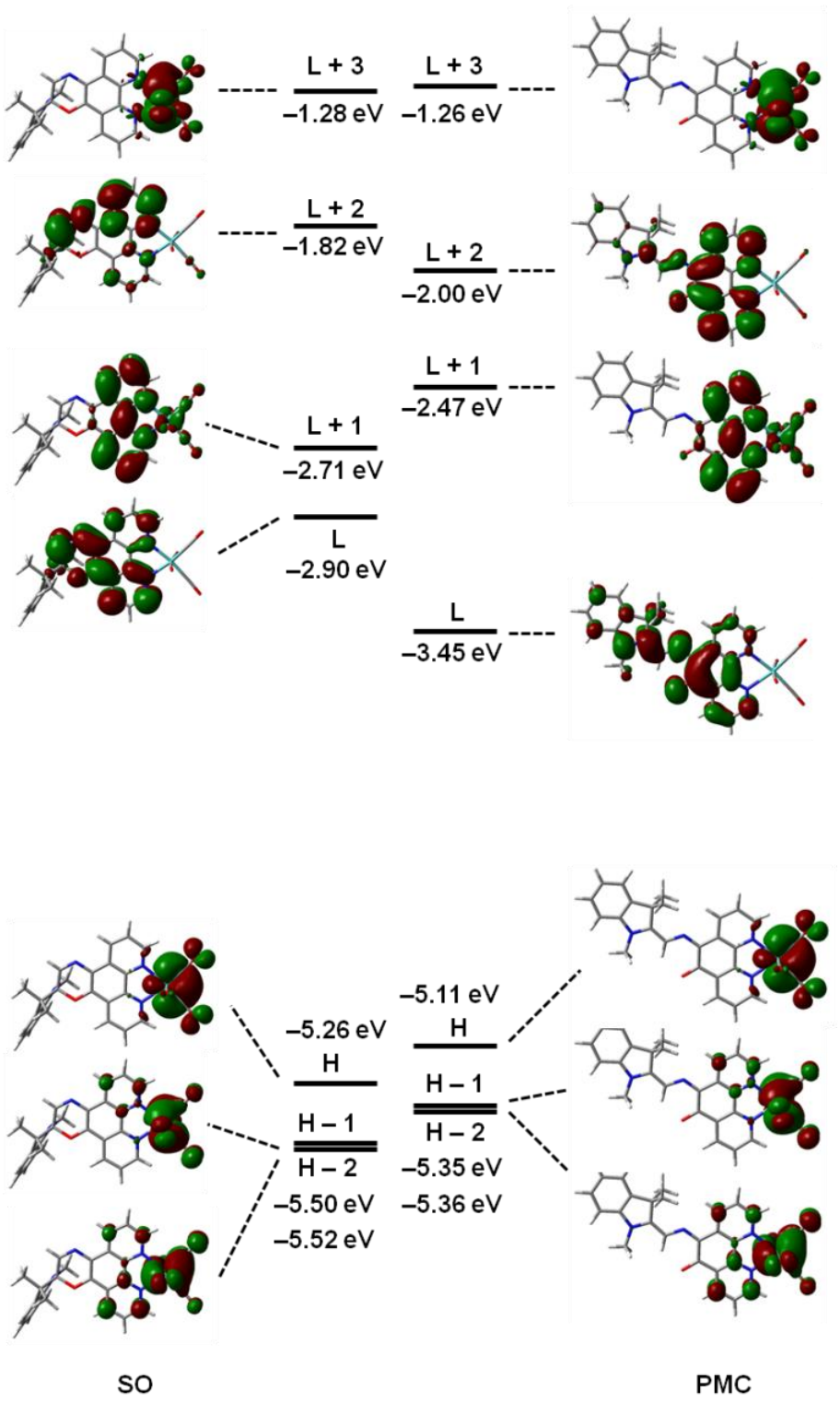

Figure 3.18. Frontier molecular orbitals of the SO and PMC forms of $Mo(CO)_4$(IPSO) calculated using DFT at the B3LYP/LANL2DZ level of theory (isovalue: MO = 0.02, density = 0.0004).

The following analysis will assume pseudo-C_{2v} symmetry for the spirooxazine complexes to facilitate discussion of the bonding interactions. The frontier MOs of $Mo(CO)_4$(IPSO) are shown in Figure 3.18. The three highest-energy occupied MOs are virtually identical for both the SO and PMC forms of the complex, and have predominantly $Mo(CO)_4$ character, with some electron density delocalization onto the diimine ligand. The three lowest-energy unoccupied MOs have predominantly ligand π^* character with similar electron density distributions and relative energies to the free ligands. In the MOs of both the SO and PMC forms, it is evident that the greatest phen(π^*)–$Mo(CO)_4$(d) mixing occurs between the fragment MOs of b_1 symmetry. In the three highest-energy occupied MOs, phen(π^*) mixing is observed to a moderate degree in the metal-based b_1-symmetry $Mo(CO)_4$(d) HOMO – 2, to a small degree in the a_2-symmetry $Mo(CO)_4$(d) HOMO – 1, and to a very small degree in the a_1-symmetry $Mo(CO)_4$(d) HOMO. In the three lowest-energy unoccupied MOs, a significant amount of $Mo(CO)_4$(d) mixing is observed in the ligand-based pseudo-b_1-symmetry phen(π^*) LUMO + 1, no $Mo(CO)_4$(d) mixing is observed in the pseudo-a_2-symmetry phen(π^*) LUMO, and only a very small amount of $Mo(CO)_4$(d) mixing is observed in the pseudo-a_2-symmetry phen(π^*) LUMO + 2. The relative molecular orbital contributions from the $Mo(CO)_4$ fragment and the ligand fragment thus parallel those described above for the $M(CO)_4$(phen) complexes. Most critical to the analysis are the differences between the SO and PMC forms of the ligands. Since the mixing between ligand and metal MOs of b_1 symmetry is primarily responsible for the Mo(d)–phen(π^*) backbonding interaction, the LUMO + 1 should be most important in determining the ligand field strength of the spirooxazines. Because this MO is lower in energy in the SO form than in the PMC form [by 0.20 eV for APSO and 0.27 eV for IPSO], the SO form is expected to be a stronger π-acceptor. Contributions from metal–ligand mixing of the a_2-symmetry MOs should have the same effect on the relative SO and PMC π-acceptor strengths as the a_2-symmetry LUMO of the SO form is significantly lower in energy than the a_2-symmetry LUMO + 2 of the PMC form. The LUMO of the PMC form, despite being lowest in energy, has no electron density on the N atoms, and would not be expected to contribute significantly to metal–ligand bonding. Overall, the conclusions from the DFT MO analysis with regard to the bonding properties of the SO and PMC forms of the

spirooxazine ligands are consistent with the experimental FT-IR and ^{13}C NMR results. In addition, if the relative energies of the b_1-symmetry low-lying unoccupied MOs are compared between phen, IPSO, and APSO, those of phen and IPSO-SO are very close in energy (–1.35 eV vs –1.30 eV), which would suggest that these ligands have similar π-acceptor strengths, while those of IPSO-PMC (–1.10 eV) and the SO and PMC forms of APSO (–1.22 and –0.95 eV, respectively) are all higher in energy, which would suggest that each of these ligands is a relatively weaker π-acceptor. Again, these results parallel the observations from FT-IR and ^{13}C NMR spectroscopy.

3.2.11. DFT MO Analysis of New Phenanthroline–Spirooxazine Derivatives

The azahomoadamantyl and indolyl spirooxazine ligands, APSO and IPSO, display very similar frontier MOs, which suggests that while spirooxazine derivatization of phen leads to significant changes to the phen-based MOs upon SO/PMC isomerization, the specific type of spirooxazine functionality, whether more or less conjugated, does not contribute significantly to the overall nature of these changes. The type of spirooxazine does somewhat influence the absolute energies of the MOs, however, and could perhaps be exploited to tune metal–ligand orbital matching. Of the three lowest-energy unoccupied MOs, the pseudo-b_1-symmetry LUMO + 1, with the appropriate symmetry to mix with the Mo(d_{xz}) fragment MO, plays the most significant role in Mo(d)–phen(π*) backbonding. To maximize differences in π-acceptor strength between the SO and PMC forms of the phenanthroline–spirooxazine ligands, one would want to maximize the energy difference between the pseudo-b_1-symmetry MOs primarily responsible for M–L orbital mixing. In APSO and IPSO, the phenanthroline moiety is derivatized at the 5- and 6- positions. As these positions have very little electron density, mixing between phenanthroline and spirooxazine fragments is not expected to be considerable. Indeed, although differences in the energies of the b_1-symmetry MOs are observed between the SO and PMC forms, greater energetic differences are observed for the a_2-symmetry MOs, which have more electron density at the 5- and 6- positions. Thus, in order to observe a greater perturbation of the pseudo-b_1-symmetry MO of phenanthroline–spirooxazines upon SO/PMC conversion, derivatization of the phen moiety at a site of greater electron density may be advantageous

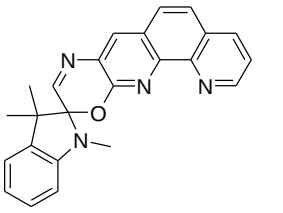

42

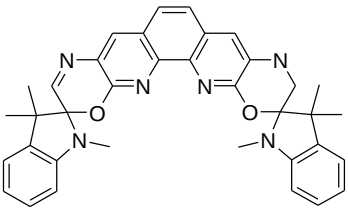

43

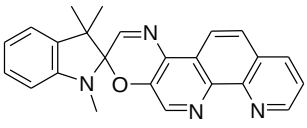

44

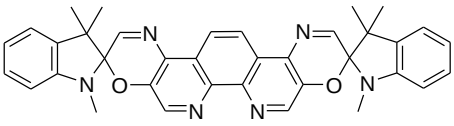

45

Phenanthroline–spirooxazines derivatized at the 2,3- or 3,4-phen positions are conceivable. Because of the symmetric nature of phenanthroline, both mono- and bis-substituted spirooxazine derivatives could be potential synthetic targets. To predict the effect of 2,3- or 3,4- vs 5,6- derivatization on the energies of the low-lying MOs of phenanthroline–spirooxazines, single-point energy calculations were performed on the optimized geometries of several indolyl spirooxazine derivatives: the mono-2,3-spirooxazine-substituted phenanthroline derivative (**42**), the bis-2,3-spirooxazine substituted phenanthroline derivative (**43**), the mono-3,4-spirooxazine-substituted phenanthroline derivative (**44**), and the bis-3,4-spirooxazine-substituted phenanthroline derivative (**45**). Geometries were optimized at the DFT/B3LYP/6-31G(d) level of theory, and again only the SO(*R*) and PMC(TTC) isomers were considered. Although the bis derivatives can potentially exist with both ring-opened and ring-closed spirooxazine substituents simultaneously, only the doubly closed or doubly opened derivatives were calculated.

The low-lying MOs for the mono-2,3-spirooxazine-substituted phenanthroline derivative (**42**) are shown in Figure 3.19. For the SO form, the LUMO and LUMO + 1 have predominantly phen(b_1, π*) and phen(a_2, π*) character, respectively, similarly to the 5,6-substituted derivatives. In this case, however, the orbital ordering is reversed, with the pseudo-b_1-symmetry MO being lower in energy. As expected, the MOs for the PMC form of the 2,3-substituted derivative show greater mixing between spirooxazine and phenanthroline fragments, as compared to the 5,6-substituted derivatives. This leads to

MOs with both spirooxazine and phenanthroline character, and a greater energy separation between the LUMO and LUMO + 1 orbitals. Both of the lowest-lying PMC MOs appear to have the appropriate symmetry to mix with the b_1-symmetry MO of d_{xz} character for a metal fragment of C_{2v} symmetry. Additionally, these both have significant electron density on the N atoms, in contrast to the 5,6-substituted derivatives, in which the LUMO has predominantly spirooxazine character and no electron density on the N atoms. In the mono-2,3-substituted derivative, the LUMO of the PMC form is ~1.1 eV lower in energy than the LUMO of the SO form, and the LUMO + 1 of the PMC form is ~0.9 eV higher in energy that the LUMO of the SO form. These are large differences in MO energies. If the LUMO of the PMC form does indeed mix significantly with the b_1-symmetry metal-based MO, then the PMC form may be a significantly stronger π-acceptor than the SO form. The effect of SO/PMC isomerization on ligand field strength would therefore be predicted to be much stronger and in the opposite direction for the 2,3-substituted derivative than for the 5,6-substituted derivatives.

The low-lying MOs for the bis-2,3-spirooxazine-substituted phenanthroline derivative (**43**) are shown in Figure 3.20. For the SO form of the bis derivative, the MOs are quite similar to those of the mono derivative. For the PMC form, two low-lying orbitals of similar energy are observed; both have a mixture of spirooxazine and phenanthroline character, but the LUMO shows more phen character with electron density on the N atoms and the LUMO + 1 more spirooxazine character with no electron density on the N atoms. If the assumption that the LUMO has the appropriate symmetry to mix with the b_1-symmetry M(d_{xz}) orbitals holds, then, as for the mono derivative, the PMC form of the bis-2,3-substituted derivative should be a significantly stronger π-acceptor than the SO form.

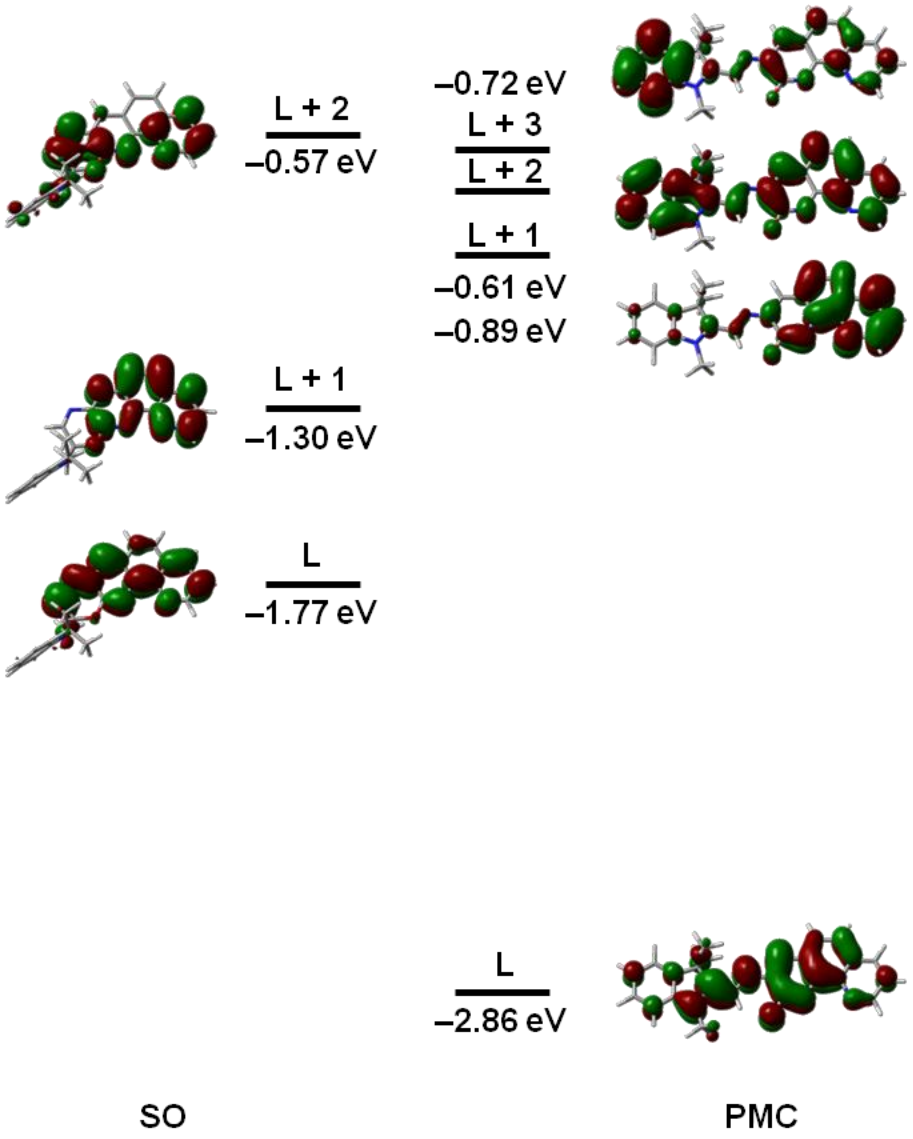

Figure 3.19. Lowest-lying unoccupied MOs of the SO and PMC forms of the mono-2,3-spirooxazine-substituted phenanthroline derivative (**42**) calculated using DFT at the B3LYP/6-31G(d) level of theory (isovalue: MO = 0.02, density = 0.0004).

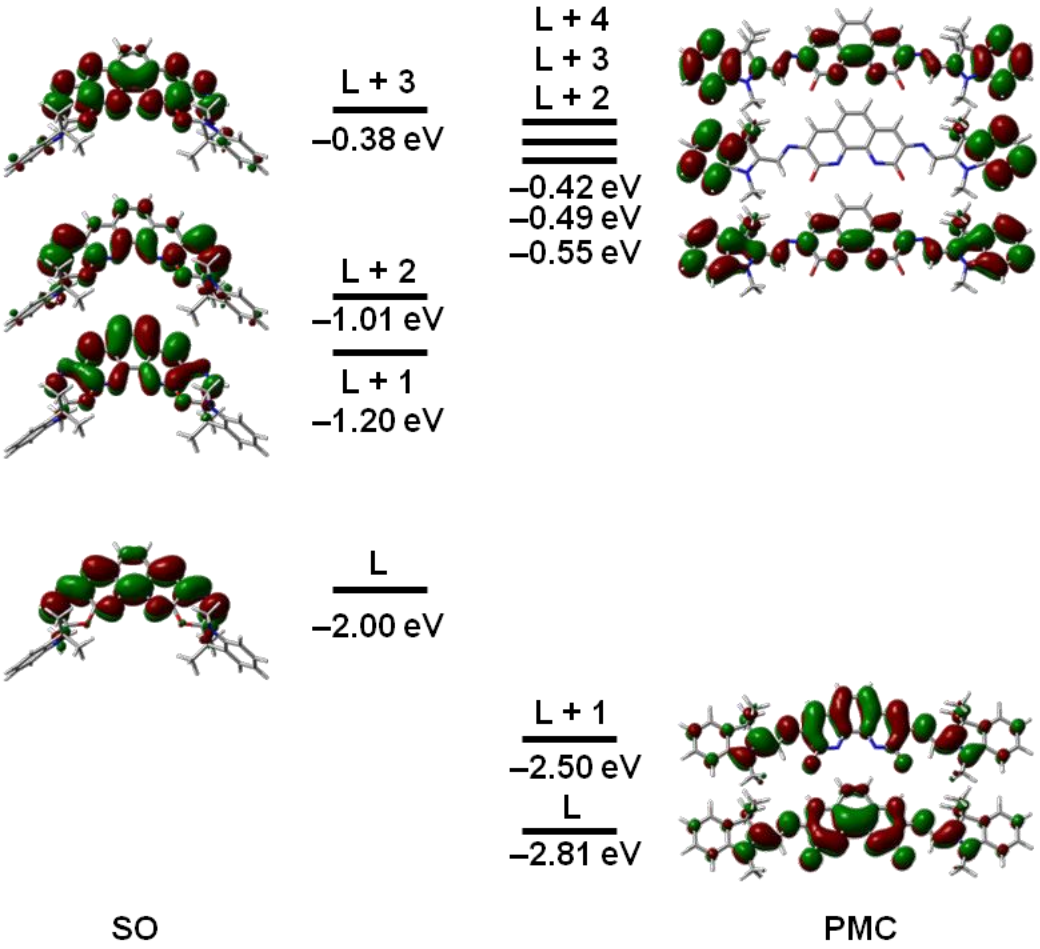

Figure 3.20. Lowest-lying unoccupied MOs of the SO and PMC forms of the bis-2,3-spirooxazine-substituted phenanthroline derivative (**43**) calculated using DFT at the B3LYP/6-31G(d) level of theory (isovalue: MO = 0.02, density = 0.0004).

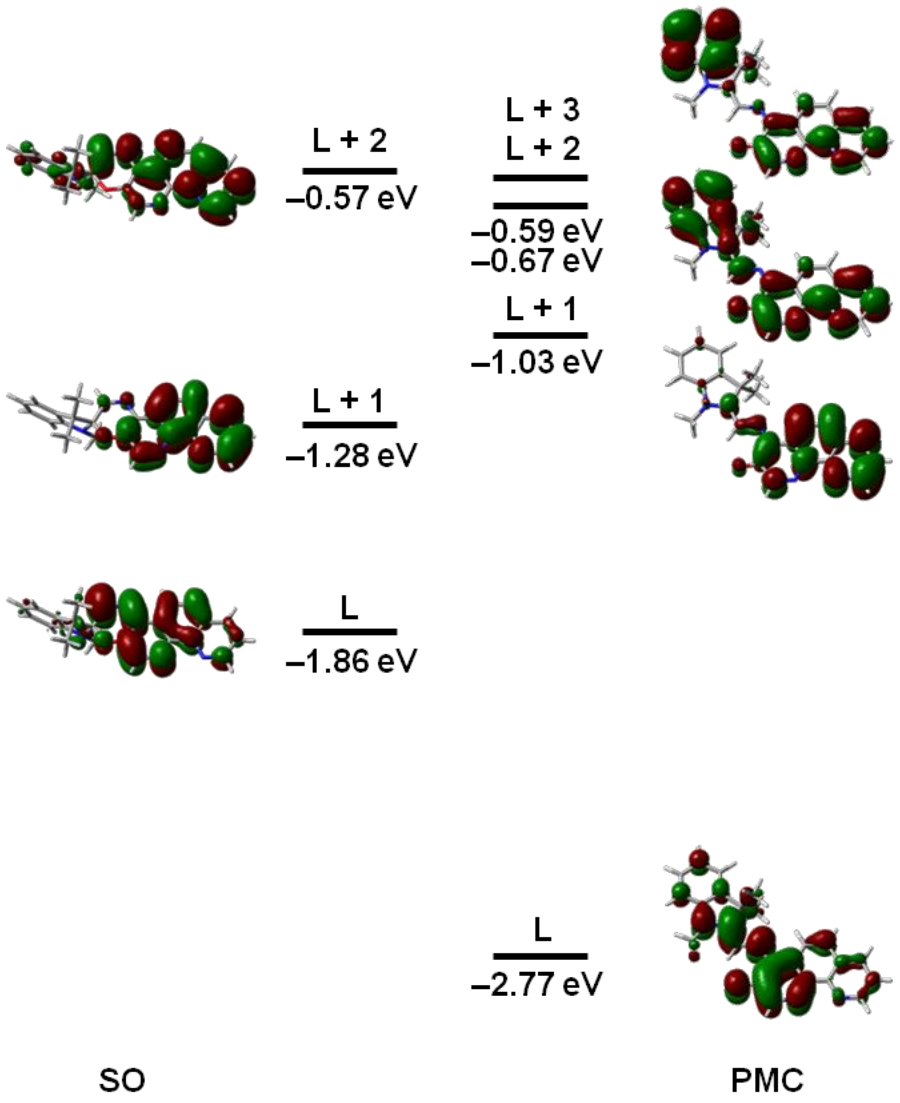

Figure 3.21. Lowest-lying unoccupied MOs of the SO and PMC forms of the mono-3,4-spirooxazine-substituted phenanthroline derivative (**44**) calculated using DFT at the B3LYP/6-31G(d) level of theory (isovalue: MO = 0.02, density = 0.0004).

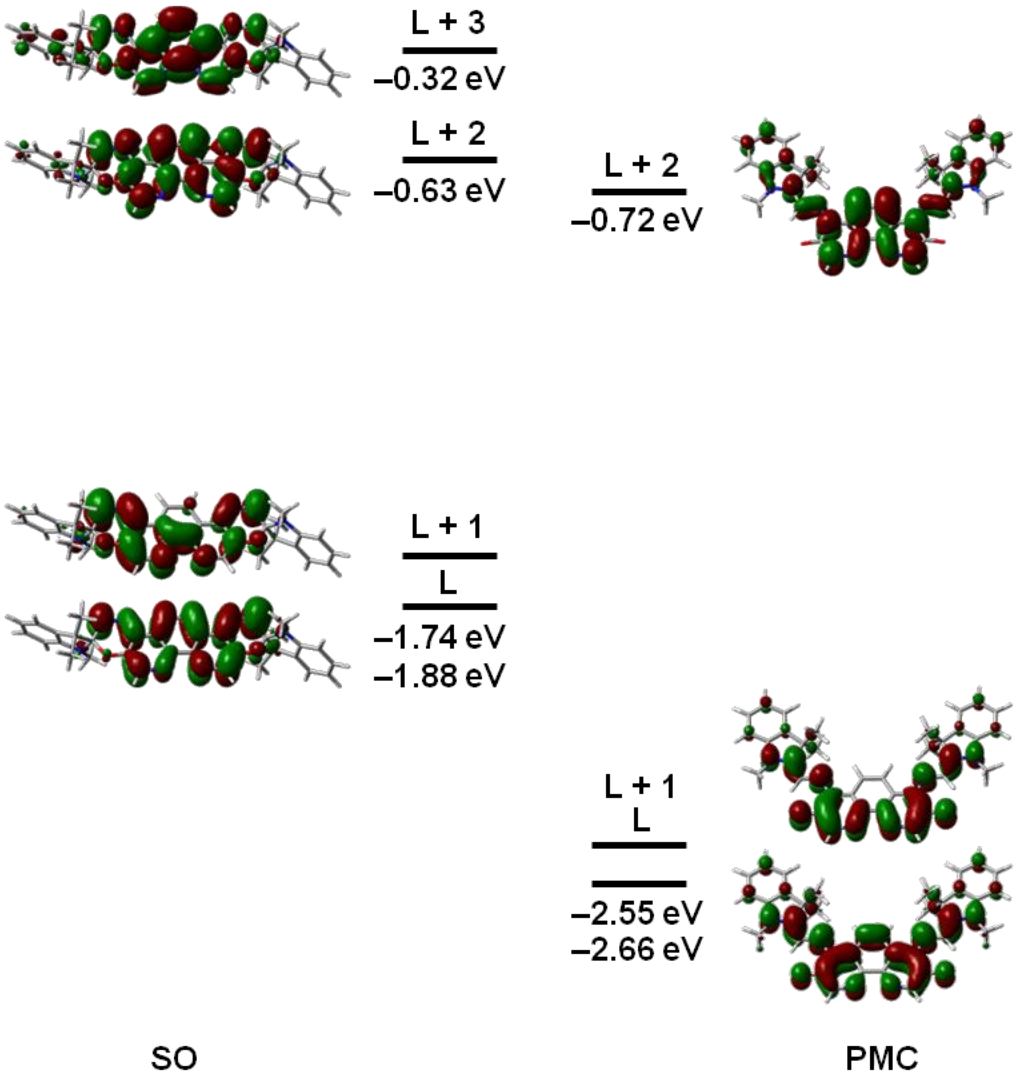

Figure 3.22. Lowest-lying unoccupied MOs of the SO and PMC forms of the bis-3,4-spirooxazine-substituted phenanthroline derivative (**45**) calculated using DFT at the B3LYP/6-31G(d) level of theory (isovalue: MO = 0.02, density = 0.0004).

The low-lying MOs for the mono-3,4-spirooxazine-substituted phenanthroline derivative (**44**) are shown in Figure 3.21. Here, considerable mixing between spirooxazine and phenanthroline fragments and MO desymmetrization is observed in both the SO and PMC forms. The distortion of the MOs leads to ambiguity regarding which spirooxazine MOs will predominantly mix with the metal-based MOs. In both the SO and PMC forms, the LUMOs have electron density on one N atom but not the other. If mixing between phen-based and metal-based fragments occurs through the LUMO, then the PMC form would be a stronger π-acceptor. If this interaction is small, and the interaction with the more symmetric b_1-symmetry MOs with greater electron density on the N atoms (i.e, the LUMO + 1 for the SO form and LUMO + 2 for the PMC form) dominates, then the SO form may be the better π-acceptor. It is also possible that this derivative simply shows a greater mix of possible backbonding pathways and that a combination of different bonding pathways must be considered in evaluating overall ligand field strength. An interesting possibility here is that PMC/SO conversion may lead to significant changes in ligand field symmetry instead of, or in addition to, changes in ligand field strength, which could have unique applications in photochromic coordination complexes.

The low-lying MOs for the bis-3,4-spirooxazine-substituted phenanthroline derivative (**45**) are shown in Figure 3.22. These are actually quite different from those of the mono derivative as they are much more symmetric, which may affect the possible bonding interactions. Here the fairly closely spaced LUMO and LUMO + 1 of the SO form have a_2 and b_1 symmetries, respectively, whereas the fairly closely spaced LUMO and LUMO + 1 of the PMC form have b_1 and a_2 symmetries, respectively. All of these low-lying MOs may foreseeably mix with metal-based MOs of corresponding symmetries. As both the PMC LUMO and LUMO + 1 are ~0.8 eV lower in energy than the SO LUMO and LUMO + 1, once again the PMC form may be predicted to be a much stronger π-acceptor in this derivative.

For all of the 2,3- or 3,4-spirooxazine-substituted phenanthroline derivatives (**42**–**45**) analyzed here, greater mixing between the spirooxazine and phenanthroline fragments is observed, as expected for substitution at sites of greater electron density. In general, the

result is that in the PMC form, mixing of spirooxazine and phenanthroline fragments leads to greater phen character for the LUMO, which, in the case of the 5,6-substituted derivatives, has only spirooxazine character and no electron density at the nitrogen atoms. Increased phen(b_1, π^*) character leads to increased electron density at the N atoms and the possibility that the PMC LUMO may interact strongly with metal fragment MOs. Whereas in the 5,6-substituted derivatives, the low-lying LUMO of the PMC form was not expected to mix with metal orbitals, and the SO form was predicted to be the stronger π-acceptor, in the 2,3- and 3,4-substituted derivatives, the effect may be reversed and more significant. Despite being potentially challenging synthetic targets and despite possible complications arising in the study of bis-photochromic derivatives, the proposed phenanthroline–spirooxazine derivatives **42**–**45** could be promising ligands for photoswitchable coordination complexes.

3.3. Summary and Conclusions

We have described an evaluation of the ligand field strength of the ring-closed SO and ring-opened PMC photoisomers of two photochromic phenanthroline–spirooxazine ligands, APSO and IPSO, where the π-acceptor strength of the ligands was assessed both spectroscopically and computationally. A change in ligand field strength between the SO and PMC forms was demonstrated through FT-IR and ^{13}C NMR analysis of molybdenum–tetracarbonyl–spirooxazine complexes, where both analyses confirmed that the SO form behaves as a stronger π-acceptor. A DFT fragment MO analysis showed that, of the low-lying unoccupied MOs in the spirooxazine ligands, the LUMO + 1, a pseudo-b_1-symmetry phen(π^*) MO, exhibits the greatest amount of mixing with the $Mo(CO)_4$ fragment and is therefore primarily responsible for the Mo(d)–phen(π^*) backbonding interaction. The relative energy of this orbital cannot be easily probed experimentally through electrochemical studies, as would be possible for the LUMO, and it can therefore be more readily studied computationally. DFT calculations predict that the LUMO + 1 is 0.2–0.3 eV lower in the SO form than in the PMC form, which implies that the SO form is a stronger π-acceptor, consistent with the FT-IR and ^{13}C NMR experimental results. Phenanthroline–spirooxazine derivatives substituted at the 2,3- or 3,4-phen positions, rather than the 5,6-position, were computationally predicted to show

greater mixing between spirooxazine and phenanthroline fragments, which could lead to greater phen(b_1, π^*) character and greater electron density on the N atoms for the LUMO of the PMC form, and could in turn lead to the PMC form being a much stronger π-acceptor than the SO form.

This is the first time that a generalized method for determining the magnitude and direction of changes in ligand field strength in photochromic ligands has been described. The methodology presented here for analyzing ligand field changes using FT-IR and ^{13}C NMR spectroscopies of metal–carbonyl complexes represents an effective way to experimentally quantify and compare ligand field changes in photochromic ligands to assess their potential as optical components for multifunctional materials. Since analogous metal–ligand bonding interactions would be expected for any combination of a wide range of photochromic phenanthroline-based ligands and metals, designing switchable multifunctional materials based on coordination complexes containing spirooxazines or other photochromic ligands may be a powerful way to introduce optical control over metal-based properties, either directly through ligand field effects or indirectly through mechanisms such as excited-state energy transfer or changes in molecular conformation.

3.4. Experimental

3.4.1. Synthesis

General. All reagents were purchased from commercial sources and used without further purification. Spectroscropy grade, dry, and deoxygenated toluene and pentane were acquired from an MBraun solvent purification system. Reactions were run under $N_{2(g)}$ or $Ar_{(g)}$ and worked up in air. ^{1}H NMR spectra were acquired with Bruker AC300, 360, or AVANCE500 spectrometers, and spectra were calibrated to the solvent residual peaks ($CDCl_3$: 7.24 ppm for ^{1}H NMR; CD_2Cl_2: 5.32 ppm for ^{1}H NMR and 53.80 ppm for ^{13}C NMR).[327] Spiro[azahomoadamantane-phenanthrolinoxazine] (APSO, **28**)[218] and spiro[indoline-phenanthrolinoxazine] (IPSO, **31**)[250] were prepared as described in Chapter 2. Molybdenum complexes were prepared from $Mo(CO)_4(pip)_2$, which was prepared from $Mo(CO)_6$ following a known procedure.[298]

$Mo(CO)_4$(APSO) (40). $Mo(CO)_4(pip)_2$ (83.9 mg, 0.222 mmol, 1.00 equiv.) and APSO (**28**) (84.8 mg, 0.221 mmol, 1.00 equiv.) were stirred in toluene (15 mL) in the absence of light at ~300 K for 19 h. The resulting precipitate was filtered and washed with toluene to yield a dark purple powder (119 mg, 90% isolated yield). Anal. Calcd for $C_{28}H_{28}MoN_4O_5 \cdot (C_6H_5CH_3)_{0.5}$: C, 58.88; H, 5.02; N 8.72. Found: C, 57.98; H, 4.68; N, 7.92. ESI-MS: *m*/*z* (%) 598 (100) $[M]^+$. ^{1}H NMR (360 MHz, CD_2Cl_2) for PMC form: δ 10.27 (s, 1H), 9.23 (dd, *J* = 5.1, 1.6 Hz, 1H), 8.91 (dd, *J* = 4.9, 1.5 Hz, 1H), 8.83 (dd, *J* = 8.0, 1.7 Hz, 1H), 8.76 (dd, *J* = 8.3, 1.5 Hz, 1H), 7.56 (dd, *J* = 8.0, 5.1 Hz, 1H), 7.45 (dd, *J* = 8.4, 5.0 Hz, 1H), 5.09 (br t, *J* = 6.1 Hz, 1H), 3.86 (septet, *J* = 2.2 Hz, 1H), 3.61 (s, 3H), 2.2–1.8 (m, 12H); for SO form: 7.79 (s, 1H) ppm (as the SO form makes up only 2% of the total concentration of the complex, only the azomethine proton resonance can be unambiguously identified). ^{13}C NMR (90 MHz, CD_2Cl_2) for PMC form: δ 223.4, 223.3, 205.7, 182.8, 171.3, 154.3, 151.3, 148.4, 142.5, 136.0, 135.3, 131.6, 131.5, 129.5, 125.1, 124.8, 123.9, 66.0, 43.7, 34.1, 33.6, 32.0, 30.2, 26.6 ppm. FT-IR (KBr): ***ν*** 2913 (m), 2849 (w), 2006 (vs), 1889 (vs), 1859 (vs), 1816 (vs), 1603 (s), 1579 (s), 1550 (s), 1494 (w), 1475 (m), 1451 (s), 1419 (s), 1408 (s), 1356 (s), 1348 (s), 1338 (m), 1324 (m), 1315 (s), 1251 (m), 1224 (vs), 1184 (w), 1127 (s, sh), 1115 (vs), 1095 (vs), 1085 (vs), 1061 (s), 1039 (s), 1013 (w), 1000 (w), 955 (w), 944 (m), 891 (w), 881 (m), 871 (w), 837 (w), 819 (m), 811 (m), 796 (w), 777 (w), 748 (w), 742 (w), 725 (s), 716 (w), 694 (m), 645 (m), 608 (m), 584 (m), 546 (w) cm^{-1}.

$Mo(CO)_4$(IPSO) (41). $Mo(CO)_4(pip)_2$ (126 mg, 0.333 mmol, 1.00 equiv.) and IPSO (**31**) (126 mg, 0.331 mmol, 1.00 equiv.) were stirred in toluene (15 mL) in the absence of light at ~300 K for 3 h. The resulting precipitate was filtered and washed with toluene to yield a blue microcrystalline powder (163 mg, 84% isolated yield). Anal. Calcd for $C_{28}H_{24}MoN_4O_5$: C, 56.76; H, 4.08; N 9.46. Found: C, 55.05; H, 3.69; N, 8.90. ESI-MS: *m*/*z* (%) 594 (100) $[M]^+$. ^{1}H NMR (360 MHz, CD_2Cl_2) for PMC form: δ 10.28 (s, 1H), 9.27 (dd, *J* = 5.2, 1.7 Hz, 1H), 9.00 (dd, *J* = 5.0, 1.4 Hz, 1H), 8.81 (dd, *J* = 8.0, 1.6 Hz, 1H), 8.76 (br d, *J* = 8.4, 1H), 7.59 (dd, *J* = 8.0, 5.2 Hz, 1H), 7.56 (dd, *J* = 8.3, 5.0 Hz, 1H), 7.51 (ddd, *J* = 7.3, 1.2, 0.5 Hz, 1H), 7.46 (td, *J* = 7.6, 1.3 Hz, 1H), 7.35 (td, *J* = 7.6, 0.9 Hz, 1H), ~7.2 (m, 1H), 3.81 (br s, 3H), 1.90 (br s, 6H); for SO form: 9.39 (dd, *J* = 5.1, 1.5 Hz, 1H), 9.31 (dd, *J* = 5.0, 1.5 Hz, 1H), 9.11 (dd, *J* = 8.4, 1.5 Hz, 1H), 8.54 (dd,

J = 8.3, 1.5 Hz, 1H), 7.94 (s, 1H), 7.78 (dd, *J* = 8.4, 5.0 Hz, 1H), 7.63 (dd, *J* = 8.3, 5.0 Hz, 1H), 7.25 (td, *J* = 7.6, 1.2 Hz, 1H), 7.15 (ddd, *J* = 7.2, 1.2, 0.6 Hz, 1H), 6.95 (td, *J* = 7.4, 0.9 Hz, 1H), 6.64 (br d, *J* = 7.7 Hz, 1H), 2.79 (s, 3H), 1.42 (s, 3H), 1.40 (s, 3H) ppm. ^{13}C NMR (125 MHz, CD_2Cl_2) for PMC and SO forms: δ 223.3, 223.1, 205.6, 205.4, 184.6, 154.9, 153.5, 153.5, 153.2, 151.2, 149.5, 148.5, 147.4, 146.5, 142.5, 140.1, 136.2, 135.8, 135.1, 132.1, 131.7, 131.6, 131.5, 131.3, 128.9, 128.8, 128.6, 128.4, 126.2, 125.4, 125.1, 125.0, 124.4, 124.4, 124.3, 123.2, 122.8, 122.0, 120.7, 120.4, 120.1, 111.3, 107.8, 107.6, 100.9, 52.5, 29.8, 28.1, 25.8, 25.7, 22.7, 20.8 ppm. FT-IR (KBr): $\boldsymbol{\nu}$ 2964 (w), 2938 (w), 2866 (w), 2008 (vs), 1893 (vs, sh), 1889 (vs), 1873 (vs, sh), 1868 (vs), 1858 (vs), 1850 (vs) 1841(vs), 1837 (vs, sh), 1829 (vs), 1604 (m), 1558 (w), 1553 (m), 1486 (w), 1473 (w), 1449 (m), 1422 (s), 1414 (s), 1387 (w), 1371 (w), 1352 (m), 1330 (s), 1306 (s), 1266 (s), 1245 (s), 1183 (w), 1169 (m), 1159 (m), 1128 (m), 1112 (s), 1090 (m), 1069 (w), 1052 (w), 1032 (m), 1019 (m), 954 (w), 932 (w), 885 (w), 807 (w), 797 (m), 755 (w), 745 (m), 728 (w), 705 (w), 643 (w), 602 (w), 582 (w), 550 (w) cm^{-1}.

$Mo(CO)_4$(phen). $Mo(CO)_4(pip)_2$ (110 mg, 0.291 mmol, 1.00 equiv.) and phenanthroline monohydrate (57.6 mg, 0.291 mmol, 1.00 equiv.) were stirred in toluene (10 mL) in the absence of light at ~300 K for 3 h. The resulting precipitate was filtered and washed with toluene to yield a shiny orange-red powder (93 mg, 82% yield). ^{1}H NMR (360 MHz, CD_2Cl_2): δ 9.44 (dd, *J* = 4.9, 1.4 Hz, 2H), 8.48 (dd, *J* = 8.2, 1.6 Hz, 2H), 7.99 (s, 2H), 7.77 (dd, *J* = 8.2, 4.9 Hz, 2H) ppm. ^{13}C NMR (90 MHz, CD_2Cl_2): δ 223.2, 205.5, 153.2, 146.5, 136.9, 130.4, 127.37, 124.7 ppm. FT-IR (KBr): $\boldsymbol{\nu}$ 3081 (w), 3063 (w), 2943 (w), 2007 (vs), 1992 (w), 1914 (sh), 1880 (s), 1872 (s), 1863 (s), 1824 (vs), 1802 (w), 1796 (w), 1776 (w), 1599 (w), 1512 (w), 1494 (w), 1446 (w), 1424 (m), 1422 (m), 1414 (m), 1409 (sh), 1339 (w), 1220 (w), 1206 (w), 1143 (m), 1104 (w), 1090 (w), 1053 (w), 987 (w), 948 (w), 871 (w), 846 (m), 771 (w), 739 (w), 724 (m), 643 (m), 603 (m), 582 (m), 551 (m) cm^{-1}.

3.4.2. X-Ray Crystallographic Analysis

A purple prism of $C_{28}H_{24}N_4O_5Mo{\cdot}C_7H_8$, having approximate dimensions of 0.04 mm × 0.12 mm × 0.22 mm, was mounted on a glass fiber. All measurements were made with a Bruker X8 APEX II diffractometer with graphite monochromated Mo-Kα radiation. The

data were collected at a temperature of –100.0 ± 0.1 °C to a maximum 2θ value of 51.1°. Data were collected in a series of φ and ω scans in 0.50° oscillations with 60.0-second exposures. The crystal-to-detector distance was 36.00 mm. Of the 15993 reflections that were collected, 5628 were unique (R_{int} = 0.034); equivalent reflections were merged. Data were collected and integrated using the Bruker SAINT[328] software package. The linear absorption coefficient, μ, for Mo-Kα radiation is 4.78 cm^{-1}. Data were corrected for absorption effects using the multi-scan technique (SADABS),[329] with minimum and maximum transmission coefficients of 0.932 and 0.981, respectively. The data were corrected for Lorentz and polarization effects. The structure was solved by direct methods.[286] The material crystallizes with one disordered molecule of toluene in the asymmetric unit. The disorder was modeled in two orientations, with a ratio of roughly 3:1 between the major and minor fragments. All non-hydrogen atoms were refined anisotropically. All hydrogen atoms were placed in calculated positions but were not refined. The final cycle of full-matrix least-squares refinement [$\Sigma w(F_o^2 - F_c^2)^2$] on F^2 was based on 5628 reflections and 412 variable parameters and converged (largest parameter shift was 0.00 times its esd) with unweighted and weighted agreement factors of $R_1 = \Sigma ||F_o| - |F_c|| / \Sigma |F_o| = 0.044$ and $wR_2 = \{\Sigma [w(F_o^2 - F_c^2)^2] / \Sigma w(F_o^2)^2\}^{1/2} = 0.074$. The standard deviation of an observation of unit weight $\{[\Sigma w(F_o^2 - F_c^2)^2/N_o - N_v)]^{1/2}$ where N_o = number of observations and N_v = number of variables} was 1.03. The weighting scheme was based on counting statistics. The maximum and minimum peaks on the final difference Fourier map corresponded to 0.40 and –0.40 $e^- \cdot Å^{-3}$, respectively. Neutral atom scattering factors were taken from Cromer and Waber.[330] Anomalous dispersion effects were included in F_{calc};[331] the values for $\Delta f'$ and $\Delta f''$ were those of Creagh and McAuley.[332] The values for the mass attenuation coefficients are those of Creagh and Hubbell.[333] All refinements were performed using the Bruker AXS SHELXTL[334] crystallographic software package.

3.4.3. Spectroscopic Methods

Electronic Absorption Spectroscopy. Electronic absorption spectroscopy was performed with an Agilent 8453 spectrometer at ~300 K on solutions prepared at concentrations of 10^{-5}–10^{-6} M in spectroscropy grade solvents. For the determination of

thermal isomerization kinetic parameters, sample solutions were transferred to 1 cm × 1 cm cuvettes, subjected to rapid uniform stirring, and exposed to steady-state multiline UV irradiation (λ_{ex} = 333.6–363.8 nm, power ≈ 30 mW) or single-line visible irradiation (λ_{ex} = 532 or 568 nm, power ≈ 45–50 mW) generated with a Spectra-Physics Stabilite 2018 mixed-gas Ar–Kr ion laser and directed through the sample cuvette perpendicularly to the sampling beam with a liquid light guide. A cuvette of acetone was placed between the sample and sampling beam to block irradiation from the spectrometer in the near-UV region (<300 nm). The rates of thermal return were determined in the absence of light after generating a photostationary state by following the absorbance kinetics at the PMC π–π* λ_{max} and fitting A_∞–A_t or A_t–A_∞ (where A_t represents the absorbance at a given time, t, and A_∞ represents the absorbance at the photostationary state, or a close approximation thereof) to a first-order monoexponential rate function ($A = A_o e^{kt}$, where A_o is the initial absorbance) by linear least-squares methods. The observed rate constants, k_{obs}, were then taken as the negative of the resulting value for k. The choice of kinetic model was assessed visually by the accuracy of the fits and by the appropriateness of the residuals, R, for the particular data set. In suspect cases, the data were additionally fit to a first-order biexponential rate function for comparison, and these fits are also given when an improvement was noted. See Appendix C for rate fitting plots.

Solution-State FT-IR. Saturated solutions were prepared in spectroscopy grade CH_2Cl_2 obtained from an MBraun solvent purification system and filtered into a solution sample cell with a transmittance window >1000 cm^{-1}. Spectra were acquired at ~300 K with a Perkin Elmer Spectrum One spectrometer with a CH_2Cl_2 background subtraction. Irradiation experiments were performed as described above for the electronic absorption spectroscopy experiments.

3.4.4. Electrochemical Methods

Cyclic voltammograms (CVs) were acquired with a BAS CV-50W Voltammetric Analyzer (with glassy carbon working, silver pseudo-reference, and platinum counter electrodes) in 0.1 M tetrabutylammonium tetrafluoroborate (TBA-TFB, Aldrich, 99%) CH_2Cl_2 and CH_3CN solutions at scan rates of 50 mV/s and temperatures of ~300 K. Spectroscropy grade, dry, and deoxygenated CH_2Cl_2 was acquired from an MBraun

solvent purification system, and CH_3CN was distilled from CaH_2 under $N_{2(g)}$. Solvents were purged with $Ar_{(g)}$ for ≥5 min prior to acquiring CVs. Potentials were referenced to the $E_{1/2}$ value of the Fc^+/Fc redox couple of an internal ferrocene standard and are reported vs SCE (0.600 V and 0.454 V vs Fc^+/Fc in 0.1 M TBA-TFB in CH_2Cl_2 and CH_3CN, respectively).[335]

3.4.5. Computational Methods

Molecular geometries of the stationary points on the potential energy surfaces of the spirooxazines were optimized with the Gaussian 03 software package[272] using density functional theory (DFT)[273] with the B3LYP functional, consisting of Becke's three-parameter hybrid exchange functional[291] combined with the Lee–Yang–Parr correlation functional.[292] Ligand geometry optimizations were performed with the 6-31G(d) or 6-31G(d,p) basis sets and Mo complex geometry optimizations were performed with the double-ζ effective core potential LANL2DZ basis set.[323-325]

Chapter 4. Photoinduced Redox-State Switching in Magnetically Bistable Spirooxazine Cobalt–Dioxolene Redox Isomers

4.1. Introduction and Background

In possession of photochromic phenanthroline–spirooxazine ligands exhibiting changes in ligand field upon photoisomerization, we sought to incorporate these into metal complexes to develop useful photoswitchable systems. In a given coordination complex, certain optical properties (e.g., energies of *d–d* or MLCT transitions), electrochemical properties (e.g., redox potentials), or magnetic properties (e.g., magnitude of spin–orbit coupling, SOC) should scale *gradually* as a function of ligand field strength or symmetry. The modulation of such properties through ligand photoisomerization could indeed provide a path to photoswitchable coordination complexes. However, an optimal way to take advantage of the modest ligand field changes observed upon isomerization of the phenanthroline–spirooxazine ligands would be to coordinate them to electronically bistable metal complexes. Classic examples of electronically bistable coordination complexes are those which exhibit spin-crossover[158-161] or redox isomerism.[336-339] In such systems, small changes in the environment of the metal (either within the coordination sphere, or through external perturbations such as variations in temperature or pressure) can potentially lead to *abrupt* changes in metal-based optical, electrochemical, or magnetic properties that are correlated with changes in oxidation and/or spin state. We have opted to couple the photochromic spirooxazine ligands, APSO (**28**) and IPSO (**31**), to redox isomeric cobalt–dioxolene complexes to obtain compounds **46** and **47**. These complexes undergo a change in oxidation state and simultaneous spin transition [low spin (ls) Co^{III} ↔ high spin (hs) Co^{II}], accompanied by significant changes in optical and magnetic properties. Of these effects, the change in magnetic spin state is particularly interesting as a nondestructive readout mechanism for a molecular switch for which the input is optical in nature, and the state of the system may be detected magnetically.

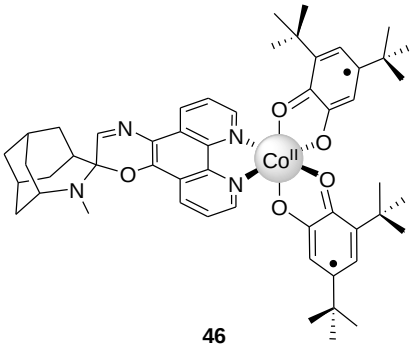

46

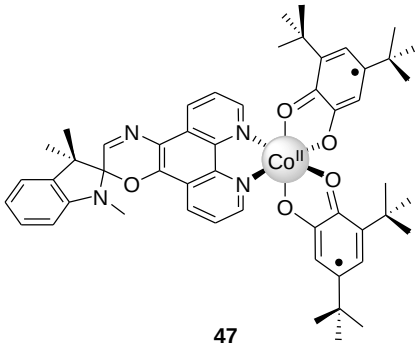

47

Photoinduced magnetic effects have been explored in several classes of coordination compounds,[164, 340-342] the most notable of which are the Prussian blue analogs,[343] spin-crossover systems,[162-166] and redox isomeric complexes.[344] In all of these systems, photoinduced magnetic effects arise from the photogeneration and trapping of metastable metal-based excited states at very low temperatures, which relax back to their ground states at temperatures well below ambient.[165] The use of photochromic ligands as a handle to optically toggle the state of a coordinated metal is a largely unexplored mechanism for eliciting photomagnetic responsivity in which the photogenerated states can remain stable at ambient temperatures. In the spirooxazine–cobalt–dioxolene systems, we hope to demonstrate that our proposed design can lead to robust room-temperature photoinduced magnetic effects and form the basis for a molecular photomagnetic switching material.

This chapter covers the synthesis of cobalt–dioxolene redox isomeric complexes **46** and **47** of the phenanthroline–spirooxazine ligands **28** and **31**, respectively. Because these systems can exist in two distinct photochromic states and two distinct redox states, characterization is both nontrivial and essential to understanding how the switching functions operate. A combination of PXRD, XRD, EA, ^{1}H NMR, FT-IR, and UV/Vis/NIR analysis is used to characterize the compounds and probe the position of the photochromic (SO/PMC) and redox (ls-Co^{III}/hs-Co^{II}) equilibria at ambient temperature. Variable-temperature (VT) ^{1}H NMR spectroscopy, UV/Vis/NIR spectroscopy, and magnetic susceptibility measurements provide information about the SO/PMC and ls-Co^{III}/hs-Co^{II} equilibria as a function of *T*. Finally, irradiation experiments are used to assess the photoresponsivity of the photochromic complexes and to investigate the correlation between light-induced SO/PMC isomerization and cobalt redox state.

4.1.1. Molecular Bistability

To meet the requirements for a molecule-based switch, a system must exhibit molecular bistability. This concept will be applied here as per the definition put forth by Kahn and Launay:[1]

> "Molecular bistability is the property of a molecular system able to evolve from a stable electronic state to another stable electronic state in a reversible and detectable fashion when applying an appropriate and controllable perturbation."

The phenomenon of molecular bistability as it relates to molecular switching is illustrated in Figure 4.1. For an ideal bistable switch (a), a reversible interconversion between states 1 and 2 occurs at a critical input parameter, I_c. An important requirement of a bistable switch is that the state of the system can be detected, as illustrated in Figure 4.1 by the change in intensity of a given readout signal along the *y* axis. Typically, the response is not as abrupt as shown in (a), and is instead more gradual, as shown in (b). In both (a) and (b), the critical input value is the same regardless of whether the conversion is occurring from state 1 to state 2 or vice versa. If this value depends on the direction of switching, the system is said to exhibit hysteresis, schematized in (c) and (d) for abrupt and gradual switching, respectively.

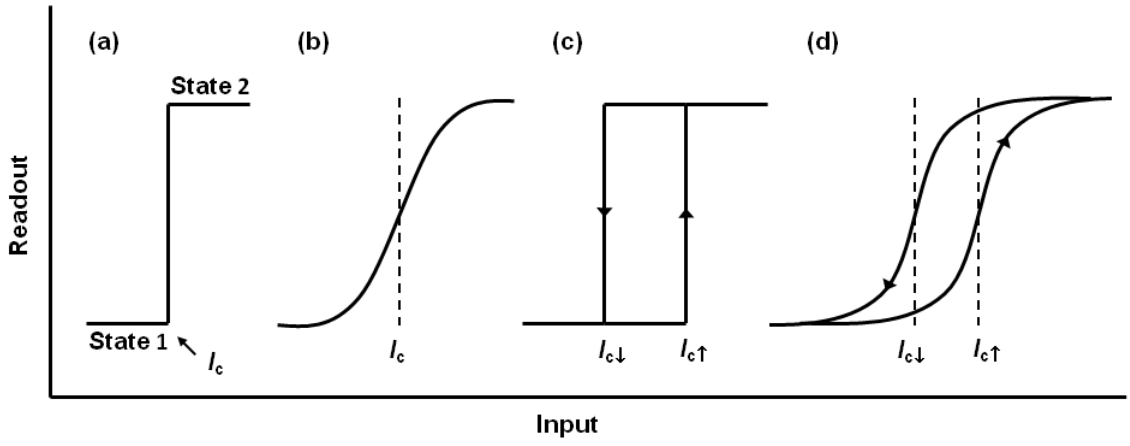

Figure 4.1. Phenomenon of molecular bistability schematized through readout vs input curves. Traces (a)–(d) are described in more detail in the text.

4.1.2. Cobalt–Dioxolene Redox Isomers

Redox isomerism (RI, also known as valence tautomerism) is a phenomenon characterized by intramolecular electron transfer (IET) between a redox-active metal and a non-innocent ligand. The quintessential redox isomeric system is the cobalt–dioxolene class of compounds. The most highly studied and well-understood compounds in this class are complexes of the $Co(DTBQ)_2(NN)$ type, where DTBQ represents a 3,5- or 3,6-di-*tert*-butyl-*ortho*-quinone ligand in either the semiquinone ($SQ^{-\bullet}$) or catecholate (Cat^{2-}) oxidation state and NN represents an ancillary diimine ligand such as 1,10-phenanthroline (phen) or 2,2′-bipyridine (bpy). Quinones—which may also be referred to as dioxolenes—are classic non-innocent ligands that can undergo a reversible one-electron reduction from a stable benzoquinone (BQ) form to a stable radical–anion semiquinone ($SQ^{-\bullet}$) form, and a further reversible one-electron reduction to a stable dianionic catecholate (Cat^{2-}) form [Scheme 4.1(a)]. In the Co–dioxolene complexes, IET from a Cat^{2-} ligand to a ls-Co^{III} metal centre results in a conversion from ls-Co^{III}(DTBCat)(DTBSQ)(NN) to hs-$Co^{II}(DTBSQ)_2$(NN). The reverse conversion occurs upon IET from hs-Co^{II} to $SQ^{-\bullet}$. The redox isomerism phenomenon is illustrated for the $Co(DTBQ)_2(phen)$[345] complex (**48**) in Scheme 4.1(b).

Scheme 4.1. (a) Reversible redox processes in non-innocent dioxolene ligands and (b) redox isomerism illustrated by the reversible conversion between ls-Co^{III}(3,5-DTBCat)(DTBSQ)(phen) and hs-$Co^{II}(3,5\text{-DTBSQ})_2$(phen) (**48**) upon intermolecular electron transfer (IET).

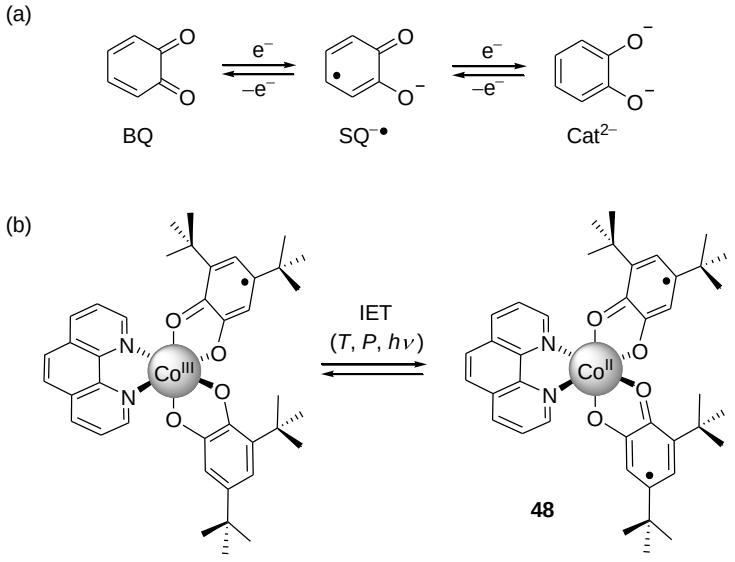

For a metal complex to be redox isomeric, it must fulfill a stringent set of requirements.[346-349] The metal and ligand frontier orbitals must be close in energy and exhibit a moderate level of mixing (i.e., the mixed-valent system should fall into a Robin–Day[350] class II classification—not electronically isolated as in class I systems nor completely delocalized as in class III systems) such that IET may occur between two distinct states. The bistability in such systems arises from a delicate thermodynamic balance of enthalpy and entropy contributions.[337]

$$\Delta G° = \Delta H° - T\Delta S° \tag{4.1}$$

The Gibbs free energy ($\Delta G°$, Equation 4.1) for the ls-Co^{III} → hs-Co^{II} reaction has a relatively small enthalpy ($\Delta H°$) contribution and a relatively large entropy ($\Delta S°$) contribution. At low T, the enthalpy term dominates the free energy of the reaction, $\Delta G°$ is positive, and the ls-Co^{III} form is most stable. At a given critical T, the $T\Delta S°$ term becomes dominant, $\Delta G°$ becomes negative, and the hs-Co^{II} form is stabilized. One of the keys to the entropy-driven bistability in Co–dioxolene complexes is the large change in electronic distribution that occurs upon IET. While the change in entropy is a function of both electronic and vibrational entropy contributions, the vibrational contribution dominates. The reduction of Co^{III} to Co^{II} accompanied by a ls → hs transition leads to the electronic population of antibonding Co^{II} orbitals. This in turn leads to longer M–L bond lengths and a greater density of associated vibrational states (as a result of more shallow potential energy wells for these vibrations, see Figure 4.2), which, from statistical mechanics arguments, contributes significantly to the greater entropy of the Co^{II} species and therefore significant entropy change upon ls-Co^{III} → hs-Co^{II} conversion.[337]

The structure (e.g., ancillary ligand) and environment (e.g., solvent polarity) of the complex should determine at which critical temperature, T_c, it undergoes IET (where T_c is defined as the temperature at which 50% of the molecules in a sample are in the ls-Co^{III} state and 50% are in the hs-Co^{II} state). Whether redox isomerism definitively occurs in a given sample and whether a conversion is gradual or abrupt depends strongly on sample medium. For a complex to undergo IET in the solid state, a large enough free volume must exist to accommodate the molecular expansion occurring upon Co^{III} → Co^{II}

conversion.[351] On the other hand, the conversion of a sample depends on intermolecular cooperativity interactions, which are typically heightened in an ordered environment such as a crystalline phase, and may be helped[345] or hindered[351] by the presence of solvent molecules in the lattice.[352] Conversion in the solution state is of a gradual nature and follows Boltzmann behaviour. Solvents of higher polarities have been found to increase T_c values.[352]

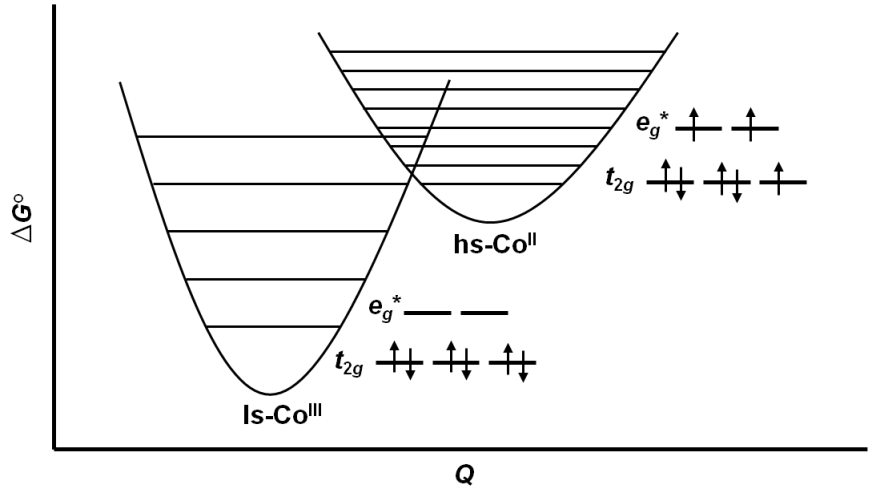

Figure 4.2. Electronic structure of ls-Co^{III} and hs-Co^{II} states of the $Co(DTBQ)_2(NN)$ system illustrating frontier orbital filling (in a pseudo-O_h coordination environment) and density of vibrational states. The reaction coordinate Q represents the Co–O bond length.

4.2. Results and Discussion

4.2.1. Theoretical Model for a Room-Temperature Spiroxazine–Cobalt–Dioxolene Photomagnetic Switch

The Co–dioxolene redox isomers display molecular bistability with more or less gradual transitions as schematized in Figure 4.1(b), and occasionally exhibit hysteresis as schematized in Figure 4.1(d). In these Co redox isomers, the input parameter is typically temperature, and the state of the complex may be detected via changes in magnetic susceptibility or optical absorbance at a particular wavelength. However, a molecular switch that relies on thermal perturbations as its input parameter may not be particularly

useful for applications unless it is possible to thermally trap a given state. For this reason, there has been ongoing interest in the light-induced excited-spin-state trapping (LIESST) effect in both redox isomeric[344, 351] and spin-crossover[162-166] coordination compounds, because one may exploit this phenomenon to control the state of a system at a given temperature using light, a practical external input parameter. However, as mentioned in Section 1.2.3, the LIESST phenomenon does not occur within ambient temperature ranges. The incorporation of photochromic ancillary ligands into cobalt–dioxolene redox isomers may provide a solution to this problem by introducing a mechanism for switching between redox states using light even at ambient temperatures. In the $Co(3,5\text{-}DTBQ)_2(IPSO)$ and $Co(3,5\text{-}DTBQ)_2(APSO)$ complexes, four distinct electronic states become accessible (Scheme 4.2) instead of the two found in traditional $Co(3,5\text{-}DTBSQ)_2(NN)$ complexes. Here, it is not only possible to induce IET between ls-Co^{III} and hs-Co^{II} forms with temperature, or to induce isomerization between SO and PMC with light, but we propose that it is possible to induce a change in the oxidation/spin state of Co through optically induced ligand photoisomerization (as shown by the dashed lines in Scheme 4.2). Because the two photoisomers of the spirooxazine ligand can remain stable at room temperature, so should the redox state of Co. As the model described here for Co–dioxolene redox isomers is very similar to that outlined by Roux et al. in the mid-90's for the ligand-driven light-induced spin change (LD-LISC) effect proposed for Fe spin-crossover materials,[156] it may be referred to as ligand-driven light-induced redox isomerism (LD-LIRI).

Scheme 4.2. Four possible electronic states of Co(3,5-DTBQ)$_2$(IPSO): (a) ls-Co^{III}(3,5-DTBCat)(3,5-DTBSQ)(IPSO-SO), (b) hs-Co^{II}(3,5-DTBSQ)$_2$(IPSO-SO), (c) ls-Co^{III}(3,5-DTBCat)(3,5-DTBSQ)(IPSO-PMC), and (d) hs-Co^{II}(3,5-DTBSQ)$_2$(IPSO-PMC).

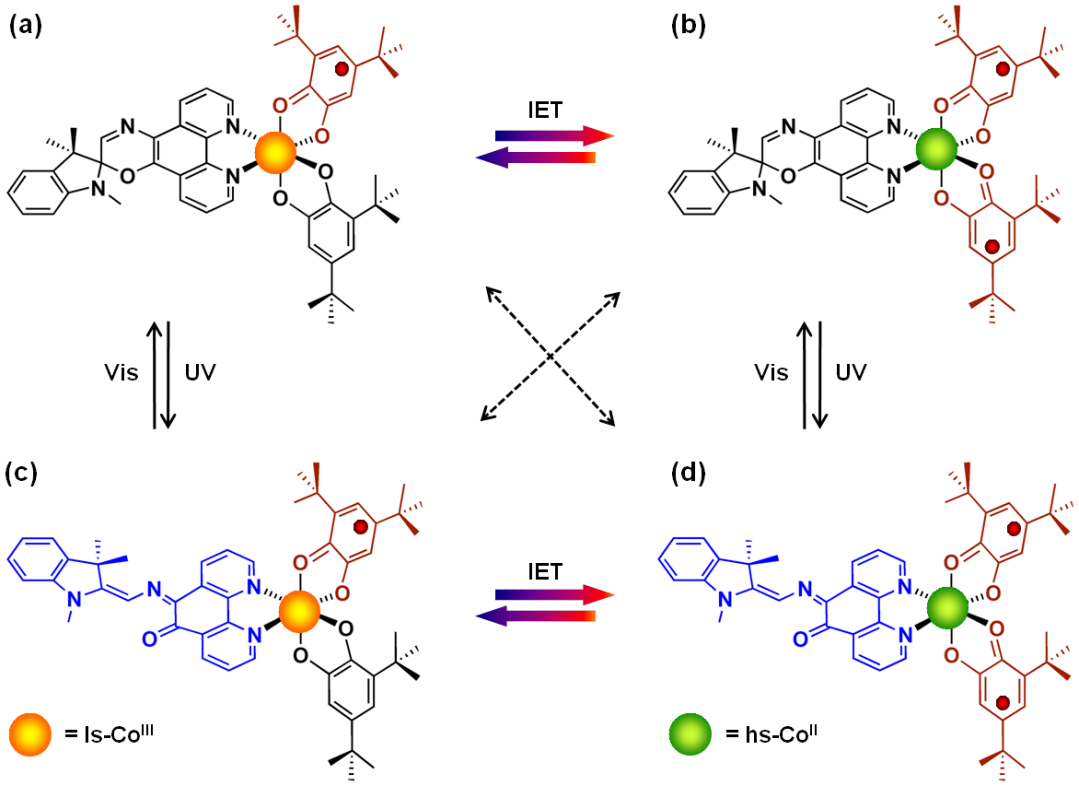

There is both experimental and theoretical precedent to support the sensitivity of the ls-Co^{III} → hs-Co^{II} equilibrium to the ligand field of the ancillary diimine ligand. In 1993, Adams et al. correlated the transition temperature, T_c, of a series of Co(3,5-DTBQ)$_2$(NN) complexes with the reduction potential of their respective diimine ligands and found a remarkably linear correlation (Figure 4.3).[345, 353] Shortly thereafter, Adams, Noodleman, and Hendrickson reported a detailed DFT computational analysis of the electronic structure of the Co(3,5-DTBQ)$_2$(phen) system, which included a discussion of ligand field effects on the stability of the ls-Co^{III} and hs-Co^{II} states.[354]

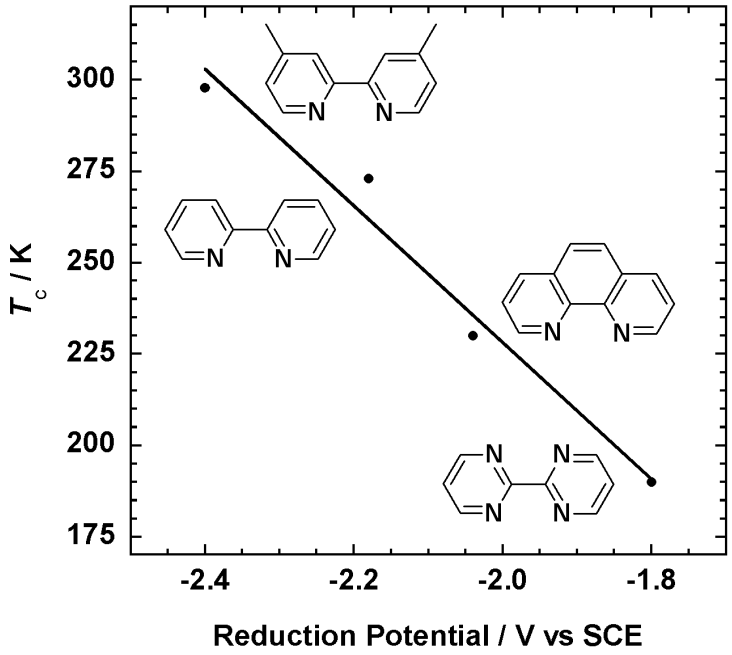

Figure 4.3. Correlation between critical temperature, T_c, for the redox isomeric ls-Co^{III} → hs-Co^{II} transition in Co(3,5-DTBQ)$_2$(NN) complexes (experimentally determined in toluene) with the reduction potential of the diimine ligand (experimentally determined in CH_3CN). A linear least-squares fit of the data gives $y = -187x - 146$ with $R^2 = 0.97$. (Figure adapted with permission from ref[337]. Copyright 2001 Wiley-VCH.)

Ligand field effects in the Co(3,5-DTBQ)$_2$(phen) system can result from both σ-donation and π-backbonding effects. A simplified schematic for the interaction of σ-donor and π-acceptor ligands with a metal ion in an octahedral coordination environment is given in Figure 4.4. A σ-donor ligand will interact with the σ-bonding e_g metal orbitals (d_{z2}, d_{x2-y2}), while a π-acceptor ligand will interact with the π-bonding t_{2g} metal orbitals (d_{xy}, d_{xz}, d_{yz}). In each case, metal-based bonding orbitals are stabilized, and the octahedral ligand field splitting parameter, ΔO_h, is increased. In the Co(3,5-DTBQ)$_2$(phen) complex, greater σ-donation preferentially stabilizes the ls-Co^{III} form. In the ls-Co^{III} form, the increased energy of the antibonding e_g* orbitals resulting from σ-donation places them further above the π* orbitals of the $SQ^{-\bullet}$ and Cat^{2-} ligands, which makes IET more energetically costly. Further, increasing the energy of the e_g* orbitals destabilizes the hs-Co^{II} form which, unlike the ls-Co^{III} form, has electron density in these orbitals. On the other hand, greater π-backbonding preferentially stabilizes the hs-Co^{II} form. Qualitatively, this can be understood from the fact that a strong π-acceptor

ligand, able to accept electron density from a coordinated metal, will preferentially stabilize the more electron-rich Co^{II} form. More rigorously, in the hs-Co^{II} species of the $Co(3,5\text{-DTBQ})_2(phen)$ system, spin polarization induces a large splitting between the α and β spin orbitals; the minority spin t_{2g} orbitals are significantly higher in energy and become much closer to the phen(π^*) orbitals; this effect does not occur in the ls-Co^{III} state. Thus the M(d)–phen(π^*) backbonding interaction is strong in the hs-Co^{II} form but essentially nonexistent in the ls-Co^{III} form. Because this backbonding interaction stabilizes the complex by stabilizing the bonding t_{2g} orbitals, and because this effect only occurs in the Co^{II} form, a stronger π-acceptor will better stabilize hs-Co^{II} over ls-Co^{III}.[354]

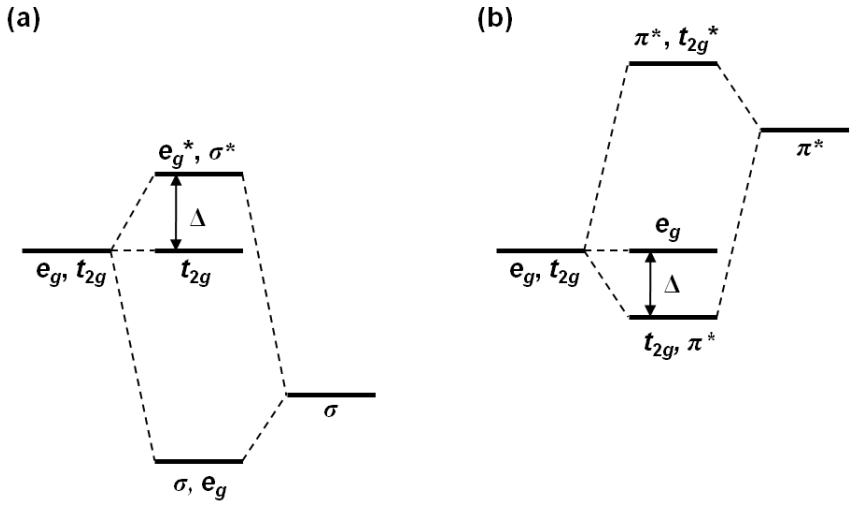

Figure 4.4. Simplified schematic for the interaction of σ-donor (a) and π-acceptor (b) ligands with metal d orbitals in an octahedral coordination environment. In each case, the O_h ligand field splitting, Δ, is shown.

The analysis of metal–ligand bonding interactions in phenanthroline–spirooxazine ligands presented in Chapter 3 demonstrated that the SO and PMC forms of these ligands have significantly different MO configurations. Although both σ-donation and π-backbonding interactions can affect the relative stabilities of the ls-Co^{III} and hs-Co^{II} forms, the linear correlation between transition temperature and diimine ligand reduction potential suggests that the π-backbonding interaction plays a more important role in the overall stabilization effect. An initial determination of the reduction potentials of the SO and PMC forms of APSO and IPSO showed that the reduction potential of the PMC form

is approximately 0.7 V more positive than that of the SO form. This result was consistent with DFT MO calculations in which the LUMO of the PMC form was found to be ~0.6–0.7 eV lower in energy than that of the SO form. However, a fragment molecular orbital analysis of the metal–ligand bonding in $Mo(CO)_4$(phen-NN) (where phen-NN represents any phen-containing ligand) complexes revealed that it is not, in fact, the LUMO of the phen-based ligand that interacts predominantly with the metal, but the LUMO + 1. This analysis should hold for the $Co(3,5\text{-DTBQ})_2$(phen-NN) complexes as the two phen-based π^* orbitals (of b_1 and a_2 symmetries under C_{2v} symmetry constraints) should be of the appropriate symmetry and energy to interact with the two metal-based orbitals of corresponding symmetries (i.e., the d_{xz} and d_{xy} orbitals in Figure 3.16) and the mixing for the 'b_1' interaction should still be most significant based on the relative electron density at the N atoms and the expected orbital overlap. It follows that because the LUMO + 1 is ~0.2–0.3 eV lower in energy for the SO form than for the PMC form, the SO form should behave as a stronger π-acceptor.

Table 4.1. Estimation of the critical transition temperature, T_c, for ls-Co^{III} → hs-Co^{II} conversion of the $Co(3,5\text{-DTBQ})_2$(NN) complexes containing the SO and PMC forms of IPSO and APSO using the estimated 'reduction potential' of the LUMO + 1.

Ligand	**Reduction Potential (LUMO)[a] / V**	**'Reduction Potential' (LUMO + 1)[b] / V**	**Estimated T_c / K**
APSO-SO		–2.24	273
APSO-PMC	–1.26[c]	–2.51	323
IPSO-SO	–1.71[d]	–2.19	264
IPSO-PMC		–2.39	301

[a]Conditions: 0.1 M TBA-TFB in deoxygenated CH_3CN; 50 mV/s scan rate, glassy carbon working electrode, silver pseudo-reference electrode, platinum counter electrode, referenced to the Fc^+/Fc redox couple and reported vs SCE. [b]Obtained by correcting the experimental reduction potential for the difference between the LUMO + 1 and the LUMO in eV from DFT calculations. [c]Taken as $E_{1/2}$. [d]Taken as E_{pc}.

The T_c values for the SO and PMC forms of IPSO and APSO were interpolated/extrapolated from the data compiled in Figure 4.3. This was done not with the reduction potentials of the ligands (correlating to the energies of the LUMO's), but with the corrected 'reduction potentials' for the LUMO + 1's, estimated by correcting the

experimental reduction potentials for the ΔE between the LUMO + 1 and LUMO extracted from DFT calculations. These values are summarized in Table 4.1. It is evident that fairly small differences in the energies of the LUMO + 1's lead to fairly substantial changes in estimated T_c values (50 K for APSO and 37 K for IPSO). In both cases, the estimated T_c values fall on either side of room temperature, with the values for the SO (273 K) and PMC (323 K) forms of APSO falling exactly 25 K below and 25 K above 298 K. This remarkable result is illustrated schematically in Figure 4.5, from which it can be seen that, in theory, at room temperature, the Co(3,5-DTBQ)$_2$(APSO) complex should exist in either the ls-Co^{III} or hs-Co^{II} state as a function of whether the spirooxazine ligand is in the SO or PMC form.

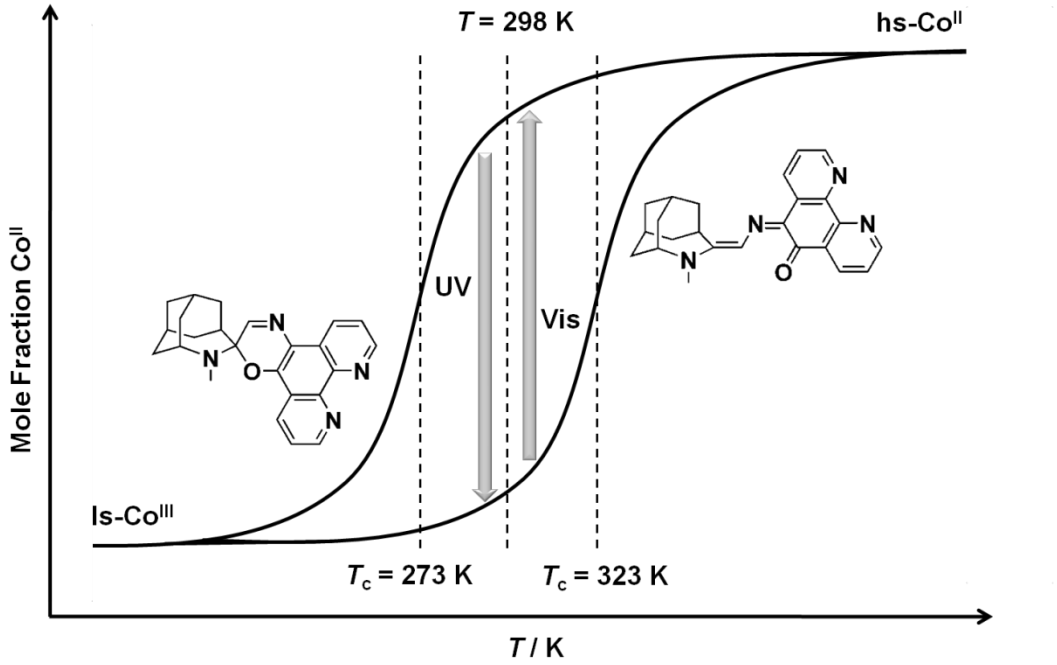

Figure 4.5. Arbitrarily abrupt model curves representing the mole fraction of Co^{II} as a function of temperature for the SO and PMC forms of Co(3,5-DTBQ)$_2$(APSO) using estimated T_c values (see text). The figure illustrates the LD-LIRI mechanism for controlling the redox state of Co through photoisomerization of the ancillary ligand at room temperature (298 K).

The analysis summarized in Table 4.1 and Figure 4.5 is based only on the LUMO + 1's of the spirooxazine ligands. If one considers the contribution of the 'a_2' metal–ligand bonding interaction, the overall conclusion is in fact strengthened because the LUMO of the SO form, exhibiting predominantly phen(π^*, a_2) character is much lower in energy than the MO of the PMC form of corresponding symmetry (i.e., the LUMO + 2). The

LUMO of the PMC form is not expected to mix significantly with the metal because there is no electron density on the nitrogen atoms. Despite the fact that the above analysis relies on numerous assumptions, it provides an enlightening model for the proposed LD-LIRI phenomenon. Importantly, even if some of the quantities cited are merely rough approximations, this analysis demonstrates that the changes in ligand field expected for the phenanthroline–spirooxazine ligands should lead to substantial changes in T_c (on the order of 50 K) in spirooxazine Co(3,5-DTBQ)$_2$(NN) systems and that the T_c values lie near room temperature, which implies that the complex should therefore be electronically labile over a practical temperature range.

4.2.2. Synthesis and Characterization

Although other synthetic routes have been reported,[355] the preparation of complexes with the generalized formula Co(DTBQ)$_2$(NN), typically follows from the reaction of $Co_2(CO)_8$, 3,5- or 3,6-DTBBQ (DTBBQ = di-*tert*-butyl-*ortho*-benzoquinone), and the desired diimine ligand. The simplest procedure involves the addition of all three reagents in solution with precipitation of the product, where the reaction solvent and temperature are chosen on the basis of the relative solubilities of the reagents and products.[356-359] Here, the oxidation of cobalt(0) octacarbonyl with liberation of CO and reduction of benzoquinone proceed to give the Co^{II}(DTBSQ)$_2$(NN) or Co^{III}(DTBSQ)(DTBCat)(NN) product. An alternative common method of preparation[345, 360-362] involves the initial synthesis of either a tetrameric Co complex, [Co^{II}_4(3,5-DTBSQ)$_8$],[363] with the 3,5-substituted benzoquinone derivative, or a tris-quinone complex, [Co^{III}(3,6-DTBSQ)$_3$],[364] with the bulkier 3,6-substituted benzoquinone derivative, followed by reaction with the diiimine ligand. A third, less common, synthetic route that we have explored is the in-situ reaction of [Co_4(3,5-DTBSQ)$_8$] in THF to form what we hypothesize to be a bis-THF complex, [Co(THF)$_2$(3,5-DTBSQ)$_2$] by analogy with the known [Mn^{III}(THF)$_2$(3,5-DTBSQ)(3,5-DTBCat)] complex,[365] followed by complexation with the diimine ligand.

The Co(3,5-DTBQ)$_2$(phen) control compound was synthesized by a modified literature procedure[345] by adding a toluene solution of phen to a toluene suspension of the Co tetramer, [Co^{II}_4(3,5-DTBSQ)$_8$]. Stirring for 2 h, followed by allowing the solution to

stand undisturbed for 5 h resulted in a dark green microcrystalline product which could be isolated by filtration. The product was then recrystallized from hot toluene following a hot filtration and gradual cooling. An analytically pure black crystalline solid was isolated as the toluene solvate, $Co(3,5\text{-}DTBQ)_2(phen)\cdot C_6H_5CH_3$.

Several methodologies and purification procedures were investigated for the synthesis of the $Co(3,5\text{-}DTBQ)_2(IPSO)$ and $Co(3,5\text{-}DTBQ)_2(APSO)$ complexes. Both derivatives could be prepared either via the Co tetramer in toluene or the THF complex in THF. In the first case, a toluene solution of IPSO or APSO was added to a toluene solution of $[Co_4(3,5\text{-}DTBSQ)_8]$, prepared either in situ from $Co_2(CO)_8$ and DBBQ or using isolated Co tetramer, and stirred for 1–2 h before removing the solvent in vacuo. In the second case, a solution of $[Co_4(3,5\text{-}DTBSQ)_8]$ in THF was stirred for ~30 min before adding a THF solution of IPSO or APSO, stirring the mixture for 1–2 h and then removing the solvent in vacuo.

For the IPSO derivative, recrystallization of the crude solid from cyclohexane either at ambient temperature (~300 K) or in the refrigerator (~285 K) gave analytically pure microcrystalline blue-green powders of $Co(3,5\text{-}DTBQ)_2(IPSO)$ in 10–60% yield.

Recrystallization of the APSO complex was more challenging. The crude solid was usually minimally soluble in hydrocarbon solvents, although different samples exhibited different solubility properties, possibly due to different aggregation behaviour. For samples that could be dissolved in sufficient quantities, no crystalline material could be isolated (from cyclohexane, toluene, THF, CH_2Cl_2, or CH_3CN), even when concentrated or stored at low temperature. $Co(3,5\text{-}DTBQ)_2(APSO)$ was therefore isolated by precipitation from toluene with pentane as an amorphous bright purple powder in 25–60% yields.

Elemental analyses for this compound exhibited higher than normal variability, most notably in the analysis of %C. Analyses on the same sample by three separate laboratories [Canadian Micronanalytical Services (Can. Micro.), University of British Columbia (UBC), and Columbia Analytical Services (CAS, formerly Desert Analytics, DA)] gave %C values ranging from 65.12 to 70.84%. For a duplicate analysis on this sample within the same laboratory (CAS), %C values were reported as 67.39 and 70.84%. Multiple samples were analyzed by the three above laboratories, and it was

found that samples analyzed by DA/CAS, for which were added a WO_3 catalyst during analysis, consistently gave higher %C values by ~2%. Thus, the results for six analyses from DA/CAS [C: 68.14 (±1.34); H: 6.69 (±0.29); Co: 6.26 (±0.42); N: 6.92 (±0.30)] and four analyses from Can. Micro/UBC [C: 65.09 (±0.55); H: 6.73 (±0.17); N: 6.91 (±0.47] were averaged both separately and together [C: 66.92 (±1.89); H: 6.70 (±0.24); Co: 6.26 (±0.42); N: 6.92 (±0.35)]. Compared to the theoretical values for Co(3,5-DTBQ)$_2$(APSO) [C: 70.65; H: 7.30; Co: 6.67; N: 6.34], the experimental values are within experimental error for Co, ~0.6% low for H, ~0.6% high for N, and ~2.5% low for C (for DA/CAS analyses) or >5% low for C (for Can. Micro/UBC analyses). Attempts to fit the average experimental formula to different combinations of mononuclear and multinuclear oligomeric stoichiometries or to account for the inclusion of solvent, THF, or H_2O were all unsuccessful. For this reason it is plausible that the differences observed between experimental and theoretical values is the result of inadequate burning of this particular sample during analysis, which could explain the higher %C values obtained upon addition of the WO_3 catalyst.

The reaction of $Co_2(CO)_8$, 3,5-DTBBQ, and APSO in MeOH gave large needle- or block-shaped dark purple-black crystals from the reaction mixture, which were isolated in 18–25% yield. Unexpectedly, these were found by X-ray analysis to be tetrameric cobalt complexes with the formula Co_4(3,5-DTBQ)$_6$(APSO)$_2$(MeO)$_2$·2MeOH (**49**) (vide infra, Section 4.2.4). Elemental analysis was consistent with this formula for both H and N, with C being ~2% low. It is possible that elemental analysis for this compound is associated with similar complications as for the mononuclear Co–APSO complex.

Electrospray ionization (ESI) mass spectrometry (MS) experiments on Co(3,5-DTBQ)$_2$(phen), Co(3,5-DTBQ)$_2$(IPSO), and Co(3,5-DTBQ)$_2$(APSO) did not show a molecular ion peak for the $[Co(3,5\text{-DTBQ})_2(NN)]^+$ fragment, but instead showed a base peak for a $[Co(3,5\text{-DTBQ})(NN)_2]^+$ fragment. Electron impact (EI) MS and MALDI experiments on Co(3,5-DTBQ)$_2$(APSO) also did not show a molecular ion peak for the $[Co(3,5\text{-DTBQ})_2(APSO)]^+$ fragment. As the high purity of the Co(3,5-DTBQ)$_2$(phen) and Co(3,5-DTBQ)$_2$(IPSO) complexes was confirmed by several techniques, this suggests that the observed $[Co(3,5\text{-DTBQ})(NN)_2]^+$ fragment is representative of an extremely small amount of the sample or is a rearrangement product

that forms in the spectrometer. Therefore, MS is not an ideal diagnostic technique for confirming the identity of these complexes.

4.2.3. PXRD Analysis

Neither single crystals of Co(3,5-DTBQ)$_2$(IPSO) nor Co(3,5-DTBQ)$_2$(APSO) could be grown. Powder X-ray diffraction (PXRD) analysis was therefore performed on the complexes to compare their crystallinity. Shimmery powder samples of Co(3,5-DTBQ)$_2$(IPSO) displayed distinct powder patterns. Through the analysis of several samples, it became evident that material isolated from cyclohexane at room temperature (~300 K) and material isolated from cyclohexane in the refrigerator (~285 K) exhibited different crystalline phases (Figure 4.6). This may be the result of the temperature-sensitive SO/PMC and ls-Co^{III}/hs-Co^{II} equilibria existing in solution, from which a given phase could easily be trapped. A representative powder sample of Co(3,5-DTBQ)$_2$(APSO), precipitated from toluene with pentane, displayed a broad, featureless PXRD pattern characteristic of an amorphous material (Figure 4.7).

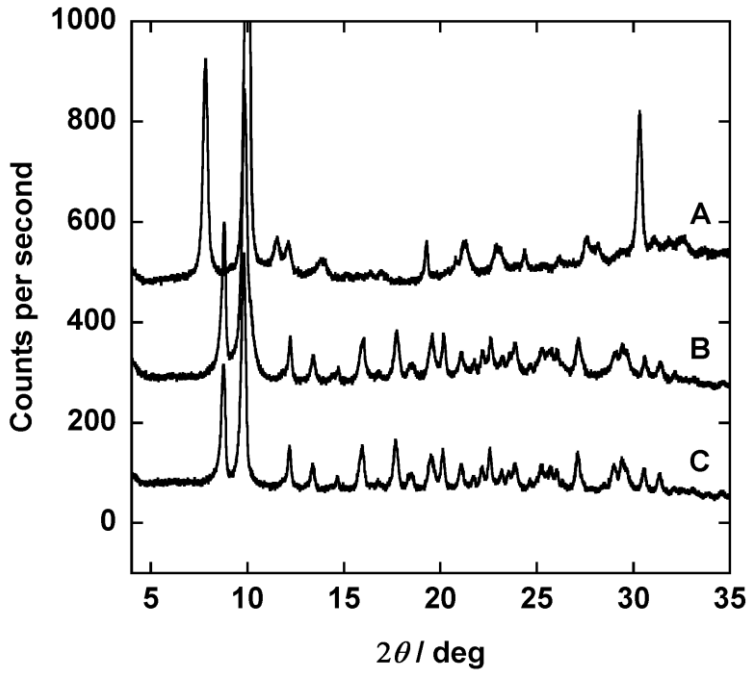

Figure 4.6. PXRD patterns of Co(3,5-DTBQ)$_2$(IPSO) complexes crystallized from cyclohexane at ~300 K (α-phase, A) and at ~285 K (β-phase, B/C).

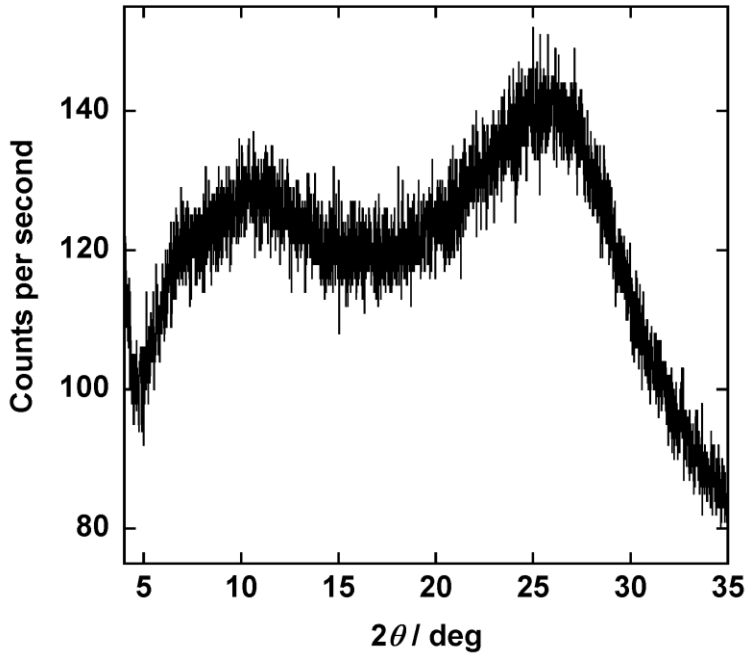

Figure 4.7. PXRD pattern of a Co(3,5-DTBQ)$_2$(APSO) powder sample.

4.2.4. Single-Crystal XRD Analysis of the Co–APSO tetramer

X-ray crystallographic analysis of the crystalline product from the reaction of [Co$_4$(3,5-DTBQ)$_8$] with APSO in MeOH was informative both in revealing the identity of the product and in determining its oxidation state.[366] Dark purple blocks and needles of the product crystallized from the MeOH reaction solution. A needle measuring 0.09 × 0.12 × 0.45 mm^3 was selected from the mother liquor and immediately mounted for data acquisition at low temperature (90 K). Unexpectedly, the product was found to be a tetrameric Co cluster with the chemical formula Co$_4$(3,5-DTBQ)$_6$(APSO)$_2$(MeO)$_2$·2MeOH, rather than the expected mononuclear Co(3,5-DTBQ)$_2$(APSO) formula. It crystallized in the monoclinic *C*2/*m* space group with one quarter molecule in the asymmetric unit, two molecules per unit cell, and two MeOH solvent molecules per complex molecule. The structure was disordered across a mirror plane, resulting in poor refinement factors (R_1 = 0.116, wR_2 = 0.300).

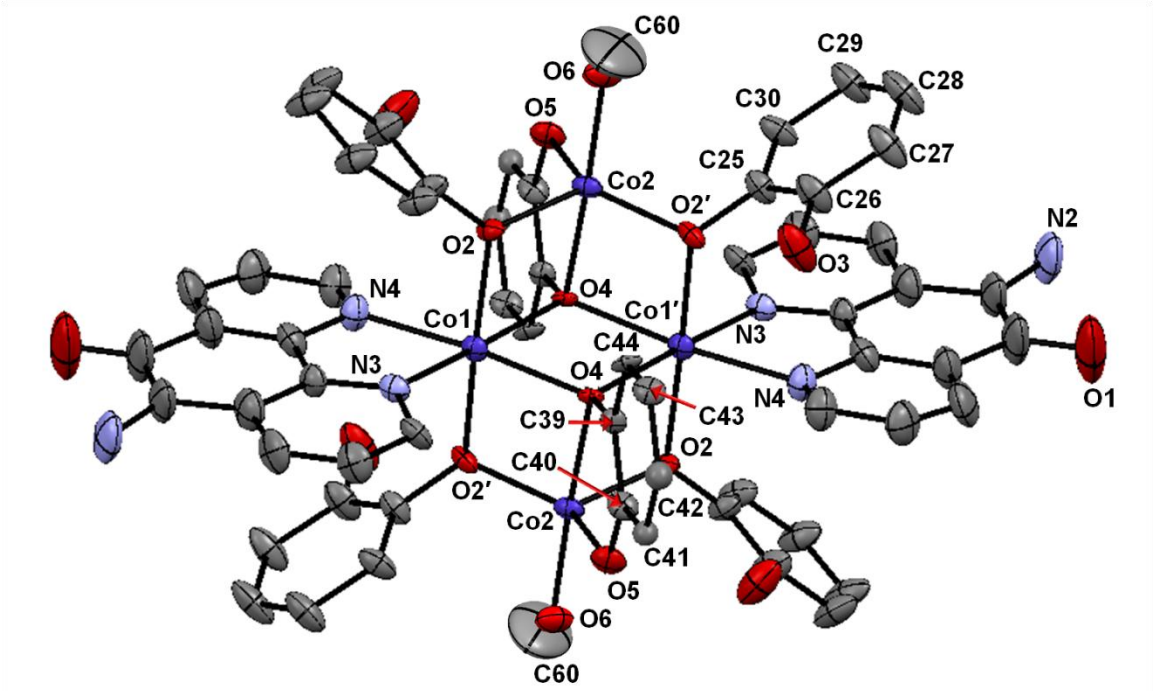

Figure 4.8. Molecular structure of $Co_4(3,5\text{-DTBQ})_6(APSO)_2(MeO)_2 \cdot 2MeOH$. Disorder, azahomoadamantyl groups, *t*-butyl groups, hydrogen atoms, and solvent molecules omitted for clarity. Ellipsoids shown at the 33% probability level.

The molecular structure of $Co_4(3,5\text{-DTBQ})_6(APSO)_2(MeO)_2 \cdot 2MeOH$ is shown in Figure 4.8, and selected bond lengths and angles are tabulated in Table 4.2. The complex contains a core of four cobalt and six oxygen atoms, the geometry of which is nearly identical to that found in the $[Co_4(3,5\text{-DTBSQ})_8]$ cluster reported in 1979 by Buchanan et al.[363] Two Co atoms [Co(1) and Co(1)′] are found in nearly octahedral coordination geometries, each being coordinated to two N atoms [N(3) and N(4)] from the APSO ligand, two triply bridging O atoms [O(4)], and two doubly bridging O atoms [O(2) and O(2)′] from $Cat^{2-}/SQ^{-\bullet}$ ligands. The two remaining Co atoms [Co(2)] possess a distorted trigonal bipyramidal geometry. They are axially coordinated to the O(6) atom from a MeO ligand and the triply bridged O(4) atom from a $Cat^{2-}/SQ^{-\bullet}$ ligand. The O(6)–Co(2)–O(4) angle is nearly 180° at 176.1°. The Co(2) atoms are equatorially coordinated to two doubly bridging O atoms [O(2) and O(2)′] and a terminally coordinated O(5) atom from a $Cat^{2-}/SQ^{-\bullet}$ ligand. The three bond angles associated with the equatorially coordinated atoms are considerably distorted from 120° [O(2)–Co(2)–O(2)′ = 115.75(15)°, O(2)–Co(2)–O(5) = 108.7(3)°, O(5)–Co(2)–O(2)′ = 131.1(3)°]. While the geometry of the core

is the same as that in Buchanan's tetramer, the coordination environment is not identical. In the $[Co_4(3,5\text{-DTBSQ})_8]$ tetramer, the Co(2) atoms are coordinated to a DTBSQ ligand with two terminally bound O atoms, while in the $Co_4(3,5\text{-DTBQ})_6(APSO)_2(MeO)_2{\cdot}2MeOH$ tetramer, the Co(2) atoms are pentacoordinate rather than hexacoordinate, and are instead coordinated to one O atom from a solvent molecule. Further, each of the four $Cat^{2-}/SQ^{-\bullet}$ ligands that are nonchelating in the $Co_4(3,5\text{-DTBQ})_6(APSO)_2(MeO)_2{\cdot}2MeOH$ complex—being merely bound to the Co(1) atoms via one oxygen atom [O(2)/O(2′)]—act as chelating ligands in the $[Co_4(3,5\text{-DTBSQ})_8]$ complex. In the tetrameric APSO complex, the four freed Co coordination sites are instead replaced by chelating APSO ligands.

Table 4.2. Selected bond lengths [Å] and angles [°] for $Co_4(3,5\text{-DTBQ})_6(APSO)_2(MeO)_2{\cdot}2MeOH$.[a]

OMe and 3,5-DTBQ ligands		**Co–O core**	
C(60)–O(6)	1.30(4)	Co(1)–O(2)	2.070(4)
C(25)–O(2)	1.354(7)	Co(1)–O(4)	2.158(7)
C(26)–O(3)	1.365(9)	Co(1)′–O(4)	2.096(7)
C(25)–(26)	1.385(10)	Co(1)–N(3)	2.128(7)
C(25)–C(30)	1.385(9)	Co(1)–N(4)	2.143(8)
C(26)–C(27)	1.413(11)	Co(2)–O(2)	1.975(4)
C(27)–C(28)	1.379(11)	Co(2)–O(2)′	1.898(5)
C(28)–C(29)	1.390(11)	Co(2)–O(4)	2.168(6)
C(29)–C(30)	1.392(10)	Co(2)–O(5)	1.930(9)
C(39)–O(4)	1.376(9)	Co(2)–O(6)	2.086(10)
C(40)–O(5)	1.391(11)	O(6)–Co(2)–O(4)	176.1
C(39)–C(40)	1.39(1)	O(2)–Co(2)–O(2)′	115.75(15)
C(39)–C(44)	1.390(6)	O(2)–Co(2)–O(5)	108.7(3)
C(40)–C(41)	1.39(2)	O(5)–Co(2)–O(2)′	131.1(3)
C(41)–C(42)	1.391(9)	O(5)–Co(2)–O(4)	81.3(4)
C(42)–C(43)	1.39(1)	O(2)–Co(2)–O(4)	85.9(2)
C(43)–C(44)	1.39(2)	O(2)′–Co(2)–O(4)	81.6(2)

[a]Formula: $C_{134}H_{178}Co_4N_8O_{16}{\cdot}2CH_3OH$. FW: 2456.71 g mol^{-1}. Crystal system: monoclinic. Space group: *C*2/*m* (no. 12). *a*: 24.684(3) Å. *b*: 24.211(3) Å. *c*: 14.843(2) Å. *β*: 115.088(3)°. *V*: 8034(2) Å^3. Z = 2. ρ_{calc} = 1.016 g cm^{-3}. *T*: 90 K. F_{000}: 2623.00. λ: 0.71073 Å. μ: 4.60 cm^{-1}. R_1: 0.116. wR_2: 0.300. $R_1 = \Sigma||F_o| - |F_c|| / \Sigma|F_o|$. $wR_2 = [\Sigma(w(F_o^2 - F_c^2)^2) / \Sigma w(F_o^2)^2]^{1/2}$; $w = 1/[\sigma^2(F_o)^2 + (0.1643P)^2 + 71.9289P]$.

Table 4.3. Bond lengths [Å] for different oxidation states of Co–dioxolene complexes.[a]

Co bonds lengths	**Co^{II}**	**Co^{III}**	**Δ**
Co–N	2.13–2.14	1.92–1.95	0.15–0.20
$Co–O_{DTBSQ}$ (terminal O or doubly bridging O)	2.02–2.09	1.90–1.92	~0.15
$Co–O_{DTBCat}$ (terminal O)		1.86–1.87	
Co–O (triply bridging O)	2.1–2.3		
Ligand bond lengths	**3,5-DTBSQ**	**3,5-DTBCat**	**Δ**
C–O	1.27–1.32	1.34–1.36	~0.06–0.07
C=C	1.32–1.39		
C–C	1.40–1.46		
C–C (Ar)		1.38–1.42	

[a]See refs[345, 363].

Because this class of Co complexes exhibits such large differences in electronic distribution between the ls-Co^{III}/hs-Co^{II} and Cat^{2-}/$SQ^{-\bullet}$ forms, the oxidation states of both the Co centres and DTBQ ligands can by determined from an analysis of the bond lengths. Although 'high-quality' structures are ideal for such an analysis,[366] the expected differences in bond lengths (0.05–0.20 Å) upon IET are considerably greater than the experimentally determined 2σ values (0.008–0.022 Å) for the bond lengths of interest. The Co–O and Co–N bond lengths are expected to be 0.10–0.20 Å longer in the hs-Co^{II} species than in the ls-Co^{III} species because the hs-Co^{II} species contains electrons in antibonding orbitals. Typical M–L bond lengths are given in Table 4.3 for closely related Co–dioxolene complexes. For the Co(1) centre in the Co–APSO complex, the Co(1)–N(3) and Co(1)–N(4) bond lengths are 2.128(7) and 2.143(8) Å, respectively, which fall cleanly within the range expected for a Co^{II} species (2.13–2.14 Å). The Co(1)–Co(2) bond length of 2.070(4) Å is also consistent with that of a Co^{II} species (2.02–2.09 Å). The bond lengths for Co(1)–O(4) and Co(1)′–O(4) are 2.158(7) and 2.096(7) Å, respectively, which are longer than expected for Co–O bonds to terminally coordinated or doubly bridging oxygen atoms, but consistent with the longer Co–O bonds to triply bridging O atoms found for the Co^{II} tetramer (2.1–2.3 Å).[363] For the Co(2) centre, all of the dioxolene-based Co–O bond lengths [Co(2)–O(5) = 1.930(9) Å, Co(2)–O(2) =

1.975(4) Å, Co(2)–O(2)′ = 1.898(5) Å] are consistent with a Co^{III} oxidation state for the metal (1.86–1.92 Å).

The oxidation state of the dioxolene ligands can also be inferred from an analysis of their C–O and C–C bond lengths. The C–O bond length for the DTBCat ligand is ~0.06 Å longer than that for the DTBSQ ligand. In addition, ligands in the $SQ^{-\bullet}$ oxidation state should exhibit C–C bonds of different bond orders alternating between greater single (>1.40 Å) and double (<1.39 Å) bond character, while ligands in the Cat^{2-} oxidation state should exhibit C–C bonds of similar length, falling within the 1.38–1.42 Å range, characteristic of an aromatic ring (Table 4.3). For the four monocoordinated dioxolene ligands in the $Co_4(3,5\text{-DTBQ})_6(APSO)_2(MeO)_2{\cdot}2MeOH$ complex, the C(25)–O(2) and C(26)–O(3) bond lengths measure 1.354(7) and 1.365(9) Å, respectively. These both fall into the range expected for a Cat^{2-} oxidation state (1.34–1.36 Å). All of the C–C bonds in the ring have bond lengths between 1.379 and 1.392 Å, with the exception of the C(26)–C(27) bond, which is slightly longer and measures 1.413(11) Å. All of these bonds are quite close in bond order and their lengths fall into the range expected for a Cat^{2-} oxidation state (1.38–1.42 Å). For the chelating dioxolene ligand, the C(39)–O(4) and C(40)–O(5) bond lengths measure 1.376(9) and 1.391(11) Å, respectively. These are both longer than expected for a typical Cat^{2-} C–O bond, but are in a fairly unique coordination environment (triply bridging O atom, pentacoordinate).

A bond-valence analysis was performed to determine the protonation states of the OMe and monocoordinate Cat^{2-} ligands using parameters from Brown and Altermatt.[367] The valency of the O(3) atom on the Cat^{2-} ligands was calculated to be 1.1, which indicates that the Cat^{2-} ligand should be protonated to achieve an overall valency of 2 for the O atom. Greater error is anticipated in the calculation of the valency for the O atom of the methoxy ligand owing to the large error for the O(6)–C(60) bond length [1.30(4) Å]. The valency was therefore calculated using C–O bond lengths of 1.26 Å and 1.34 Å to obtain a valency range of 1.5–1.8. As these values fall between 1 and 2, whether or not the methoxy ligand is protonated is ambiguous; however, because the values lie closer to 2, the methoxy ligand is most likely not protonated. In further support of this analysis, the Co(2)–O(6) bond length of 2.086(10) Å is closer to that expected for a Co^{II}–O_{MeO} bond [2.09(2) Å] than that expected for a Co^{II}–O_{MeOH} bond [2.19(1) Å].[368] Here, the cobalt

oxidation states being compared differ; however, the bond length for a $Co^{III}–O_{MeOH}$ bond has also been reported to be 2.196(5) Å,[369] and the corresponding $Co^{III}–O_{MeO}$ bond length would therefore be expected to be slightly shorter, as is observed. Finally, to balance the +10 charge for a tetranuclear complex containing two Co^{II} ions and two Co^{III} ions, the complex is most reasonably represented by the formula $Co^{II}_2Co^{III}_2$(3,5-DTBCat)$_2$(3,5-DTBCatH)$_4$(APSO)$_2$(MeO)$_2$, which corroborates the bond-valence analysis.

4.2.5. ^{1}H NMR Spectroscopy

^{1}H NMR analysis proved to be a particularly useful method of characterization for the paramagnetic Co–dioxolene complexes. ^{1}H NMR spectra were acquired for Co(3,5-DTBQ)$_2$(phen), Co(3,5-DTBQ)$_2$(IPSO), Co(3,5-DTBQ)$_2$(APSO), and Co$_4$(3,5-DTBQ)$_6$(APSO)$_2$(MeO)$_2$. In all cases, the samples were prepared in degassed toluene-d_8 solutions in an inert atmosphere argon glovebox.

^{1}H NMR analysis of the most simple Co(3,5-DTBQ)$_2$(phen) complex (Figure 4.9) provides an overview of the key NMR features of the Co–dioxolene complexes. ^{1}H NMR signals at ~99, 34, 19, and 12 ppm integrating to ~2 protons each are assigned to the four sets of two equivalent phen protons. The downfield shifts for the signals are consistent with coordination to a paramagnetic Co^{II} centre. The phenanthroline signals may be assigned by comparison with the Co^{II}(phen)$_3$(PF_6)$_2$ complex,[370] which displays analogous shifts for the phen ligand. Thus, the most downfield signal at ~99 ppm is assigned to the 2-H and 9-H resonances, the next most downfield signal at ~34 ppm is assigned to the 3-H and 8-H resonances, the signal at ~19 ppm is assigned to the 5-H and 6-H resonances, and finally the signal at ~12 ppm is assigned to the 4-H and 7-H resonances. Slightly broad signals at ~15 and ~2 ppm integrating to ~18 protons each are assigned to two sets of two equivalent *t*-butyl groups (i.e., those on the 3-position of each quinone ligand and those on the 5-position of each quinone ligand). The broadened and shifted signals are consistent with the *t*-butyl groups being in a paramagnetic environment. Very weak signals at 0.78, 1.14, 5.90, and 6.60 ppm are assigned to free DTBBQ ligand, typically observed in small amounts (<1%) in the ^{1}H NMR spectra of the Co–dioxolene complexes.

The ^{1}H NMR spectrum of the Co(3,5-DTBQ)$_2$(IPSO) complex is shown in Figure 4.10, and displays similar features as that of the phen complex. Signals assigned to the coordinated IPSO ligand exhibit similar shifts and splitting patterns as those of the free ligand, and it is evident that the coordinated spirooxazine is predominantly in the SO form. Resonances corresponding to the azomethine protons of the SO and PMC forms of IPSO are observed at 7.98 and 9.33 ppm, respectively. The relative intensities of these peaks (0.98 and 0.064, respectively) can be used to calculate a K_T value of 0.07 for the SO/PMC equilibrium (i.e., the complex exists as 6% PMC form in toluene-d_8). Singlets integrating to ~3 at 0.96, 0.99, and 2.33 ppm are assigned to the methyl groups of the SO form of the IPSO ligand. The corresponding methyl peaks for the PMC form can be observed at 1.57 (likely two overlapping signals) and 2.83 ppm. Multiplets corresponding to the four aromatic protons on the indolyl portion of the SO form of IPSO are observed between 6 and 7 ppm. No signals are observed within the 7–9 ppm range where the phenanthroline protons of IPSO are expected. However, downfield-shifted signals are observed for the 2-H and 9-H (~98 ppm), 3-H and 8-H (~34 ppm), and 4-H and 7-(~13 ppm) phen resonances of IPSO in analogy with the Co(3,5-DTBQ)$_2$(phen) complex. For the IPSO complex, four distinct peaks are observed for each set of phen resonances; this is most clearly seen for the peaks at ~34 ppm shown in Figure 4.10. Here, the asymmetry of the ligand results in a slightly shifted signal for each of the sets of resonances (e.g., 2-H vs 9-H). In addition, a corresponding set of two peaks of weaker intensity (~5–10%) may be assigned to the PMC form of the complex, consistent with the expected SO/PMC equilibrium. The signals for the 2-H and 9-H phen protons of the PMC form expected near 98 ppm are presumably too broad to observe. Broad peaks integrating to ~18 at 1.7 and 14.2 ppm are assigned to *t*-butyl groups. Two additional signals are observed near the signal at 14.2 ppm: one at 13.5 ppm and one at 14.7 ppm. The assignment of these peaks is uncertain, although they may originate from *t*-butyl groups on different coordination isomers as a result of the asymmetry of the phenanthroline–spirooxazine ligand.

The ^{1}H NMR spectrum of the Co(3,5-DTBQ)$_2$(APSO) complex in toluene-d_8 (Figure 4.11) is more complicated than those of the phen and IPSO complexes. This may stem from a more complicated solution-state equilibrium in the case of the APSO complex,

which could include multiple possible PMC *cis*/*trans* isomers or PMC aggregates. Nevertheless the ^{1}H NMR spectrum of Co(3,5-DTBQ)$_2$(APSO) displays many of the same features as that of Co(3,5-DTBQ)$_2$(IPSO). For the APSO complex, numerous signals are observed in the 30–50 ppm range, in contrast to the IPSO complex, for which only four distinct signals are observed. For Co(3,5-DTBQ)$_2$(APSO), three sets of two signals may be clearly detected in this range (with relative intensities of 10:2:1)—in addition to several weaker signals—which suggests that at least three distinct phenanthroline-containing species of similar composition exist in equilibrium under these conditions. These species may be different PMC *cis*/*trans* isomers. The SO form may also be present in solution, although one would expect that this species be present in very low concentration by analogy with the Mo(CO)$_4$(APSO) complex, for which no SO form could be observed in toluene solution by ^{1}H NMR (Chapter 3). Corresponding signals for the two dominant species are observed with similar intensity ratios at 85–100 ppm (2-H and 9-H phen resonances), 14–15 ppm (*t*-butyl resonances), 12–13 ppm (4-H and 7-H phen resonances), and 10–11 ppm (PMC azomethine resonance).

The ^{1}H NMR spectrum for Co$_4$(3,5-DTBQ)$_6$(APSO)$_2$(MeO)$_2$ (not shown) is very complicated and significantly broadened, which is likely due to the paramagnetism of the sample. Peaks originating from the azahomoadamantyl group are clearly visible, but no other signals (e.g., phen, *t*-butyl) can be assigned. It is evident that it behaves very differently by NMR than does the Co(3,5-DTBQ)$_2$(APSO) complex.

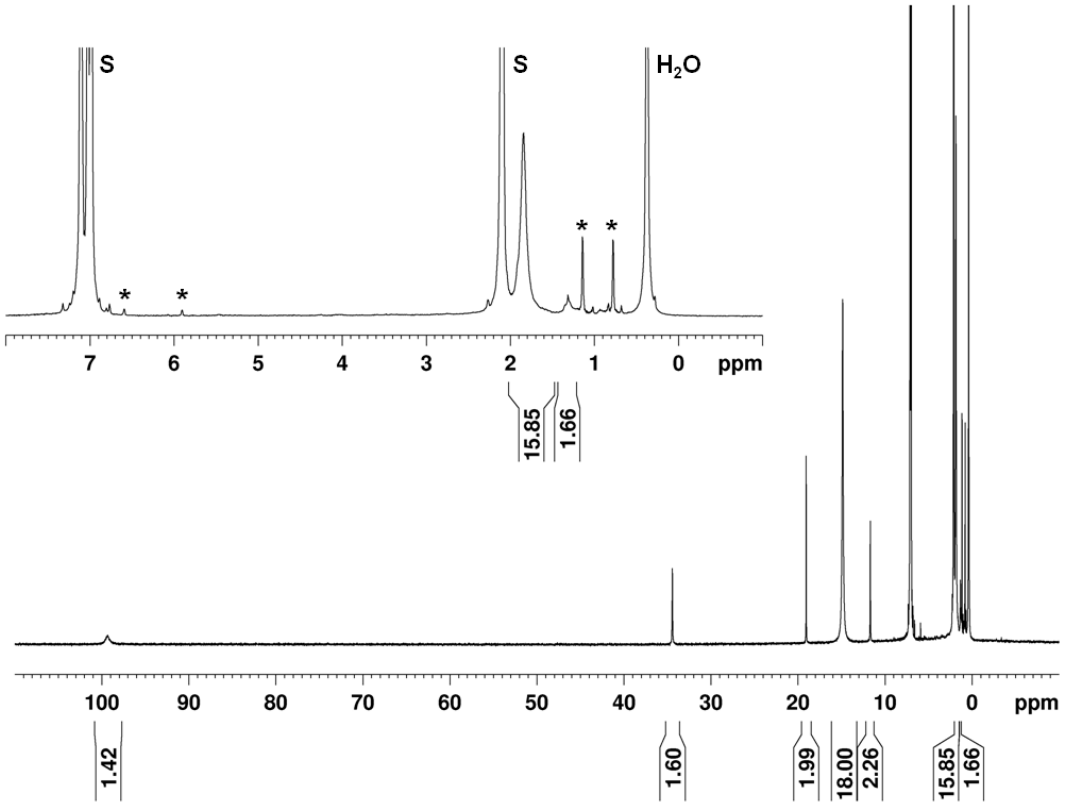

Figure 4.9. ^{1}H NMR spectrum of Co(3-5-DTBQ)$_2$(phen)·$C_6H_5CH_3$ in toluene-d_8 at 360 MHz at ~300 K (S = solvent: toluene; * = free DBBQ).

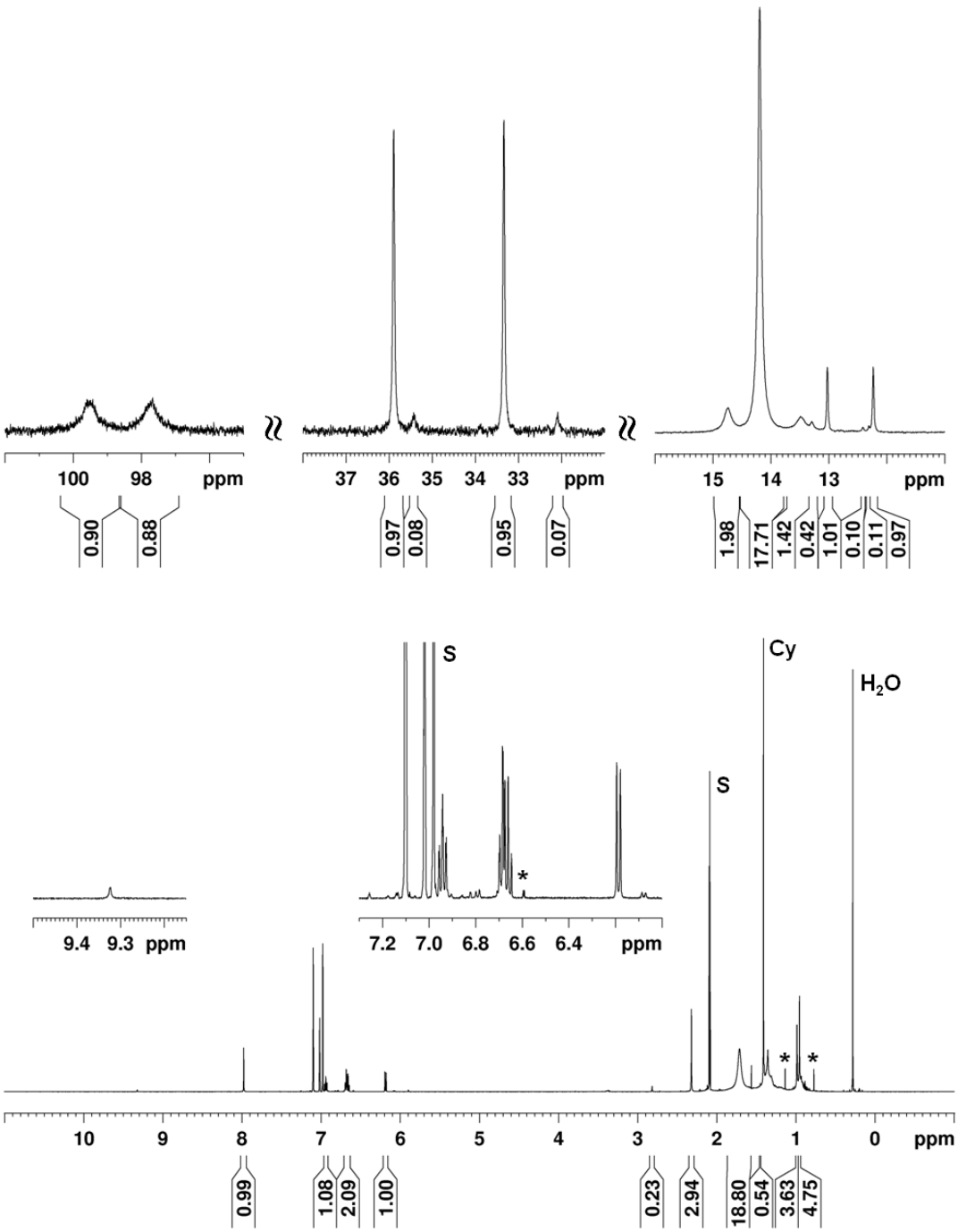

Figure 4.10. ^{1}H NMR spectrum of Co(3,5-DTBQ)$_2$(IPSO) in toluene-d_8 at 500 MHz at ~300 K (S = solvent: toluene; Cy = cyclohexane; * = free DBBQ; the integration of the peak at 9.33 ppm is 0.07).

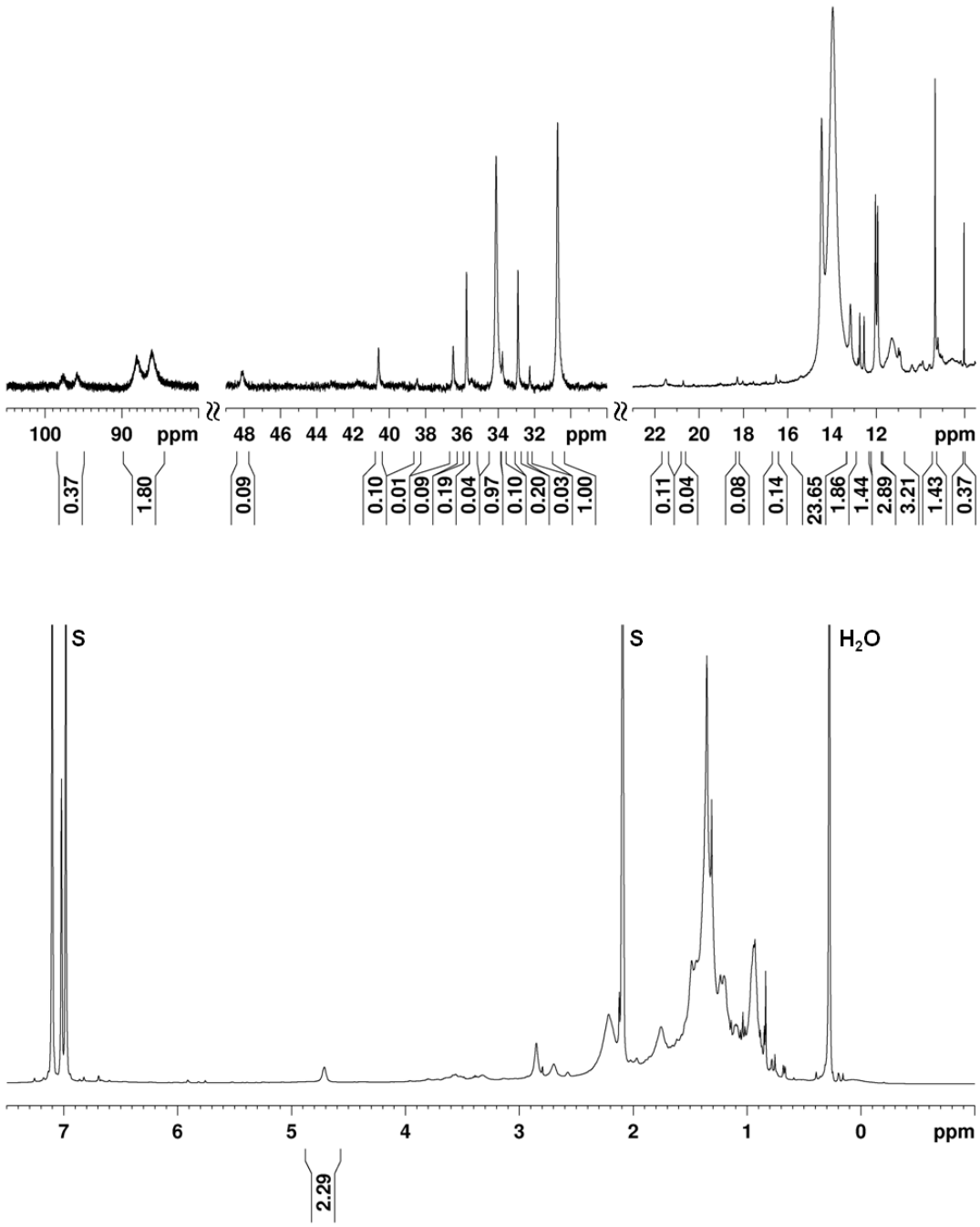

Figure 4.11. ^{1}H NMR spectrum of Co(3,5-DTBQ)$_2$(APSO) in toluene-d_8 at 500 MHz at ~ 300 K (S = solvent: toluene).

An Evan's method study was performed for each of the Co(3,5-DTBQ)$_2$(phen), Co(3,5-DTBQ)$_2$(IPSO), Co(3,5-DTBQ)$_2$(APSO), and Co$_4$(3,5-DTBQ)$_6$(APSO)$_2$(MeO)$_2$ complexes in CD_2Cl_2. This study not only allowed the determination of solution-state magnetic susceptibilities (see Section 4.2.9), but allowed the observation of the VT behaviour of the ^{1}H NMR spectra.

The VT ^{1}H NMR spectrum for Co(3,5-DTBQ)$_2$(phen) is shown in Figure 4.12. It is first noteworthy that slight differences are observed between the ambient-temperature ^{1}H NMR spectra acquired in CD_2Cl_2 and toluene. In both solvents, the signals for the phen and *t*-butyl proton resonances are readily apparent, but these are shifted more upfield in CD_2Cl_2. Additionally, new, low intensity peaks appear in the CD_2Cl_2 spectrum (at ~83, 32, 25, 19, and 12 ppm); each of these peaks appears to be associated with one of the phen proton resonances. The origin of these new signals is not clear, although the formation of a minor side product in CD_2Cl_2 is possible. Cador et al. have reported the observation of ligand disproportionation and solvolysis reactions by NMR for Co–dioxolene complexes in polar solvents.[347] These new signals exhibit pronounced temperature dependence and most move downfield with decreasing temperature. In contrast, the dominant phen proton resonances move upfield with decreasing temperature, with the more downfield signals showing more pronounced upfield shifts. The signals also broaden with decreasing temperature. Importantly, upon conversion from hs-Co^{II} to ls-Co^{III} with decreasing temperature, we do not observe the disappearance of one set of signals and the appearance of a new set of signals, but rather we observe a shifting and broadening of the same set of signals. This suggests that the hs-Co^{II} ↔ ls-Co^{III} interconversion upon ligand-to-metal IET is a dynamic process that is rapid on the NMR timescale. Thus the observed signals represent an average of the hs-Co^{II} and ls-Co^{III} resonances. When the phen signals move upfield with decreasing temperature, this represents a shift in the equilibrium toward ls-Co^{III}, in which the phenanthroline is coordinated to a diamagnetic ls-Co^{III} centre. In addition, as only two *t*-butyl signals are observed at any point, this indicates that the two dioxolene ligands are equivalent on the NMR timescale, and in the case of the ls-Co^{III}(SQ$^{-\bullet}$)(Cat^{2-}) species, IET between the ligands must occur on a timescale faster than the experiment.[371] Because the phen signals are still shifting between 290 and 300 K, this suggests that the system is not yet in 100%

hs-Co^{II} form at 300 K. The fact that these same signals are more downfield in toluene at 300 K also suggests that more of the Co^{II} form is present in toluene, if not 100%. Indeed, studies have shown that more polar solvents increase T_c values.[352] Additionally, the fact that no clear signals are evident at 200 K suggests that the equilibrium has not yet reached 100% ls-Co^{III} at this temperature. The *t*-butyl signals are much broader in CD_2Cl_2 than in toluene, particularly the more downfield of the two, which again highlights the differences in the dynamic interconversion process between the two solvent systems. With decreasing temperature, the more upfield *t*-butyl signal first shifts slightly more upfield, then slightly downfield with decreasing temperature, all the while broadening significantly until it is no longer observable below 220 K. At the same time, the second *t*-butyl signal shifts ever so slightly downfield while broadening to a nearly flat baseline at 270 K. Overall, the redox isomeric hs-Co^{II} → ls-Co^{III} conversion with decreasing temperature is very clear from the VT ^{1}H NMR data.

The VT ^{1}H NMR spectrum of Co(3,5-DTBQ)$_2$(IPSO) in CD_2Cl_2 is shown in Figure 4.13. As for the phen analog, the spectrum of the IPSO complex is more complicated in CD_2Cl_2 than in toluene. The key signals (i.e., the three sets of two phen proton resonances and the two *t*-butyl resonances) exhibit very similar shifts and similar temperature-dependent behaviour as those of the phen analog, which would indicate that the IPSO complex behaves similarly to the phen complex in terms of its redox isomeric conversion. The weaker signals assigned to the PMC form of the complex in toluene-d_8 are not readily apparent in the CD_2Cl_2 spectrum, although additional signals are observed that are associated with the phen moiety (e.g., at ~82 and 30/34 ppm). By analogy with the phen complex, it seems plausible that these additional signals may originate from a decomposition product rather than from the PMC form for two reasons: first, these signals shift downfield with decreasing temperature rather than upfield, as would be expected for hs-Co^{II} → ls-Co^{III} conversion; second, these signals are not found in the same relative positions as those observed in toluene (i.e., in toluene, the minor signals at ~34 ppm were found to be more upfield than the major signals rather than more downfield, as is observed in CD_2Cl_2). Overall, despite a slightly more complicated spectrum and perhaps a small amount of sample decomposition in CD_2Cl_2, the

$Co(3,5\text{-}DTBQ)_2(IPSO)$ complex demonstrates temperature-dependent redox isomeric behaviour very similar to that observed in the $Co(3,5\text{-}DTBQ)_2(phen)$ complex.

As anticipated, the $Co(3,5\text{-}DTBQ)_2(APSO)$ complex displays a more complicated VT ^1H NMR spectrum in CD_2Cl_2 than in toluene-d_8. Still, several features associated with hs-Co^{II} → ls-Co^{III} conversion can be observed with decreasing temperature. The phen resonances at ~45, 22, and 10 ppm shift upfield and broaden as the temperature is lowered. In addition, the broad *t*-butyl signal at ~15 ppm quickly broadens with decreasing temperature. Most interestingly, for $Co(3,5\text{-}DTBQ)_2(APSO)$, many peaks actually appear and sharpen at lower temperature. This is observed for several signals at ~9 ppm, and for signals at ~8.1, 7.6, and 6.5 ppm. The signals between 7 and 9 ppm may originate from phen protons of the ls-Co^{III} species, which could suggest that there is more of the ls-Co^{III} form in the $Co(3,5\text{-}DTBQ)_2(APSO)$ complex than in the phen and IPSO complexes within the 200–250 K temperature range. Overall, the redox isomerism of the Co–APSO complex is corroborated by the VT ^1H NMR data, although the complicated nature of the spectrum obscures further interpretation.

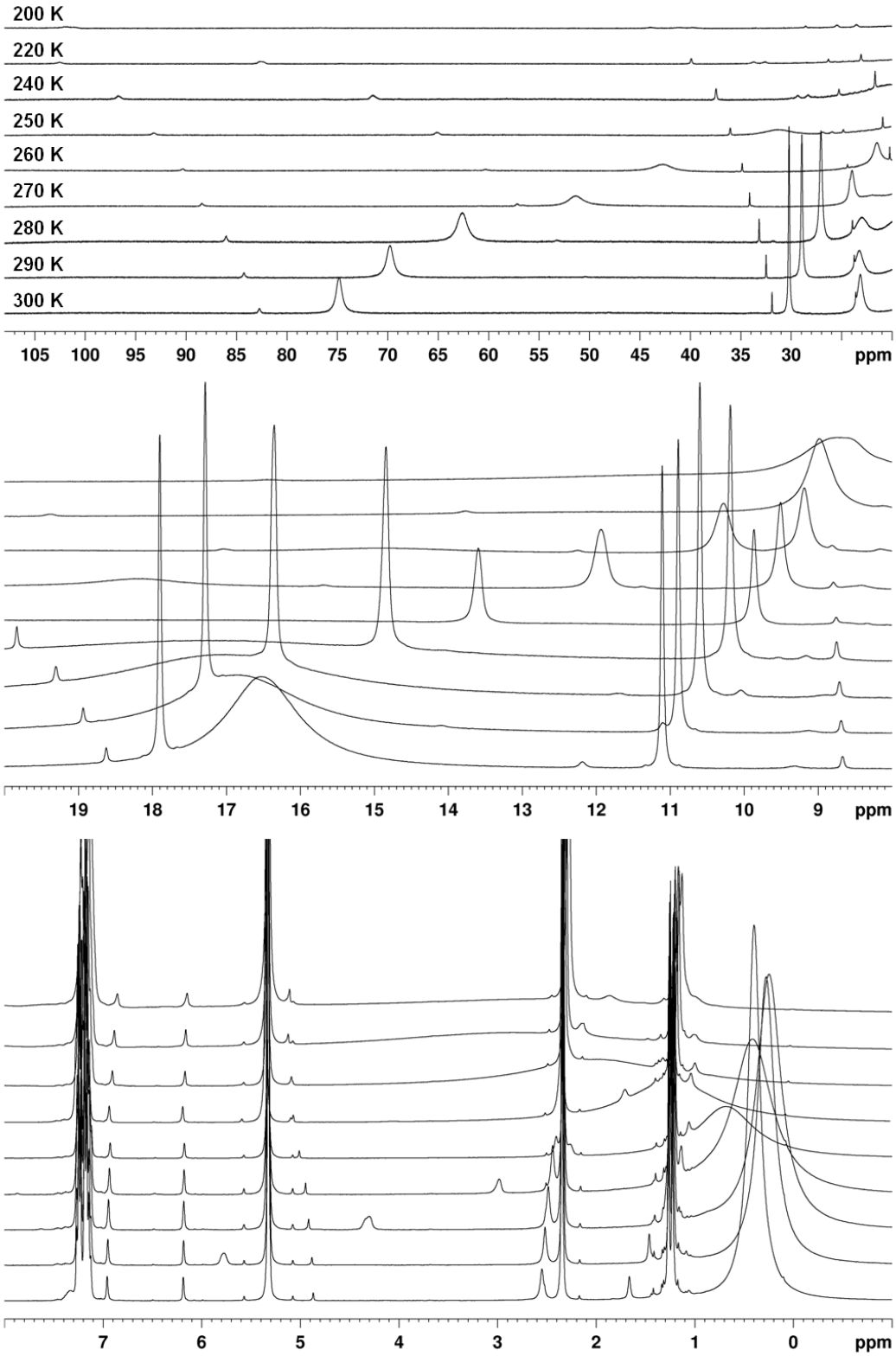

Figure 4.12. Variable temperature ^{1}H NMR spectrum of $Co(3,5\text{-}DTBQ)_2(phen)\cdot C_6H_5CH_3$ in CD_2Cl_2 at 360 MHz.

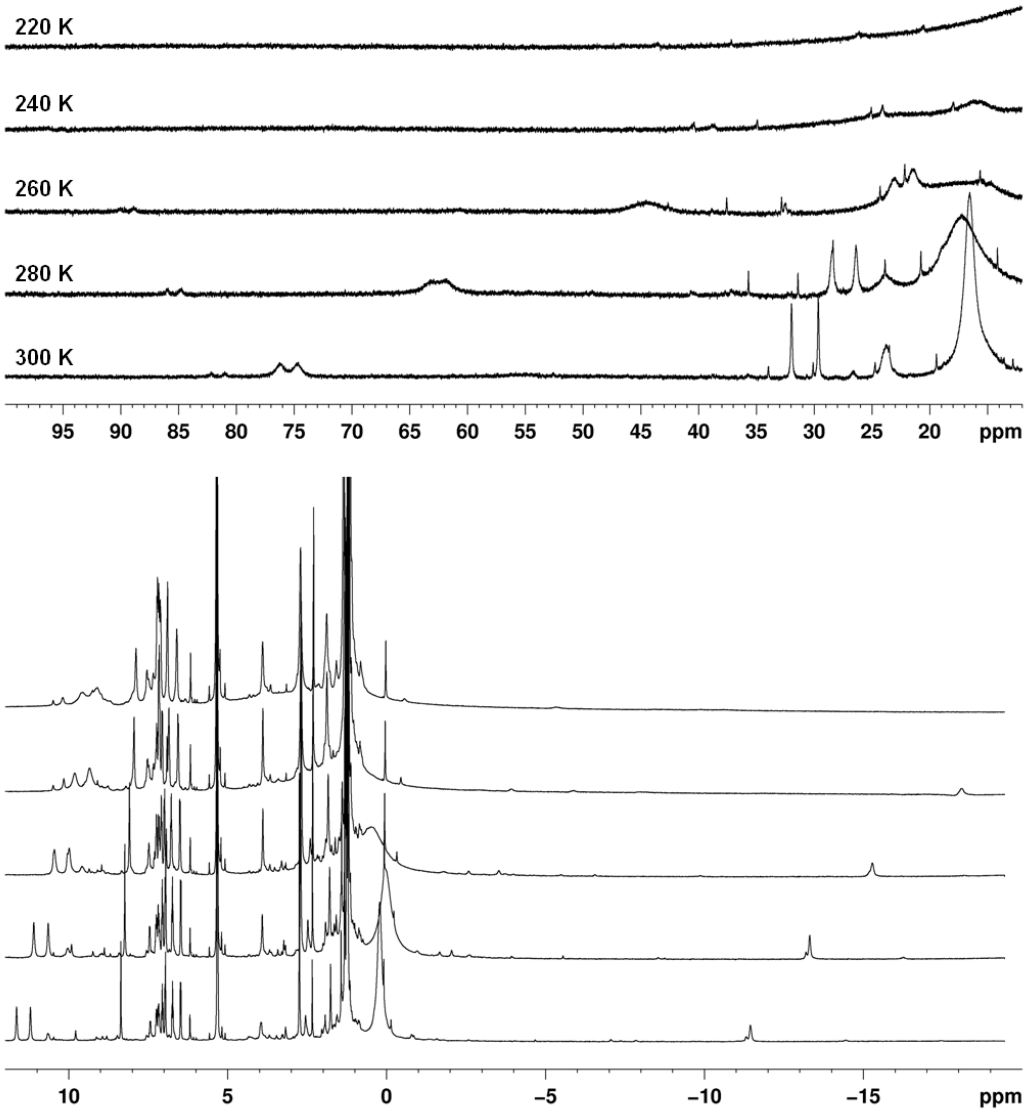

Figure 4.13. Variable temperature ^{1}H NMR spectrum of Co(3,5-DTBQ)$_2$(IPSO) in CD_2Cl_2 at 360 MHz.

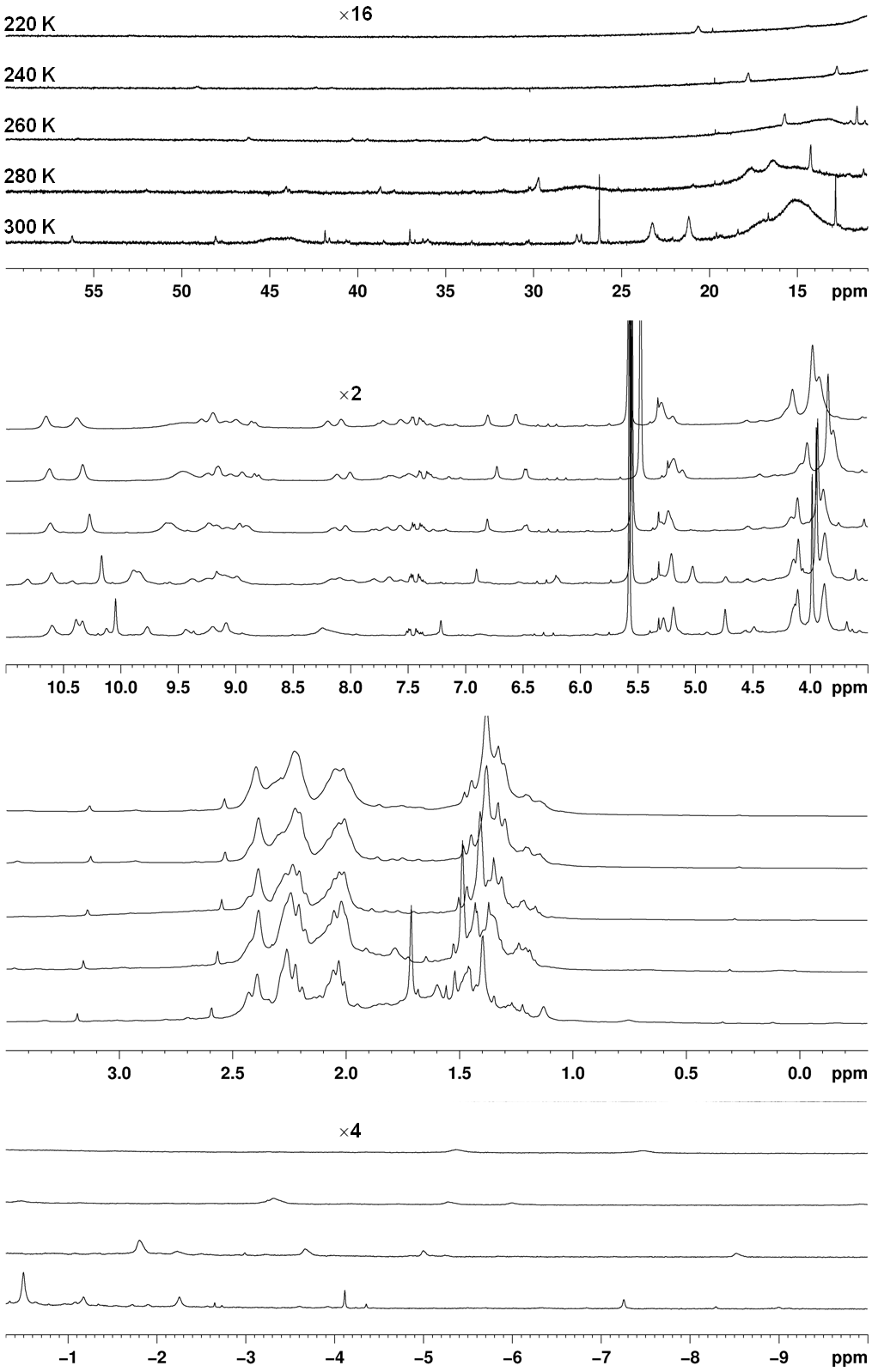

Figure 4.14. Variable temperature ^{1}H NMR spectrum of Co(3,5-DTBQ)$_2$(APSO) in CD_2Cl_2 at 500 MHz.

4.2.6. FT-IR Spectroscopy

The FT-IR spectrum of Co(3,5-DTBQ)$_2$(APSO) was analyzed to identify potential diagnostic peaks. The fingerprint IR region of this class of Co complexes typically contains valuable information concerning the redox state of the dioxolene ligands. Distinct peaks associated with either the Cat^{2-} or $SQ^{-\bullet}$ forms of the ligand have been identified. Intense peaks between 1240 and 1280 cm^{-1} are typically associated with a C–O stretching mode of coordinated Cat^{2-} ligands.[357, 372, 373] Bands between 1470 and 1490 cm^{-1} have been assigned to the aromatic ring stretching mode of the Cat^{2-} form,[372, 374] while other bands between 1420 and 1490 cm^{-1} have been assigned to the C–O stretching mode of the $SQ^{-\bullet}$ form.[375, 376] However, bands in the 1420–1430 cm^{-1} region have also been shown to correlate with the Cat^{2-} form.[373, 374] There is therefore some ambiguity regarding the assignment of peaks in the 1400–1500 cm^{-1} range, as peaks from both forms are present here.

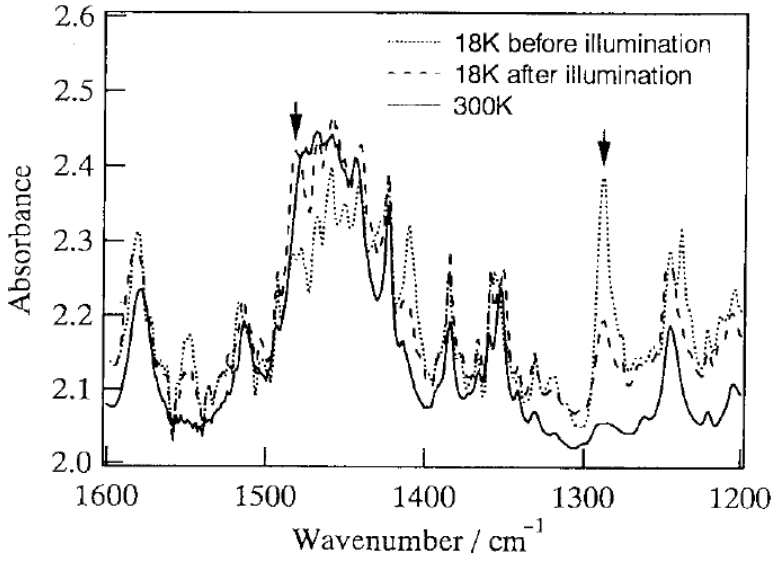

Figure 4.15. FT-IR spectrum of Co(3,5-DTBQ)$_2$(phen) at 300 K, 18 K, and after illumination (532 nm, ~30 mW/cm^2) at 18 K. The sample medium was not specified. (Figure reproduced with permission from ref[373]. Copyright 2001 Chemical Society of Japan.)

The VT FT-IR spectrum of Co(3,5-DTBQ)$_2$(phen) reported by Sato et al. (Figure 4.15) sheds some light on the assignment of these features. Here it is clear that strong bands at ~1280 cm^{-1} and ~1420 cm^{-1} are associated with the Cat^{2-} ligand, while bands at ~1430 and 1490 cm^{-1} are evident for both hs-$Co^{II}(SQ^{-\bullet})_2$ and ls-$Co^{III}(SQ^{-\bullet})(Cat^{2-})$ species. There

is also a feature at ~1230 cm^{-1} only observed in the ls-Co^{III} form of the spectrum, which is not mentioned by the authors, but may be a diagnostic band for this system.

The FT-IR spectrum of Co(3,5-DTBQ)$_2$(APSO) was analyzed by comparison to the spectra of APSO and Co(3,5-DTBQ)$_2$(phen) in the context of the literature assignments. Spectra of CCl_4 solutions at ~300 K are displayed in Figure 4.16. For the Co(3,5-DTBQ)$_2$(APSO) complex, the band at 1036 cm^{-1} appears to belong to the Co(diox)$_2$ functionality, while the peak at 1102 cm^{-1} appears in the spectra of both APSO and Co(3,5-DTBQ)$_2$(phen), and may represent overlapping signals originating from both spiroooxazine and dioxolene ligands as it is very strong. The spectrum of Co(3,5-DTBQ)$_2$(APSO) displays a broad feature with two peaks at 1127 and 1135 cm^{-1} in addition to a shoulder at 1119 cm^{-1}. This feature is not observed in the spectrum of the phen complex, which suggests that it arises from the spirooxazine ligand, although only one distinct peak is observed in this region in the spectrum for APSO. The region spanning 1200 to 1300 cm^{-1} contains peaks associated with both the APSO ligand and the Co(diox)$_2$ functionality. The band at 1228 cm^{-1} corresponds to an identical band in the spectrum of the free ligand; however it is significantly more intense in the spectrum of the Co(3,5-DTBQ)$_2$(APSO) complex. It is possible that this band represents overlapping vibrations originating from the spirooxazine and the ls-Co^{III}–dioxolene functionality, by analogy with the low-temperature spectrum of Co(3,5-DTBQ$_2$)(phen) from Figure 4.15. Features at 1246 and 1260 cm^{-1} more closely match those observed in the Co(3,5-DTBQ)$_2$(phen) spectrum, although there is a very intense band at 1250 cm^{-1} in the spectrum for APSO which could also be contributing in this region. Peaks in the 1300–1400 cm^{-1} range appear to originate almost exclusively from the APSO ligand. Finally, bands within the 1400–1500 cm^{-1} range can be attributed to both APSO and Co(diox)$_2$ moieties. A band at 1416 cm^{-1} corresponds exactly with a peak in the APSO spectrum, while a band at 1425 cm^{-1} does not correlate directly with one from either of the parent compounds. Peaks at 1446, 1460, and 1480 cm^{-1} correspond very closely with similar peaks in the spectrum of Co(3,5-DTBQ)$_2$(phen). The peaks in the 1400 to 1500 cm^{-1} range are clearly important features in the FT-IR spectra of Co–dioxolene complexes, as evidenced by their dominance in the spectrum of the Co(3,5-DTBQ)$_2$(phen) complex. However, their use in assigning relative concentrations

of Co^{II} and Co^{III} is somewhat ambiguous as the multiple peaks can be assigned to both $SQ^{-\bullet}$ and Cat^{2-} ligands. The absence of the strong peak at ~1490 cm^{-1} for the APSO complex that is found in the spectrum of the phen complex, and which has been more often assigned to a $SQ^{-\bullet}$ stretch, may indicate that the APSO complex has a substantial contribution from the ls-Co^{III} species under these conditions. Overall, it is fairly clear that the spectrum shows bands from both spirooxazine and $Co(diox)_2$ moieties, although the assignment of peaks to $SQ^{-\bullet}$ or Cat^{2-} species can only be done tentatively.

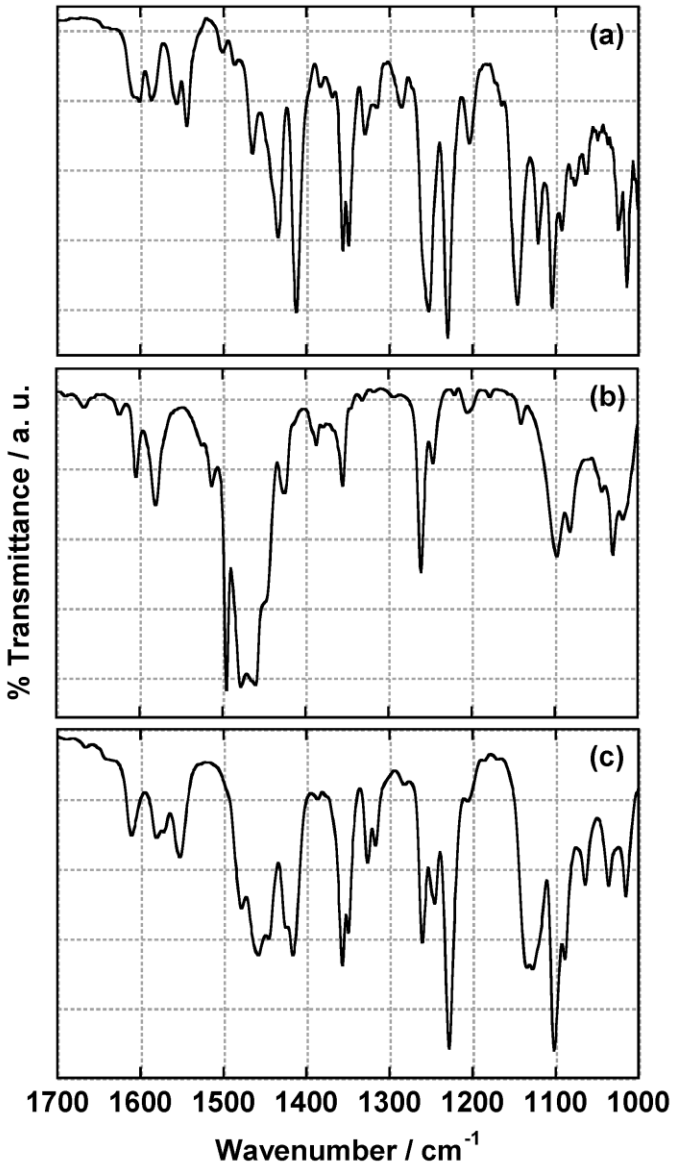

Figure 4.16. FT-IR spectra of APSO (a), $Co(3,5\text{-}DTBQ)_2(phen)$ (b), and $Co(3,5\text{-}DTBQ)_2(APSO)$ (c) in CCl_4 at ~300 K.

4.2.7. Electronic Absorption Spectroscopy

UV/Vis/NIR electronic absorption spectroscopy is a particularly useful way to gain insight into the redox isomeric behaviour of Co–dioxolene complexes. Before analyzing the spirooxazine complexes, it will be useful to review the spectral features for Co(3,5 DTBQ)$_2$(phen). The variable temperature UV/Vis spectrum of the phen complex in toluene is shown in Figure 4.17. At 295 K, the spectrum displays features predominantly associated with the hs-Co^{II} form. The complex exhibits high absorbance throughout the visible region (ε = 2000–3500 cm^{-1}·M^{-1}). The dominant feature is a broad band at ~765 nm assigned as a MLCT band,[354] with a shoulder at ~640 nm, and absorption tailing into the low-energy range of the visible region and into the NIR region. An additional band at ~540 nm is readily apparent, and has been assigned to ligand-field (LF) transitions.[354] Strong absorbance is also observed between 400–500 nm, which may also be associated with LF transitions. Changes in the UV/Vis electronic absorption spectrum with temperature (Figure 4.17) are consistent with redox isomerism; the presence of isosbestic points indicate a clean conversion between the hs-Co^{II} and ls-Co^{III} species. At low temperature, the dominant spectral feature characteristic of the ls-Co^{III} species is a strong band at ~600 nm. For the ls-Co^{III} form, the spectrum still exhibits relatively high absorbance intensity throughout the visible and into the NIR regions. The band at 600 nm and other bands throughout the visible region have been assigned to transitions with predominantly π–π* character.[354]

Another key feature of the Co(3,5-DTBQ)$_2$(NN) class of compounds is strong absorbance in the NIR region, as illustrated in the spectrum of a polystyrene film of Co(3,5-DTBQ)$_2$(phen) in Figure 4.18. Most notably, a broad band at ~2500 nm (~4000 cm^{-1}) and a less intense band at ~1700 nm are observed at low temperature and are associated with the ls-Co^{III} form alone. The origin of the band at ~2500 nm is controversial; it has been assigned as either a Cat^{2-}(π*)–Co^{III}(e_g*) LMCT transition or an intervalence charge transfer (IVCT) occurring between Cat^{2-}(π*) and SQ$^{-\bullet}$(π*) ligands in the ls-Co^{III} species. Adams, Noodleman, and Hendrickson assigned the CT band to a ligand-based IVCT on the basis of DFT calculations of the localized electronic states of Co(3,5-DTBQ)$_2$(phen), even though the energy for interligand transition was calculated to be ~1200 cm^{-1} and the energy for the ligand-to-metal transition was calculated to be

~7600 cm^{-1} (compared to an experimental value of ~4000 cm^{-1}).[354] Later, Klokishner and Reu theoretically modeled the optical CT band taking into account vibrational coupling and electron transfer processes, and were able to qualitatively reproduce the experimental band. This model predicted the origin of the band to be a Cat^{2-}–Co^{III} transition.[377] In an experimental study of the $Co^{III}(Cat^{2-})(SQ^{-\bullet})/Co^{III}(SQ^{-\bullet})_2/Co^{III}(Cat^{2-})_2$ redox series, the $Co^{III}(Cat^{2-})(SQ^{-\bullet})$ compound alone was found to display a band at ~2500 nm, suggesting that the transition arises only in the mixed-ligand system and must be assigned to an interligand process.[378] Finally, just recently, Evangelio et al. calculated the transition energies for the ligand-to-metal and ligand-to-ligand transitions using CASSCF and CASSPT2 single-point energy calculations (from X-ray geometries) on different spin states of a related class of Co redox isomeric Co^{III}(Cat-N-BQ)(Cat-N-SQ)/Co^{II}(Cat-N-BQ)$_2$ complexes containing Schiff-base iminoquinone ligands. The authors calculated an energy of 4500 cm^{-1} for the LMCT transition and of 700 cm^{-1} for the LLCT.[371] As the calculated energy for the LMCT transition is quite close to the experimental energy for the NIR band, this may provide further evidence for its assignment as a $Cat^{2-}(\pi^*)$–$Co^{III}(e_g^*)$ transition.

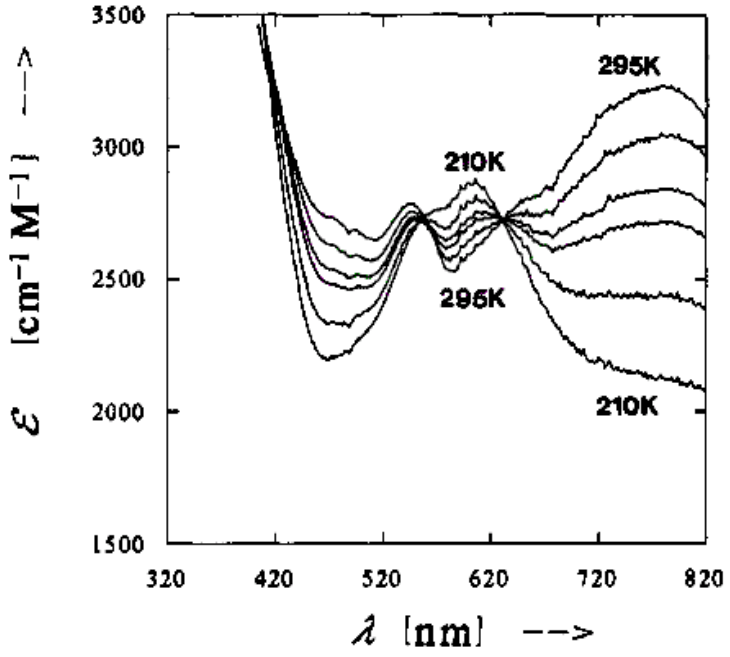

Figure 4.17. Variable-temperature UV/Vis absorption spectrum of a toluene solution of Co(3,5 DTBQ)$_2$(phen)·$C_6H_5CH_3$ at 295, 260, 240, 230, 220, and 210 K. (Figure reproduced with permission from ref[345]. Copyright 1993 American Chemical Society.)

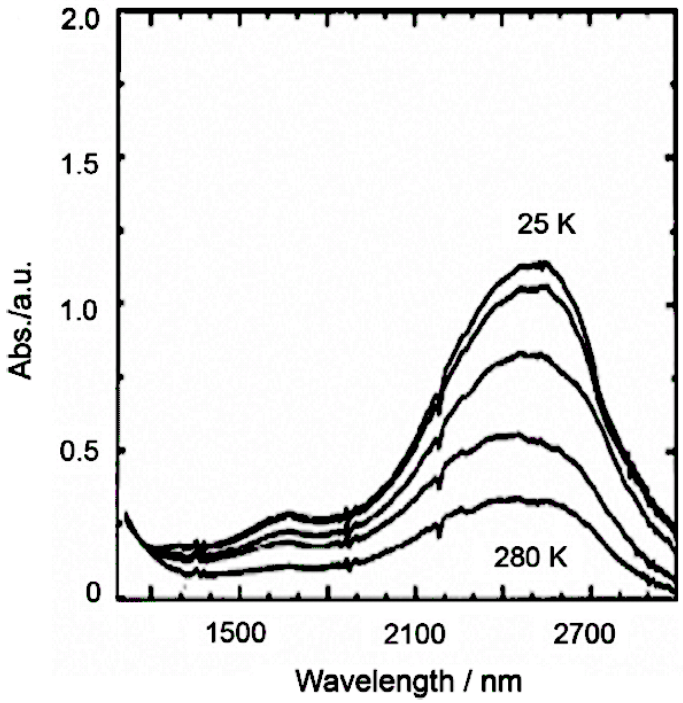

Figure 4.18. Variable-temperature NIR absorption spectrum of a polystyrene film of $Co(3,5\ DTBQ)_2(phen)$ at 280, 200, 150, 80, and 25 K. (Figure reproduced with permission from ref[378]. Copyright 2008 Elsevier.)

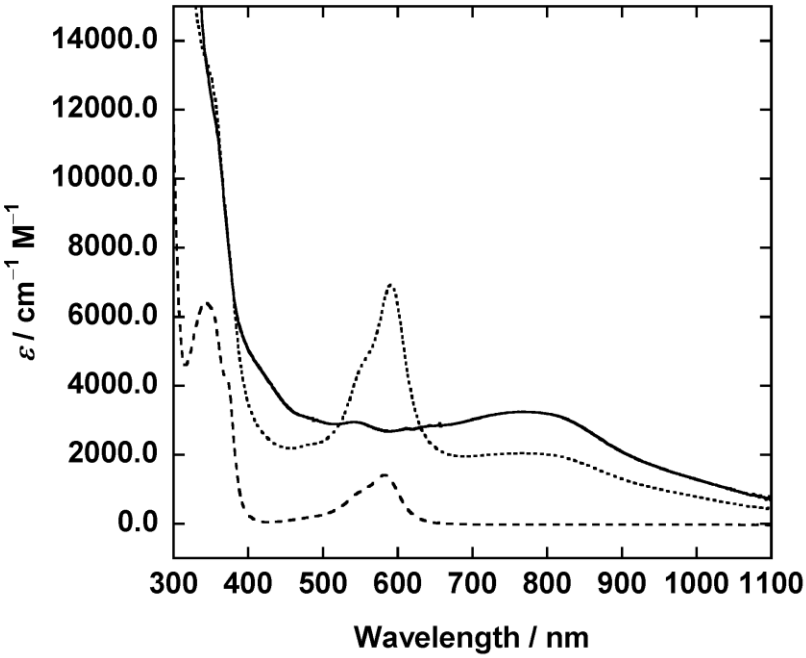

Figure 4.19. UV/Vis electronic absorption spectra of $Co(3,5\text{-}DTBQ)_2(phen)$ (—), IPSO (— —), and $Co(3,5\text{-}DTBQ)_2(IPSO)$ (▪▪▪▪) in toluene at ~300 K.

Before the spectra of the spirooxazine–cobalt–dioxolene complexes are discussed, a note should be made regarding extinction coefficients. Because these complexes exist in a four-state equilibrium, the uncorrected extinction coefficients represent contributions from each of the species in solution at a given total concentration. As spectra are compared using uncorrected extinction coefficients, one must be sure to note that the relative band intensities are not only a reflection of relative transition probabilities but also of the relative concentrations of different species in solution.

The spectrum of Co(3,5-DTBQ)$_2$(IPSO) is shown in Figure 4.19, along with the spectra of Co(3,5-DTBQ)$_2$(phen) and IPSO in toluene at ~300 K. The spectrum of the IPSO complex exhibits a prominent PMC-based π–π* CT transition with a λ_{max} of 590 nm, slightly bathochromically shifted from that of the free ligand (582 nm). Under these experimental conditions, the IPSO complex exists as ~7% PMC form as determined by ^{1}H NMR spectroscopy (vide supra, Section 4.2.5). The free ligand, IPSO, exists as only ~2% PMC form, which explains the discrepancy between the observed intensities for the PMC peaks. If the extinction coefficients for the PMC band are corrected for the concentration of the PMC form, these values become 99000 $cm^{-1}\cdot M^{-1}$ for Co(3,5-DTBQ)$_2$(IPSO) compared to 70000 $cm^{-1}\cdot M^{-1}$ for IPSO. The spectrum of the Co(3,5-DTBQ)$_2$(IPSO) complex also exhibits the same features as that of the phen complex, namely a broad band centered at ~765 nm ($\varepsilon \approx 2000$ $cm^{-1}\cdot M^{-1}$) with absorbance tailing beyond 1100 nm and into the NIR region. In addition, considerable absorbance intensity is observed between 400–500 nm, although it is difficult to ascertain specific features of the Co–dioxolene bands between 400–700 nm, as they are obscured by the intense PMC absorption. When a toluene solution of Co(3,5-DTBQ)$_2$(IPSO) is left open to air, a steady decomposition process is observed, as shown in Figure 4.20. Over time, a decrease in both the PMC π–π* and hs-Co^{II} MLCT bands is observed and, importantly, this process is accompanied by the formation of a new band at ~400 nm. This band has been attributed to the free DBBQ species which absorbs at this wavelength. This gives some insight into the decomposition pathway, which may involve oxidation and decomplexation of the dioxolene ligand, consistent with the observation of a small amount of free DBBQ in the ^{1}H NMR spectra of the Co–dioxolene complexes (vide supra, Section 4.2.5). The diffuse reflectance spectrum of a powder sample of Co(3,5-

DTBQ)$_2$(IPSO) in $BaSO_4$ is shown in Figure 4.21. The solid-state spectrum is similar to the solution-state spectrum, and is dominated by the PMC π–π* band with λ_{max} at 595 nm.

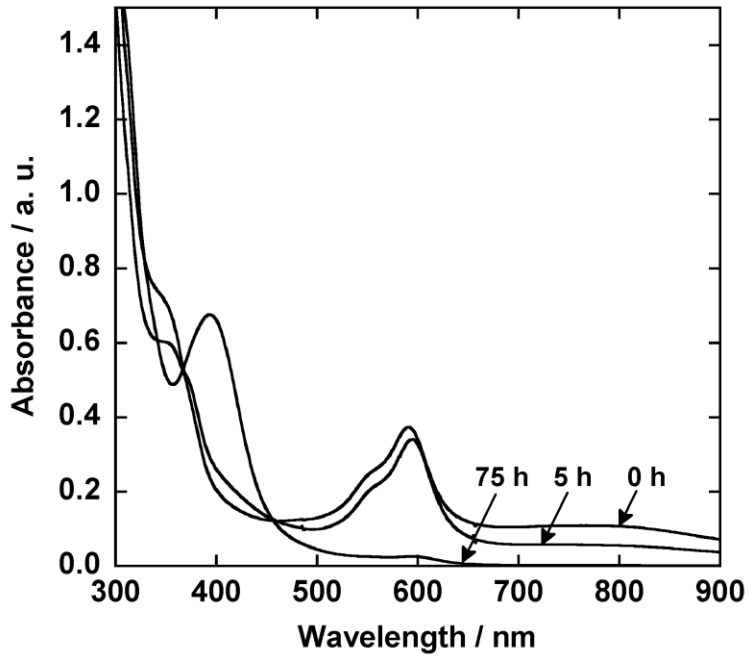

Figure 4.20. UV/Vis electronic absorption spectrum of Co(3,5-DTBQ)$_2$(IPSO) in toluene over time at ~300 K during exposure to air.

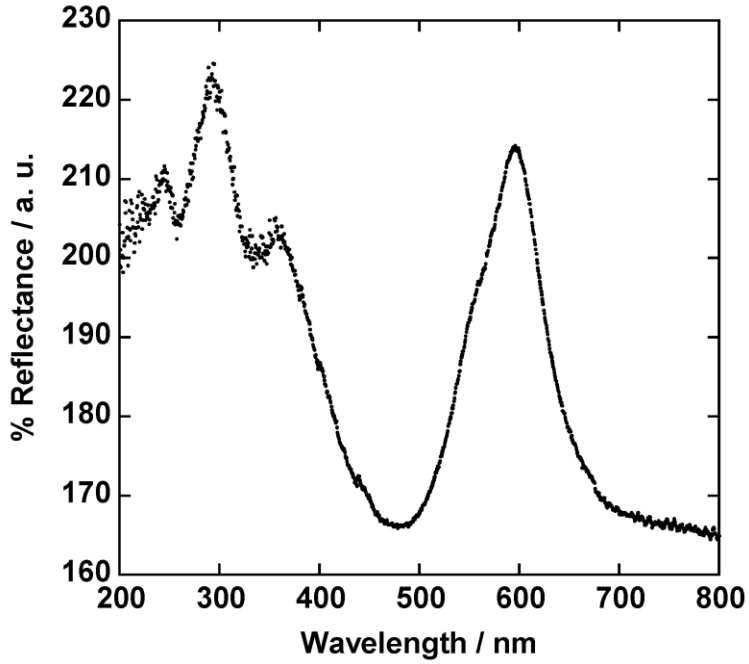

Figure 4.21. Diffuse reflectance spectrum of Co(3,5-DTBQ)$_2$(IPSO) in $BaSO_4$ at ~300 K.

Variable-temperature electronic absorption spectra of Co(3,5-DTBQ)$_2$(IPSO) are shown in the UV/Vis region for a toluene solution in Figure 4.22 and in the Vis/NIR region for a thin film in Figure 4.23. The observed spectral changes indicate a hs-Co^{II} → ls-Co^{III} redox isomeric conversion with decreasing temperature. In the visible region, the dominant spectral change is a decrease in the Co^{II}-based MLCT band at ~765 nm when the temperature is lowered to 196 K. The PMC π–π* band also increases in intensity, consistent with stabilization of the PMC form at low temperature, as is observed for uncoordinated spirooxazine ligands. At low temperature, there is still strong absorption throughout the visible region. The spectral changes are fully reversible upon warming to room temperature. In the NIR region, a strong band at ~2400 nm and a weaker band at ~1500 nm grow in upon decreasing the temperature from 300 to 200 K. This temperature dependence is analogous to that of Co(3,5-DTBQ)$_2$(phen) (Figure 4.18). Again, this change is reversible upon warming. Because spectral changes are observed at both the low-*T* and high-*T* limits for the VT-NIR data, it is apparent that some mixture of ls-Co^{III} and hs-Co^{II} species exists over the full temperature range studied here.

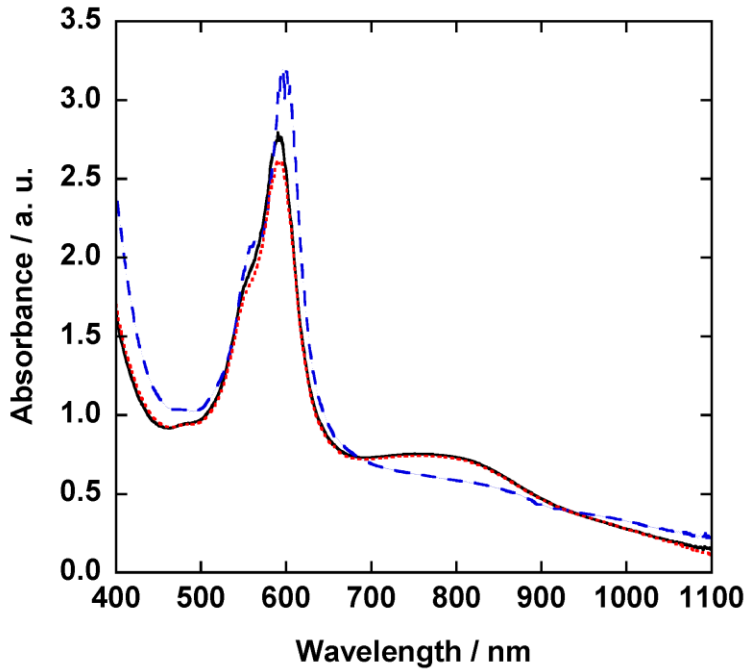

Figure 4.22. Variable-temperature UV/Vis absorption spectrum of Co(3,5-DTBQ)$_2$(IPSO) in toluene at 299 K (—), after cooling at 196 K (– –), and after warming at 291 K (▪▪▪▪).

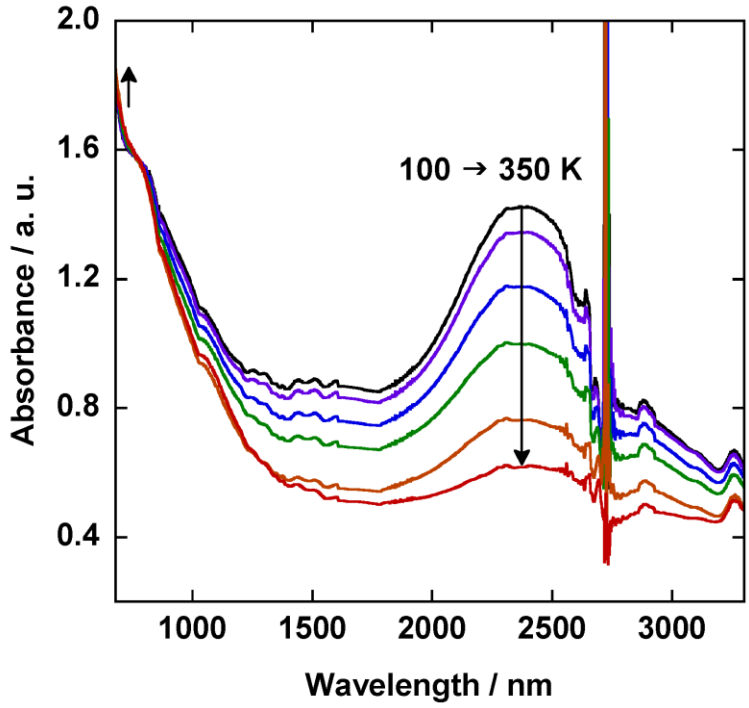

Figure 4.23. Variable-temperature Vis/NIR absorption spectrum of a thin film of $Co(3,5\text{-}DTBQ)_2(IPSO)$ measured from 100 to 350 K in 50 K increments.

UV/Vis electronic absorption spectra of $Co(3,5\text{-}DTBQ)_2(APSO)$ and $Co_4(3,5\text{-}DTBQ)_6(APSO)_2(MeO)_2$ in toluene at ~300 K are shown in Figure 4.24, along with spectra of $Co(3,5\text{-}DTBQ)_2(phen)$ and APSO. In the mononuclear and tetranuclear APSO complexes, a strong PMC π–π^* band is observed, in both cases with λ_{max} at 555 nm, the same as for the free APSO ligand. For the Co–APSO complexes, the concentration of PMC species in solution cannot be unambiguously extracted from the ^{1}H NMR data like it can for the Co–IPSO complexes (vide supra, Section 4.2.5). However, if we assume that the monomeric and tetrameric Co–APSO complexes exhibit comparable SO/PMC equilibria (i.e., predominantly in the PMC form as expected for coordination complexes of APSO) under similar conditions (toluene, r.t. solutions)—an assumption which is not unfounded as the APSO ligand has a similar coordination environment in both cases—the extinction coefficient of the PMC form at λ_{max} = 555 nm is significantly greater in the tetramer ($\varepsilon_{PMC,555} \geq 84000$ $cm^{-1}{\cdot}M^{-1}$) than in the monomer ($\varepsilon_{PMC,555} \geq 33000$ $cm^{-1}{\cdot}M^{-1}$), particularly if one takes into account that the PMC ligand makes up a lower stoichiometric ratio in the former than in the latter. For comparison, the value of $\varepsilon_{PMC,555}$

for APSO in toluene is 43000 $cm^{-1}{\cdot}M^{-1}$, which reveals that the extinction coefficient for the monomer is slightly lower than that of the free ligand, while that of the tetramer is about twice as large.

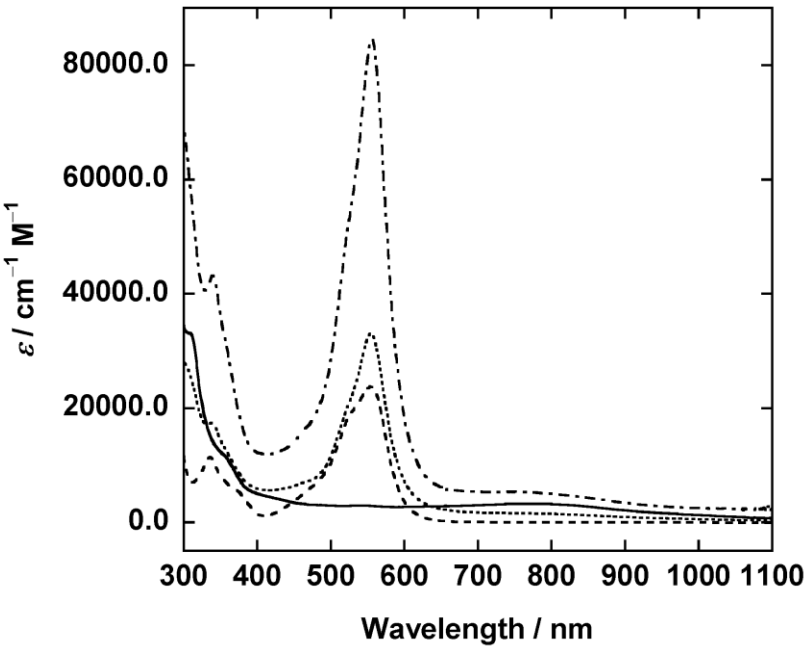

Figure 4.24. UV/Vis absorption spectra of $Co(3,5\text{-}DTBQ)_2(phen)$ (—), APSO (— —), $Co(3,5\text{-}DTBQ)_2(APSO)$ (▪▪▪▪), and $Co_4(3,5\text{-}DTBQ)_6(APSO)_2(MeO)_2$ (— ▪ —) in toluene at ~300 K.

The Co–APSO complexes also display features associated with the Co–dioxolene portion of the molecule, which include significant absorbance between 400 and 500 nm, but most notably a broad Co^{II} MLCT band at ~750 nm. This band is significantly more intense in the tetramer than in the monomer. The extinction coefficient at 750 nm for the tetramer is ~5400 $cm^{-1}{\cdot}M^{-1}$ and that for the monomer is ~1600 $cm^{-1}{\cdot}M^{-1}$. In contrast, ε_{750} for $Co(3,5\text{-}DTBQ)_2(phen)$ is 3300 $cm^{-1}{\cdot}M^{-1}$. The lower MLCT absorbance intensity for the $Co(3,5\text{-}DTBQ)_2(APSO)$ complex suggests that it may exist in a lower concentration of Co^{II} form than the Co–phen complex at room temperature or that the extinction coefficient for this transition may simply be smaller for the APSO complex. For the monomeric $Co(3,5\text{-}DTBQ)_2(APSO)$ complex, ε varies from sample to sample on the order of 1000 $cm^{-1}{\cdot}M^{-1}$ throughout the visible region, which may suggest differences in composition between samples. The high absorbance in $Co_4(3,5\text{-}DTBQ)_6(APSO)_2(MeO)_2$

may be the result of a greater concentration of hs-Co^{II} species or simply the different electronic structure of this material.

If a toluene solution of $Co(3,5\text{-}DTBQ)_2(APSO)$ is left open to air, decomposition is observed, as for the IPSO analog (Figure 4.25). Here again, in addition to a decrease in the intensity of the PMC π–π* CT and hs-Co^{II} MLCT bands over time, an increase in the intensity of a new band at ~400 nm is simultaneously observed.

The solid-state diffuse reflectance spectrum of a powder sample of $Co(3,5\text{-}DTBQ)_2(APSO)$ in $BaSO_4$ (Figure 4.26) is dominated by the PMC π–π* band, though in the solid-state the observed λ_{max} of 542 nm exhibits a significant hypsochromic shift from that observed in the solution state (555 nm).

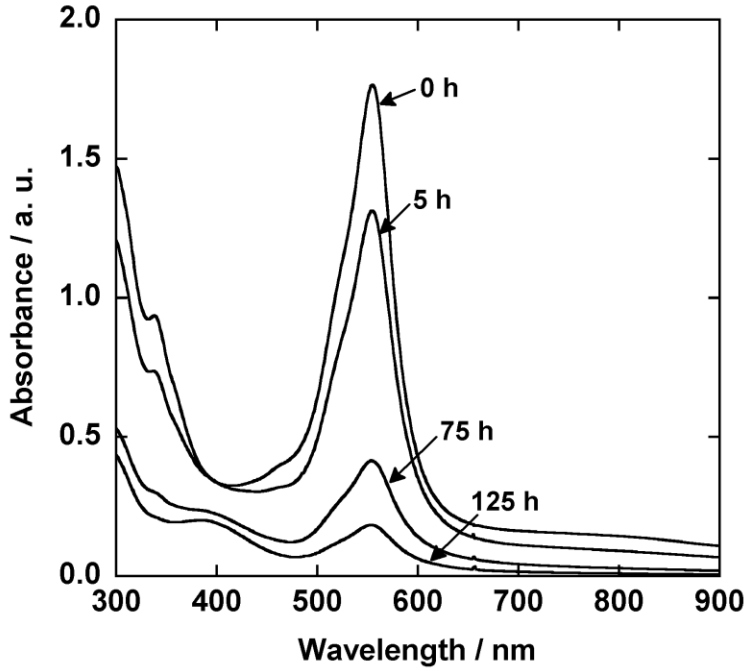

Figure 4.25. UV/Vis absorption spectrum of $Co(3,5\text{-}DTBQ)_2(APSO)$ in toluene over time at ~300 K.

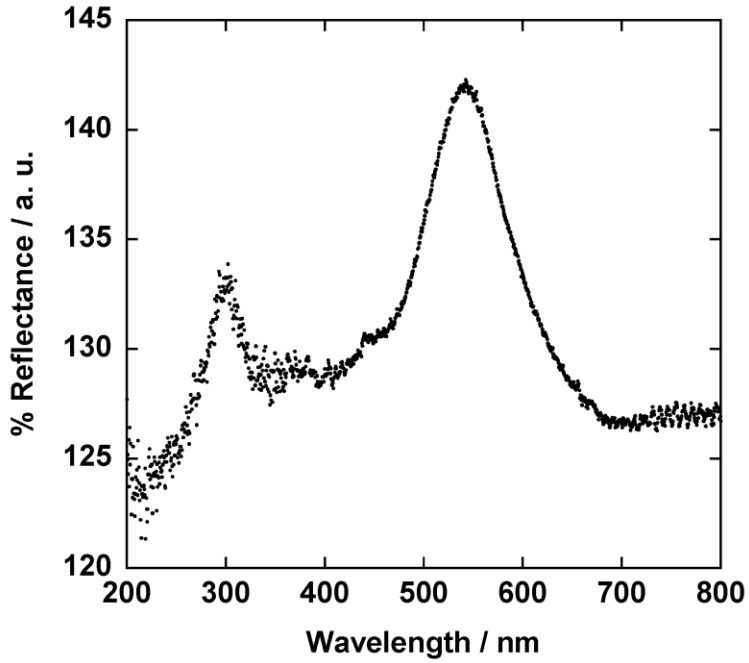

Figure 4.26. Diffuse reflectance spectrum of $Co(3,5\text{-}DTBQ)_2(APSO)$ in $BaSO_4$ at ~300 K.

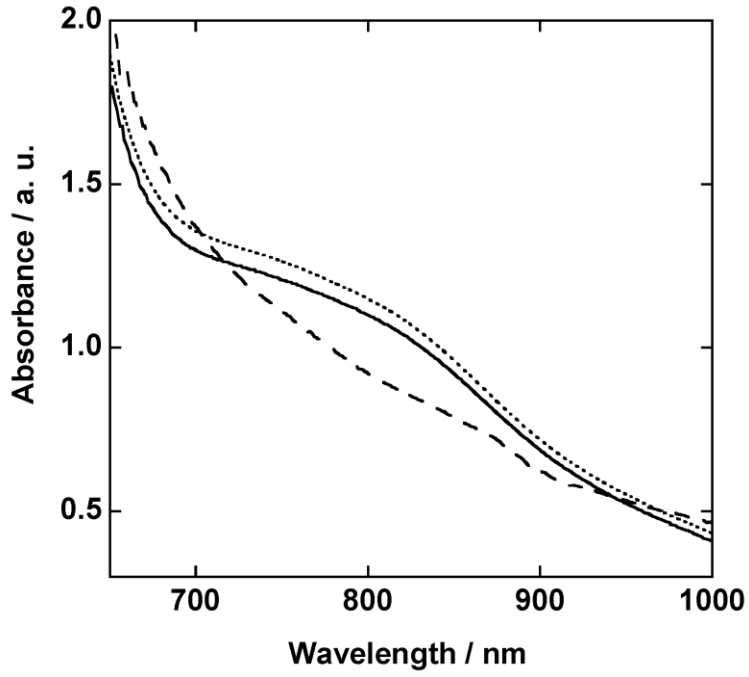

Figure 4.27. Variable-temperature electronic absorption spectrum of $Co(3,5\text{-}DTBQ)_2(APSO)$ in toluene at 299 K (▬), after cooling at 196 K (▬ ▬), and after warming at 291 K (▪▪▪▪).

The VT UV/Vis electronic absorption spectrum of a toluene solution of Co(3,5-DTBQ)$_2$(APSO) is shown in Figure 4.27. As the APSO complex exists predominantly as the PMC form in solution, the PMC π–π* and hs-Co^{II} MLCT bands cannot be easily monitored simultaneously due to the very different intensities of the two transitions. Therefore, a concentrated solution was prepared and only the MLCT band was monitored. When the solution temperature was decreased from 299 to 196 K, the MLCT band decreased in intensity, consistent with hs-Co^{II} → ls-Co^{III} conversion, and this change was reversible upon warming of the solution. From VT studies of the parent APSO ligand, the PMC π–π* band is expected to increase at low temperatures with stabilization of the PMC form.

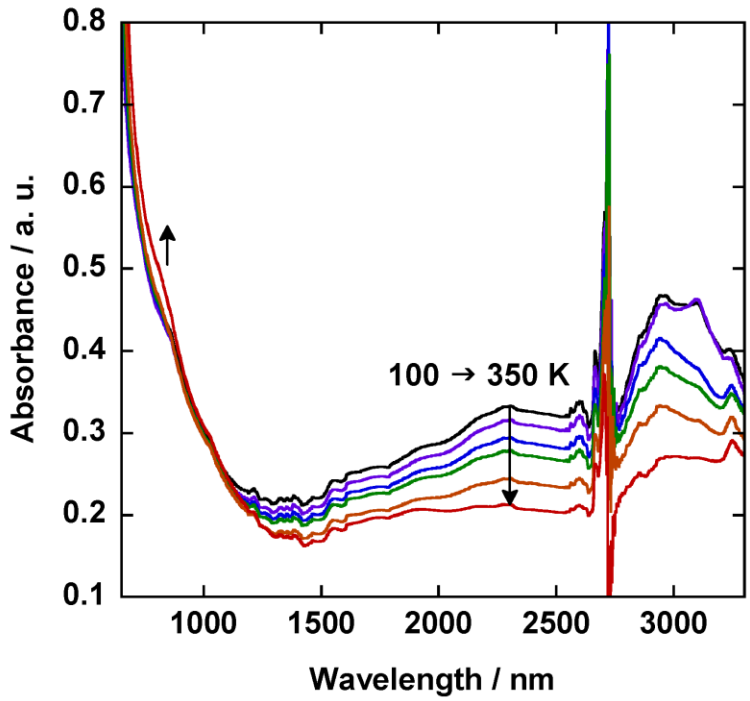

Figure 4.28. Variable-temperature Vis/NIR electronic absorption spectrum of a thin film of Co(3,5-DTBQ)$_2$(APSO) monitored from 100 to 350 K in 50 K increments. The feature between 2600 and 2800 nm is due to the infrasil quartz/water background correction.

The VT Vis/NIR absorption spectrum of a thin film of Co(3,5-DTBQ)$_2$(APSO) is shown in Figure 4.28. In the visible region, an increase in the absorbance in the 700–800 nm range with increasing temperature is consistent with ls-Co^{III} → hs-Co^{II}

conversion. In the NIR region, the absorbance between 1200 and 3300 nm decreases with increasing temperature, also consistent with ls-Co^{III} → hs-Co^{II} conversion. The overall change in absorbance intensity in the NIR region is not as pronounced for the Co–APSO complex as it is for the Co–phen and Co–IPSO complexes. In addition, the overall intensity of the band at ~2500 nm varies from sample to sample. An interesting aspect of the spectra shown in Figure 4.28 is the low-energy feature at ~2850 nm (~3500 cm^{-1}). This feature is not typically very pronounced in spectra of Co–dioxolene complexes, as exemplified by the spectra for the $Co(3,5\text{-}DTBQ)_2(phen)$ (Figure 4.18) and $Co(3,5\text{-}DTBQ)_2(IPSO)$ (Figure 4.23) complexes shown above, as well as several examples from the literature.[358, 379] For these compounds, it is possible that the low-energy feature is simply shifted in energy or, likely, very weak in comparison to the prominent band at ~2500 nm (~4000 cm^{-1}). This lower-energy spectral feature is, however, evident in several Co–dioxolene complexes reported in the literature.[357, 380] Hearns et al.[357] deconvoluted the absorbance band in the NIR region as a function of temperature for a dinuclear $Co_2(3,5\text{-}DTBQ)_4(NN\text{-}NN)$ complex (where NN-NN is a 4,6-di-2′-pyridylpyrimidine ligand with two bidentate diimine chelating sites) and found two distinct bands [a more intense higher energy band at ~4900 cm^{-1} (~2050 nm) and a less intense lower energy band at ~3900 cm^{-1} (~2450 nm)] which displayed distinctly different temperature dependence. This result suggests that the low-energy feature is in fact a distinct band. The authors tentatively proposed that the second low-energy band originated from an IVCT between Cat^{2-} and $SQ^{-\bullet}$ ligands on neighbouring Co sites rather than on the same Co site, which was supported by the trends in VT behaviours for the two bands. For $Co(3,5\text{-}DTBQ)_2(APSO)$, the low-energy feature at ~3000 nm may simply appear more prominent relative to the band at ~2500 nm because the latter is quite weak in intensity, even at low temperatures.

The VT Vis/NIR absorption spectrum of a thin film of $Co_4(3,5\text{-}DTBQ)_6(APSO)_2(MeO)_2$ is shown in Figure 4.29. Upon increasing the temperature from 100 to 300 K, the spectrum displays both an increase in absorbance in the 700–800 nm range and a decrease in absorbance throughout the NIR region, both consistent with ls-Co^{III} → hs-Co^{II} redox isomeric conversion. For the Co–APSO tetramer, features at ~1700, 2400 nm, and 2900 nm are all clearly observed in the NIR spectrum, as for the

Co–phen and Co–IPSO complexes. However, the relative change in the most intense mid-energy band at ~2400 nm is smallest for the Co–APSO complex. For both mononuclear and tetranuclear Co–APSO complexes, it is possible that less of the complex converts to the ls-Co^{III} form at low temperature, but it is also possible that the extinction coefficient for this transition is smaller for these systems.

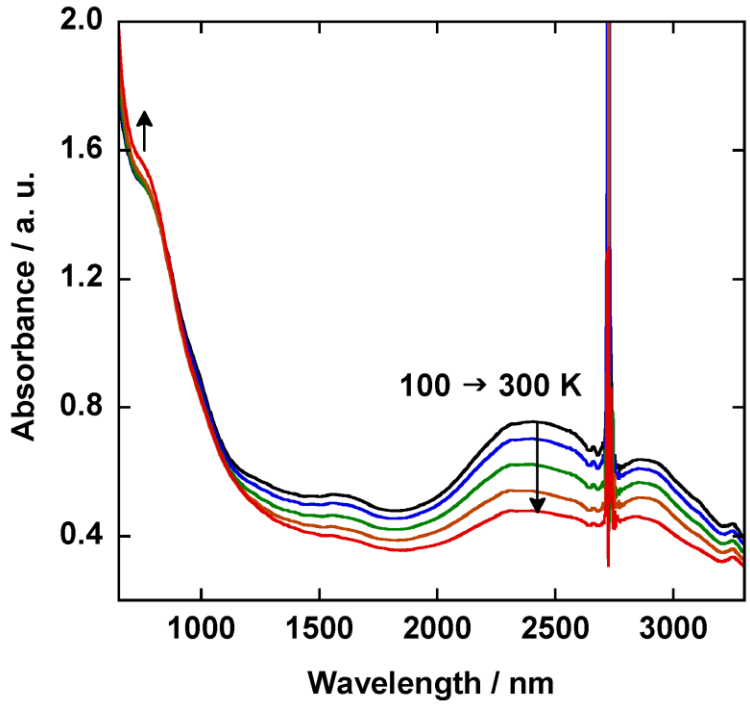

Figure 4.29. Variable-temperature Vis/NIR electronic absorption spectra of a thin film of $Co_4(3,5\text{-DTBQ})_6(APSO)_2(MeO)_2$ (100, 150, 200, 250, 300 K). The feature between 2600 and 2800 nm is due to the infrasil quartz/water background correction.

4.2.8. Solution-State Photochromism

All of the spirooxazine Co–dioxolene complexes were found to be photoresponsive. For $Co(3,5\text{-DTBQ})_2(IPSO)$, photochromism was investigated by irradiating the sample with UV light. In a toluene solution of the complex at ~300 K, UV irradiation induces an increase in the PMC π–π^* band (λ_{max} = 590 nm, with shoulders at ~555 and 485 nm) before a photostationary state (PSS) is achieved (Figure 4.30). The photoresponsivity of the complex under the experimental conditions (ΔK_{UV}), the difference between

equilibrium constants at the PSS, K_{UV} (0.12), and at thermal equilibrium, K_T (0.07), was found to be 0.05, which is lower than that of the free IPSO ligand in toluene (K_T = 0.02, K_{UV} = 0.23, ΔK_{UV} = 0.21). In other words, only 6% of the molecules in solution isomerize from the SO to the PMC form before a PSS is reached. The isomerization process is thermally reversible in the absence of light with an observed rate constant, k_{obs}, of 1×10^{-1} s^{-1} if fit by a first-order monoexponential rate function (R = 0.99653) or with rate constants of 1×10^{-1} s^{-1} (75%) and 6×10^{-1} s^{-1} (25%) if fit by a first-order biexponential rate function (R = 0.99942). As for the Mo complexes, the possibility of two rate components may be indicative of multiple PMC isomers in solution. In either case, the rate constants are comparable to that of IPSO (2×10^{-1} s^{-1}) in toluene.

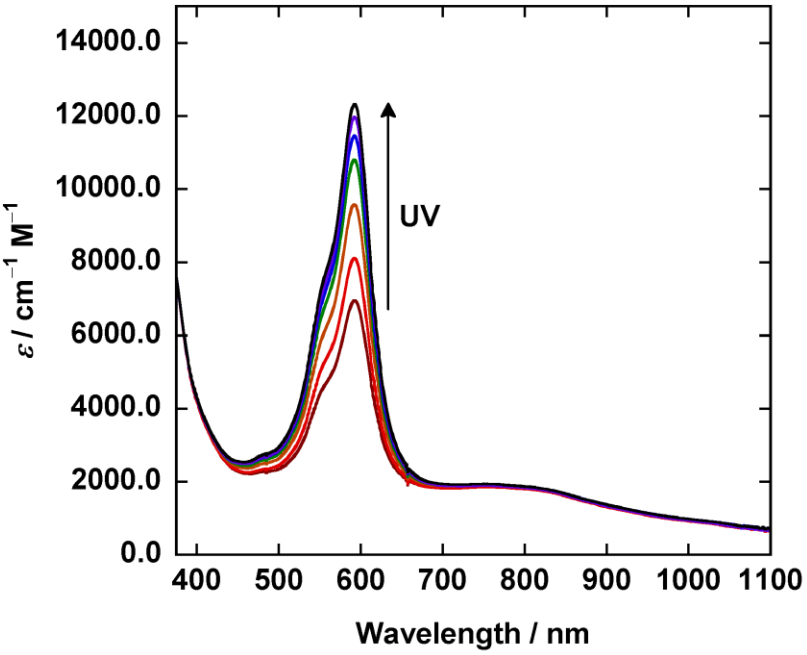

Figure 4.30. UV/Vis electronic absorption spectra of Co(3,5-DTBQ)$_2$(IPSO) in toluene at ~300 K upon UV irradiation (100 mW).

The photochromism of the Co–APSO complexes may be monitored by irradiation with visible light, as metal APSO complexes exist predominantly in the PMC form. For a toluene solution of Co(3,5-DTBQ)$_2$(APSO) at ~300 K, visible irradiation induces a decrease in the PMC π–π* absorption band, as expected for PMC → SO conversion (Figure 4.31). The photoresponsivity of the APSO complex to visible light is much

greater than that of the analogous IPSO complex to UV light. Although the value of ΔK_{Vis} cannot be precisely determined because the value of K_T is not exactly known, one may estimate a figure for the sake of comparison. If we assume a K_T value of 20 (i.e., 95% PMC), we may calculate the equilibrium constant at the PSS under these conditions, K_{Vis}, as 0.3 (i.e., 30% PMC form), to give a ΔK_{UV} value of ~19.7. The data therefore suggest that >60% of the molecules in solution photoisomerize from the PMC to the SO form. In comparison, in a toluene solution of APSO, the photoresponsivity to visible light is closer to ΔK_{Vis} = 0.4 (i.e., 10% PMC → SO conversion), which is significanty lower. Finally, these changes are thermally reversible in the absence of light [$k_{obs} = 2\times10^{-2}$ s^{-1} if fit by a first-order monoexponential rate function (R = 0.99916) or $k_{obs} = 2\times10^{-2}$ s^{-1} (80%) and 1×10^{-2} s^{-1} (20%) if fit by a first-order biexponential rate function (R = 0.99909)] (in comparison, $k_{obs} = 2\times10^{-1}$ s^{-1} for APSO in toluene). The photochromic properties of the Co–APSO tetramer are nearly identical to those of the monomer, both in terms of photoresponsivity and rates of thermal relaxation.

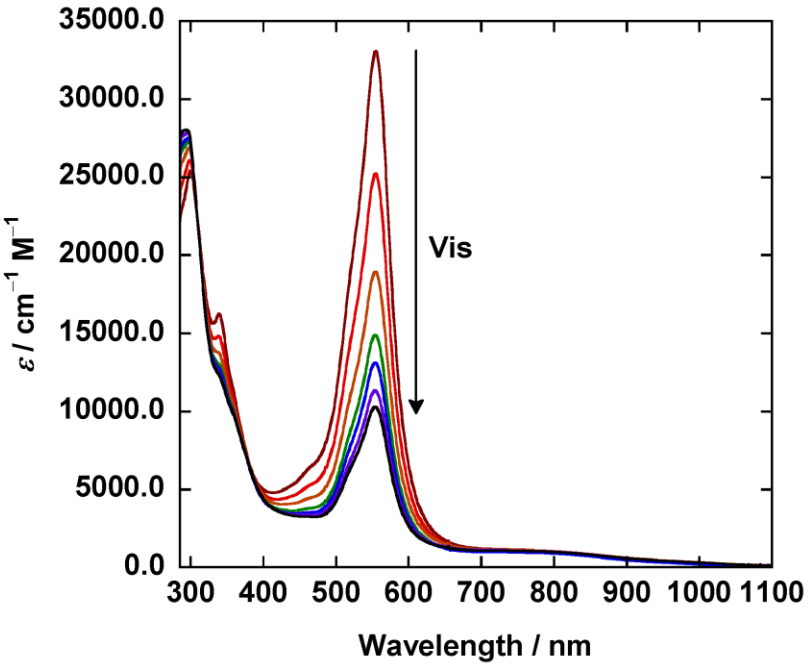

Figure 4.31. UV/Vis electronic absorption spectrum of Co(3,5-DTBQ)$_2$(APSO) in toluene at ~300 K upon visible irradiation (λ_{ex} = 568 nm, 60 mW).

4.2.9. Magnetic Susceptibility Measurements

The analysis of variable-temperature magnetic susceptibility data is another way to probe the redox isomeric processes occurring in Co–dioxolene complexes. This is nicely illustrated by looking at the magnetic behaviour of the toluene solvate of Co(3,5-DTBQ)$_2$(phen) shown in Figure 4.32, representative of that typically reported for this compound.[345] At 300 K, the magnetic moment, χT, of this material has a value of 4.02 emu·K·mol^{-1}, consistent with a hs-Co^{II}(SQ$^{-\bullet}$)$_2$ species in which the Co^{II} centre has a *g*-value greater than 2 as a result of SOC effects. With decreasing temperature, the magnetic moment drops rapidly within a span of ~20 K, with the mid-point of this drop, T_c, being ~240 K. At temperatures of 100 K and below, χT has a value of 0.39 emu·K·mol^{-1}, very close to the value of the spin-only magnetic moment expected for a ls-Co^{III}(Cat^{2-})(SQ$^{-\bullet}$) species containing only one radical (0.375 emu·K·mol^{-1}). Finally, at very low temperature (<6 K), χT again drops rapidly, consistent with intermolecular antiferromagnetic interactions. The data presented in Figure 4.32 also illustrates the effect of environment on the redox isomeric transition in these types of complexes. The abrupt transition observed in the solid state is a result of cooperative intermolecular interactions in the highly crystalline material facilitated by the presence of lattice solvent molecules.[345] The solution-state magnetic susceptibility from 200 to 300 K obtained by Evan's method in CD_2Cl_2 is shown alongside the solid-state data. In solution, the ls-Co^{III}/hs-Co^{II} transition is more gradual than in the solid state, and the complex does not reach either 100% ls-Co^{III} or 100% hs-Co^{II} form within the observed temperature range. The onset of redox isomerism with increasing temperature occurs at ~250 K, and the T_c in solution (specifically, relatively polar CD_2Cl_2) is greater than the T_c obtained for the crystalline toluene solvate (240 K).

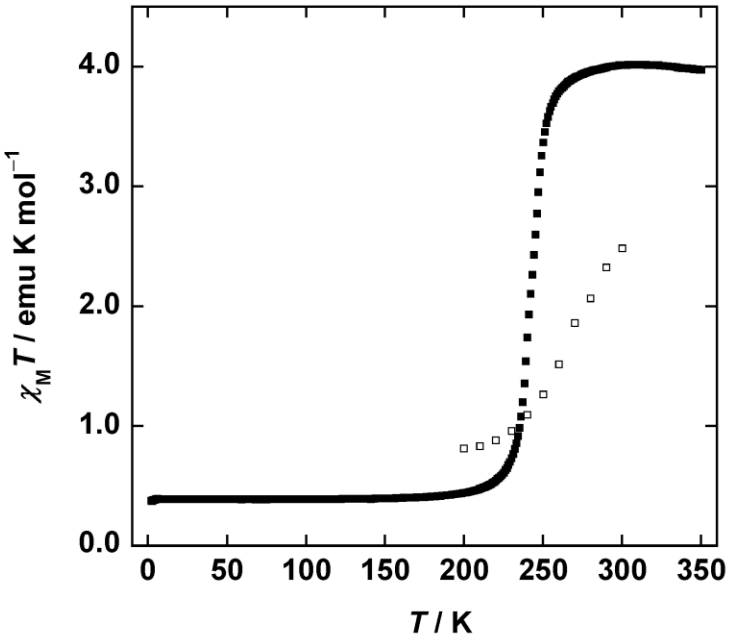

Figure 4.32. Temperature dependence of the magnetic moment (χT) of $Co(3,5\text{-}DTBQ)_2(phen)\cdot C_6H_5CH_3$ in the crystalline state at 10000 Oe (2 → 350 K, ■) and in CD_2Cl_2 (200–300 K, □) as determined by Evan's method with a 360 MHz spectrometer.

Curves of the magnetic moment as a function of temperature for powder and CD_2Cl_2 samples of $Co(3,5\text{-}DTBQ)_2(IPSO)$ are shown in Figure 4.33. Solid-state data is shown for a microcrystalline sample crystallized from cyclohexane at ~300 K (α phase) and a microcrystalline sample crystallized from cyclohexane at ~285 K (β phase). Samples crystallized under the two different sets of conditions reproducibly display different VT magnetic behaviour, which is consistent with them being composed of different crystalline phases, as supported by PXRD data (vide supra, Section 4.2.3). The α-phase samples show a magnetic moment at 350 K consistent with dominance of the hs-Co^{II} form (3.75 emu·K·mol^{-1}). The magnetic moment remains fairly stable with decreasing temperature until ~100 K when a fairly abrupt decrease in χT is observed before it reaches a limiting value of 0.07 emu·K·mol^{-1} at 2 K. It is not certain whether the observed decrease in χT is caused by a redox isomeric transition to the ls-Co^{III} species at lower temperatures or antiferromagnetic exchange in the hs-$Co^{II}(SQ^{-\bullet})_2$ form, although the redox isomeric transition would be expected at much higher temperatures by analogy with comparable systems. In the β-phase, the Co–IPSO complex displays gradual χT vs T behaviour. At 350 K, the magnetic moment is 1.53 emu·K·mol^{-1}, consistent with a

mixture of ls-Co^{III} and hs-Co^{II} species. A gradual and uneven decrease in χT is observed with decreasing temperature, with a hump at ~250 K, until ~150 K at which a point a plateau is reached with χT = 0.52 emu·K·mol^{-1} before a more abrupt drop in χT occurs below 20 K. It is apparent that the magnetic moment is too high for the sample to consist entirely of the ls-Co^{III} form at low temperature (20–200 K), although it should be the dominant species in the equilibrium. Neither a full conversion to ls-Co^{III} nor hs-Co^{II} is observed within the temperature range monitored, but a clear redox isomeric transition is observed for these samples. A very subtle hysteretic effect is observed in microcrystalline powder samples of Co(3,5-DTBQ)$_2$(IPSO) upon temperature cycling, as shown in Figure 4.34 for a low-to-high temperature scan followed by a high-to-low temperature scan. This effect could be associated with a slight phase change; however, more interestingly, because this complex contains a photochromic spirooxazine ligand that is also thermochromic, the hysteresis might be caused by a subtle memory effect associated with this thermochromism (for which the kinetics in the solid state might be slow or on the order of the timescale of the experiment). Solution-state VT magnetic susceptibility data were also obtained for Co(3,5-DTBQ)$_2$(IPSO) using Evan's method in CD_2Cl_2, as shown alongside the solid-state data in Figure 4.33. The solution-state data for Co(3,5-DTBQ)$_2$(IPSO) is more consistent with the analogous data for the Co(3,5-DTBQ)$_2$(phen) sample than the solid-state data: the onset of a ls-Co^{III} → hs-Co^{II} transition is observed at ~250 K, and the overall magnetic moment displays a steady increase from 0.73 emu·K·mol^{-1} at 200 K to 1.94 emu·K·mol^{-1} at 300 K.

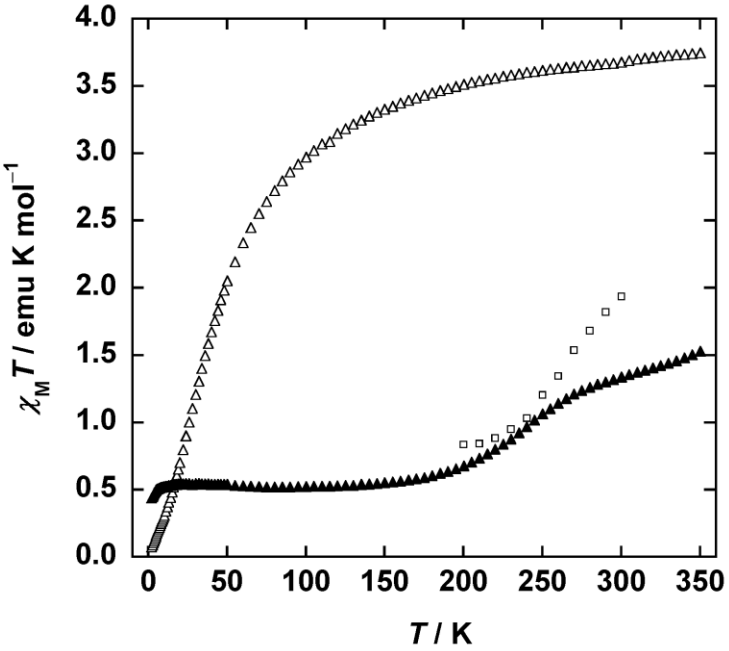

Figure 4.33. Temperature dependence of the magnetic moment (χT) of Co(3,5-DTBQ)$_2$(IPSO) in the microcrystalline state at 10000 Oe [recrystallized from cyclohexane at ~300 K (α phase, Δ) and ~285 K (β phase, ▲)] and in CD_2Cl_2 (□) as determined by Evan's method with a 360 MHz spectrometer.

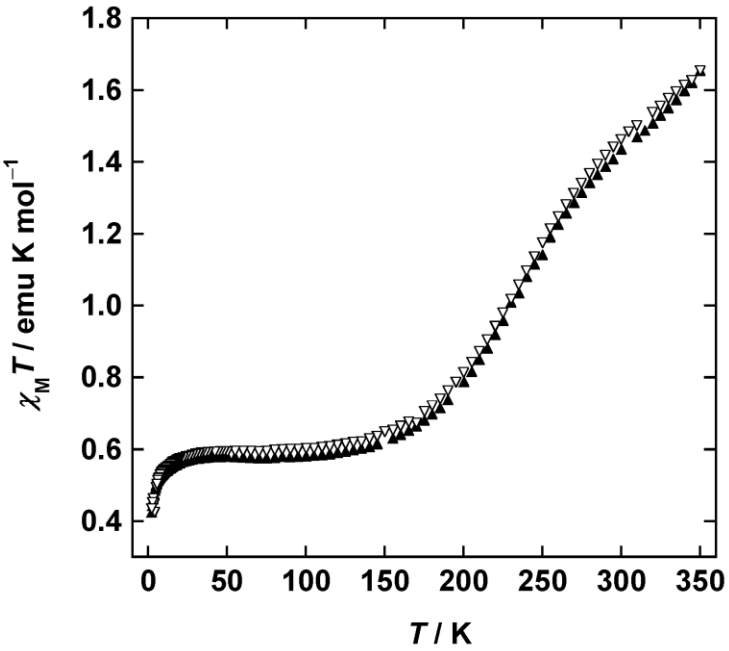

Figure 4.34. Temperature dependence of the magnetic moment (χT) of a microcrystalline sample of Co(3,5-DTBQ)$_2$(IPSO) (β phase) at 10000 Oe over two temperature cycles [2 → 350 K (▲), 350 → 2 K (▽)].

The Co(3,5-DTBQ)$_2$(APSO) powder samples demonstrate fairly reproducible VT magnetic behaviour. Representative χT vs T curves for solid-state and solution-state samples are shown in Figure 4.35. For the powder sample, the magnetic moment is 1.61 emu·K·mol^{-1} at 350 K, consistent with a mixture of ls-Co^{III} and hs-Co^{II} species at this temperature. With decreasing temperature, the magnetic moment decreases gradually from 350 to 300 K, even more gradually below 300 K, and then more abruptly below 100 K, before reaching a limiting moment of 0.55 emu·K·mol^{-1} at 2 K. Clearly, the ls-Co^{III}/hs-Co^{II} redox isomeric conversion is not complete over the 2–350 K temperature range, and a χT value between ~1.2 and 1.6 emu·K·mol^{-1} within the 100–350 K range points to the existence of a metastable equilibrium of both ls-Co^{III} and hs-Co^{II} forms at these temperatures. The Co(3,5-DTBQ)$_2$(APSO) complex also shows a slight hysteresis effect in the solid state, as in the IPSO analog. Representative data is shown in Figure 4.36, where the magnetization was measured over three temperature cycles (2 → 350 K, 350 → 2 K, 350 → 2 K). After an initial heating scan from 2 to 350 K, a cooling scan revealed slightly different χT behaviour, notably a smoothing of the higher temperature data, where instead of demonstrating a dip at ~300 K, the data show a slight bump at ~250 K. Interestingly, during the subsequent heating scan, the hysteresis effect decreased considerably and the χT values followed a path quite similar to the second high-T to low-T scan rather than the initial low-T to high-T scan. The post-heating data is in fact very reminiscent of the data obtained for the Co(3,5-DTBQ)$_2$(IPSO) samples in the β phase, except that the overall magnetic moment is higher for the APSO derivative. Finally, a solution-state Evan's method analysis was performed for Co(3,5-DTBQ)$_2$(APSO) in CD_2Cl_2 between 200 and 300 K (Figure 4.35). The sample exhibits a low-temperature magnetic moment of ~1.1 emu·K·mol^{-1}, which is higher than that observed in the analogous phen and IPSO complexes (~0.8 emu·K·mol^{-1}), but is consistent with the higher overall magnetic moment observed for the APSO complex in the solid state. The onset of ls-Co^{III} → hs-Co^{II} conversion is observed, however, and this happens at a slightly higher temperature than in the phen and IPSO complexes. Ultimately, a χT value of 1.74 emu·K·mol^{-1} is observed at 300 K, which is significantly higher than that achieved in the solid state.

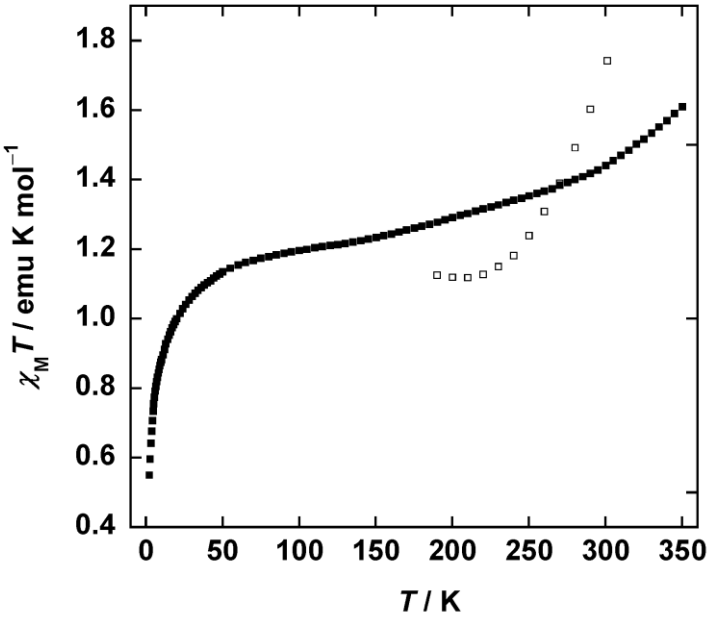

Figure 4.35. Temperature dependence of the magnetic moment (χT) of Co(3,5-DTBQ)$_2$(APSO) as a powder at 10000 Oe (2 → 350 K, ■) and in CD_2Cl_2 (200–300 K, □) as determined by Evan's method with a 360 MHz spectrometer.

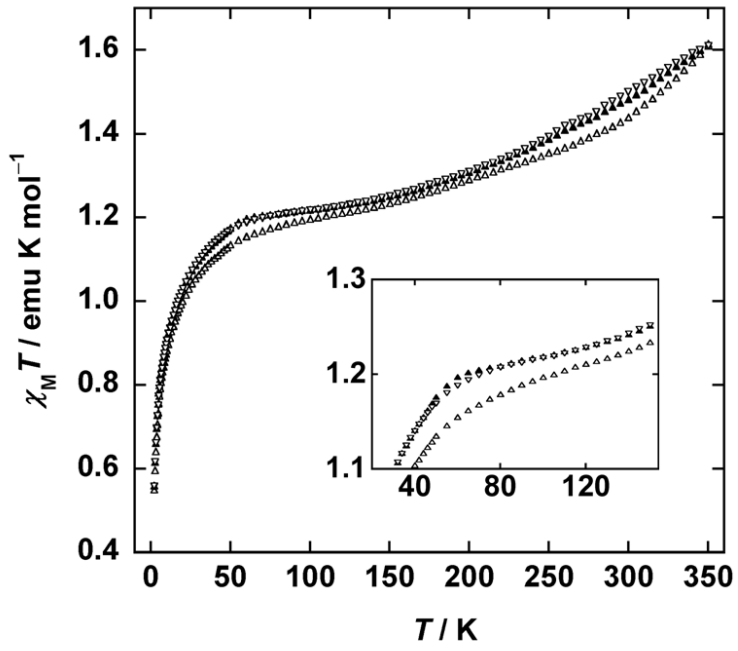

Figure 4.36. Temperature dependence of the magnetic moment (χT) of a powder sample of Co(3,5-DTBQ)$_2$(APSO) at 10000 Oe over three temperature cycles [2 → 350 K (Δ), 350 → 2 K (▽), and 2 → 350 K (▲)].

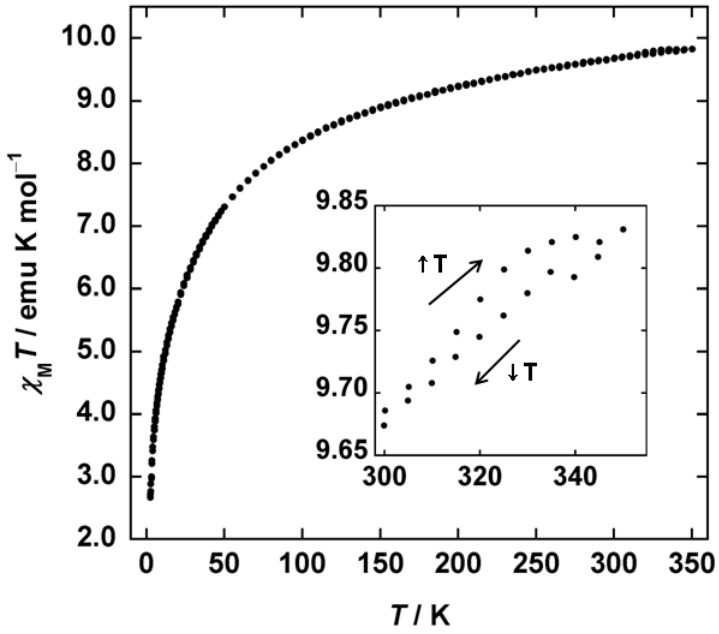

Figure 4.37. Temperature dependence (2 → 350 → 2 K) of the magnetic moment (χT) of Co_4(3,5-DTBQ)$_6$(APSO)$_2$(MeO)$_2$·2MeOH in the crystalline state at 10000 Oe. The inset shows the behaviour at high temperature (>300 K).

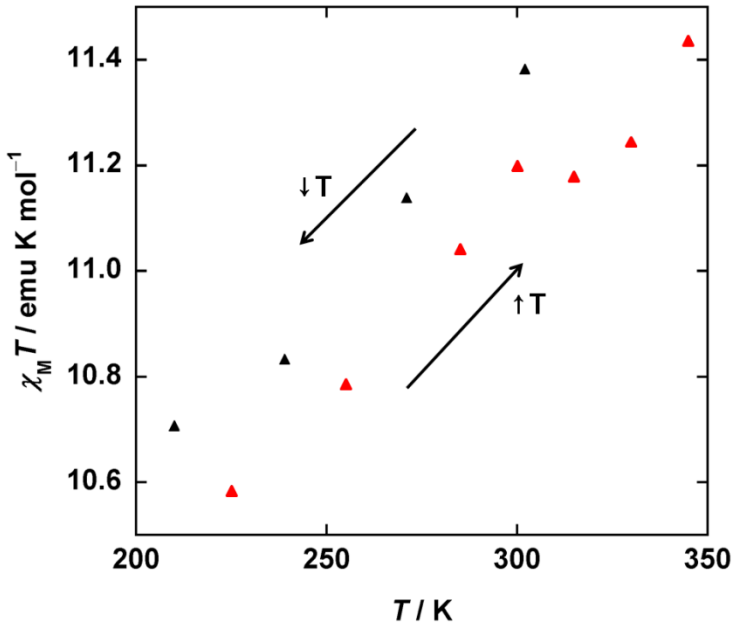

Figure 4.38. Temperature dependence [decreasing temperature 302 → 271 → 239 → 210 K (▲); increasing temperature 225 → 255 →285 →300 →315 → 330 → 345 K (▲)] of the magnetic moment (χT) of Co_4(3,5-DTBQ)$_6$(APSO)$_2$(MeO)$_2$·2MeOH in toluene-d_8 as determined by Evan's method with a 360 MHz spectrometer.

The magnetic moment as a function of temperature for a sample of the Co–APSO tetramer is shown in Figure 4.37. Low-temperature X-ray analysis of this compound suggested the existence of a $Co^{II}_2Co^{III}_2(Cat^{2-})_6$ species at 90 K, which has a spin-only magnetic moment of 3.75 emu·K·mol^{-1}. If we assume that a complete redox isomeric conversion takes place below 350 K (i.e., an IET between two Co^{III} centres and two Cat^{2-} ligands), we would expect a $Co^{II}_4(SQ^{-\bullet})_2(Cat^{2-})_4$ species at high temperature, the spin-only magnetic moment of which is 8.25 emu·K·mol^{-1}. However, hs-Co^{II} is expected to exhibit SOC effects, and the expected magnetic moments for this complex could conceivably be as high as ~7 emu·K·mol^{-1} for the $Co^{II}_2Co^{III}_2(Cat^{2-})_6$ species and as high as ~15 emu·K·mol^{-1} for the $Co^{II}_4(SQ^{-\bullet})_2(Cat^{2-})_4$ species. These estimates do not account for strong exchange interactions. The experimental magnetic moment of the tetramer was found to be 9.82 emu·K·mol^{-1} at 350 K. It is difficult to use this result to estimate the Co^{III}/Co^{II} equilibrium in the sample, although it can be said that the magnetic moment at 350 K is higher than expected for a $Co^{II}_2Co^{III}_2(Cat^{2-})_6$ alone, and therefore some amount of redox isomeric conversion is expected. With decreasing temperature, the magnetic moment shows a gradual decrease which becomes more abrupt below 100 K to reach a limiting χT value of 2.67 emu·K·mol^{-1} at 2.5 K. A subtle hysteresis effect with some unusual features is observed for this compound above 300 K. Solution-state magnetic susceptibility data for the Co–APSO tetramer were acquired in toluene-d_8 using Evan's method (Figure 4.38). For the data acquisition, the temperature was decreased in 30 K increments, and then increased in 30 K increments to fill the intervals at every 15 K. The high-to-low *T* scan and low-to-high *T* scan did not overlap smoothly, and it was immediately assumed that this was evidence for a change in sample composition over time or after cooling. However, a comparison of the solid-state and solution-state data show remarkably—or coincidentally—similar features, which may suggest that the observed hysteresis is a property of the system and not an experimental artifact, although for hysteresis to exist in solution, the kinetics controlling the effect must be slow on the solution-phase NMR timescale. Overall, the magnetic moment of Co_4(3,5-DTBQ)$_6$(APSO)$_2$(MeO)$_2$·2MeOH in toluene-d_8 increases gradually from 10.70 emu·K·mol^{-1} at 200 K to 11.43 emu·K·mol^{-1} at 350 K, consistent with the gradual

increase over this temperature range observed for the solid-state sample but with the overall χT value being about 1.5 emu·K·mol^{-1} higher.

4.2.10. Correlation of Photochromic State with Redox Isomeric State

After confirming that all of the Co complexes were both photochromic and redox isomeric, we sought to investigate the correlation between photochromic state and redox state to determine whether the two processes are in fact coupled (i.e., whether the SO and PMC forms preferentially stabilize one Co redox state over the other). As an attempt to correlate the two processes, the behaviour of the hs-Co^{II} MLCT band at ~800 nm in the visible region, the ls-Co^{III} CT band at ~2500 nm (~4000 cm^{-1}) in the NIR region, and the fingerprint IR regions were monitored spectroscopically as a function of photoisomerization.

In the UV/Vis spectra, the behaviour of the hs-Co^{II} MLCT band upon spirooxazine photoisomerization is convoluted with the large changes occurring for the PMC π–π* CT band. The spectra for both Co(3,5-DTBQ)$_2$(IPSO) and Co(3,5-DTBQ)$_2$(APSO) were therefore deconvoluted between 500 and 1000 nm in order to differentiate the overall behaviour of each band. It is known from the electronic absorption spectra of IPSO and APSO (Figure 2.6), that the PMC π–π* band is made up of three vibrational bands, ν(1), ν(2), and ν(3). However, the highest-energy ν(3) band between 400 and 500 nm only makes up ≤10% of the total peak area. It is also known from the electronic absorption spectrum of Co(3,5-DTBQ)$_2$(phen) (Figure 4.17) that as many as five or six Co-based transitions occur throughout the visible region, but that the hs-Co^{II} MLCT band is the most prominent when the hs-Co^{II} form is dominant. In theory, therefore, there are many contributions to the UV/Vis spectra of the Co–spirooxazine complexes. In practice, however, the spectra were successfully deconvoluted (R^2 = 0.999) into three major bands using Lorentzian functions (attempts to fit more bands or to use Gaussian functions were unsuccessful), where the bands could be assigned as the ν(1) and ν(2) vibronic transitions of the PMC π–π* CT band and the hs-Co^{II} MLCT band. This data is shown for one spectrum each of Co(3,5-DTBQ)$_2$(IPSO) (from Figure 4.30) and Co(3,5-DTBQ)$_2$(APSO) (from Figure 4.31) in Figure 4.39(a) and Figure 4.40(a), respectively. In both cases, the peak areas for the combined PMC-based bands and the hs-Co^{II} MLCT band were plotted

as a function of irradiation time, and, in both cases, the PMC and MLCT bands show the opposite behaviour with roughly the same monoexponential kinetics. It can be seen that for Co(3,5-DTBQ)$_2$(IPSO) [Figure 4.39(b)], as the PMC band increases with UV irradiation, indicative of SO → PMC isomerization, the hs-Co^{II} MLCT band decreases, indicative of hs-Co^{II} → ls-Co^{III} conversion. For Co(3,5-DTBQ)$_2$(APSO) [Figure 4.40(b)], as the PMC band decreases with visible irradiation, indicative of PMC → SO isomerization, the hs-Co^{II} MLCT band increases, indicative of ls-Co^{III} → hs-Co^{II} conversion. Therefore, for both Co(3,5-DTBQ)$_2$(APSO) and Co(3,5-DTBQ)$_2$(IPSO), the UV/Vis data supports a correlation between SO/PMC photoisomerization and the redox state of the cobalt centre, and suggests that the SO form stabilizes the hs-Co^{II} form. This result is consistent with the theoretical model proposed in Section 4.2.1.

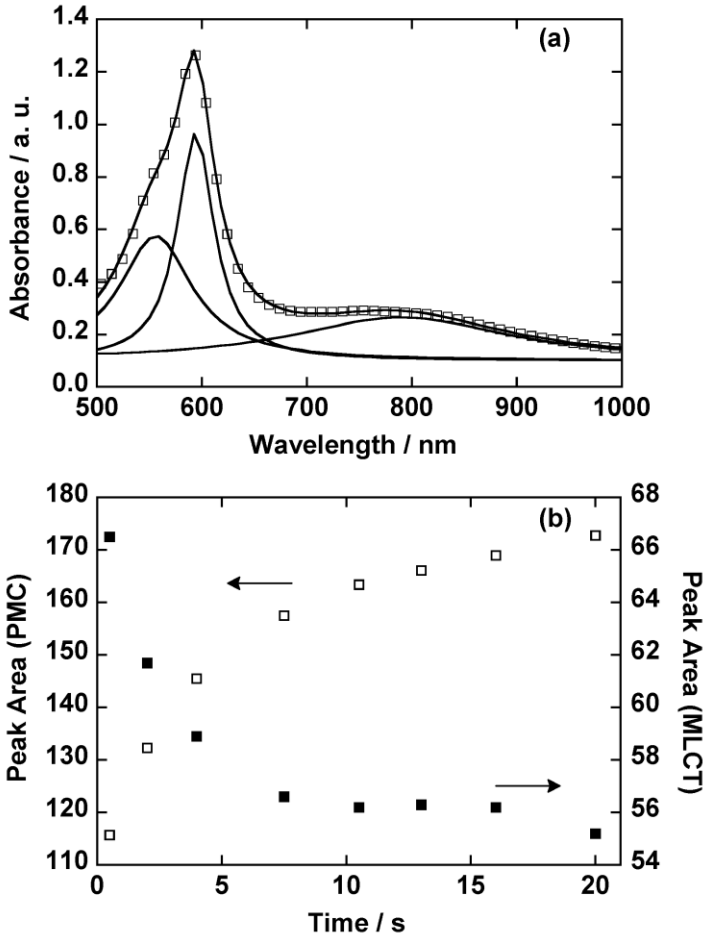

Figure 4.39. (a) Lorentzian deconvolution [—] and experimental data [□] for the electronic absorption spectrum of Co(3,5-DTBQ)$_2$(IPSO) in toluene. (b) Peak areas of the combined PMC CT *ν*(1) and *ν*(2) bands [□], and of the hs-Co^{II} MLCT band [■] as a function of UV irradiation time (corresponding to spectra from Figure 4.30).

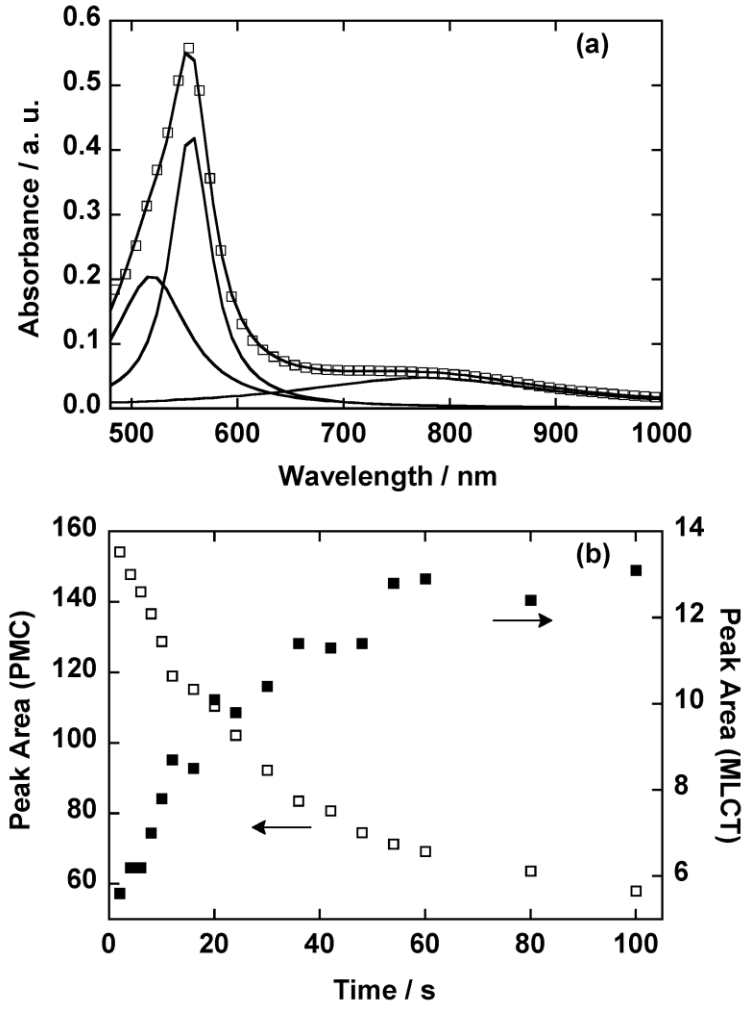

Figure 4.40. (a) Lorentzian deconvolution [—] and experimental data [□] for the electronic absorption spectrum of Co(3,5-DTBQ)$_2$(APSO) in toluene. (b) Peak areas of the combined PMC CT ν(1) and ν(2) bands [□], and of the hs-Co^{II} MLCT band [■] as a function of visible irradiation time (corresponding to spectra from Figure 4.31).

FT-IR/NIR spectroscopy was used to monitor both the fingerprint and IVCT spectral regions upon photoisomerization of Co(3,5-DTBQ)$_2$(APSO) to probe the possible correlation between the SO/PMC photochromic equilibrium and the ls-Co^{III}/hs-Co^{II} redox isomeric equilibrium. The irradiation of a CCl_4 solution of Co(3,5-DTBQ)$_2$(APSO) with visible light at ~300 K leads to dramatic changes in the FT-IR spectrum, which are nearly perfectly thermally reversible after the irradiation is stopped [Figure 4.41(a)]. After irradiation, the majority of the bands in the fingerprint region show a decrease in intensity, typical of PMC → SO isomerization, as found in APSO and other APSO-containing systems. To help in the deconvolution of changes associated with APSO

PMC → SO isomerization from changes associated with a change in cobalt redox state, the difference spectrum for the irradiation of the Co–APSO complex shown in Figure 4.41(a) was plotted alongside that for a CCl_4 solution of APSO subjected to the same irradiation experiment [Figure 4.41(b)] (note that the photoresponsivity of APSO is much lower than that of the Co–APSO complex, but changes are clearly discernible when the data is plotted as a difference spectrum). The result is given in Figure 4.41(c), where possible changes associated with a redox isomeric conversion are marked by asterisks. The band at 1036 cm^{-1}, which may be dioxolene-based (vide supra, Section 4.2.6), shows a decrease in intensity with irradiation. A very strong drop in intensity is observed for the band at 1228 cm^{-1}. This parallels a drop observed in an analogous band for the free ligand upon PMC → SO isomerization, although the magnitude of the effect observed for the cobalt complex suggests that there may also be a contribution from a change in redox state, specifically a ls-Co^{III} → hs-Co^{II} conversion if this band is in fact associated with the ls-Co^{III} form as suggested by the VT FT-IR spectrum of $Co(3,5\text{-}DTBQ)_2(phen)$ (Figure 4.15). A subtle decrease in intensity is observed for the band at 1261 cm^{-1}. This band may most confidently be assigned to a dioxolene ligand in the catecholate redox state by analogy with the majority of the literature on the topic,[357, 372, 373] which would make this decrease also indicative of ls-Co^{III} → hs-Co^{II} conversion. The band at 1425 cm^{-1}, which has been empirically associated with the catecholate form,[373, 374] appears to exhibit a drop in intensity as well. Changes occurring between 1440 and 1480 cm^{-1} are certainly evident, although their origin in less clear, which is not surprising as this region likely contains contributions from both $SQ^{-\bullet}$ and Cat^{2-} species. Changes in the spectrum of the Co–APSO complex between 1300 and 1400 cm^{-1} as well as 1500 and 1600 cm^{-1} appear closely correlated with changes occurring for the APSO ligand alone upon PMC → isomerization. Overall, the data is consistent with reversible PMC → SO isomerization upon irradiation with visible light, and may also tentatively support a simultaneous ls-Co^{III} → hs-Co^{II} conversion.

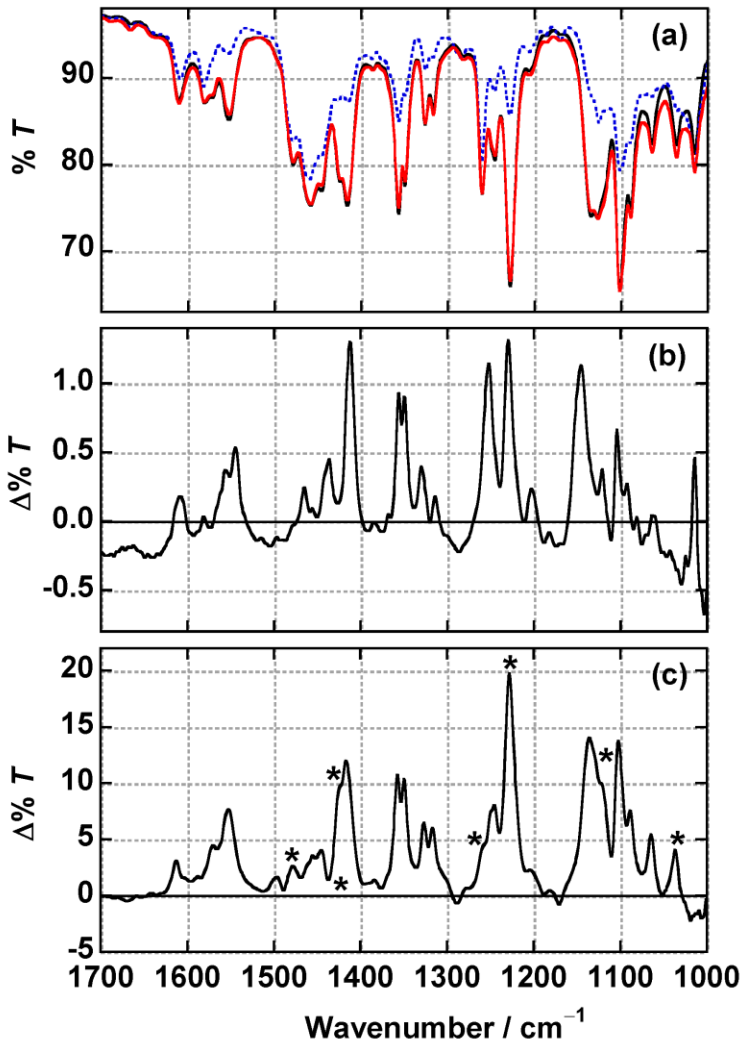

Figure 4.41. (a) FT-IR spectrum of a CCl_4 solution of Co(3,5-DTBQ)$_2$(APSO) at ~300 K before (—) and after (▪▪▪▪) 10 min of steady-state visible irradiation (568 nm, 150 mW), and after thermal relaxation for 9 min (—). (b) Changes in % transmittance of a CCl_4 solution of APSO at ~300 K upon visible irradiation. (c) Changes in % transmittance of the spectrum of Co(3,5-DTBQ)$_2$(APSO) from (a). [Horizontal lines indicate 0% change in %*T*; asterisks highlight possible differences between the two spectra shown in (b) and (c)].

The spectral features of the NIR IVCT region for the same Co(3,5-DTBQ)$_2$(APSO) sample irradiated in CCl_4 are displayed in Figure 4.42. The broad band associated with IVCT in the ls-Co^{III} form of the complex exhibits a partially reversible decrease in intensity following irradiation of the sample with visible light. Because a quantitative interpretation of the spectral changes using this plot alone is hindered by the pronounced shift in baseline occurring over the course of the experiment, the total peak area of the

IVCT band was plotted as a function of time and compared to the peak area of a second major peak from the fingerprint region (Figure 4.43). This plot shows that irradiation leads to quite a large decrease in the intensity of the IVCT band—the total peak area is reduced by over half. After thermal equilibration in the absence of light, the peak intensity returns to ~3/4 of its original intensity, which demonstrates that the effect is partially reversible. The decrease in the IVCT band corroborates some degree of ls-Co^{III} → hs-Co^{II} conversion upon PMC → SO isomerization. Insight into the lack of reversibility of the process may be gained through a closer inspection of the sample solution cell (Figure 4.44). Here we see that, whereas the CCl_4 solution of $Co(3,5\text{-}DTBQ)_2(APSO)$ began as an intensely coloured purple solution and became a clear, colourless solution immediately after visible irradiation, the formation of a purple solid is observed after thermal relaxation. The observed phase change could suggest that the drastic change in composition induced by irradiation of the saturated solution in the cell causes some precipitation or aggregation of the product upon thermal return.

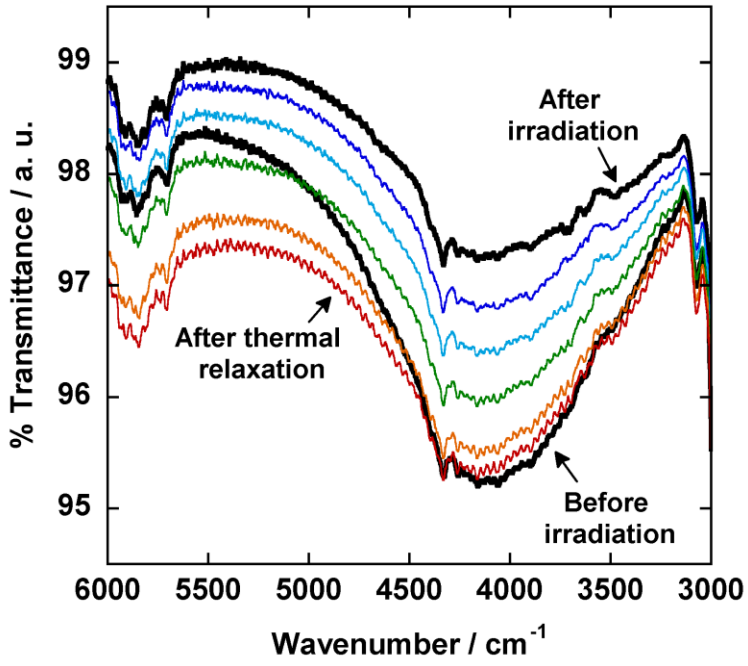

Figure 4.42. FT-IR spectrum (IVCT region) of a CCl_4 solution of $Co(3,5\text{-}DTBQ)_2(APSO)$ before and after (dark traces) 10 min of visible irradiation (568 nm, 150 mW) and during thermal relaxation for 9 min (coloured traces) at ~300 K.

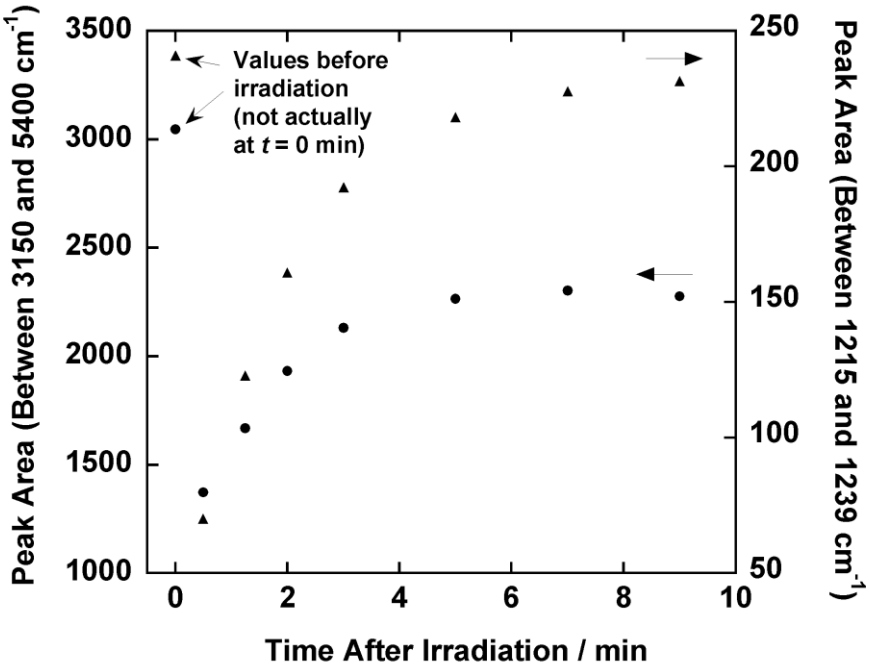

Figure 4.43. Changes in peak areas for the IVCT band (Figure 4.42) and the1230-cm^{-1} peak [Figure 4.41(a)] for a CCl_4 solution of Co(3,5-DTBQ)$_2$(APSO) after visible irradiation and thermal relaxation.

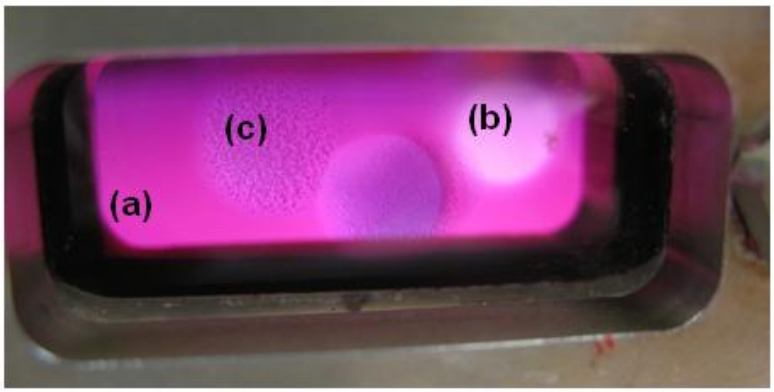

Figure 4.44. FT-IR solution cell containing a CCl_4 solution of Co(3,5-DTBQ)$_2$(APSO) before visible irradiation (a), very shortly after irradiation (b), and following thermal relaxation (c).

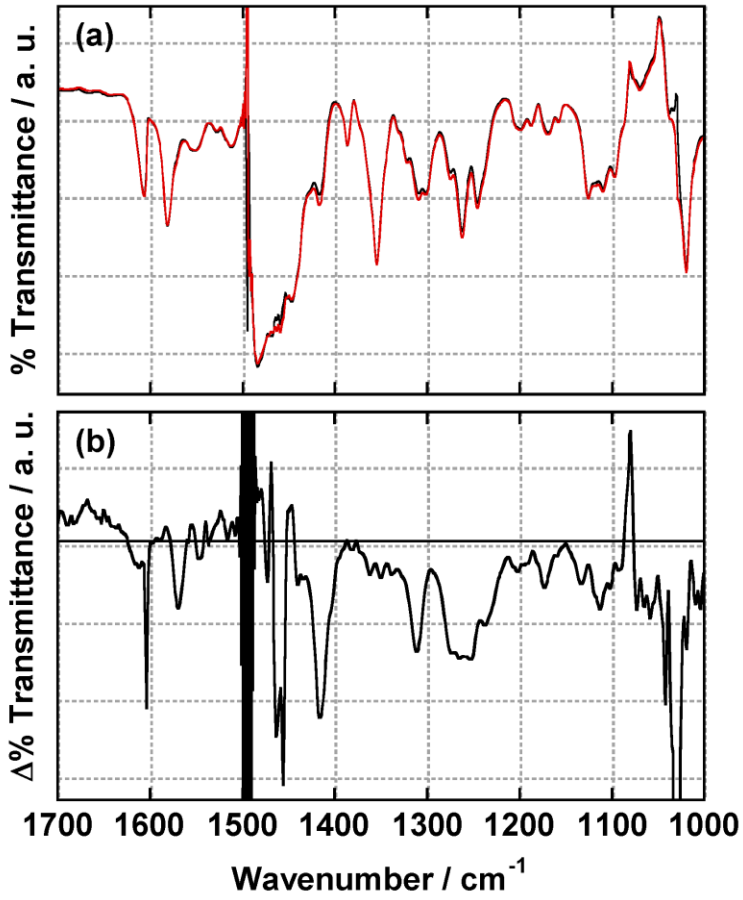

Figure 4.45. (a) FT-IR spectrum of a toluene solution of Co(3,5-DTBQ)$_2$(IPSO) before (—) and after (—) 10 min of UV irradiation at ~300 K. (b) Difference FT-IR spectrum for the above data. The horizontal line indicates 0% change. The discontinuity at ~1500 cm^{-1} is from the toluene background correction.

The same FT-IR analysis was performed for a saturated toluene solution of Co(3,5-DTBQ)$_2$(IPSO) upon UV irradiation. The fingerprint region of the FT-IR spectrum before and after 10 min of UV irradiation is shown in Figure 4.45(a), while the corresponding difference spectrum is plotted in Figure 4.45(b). As can be seen in Figure 4.45(a), the photoresponsivity of the complex is quite low and only very subtle changes in the spectrum can be observed. However, a plot of the difference spectrum highlights these changes very clearly. Most of the bands show an increase in intensity, in contrast to the Co–APSO sample. The spirooxazine-based peaks are expected to increase in intensity upon SO → PMC isomerization, and many of the spectral changes are likely associated with this process. A careful analysis of the difference spectrum reveals that bands at 1081, 1449, and 1470 cm^{-1} display a decrease in intensity, while bands at 1030, 1260,

1311, 1417, 1456, and 1463 cm^{-1} display an increase in intensity immediately following UV irradiation of the sample. Of these, bands at 1030, 1260 (Cat^{2-} C–O), 1417, 1463, and possibly 1311 cm^{-1} all exhibit a change in the opposite direction from those observed for the APSO complex. Most notably, there is good evidence that the peak at 1260 cm^{-1} can be assigned to a Cat^{2-} C–O stretching mode, and that bands at 1417 and 1463 cm^{-1} may be assigned to Cat^{2-} aromatic ring stretching modes. If these assignments are accurate, the results corroborate an increase in the concentration of Cat^{2-} species in solution, consistent with preferential stabilization of the ls-Co^{III} form upon SO → PMC photoisomerization. Although a moderately intense IVCT band could be identified in the spectrum, no clear changes in its intensity could be observed following UV irradiation.

On the whole, the behaviour of the hs-Co^{II} MLCT band, the ls-Co^{III} IVCT band, and several bands in the IR fingerprint region upon SO/PMC photoisomerization of the Co–dioxolene–spirooxazine complexes corroborate a relationship between the photochromic state of the spirooxazine ligand and redox state of the Co centre. For both $Co(3,5\text{-}DTBQ)_2$(IPSO) and $Co(3,5\text{-}DTBQ)_2$(APSO) complexes, the observed changes in the $Co(diox)_2$ spectral features are consistent with stabilization of the hs-Co^{II} species in the SO form of the spirooxazine ligand, a result which is consistent with the theoretical model outlined in section 4.2.1.

4.3 Summary and Conclusions

$Co(3,5\text{-}DTBQ)_2$(IPSO) was successfully synthesized and found to behave as expected for $Co(DTBQ)_2$(NN) complexes [with the prototypical system being $Co(3,5\text{-}DTBQ)_2$(phen)] on the basis of VT ^{1}H NMR and UV/Vis/NIR electronic absorption spectroscopy. The expected paramagnetically shifted ^{1}H NMR signals are observed and exhibit VT shifts associated with ls-Co^{III} → hs-Co^{II} redox isomerism with increasing temperature. The characteristic hs-Co^{II} MLCT band is observed in the visible electronic absorption spectrum as well as the characteristic ls-Co^{III} IVCT band in the NIR spectrum; both bands display temperature-dependent changes nearly identical to those observed for $Co(3,5\text{-}DTBQ)_2$(phen). Two microcrystalline phases were reproducibly isolated from cyclohexane by crystallization at either ~300 K or 285 K, as confirmed by PXRD analysis. The phases exhibit different VT magnetic susceptibility behaviour,

neither being particularly similar to that of the Co(3,5-DTBQ)$_2$(phen) toluene solvate: one phase shows a gradual, discontinuous conversion between ls-Co^{III} and hs-Co^{II}, while the other phase does not show evidence for a conversion to ls-Co^{III} at all. The solution-state magnetic behaviour determined using Evan's method, however, is very similar to that of the phen analog. The IPSO complex is photochromic and exhibits SO → PMC upon exposure to UV light; however, the photoresponsivity is quite low, and only ~5% of the molecules photoisomerize under experimental conditions in a toluene solution.

The Co(3,5-DTBQ)$_2$(APSO) complex displays ^{1}H NMR and UV/Vis/NIR features characteristic of typical Co(DTBQ)$_2$(NN) systems, although with some variation from the analogous Co–phen and Co–IPSO complexes. Amorphous powders were reproducibly isolated that displayed fairly consistent spectral features. The solid-state temperature-dependent magnetic behaviour showed a very gradual conversion from ls-Co^{III} at low temperature to hs-Co^{II} at higher temperature, with the onset of a more abrupt conversion at >300 K. The Co(3,5-DTBQ)$_2$(APSO) complex exhibits excellent photochromic properties with high photoresponsivity to visible light, which makes this material a good candidate for the application of ligand-driven light-induced redox isomerism (LD-LIRI).

For the Co(3,5-DTBQ)$_2$(IPSO) and Co(3,5-DTBQ)$_2$(APSO) complexes, an analysis of the hs-Co^{II} MLCT band, ls-Co^{III} IVCT band, and Cat^{2-}/SQ$^{-\bullet}$ bands in the IR fingerprint region as a function of SO/PMC isomerization reveals a correlation between the state of the photochromic spirooxazine ligand and the redox isomeric state of the Co(diox)$_2$ moiety. For both Co–IPSO and Co–APSO complexes, the observed correlations suggest that the SO form of the spirooxazine ligand preferentially stabilizes the hs-Co^{II} redox isomeric state. This behaviour is consistent with the theoretical model for ligand-driven light-induced redox isomerism (LD-LIRI) proposed for these systems. Here the effect of the ancillary ligand on relative ls-Co^{III}/hs-Co^{II} stabilization is correlated with ligand π-acceptor strength, and in the Co–spirooxazine systems, the stronger π-acceptor ability of the SO form would serve to stabilize the more electron rich hs-Co^{II} redox state. As expected from estimated T_c values, both Co–IPSO and Co–APSO complexes exist as an equilibrium of ls-Co^{III}/hs-Co^{II} species at room temperature, and therefore under these conditions, the complexes exist in an electronically bistable state such that perturbation with light can modulate the redox equilibrium. They therefore demonstrate the molecular

bistability illustrated in Figure 4.5, and meet theoretical requirements for room-temperature reversibly photoswitchable materials.

The Co–APSO tetramer was the only one of the three synthesized Co–dioxolene–spirooxazine complexes that could be isolated in a single-crystalline form (vs a microcrystalline powder in the case of the IPSO derivative). Its identity as a tetranuclear Co complex was confirmed through XRD analysis, in which its oxidation state at low temperature was identified as $Co^{II}_2Co^{III}_2$(3,5-DTBCatH)$_4$(3,5-DTBCat)$_2$(APSO)$_2$(MeO)$_2$·2MeOH. The complex exhibits distinct spectral features associated with the Co–dioxolene class of redox isomers, namely a strong hs-Co^{II} MLCT band in the visible region and a ls-Co^{III} IVCT band in the NIR region. The IVCT band displays substantial temperature dependence, as typically observed in Co–dioxolene redox isomeric materials, which suggests that the Co–APSO tetramer is indeed redox isomeric. The temperature-dependent behaviour of the magnetic moment does not show a clear redox transition: in both solid and solution states a very gradual increase in magnetic moment is observed with increasing temperature. However, the high temperature moment is higher than would be expected for the low-temperature redox state suggested by XRD analysis. This complex is interesting in its own right as it is the first multinuclear complex of this geometry to show redox isomerism. It also displays strong photoresponsivity comparable to the Co–APSO monomer. The combination of the ease of synthesis, rich spectral features, photochromism, and redox isomerism in this material make it a promising candidate for ligand-driven light-induced redox isomerism.

4.4. Experimental

4.4.1. Synthesis

General synthetic procedures. All reagents were purchased from commercial sources and used without further purification. Cyclohexane was dried over and distilled from P_2O_5, and degassed using freeze-pump-thaw cycles. Spectroscopic-grade, dry, and deoxygenated hexane, pentane, toluene, THF, and CH_2Cl_2 were acquired from an MBraun solvent purification system. The synthesis and purification procedures for all metal complexes were executed under the strict exclusion of air; manipulations were performed using standard Schlenk line techniques under $N_{2(g)}$ or $Ar_{(g)}$ or in an inert

atmosphere $Ar_{(g)}$ glovebox. ^{1}H NMR spectra were acquired with Bruker AC300, AVANCE360, or AVANCE500 spectrometers, and spectra were calibrated to the solvent residual peaks.[283] FT-IR spectra were acquired with a Perkin Elmer Spectrum One spectrometer, and electronic absorption UV/Vis/NIR spectra were acquired with Agilent 8453 and PE Lambda 1050 spectrophotometers. Elemental analyses were performed by Desert Analytics, Columbia Analytical Servies (formerly Desert Analytics), Canadian Microanalytical Services, and the University of British Columbia. Details for mass spectrometry measurements are given in Section 4.4.4. APSO and IPSO were prepared as described in Chapter 2. Both $[Co(3,5\text{-}DTBSQ)_2]_4$[363] and $Co(3,5\text{-}DTBQ)_2(phen)\cdot C_6H_5CH_3$[345] were prepared according to literature methods using toluene as the solvent.

Co(3,5-DTBQ)$_2$(IPSO). $[Co(3,5\text{-}DTBSQ)_2]_4$ (108 mg, 0.0540 mol, 1.00 equiv.) was stirred in dry THF (15 mL) for 1.5 h, whereupon the solution changed from a dark green suspension to a blue-green solution. To this was added a solution of IPSO (81.9 mg, 0.215 mol, 3.98 equiv.) in THF (7 mL) to give a blue solution which was stirred for 3 h before removing the solvent in vacuo and redissolving the solid in cyclohexane. After allowing the material to recrystallize over the course of a number of weeks under an inert atmosphere, a dark green solid was recovered and washed with pentane in a yield of 25%. This compound was observed to be quite sensitive to decomposition through exposure to O_2 in solution, as evidenced by ^{1}H NMR and electronic absorption spectroscopy, but stable in the solid state. Anal. Calcd for $C_{52}H_{60}CoN_4O_5$: C, 70.97; H, 6.87; N, 6.37. Found: C, 70.85; H, 7.04, N, 5.99 (average of a duplicate analysis). ESI-MS: *m*/*z* (%) 1039 (100) $[Co(3,5\text{-}DTBQ)(IPSO)_2]^+$, 243 (50) $[DTBQ + Na]^+$. ^{1}H NMR (500 MHz, toluene-d_8) tentative assignment of SO form: δ 99.5 (br s, 1H, phen), 97.7 (br s, 1H, phen), 35.9 (br s, 1H, phen), 33.3 (br s, 1H, phen), 14.2 (br s, 18H, *t*-butyl), 13.0 (br s, 1H, phen), 12.2 (br s, 1H, phen), 7.98 (s, 1H), 6.94 (td, J = 6.9, 1.5 Hz, 1H), 6.69 (dd, J = 7.3, 1.4 Hz, 1H), 6.66 (br t, J = 7.1 Hz, 1H), 6.19 (d, 7.9 Hz, 1H), 2.33 (s, 3H, CH_3), 1.7 (br s, 18H, *t*-butyl), 0.99 (s, 3H, CH_3), 0.96 (s, 3H, CH_3); of PMC form: δ 35.4 (br s, 1H, phen), 32.1 (br s, 1H, phen), 13.3 (br s, 1H, phen), 12.4 (br s, 1H, phen) [or 12.3 (br s, 1H, phen)], 9.33 (s, 1H), 2.83 (s, 3H, CH_3), 1.57 (s, 3H, CH_3). FT-IR (KBr): $\boldsymbol{\nu}$ 3055 (w), 2959 (vs), 2904 (s), 2865 (s), 1602 (w), 1578 (s), 1559 (w), 1514 (m), 1468 (vs), 1458

(vs), 1444 (vs), 1423 (s), 1413 (m), 1385 (m), 1366 (m), 1359 (w), 1353 (s), 1341 (w), 1332 (w), 1288 (w), 1261 (w), 1245 (s), 1220 (w), 1204 (m), 1143 (w), 1094 (m), 1045 (w), 1028 (m), 1022 (m), 985 (s), 931 (w), 906 (m), 860 (m), 855 (m), 846 (vs), 825 (m), 801 (w), 786 (m), 775 (m), 744 (w), 728 (vs), 696 (m), 673 (w), 653 (m), 640 (m), 602 (w), 570 (w), 539 (w), 494 (w), 467 (m) cm^{-1}.

Co(3,5-DTBQ)$_2$(APSO). [Co(3,5-DTBSQ)$_2$]$_4$ (107 mg, 0.0535 mmol, 1.00 equiv.) was stirred in dry THF (10 mL) for 0.5 h. To this was added a solution of APSO (82.4 mg, 0.214 mmol, 4.01 equiv.) in THF (10 mL). The mixture was stirred for 1 h, before removing the solvent in vacuo. The crude product was then brought into toluene (~10 mL), filtered through a filter stick to remove undissolved solid, and precipitated with pentane (~20 mL). The solid was collected on a filter stick and rinsed with pentane, and a bright purple powder was collected (120 mg, 63% yield). Anal. Calcd for $C_{52}H_{64}CoN_4O_5$: C, 70.65; H, 7.30; Co, 6.67; N, 6.34. Found: C, 66.92 (±1.89); H, 6.70 (±0.24); Co, 6.26 (±0.42); N, 6.92 (±0.35) (average of ten analyses on different samples). ESI-MS: *m*/*z* (%) 1051 (90) [Co(3,5-DTBQ)(APSO)$_2$ + 4H]$^+$, 244 (100) [DTBQ + Na]$^+$. ESI-MS, MALDI: *m*/*z* 1047 [Co(3,5-DTBQ)(APSO)$_2$]$^+$. FT-IR (KBr): ***ν*** 2952 (vs), 2915 (vs), 2870 (m), 1606 (m), 1580 (m), 1556 (m), 1475 (s, sh), 1462 (s, sh), 1455 (vs), 1426 (s), 1414 (s), 1385 (m), 1356 (s), 1349 (s), 1325 (m), 1317 (m), 1280 (w), 1242 (m), 1226 (vs), 1124 (vs), 1100 (vs), 1089 (s), 1063 (m), 1037 (m), 1014 (m), 1001 (w), 984 (w), 957 (m), 947 (w), 906 (w), 884 (w), 859 (w), 840 (vw), 826 (vw), 811 (vw), 788 (w), 746 (m), 732 (w), 705 (vw), 695 (vw), 602 (w) cm^{-1}.

Co$_4$(3,5-DTBQH)$_4$(3,5-DTBQ)$_2$(APSO)$_2$(MeO)$_2$·2MeOH. To a stirring MeOH (15 mL) solution of APSO (77.3 mg, 0.201 mmol, 1.00 equiv.) and DBBQ (132.9 mg, 0.603 mmol, 3.00 equiv.), was added a MeOH (10 mL) solution of $Co_2(CO)_8$ (68.9 mg, 0.201 mmol, 1.00 equiv.). The solution was stirred in a sealed Schlenk flask under N_2 in the absence of light for 1.5 h, before placing the flask in a vibration-free dark location. After ~48 h, the product was filtered and washed with MeOH, and a dark purple crystalline material was isolated (42 mg, 10% yield). Anal. Calcd for $C_{134}H_{178}Co_4N_8O_{16}$·2$CH_3OH$: C, 66.49; H, 7.63; N, 4.56. Found: C, 64.32; H, 7.16, N, 4.64 (average of two determinations for two samples). FT-IR (KBr): ***ν*** 3442 (s, br), 3074 (w), 2952 (s), 2909 (s), 2869 (m), 1747 (w), 1714 (w) 1608 (m), 1580 (m), 1556 (m),

1478 (s), 1454 (s), 1446 (s), 1416 (s), 1388 (w), 1357 (s), 1350 (s), 1326 (m), 1316 (m), 1306 (m), 1260 (m, sh), 1244 (m), 1227 (s), 1127 (s), 1101 (s), 1088 (m), 1066 (m), 1037 (m), 1015 (m), 2000 (w), 984 (m), 957 (m), 946 (w), 908 (w), 884 (w), 827 (w), 809 (w), 745 (m), 732 (m), 659 (w), 653 (w) cm^{-1}.

4.4.2. PXRD Analysis

PXRD data were acquired with a Rigaku Miniflex Diffractometer at ambient temperature (~300 K). Cr radiation was used at 30 kV and 15 mA with a V Kβ filter, a 4.2° scattering slit, and a 0.3 mm receiving slit. Data were acquired in FT mode, with a step width of 0.01° and a count time of 10.0 s per step between 3 or 4 to 35° (2θ). (Preliminary scans did not show any significant peaks above this value.) Samples were prepared in two ways. If only a small amount of material was available, they were prepared by suspending a small amount of powder in a minimal amount of Et_2O and dropcasting a thin film of material onto a glass microscope slide. The remaining samples were prepared by filling an indented silicon zero-background holder with powder.

4.4.3. Single-Crystal X-Ray Crystallographic Analysis

A purple needle crystal of $C_{134}H_{178}Co_4N_8O_{16}{\cdot}2CH_3OH$ having approximate dimensions of 0.09 × 0.12 × 0.45 mm^3 was mounted on a glass fiber. All measurements were made on a Bruker APEX DUO diffractometer with graphite monochromated Mo-Kα radiation.

The data were collected at a temperature of –183.0 ± 0.1 °C to a maximum 2θ value of 45.0°. Data were collected in a series of φ and ω scans in 0.5° oscillations with 20.0-second exposures. The crystal-to-detector distance was 40.00 mm.

Of the 41004 reflections that were collected, 5418 were unique (R_{int} = 0.052); equivalent reflections were merged. Data were collected and integrated using the Bruker SAINT[381] software package. The linear absorption coefficient, μ, for Mo-Kα radiation is 4.60 cm^{-1}. Data were corrected for absorption effects using the multi-scan technique (SADABS),[329] with minimum and maximum transmission coefficients of 0.825 and 0.959, respectively. The data were corrected for Lorentz and polarization effects.

The structure was solved by direct methods.[286] The material crystallizes in space group *C*2/*m*, with one-quarter molecule in the asymmetric unit. The molecule is completed by rotation about a two-fold axis and reflection across a mirror plane. Since the molecule

does not possess mirror symmetry this results in disorder across the mirror plane. All non-hydrogen atoms except C(41) and C(42) were refined anisotropically. The OH hydrogen H(30) was located in a difference map and refined isotropically. All other hydrogen atoms were placed in calculated positions. The final cycle of full-matrix least-squares refinement [least-squares function minimized: $\Sigma w(F_o^2 - F_c^2)^2$] on F^2 was based on 5418 reflections and 596 variable parameters and converged (largest parameter shift was 0.00 times its esd) with unweighted and weighted agreement factors of:

$$R_1 = \Sigma||F_o| - |F_c|| / \Sigma|F_o| = 0.116$$

$$wR_2 = [\Sigma(w(F_o^2 - F_c^2)^2) / \Sigma w(F_o^2)^2]1/2 = 0.300$$

The standard deviation of an observation of unit weight $\{[\Sigma w(F_o^2 - F_c^2)^2/N_o - N_v)]^{1/2}$, where N_o = number of observations and N_v = number of variables} was 1.12. The weighting scheme was based on counting statistics. The maximum and minimum peaks on the final difference Fourier map corresponded to 1.04 and –0.56 $e^-/Å^3$, respectively.

Neutral atom scattering factors were taken from Cromer and Waber.[330] Anomalous dispersion effects were included in F_{calc};[331] the values for $\Delta f'$ and $\Delta f''$ were those of Creagh and McAuley.[332] The values for the mass attenuation coefficients are those of Creagh and Hubbell.[333] All refinements were performed using the SHELXL-97[334] via the WinGX[382] interface.

4.4.4. Spectroscopic Methods

Mass Spectrometry (UVic). Mass spectra were acquired with a Q-Tof2 ESI hybrid quadrupole time-of-flight mass spectrometer with the following settings: MCP voltage – 2800 V, capillary voltage – 3 kV, cone voltage – 20 V, source temp. – 80 °C, desolvation temp. 250 °C. Samples were dissolved in CH_2Cl_2 and diluted with CH_3OH.

Mass Spectrometry (UBC). The ESI mass spectrum of Co(3,5-DTBQ)$_2$(APSO) was obtained on a Water/Micromass LCT time-of-flight mass spectrometer equipped with an electrospray ion source. The sample was dissolved in dichloromethane and diluted with methanol. The working solution concentration was about 25 to 50 µM. The sample

solution was infused to the LCT at a flow rate of 20 μL/min. MALDI was performed on Co(3,5-DTBQ)$_2$(APSO) with DCTB as a matrix. The EI mass spectrum of APSO was obtained using a double-focusing Kratos MS-50 mass spectrometer coupled with a MASPEC data system. The sample was introduced using a direct insertion probe. Operation conditions: source *T* – 150 °C, ionization energy – 70 eV.

Diffuse Reflectance Spectroscopy. Spectra of Co(3,5-DTBQ)$_2$(IPSO) and Co(3,5-DTBQ)$_2$(APSO) were acquired with a Cary 100 spectrometer equipped with an integrating sphere. The sample was prepared by grinding 1.1% of sample in $BaSO_4$ and loading this into a quartz sample cell. The spectrum was corrected with a blank $BaSO_4$ background.

Variable-Temperature Electronic Absorption Spectroscopy. Solution-state variable-temperature UV/Vis experiments for Co(3,5-DTBQ)$_2$(IPSO) and Co(3,5-DTBQ)$_2$(APSO) were performed with an Agilent 8453 spectrophotometer. Solutions (10^{-5} M) were prepared in spectroscopic-grade deoxygenated toluene acquired from an MBraun solvent purification system and were transferred to a long-stemmed quartz cuvette sealed under N_2 with a septum. The cuvettes were then immersed in a quartz dewar filled with spectroscopic-grade acetone. A spectrum was acquired at 300 K before cooling the acetone solution to 196 K with dry ice, removing water condensation from the outside of the dewar with acetone, and quickly acquiring a low-temperature spectrum. A final spectrum was acquired after warming the solution to near room temperature. It was not possible to acquire spectra at intermediate temperatures as the thawing of the dry ice released gas bubbles which created excessive spectral noise. Attempts at reproducing these results using the Oxford cryostat (vide infra) were unsuccessful due to difficulties in correcting for temperature-dependent background effects in the solution state.

Solid-state VT Vis/NIR electronic absorption spectroscopy experiments were performed on thin films of the Co complexes with a Perkin Elmer (PE) Lambda 1050 spectrophotometer using a standard scan method. Thin films were dropcast onto infrasil quartz discs (17 mm diameter, 1 mm thick) from concentrated CH_2Cl_2 (spectroscopic grade) solutions and allowed to air dry. Temperature control was achieved using an Oxford OptistatCF continuous flow static exchange gas cryostat system fitted with inner

sapphire windows (for high-temperature VT capabilities) and middle and outer infrasil quartz windows (for a reasonably clear spectral window between 300–3300 nm). Background corrections were performed by correcting for a blank spectrum of the cryostat containing a blank infrasil quartz disc at room temperature. VT experiments were typically performed by acquiring a spectrum at 300 K, cooling the cryostat to 80 K with liquid nitrogen, and acquiring spectra while heating the cryostat sample chamber in increments. The sample chamber was allowed to equilibrate for ~20–30 min after attaining the desired temperature before acquiring each spectrum.

UV/Vis Irradiation Experiments. Irradiation experiments were performed with a Agilent 8453 spectrophotometer. Sample solutions were prepared in spectroscopic-grade solvents under N_2 and transferred to 1 cm × 1 cm quartz cuvettes. Care was taken to avoid oxygen exposure of the samples by either passing a stream of N_2 over the cuvette during the experiment or using air-tight cuvettes. Solutions were continuously stirred using micro (1 × 6 mm) stir bars or specially designed round cuvette stir bars. Continuous multiline UV (λ_{ex} = 333.6–363.8 nm) or single-line visible (514, 532, or 568 nm) irradiation (30–150 mW) was generated using a Spectra-Physics Stabilite 2018 mixed-gas Ar–Kr ion laser and directed through the sample cuvette perpendicularly to the sampling beam with a liquid light guide. For samples sensitive to UV-induced decomposition, a cuvette of acetone was placed between the sample and sampling beam to block irradiation from the spectrometer in the near-UV region (<300 nm). The rates of thermal return were determined in the absence of light after generating a photostationary state by following the absorbance kinetics at the PMC π–π^* λ_{max} and fitting A_∞–A_t or A_t–A_∞ (where A_t represents the absorbance at a given time, t, and A_∞ represents the absorbance at the photostationary state, or a close approximation thereof) to both first-order monoexponential ($A = A_o e^{kt}$, where A_o is the initial absorbance) and biexponential rate ($A = A_o e^{kt} + B_o e^{k't}$) functions by linear least-squares methods. The observed rate constants, k_{obs}, were then taken as the negative of the resulting value for k. See Appendix C for rate fitting plots.

FT-IR/NIR Irradiation Experiments. Saturated solutions of the complexes were prepared under nitrogen or argon gas in deoxygenated spectroscopic-grade toluene from an MBraun solvent purification system or CCl_4 (washed with $NaOH_{(aq)}$ then water,

passed through a silica gel plug, dried over $MgSO_4$, distilled from P_2O_5, and freeze-pump-thawed). Solutions were briefly transferred in air before filtering into an IR solution cell fitted with windows transparent in the IR/NIR region (>1000 cm^{-1}). Spectra were acquired with a Perkin Elmer Spectrum One spectrometer. Irradiation experiments were performed using the same laser setup as described in the previous section, but with the laser beam directed onto a focused spot (~1 cm^2) of the solution cell in between FT-IR scans.

4.4.5. Solution-State Magnetic Measurements – Evan's Method

The Evan's method experiment was performed in CD_2Cl_2 for Co(3,5-DTBQ)$_2$(phen), Co(3,5-DTBQ)$_2$(IPSO), and Co(3,5-DTBQ)$_2$(APSO) for solubility reasons in order to precisely determine solution concentrations. The experiment was performed in toluene-d_8 for Co_4(3,5-DTBQ)$_6$(APSO)$_2$(MeO)$_2$·2MeOH. CD_2Cl_2 was obtained from ampules and toluene-d_8 was deoxygenated using the freeze-pump-thaw method. In at inert atmosphere argon glovebox, 5–10 mg of the complexes were dissolved in 1.00 mL of solvent, and the solutions were transferred into 5-mm NMR tubes fitted with a coaxial insert tube filled with pure deuterated solvent. The tubes were capped and sealed with parafilm. ^{1}H NMR spectra were acquired with a Bruker AVANCE360 NMR spectrometer between 200 and 300 K for CD_2Cl_2 solutions or 200 and 350 K for toluene-d_8 solutions. Evan's method was used to determine the solution-state magnetic susceptibility of the samples by monitoring the frequency shift of the $CDHCl_2$ or $C_6D_5CD_2H$ proton resonance. The gram magnetic susceptibility of the samples, χ_g, was calculated with Equation 4.2,[383-385]

$$\chi_g = -\frac{3\Delta\nu}{4\pi m\nu} + \chi_{g0} + \chi_{g0}\frac{\rho_0 - \rho_s}{m} \tag{4.2}$$

where $\Delta\nu$ (Hz) is the shift between the resonances for the solvent-containing solute and the reference solvent, ν (Hz) is the operating frequency of the NMR spectrometer, m is the mass (g) of paramagnetic solute in 1.00 mL of solvent, χ_{g0} is the gram magnetic susceptibility of the solvent, ρ_0 is the density of the pure solvent, and ρ_s is the density of the solvent-containing solute. The m term was corrected for the change in solvent density at each temperature.[386] The temperature-dependent density of the solvents was

approximated by applying the very nearly linear behaviour of the density in the temperature range of interest[387] to the known solvent densities at 298 K (CD_2Cl_2 = 1.362 g/mL, toluene-d_8 = 0.943 g/mL). The second and third terms in Equation 4.2 were neglected.[388] The molar susceptibilities, χ_M, were calculated from the χ_g values and were subsequently corrected for the diamagnetic contribution of the complex, χ_d (same as those used for the solid-state magnetic measurements, vide infra, Section 4.4.6), to obtain the paramagnetic contribution to the magnetic moment, $\chi_M T$.

4.4.6. Solid-State Magnetic Measurements

DC-SQUID measurements were obtained with a Quantum Design Magnetic Property Measurement System at a field of 10000 Oe. Powder samples of ~10–15 mg were weighed into gelules, sealed with Kapton tape, and inserted into straw tubes. The diamagnetic moments of the samples were calculated using Pascal's constants for atomic diamagnetic contributions to get correction values of -5.159×10^{-4} emu·K·mol^{-1} for Co^{II}(3,5-DTBQ)$_2$(IPSO), -5.277×10^{-4} emu·K·mol^{-1} for Co^{II}(3,5-DTBQ)$_2$(APSO), and -1.453×10^{-3} emu·K·mol^{-1} for Co^{II}_4(3,5-DTBQH)$_4$(3,5-DTBQ)$_2$(APSO)$_2$(MeO)$_2$·2MeOH. For Co^{II}(3,5-DTBQ)$_2$(phen)·$C_6H_5CH_3$, the diamagnetic correction from Pascal's constants was -4.604×10^{-4} emu·K·mol^{-1}, however the diamagnetic corrected obtained by the slope method (-1.1106×10^{-3} emu·K·mol^{-1}) was approximately twice the magnitude and gave much nicer data so was therefore used in the data workup. The diamagnetic correction for the gelule and insertion tube is quite small, with a value of -2.4×10^{-7} emu·K·mol^{-1} and was therefore not included in the correction as it had a negligible contribution to the data.

Chapter 5. Conclusions and Future Work

Toward the goal of designing new photoswitchable multifunctional materials, this thesis has examined a class of phenanthroline–spirooxazine ligands and metal complexes thereof. Although photochromic ligands and coordinated metal ions may interact through a number of mechanisms, we were specifically focused on investigating the changes in ligand field strength occuring upon photoisomerization between spirooxazine (SO) and photomerocyanine (PMC) forms and exploiting these changes to modulate metal-based properties. The thesis convered three main studies: (1) an analysis of chemical substituent and medium effects on the ligands themselves; (2) an evaluation of the ligand field strengths of the phenanthroline–spirooxazine ligands; and (3) a study of coordination complexes combining the optically bistable photochromic ligand with a magnetically bistable metal centre designed in such a way that photoisomerization of the ligand was expected to modulate the redox state of the metal.

Chapter 2 presented a thorough study of substituent and medium effects on two phenanthroline–spiroxazine derivatives: spiro[indoline-phenanthrolinoxazine] (IPSO, **28**) and spiro[azahomoadamantyl-phenanthrolinoxazine] (APSO, **31**). The molecular structures of the PMC forms of both spirooxazines were elucidated to determine the relative contributions of the canonical quinoidal and zwitterionic resonance forms in different media. The azahomoadamantyl derivative, APSO, was found to be more zwitterionic than the indolyl derivative, IPSO. The zwitterionic character of APSO in the solid state was confirmed by X-ray diffraction analysis via an analysis of the degree of bond-length alternation throughout the conjugated bridge. The solution-state structures of the two derivatives were inferred through an analysis of the solvent-dependent vibrational profiles and solvatochromism of the PMC π–π^* CT band. Comparing the spectroscopy for the two compounds revealed that both derivatives exhibit a range of relative quinoidal and zwitterionic character, with more zwitterionic character in increasingly polar solvents, but with the APSO derivative displaying more zwitterionic character at any given polarity. X-ray analyses for photomerocyanines are extremely rare, so the study presented here not only allowed us to confirm the zwitterionic structure of the PMC form of APSO, but also allowed us to probe the effect of the crystalline lattice on the PMC

molecular structure. A comparison of two different crystal structures revealed that, in each lattice, the PMC has a different relative degree of zwitterionic character. Additionally, the high degree of zwitterionic character observed in the crystal structures suggested that the lattice behaves as a relatively strong dielectric upon comparison to the solution-state behaviour, where evidence of a zwitterionic structure was only observed in higher polarity solvents.

One of the most revealing aspects of this study was the observation of significant zwitterionic character in the azahomoadamantyl derivative relative to the indolyl derivative. In the literature, spiropyrans and spirooxazines that have been reported to possess a zwitterionic structure, based on either direct or indirect evidence, typically display similar properties such as a more stable PMC form and slower rates of thermal relaxation, as was observed for APSO. However, these zwitterionic spiropyrans and spirooxazines are also all derivatized with strong electron-withdrawing groups on the oxazine moiety. While the substitution of electron-donating groups on the amine moiety is expected to increase the zwitterionic character of spiropyrans and spirooxazines, this has not been observed in the literature for indolyl derivatives with, for example, methoxy substituents. Therefore, the strong electronic effect of the azahomoadamantyl group is quite unique. An obvious direction for future research would involve the synthesis of azahomoadamantyl spirooxazines that are also functionalized with strong EWGs on the oxazine moiety such as the methylated isoquinoline or nitro naphthalene derivatives **50** and **51**. The combined effects of the electron-donating and electron-withdrawing substituents could lead to spirooxazines with unprecedented properties such as extremely stable PMC forms and extremely slow rates of thermal relaxation.

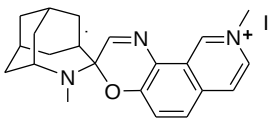

50

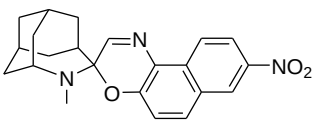

51

In general, azahomoadamantyl spirooxazine derivatives as a class exhibit an intriguing set of photochromic properties, but these compounds have been insufficiently studied in comparison to the indolyl derivatives that have been studied in depth over the last several

decades. The investigation of photochemical and photophysical mechanisms and parameters through transient absorption studies and computations should prove very useful. Because the azahomoadamantyl derivativatization of spirooxazines has been shown to lead to solid-state photochromism,[217] this class of molecules should also be studied more thoroughly in the solid state and other constrained matrices. The synthesis and characterization of a series of azahomoadamantyl spirooxazine derivatives could prove valuable toward generalizing spirooxazine structure–property relationships and developing novel materials for switching applications.

A final critical problem that remains to be solved regarding the azahomoadamantyl spirooxazine derivatives concerns the UV-induced decomposition process that occurs in the phenanthroline derivative but not in other derivatives such as the quinoline and isoquinoline analogs. Solving this problem is particularly important if APSO is to be used in coordination complexes for reversible photoswitching applications.

Questions regarding the molecular structure of merocyanines and how it is affected by medium still remain, as evidenced by the ongoing studies in this field. The study described here provides a piece of the puzzle, which will be particularly relevant to spirooxazine-based photomerocyanines. However, questions still remain to be unambiguously answered. In the case of merocyanines in general: How do the solvatochromism and solvent-dependent vibrational profile directly correlate to the true molecular structure? What specific solvent interactions play a role? How can the inconsistencies between computational and experimental results be rectified? In the case of spiroxazines specifically: Is it best to represent the PMC form as a combination of the canonical resonance forms as **A** and **B** (Scheme 2.1) or is there a more accurate representation? What correlations can be drawn between the relative degrees of quinoidal and zwitterionic character and photochromic parameters? What structure–property relationships can ultimately be drawn? And what role does the medium play? Surely the opportunity to study more spirooxazine PMC crystal structures based on the more easily crystallizable azahomoadamantyl derivatives, in combination with spectroscopic studies, could prove to be enlightening in making further progress on this topic.

In Chapter 3, the phenanthroline–spirooxazine ligands APSO and IPSO were again examined from a fundamental perspective, but this time in the context of the metal–

ligand bonding interactions and ultimately ligand field strengths of the SO and PMC photoisomers. Empirically, the spectroscopic analysis of the carbonyl signals of molybdenum–tetracarbonyl–spirooxazine complexes by ^{13}C NMR and FT-IR methods showed that the SO form is a better π-acceptor than the PMC form. Theoretically, the SO and PMC forms were shown to have very different frontier molecular orbitals, although those for APSO and IPSO were quite similar to each other. In terms of the metal–ligand π-backbonding interaction, it was found that the predominant bonding pathway is via the pseudo-b_1-symmetry phen(π^*) LUMO + 1 of the ligand and the b_1-symmetry d_{xz} MO of the metal. Because the LUMO + 1 of the SO form is 0.2–0.3 eV lower in energy than that of the PMC form, the SO form is expected to be a stronger π-acceptor.

Unfortunately, of the low-lying MOs in the phenanthroline–spirooxazine derivatives, the b_1-symmetry phen(π^*) MO is actually the least perturbed by spirooxazine derivatization as it has minimal electron density at the 5- and 6-positions of functionalization. This suggests that a future direction of work could be the synthesis and characterization of phenanthroline–spirooxazine derivatives functionalized at positions of greater phen(b_1, π^*) electron density, such as at the 2,3- or 3,4-positions. The possibility of unsymmetrical phenanthroline derivatization leads to both mono-spirooxazine-substituted and bis-spirooxazine-subsituted phenanthroline ligands being synthetic targets. A preliminary DFT MO analysis of spirooxazines **42**–**45** suggests that the bonding phen(π^*) MOs are more perturbed and show greater spirooxazine character when derivatized at these alternative positions. In addition, the LUMO of the PMC form has both phen(b_1) and spirooxazine character (in contrast to the 5,6-spirooxazine-substituted derivative in which it has only spirooxazine character) and therefore may show significant mixing with the metal upon coordination. This would imply that for the proposed phenanthroline-spirooxazine targets **42**–**45**, the PMC form may in fact be the better π-acceptor. Having a series of derivatives in which either the SO form or the PMC form is a stronger π-acceptor would add flexibility to the applications of phenanthroline—spirooxazine ligands for ligand field switching in bistable metal complexes. It remains to be determined whether the proposed derivatives are synthetically accessible, how their ligand field strength measures up empirically [which can be determined via spectroscopic analysis of their $Mo(CO)_4(NN)$ complexes], and

how they behave photochromically. The bis-substituted derivatives are particularly interesting as they may show greater changes in ligand field, but may also show more complicated photochromic behaviour as they can exist in a greater number of photochromic states. It may be valuable to analyze the photochromic mechanism of these derivatives from a computational angle[389] before embarking on a potentially challenging synthetic excursion.

In addition to the spirooxazine derivatives studied here, other classes of photochromic ligands may be of interest in the context of ligand field switching. As a first step, one can look to the recent literature for inspiration, wherein a plethora of photochromic ligands have been reported. Many of these are not expected to show significant changes in ligand field upon photoisomerization. However, several photochromic systems could be of interest in this regard, such as the azobenzene derivative **52**[167] or the terarylene derivative **53**.[183] It could be valuable to more rigorously evaluate the ligand field changes in these systems through a combination of DFT MO calculations and molybdenum–carbonyl spectroscopic studies in order to evaluate their potential for switching the properties of coordinated metals via changes in ligand field strength.

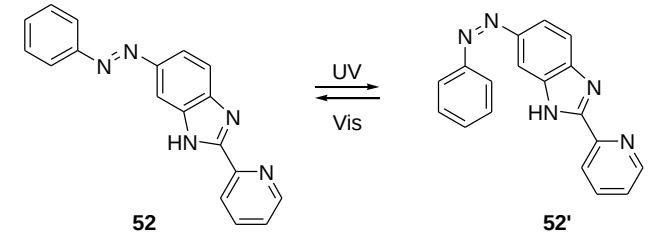

52 **52'**

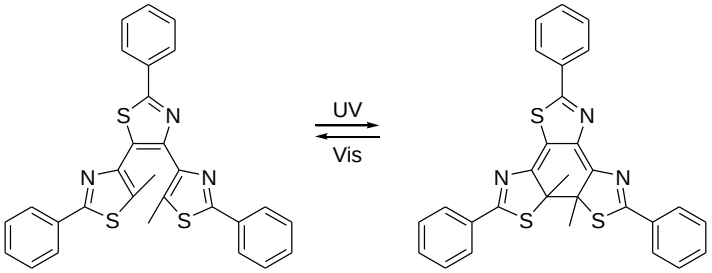

53 **53'**

Finally, the study of the molybdenum–tetracarbonyl–spirooxazine complexes described here raises further questions regarding the effects of metal complexation on spirooxazine

photochromic properties. Explicitly: Why does metal complexation have different effects on APSO and IPSO? What is the difference between the effects of second row metals vs first row metals? Such questions can be investigated through a more systematic analysis of the photochemical and photophysical properties of APSO metal complexes. An interesting observation that emerged from this study was the ^{1}H NMR evidence for multiple PMC isomers of $Mo(CO)_4$(APSO) in DMSO-d_6. Pursuing this result experimentally through variable-temperature and NOESY NMR spectroscopy and variable-temperature kinetic studies to determine thermodynamic and kinetic parameters, in combination with DFT energy calculations for the ground and excited states of the different possible isomers, could lead to greater insight as regards the thermodynamics and kinetics of the isomers of APSO and metal complexes thereof, and how these relate to the indolyl class.

Chapter 4 described the synthesis of cobalt–dioxolene–spirooxazine complexes in which an optically bistable photochromic ligand is coupled to a magnetically bistable cobalt redox isomer. The complexes exist in a four-state equilibrium, and, under most conditions, exist as a mixture of multiple states. The Co–spirooxazine complexes exhibited a series of spectroscopic and magnetic features associated with the Co–dioxolene class of compounds. Both thermal and optical stimuli could be used to perturb the redox isomeric and photochromic equilibria, which could be monitored spectroscopically or magnetically. Because the SO and PMC forms of the photochromic spirooxazine ligand were found to have different π-acceptor strengths, it was predicted that they would preferentially stabilize one cobalt redox state over the other. On the basis of empirical trends from the literature, it was predicted that the SO form, being the better π-acceptor, would better stabilize the Co^{II} form, and that the transition temperature, T_c, between ls-Co^{III} and hs-Co^{II} states would be at approximately room temperature for these spirooxazine complexes. Analysis of the spectroscopic features as a function of irradiation and SO/PMC photoisomerization demonstrated that at room temperature, the photochromic and redox states are coupled and that stabilization of the SO form leads to stabilization of the hs-Co^{II} form. These complexes therefore fulfill the requirements for a room-temperature photoswitchable coordination complex in which the properties of the metal can be reversibly modulated using two different wavelengths of light.

As these systems are quite complicated and some of their fundamental electronic properties are still not well understood (e.g., the nature of the ls-Co^{III} IVCT transition), it could be worthwhile to expand on the work of Adams, Hendrickson, and Noodleman from 1997[354] and subsequent theoretical studies and rigorously calculate the electronic properties of the system. In particular it would be useful to absolutely assign spectral features and, for the spirooxazine complexes, to get a thorough handle on the metal–ligand bonding interactions in the SO and PMC forms. The next major hurdle is the study of photoinduced changes in magnetic state in the solid state. Photoinduced magnetic effects can be studied in the SQUID magnetometer. In terms of photoinduced magnetic effects (vs photoinduced changes in redox state), it would be relevant to distinguish contributions from the change in redox state upon SO/PMC isomerization from contributions from changes in spin–orbit coupling (SOC) arising from changes in ligand symmetry. This could be better understood by studying control spirooxazine Co^{II} complexes that are not expected to be redox isomeric. Corroboration of the photoinduced changes in redox state should also be accomplished with other experiments, including diffuse reflectance spectroscopy to monitor electronic absorption bands in the solid state, and X-ray absorption spectroscopy (XAS) or photoemission spectroscopy (PES) to rigorously probe the metal oxidation state as a function of irradiation. As XAS is a bulk technique and PES is a surface-sensitive technique, the latter may be more useful for investigating surface irradiation effects in the solid samples.

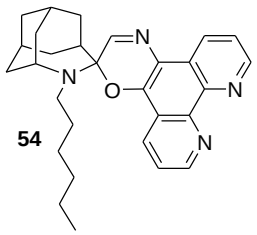

54

It may also be useful to explore synthetic variations on these complexes to potentially obtain materials that are more crystalline and/or easier to isolate. Because the switching properties of Co–dioxolene redox isomers are so dependent on intermolecular interactions, this could have a dramatic effect on material properties. Some straightforward synthetic modifications could include the synthesis of complexes

containing spirooxazines with long alkyl chains (e.g., derivative **54**) in order to possibly improve solid-state cooperativity interactions or the use of 3,6-di-*tert*-butyl-*ortho*-quinone ligands, as these may inhibit the formation of oligomers, possibly making the crystallization of mononuclear complexes easier.

On a big-picture level, other applications of the ligand field switching mechanism in phenanthroline–spirooxazine coordination complexes could include coordination to Fe spin-crossover systems to effectively control LD-LISC. Further, these ligands likely show a change in local ligand field symmetry, and one could apply such a change to the photoswitching of luminescence in lanthanide complexes or of magnetism in complexes sensitive to the degree of SOC (e.g., hs-Co^{II}). It could also be of interest to further investigate how spirooxazines behave as bridging ligands to see if they can mediate electron/energy transfer by a change in conjugation in the same fashion as the DTEs.

In the introduction, applications for photoswitchable molecular materials were discussed in the context of optical data storage, optically controlled electronics, molecular machines, and functional surfaces. The majority of these applications are longer-term prospects. For most of these, bridging the gap between the current state-of-the-art and eventual technologies is mainly a function of improving auxiliary technologies (e.g., photonic technologies for optical data storage or optically controlled electronics) or fundamental knowledge (e.g., accessing single molecules for molecular electronics) moreso than available materials. Because the direction of future technological progress is relatively uncertain, it makes sense to place the study of fundamental properties of molecular systems on an equal playing field as the synthesis and characterization of novel molecular systems. In the spirooxazine–metal complexes described here, many fundamental photochemical and photophysical pathways need to be understood for both the photochromic ligands and the photochromic metal complexes. The metal–ligand interaction mechanisms can be more thoroughly fleshed out; for example, it would be relevant to analyze the relative effect of ligand field symmetry changes in the phenanthroline–spirooxazine ligands. Another crucial direction will be to focus on analysis in the crystalline state or other solid matrices, as this will be the medium for many possible applications. Along this same line of thought, it will be useful to develop ways to arrange these molecules on surfaces or in periodic materials, be this

via self-assembly processes, the formation of homogeneous nanocrystals, or other methods. A focus on these key fundamental directions will advance the goal of integrating synthetically tunable molecular materials into functional devices.

Bibliography

1. Kahn, O.; Launay, J. P., Molecular bistability; an overview. *Chemtronics* **1988**, *3*, 140−151.

2. Dowben, P. A.; Miller, A., *Surface Segregation Phenomena*. CRC Press: Boston, 1990; p 440.

3. Balzani, V.; Credi, A.; Venturi, M., The bottom-up approach to molecular-level devices and machines. *Chem. Eur. J.* **2002**, *8*, 5524–5532.

4. Kirchain, R.; Kimerling, L., A roadmap for nanophotonics. *Nature Photon.* **2007**, *1*, 303–305.

5. Jenkins, A., The road to nanophotonics. *Nature Photon.* **2008**, *2*, 258−260.

6. John, S., Light control at will. *Nature* **2009**, *460*, 337−337.

7. Cai, W.; Brongersma, M. L., Plasmonics gets transformed. *Nature Nanotech.* **2010**, *5*, 485−486.

8. Brongersma, M. L.; Shalaev, V. M., The Case for Plasmonics. *Science* **2010**, *328*, 440−441.

9. Lal, S.; Link, S.; Halas, N. J., Nano-optics from sensing to waveguiding. *Nature Photon.* **2007**, *1*, 641−648.

10. Caulfield, H. J.; Dolev, S., Why future supercomputing requires optics. *Nature Photon.* **2010**, *4*, 261−263.

11. Caulfield, H. J., Perspectives in optical computing. *Computer* **1998**, *31*, 22–25.

12. Mitkas, P. A.; Betzos, G. A.; Irakliotis, L. J., Optical processing paradigms for electronic computers. *Computer* **1998**, *31*, 45−51.

13. Moore, G. E., Cramming more components onto integrated circuits. *Electronics* **1965**, *38*, 114−117.

14. Moore, G. E., Progress in digital integrated electronics. *Digest of the 1975 International Electron Devices Meeting* **1975**, 11−13.

15. Carroll, R. L.; Gorman, C. B., The genesis of molecular electronics. *Angew. Chem. Int. Ed.* **2002**, *41*, 4379–4400.

16. Balzani, V.; Credi, A.; Venturi, M., Processing energy and signals by molecular and supramolecular systems. *Chem. Eur. J.* **2008**, *14*, 26–39.

17. Mirkin, C. A.; Ratner, M. A., Molecular Electronics. *Annu. Rev. Phys. Chem.* **1992**, *43*, 719–754.

18. Joachim, C.; Gimzewski, J. K.; Aviram, A., Electronics using hybrid-molecular and mono-molecular devices. *Nature* **2000**, *408*, 541–548.

19. Aviram, A.; Ratner, M. A., Molecular Rectifiers. *Chem. Phys. Lett.* **1974**, *29*, 277–283.

20. Mendes, P. M.; Flood, A. H.; Stoddart, J. F., Nanoelectronic devices from self-organized molecular switches. *Appl. Phys. A: Mater. Sci. Process.* **2005**, *80*, 1197–1209.

21. Jiang, G. Y.; Song, Y. L.; Guo, X. F.; Zhang, D. Q.; Zhu, D. B., Organic functional molecules towards information processing and high-density information storage. *Adv. Mater.* **2008**, *20*, 2888–2898.

22. Pease, A. R.; Jeppesen, J. O.; Stoddart, J. F.; Luo, Y.; Collier, C. P.; Heath, J. R., Switching devices based on interlocked molecules. *Acc. Chem. Res.* **2001**, *34*, 433–444.

23. Gust, D.; Moore, T. A.; Moore, A. L., Molecular switches controlled by light. *Chem. Commun.* **2006**, 1169–1178.

24. Zacharias, P.; Gather, M. C.; Köhnen, A.; Rehmann, N.; Meerholz, K., Photoprogrammable Organic Light-Emitting Diodes. *Angew. Chem. Int. Ed.* **2009**, *48*, 4038–4041.

25. Shen, Q.; Cao, Y.; Liu, S.; Steigerwald, M. L.; Guo, X. F., Conformation-Induced Electrostatic Gating of the Conduction of Spiropyran-Coated Organic Thin-Film Transistors. *J. Phys. Chem. C* **2009**, *113*, 10807–10812.

26. Namiki, K.; Sakamoto, A.; Murata, M.; Kume, S.; Nishihara, H., Reversible photochromism of a ferrocenylazobenzene monolayer controllable by a single green light source. *Chem. Commun.* **2007**, 4650–4652.

27. Milder, M. T. W.; Areephong, J.; Feringa, B. L.; Browne, W. R.; Herek, J. L., Photoswitchable molecular wires: From a sexithiophene to a dithienylethene and back. *Chem. Phys. Lett.* **2009**, *479*, 137–139.

28. de Silva, A. P.; McClenaghan, N. D., Molecular-scale logic gates. *Chem. Eur. J.* **2004**, *10*, 574-586.

29. Andréasson, J.; Pischel, U., Smart molecules at work – mimicking advanced logic operations. *Chem. Soc. Rev.* **2010**, *39*, 174–188.

30. Szacilowski, K., Digital information processing in molecular systems. *Chem. Rev.* **2008**, *108*, 3481–3548.

31. Browne, W. R.; Feringa, B. L., Light Switching of Molecules on Surfaces. *Annu. Rev. Phys. Chem.* **2009**, *60*, 407–428.

32. McCreery, R. L.; Bergren, A. J., Progress with Molecular Electronic Junctions: Meeting Experimental Challenges in Design and Fabrication. *Adv. Mater.* **2009**, *21*, 4303–4322.

33. Tour, J. M., Molecular electronics. Synthesis and testing of components. *Acc. Chem. Res.* **2000**, *33*, 791–804.

34. Haick, H.; Cahen, D., Contacting organic molecules by soft methods: Towards molecule-based electronic devices. *Acc. Chem. Res.* **2008**, *41*, 359–366.

35. Mustroph, H.; Stollenwerk, M.; Bressau, V., Current Developments in Optical Data Storage with Organic Dyes. *Angew. Chem. Int. Ed.* **2006**, *45*, 2016–2035.

36. van de Nes, A. S.; Braat, J. J. M.; Pereira, S. F., High-density optical data storage. *Rep. Prog. Phys.* **2006**, *69*, 2323–2363.

37. Dvornikov, A. S.; Liang, Y. C.; Rentzepis, P. A., Ultra-high-density non-destructive readout, rewritable molecular memory. *Res. Chem. Intermed.* **2004**, *30*, 545–561.

38. Dvornikov, A. S.; Walker, E. P.; Rentzepis, P. M., Two-Photon Three-Dimensional Optical Storage Memory. *J. Phys. Chem. A* **2009**, *113*, 13633–13644.

39. Cumpston, B. H.; Ananthavel, S. P.; Barlow, S.; Dyer, D. L.; Ehrlich, J. E.; Erskine, L. L.; Heikal, A. A.; Kuebler, S. M.; Lee, I. Y. S.; McCord-Maughon, D.; Qin, J. Q.; Rockel, H.; Rumi, M.; Wu, X.-L.; Marder, S. R.; Perry, J. W., Two-photon

polymerization initiators for three-dimensional optical data storage and microfabrication. *Nature* **1999**, *398*, 51–54.

40. Ashley, J.; Bernal, M.-P.; Burr, G. W.; Coufal, H.; Guenther, H.; Hoffnagle, J. A.; Jefferson, C. M.; Marcus, B.; Macfarlane, R. M.; Shelby, R. M.; Sincerbox, G. T., Holographic data storage. *IBM J. Res. Dev.* **2000**, *44*, 341–368.

41. Hesselink, L.; Orlov, S. S.; Bashaw, M. C., Holographic data storage systems. *Proc. IEEE* **2004**, *92*, 1231–1280.

42. Corredor, C. C.; Huang, Z.-L.; Belfield, K. D., Two-photon 3D optical data storage via fluorescence modulation of an efficient fluorene dye by a photochromic diarylethene. *Adv. Mater.* **2006**, *18*, 2910–2914.

43. Corredor, C. C.; Huang, Z.-L.; Belfield, K. D.; Morales, A. R.; Bondar, M. V., Photochromic polymer composites for two-photon 3D optical data storage. *Chem. Mater.* **2007**, *19*, 5165–5173.

44. Yesodha, S. K.; Pillai, C. K. S.; Tsutsumi, N., Stable polymeric materials for nonlinear optics: a review based on azobenzene systems. *Prog. Polym. Sci.* **2004**, *29*, 45–74.

45. Hampp, N., Bacteriorhodopsin as a photochromic retinal protein for optical memories. *Chem. Rev.* **2000**, *100*, 1755–1776.

46. Kawata, S.; Kawata, Y., Three-Dimensional Optical Data Storage Using Photochromic Materials. *Chem. Rev.* **2000**, *100*, 1777–1788.

47. Nagashima, S.; Murata, M.; Nishihara, H., A ferrocenylspiropyran that functions as a molecular photomemory with controllable depth. *Angew. Chem. Int. Ed.* **2006**, *45*, 4298–4301.

48. Freitas, R. F.; Wilcke, W. W., Storage-class memory: The next storage system technology. *IBM J. Res. Dev.* **2008**, *52*, 439–447.

49. Feynman, R. P., There's plenty of room at the bottom. *Caltech Engineering and Science* **1960**, *2*, 23–36.

50. Drexler, K. E., Molecular Engineering: An Approach to the Development of General Capabilities for Molecular Manipulation. *Proc. Natl. Acad. Sci. U. S. A.* **1981**, *78*, 5275–5278.

51. Drexler, K. E., *Nanosystems – Molecular Machinery, Manufacturing, and Computation*. John Wiley & Sons, Inc.: New York, 1992; p 556.

52. Drexler, K. E., *Engines of Creation*. Anchor Press: Garden City, New York, 1986; p 298.

53. *Productive Nanosystems – A Technology Roadmap*; Battelle Memorial Institute and Foresight Nanotech Institute: 2007.

54. Jones, R. A. L., *Soft Machines - Nanotechnology and Life*. Oxford University Press: New York, 2004; p 238.

55. Feringa, B. L., In control of motion: From molecular switches to molecular motors. *Acc. Chem. Res.* **2001**, *34*, 504–513.

56. Feringa, B. L., The art of building small: From molecular switches to molecular motors. *J. Org. Chem.* **2007**, *72*, 6635–6652.

57. Balzani, V.; Venturi, M.; Credi, A., *Molecular Devices and Machines – A Journey Into the Nanoworld*. Wiley: Weinheim, 2003.

58. Kay, E. R.; Leigh, D. A.; Zerbetto, F., Synthetic molecular motors and mechanical machines. *Angew. Chem. Int. Ed.* **2007**, *46*, 72–191.

59. Ballardini, R.; Balzani, V.; Credi, A.; Gandolfi, M. T.; Venturi, M., Artificial molecular-level machines: Which energy to make them work? *Acc. Chem. Res.* **2001**, *34*, 445–455.

60. Venturi, M.; Balzani, V.; Ballardini, R.; Credi, A.; Gandolfi, M. T., Towards molecular photochemionics. *Int. J. Photoenergy* **2004**, *6*, 1–10.

61. Muraoka, T.; Kinbara, K.; Kobayashi, Y.; Aida, T., Light-driven open−close motion of chiral molecular scissors. *J. Am. Chem. Soc.* **2003**, *125*, 5612−5613.

62. Norikane, Y.; Tamaoki, N., Light-driven molecular hinge: A new molecular machine showing a light-intensity-dependent photoresponse that utilizes the trans−cis isomerization of azobenzene. *Org. Lett.* **2004**, *6*, 2595–2598.

63. Murakami, H.; Kawabuchi, A.; Matsumoto, R.; Ido, T.; Nakashima, N., A multi-mode-driven molecular shuttle: Photochemically and thermally reactive azobenzene rotaxanes. *J. Am. Chem. Soc.* **2005**, *127*, 15891−15899.

64. Zhou, M. G.; Liang, X. G.; Mochizuki, T.; Asanuma, H., A Light-Driven DNA Nanomachine for the Efficient Photoswitching of RNA Digestion. *Angew. Chem. Int. Ed.* **2010**, *49*, 2167–2170.

65. Wurthner, F.; Rebek, J., Light-Switchable Catalysis in Synthetic Receptors. *Angew. Chem. Int. Ed.* **1995**, *34*, 446–448.

66. Stoll, R. S.; Peters, M. V.; Kuhn, A.; Heiles, S.; Goddard, R.; Buhl, M.; Thiele, C. M.; Hecht, S., Photoswitchable Catalysts: Correlating Structure and Conformational Dynamics with Reactivity by a Combined Experimental and Computational Approach. *J. Am. Chem. Soc.* **2009**, *131*, 357−367.

67. Sud, D.; Norsten, T. B.; Branda, N. R., Photoswitching of stereoselectivity in catalysis using a copper dithienylethene complex. *Angew. Chem. Int. Ed.* **2005**, *44*, 2019–2021.

68. Sud, D.; Wigglesworth, T. J.; Branda, N. R., Creating a reactive enediyne by using visible light: Photocontrol of the bergman cyclization. *Angew. Chem. Int. Ed.* **2007**, *46*, 8017–8019.

69. Shao, Q.; Xing, B. G., Photoactive molecules for applications in molecular imaging and cell biology. *Chem. Soc. Rev.* **2010**, *39*, 2835–2846.

70. Terazono, Y.; Kodis, G.; Andréasson, J.; Jeong, G. J.; Brune, A.; Hartmann, T.; Dürr, H.; Moore, A. L.; Moore, T. A.; Gust, D., Photonic control of photoinduced electron transfer via switching of redox potentials in a photochromic moiety. *J. Phys. Chem. B* **2004**, *108*, 1812−1814.

71. Alfimov, M. V.; Fedorova, O. A.; Gromov, S. P., Photoswitchable molecular receptors. *J. Photochem. Photobiol., A* **2003**, *158*, 183–198.

72. Crano, J. C.; Flood, T.; Knowles, D.; Kumar, A.; Van Gemert, B., Photochromic compounds: Chemistry and application in ophthalmic lenses. *Pure Appl. Chem.* **1996**, *68*, 1395–1398.

73. Cheng, T.; Lin, T.; Brady, R.; Wang, X., Photochromic fabrics with improved durability and photochromic performance. *Fibers and Polymers* **2008**, *9*, 521−526.

74. Mennig, M.; Fries, K.; Lindenstruth, M.; Schmidt, H., Development of fast switching photochromic coatings on transparent plastics and glass. *Thin Solid Films* **1999**, *351*, 230–234.

75. Klajn, R.; Wesson, P. J.; Bishop, K. J. M.; Grzybowski, B. A., Writing Self-Erasing Images using Metastable Nanoparticle "Inks". *Angew. Chem. Int. Ed.* **2009**, *48*, 7035–7039.

76. Banghart, M.; Borges, K.; Isacoff, E.; Trauner, D.; Kramer, R. H., Light-activated ion channels for remote control of neuronal firing. *Nat. Neurosci.* **2004**, *7*, 1381–1386.

77. Koçer, A.; Walko, M.; Meijberg, W.; Feringa, B. L., A light-actuated nanovalve derived from a channel protein. *Science* **2005**, *309*, 755–758.

78. Dri, C.; Peters, M. V.; Schwarz, J.; Hecht, S.; Grill, L., Spatial periodicity in molecular switching. *Nature Nanotech.* **2008**, *3*, 649–653.

79. Ubukata, T.; Fujii, S.; Yokoyama, Y., Reversible phototriggered micromanufacturing using amorphous photoresponsive spirooxazine film. *J. Mater. Chem.* **2009**, *19*, 3373–3377.

80. Tsujioka, T.; Sesumi, Y.; Takagi, R.; Masui, K.; Yokojima, S.; Uchida, K.; Nakamura, S., Selective metal deposition on photoswitchable molecular surfaces. *J. Am. Chem. Soc.* **2008**, *130*, 10740−10747.

81. Riskin, M.; Gutkin, V.; Felner, I.; Willner, I., Photochemical and electrochemical encoding of erasable magnetic patterns. *Angew. Chem. Int. Ed.* **2008**, *47*, 4416–4420.

82. Rosario, R.; Gust, D.; Garcia, A. A.; Hayes, M.; Taraci, J. L.; Clement, T.; Dailey, J. W.; Picraux, S. T., Lotus effect amplifies light-induced contact angle switching. *J. Phys. Chem. B* **2004**, *108*, 12640–12642.

83. Mark, D.; Haeberle, S.; Roth, G.; von Stetten, F.; Zengerle, R., Microfluidic lab-on-a-chip platforms: requirements, characteristics and applications. *Chem. Soc. Rev.* **2010**, *39*, 1153–1182.

84. Berná, J.; Leigh, D. A.; Lubomska, M.; Mendoza, S. M.; Pérez, E. M.; Rudolf, P.; Teobaldi, G.; Zerbetto, F., Macroscopic transport by synthetic molecular machines. *Nature Mater.* **2005**, *4*, 704–710.

85. Browne, W. R., Photochemistry of immobilized photoactive compounds. *Coord. Chem. Rev.* **2008**, *252*, 2470–2479.

86. Russew, M.-M.; Hecht, S., Photoswitches: From Molecules to Materials. *Adv. Mater.* **2010**, *22*, 3348–3360.

87. Feringa, B. L.; van Delden, R. A.; Koumura, N.; Geertsema, E. M., Chiroptical molecular switches. *Chem. Rev.* **2000**, *100*, 1789–1816.

88. Yildiz, I.; Deniz, E.; Raymo, F. M., Fluorescence modulation with photochromic switches in nanostructured constructs. *Chem. Soc. Rev.* **2009**, *38*, 1859–1867.

89. Gromov, S. P., Molecular meccano for light-sensitive and light-emitting nanosized systems based on unsaturated and macrocyclic compounds. *Russ. Chem. Bull.* **2008**, *57*, 1325–1350.

90. Raymo, F. M.; Tomasulo, M., Electron and energy transfer modulation with photochromic switches. *Chem. Soc. Rev.* **2005**, *34*, 327–336.

91. Tian, H.; Wang, S., Photochromic bisthienylethene as multi-function switches. *Chem. Commun.* **2007**, 781–792.

92. Irie, M., Diarylethenes for Memories and Switches. *Chem. Rev.* **2000**, *100*, 1685–1716.

93. Berkovic, G.; Krongauz, V.; Weiss, V., Spiropyrans and spirooxazines for memories and switches. *Chem. Rev.* **2000**, *100*, 1741–1753.

94. Dürr, H.; Bouas-Laurent, H., *Photochromism: Molecules and Systems*. Elsevier: New York, 2003.

95. Crano, J. C.; Guglielmetti, R. J., *Organic Photochromic and Thermochromic Compounds*. Kluwer Academic Publishers: New York, 2002; Vol. 1, 2.

96. Bertelson, R. C., Chapter III: Photochromic Processes Involving Heterolytic Cleavage. In *Techniques of Chemistry Volume III: Photochromism*, Brown, G. H., Ed. Wiley-Interscience: New York, 1971.

97. Peters, A.; McDonald, R.; Branda, N. R., Regulating pi-conjugated pathways using a photochromic 1,2-dithienylcyclopentene. *Chem. Commun.* **2002**, 2274–2275.

98. Lin, H.; Wei, Z. M.; Xiang, J. F.; Xu, W.; Zhu, D. B., Electrical switching of 1,2-bis(2-methyl-5-phenyl-3-thienyl) perfluorocyclopentene in the solid state. *Chemphyschem* **2009**, *10*, 1996–1999.

99. Tsuji, Y.; Staykov, A.; Yoshizawa, K., Orbital view concept applied on photoswitching systems. *Thin Solid Films* **2009**, *518*, 444–447.

100. Kawai, T.; Koshido, T.; Yoshino, K., Optical and Dielectric Properties of Photochromic Dye in Amorphous State and Its Application. *Appl. Phys. Lett.* **1995**, *67*, 795–797.

101. Tanio, N.; Irie, M., Refractive Index of Organic Photochromic Dye-Amorphous Polymer Composites. *Jpn. J. Appl. Phys., Part 1* **1994**, *33*, 3942–3946.

102. Yokoyama, Y.; Uchida, S.; Yokoyama, Y.; Sugawara, Y.; Kurita, Y., Diastereoselective photochromism of an (*R*)-binaphthol-condensed indolylfulgide. *J. Am. Chem. Soc.* **1996**, *118*, 3100–3107.

103. Zimmerman, G.; Chow, L.-Y.; Paik, U.-J., The Photochemical Isomerization of Azobenzene. *J. Am. Chem. Soc.* **1958**, *80*, 3528–3531.

104. Shinkai, S.; Nakaji, T.; Nishida, Y.; Ogawa, T.; Manabe, O., Photoresponsive Crown Ethers. 1. Cis–Trans Isomerism of Azobenzene as a Tool to Enforce Conformational Changes of Crown Ethers and Polymers. *J. Am. Chem. Soc.* **1980**, *102*, 5860–5865.

105. Ueno, A.; Takahashi, K.; Osa, T., Photocontrol of Catalytic Activity of Capped Cyclodextrin. *J. Chem. Soc., Chem. Commun.* **1981**, 94–96.

106. Irie, M.; Mohri, M., Thermally Irreversible Photochromic Systems. Reversible Photocyclization of Diarylethene Derivatives. *J. Org. Chem.* **1988**, *53*, 803–808.

107. Hanazawa, M.; Sumiya, R.; Horikawa, Y.; Irie, M., Thermally Irreversible Photochromic Systems. Reversible Photocyclization of 1,2-Bis(2-methylbenzo[*b*]thiophen-3-yl)perfluorocycloalkene Derivatives. *J. Chem. Soc., Chem. Commun.* **1992**, 206–207.

108. Gilat, S. L.; Kawai, S. H.; Lehn, J.-M., Light-Triggered Electrical and Optical Switching Devices. *J. Chem. Soc., Chem. Commun.* **1993**, 1439–1442.

109. Shim, S. D.; Joo, T. H.; Bae, S. C.; Kim, K. S.; Kim, E. Y., Ring opening dynamics of a photochromic diarylethene derivative in solution. *J. Phys. Chem. A* **2003**, *107*, 8106–8110.

110. Minkin, V. I., Photo-, thermo-, solvato-, and electrochromic spiroheterocyclic compounds. *Chem. Rev.* **2004**, *104*, 2751–2776.

111. Nicole, L.; Rozes, L.; Sanchez, C., Integrative Approaches to Hybrid Multifunctional Materials: From Multidisciplinary Research to Applied Technologies. *Adv. Mater.* **2010**, *22*, 3208–3214.

112. Fukaminato, T.; Umemoto, T.; Iwata, Y.; Yokojima, S.; Yoneyama, M.; Nakamura, S.; Irie, M., Photochromism of diarylethene single molecules in polymer matrices. *J. Am. Chem. Soc.* **2007**, *129*, 5932–5938.

113. Natansohn, A.; Rochon, P., Photoinduced motions in azo-containing polymers. *Chem. Rev.* **2002**, *102*, 4139–4175.

114. Ichimura, K., Photoalignment of liquid-crystal systems. *Chem. Rev.* **2000**, *100*, 1847–1873.

115. Lebeau, B.; Sanchez, C., Sol-gel derived hybrid inorganic-organic nanocomposites for optics. *Curr. Opin. Solid State Mater. Sci.* **1999**, *4*, 11–23.

116. Kinashi, K.; Kita, H.; Misaki, M.; Koshiba, Y.; Ishida, K.; Ueda, Y.; Ishihara, M., Fabrication and optical properties of photochromic compound/clay hybrid films. *Thin Solid Films* **2009**, *518*, 651–655.

117. Fujita, W.; Awaga, K., Reversible Structural Transformation and Drastic Magnetic Change in a Copper Hydroxides Intercalation Compound. *J. Am. Chem. Soc.* **1997**, *119*, 4563–4564.

118. Kojima, N.; Okubo, M.; Shimizu, H.; Enomoto, M., Control of magnetism by isomerization of intercalated molecules in organic-inorganic hybrid systems. *Coord. Chem. Rev.* **2007**, *251*, 2665–2673.

119. Taguchi, M.; Yamada, K.; Suzuki, K.; Sato, O.; Einaga, Y., Photoswitchable magnetic nanoparticles of Prussian blue with amphiphilic azobenzene. *Chem. Mater.* **2005**, *17*, 4554–4559.

120. Shimizu, H.; Okubo, M.; Nakamoto, A.; Enomoto, M.; Kojima, N., Enhancement of the Curie Temperature by Isomerization of Diarylethene (DAE) for an Organic–Inorganic Hybrid System: $Co_4(OH)_7(DAE)_{0.5}$.3H2O. *Inorg. Chem.* **2006**, *45*, 10240–10247.

121. Pieroni, O.; Fissi, A.; Viegi, A.; Fabbri, D.; Ciardelli, F., Modulation of the Chain Conformation of Spiropyran-Containing Poly(L-Lysine) by the Combined Action of Visible Light and Solvent. *J. Am. Chem. Soc.* **1992**, *114*, 2734–2736.

122. Ciardelli, F.; Fabbri, D.; Pieroni, O.; Fissi, A., Photomodulation of Polypeptide Conformation by Sunlight in Spiropyran-Containing Poly(L-Glutamic Acid). *J. Am. Chem. Soc.* **1989**, *111*, 3470–3472.

123. Tian, Z. Y.; Wu, W. W.; Li, A. D. Q., Photoswitchable Fluorescent Nanoparticles: Preparation, Properties and Applications. *Chemphyschem* **2009**, *10*, 2577–2591.

124. Tian, Z.; Wu, W.; Wan, W.; Li, A. D. Q., Single-Chromophore-Based Photoswitchable Nanoparticles Enable Dual-Alternating-Color Fluorescence for Unambiguous Live Cell Imaging. *J. Am. Chem. Soc.* **2009**, *131*, 4245–4252.

125. Mikami, R.; Taguchi, M.; Yamada, K.; Suzuki, K.; Sato, O.; Einaga, Y., Reversible Photo-Switching of the Magnetization of Iron Oxide Nanoparticles at Room Temperature. *Angew. Chem. Int. Ed.* **2004**, *43*, 6135–6139.

126. Wu, T.; Zou, G.; Hu, J. M.; Liu, S. Y., Fabrication of Photoswitchable and Thermotunable Multicolor Fluorescent Hybrid Silica Nanoparticles Coated with Dye-Labeled Poly(N-isopropylacrylamide) Brushes. *Chem. Mater.* **2009**, *21*, 3788–3798.

127. Zhou, Z. G.; Hu, H.; Yang, H.; Yi, T.; Huang, K. W.; Yu, M. X.; Li, F. Y.; Huang, C. H., Up-conversion luminescent switch based on photochromic diarylethene and rare-earth nanophosphors. *Chem. Commun.* **2008**, 4786–4788.

128. Wesenhagen, P.; Areephong, J.; Landaluce, T. F.; Heureux, N.; Katsonis, N.; Hjelm, J.; Rudolf, P.; Browne, W. R.; Feringa, B. L., Photochromism and electrochemistry of a dithienylcyclopentene electroactive polymer. *Langmuir* **2008**, *24*, 6334–6342.

129. Li, Y.; Wong, K. M.-C.; Tam, A. Y.-Y.; Wu, L.; Yam, V. W.-W., Thermo- and Acid-Responsive Photochromic Spironapthoxazine-Containing Organogelators. *Chem. Eur. J.* **2010**, *16*, 8690–8698.

130. Jiang, G. Y.; Wang, S.; Yuan, W. F.; Jiang, L.; Song, Y. L.; Tian, H.; Zhu, D. B., Highly fluorescent contrast for rewritable optical storage based on photochromic bisthienylethene-bridged naphthalimide dimer. *Chem. Mater.* **2006**, *18*, 235–237.

131. Andréasson, J.; Straight, S. D.; Bandyopadhyay, S.; Mitchell, R. H.; Moore, T. A.; Moore, A. L.; Gust, D., A molecule-based 1:2 digital demultiplexer. *J. Phys. Chem. C* **2007**, *111*, 14274–14278.

132. Ko, C.-C.; Yam, V. W.-W., Transition metal complexes with photochromic ligands – photosensitization and photoswitchable properties. *J. Mater. Chem.* **2010**, *20*, 2063–2070.

133. Kume, S.; Nishihara, H., Metal-based photoswitches derived from photoisomerization. In *Struct Bond*, Springer-Verlag: Berlin, 2007; Vol. 123, pp 79–112.

134. Kume, S.; Nishihara, H., Photochrome-coupled metal complexes: molecular processing of photon stimuli. *Dalton Trans.* **2008**, 3260–3271.

135. Belser, P.; De Cola, L.; Hartl, F.; Adamo, V.; Bozic, B.; Chriqui, Y.; Iyer, V. M.; Jukes, R. T. F.; Kuhni, J.; Querol, M.; Roma, S.; Salluce, N., Photochromic switches incorporated in bridging ligands: A new tool to modulate energy-transfer processes. *Adv. Funct. Mater.* **2006**, *16*, 195–208.

136. Myles, A. J.; Branda, N. R., 1,2-dithienylethene photochromes and non-destructive erasable memory. *Adv. Funct. Mater.* **2002**, *12*, 167–173.

137. Huynh, M. H. V.; Dattelbaum, D. M.; Meyer, T. J., Exited state electron and energy transfer in molecular assemblies. *Coord. Chem. Rev.* **2005**, *249*, 457–483.

138. Fernández-Acebes, A.; Lehn, J.-M., Optical switching and fluorescence modulation properties of photochromic metal complexes derived from dithienylethene ligands. *Chem. Eur. J.* **1999**, *5*, 3285–3292.

139. Wenger, O. S.; Henling, L. M.; Day, M. W.; Winkler, J. R.; Gray, H. B., Rhenium(I) tricarbonyl complexes with photoisomerizable ligands. *Polyhedron* **2004**, *23*, 2955–2958.

140. Ko, C.-C.; Kwok, W.-M.; Yam, V. W.-W.; Phillips, D. L., Triplet MLCT Photosensitization of the Ring-Closing Reaction of Diarylethenes by Design and Synthesis of a Photochromic Rhenium(I) Complex of a Diarylethene-Containing 1,10-Phenanthroline Ligand. *Chem. Eur. J.* **2006**, *12*, 5840–5848.

141. Ko, C.-C.; Wu, L.-X.; Wong, K. M.-C.; Zhu, N.; Yam, V. W.-W., Synthesis, Characterization and Photochromic Studies of Spirooxazine-Containing 2,2'-Bipyridine Ligands and Their Rhenium(I) Tricarbonyl Complexes. *Chem. Eur. J.* **2004**, *10*, 766–776.

142. Pourrieux, G.; Fagalde, F.; Romero, I.; Fontrodona, X.; Parella, T.; Katz, N. E., Electron-, Proton-, and Photon-Induced Spectroscopic Changes in Chromophore-Quencher Tricarbonyl(2,2'-Bipyridine)rhenium(I) Complexes with 4,4'-Azobis(pyridine). *Inorg. Chem.* **2010**, *49*, 4084–4091.

143. Kim, H. J.; Jang, J. H.; Choi, H.; Lee, T.; Ko, J.; Yoon, M.; Kim, H.-J., Photoregulated fluorescence switching in axially coordinated tin(IV) porphyrinic dithienylethene. *Inorg. Chem.* **2008**, *47*, 2411–2415.

144. Lee, I.; You, Y.; Lim, S. J.; Park, S. Y., Reversible photon-mode phosphorescence switching of heteroleptic cyclometalated iridium(III) complexes via photochromic bisthienylethene switch linked to ancillary ligand. *Chem. Lett.* **2007**, *36*, 888–889.

145. Jukes, R. T. F.; Adamo, V.; Hartl, F.; Belser, P.; De Cola, L., Photochromic dithienylethene derivatives containing Ru(II) or Os(II) metal units. Sensitized photocyclization from a triplet state. *Inorg. Chem.* **2004**, *43*, 2779–2792.

146. Zhao, H.; Al-Atar, U.; Pace, T. C. S.; Bohne, C.; Branda, N. R., High-contrast fluorescence switching using a photoresponsive dithienylethene coordination compound. *J. Photochem. Photobiol., A* **2008**, *200*, 74–82.

147. Yun, C.; You, J.; Kim, J.; Huh, J.; Kim, E., Photochromic fluorescence switching from diarylethenes and its applications. *J Photochem. Photobiol., C* **2009**, *10*, 111–129.

148. Weiss, E. A.; Wasielewski, M. R.; Ratner, M. A., Molecules as Wires: Molecule-Assisted Movement of Charge and Energy. In *Top. Curr. Chem.*, De Cola, L., Ed. Springer-Verlag: Berlin, 2005; Vol. 257, pp 103–133.

149. Scandola, F.; Indelli, M. T.; Chiorboli, C.; Bignozzi, C. A., Photoinduced Electron and Energy Transfer in Polynuclear Complexes. In *Topics in Current Chemistry 158: Photoinduced Electron Transfer II*, Mattay, J., Ed. Springer-Verlag: Berlin, 1990; pp 73-149.

150. Tsuchiya, S., Intramolecular electron transfer of diporphyrins comprised of electron-deficient porphyrin and electron-rich porphyrin with photocontrolled isomerization. *J. Am. Chem. Soc.* **1999**, *121*, 48–53.

151. Fraysse, S.; Coudret, C.; Launay, J. P., Synthesis and properties of dinuclear complexes with a photochromic bridge: An intervalence electron transfer switching "on" and "off". *Eur. J. Inorg. Chem.* **2000**, 1581–1590.

152. Launay, J. P., Long-distance intervalence electron transfer. *Chem. Soc. Rev.* **2001**, *30*, 386–397.

153. Matsuda, K.; Irie, M., Effective photoswitching of intramolecular magnetic interaction by diarylethene: Backgrounds and applications. *Polyhedron* **2005**, *24*, 2477–2483.

154. Takayama, K.; Matsuda, K.; Irie, M., Photoswitching of the magnetic interaction between a copper(II) ion and a nitroxide radical by using a photochromic spin coupler. *Chem. Eur. J.* **2003**, *9*, 5605–5609.

155. Boillot, M. L.; Zarembowitch, J.; Sour, A., Ligand-driven light-induced spin change (LD-LISC): a promising photomagnetic effect. *Top Curr Chem* **2004**, *234*, 261–276.

156. Roux, C.; Zarembowitch, J.; Gallois, B.; Granier, T.; Claude, R., Toward Ligand-Driven Light-Induced Spin Change. Influence of the Configuration of 4-Styrylpyridine (stpy) on the Magnetic Properties of $Fe^{II}(stpy)_4(NCS)_2$ Complexes. Crystal Structures of the Spin-Crossover Species Fe(*trans*-stpy)$_4$(NCS)$_2$ and of the High-Spin Species Fe(*cis*-stpy)$_4$(NCS)$_2$. *Inorg. Chem.* **1994**, *33*, 2273–2279.

157. Boillot, M.-L.; Roux, C.; Audiere, J.-P.; Dausse, A.; Zarembowitch, J., Ligand-driven light-induced spin change in transition-metal complexes: Selection of an appropriate system and first evidence of the effect, in Fe^{II}(4-styrylpyridine)$_4$(NCBPh$_3$)$_2$. *Inorg. Chem.* **1996**, *35*, 3975–3980.

158. Bousseksou, A.; Molnár, G.; Matouzenko, G., Switching of Molecular Spin States in Inorganic Complexes by Temperature, Pressure, Magnetic Field and Light: Towards Molecular Devices. *Eur. J. Inorg. Chem.* **2004**, 4353–4369.

159. Murray, K. S., Advances in polynuclear iron(II), iron(III) and cobalt(II) spin-crossover compounds. *Eur. J. Inorg. Chem.* **2008**, 3101–3121.

160. Létard, J. F.; Guionneau, P.; Goux-Capes, L., Towards spin crossover applications. *Top. Curr. Chem.* **2004**, *235*, 221–249.

161. Kahn, O.; Krober, J.; Jay, C., Spin Transition Molecular Materials for Displays and Data Recording. *Adv. Mater.* **1992**, *4*, 718–728.

162. Létard, J.-F.; Guionneau, P.; Nguyen, O.; Costa, J. S.; Marcén, S.; Chastanet, G.; Marchivie, M.; Goux-Capes, L., A Guideline to the Design of Molecular-Based Materials with Long-Lived Photomagnetic Lifetimes. *Chem. Eur. J.* **2005**, *11*, 4582–4589.

163. Létard, J.-F., Photomagnetism of iron(II) spin crossover complexes - the *T*(LIESST) approach. *J. Mater. Chem.* **2006**, *16*, 2550–2559.

164. Sato, O., Optically Switchable Molecular Solids: Photoinduced Spin-Crossover, Photochromism, and Photoinduced Magnetization. *Acc. Chem. Res.* **2003**, *36*, 692–700.

165. Halcrow, M. A., Trapping and manipulating excited spin states of transition metal compounds. *Chem. Soc. Rev.* **2008**, *37*, 278–289.

166. Bousseksou, A.; Molnár, G.; Real, J. A.; Tanaka, K., Spin crossover and photomagnetism in dinuclear iron(II) compounds. *Coord. Chem. Rev.* **2007**, *251*, 1822–1833.

167. Hasegawa, Y.; Kume, S.; Nishihara, H., Reversible light-induced magnetization change in an azobenzene-attached pyridylbenzimidazole complex of iron(II) at room temperature. *Dalton Trans.* **2009**, 280–284.

168. Boillot, M.-L.; Chantraine, S.; Zarembowitch, J.; Lallemand, J.-Y.; Prunet, J., First ligand-driven light-induced spin change *at room temperature* in a transition-metal molecular compound. *New J. Chem.* **1999**, *23*, 179–183.

169. Sour, A.; Boillot, M.-L.; Rivière, E.; Lesot, P., First evidence of a photoinduced spin change in an Fe^{III} complex using visible light at room temperature. *Eur. J. Inorg. Chem.* **1999**, 2117–2119.

170. Boillot, M.-L.; Sour, A.; Delhaès, P.; Mingotaud, C.; Soyer, H., A photomagnetic effect for controlling spin states of Iron(II) complexes in molecular materials. *Coord. Chem. Rev.* **1999**, *192*, 47–59.

171. Senechal-David, K.; Zaman, N.; Walko, M.; Halza, E.; Riviere, E.; Guillot, R.; Feringa, B. L.; Boillot, M. L., Combining organic photochromism with inorganic paramagnetism - optical tuning of the iron(II) electronic structure. *Dalton Trans.* **2008**, 1932–1936.

172. Boillot, M. L.; Pillet, S.; Tissot, A.; Riviere, E.; Claiser, N.; Lecomte, C., Ligand-Driven Light-Induced Spin Change Activity and Bidirectional Photomagnetism of Styrylpyridine Iron(II) Complexes in Polymeric Media. *Inorg. Chem.* **2009**, *48*, 4729–4736.

173. Kolb, J. S.; Thomson, M. D.; Novosel, M.; Senechal-David, K.; Riviere, E.; Boillot, M. L.; Roskos, H. G., Characterization of Fe(II) complexes exhibiting the ligand-driven light-induced spin-change effect using SQUID and magnetic circular dichroism. *C. R. Chimie* **2007**, *10*, 125–136.

174. Morimoto, M.; Irie, M., Photochromism of diarylethene single crystals: crystal structures and photochromic performance. *Chem. Commun.* **2005**, 3895–3905.

175. Tani, K.; Ishibashi, Y.; Miyasaka, H.; Kobatake, S.; Irie, M., Dynamics of cyclization, cycloreversion, and multiphoton-gated reaction of a photochromic diarylethene derivative in crystalline phase. *J. Phys. Chem. C* **2008**, *112*, 11150–11157.

176. Matsuda, K.; Takayama, K.; Irie, M., Photochromism of metal complexes composed of diarylethene ligands and Zn(II), Mn(II), and Cu(II) hexafluoroacetylacetonates. *Inorg. Chem.* **2004**, *43*, 482–489.

177. Samachetty, H. D.; Branda, N. R., Photomodulation of Lewis basicity in a pyridine-functionalized 1,2-dithienylcyclopentene. *Chem. Commun.* **2005**, 2840–2842.

178. Samachetty, H. D.; Lemieux, V.; Branda, N. R., Modulating chemical reactivity using a photoresponsive molecular switch. *Tetrahedron* **2008**, *64*, 8292–8300.

179. Lemieux, V.; Spantulescu, M. D.; Baldridge, K. K.; Branda, N. R., Modulating the Lewis acidity of boron using a photoswitch. *Angew. Chem. Int. Ed.* **2008**, *47*, 5034–5037.

180. Yam, V. W. W.; Ko, C. C.; Zhu, N. Y., Photochromic and luminescence switching properties of a versatile diarylethene-containing 1,10-phenanthroline ligand and its rhenium(I) complex. *J. Am. Chem. Soc.* **2004**, *126*, 12734–12735.

181. Ngan, T.-W.; Ko, C.-C.; Zhu, N.; Yam, V. W.-W., Syntheses, Luminescence Switching, and Electrochemical Studies of Photochromic Dithienyl-1,10-phenanthroline Zinc(II) Bis(thiolate) Complexes. *Inorg. Chem.* **2007**, *46*, 1144–1152.

182. Nakagawa, T.; Atsumi, K.; Nakashima, T.; Hasegawa, Y.; Kawai, T., Reversible Luminescence Modulation in Photochromic Europium(III) Complex Having Triangle Terthiazole Ligands. *Chem. Lett.* **2007**, *36*, 372–373.

183. Nakagawa, T.; Hasegawa, Y.; Kawai, T., Photoresponsive europium(III) complex based on photochromic reaction. *J. Phys. Chem. A* **2008**, *112*, 5096–5103.

184. Nakagawa, T.; Hasegawa, Y.; Kawai, T., Nondestructive luminescence intensity readout of a photochromic lanthanide(III) complex. *Chem. Commun.* **2009**, 5630–5632.

185. Werts, M. H. V., Making sense of lanthanide luminescence. *Sci. Prog.* **2005**, *88*, 101–131.

186. Bünzli, J.-C. G.; Piguet, C., Taking advantage of luminescent lanthanide ions. *Chem. Soc. Rev.* **2005**, *34*, 1048–1077.

187. de Sá, G. F.; Malta, O. L.; de Mello Donegá, C.; Simas, A. M.; Longo, R. L.; Santa-Cruz, P. A.; da Silva Jr, E. F., Spectroscopic properties and design of highly luminescent lanthanide coordination complexes. *Coord. Chem. Rev.* **2000**, *196*, 165–195.

188. Hasegawa, Y.; Yamamuro, M.; Wada, Y.; Kanehisa, N.; Kai, Y.; Yanagida, S., Luminescent polymer containing the Eu(III) complex having fast radiation rate and high emission quantum efficiency. *J. Phys. Chem. A* **2003**, *107*, 1697–1702.

189. Kopelman, R. A.; Paquette, M. M.; Frank, N. L., Photoprocesses and magnetic behavior of photochromic transition metal indoline[phenanthrolinospirooxazine] complexes: Tunable photochromic materials. *Inorg. Chim. Acta* **2008**, *361*, 3570–3576.

190. Juhász, G.; Matsuda, R.; Kanegawa, S.; Inoue, K.; Sato, O.; Yoshizawa, K., Bistability of Magnetization without Spin-Transition in a High-Spin Cobalt(II) Complex due to Angular Momentum Quenching. *J. Am. Chem. Soc.* **2009**, *131*, 4560−4561.

191. Wurthner, F.; Rebek, J., Photoresponsive Synthetic Receptors: Binding-Properties and Photocontrol of Catalytic Activity. *J. Chem. Soc., Perkin Trans. 2* **1995**, 1727−1734.

192. Cacciapaglia, R.; Di Stefano, S.; Mandolini, L., The bis-barium complex of a butterfly crown ether as a phototunable supramolecular catalyst. *J. Am. Chem. Soc.* **2003**, *125*, 2224–2227.

193. Segarra-Maset, M. D.; van Leeuwen, P. W. N. M.; Freixa, Z., Light Switches the Ligand! Photochromic Azobenzene-Phosphanes. *Eur. J. Inorg. Chem.* **2010**, 2075–2078.

194. Liu, Z. L.; Jiang, L.; Liang, Z.; Gao, Y. H., Photo-switchable molecular devices based on metal-ionic recognition. *Tetrahedron Lett.* **2005**, *46*, 885–887.

195. Winkler, J. D.; Bowen, C. M.; Michelet, V., Photodynamic fluorescent metal ion sensors with parts per billion sensitivity. *J. Am. Chem. Soc.* **1998**, *120*, 3237–3242.

196. Radu, A.; Scarmagnani, S.; Byrne, R.; Slater, C.; Lau, K. T.; Diamond, D., Photonic modulation of surface properties: a novel concept in chemical sensing. *J. Phys. D: Appl. Phys.* **2007**, *40*, 7238–7244.

197. Filley, J.; Ibrahim, M. A.; Nimlos, M. R.; Watt, A. S.; Blake, D. M., Magnesium and calcium chelation by a bis-spiropyran. *J. Photochem. Photobiol., A* **1998**, *117*, 193–198.

198. Wojtyk, J. T. C.; Kazmaier, P. M.; Buncel, E., Effects of metal ion complexation on the spiropyran-merocyanine interconversion: development of a thermally stable photo-switch. *Chem. Commun.* **1998**, 1703–1704.

199. Wojtyk, J. T. C.; Kazmaier, P. M.; Buncel, E., Modulation of the spiropyran-merocyanine reversion via metal-ion selective complexation: Trapping of the "Transient" cis-merocyanine. *Chem. Mater.* **2001**, *13*, 2547–2551.

200. Chibisov, A. K.; Gorner, H., Complexes of spiropyran-derived merocyanines with metal ions: relaxation kinetics, photochemistry and solvent effects. *Chem. Phys.* **1998**, *237*, 425–442.

201. Gorner, H.; Chibisov, A. K., Complexes of spiropyran-derived merocyanines with metal ions. *J. Chem. Soc., Faraday Trans.* **1998**, *94*, 2557–2564.

202. Fukushima, K.; Vandenbos, A. J.; Fujiwara, T., Spiropyran dimer toward photo-switchable molecular machine. *Chem. Mater.* **2007**, *19*, 644–646.

203. Kumar, S.; Watkins, D. L.; Fujiwara, T., A tailored spirooxazine dimer as a photoswitchable binding tool. *Chem. Commun.* **2009**, 4369–4371.

204. Guo, X. F.; Zhang, D. Q.; Zhang, G. X.; Zhu, D. B., Monomolecular logic: "Half-adder" based on multistate/multifunctional photochromic spiropyrans. *J. Phys. Chem. B* **2004**, *108*, 11942−11945.

205. Hirshberg, Y., Reversible Formation and Eradication of Colors by Irradiation at Low Temperatures - A Photochemical Memory Model. *J. Am. Chem. Soc.* **1956**, *78*, 2304–2312.

206. Bahr, J. L.; Kodis, G.; de la Garza, L.; Lin, S.; Moore, A. L.; Moore, T. A.; Gust, D., Photoswitched singlet energy transfer in a porphyrin-spiropyran dyad. *J. Am. Chem. Soc.* **2001**, *123*, 7124–7133.

207. Tanaka, M.; Nakamura, M.; Salhin, M. A. A.; Ikeda, T.; Kamada, K.; Ando, H.; Shibutani, Y.; Kimura, K., Synthesis and photochromism of spirobenzopyran derivatives bearing an oxymethylcrown ether moiety: Metal ion-induced switching between positive and negative photochromisms. *J. Org. Chem.* **2001**, *66*, 1533–1537.

208. Tanaka, M.; Ikeda, T.; Xu, Q.; Ando, H.; Shibutani, Y.; Nakamura, M.; Sakamoto, H.; Yajima, S.; Kimura, K., Synthesis and photochromism of spirobenzopyrans and spirobenzothiapyran derivatives bearing monoazathiacrown ethers and noncyclic analogues in the presence of metal ions. *J. Org. Chem.* **2002**, *67*, 2223–2227.

209. Inouye, M.; Akamatsu, K.; Nakazumi, H., New crown spirobenzopyrans as light- and ion-responsive dual-mode signal transducers. *J. Am. Chem. Soc.* **1997**, *119*, 9160–9165.

210. Fedorova, O. A.; Strokach, Y. P.; Gromov, S. P.; Koshkin, A. V.; Valova, T. M.; Alfimov, M. V.; Feofanov, A. V.; Alaverdian, I. S.; Lokshin, V. A.; Samat, A.; Guglielmetti, R.; Girling, R. B.; Moore, J. N.; Hester, R. E., Effect of metal cations on the photochromic properties of spironaphthoxazines conjugated with aza-15(18)-crown-5(6) ethers. *New J. Chem.* **2002**, *26*, 1137−1145.

211. Querol, M.; Bozic, B.; Salluce, N.; Belser, P., Synthesis, metal complex formation, and switching properties of spiropyrans linked to chelating sites. *Polyhedron* **2003**, *22*, 655–664.

212. Khairutdinov, R. F.; Giertz, K.; Hurst, J. K.; Voloshina, E. N.; Voloshin, N. A.; Minkin, V. I., Photochromism of Spirooxazines in Homogeneous Solution and Phospholipid Liposomes. *J. Am. Chem. Soc.* **1998**, *120*, 12707−12713.

213. Yam, V. W.-W.; Ko, C.-C.; Wu, L.-X.; Wong, K. M.-C.; Cheung, K.-K., Syntheses, Crystal Structure, and Photochromic Properties of Rhenium(I) Complexes Containing the Spironaphthoxazine Moiety. *Organometallics* **2000**, *19*, 1820−1822.

214. Patel, D. G. Organic Dyes for Photoswitching and Photovoltaic Applications. University of Washington, Washington, 2007.

215. Kopelman, R. A. Photochromic Spirooxazine Metal Complexes. University of Washington, Seattle, 2004.

216. Kopelman, R. A.; Snyder, S. M.; Frank, N. L., Tunable Photochromism of Spirooxazines via Metal Coordination. *J. Am. Chem. Soc.* **2003**, *125*, 13684−13685.

217. Patel, D. G.; Benedict, J. B.; Kopelman, R. A.; Frank, N. L., Photochromism of a spirooxazine in the single crystalline phase. *Chem. Commun.* **2005**, 2208–2210.

218. Patel, D. G.; Paquette, M. M.; Kopelman, R. A.; Kaminsky, W.; Ferguson, M. J.; Frank, N. L., A Solution- and Solid-State Investigation of Medium Effects on Charge Separation in Metastable Photomerocyanines. *J. Am. Chem. Soc.* **2010**, *132*, 12568–12586.

219. Chamontin, K.; Lokshin, V.; Samat, A.; Guglielmetti, R.; Dubest, R.; Aubard, J., Synthesis and photochromic properties of new spiro[azahomoadamantane-naphthoxazines]. *Dyes Pigm.* **1999**, *43*, 119–125.

220. Chamontin, K.; Lokshin, V.; Guglielmetti, R.; Samat, A.; Pèpe, G., 4-methylspiro[4-azahomoadamantane-5,3'-[3'*H*]naphth[2,1-*b*][1,4]oxazine], a new photochromic spirooxazine. *Acta Crystallogr., Sect. C: Cryst. Struct. Commun.* **1998**, *54*, 670–672.

221. Tamai, N.; Miyasaka, H., Ultrafast dynamics of photochromic systems. *Chem. Rev.* **2000**, *100*, 1875–1890.

222. Onai, Y.; Mamiya, M.; Kiyokawa, T.; Okuwa, K.; Kobayashi, M.; Shinohara, H.; Sato, H., Colored Merocyanine Aggregates: Long-Lived Crystals of Large-Size (10–100 μM) and Deaggregation of Small Aggregates in Solutions. *J. Phys. Chem.* **1993**, *97*, 9499–9505.

223. Krongauz, V. A.; Fishman, S. N.; Goldburt, E. S., Quasi-Crystals - Growth from Photochromic Spiropyrans on Irradiation in a Constant Electric-Field. *J. Phys. Chem.* **1978**, *82*, 2469–2474.

224. Hirano, M.; Osakada, K.; Nohira, H.; Miyashita, A., Crystal and solution structures of photochromic spirobenzothiopyran. First full characterization of the meta-stable colored species. *J. Org. Chem.* **2002**, *67*, 533–540.

225. Artemova, N. K.; Smirnov, V. A.; Rogachev, B. G.; Shilov, G. V.; Aldoshin, S. M., Photo- and thermochromic properties of 1',3',3'-trimethyl-6-nitro-8-pyridiniomethylspiro[2*H*-[1]benzopyran-2,2'-indoline] chloride in the crystalline state. *Russ. Chem. Bull.* **2006**, *55*, 1605–1611.

226. Naumov, P.; Yu, P.; Sakurai, K., Electronic tera-order stabilization of photoinduced metastable species: Structure of the photochromic product of spiropyran determined with in situ single crystal X-ray photodiffraction. *J. Phys. Chem. A* **2008**, *112*, 5810–5814.

227. Aldoshin, S. M., Spiropyrans: structural features and photochemical properties. *Russ. Chem. Rev.* **1990**, *59*, 663–685.

228. Aakeröy, C. B.; Hurley, E. P.; Desper, J.; Natali, M.; Douglawi, A.; Giordani, S., The balance between closed and open forms of spiropyrans in the solid state. *Crystengcomm* **2010**, *12*, 1027–1033.

229. Hobley, J.; Malatesta, V.; Millini, R.; Montanari, L.; Parker, W. O. N., Proton exchange and isomerisation reactions of photochromic and reverse photochromic spiro-pyrans and their merocyanine forms. *Phys. Chem. Chem. Phys.* **1999**, *1*, 3259–3267.

230. Keum, S.-R.; Hur, M.-S.; Kazmaier, P. M.; Buncel, E., Thermochromic and Photochromic Dyes: Indolino-Benzospiropyrans.1. UV-Vis Spectroscopic Studies of 1,3,3-Spiro(2*H*-1-Benzopyran-2,2'-Indolines) and the Open-Chain Merocyanine Forms; Solvatochromism and Medium Effects on Spiro Ring Formation. *Can. J. Chem.* **1991**, *69*, 1940–1947.

231. Wojtyk, J. T. C.; Wasey, A.; Kazmaier, P. M.; Hoz, S.; Buncel, E., Thermal reversion mechanism of N-functionalized merocyanines to spiropyrans: A solvatochromic, solvatokinetic, and semiempirical study. *J. Phys. Chem. A* **2000**, *104*, 9046–9055.

232. Laréginie, P.; Lokshin, V.; Samat, A.; Guglielmetti, R.; Pèpe, G., First permanent opened forms in spiro[indoline-oxazine] series: Synthesis and structural elucidation. *J. Chem. Soc., Perkin Trans. 2* **1996**, 107–111.

233. Song, H. F.; Chen, K. C.; Tian, H., Alkali induced chromics and stable single crystal of opened-ring form of a new spirooxazine. *Dyes Pigm.* **2005**, *67*, 1–7.

234. Pottier, E.; Dubest, R.; Guglielmetti, R.; Tardieu, P.; Kellmann, A.; Tfibel, F.; Levoir, P.; Aubard, J., Substituent, Heteroatom, and Solvent Effects on the Thermal-Bleaching Kinetics and Absorption-Spectra of Photomerocyanines Issued from Spiro[Indoline-Oxazines]. *Helv. Chim. Acta* **1990**, *73*, 303–315.

235. Metelitsa, A. V.; Micheau, J. C.; Voloshin, N. A.; Voloshina, E. N.; Minkin, V. I., Kinetic and thermodynamic investigations of the photochromism and solvatochromism of semipermanent merocyanines. *J. Phys. Chem. A* **2001**, *105*, 8417–8422.

236. Pozzo, J.-L.; Samat, A.; Guglielmetti, R.; De Keukeleire, D., Solvatochromic and Photochromic Characteristics of New 1,3-Dihydrospiro[2*H*-indole-2,2'-[2*H*]-bipyrido[3,2-*f*][2,3-*h*][1,4]benzoxazines]. *J. Chem. Soc., Perkin Trans. 2* **1993**, 1327–1332.

237. Nakamura, S.; Uchida, K.; Murakami, A.; Irie, M., Ab Initio MO and ^{1}H NMR NOE Studies of Photochromic Spironaphthoxazine. *J. Org. Chem.* **1993**, *58*, 5543–5545.

238. Malatesta, V.; Neri, C.; Wis, M. L.; Montanari, L.; Millini, R., Thermal and photodegradation of photochromic spiroindolinenaphthooxazines and -pyrans: Reaction with nucleophiles. Trapping of the merocyanine zwitterionic form. *J. Am. Chem. Soc.* **1997**, *119*, 3451–3455.

239. Chibisov, A. K.; Görner, H., Photoprocesses in spirooxazines and their merocyanines. *J. Phys. Chem. A* **1999**, *103*, 5211–5216.

240. Sheng, Y. H.; Leszczynski, J.; Garcia, A. A.; Rosario, R.; Gust, D.; Springer, J., Comprehensive theoretical study of the conversion reactions of spiropyrans: Substituent and solvent effects. *J. Phys. Chem. B* **2004**, *108*, 16233–16243.

241. Metelitsa, A. V.; Lokshin, V.; Micheau, J. C.; Samat, A.; Guglielmetti, R.; Minkin, V. I., Photochromism and solvatochromism of push-pull or pull-push spiroindolinenaphthoxazines. *Phys. Chem. Chem. Phys.* **2002**, *4*, 4340–4345.

242. Mishra, A.; Behera, R. K.; Behera, P. K.; Mishra, B. K.; Behera, G. B., Cyanines during the 1990s: A review. *Chem. Rev.* **2000**, *100*, 1973–2011.

243. Jacques, P., On the Relative Contributions of Nonspecific and Specific Interactions to the Unusual Solvatochromism of a Typical Merocyanine Dye. *J. Phys. Chem.* **1986**, *90*, 5535–5539.

244. Buncel, E.; Rajagopal, S., Solvatochromism and Solvent Polarity Scales. *Acc. Chem. Res.* **1990**, *23*, 226–231.

245. da Silva, L.; Machado, C.; Rezende, M. C., On the Solvatochromic Reversal of Merocyanine Dyes. Part 1. The UV-Vis Spectroscopic Behavior of Vinylogous γ-Pyridones. *J. Chem. Soc., Perkin Trans. 2* **1995**, 483–488.

246. Lokshin, V.; Samat, A.; Guglielmetti, R., Synthesis of photochromic spirooxazines from 1-amino-2-naphthols. *Tetrahedron* **1997**, *53*, 9669–9678.

247. Paw, W.; Eisenberg, R., Synthesis, Characterization, and Spectroscopy of Dipyridocatecholate Complexes of Platinum. *Inorg. Chem.* **1997**, *36*, 2287–2293.

248. Terent'ev, P. B.; Stankyavichyus, A. P., Mass-spectrometric behavior of 9-hydroxy-10-nitrosophenanthrene and its diaza analogues. *Chem. Heterocycl. Compd.* **1988**, *24*, 1258–1262.

249. Sasaki, T.; Eguchi, S.; Toi, N., Synthesis of Adamantane Derivatives. 42. Novel Synthesis of 5-Methylene-4-azahomoadamantane Derivatives from 2-Methyl-2-hydroxyadamantane and Their Carbon-13 Nuclear Magnetic Resonance Spectra. *J. Org. Chem.* **1978**, *43*, 3810–3813.

250. Paquette, M. M.; Kopelman, R. A.; Beitler, E.; Frank, N. L., Incorporating optical bistability into a magnetically bistable system: a photochromic redox isomeric complex. *Chem. Commun.* **2009**, 5424–5426.

251. Atkins, P.; de Paula, J., *Physical Chemistry*. 7th Edition ed.; W. H. Freeman and Company: New York, 2002; p 876.

252. Anslyn, E. V.; Dougherty, D. A., *Modern Physical Organic Chemistry*. University Science Books: Sausalito, CA, 2006; p 388–389.

253. Nangia, A., Nomenclature in Crystal Engineering. In *Encyclopedia of Supramolecular Chemistry*, Atwood, J. L.; Steed, J. W., Eds. Taylor & Francis: New York, 2004; pp 967–972.

254. Allen, F. H.; Kennard, O.; Watson, D. G.; Brammer, L.; Orpen, A. G.; Taylor, R., Tables of Bond Lengths Determined by X-Ray and Neutron-Diffraction. 1. Bond Lengths in Organic-Compounds. *J. Chem. Soc., Perkin Trans. 2* **1987**, S1–S19.

255. Hiramatsu, T.; Yoshida, H.; Sato, N., Solvent-Dependent Structural and Electronic Behaviors of a Push-Pull Molecule: {4-[4,5-Bis(methylsulfanyl)-1,3-dithiol-2-ylidene]cyclohexa-2,5-dien-1-ylidene}malononitrile. *J. Phys. Chem. A* **2009**, *113*, 9174–9179.

256. Mustroph, H.; Reiner, K.; Mistol, J.; Ernst, S.; Keil, D.; Hennig, L., Relationship between the Molecular Structure of Cyanine Dyes and the Vibrational Fine Structure of their Electronic Absorption Spectra. *Chemphyschem* **2009**, *10*, 835-840.

257. Catalán, J.; Mena, E.; Meutermans, W.; Elguero, J., Solvatochromism of a Typical Merocyanine: Stilbazolium Betaine and Its 2,6-Di-*tert*-butyl Derivative. *J. Phys. Chem.* **1992**, *96*, 3615–3621.

258. Würthner, F.; Archetti, G.; Schmidt, R.; Kuball, H.-G., Solvent effect on color, band shape, and charge-density distribution for merocyanine dyes close to the cyanine limit. *Angew. Chem. Int. Ed.* **2008**, *47*, 4529–4532.

259. Ernsting, N. P.; Arthen-Engeland, T., Photochemical Ring-Opening Reaction of Indolinospiropyrans Studied by Subpicosecond Transient Absorption. *J. Phys. Chem.* **1991**, *95*, 5502–5509.

260. Botrel, A.; Lebeuze, A.; Jacques, P.; Strub, H., Solvatochromism of a Typical Merocyanine Dye – a Theoretical Investigation through the CNDO/SCI Method Including Solvatation. *J. Chem. Soc., Faraday Trans. 2* **1984**, *80*, 1235–1252.

261. Reichardt, C., Solvatochromic Dyes as Solvent Polarity Indicators. *Chem. Rev.* **1994**, *94*, 2319–2358.

262. Cleveland, W. S., Robust locally weighted regression and smoothing scatterplots. *J. Am. Stat. Assoc.* **1979**, *74*, 829–836.

263. Niedbalska, M.; Gruda, I., Effect of Substituents on the Solvatochromism of Stilbazolium Merocyanines. *Can. J. Chem.* **1990**, *68*, 691–695.

264. Tsukada, M.; Mineo, Y.; Itoh, K., Resonance Raman and Surface-Enhanced Resonance Raman Scattering Study on the Structure of a Merocyanine Dye, 4-(2-(4-Hydroxyphenyl)Ethenyl)-1-Methylpyridinium. *J. Phys. Chem.* **1989**, *93*, 7989–7992.

265. Benson, H. G.; Murrell, J. N., Some Studies of Benzenoid-Quinonoid Resonance. Part 2. The Effect of Solvent Polarity on the Structure and Properties of Merocyanine Dyes. *J. Chem. Soc., Faraday Trans. 2* **1972**, *68*, 137–143.

266. Albert, I. D. L.; Marks, T. J.; Ratner, M. A., Rational design of molecules with large hyperpolarizabilities. Electric field, solvent polarity, and bond length alternation effects on merocyanine dye linear and nonlinear optical properties. *J. Phys. Chem.* **1996**, *100*, 9714–9725.

267. Morley, J. O.; Morley, R. M.; Docherty, R.; Charlton, M. H., Fundamental studies on Brooker's merocyanine. *J. Am. Chem. Soc.* **1997**, *119*, 10192–10202.

268. Baraldi, I.; Momicchioli, F.; Ponterini, G.; Vanossi, D., Solvent effects within the CS INDO method. Geometrical distortion and solvatochromism of merocyanine dyes. *Chem. Phys.* **1998**, *238*, 353–364.

269. Abdel-Halim, S. T., Solvatochromism of a Typical Merocyanine Dye - Further Investigations. *J. Chem. Soc., Faraday Trans.* **1993**, *89*, 55–57.

270. Kulinich, A. V.; Derevyanko, N. A.; Ishchenko, A. A., Electronic structure and solvatochromism of merocyanines based on N,N-diethylthiobarbituric acid. *J. Photochem. Photobiol., A* **2007**, *188*, 207–217.

271. Bagno, A.; Rastrelli, F.; Saielli, G., Toward the complete prediction of the ^{1}H and ^{13}C NMR spectra of complex organic molecules by DFT methods: Application to natural substances. *Chem. Eur. J.* **2006**, *12*, 5514–5525.

272. Frisch, M. J.; Trucks, G. W.; Schlegel, H. B.; Scuseria, G. E.; Robb, M. A.; Cheeseman, J. R.; Montgomery, J. A.; Vreven, T. J.; Kudin, K. N.; Burant, J. C.; Millam, J. M.; Iyengar, S. S.; Tomasi, J.; Barone, V.; Mennucci, B.; Cossi, M.; Scalmani, G.; Rega, N.; Petersson, G. A.; Nakatsuji, H.; Hada, M.; Ehara, M.; Toyota, K.; Fukuda, R.; Hasegawa, J.; Ishida, M.; Nakajima, T.; Honda, Y.; Kitao, O.; Nakai, H.; Klene, M.; Li, X.; Knox, J. E.; Hratchian, H. P.; Cross, J. B.; Bakken, V.; Adamo, C.; Jaramillo, J.; Gomperts, R.; Stratmann, R. E.; Yazyev, O.; Austin, A. J.; Cammi, R.; Pomelli, C.; Ochterski, J. W.; Ayala, P. Y.; Morokuma, K.; Voth, G. A.; Salvador, P.; Dannenberg, J. J.; Zakrzewski, V. G.; Dapprich, S.; Daniels, A. D.; Strain, M. C.; Farkas, O.; Malick, D. K.; Rabuck, A. D.; Raghavachari, K.; Foresman, J. B.; Ortiz, J. V.; Cui, Q.; Baboul, A. G.; Clifford, S.; Cioslowski, J.; Stefanov, B. B.; Liu, G.; Liashenko, A.; Piskorz, P.; Komaromi, I.; Martin, R. L.; Fox, D. J.; Keith, T.; Al-Laham, M. A.; Peng, C. Y.; Nanayakkara, A.; Challacombe, M.; Gill, P. M. W.; Johnson, B.; Chen, W.; Wong, M.

W.; Gonzalez, C.; Pople, J. A. *Gaussian 03, Revision E.01*, Gaussian, Inc.: Wallingford CT, 2004.

273. Ziegler, T., Approximate Density Functional Theory as a Practical Tool in Molecular Energetics and Dynamics. *Chem. Rev.* **1991**, *91*, 651–667.

274. El-Azhary, A. A.; Suter, H. U., Comparison between optimized geometries and vibrational frequencies calculated by the DFT methods. *J. Phys. Chem.* **1996**, *100*, 15056–15063.

275. Maurel, F.; Aubard, J.; Rajzmann, M.; Guglielmetti, R.; Samat, A., A quantum chemical study of the ground state ring opening/closing of photochromic 1,3,3-trimethylspiro[indoline-2,3'-naphtho[2,1-*b*]-[1,4]oxazine]. *J. Chem. Soc., Perkin Trans. 2* **2002**, 1307–1315.

276. Minkin, V. I.; Metelitsa, A. V.; Dorogan, I. V.; Lukyanov, B. S.; Besugliy, S. O.; Micheau, J.-C., Spectroscopic and theoretical evidence for the elusive intermediate of the photoinitiated and thermal rearrangements of photochromic spiropyrans. *J. Phys. Chem. A* **2005**, *109*, 9605–9616.

277. Hargittai, I., Variations of Molecular Geometry from Electron Diffraction. *Pure Appl. Chem.* **1989**, *61*, 651–660.

278. Chiang, J. F.; Song, J. J., Molecular Structures of 4-Nitro-, 4-Methyl- and 4-Chloro-Pyridine-*N*-Oxides. *J. Mol. Struct.* **1982**, *96*, 151–162.

279. Choi, C. H.; Kertesz, M.; Karpfen, A., The effects of electron correlation on the degree of bond alternation and electronic structure of oligomers of polyacetylene. *J. Chem. Phys.* **1997**, *107*, 6712–6721.

280. Masunov, A. M.; Tretiak, S., Prediction of two-photon absorption properties for organic chromophores using time-dependent density-functional theory. *J. Phys. Chem. B* **2004**, *108*, 899–907.

281. Domínguez, M.; Rezende, M. C., Towards a unified view of the solvatochromism of phenolate betaine dyes. *J. Phys. Org. Chem.* **2010**, *23*, 156–170.

282. Maurel, F.; Aubard, J.; Millie, P.; Dognon, J. P.; Rajzmann, M.; Guglielmetti, R.; Samat, A., Quantum chemical study of the photocoloration reaction in the napthoxazine series. *J. Phys. Chem. A* **2006**, *110*, 4759–4771.

283. NMR Solvent Data Chart. Cambridge Isotope Labs.

284. Dickeson, J. E.; Summers, L. A., Derivatives of 1,10-Phenanthroline-5,6-Quinone. *Aust. J. Chem.* **1970**, *23*, 1023–1027.

285. *Apex2 (Version 2.1–4), SAINT (Version 7.34A), SADABS (Version 2007/4)*, Bruker AXS Inc.: Madison, Wisconsin, USA, 2007.

286. Altomare, A.; Burla, M. C.; Camalli, M.; Cascarano, G. L.; Giacovazzo, C.; Guagliardi, A.; Moliterni, A. G. G.; Polidori, G.; Spagna, R., SIR97: a new tool for crystal structure determination and refinement. *J. Appl. Crystallogr.* **1999**, *32*, 115–119.

287. Sheldrick, G. M. *SHELXL97: Program for the Refinement of Crystal Structures*, University of Gottingen: Germany, 1997.

288. Mackay, S.; Edwards, C.; Henderson, A.; Gilmore, C.; Stewart, N.; Shankland, K.; Donald, A. *MaXus: A computer program for the solution and refinement of crystal structures from diffraction data*, University of Glasgow: Scotland, 1997.

289. Waasmaier, D.; Kirfel, A., New Analytical Scattering-Factor Functions for Free Atoms and Ions. *Acta Crystallographica Section A* **1995**, *51*, 416–431.

290. Sheldrick, G. M., A short history of SHELX. *Acta Crystallogr. Sect. A* **2008**, *64*, 112–122.

291. Becke, A. D., Density-Functional Thermochemistry. III. The Role of Exact Exchange. *J. Chem. Phys.* **1993**, *98*, 5648–5652.

292. Lee, C. T.; Yang, W. T.; Parr, R. G., Development of the Colle-Salvetti Correlation-Energy Formula into a Functional of the Electron-Density. *Phys. Rev. B* **1988**, *37*, 785–789.

293. Graham, W. A. G., An Approach to the Separation of Inductive and Mesomeric Effects in Complexes of the Types $LMn(CO)_5$ and $LMo(CO)_5$. *Inorg. Chem.* **1968**, *7*, 315–321.

294. Hocking, R. K.; Hambley, T. W., Database analysis of transition metal carbonyl bond lengths: Insight into the periodicity of π back-bonding, σ donation, and the factors affecting the electronic structure of the TM–CO moiety. *Organometallics* **2007**, *26*, 2815–2823.

295. Tolman, C. A., Electron Donor-Acceptor Properties of Phosphorus Ligands - Substituent Additivity. *J. Am. Chem. Soc.* **1970**, *92*, 2953–2956.

296. Barbeau, C.; Turcotte, J., Donor–Acceptor Powers of Ligands in $Mo(CO)_6$ Derivatives. *Can. J. Chem.* **1976**, *54*, 1603–1611.

297. Cotton, F. A.; Wilkinson, G., *Advanced Inorganic Chemistry*. 4th ed.; John Wiley & Sons: Toronto, 1980.

298. Darensbourg, D. J.; Kump, R. L., A Convenient Synthesis of cis-$Mo(CO)_4L_2$ Derivatives (L = Group 5A Ligand) and a Qualitative Study of Their Thermal Reactivity toward Ligand Dissociation. *Inorg. Chem.* **1978**, *17*, 2680–2682.

299. Kraihanzel, C. A.; Cotton, F. A., Vibrational Spectra and Bonding in Metal Carbonyls .2. Infrared Spectra of Amine-Substituted Group 6 Carbonyls in Co Stretching Region. *Inorg. Chem.* **1963**, *2*, 533–534.

300. Ernst, S.; Kaim, W., Coordination Characteristics of Four Isomeric α-Diimine Ligands. π Molecular Orbital Perturbation Calculations for the Bidiazines and Their Correlation with the Properties of Group-6 Metal-Carbonyl-Complexes. *J. Am. Chem. Soc.* **1986**, *108*, 3578–3586.

301. Bruins Slot, H. J.; Murrall, N. W.; Welch, A. J., Structure of Tetracarbonyl(phenanthroline)molybdenum(0), $[Mo(CO)_4(C_{12}H_8N_2)]$, at 185 K. *Acta Crystallogr., Sect. C: Cryst. Struct. Commun.* **1985**, *41*, 1309–1312.

302. Makedonas, C.; Mitsopoulou, C. A., $W(CO)_4$(diimine) structure revised – Correlating structure to π^* back-bonding. *Eur. J. Inorg. Chem.* **2007**, 110–119.

303. Hobley, J.; Malatesta, V., Energy barrier to TTC-TTT isomerisation for the merocyanine of a photochromic spiropyran. *Phys. Chem. Chem. Phys.* **2000**, *2*, 57–59.

304. Delbaere, S.; Bochu, C.; Azaroual, N.; Buntinx, G.; Vermeersch, G., NMR studies of the structure of the photoinduced forms of photochromic spironaphthoxazines. *J. Chem. Soc., Perkin Trans. 2* **1997**, 1499–1501.

305. Berthet, J.; Delbaere, S.; Carvalho, L. M.; Vermeersch, G.; Coelho, P. J., Unprecedented coexistence of a spirooxazine and its four transoid photomerocyanines. *Tetrahedron Lett.* **2006**, *47*, 4903–4905.

306. Manuta, D. M.; Lees, A. J., Emission and Photochemistry of $M(CO)_4$(diimine) (M = Cr, Mo, W) Complexes in Room-Temperature Solution. *Inorg. Chem.* **1986**, *25*, 1354–1359.

307. Cotton, F. A.; Kraihanz.Cs, Vibrational Spectra and Bonding in Metal Carbonyls.I. Infrared Spectra of Phosphine-Substituted Group VI Carbonyls in CO Stretching Region. *J. Am. Chem. Soc.* **1962**, *84*, 4432–4438.

308. Cotton, F. A., Vibrational Spectra and Bonding in Metal Carbonyls. III. Force Constants and Assignments of CO Stretching Modes in Various Molecules; Evaluation of CO Bond Orders. *Inorg. Chem.* **1964**, *3*, 702–711.

309. Shiu, K.-B.; Wang, S.-L.; Liao, F.-L., Organotransition-metal complexes of multidentate ligands XVI. On the nature of the sigma-donicity of the saturated nitrogen ligands; chelate-assisted weakening of the alpha-N-H bond: synthesis, and spectral and structural study of $[Mo(N\text{-}N)(CO)_4]$ (N-N = saturated nitrogen bidentate ligands). *J. Organomet. Chem.* **1991**, *420*, 207–215.

310. Hutchinson, B.; Nakamoto, K., Infrared Spectra of Group VI B Metal Carbonyls Containing Heterocyclic Diamines. *Inorg. Chim. Acta* **1969**, *3*, 591-595.

311. Clauti, G.; Zassinovich, G.; Mestroni, G., Carbonyl Complexes of Rh(I), Ir(I) and Mo(0) Containing Substituted Derivatives of 1,10-Phenanthroline and 2,2'-Bipyridine. *Inorg. Chim. Acta* **1986**, *112*, 103–106.

312. Kulasingham, G. C.; McWhinnie, W. R., The infrared spectra of some tetracarbonylmolybdenum complexes in the regions 2500–1750 cm^{-1} and 667–222 cm^{-1}. *J. Less Common Met.* **1966**, *10*, 72–74.

313. Gansow, O. A.; Kimura, B. Y.; Dobson, G. R.; Brown, R. A., Carbon-13 Nuclear Magnetic Resonance of Some Group VIb Metal Carbonyls and Derivatives. *J. Am. Chem. Soc.* **1971**, *93*, 5922–5924.

314. Mann, B. E., Carbon-13 Nuclear Magnetic-Resonance Spectra of Some Carbonyl Complexes of Chromium, Molybdenum, and Tungsten. *J. Chem. Soc., Dalton Trans.* **1973**, 2012–2015.

315. Bard, A. J.; Faulkner, L. R., *Electrochemical Methods – Fundamentals and Applications*. 2nd ed.; John Wiley & Sons, Inc.: Toronto, 2001.

316. Perrier, A.; Maurel, F.; Perpète, E. A.; Wathelet, V.; Jacquemin, D., Spectral Properties of Spirooxazine Photochromes: TD-DFT Insights. *J. Phys. Chem. A* **2009**, *113*, 13004–13012.

317. Ernst, S.; Vogler, C.; Klein, A.; Kaim, W.; Zalis, S., π^* molecular orbital crossing $a_2(\chi)/b_1(\psi)$ in 1,10-phenanthroline derivatives. Ab initio calculations and EPR/ENDOR

studies of the 4,7-diaza-1,10-phenanthroline radical anion and its $M(CO)_4$ complexes (M=Cr, Mo, W). *Inorg. Chem.* **1996**, *35*, 1295–1300.

318. Klein, A.; Kaim, W.; Waldhor, E.; Hausen, H. D., Different Orbital Occupation by an Added Single Electron in 1,10-Phenanthroline and Its 3,4,7,8-Tetramethyl Derivative. Evidence from Electron Paramagnetic Resonance Spectroscopy of the Anion Radicals and of Their Dimesitylplatinum(II) Complexes. X-Ray Molecular-Structure of Dimesityl(1,10-Phenanthroline)Platinum(II). *J. Chem. Soc., Perkin Trans. 2* **1995**, 2121–2126.

319. Elian, M.; Hoffmann, R., Bonding Capabilities of Transition-Metal Carbonyl Fragments. *Inorg. Chem.* **1975**, *14*, 1058–1076.

320. Richardson, D. E., The Angular Overlap Model as a Unified Bonding Model for Main-Group and Transition-Metal Compounds - a Version Suitable for Undergraduate Inorganic Students. *J. Chem. Educ.* **1993**, *70*, 372–380.

321. Yang, L.; Feng, J. K.; Ren, A. M., Theoretical studies of ground and excited electronic states of complexes M(CO)4(phen) (M=Cr, Mo, W; phen=1,10-phenanthroline). *Synth. Met.* **2005**, *152*, 265–268.

322. Farrell, I. R.; Hartl, F.; Zalis, S.; Mahabiersing, T.; Vlcek, A., The spectroscopic, electrochemical and photophysical effects of the b_1/a_2 π^* lowest unoccupied molecular orbital switching in $[M(CO)_4(N,N)]$ (M = Cr or W; N,N = 1,10-phenanthroline or 3,4,7,8-tetramethyl-1,10-phenanthroline). An experimental and DFT computational study. *J. Chem. Soc., Dalton Trans.* **2000**, 4323–4331.

323. Hay, P. J.; Wadt, W. R., Ab *initio* Effective Core Potentials for Molecular Calculations. Potentials for the Transition-Metal Atoms Sc to Hg. *J. Chem. Phys.* **1985**, *82*, 270–283.

324. Wadt, W. R.; Hay, P. J., Ab *initio* Effective Core Potentials for Molecular Calculations. Potentials for Main Group Elements Na to Bi. *J. Chem. Phys.* **1985**, *82*, 284–298.

325. Hay, P. J.; Wadt, W. R., Ab *initio* Effective Core Potentials for Molecular Calculations. Potentials for K to Au Including the Outermost Core Orbitals. *J. Chem. Phys.* **1985**, *82*, 299–310.

326. Aldoshin, S. M.; Chuev, I. I.; Filipenko, O. S.; Utenyshev, A. N.; Lokshin, V.; Larégenie, P.; Samat, A.; Guglielmetti, R., Structures and photochromic properties of substituted spiroindolinonaphthoxazines. *Russ. Chem. Bull.* **1998**, *47*, 1089–1097.

327. Zilker, S. J., Holographic data storage - The materials challenge. *Chemphyschem* **2002**, *3*, 333–334.

328. *SAINT*, Version 7.53A; Bruker AXS Inc.: Madison, Wisconsin, USA, 1997–2008.

329. *SADABS*, V2008/1; Bruker AXS Inc.: Madison, Wisconsin, USA, 2008.

330. Cromer, D. T.; Waber, J. T., Table 2.2A. In *International Tables for X-ray Crystallography*, The Kynoch Press: Birmingham, England, 1974; Vol. IV.

331. Ibers, J. A.; Hamilton, W. C., Dispersion Corrections and Crystal Structure Refinements. *Acta Crystallogr.* **1964**, *17*, 781–782.

332. Creagh, D. C.; McAuley, W. J., Table 4.2.6.8. In *International Tables for Crystallography*, Wilson, A. J. C., Ed. Kluwer Academic Publishers: Boston, 1992; Vol. C, pp 219–222.

333. Creagh, D. C.; Hubbell, J. H., Table 4.2.4.3. In *International Tables for Crystallography*, Wilson, A. J. C., Ed. Kluwer Academic Publishers: Boston, 1992; Vol. C, pp 200–206.

334. *SHELXTL*, Version 5.1; Bruker AXS Inc.: Madison, Wisconsin, USA, 1997.

335. Bao, D. D.; Millare, B.; Xia, W.; Steyer, B. G.; Gerasimenko, A. A.; Ferreira, A.; Contreras, A.; Vullev, V. I., Electrochemical Oxidation of Ferrocene: A Strong Dependence on the Concentration of the Supporting Electrolyte for Nonpolar Solvents. *J. Phys. Chem. A* **2009**, *113*, 1259–1267.

336. Pierpont, C. G., Studies on charge distribution and valence tautomerism in transition metal complexes of catecholate and semiquinonate ligands. *Coord. Chem. Rev.* **2001**, *216*, 99–125.

337. Shultz, D. A., Valence Tautomerism in Dioxolene Complexes of Cobalt. In *Magnetism: Molecules to Materials II*, Miller, J. S.; Drillon, M., Eds. Wiley-VCH: Weinheim, 2001; pp 281–306.

338. Evangelio, E.; Ruiz-Molina, D., Valence tautomerism: New challenges for electroactive ligands. *Eur. J. Inorg. Chem.* **2005**, 2957–2971.

339. Hendrickson, D. N.; Pierpont, C. G., Valence tautomeric transition metal complexes. *Top Curr Chem* **2004**, *234*, 63–95.

340. Sato, O.; Tao, J.; Zhang, Y.-Z., Control of Magnetic Properties through External Stimuli. *Angew. Chem. Int. Ed.* **2007**, *46*, 2152–2187.

341. Gutlich, P.; Garcia, Y.; Woike, T., Photoswitchable coordination compounds. *Coord. Chem. Rev.* **2001**, *219–221*, 839–879.

342. Einaga, Y., Photo-switching magnetic materials. *J Photochem. Photobiol., C* **2006**, *7*, 69–88.

343. Sato, O.; Iyoda, T.; Fujishima, A.; Hashimoto, K., Photoinduced Magnetization of a Cobalt-Iron Cyanide. *Science* **1996**, *272*, 704–705.

344. Sato, O.; Cui, A.; Matsuda, R.; Tao, J.; Hayami, S., Photo-induced Valence Tautomerism in Co Complexes. *Acc. Chem. Res.* **2007**, *40*, 361–369.

345. Adams, D. M.; Dei, A.; Rheingold, A. L.; Hendrickson, D. N., Bistability in the $[Co^{II}(semiquinonate)_2]$ to $[Co^{III}(catecholate)(semiquinonate)]$ Valence-Tautomeric Conversion. *J. Am. Chem. Soc.* **1993**, *115*, 8221–8229.

346. Dei, A., Correlations between Optical Charge Transfer Energies and Electrochemical Data - the Iron(III)–Catecholato System. *Inorg. Chem.* **1993**, *32*, 5730–5733.

347. Cador, O.; Chabre, F.; Dei, A.; Sangregorio, C.; Van Slageren, J.; Vaz, M. G. F., Temperature-induced solid-state valence tautomeric interconversion in two cobalt-Schiff base diquinone complexes. *Inorg. Chem.* **2003**, *42*, 6432–6440.

348. Bencini, A.; Caneschi, A.; Carbonera, C.; Dei, A.; Gatteschi, D.; Righini, R.; Sangregorio, C.; Van Slageren, J., Tuning the physical properties of a metal complex by molecular techniques: the design and the synthesis of the simplest cobalt-*o*-dioxolene complex undergoing valence tautomerism. *J. Mol. Struct.* **2003**, *656*, 141–154.

349. Evangelio, E.; Ruiz-Molina, D., Valence tautomerism: More actors than just electroactive ligands and metal ions. *C. R. Chimie* **2008**, *11*, 1137–1154.

350. Robin, M. B.; Day, P., In *Advances in Inorganic Chemistry and Radiochemistry*, Emeléus, H. J.; Sharpe, A. G., Eds. Academic Press: New York, 1967; Vol. 10, p 247.

351. Schmidt, R. D.; Shultz, D. A.; Martin, J. D.; Boyle, P. D., Goldilocks Effect in Magnetic Bistability: Remote Substituent Modulation and Lattice Control of Photoinduced Valence Tautomerism and Light-Induced Thermal Hysteresis. *J. Am. Chem. Soc.* **2010**, *132*, 6261–6273.

352. Evangelio, E.; Rodriguez-Blanco, C.; Coppel, Y.; Hendrickson, D. N.; Sutter, J. P.; Campo, J.; Ruiz-Molina, D., Solvent effects on valence tautomerism: A comparison between the interconversion in solution and solid state. *Solid State Sciences* **2009**, *11*, 793–800.

353. Kawanishi, Y.; Kitamura, N.; Tazuke, S., Dependence of Spectroscopic, Electrochemical, and Excited-State Properties of Tris Chelate Ruthenium(II) Complexes on Ligand Structure. *Inorg. Chem.* **1989**, *28*, 2968–2975.

354. Adams, D. M.; Noodleman, L.; Hendrickson, D. N., Density functional study of the valence-tautomeric interconversion low-spin $[Co^{III}(SQ)(Cat)(phen)] \leftrightarrow$ high-spin $[Co^{II}(SQ)_2(phen)]$. *Inorg. Chem.* **1997**, *36*, 3966–3984.

355. Imaz, I.; Maspoch, D.; Rodríguez-Blanco, C.; Pérez-Falcón, J. M.; Campo, J.; Ruiz-Molina, D., Valence-tautomeric metal–organic nanoparticles. *Angew. Chem. Int. Ed.* **2008**, *47*, 1857–1860.

356. Jung, O.-S.; Pierpont, C. G., Low-Energy Cobalt(III)-Catechol Electron Transfer. Subtle Coligand Bonding Effects for Co^{III}(N-N)(3,6-DBSQ)(3,6-DBCat) (N-N = 1,10-Phenanthroline, 5-Nitro-1,10-phenanthroline; DBSQ = Di-*tert*-butylsemiquinonate; DBCat = Di-*tert*-butylcatecholato). *J. Am. Chem. Soc.* **1994**, *116*, 1127–1128.

357. Hearns, N. G. R.; Korčok, J. L.; Paquette, M. M.; Preuss, K. E., Dinuclear cobalt bis(dioxolene) complex exhibiting two sequential thermally induced valence tautomeric transitions. *Inorg. Chem.* **2006**, *45*, 8817–8819.

358. Kiriya, D.; Chang, H.-C.; Kamata, A.; Kitagawa, S., Polytypic phase transition in alkyl chain-functionalized valence tautomeric complexes. *Dalton Trans.* **2006**, 1377–1382.

359. Liang, H.; Cha, M. S.; Lee, Y.-A.; Lee, S. S.; Jung, O.-S., First bistable monocobalt complex with six free nitrogen donors: 3,5-Di-*tert*-butylbenzoquinonatocobalt complex containing triethanolaminetriisonicotinate. *Inorg. Chem. Commun.* **2007**, *10*, 71–73.

360. Yamaguchi, A.; Awaga, K., Inner- and outer-sphere magnetic moments in the cobalt–quinone valence tautomeric system. *J. Mater. Chem.* **2001**, *11*, 2142–2145.

361. Naumov, P.; Belik, A. A., Effects of secondary ligand and excitation on the thermally induced and photoinduced valence tautomerism semiquinonate − catecholate. *Inorg. Chem. Commun.* **2008**, *11*, 465–469.

362. Kiriya, D.; Chang, H.-C.; Kitagawa, S., Molecule-based valence tautomeric bistability synchronized with a macroscopic crystal-melt phase transition. *J. Am. Chem. Soc.* **2008**, *130*, 5515–5522.

363. Buchanan, R. M.; Fitzgerald, B. J.; Pierpont, C. G., Semiquinone Radical Anion Coordination to Divalent Cobalt and Nickel. Structural Features of the Bis(3,5-di-*tert*-butyl-1,2-semiquinone)cobalt(II) Tetramer. *Inorg. Chem.* **1979**, *18*, 3439–3444.

364. Lange, C. W.; Conklin, B. J.; Pierpont, C. G., Radical Superexchange in Semiquinone Complexes Containing Diamagnetic Metal Ions. 3,6-Di-*tert*-Butyl-1,2-Semiquinonate Complexes of Zinc(II), Cobalt(III), Gallium(III), and Aluminum(III). *Inorg. Chem.* **1994**, *33*, 1276–1283.

365. Attia, A. S.; Pierpont, C. G., New semiquinone/catecholate complexes that exhibit valence tautomerism. Synthesis and characterization of $Mn^{III}(thf)_2$(3,6-DBSQ)(3,6-DBCat) and observations on the Mn^{IV}(3,6-DBSQ)$_2$(3,6-DBCat)/Mn^{III}(3,6-DBSQ)$_3$ equilibrium in the solid state. *Inorg. Chem.* **1998**, *37*, 3051–3056.

366. Chaudhuri, P.; Verani, C. N.; Bill, E.; Bothe, E.; Weyhermuller, T.; Wieghardt, K., Electronic structure of bis(*o*-iminobenzosemiquinonato)metal complexes (Cu, Ni, Pd). The art of establishing physical oxidation states in transition-metal complexes containing radical ligands. *J. Am. Chem. Soc.* **2001**, *123*, 2213–2223.

367. Brown, I. D.; Altermatt, D., Bond-Valence Parameters Obtained from a Systematic Analysis of the Inorganic Crystal Structure Database. *Acta Crystallogr., Sect. B: Struct. Sci.* **1985**, *41*, 244–247.

368. Berry, J. F.; Cotton, F. A.; Liu, C. Y.; Lu, T. B.; Murillo, C. A.; Tsukerblat, B. S.; Villagrán, D.; Wang, X. P., Modeling Spin Interactions in a Cyclic Trimer and a Cuboidal Co_4O_4 core with Co(II) in Tetrahedral and Octahedral Environments. *J. Am. Chem. Soc.* **2005**, *127*, 4895–4902.

369. Wang, F.-M.; Lu, C.-S.; Li, Y.-Z.; Meng, Q.-J., A tetranuclear cobalt(III) cluster with 2-(hydroxymethyl) pyridine ligands. *Acta Crystallogr. Sect. E: Struct. Rep. Online* **2010**, *66*, M594–U1136.

370. Bertini, I.; Wilson, L. J., $Ni(phen)_3^{2+}$–$Co(phen)_3^{2+}$ System: Evaluation of Dipolar Proton Magnetic Resonance Shift Contribution in Paramagnetic Cobalt(II) Complexes. *J. Chem. Soc. A* **1971**, 489–492.

371. Evangelio, E.; Bonnet, M.-L.; Cabañas, M.; Nakano, M.; Sutter, J.-P.; Dei, A.; Robert, V.; Ruiz-Molina, D., Coexistence of Two Thermally Induced Intramolecular Electron Transfer Processes in a Series of Metal Complexes [M(Cat-N-BQ)(Cat-N-

SQ)]/[M(Cat-N-BQ)$_2$] (M = Co, Fe, and Ni) bearing Non-Innocent Catechol-Based Ligands: A Combined Experimental and Theoretical Study. *Chem. Eur. J.* **2010**, *16*, 6666–6677.

372. Wicklund, P. A.; Brown, D. G., Synthesis and Characterization of Some Cobalt(III) Catechol Complexes. *Inorg. Chem.* **1976**, *15*, 396–400.

373. Sato, O.; Hayami, S.; Gu, Z.-z.; Seki, K.; Nakajima, R.; Fujishima, A., Photo-Induced Long-Lived Intramolecular Electron Transfer in a Co Valence Tautomeric Complex. *Chem. Lett.* **2001**, 874–875.

374. Caneschi, A.; Dei, A.; de Biani, F. F.; Gütlich, P.; Ksenofontov, V.; Levchenko, G.; Hoefer, A.; Renz, F., Pressure- and temperature-induced valence tautomeric interconversion in a *o*-dioxolene adduct of a cobalt-tetraazamacrocycle complex. *Chem. Eur. J.* **2001**, *7*, 3926–3930.

375. Arzberger, S.; Soper, J.; Anderson, O. P.; la Cour, A.; Wicholas, M., Synthesis and structure of an air-stable, free-radical cobalt(III) semiquinone complex. *Inorg. Chem.* **1999**, *38*, 757–761.

376. Lynch, M. W.; Valentine, M.; Hendrickson, D. N., Mixed-Valence Semi-Quinone Catecholate Iron Complexes. *J. Am. Chem. Soc.* **1982**, *104*, 6982-6989.

377. Klokishner, S. I.; Reu, O. S., Vibronic dynamic problem of the valence tautomeric interconversion [low-spin Co(III)(N N)(sq)(cat)] ↔ [high-spin Co(II)(N N)(sq)$_2$]. Magnetic properties and charge-transfer band. *Chem. Phys.* **2003**, *286*, 115−126.

378. Evangelio, E.; Hendrickson, D. N.; Ruiz-Molina, D., Intramolecular electron transfer in the mixed-valence [Co(3,5-DTBCat)(3,5-DTBSQ)(bpy)] complex: Beyond valence tautomerism. *Inorg. Chim. Acta* **2008**, *361*, 3403−3409.

379. Shultz, D. A.; Kumar, R. K.; Bin-Salamon, S.; Kirk, M. L., Valence tautomerization and exchange coupling in a cobalt-nitronylnitroxide-semiquinone complex. *Polyhedron* **2005**, *24*, 2876–2879.

380. Jung, O. S.; Park, S. H.; Lee, Y. A.; Chae, H. K.; Sohn, Y. S., Distinct oxidation-state change dependent on remote group of coligand. (X_2-phen)Co(3,6-DBBQ)$_2$ (X_2-phen=4,7-disubstituted-1,10-phenanthroline; 3,6-DBBQ=3,6-di-*tert*-butyl-1,2-benzoquinone). *Bull. Korean Chem. Soc.* **1996**, *17*, 1085–1087.

381. *SAINT*, Version 7.68A; Bruker AXS Inc.: Madison, Wisconsin, USA, 1997–2010.

382. Farrugia, L. J., WinGX – V1.70. *J. Appl. Crystallogr.* **1999**, *32*, 837.

383. Schubert, E. M., Utilizing the Evans Method with a Superconducting NMR Spectrometer in the Undergraduate Laboratory. *J. Chem. Educ.* **1992**, *69*, 62–62.

384. Evans, D. F., The Determination of the Paramagnetic Susceptibility of Substances in Solution by Nuclear Magnetic Resonance. *J. Chem. Soc.* **1959**, 2003–2005.

385. Crawford, T. H.; Swanson, J., Temperature Dependent Magnetic Measurements and Structural Equilibria in Solution. *J. Chem. Educ.* **1971**, *48*, 382.

386. Ostfeld, D.; Cohen, I. A., A Cautionary Note on the Use of the Evans Method for Magnetic Measurements. *J. Chem. Educ.* **1972**, *49*, 829.

387. Yaws, C. L., *Physical Properties - A Guide to the Physical, Thermodynamic and Transport Property Data of Industrially Important Chemical Compounds*. McGraw-Hill: New York, 1977.

388. Grant, D. H., Paramagnetic-Susceptibility by NMR - the Solvent Correction Reexamined. *J. Chem. Educ.* **1995**, *72*, 39–40.

389. Jacquemin, D.; Perpète, E. A.; Maurel, F.; Perrier, A., Doubly Closing or Not? Theoretical Analysis for Coupled Photochromes. *J. Phys. Chem. C* **2010**, *114*, 9489–9497.

Appendix A. NMR Spectra

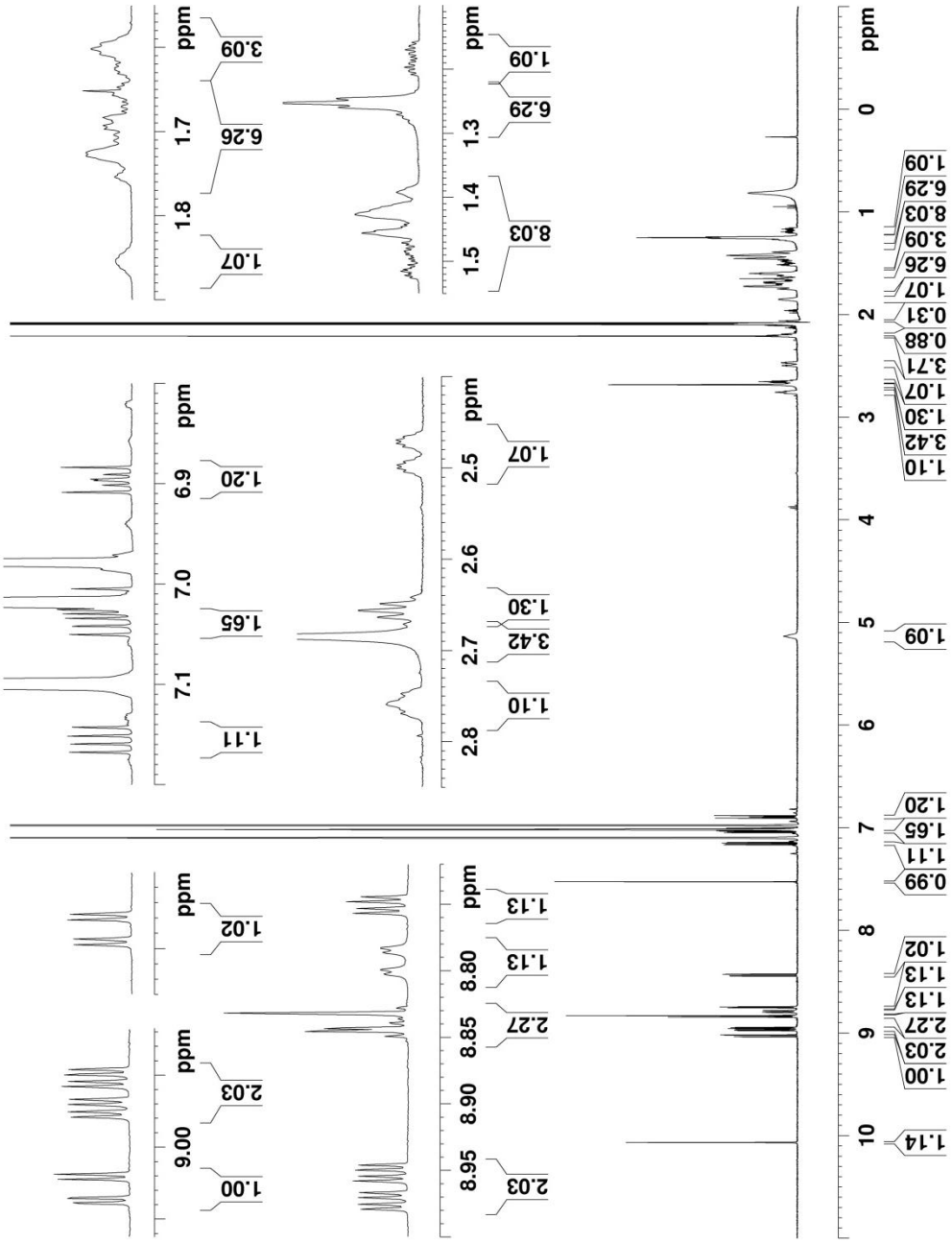

Figure A1. ^{1}H NMR spectrum of APSO in toluene-d_8 (500 MHz, ~300 K).

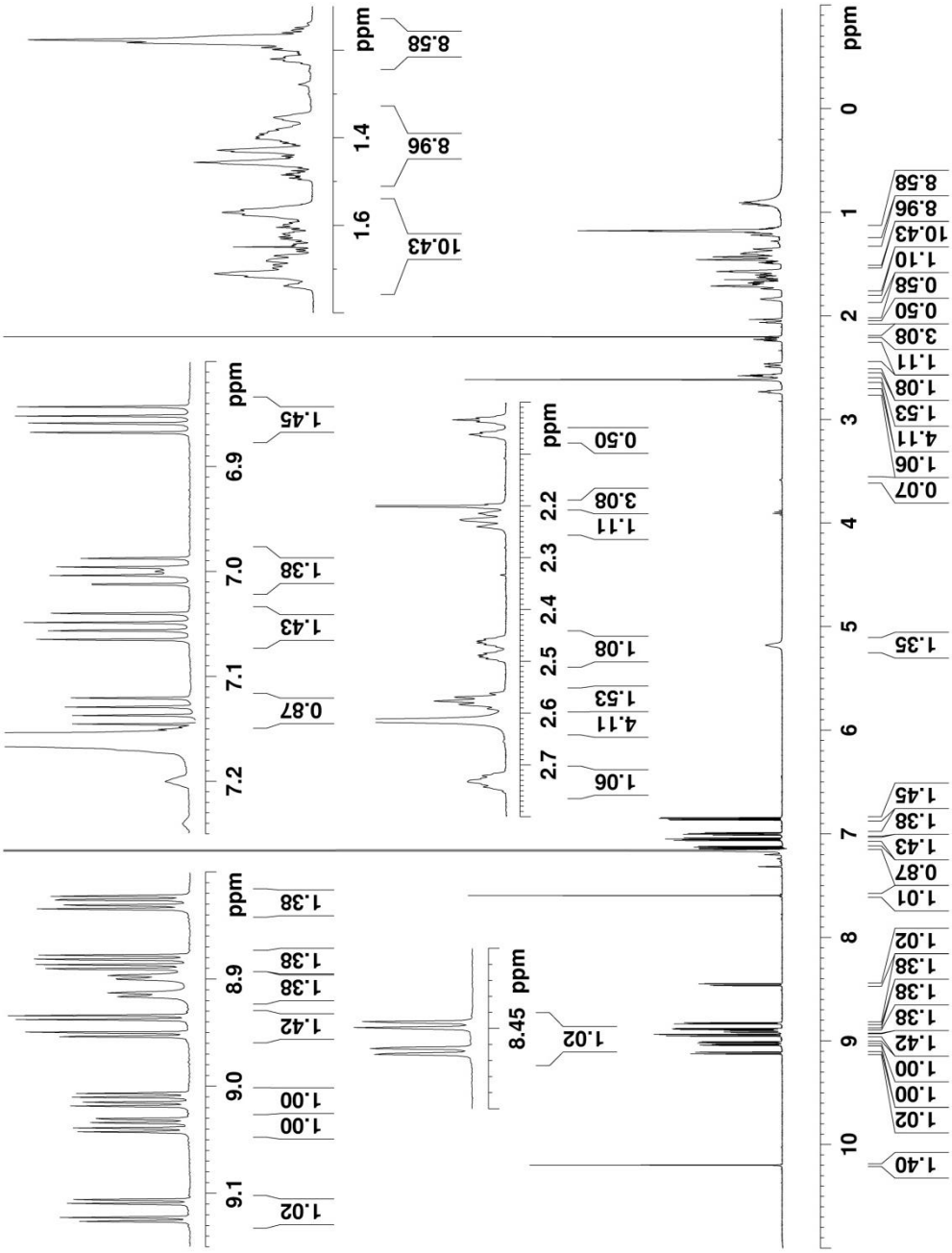

Figure A2. ^{1}H NMR spectrum of APSO in benzene-d_6 (500 MHz, ~300K).

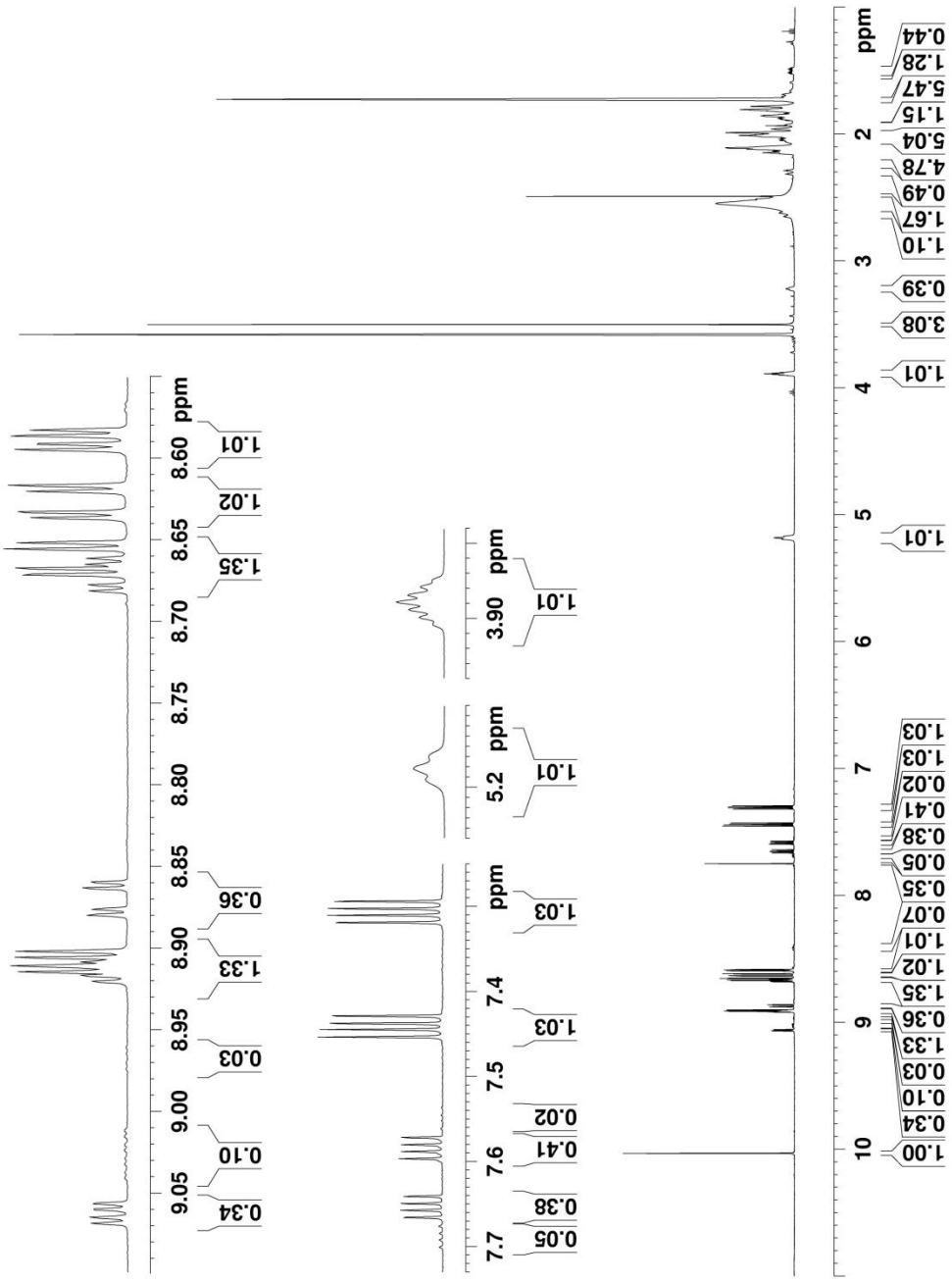

Figure A3. ^{1}H NMR spectrum of APSO in THF-d_8 (500 MHz, ~300 K).

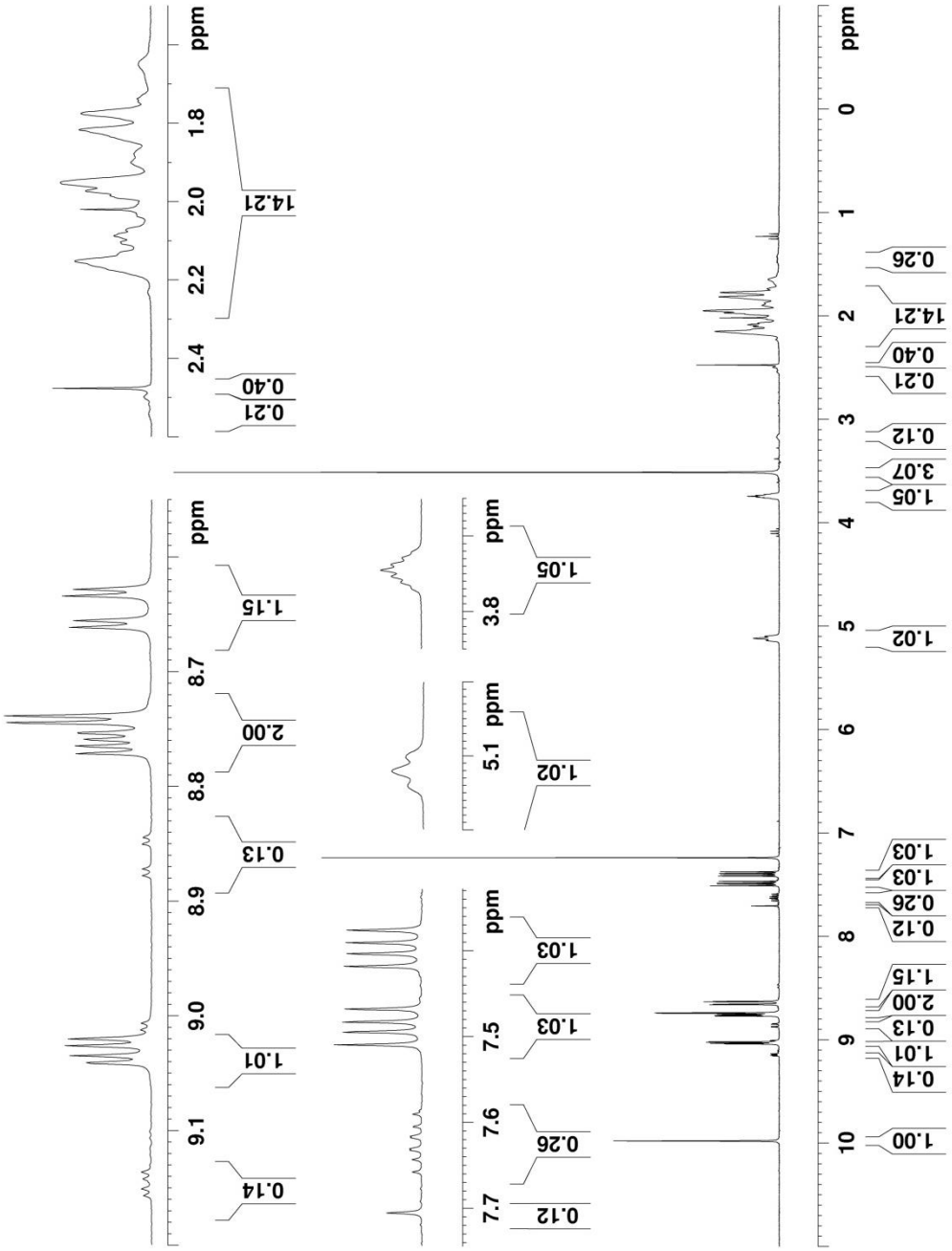

Figure A4. ^{1}H NMR spectrum of APSO in $CDCl_3$ (300 MHz, ~300 K).

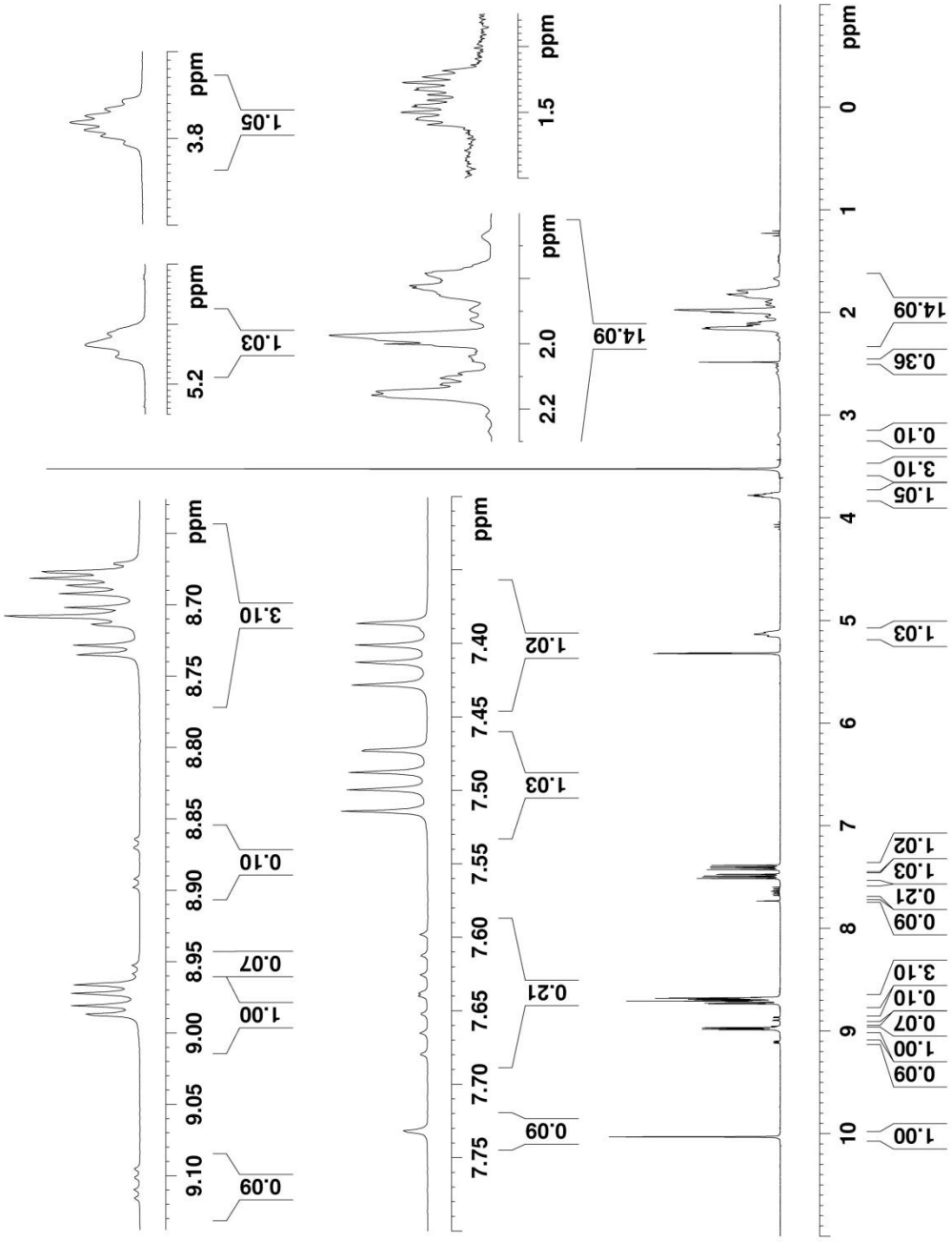

Figure A5. ^{1}H NMR spectrum of APSO in CD_2Cl_2 (300 MHz, ~300 K).

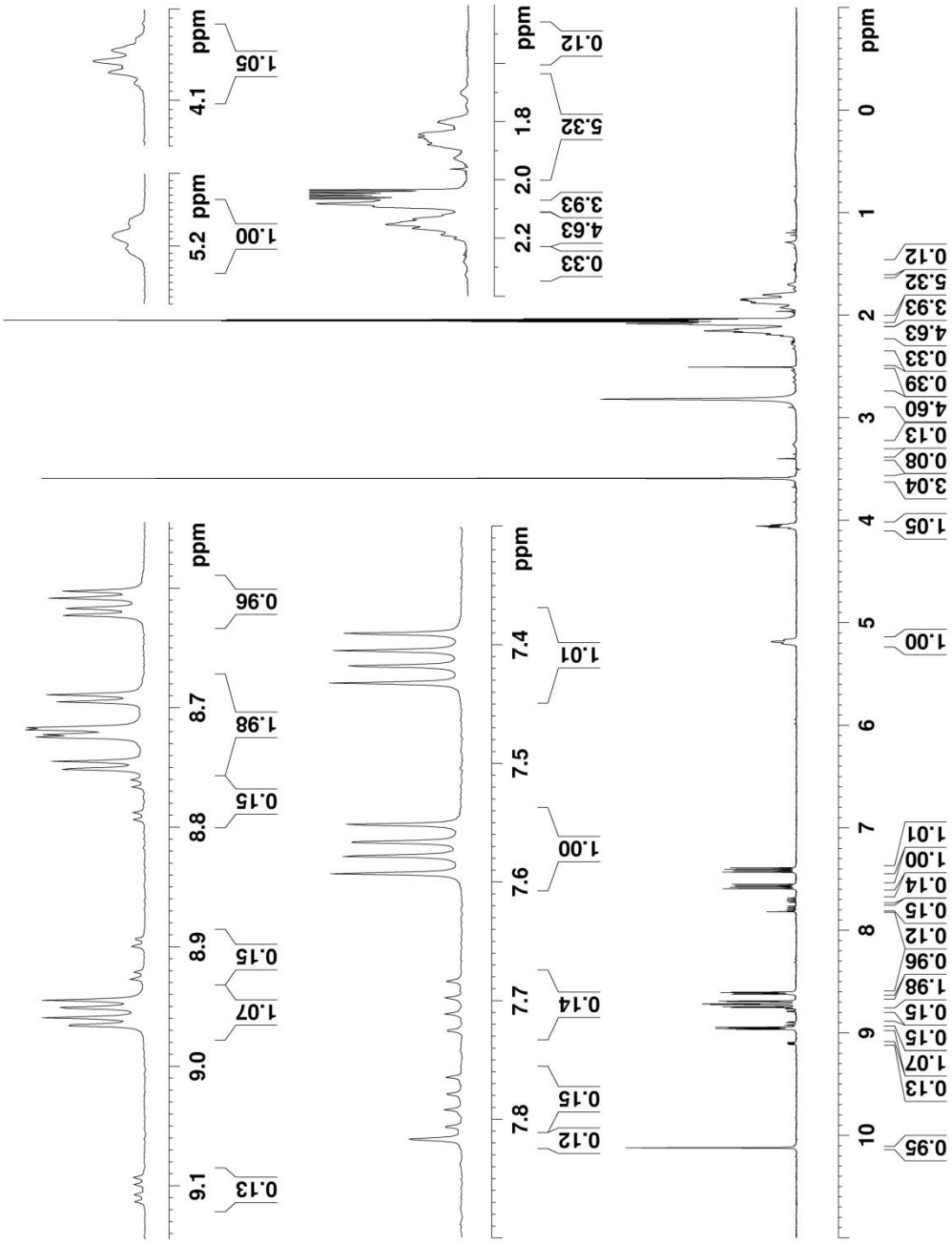

Figure A6. ^{1}H NMR spectrum of APSO in acetone-d_6 (300 MHz, ~300 K).

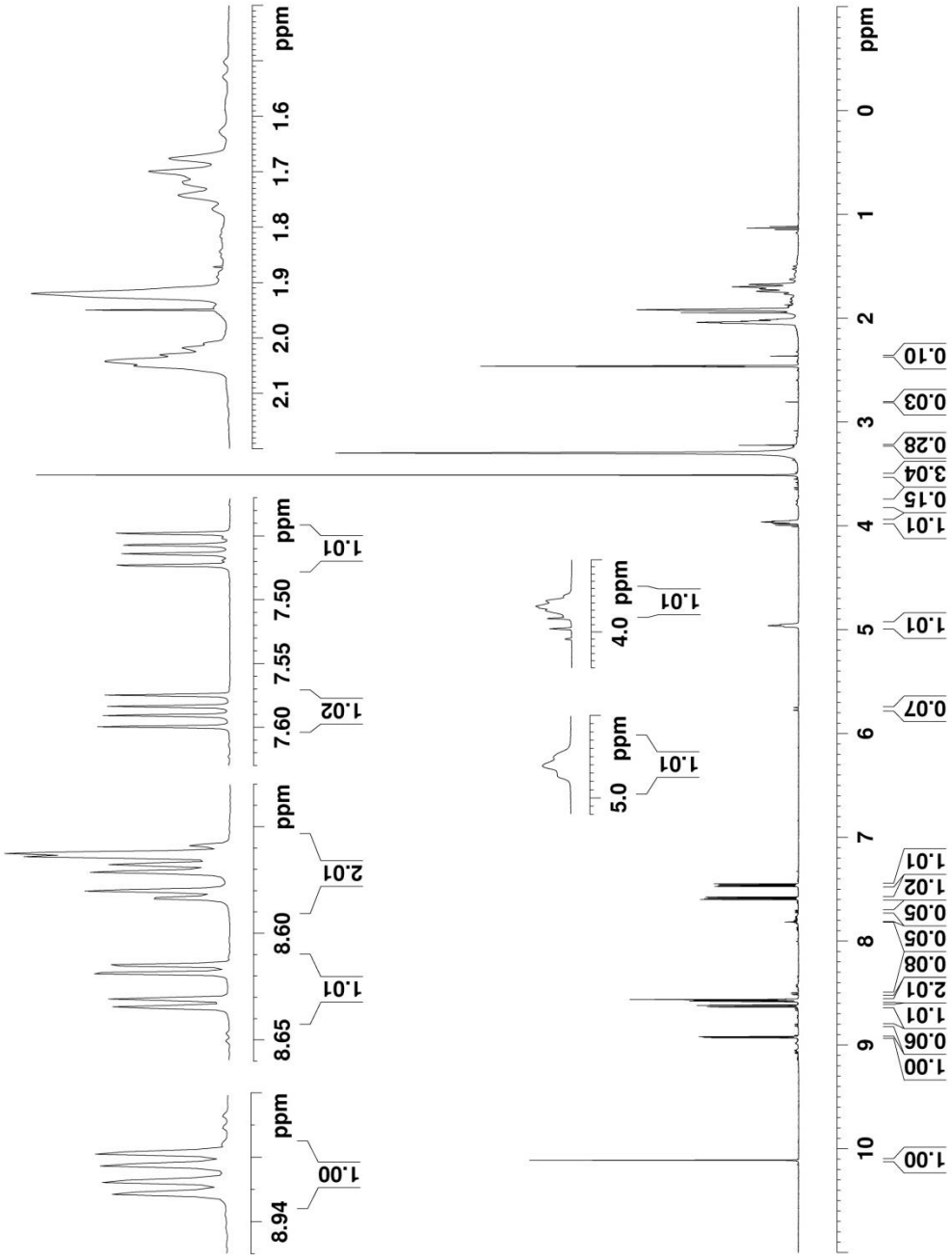

Figure A7. ^{1}H NMR spectrum of APSO in DMSO-d_6 (500 MHz, ~300 K).

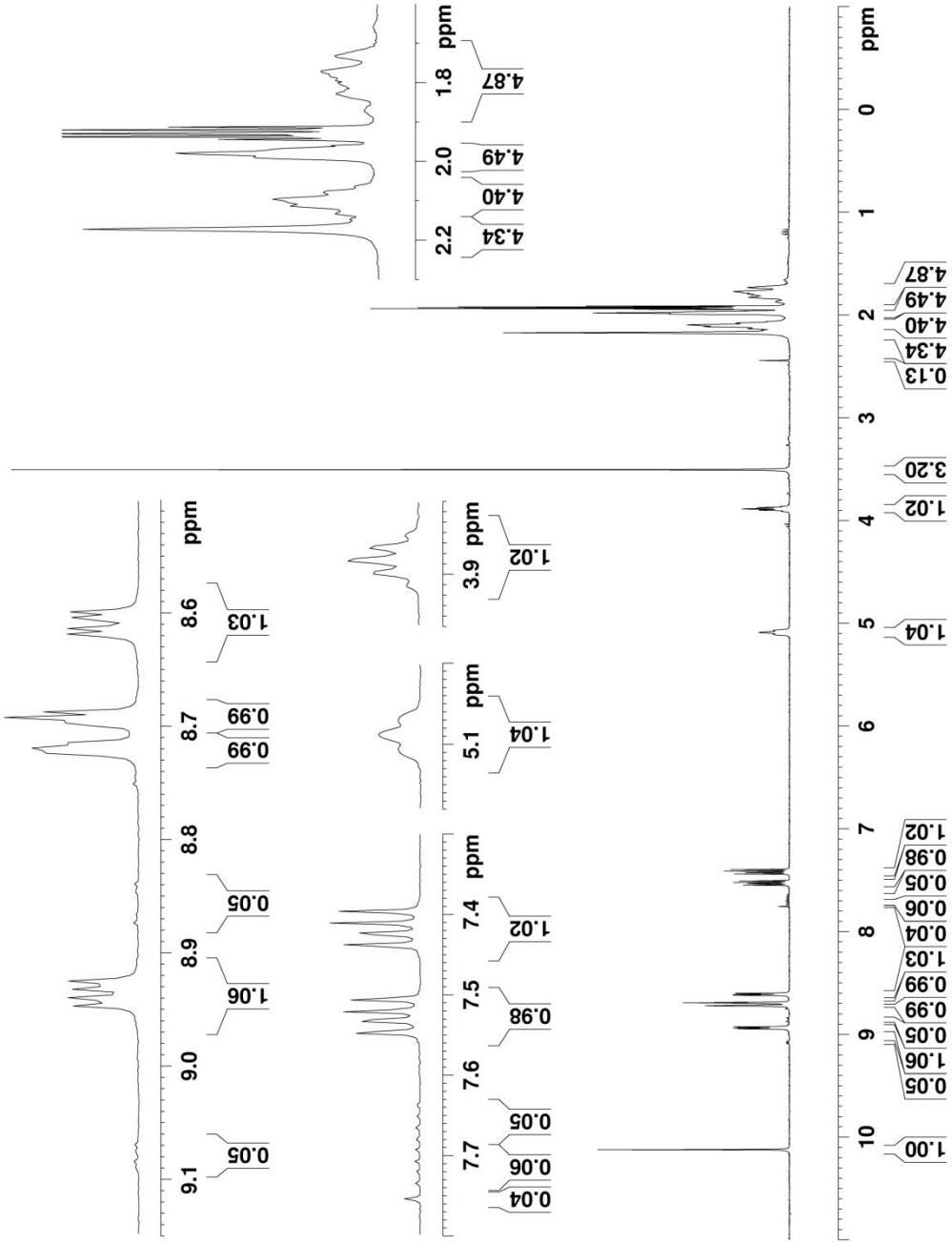

Figure A8. ^{1}H NMR spectrum of APSO in CD_3CN (300 MHz, ~300 K).

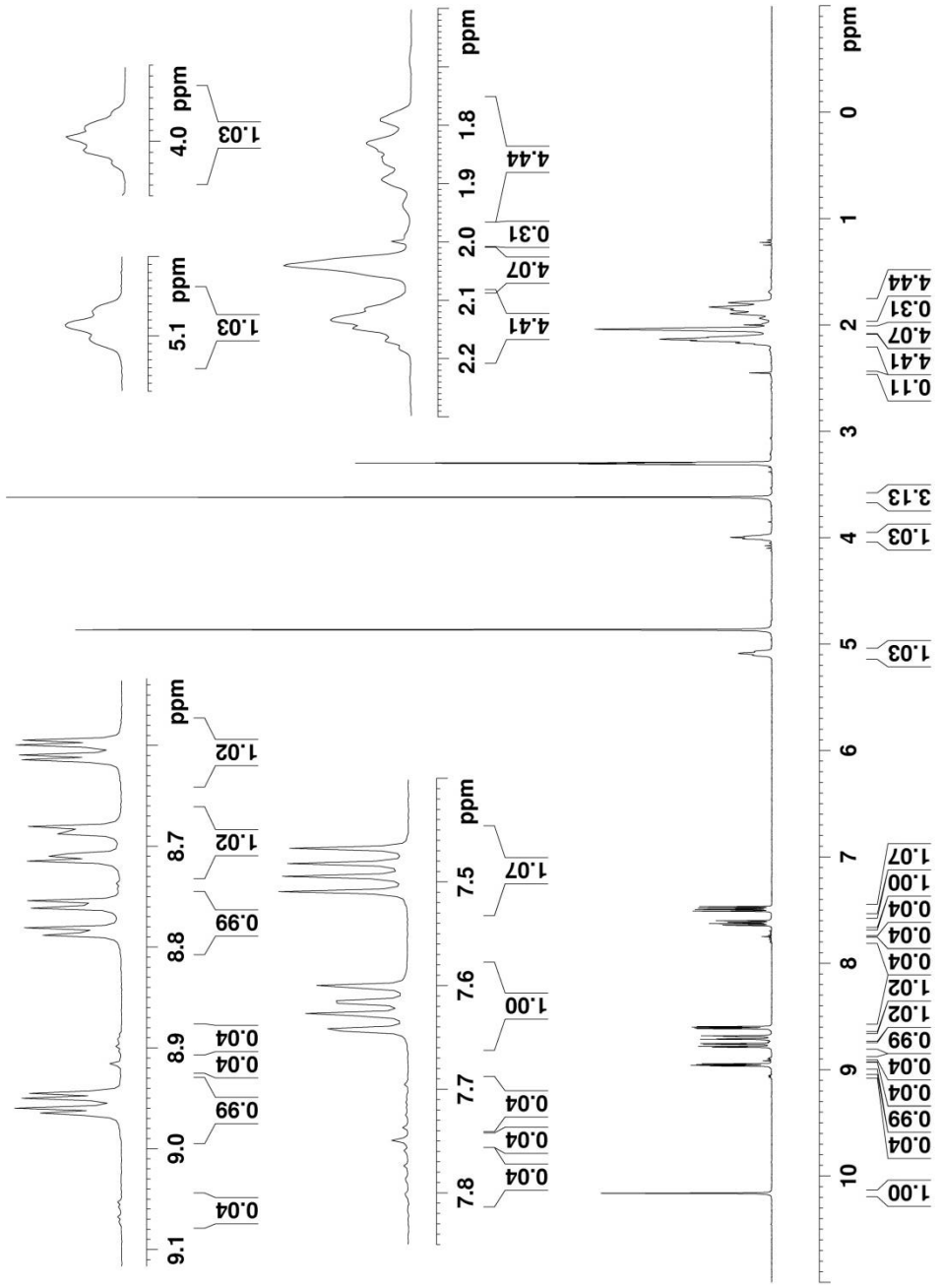

Figure A9. ^{1}H NMR spectrum of APSO in CD_3OD (300 MHz, ~300 K).

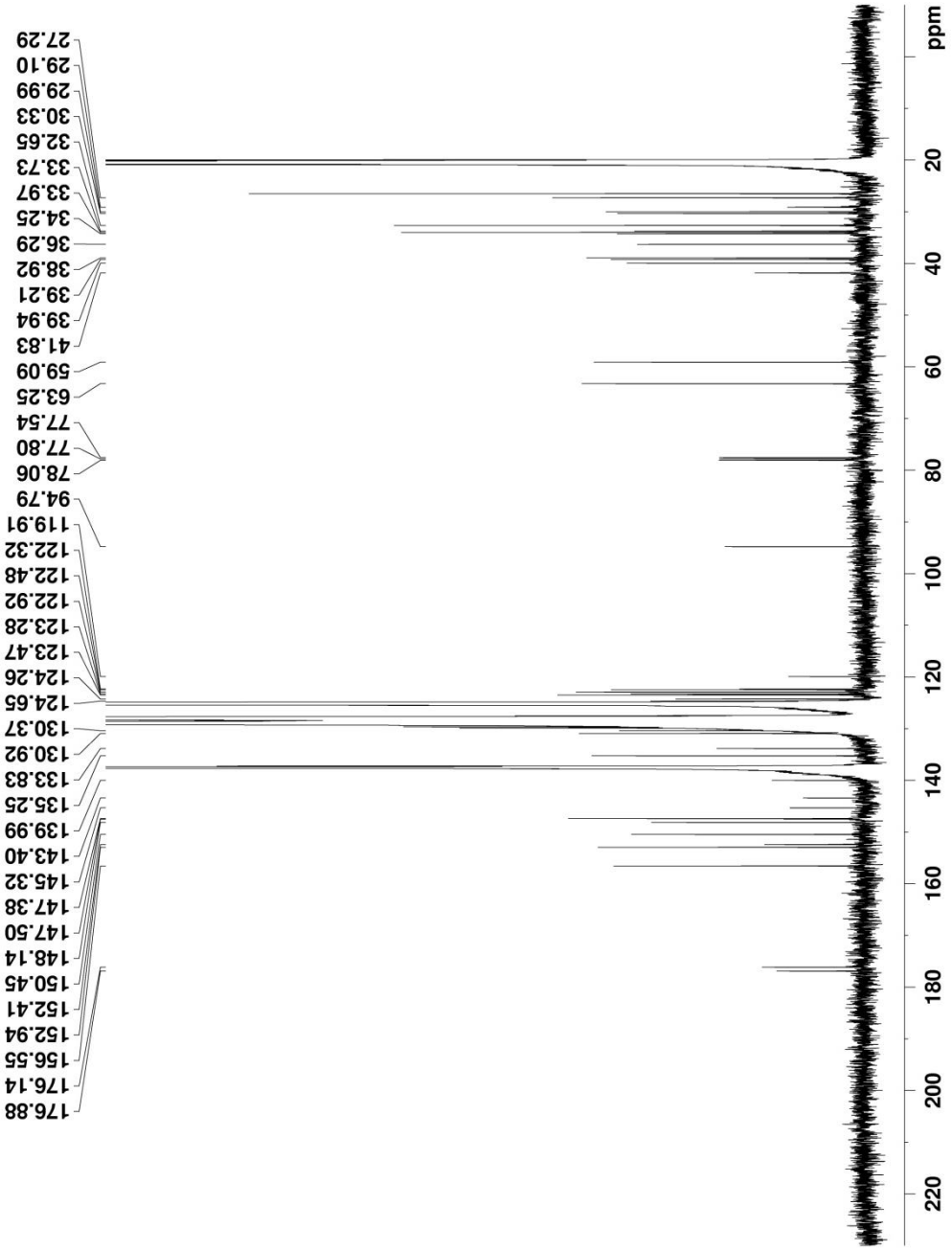

Figure A10. ^{13}C NMR spectrum of APSO in toluene-d_8 (125 MHz, ~300 K).

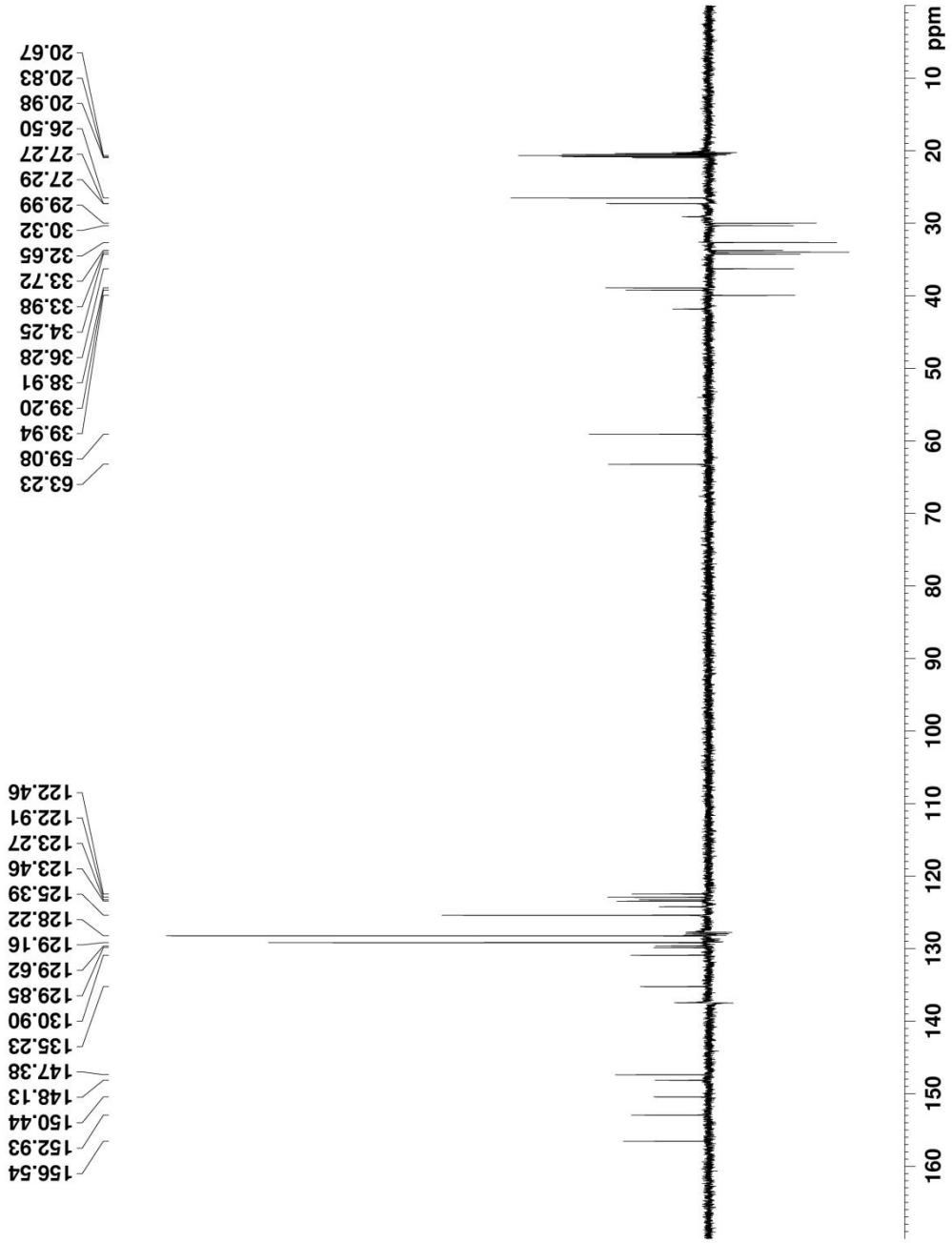

Figure A11. DEPT-135 spectrum of APSO in toluene-d_8 (125 MHz, ~300 K).

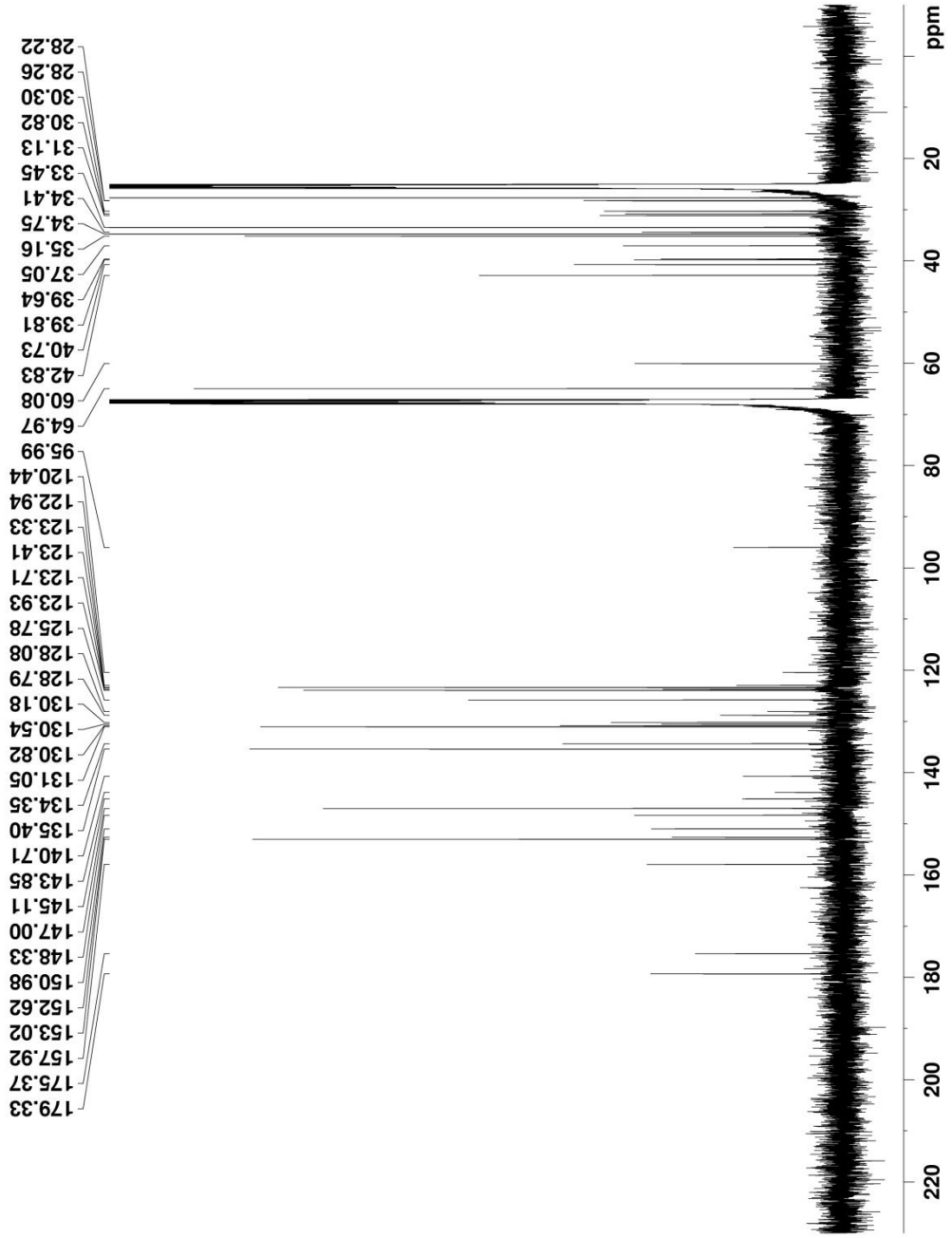

Figure A12. ^{13}C NMR spectrum of APSO in THF-d_8 (125 MHz, ~300 K).

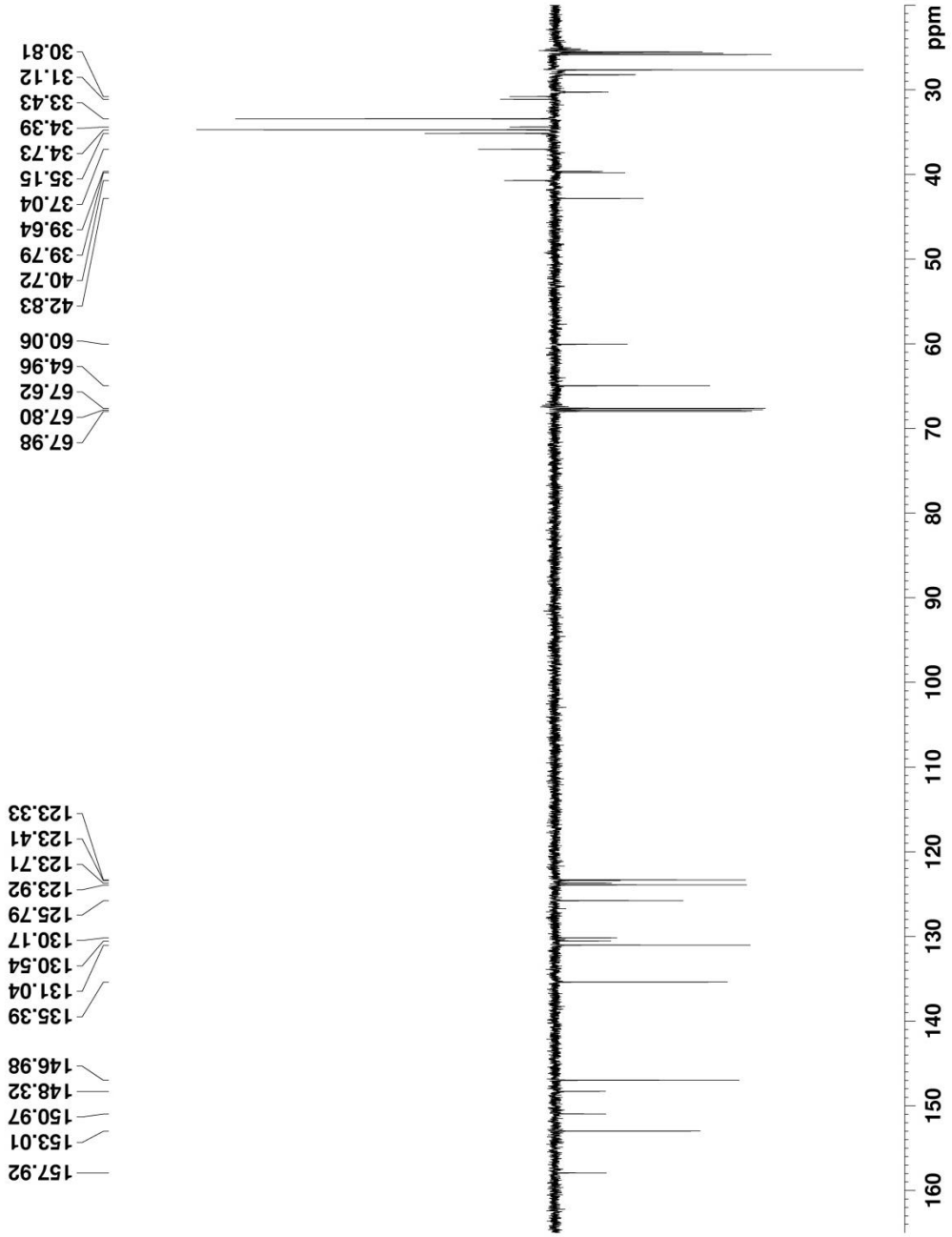

Figure A13. DEPT-135 spectrum of APSO in THF-d_8 (125 MHz, ~300 K).

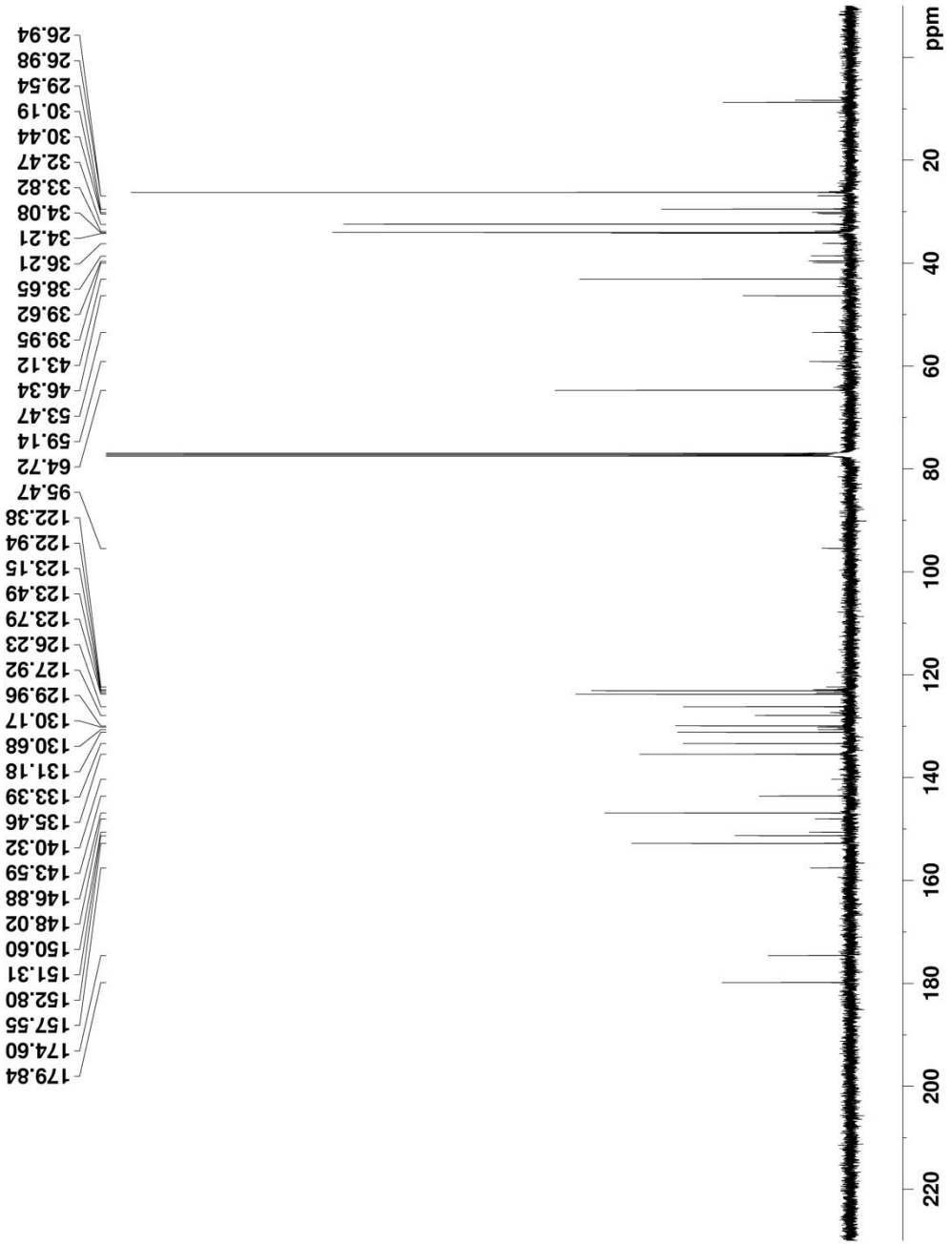

Figure A14. ^{13}C NMR spectrum of APSO in $CDCl_3$ (125 MHz, ~300 K).

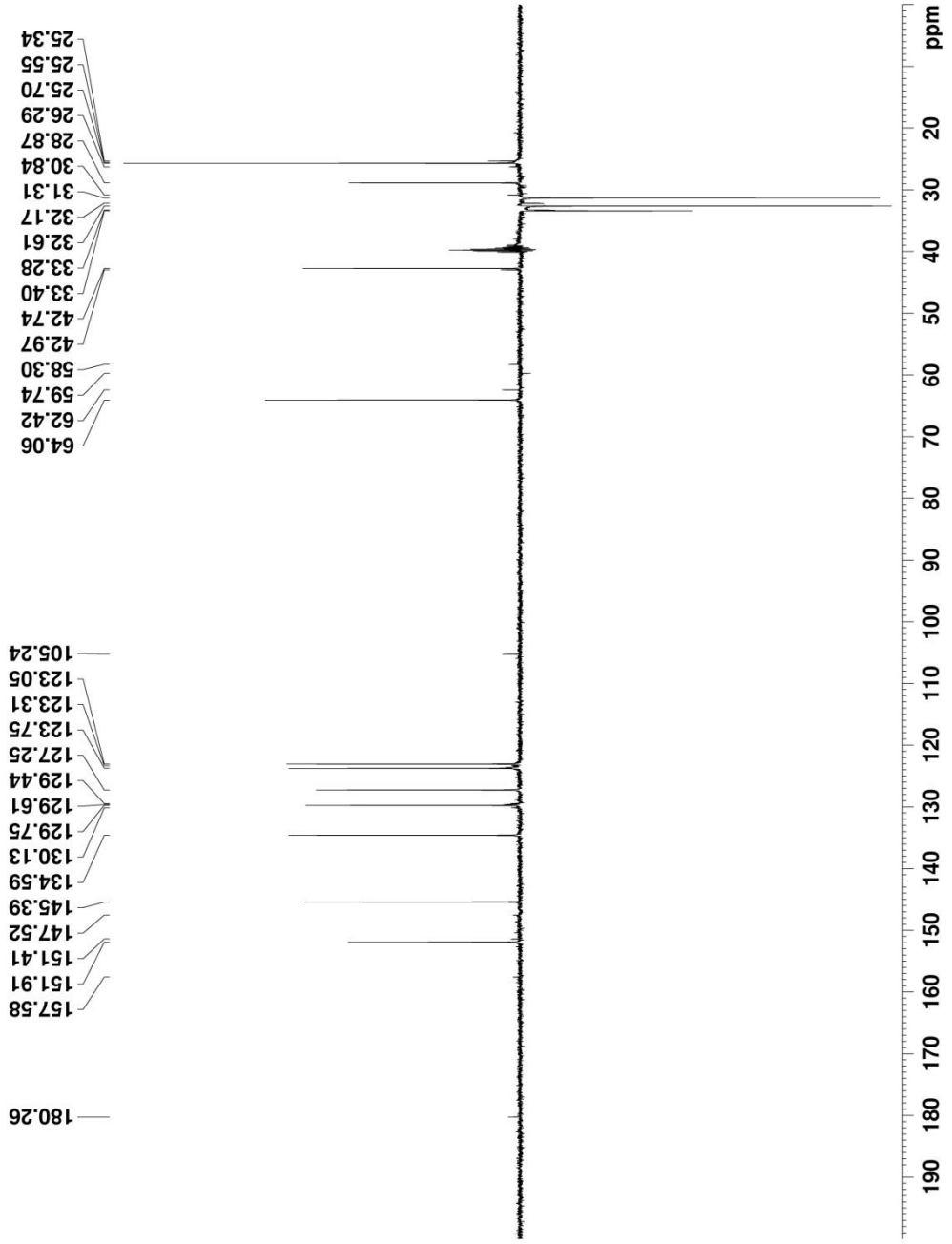

Figure A15. DEPT-135 spectrum of APSO in DMSO-d_6 (125 MHz, ~300 K).

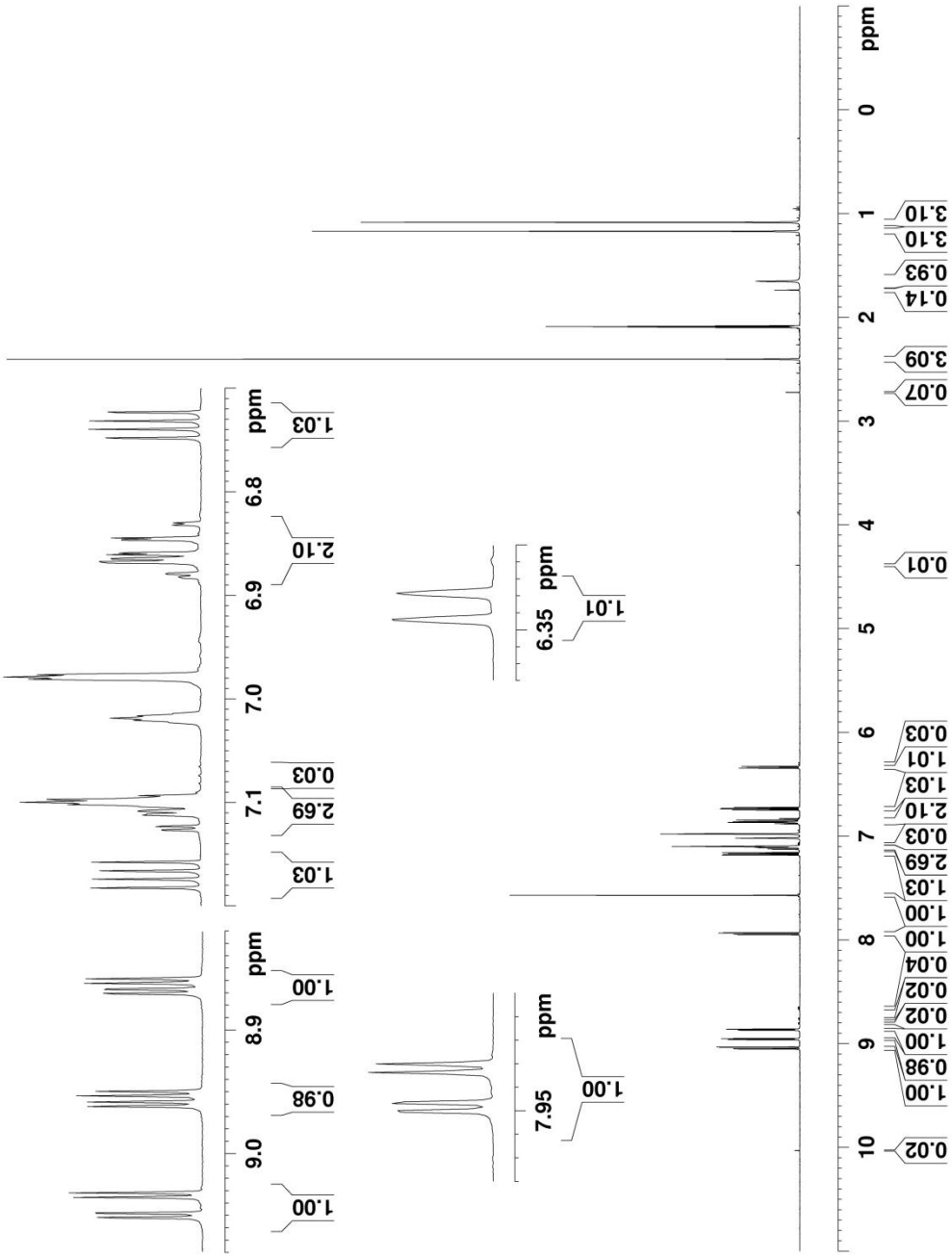

Figure A16. ^{1}H NMR spectrum of IPSO in toluene-d_8 (500 MHz, ~300 K).

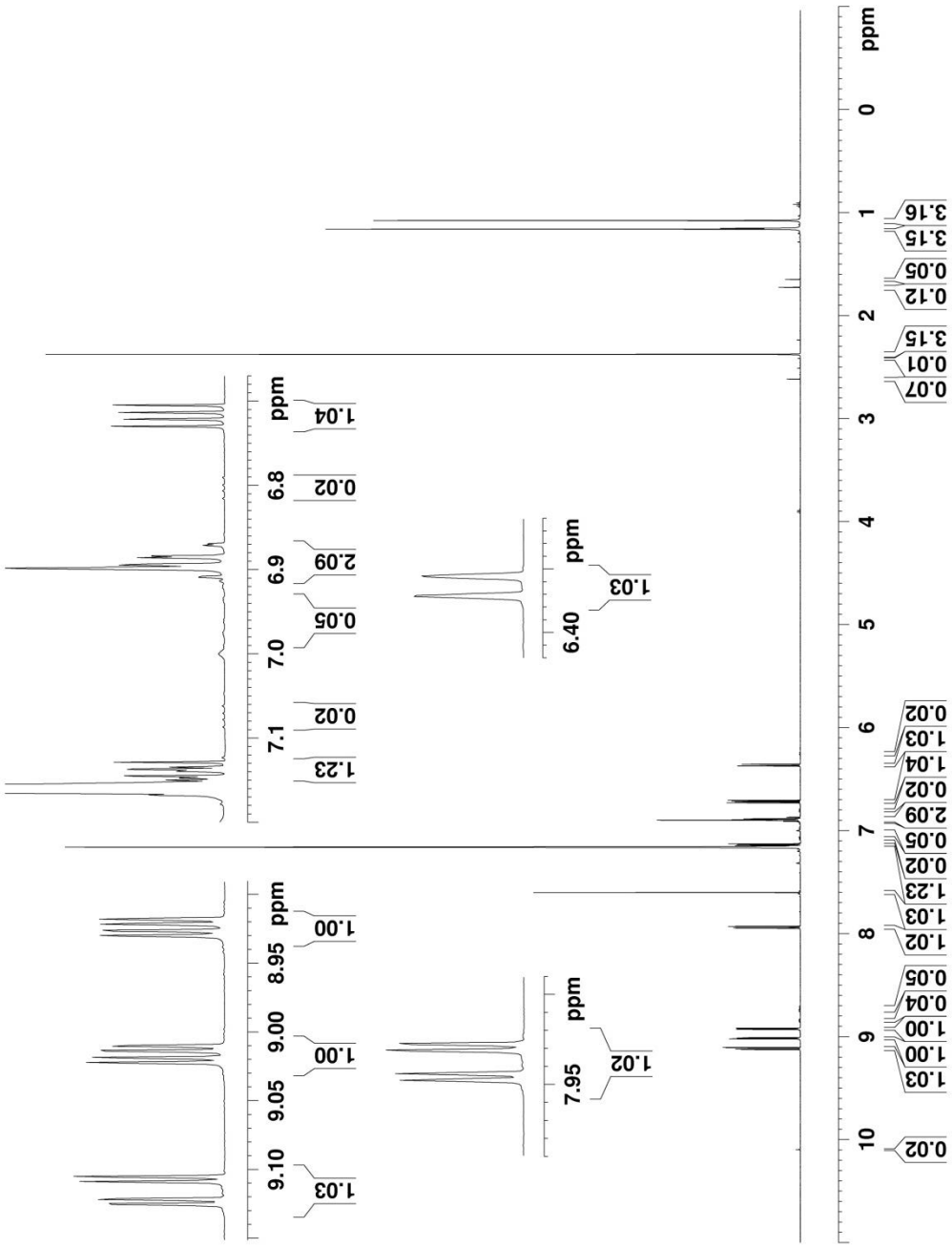

Figure A17. ^{1}H NMR spectrum of IPSO in benzene-d_6 (500 MHz, ~300K).

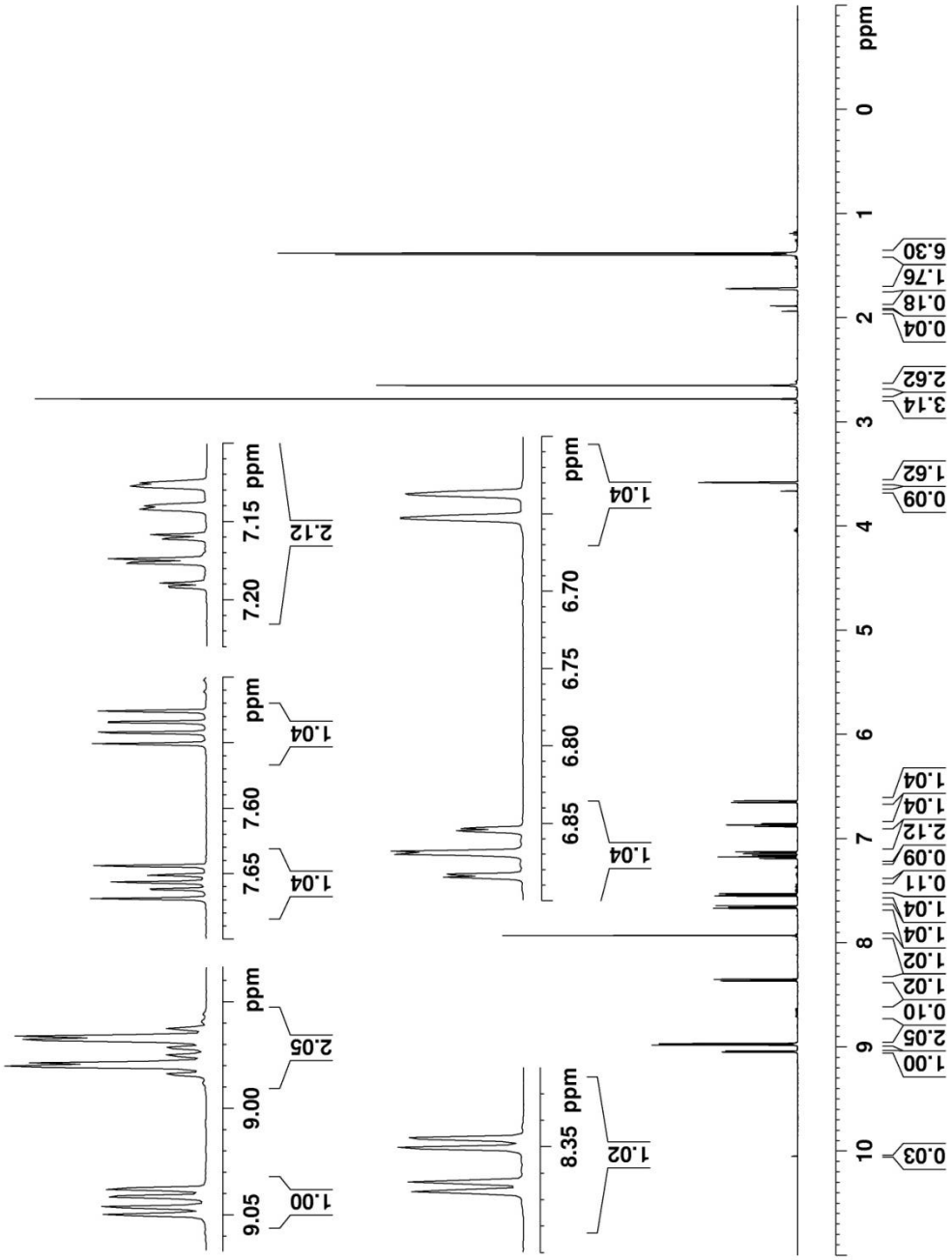

Figure A18. ^{1}H NMR spectrum of IPSO in THF-d_8 (500 MHz, ~300 K).

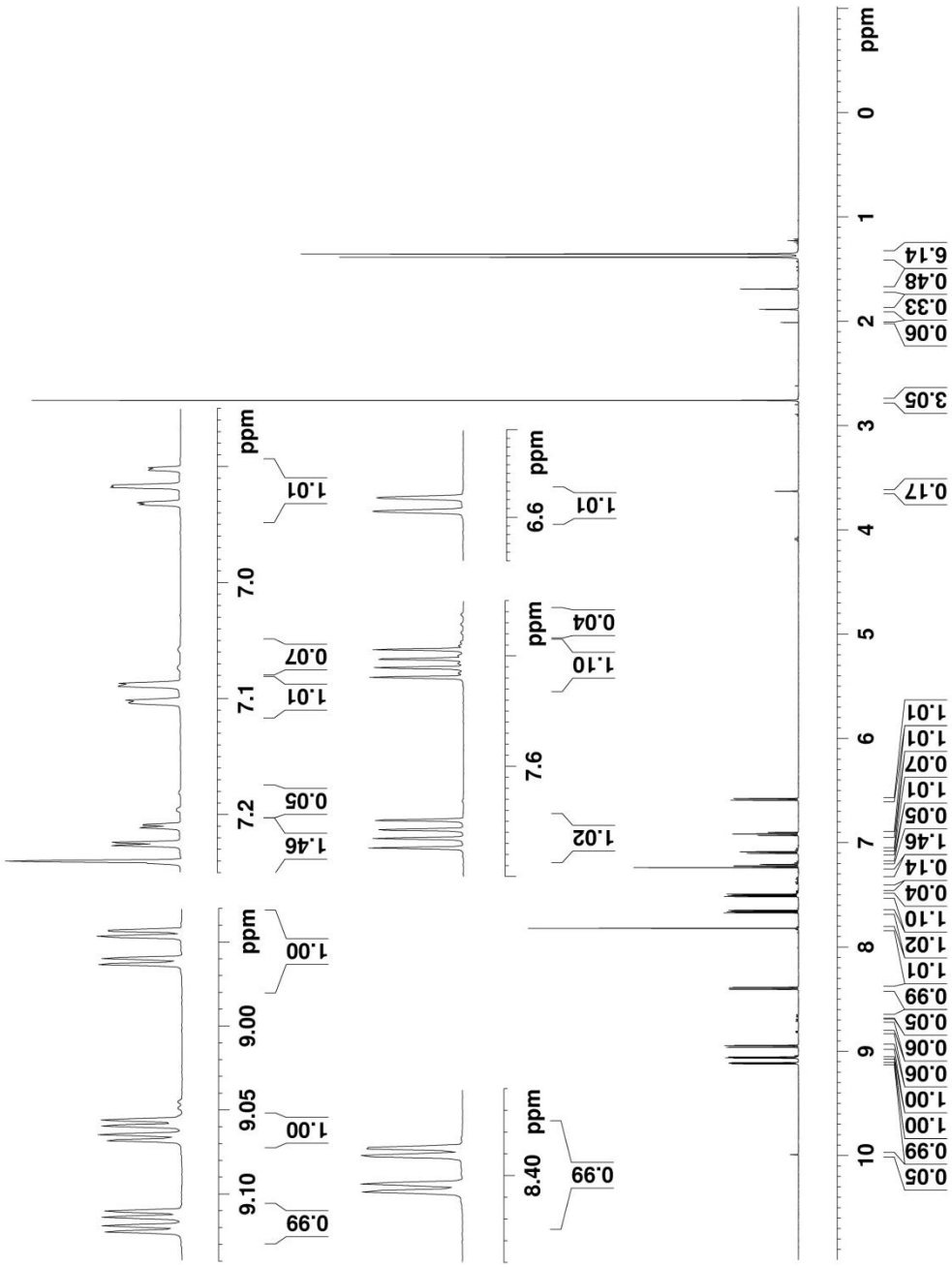

Figure A19. ^{1}H NMR spectrum of IPSO in $CDCl_3$ (500 MHz, ~300 K).

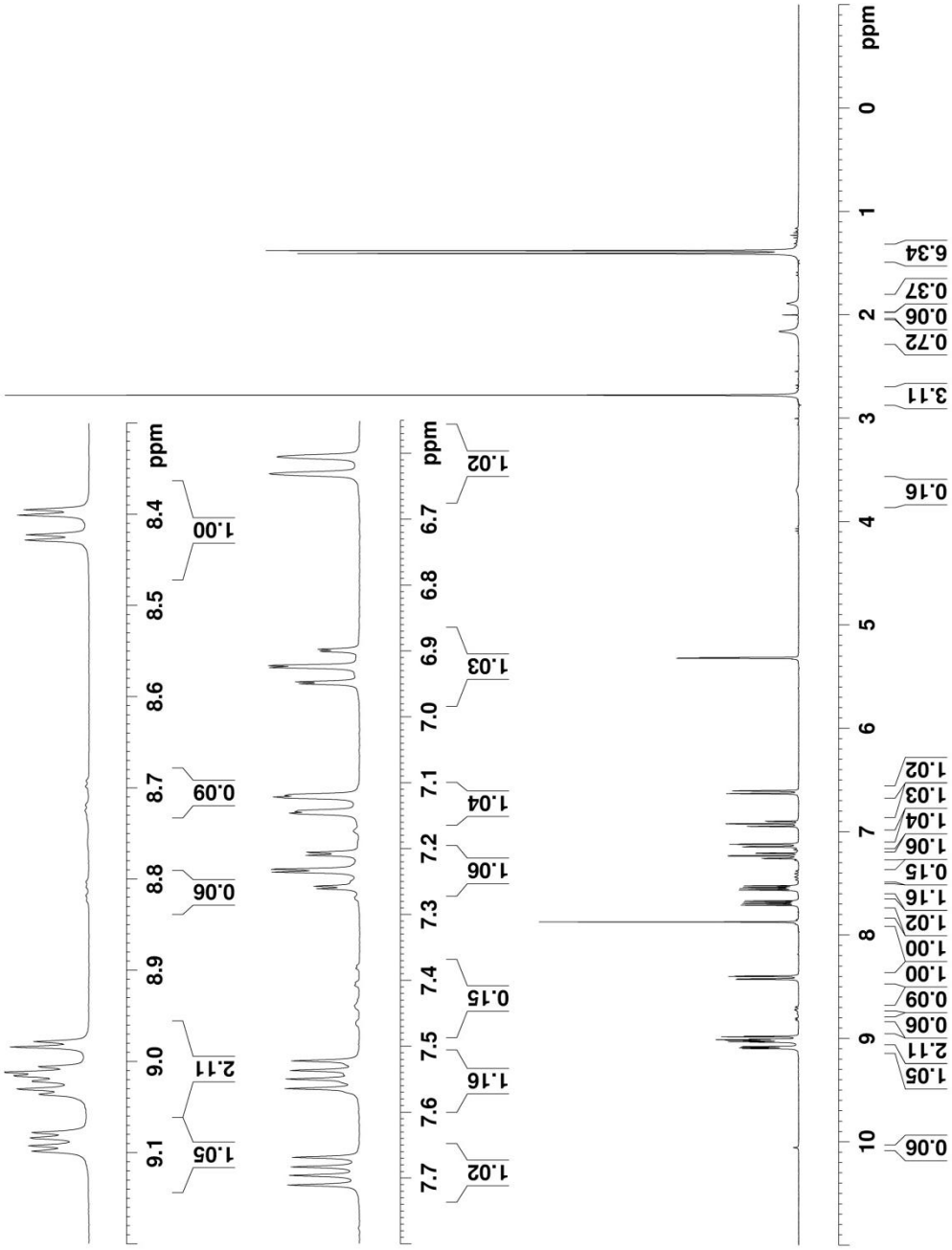

Figure A20. ^{1}H NMR spectrum of IPSO in CD_2Cl_2 (300 MHz, ~300 K).

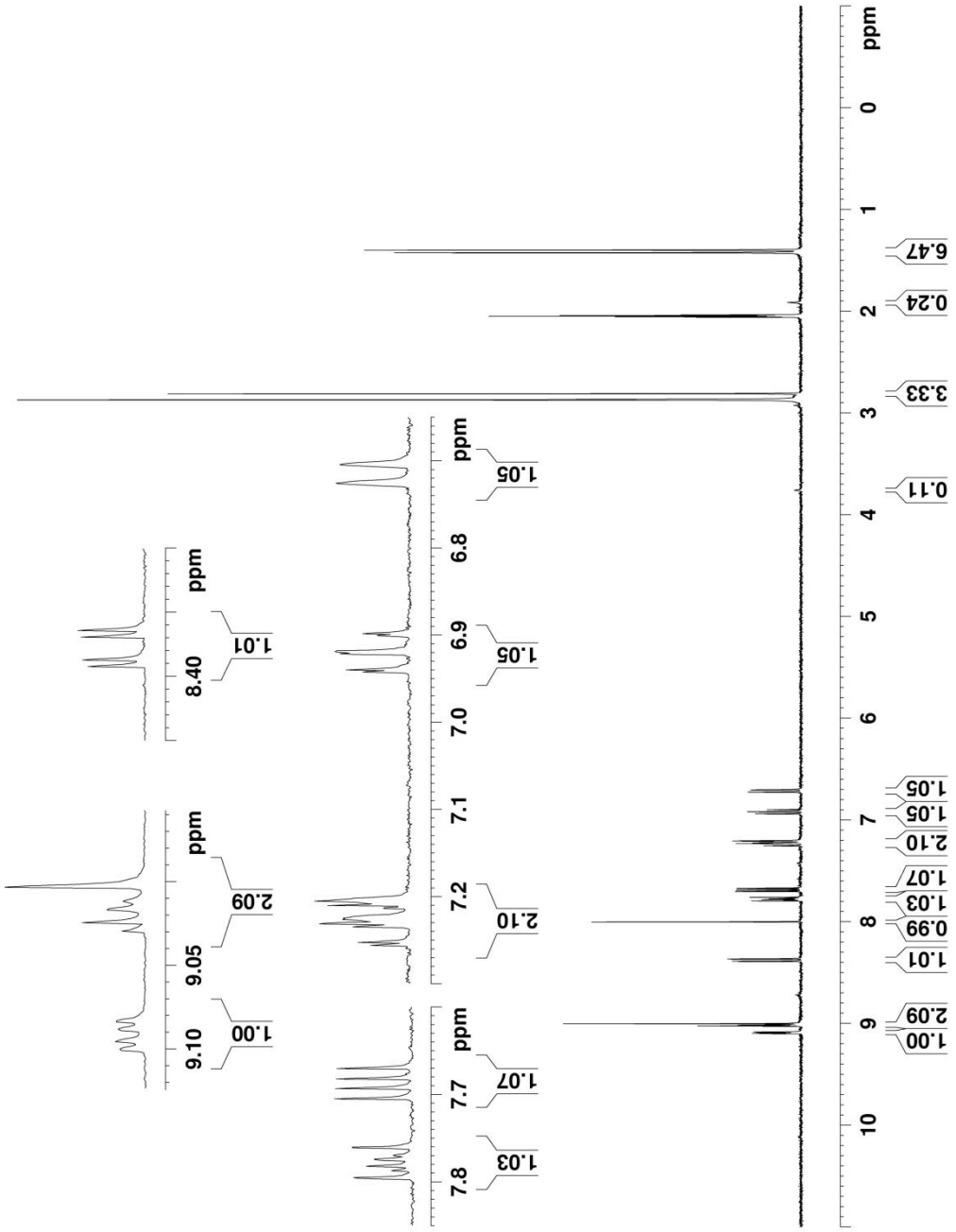

Figure A21. ^{1}H NMR spectrum of IPSO in acetone-d_6 (360 MHz, ~300 K).

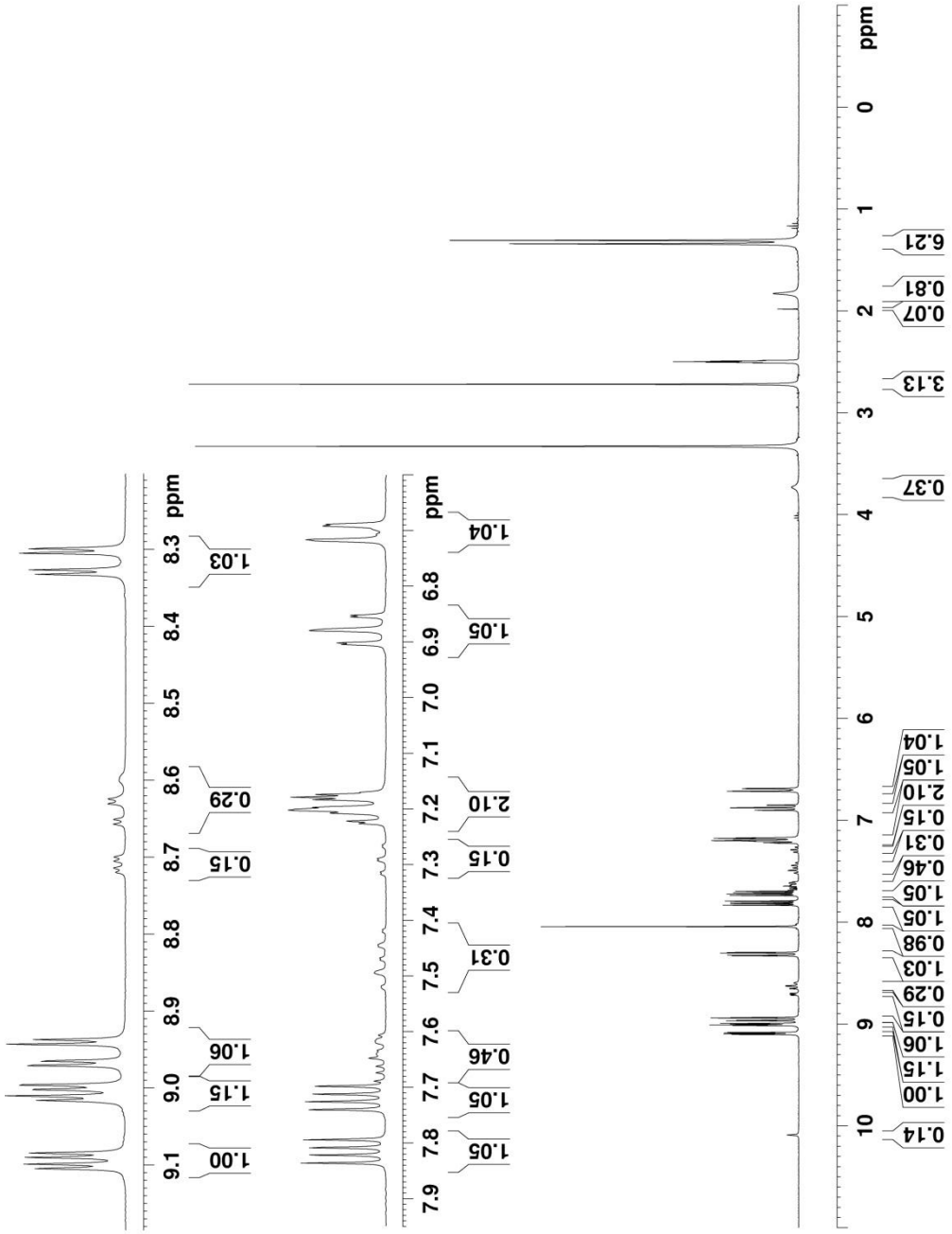

Figure A22. ^{1}H NMR spectrum of IPSO in DMSO-d_6 (300 MHz, ~300 K).

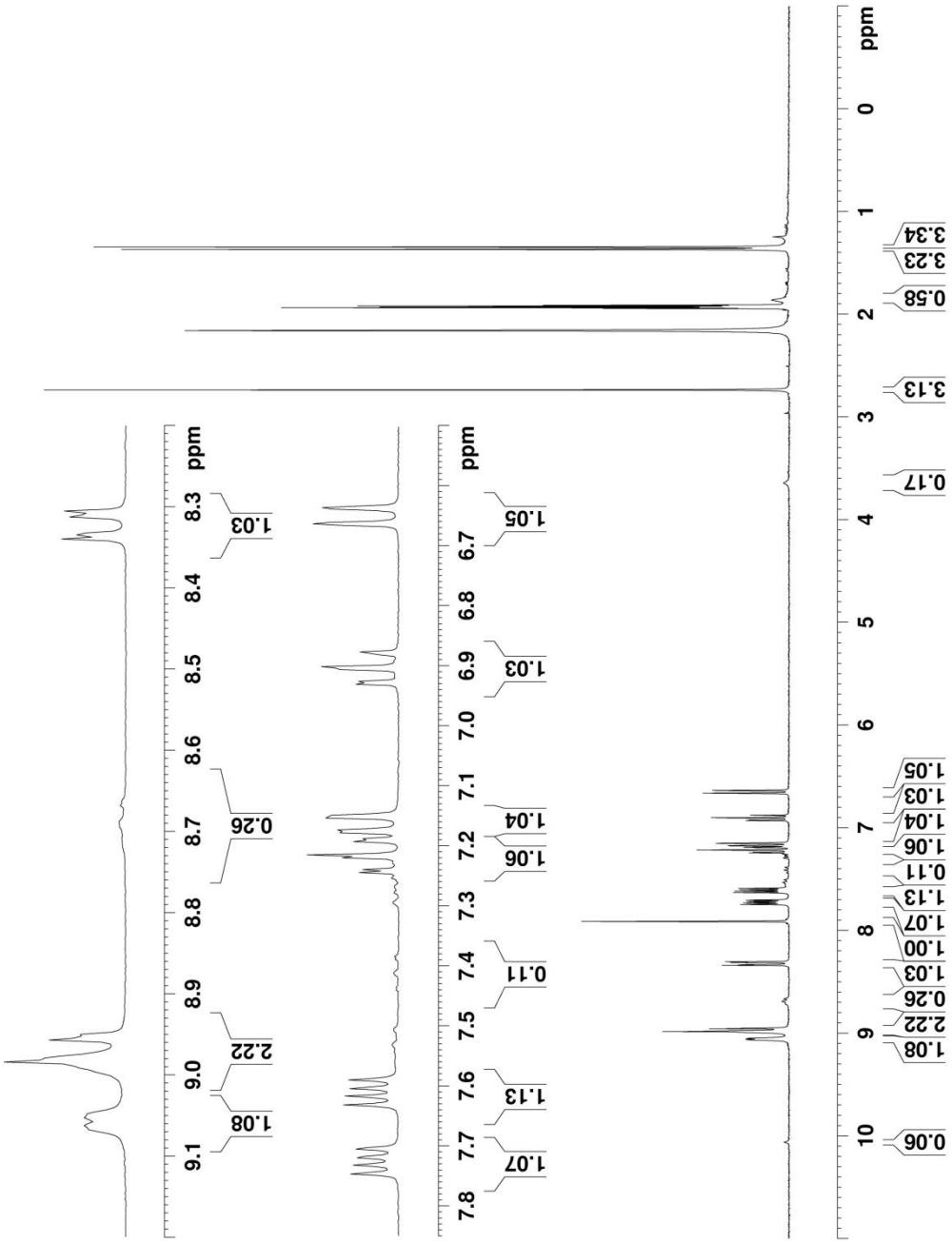

Figure A23. ^{1}H NMR spectrum of IPSO in CD_3CN (300 MHz, ~300 K).

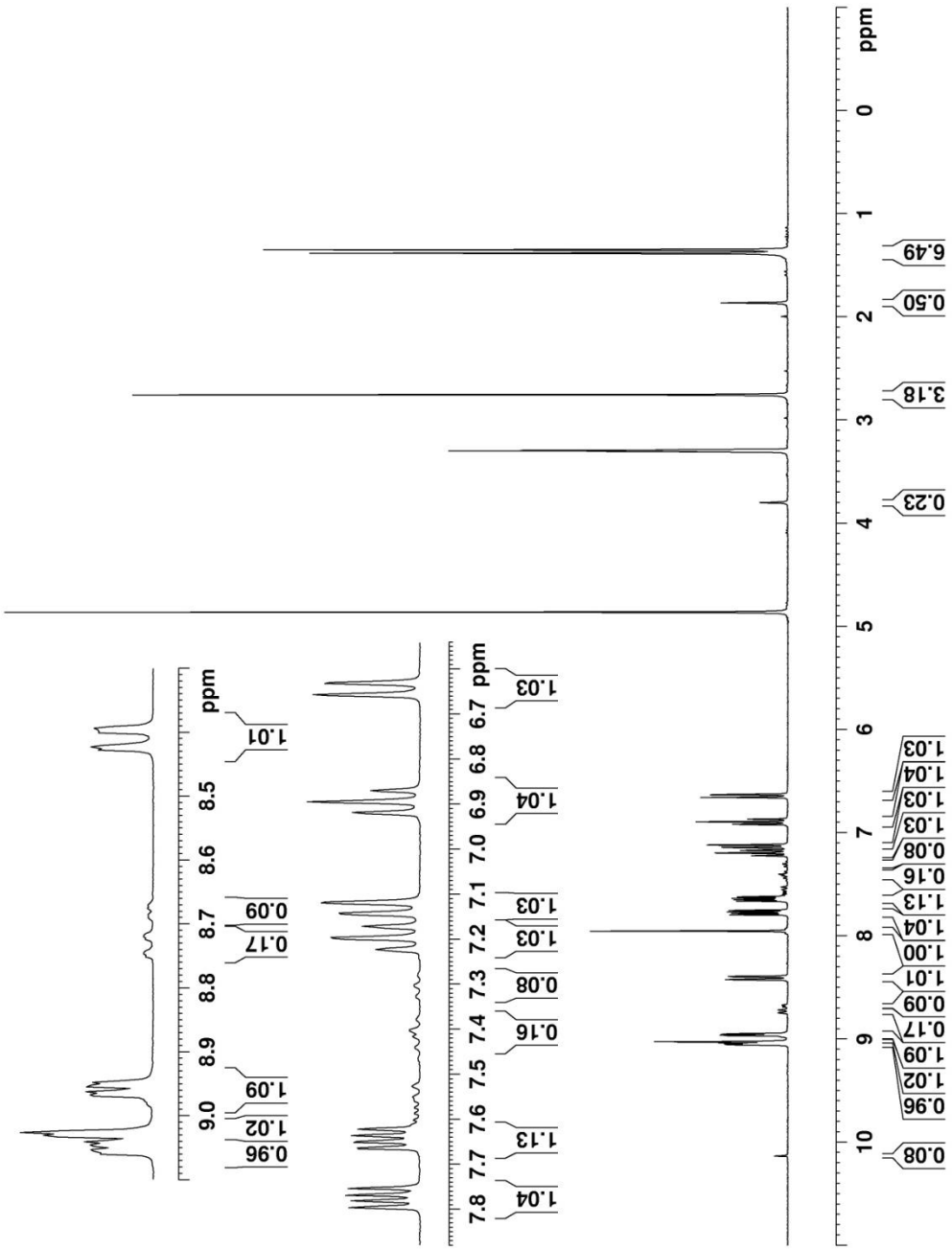

Figure A24. ^{1}H NMR spectrum of IPSO in CD_3OD (300 MHz, ~300 K).

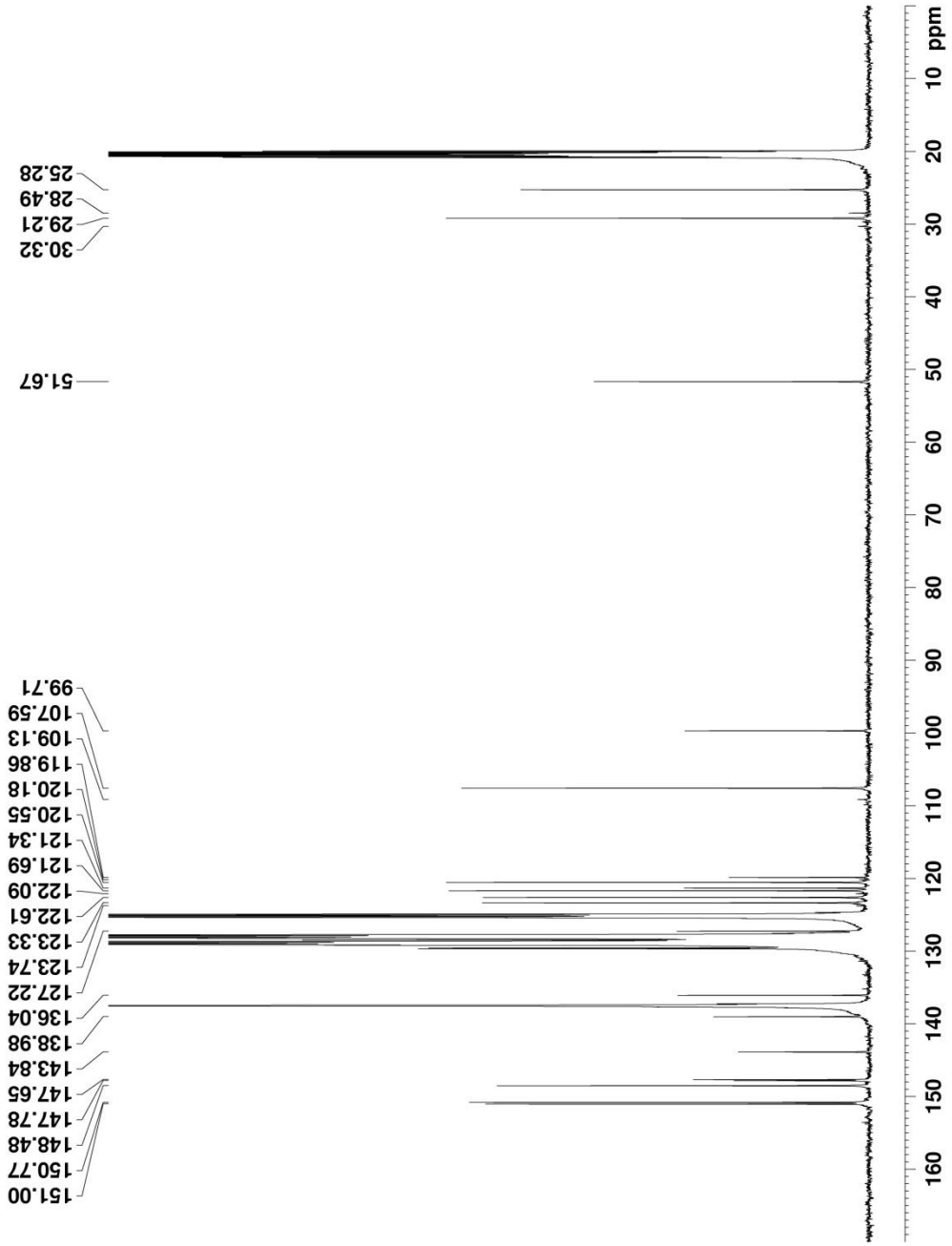

Figure A25. ^{13}C NMR spectrum of IPSO in toluene-d_8 (125 MHz, ~300 K).

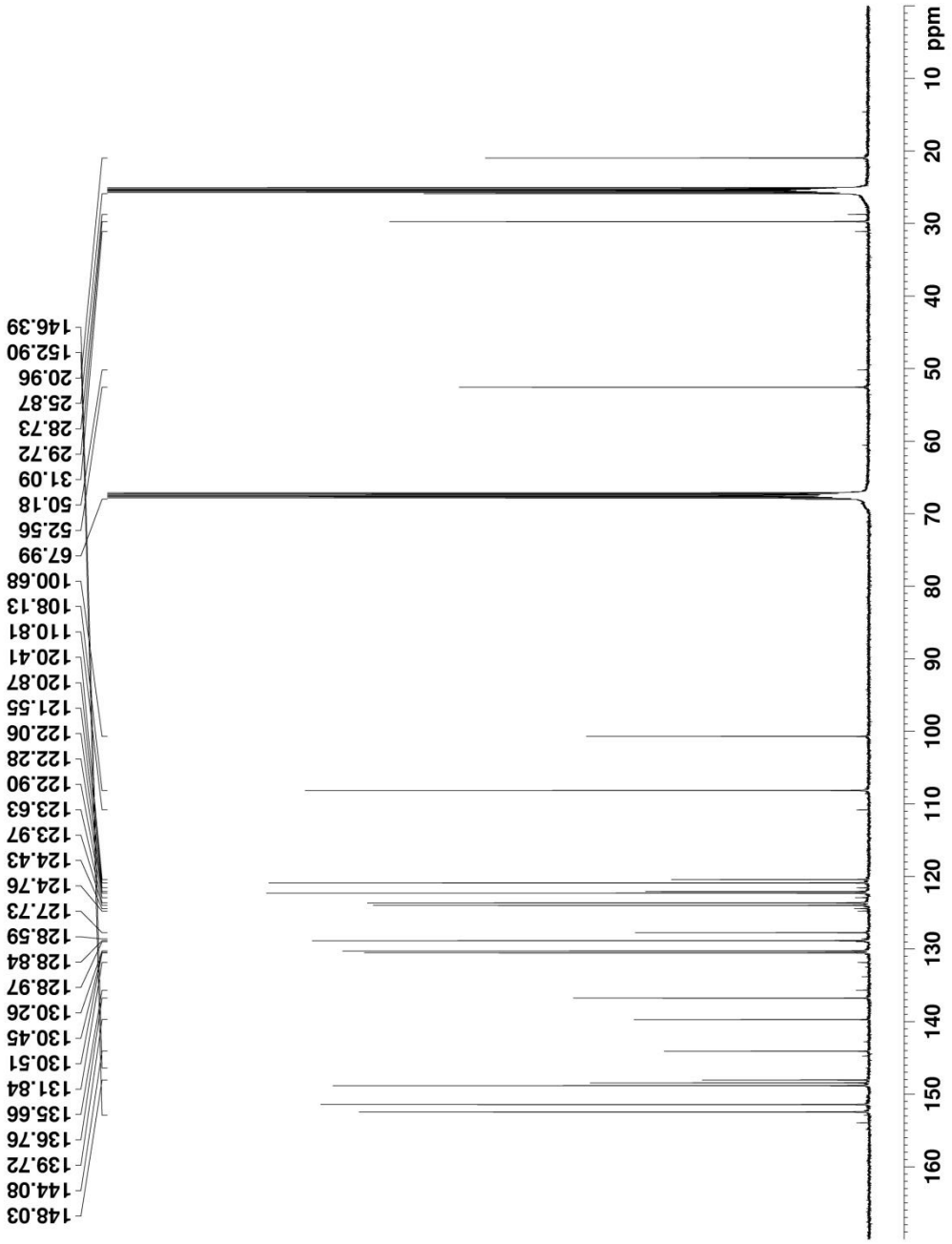

Figure A26. ^{13}C NMR spectrum of IPSO in THF-d_8 (125 MHz, ~300 K).

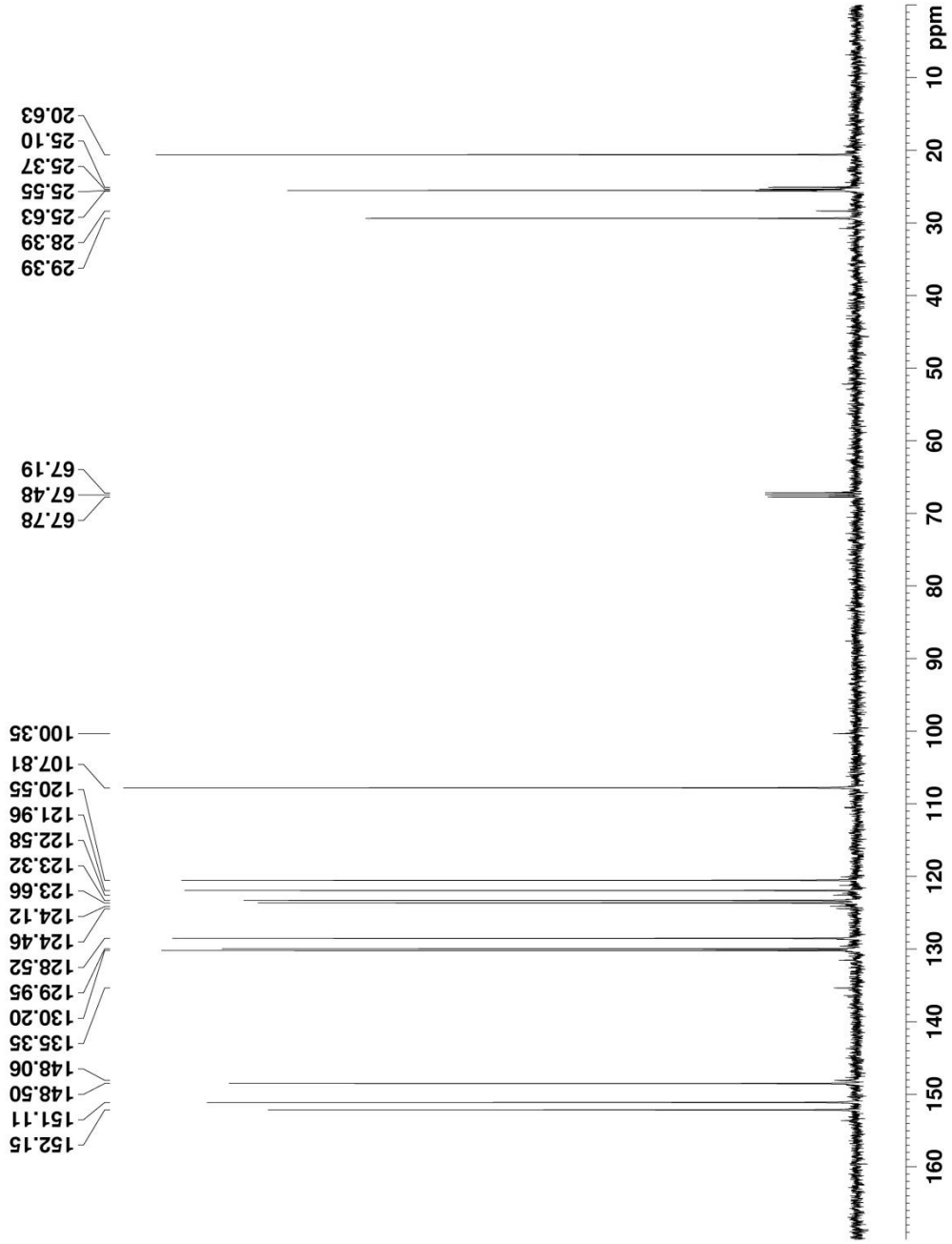

Figure A27. DEPT-135 spectrum of IPSO in THF-d_8 (75 MHz, ~300 K).

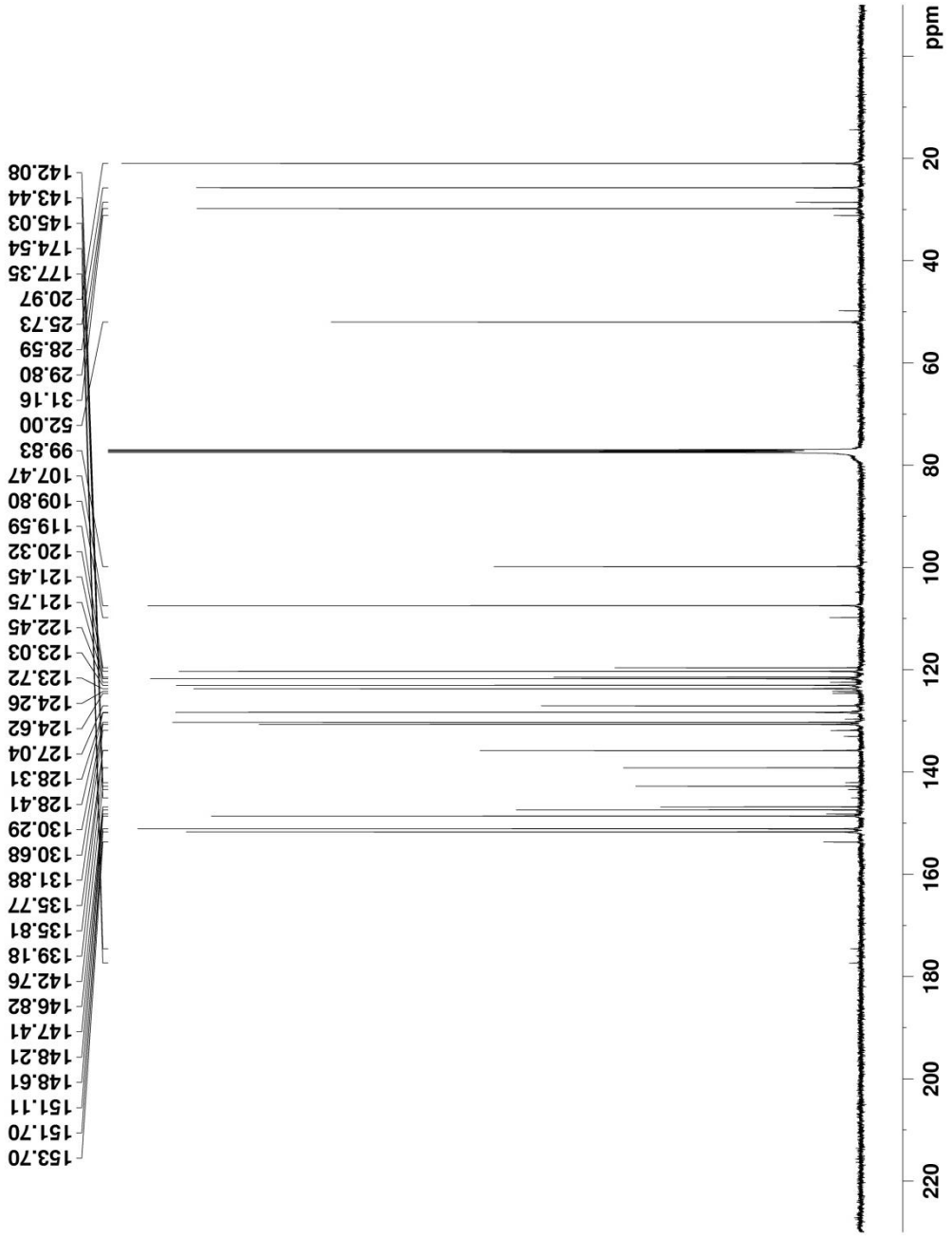

Figure A28. ^{13}C NMR spectrum of IPSO in $CDCl_3$ (125 MHz, ~300 K).

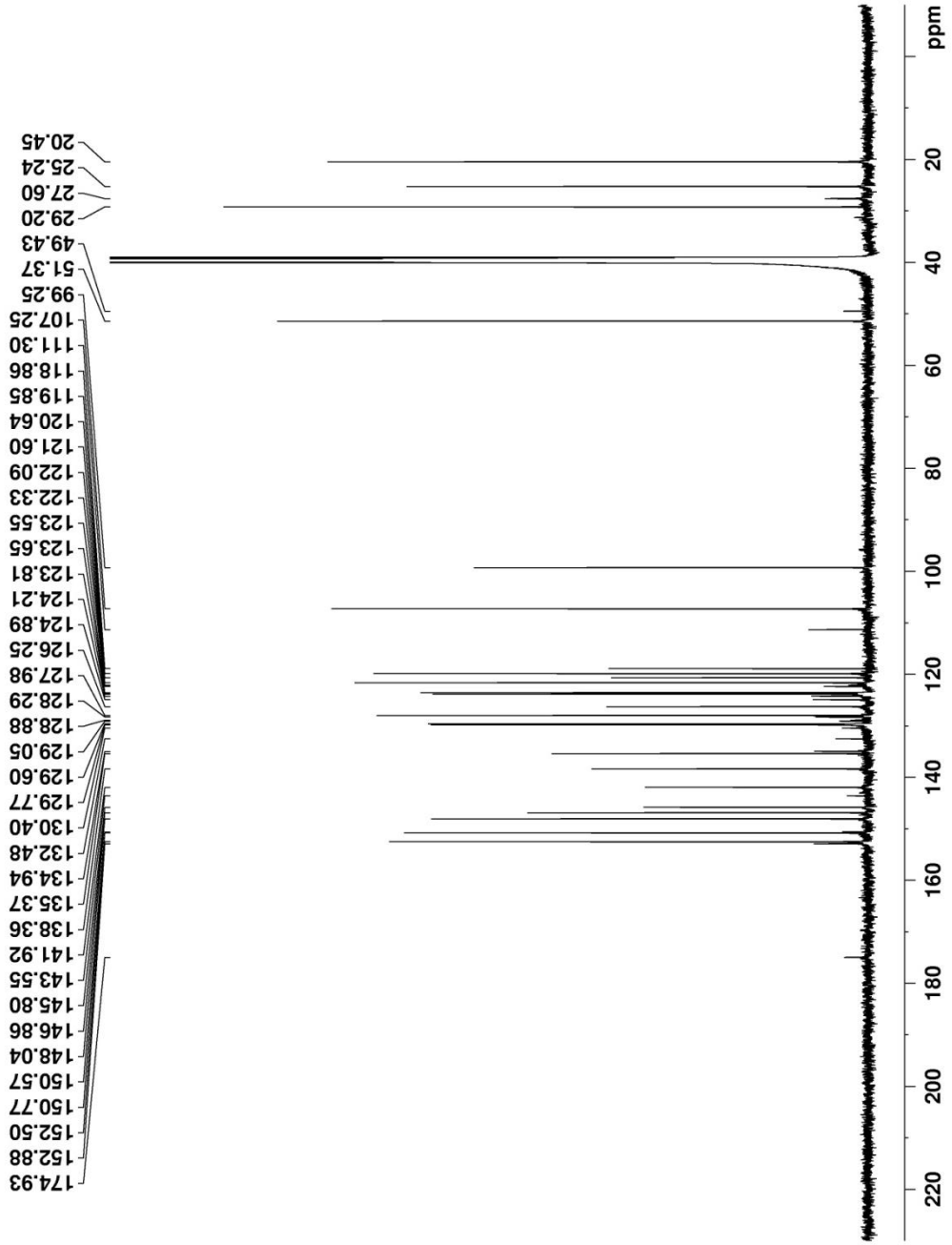

Figure A29. ^{13}C NMR spectrum of IPSO in DMSO-d_6 (125 MHz, ~300 K).

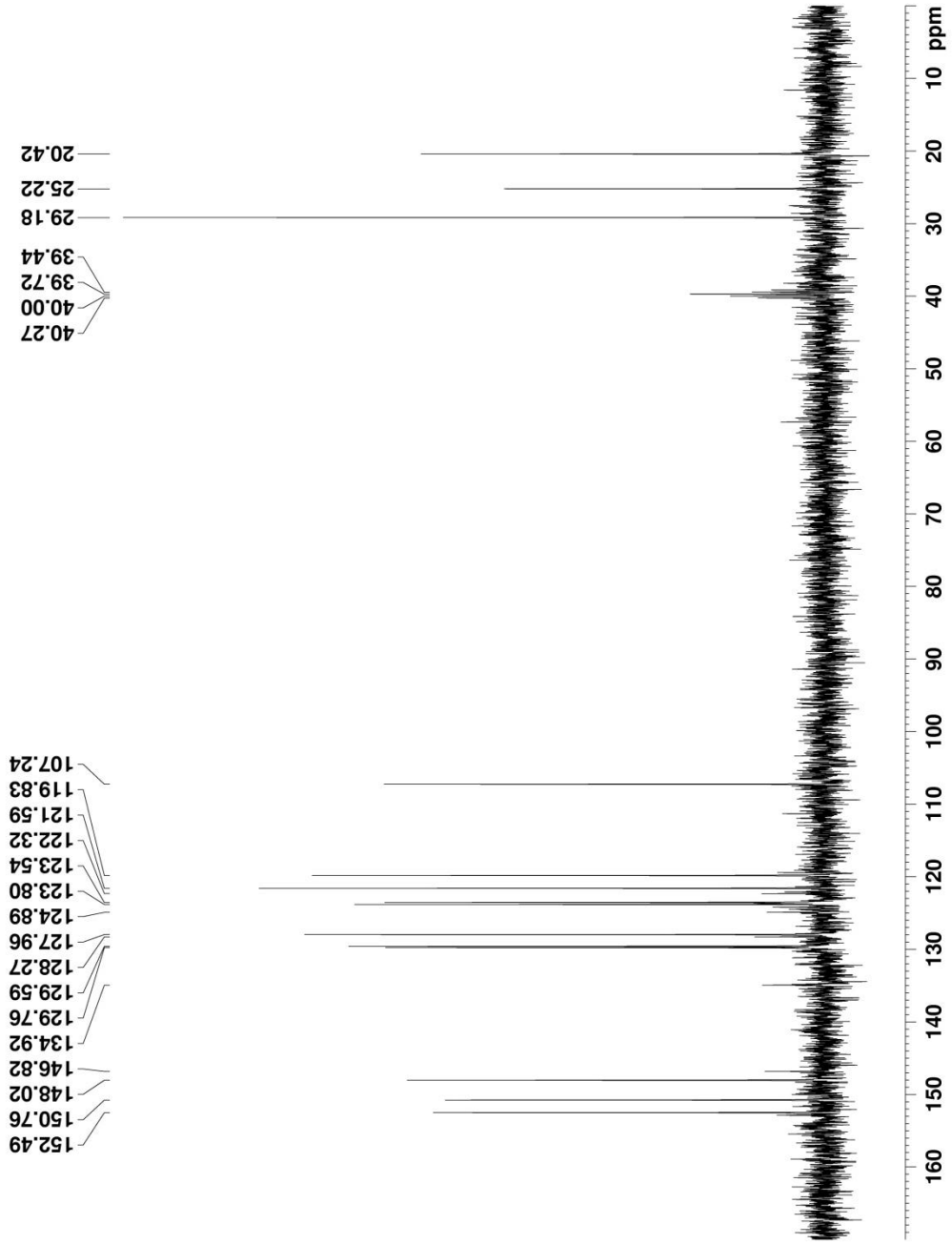

Figure A30. DEPT-135 spectrum of IPSO in DMSO-d_6 (75 MHz, ~300 K).

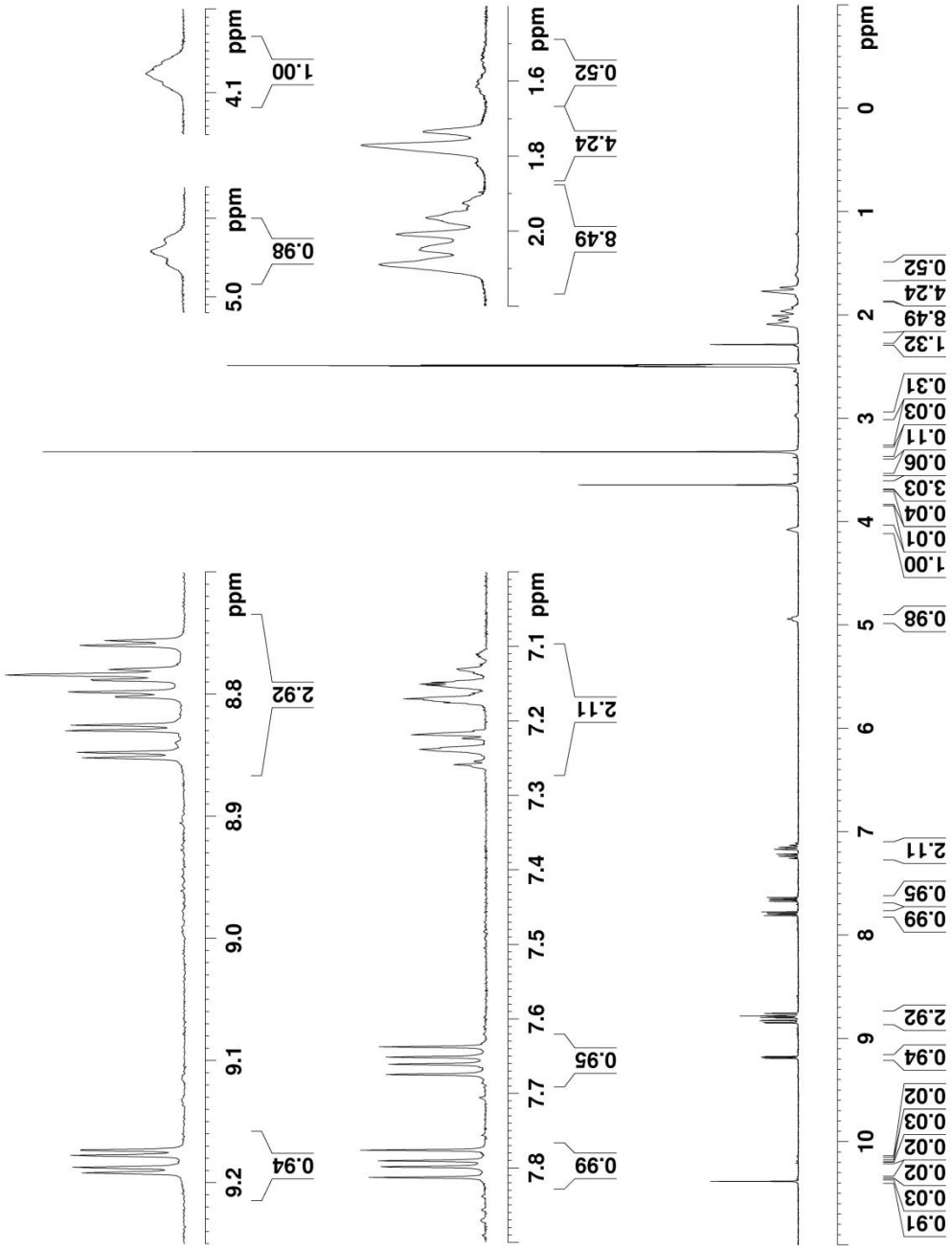

Figure A31. ^{1}H NMR spectrum of $Mo(CO)_4$(APSO) in DMSO-d_6 (360 MHz, ~300 K).

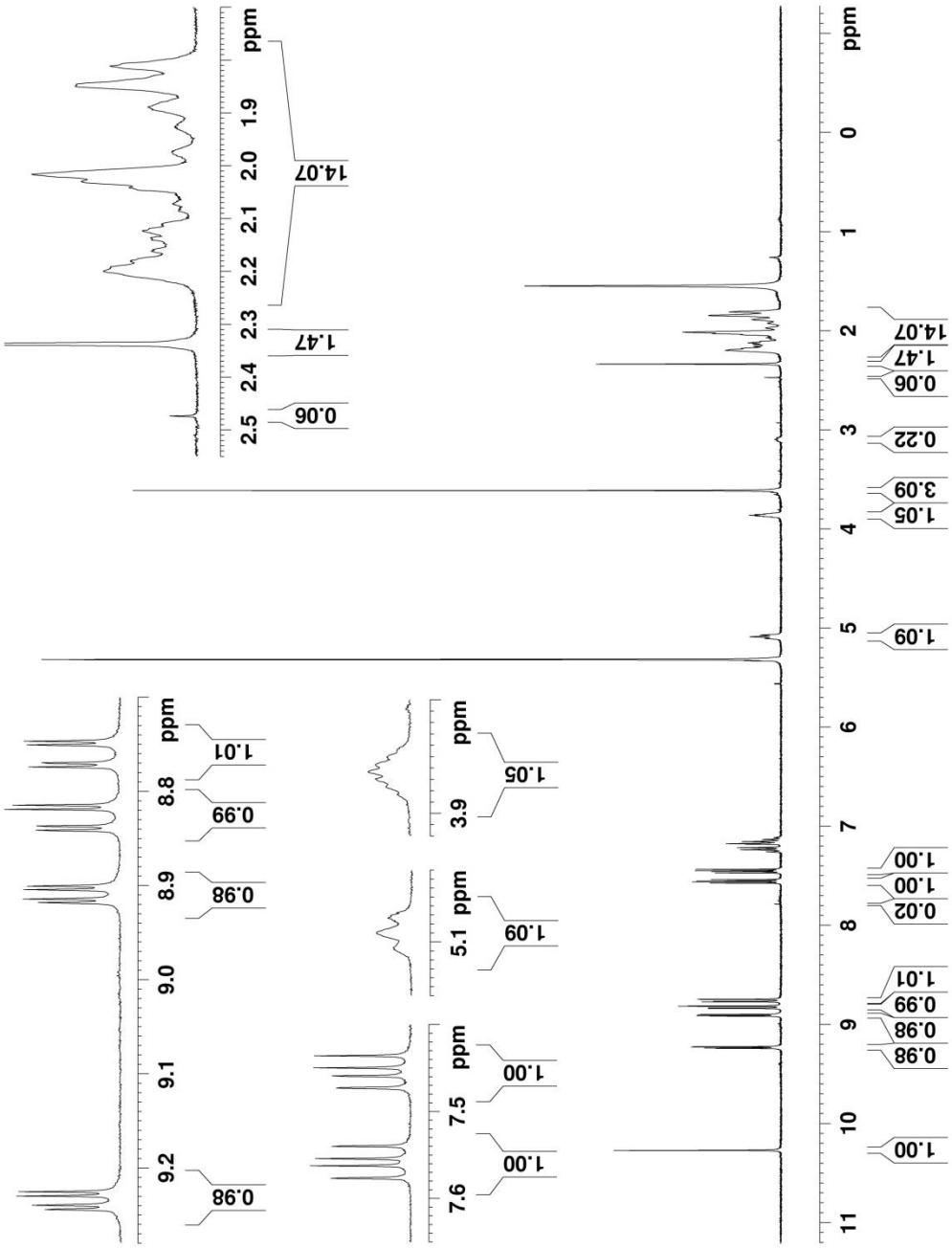

Figure A32. ^{1}H NMR spectrum of $Mo(CO)_4$(APSO) in CD_2Cl_2 (360 MHz, ~300 K).

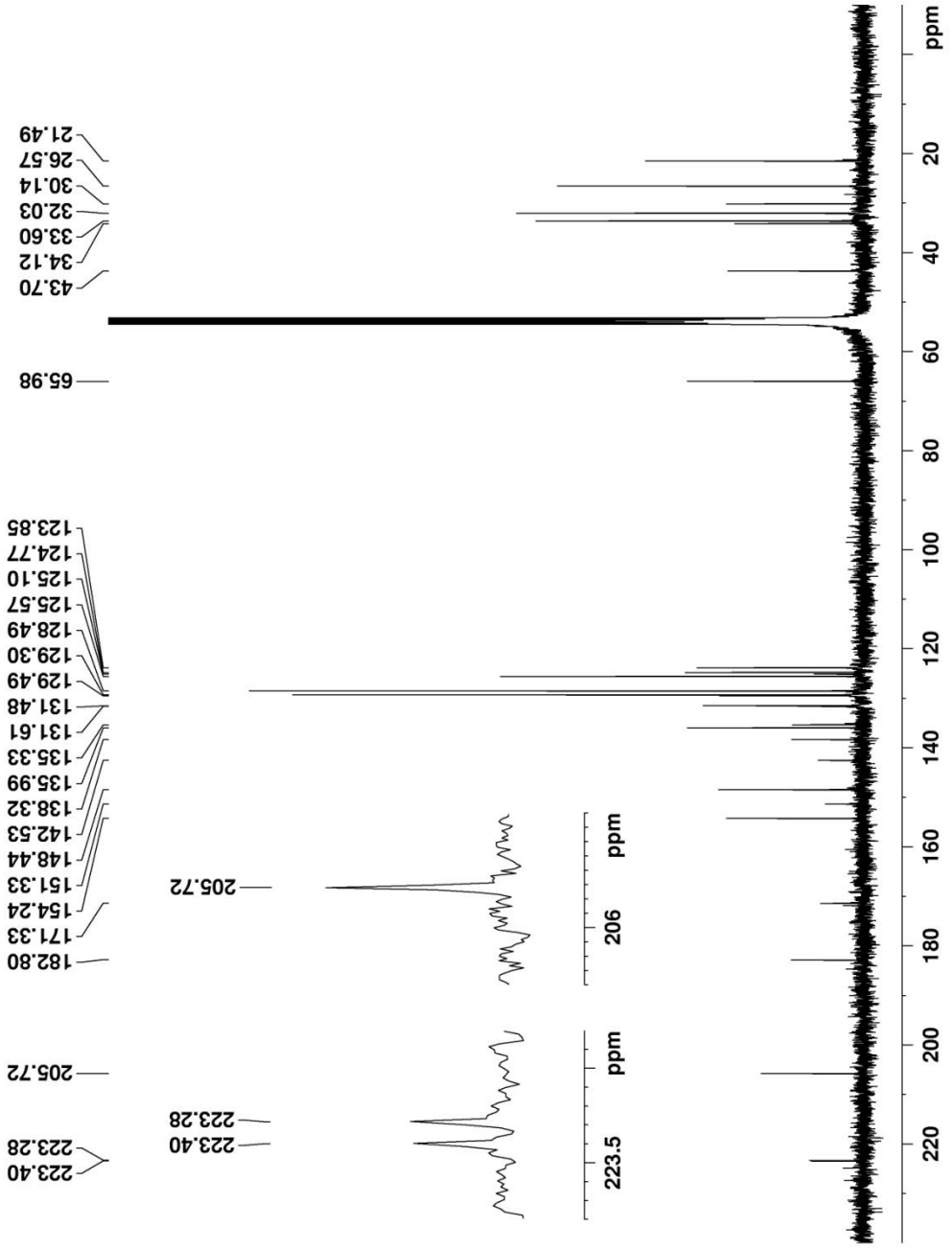

Figure A33. ^{13}C NMR spectrum of $Mo(CO)_4$(APSO) in CD_2Cl_2 (90 MHz, ~300 K).

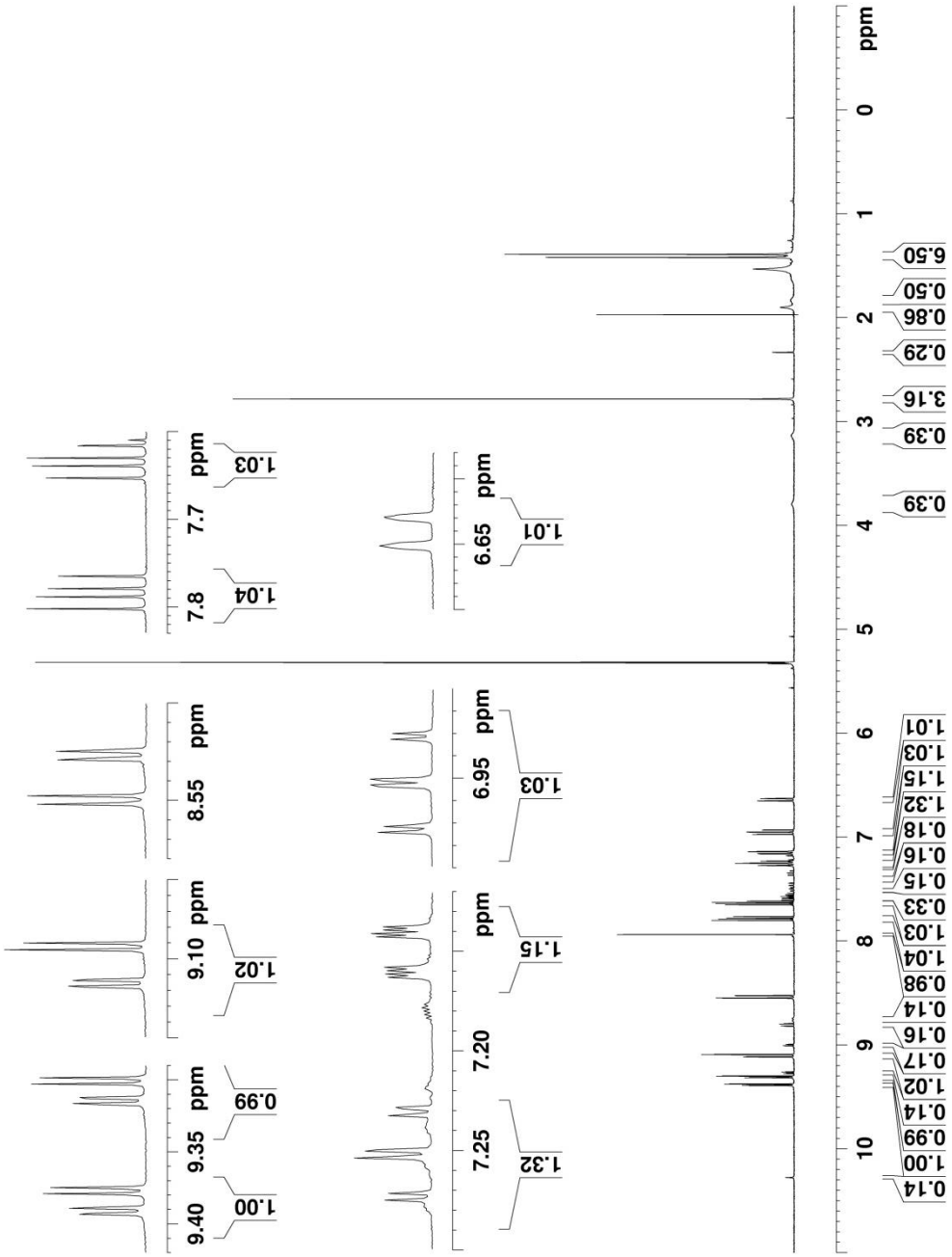

Figure A34. ^{1}H NMR spectrum of $Mo(CO)_4$(IPSO) in CD_2Cl_2 (360 MHz, ~300 K).

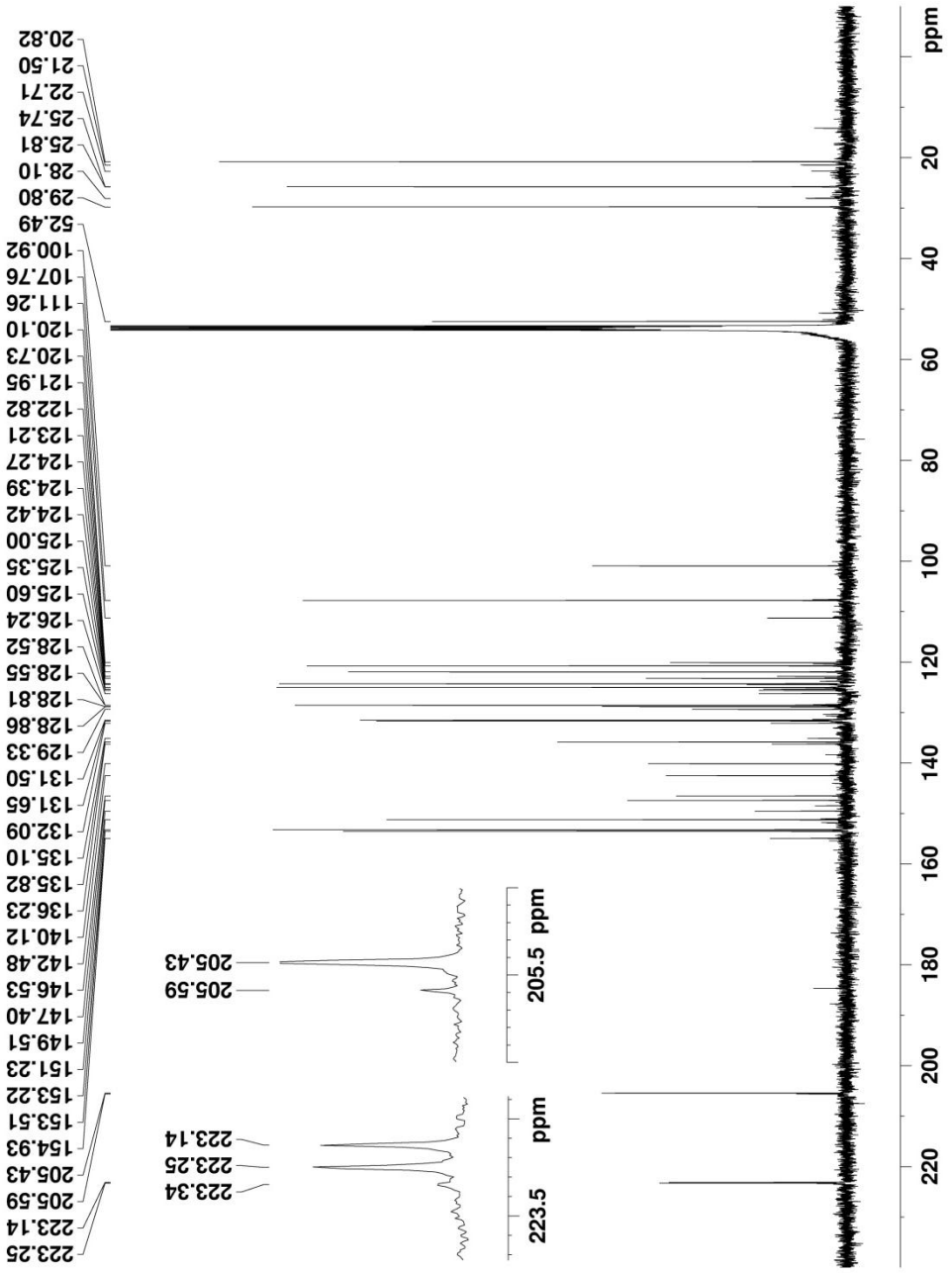

Figure A35. ^{13}C NMR spectrum of $Mo(CO)_4$(IPSO) in CD_2Cl_2 (90 MHz, ~300 K).

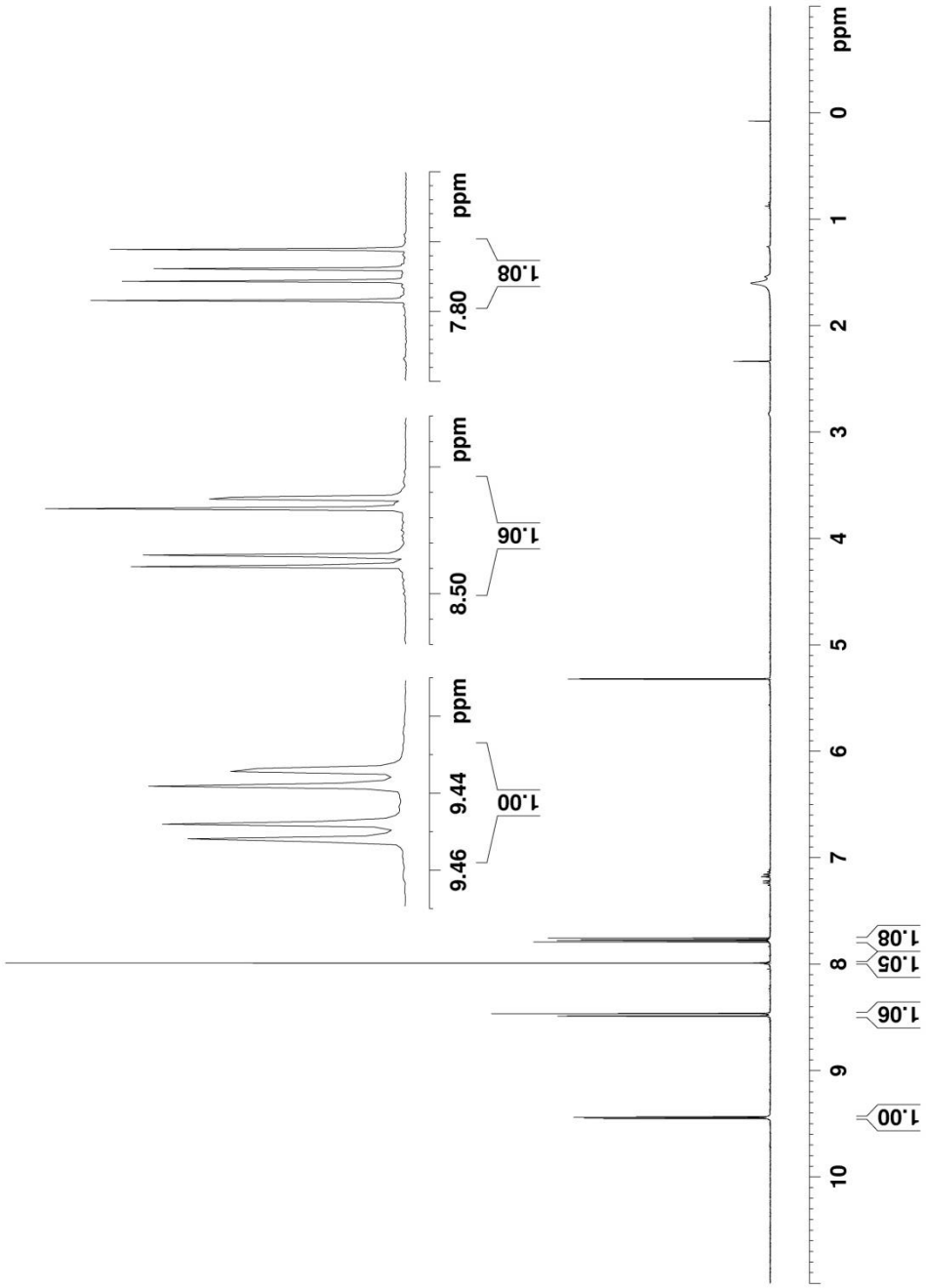

Figure A36. ^{1}H NMR spectrum of $Mo(CO)_4(phen)$ in CD_2Cl_2 (360 MHz, ~300 K).

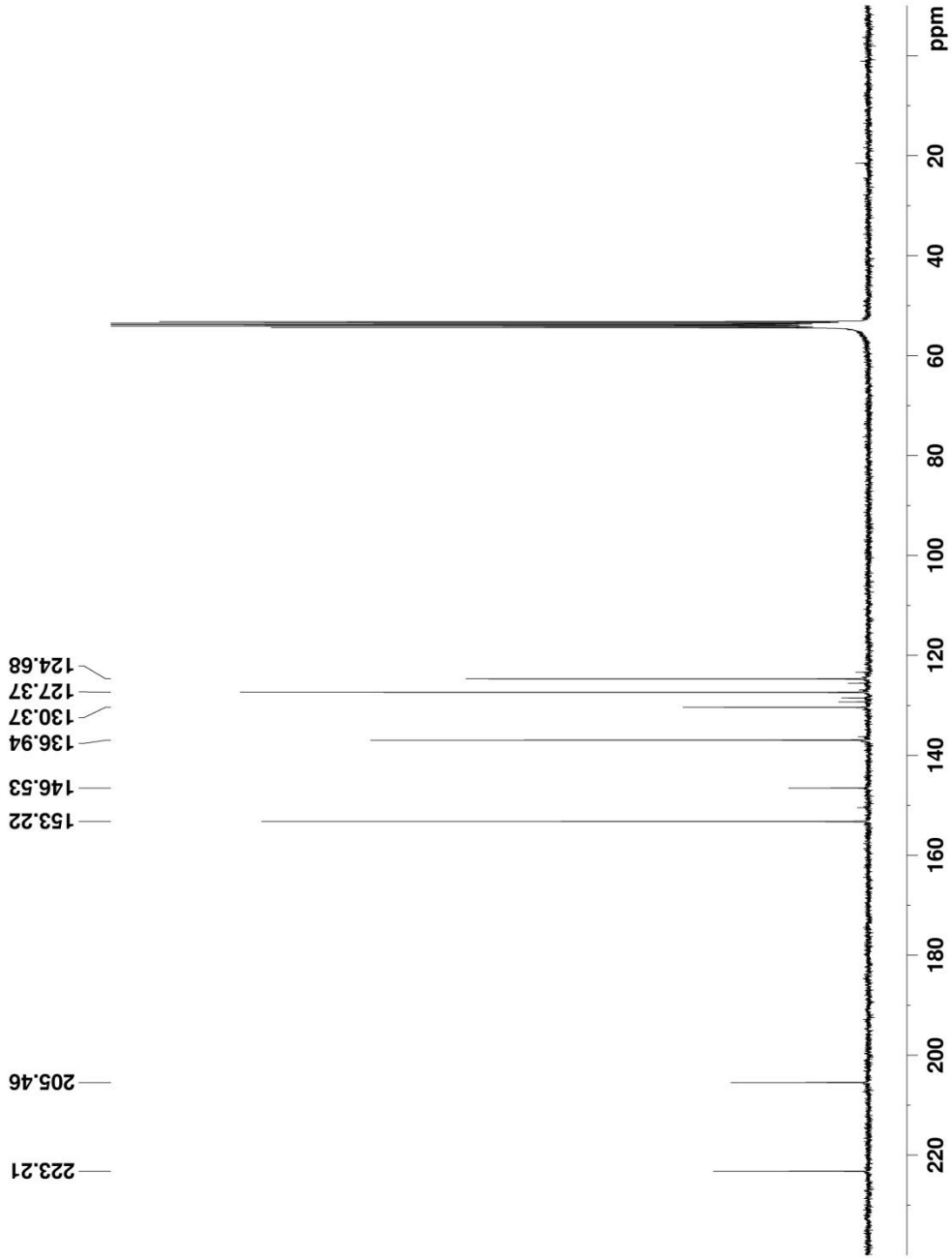

Figure A37. ^{13}C NMR spectrum of $Mo(CO)_4(phen)$ in CD_2Cl_2 (90 MHz, ~300 K).

Appendix B. Crystallographic Data

Table B1. Crystallographic data and refinement parameters for APSO-PMC-I (**28**-PMC-I), APSO-PMC-II (**28**-PMC-II), $Mo(CO)_4$(APSO-PMC) (**40**-PMC), and Co_4(3,5-DTBCatH)$_4$(DTBCat)$_2$(APSO-PMC)$_2$(MeO)$_2$·2MeOH (**49**-PMC).

Table B2. Bond lengths [Å] for APSO-PMC-I.

Table B3. Bond angles [°] for APSO-PMC-I.

Table B4. Bond lengths [Å] for APSO-PMC-II.

Table B5. Bond angles [°] for APSO-PMC-II.

Table B6. Bond lengths [Å] for $Mo(CO)_4$(APSO-PMC).

Table B7. Bond angles [°] for $Mo(CO)_4$(APSO-PMC).

Table B8. Bond lengths [Å] for **49**-PMC.

Table B9. Bond angles [°] for **49**-PMC.

Table B1. Crystallographic data and refinement parameters for APSO-PMC-I (**28**-PMC-I), APSO-PMC-II (**28**-PMC-II), $Mo(CO)_4$(APSO-PMC) (**40**-PMC), and Co_4(3,5-DTBCatH)$_4$(DTBCat)$_2$(APSO-PMC)$_2$(MeO)$_2$·2MeOH (**49**-PMC).

	28-PMC-I	**28-PMC-II**	**40-PMC**	**49-PMC**
Formula	$C_{24}H_{24}N_4O$	$C_{24}H_{24}N_4O{\cdot}3H_2O$	$C_{28}H_{28}MoN_4O_5{\cdot}C_6H_5CH_3$	$C_{134}H_{178}Co_4N_8O_{16}{\cdot}2CH_3OH$
FW / g mol^{-1}	384.47	438.52	684.59	2456.71
Temperature / K	110(2)	193(2)	173(2)	90.0(1)
Wavelength / Å	0.71073	0.71073	0.71073	0.71073
Crystal habit / color	Prism / purple	Block / purple	Prism / purple	Needle / purple
Crystal size / mm	0.22 × 0.15 × 0.12	0.53 × 0.22 × 0.17	0.04 × 0.12 × 0.22	0.09 × 0.12 × 0.45
Crystal system	Monoclinic	Monoclinic	Triclinic	Monoclinic
Space group	*C*2/*c* (no. 15)	*P*2$_1$/*n* (no. 14)	*P*–1 (no. 2)	*C*$_2$/*m* (no. 12)
Unit cell parameters				
a / Å	18.7530(18)	6.6536(12)	7.8137(8)	24.684(3)
b / Å	8.7476(8)	16.165(3)	9.9057(11)	24.211(3)
c / Å	24.797(3)	20.809(4)	14.0837(16)	14.843(2)
α / °			84.895(5)	
β / °	108.605(5)	93.277(2)	77.368(5)	115.088(3)
γ / °			81.828(5)	
V / Å^3	3855.3(7)	2234.4(7)	3178.6(2)	8034(2)
Z	8	4	2	2
D_{calcd} / g·cm^{-3}	1.325	1.304	1.482	1.016
μ	0.083 mm^{-1}	0.090 mm^{-1}	4.78 cm^{-1}	4.60 cm^{-1}
F(000)	1632	936	704	2623
Max. and min. transmission	0.9901 and 0.9819	0.9849 and 0.9538	0.981 and 0.932	0.959 and 0.825
Theta range for data collection / °	2.29 to 26.37	1.60 to 25.25	1.98 to 25.57	2.24 to 22.51
Index ranges	$-22 \le h \le 23$, $-10 \le k \le 10$, $-30 \le l \le 30$	$-7 \le h \le 7$, $-19 \le k \le 19$, $-24 \le l \le 24$	$-11 \le h \le 12$, $-13 \le k \le 10$, $-17 \le l \le 17$	$-26 \le h \le 26$, $-26 \le k \le 26$, $-15 \le l \le 15$
Refl. collected	37730	23144	15993	41004
Independent reflections	3877 (R_{int} = 0.0977)	4020 (R_{int} = 0.0661)	5628 (R_{int} = 0.034)	5418 (R_{int} = 0.052)
GOF on F^2	1.005	1.149	1.032	1.122
Final *R* indices [$I>2\sigma(I)$]				
R_1	0.0469[a]	0.0906[b]	0.0310[c]	0.0930[d]
wR_2	0.1174[a]	0.2458[b]	0.0690[c]	0.269[d]
Largest diff. peak and hole / e$^-$·Å^{-3}	0.300 / –0.198	0.906 / –0.448	0.40 / –0.40	1.04 / –0.56

[a] $R_1 = \Sigma||F_o| - |F_c||/\Sigma|F_o|$; $wR_2 = [\Sigma w(F_o^2 - F_c^2)^2/\Sigma w(F_o^2)]^{1/2}$; $w = [\sigma^2(F_o^2) + (0.0735P)^2 + 2.1923P]^{-1}$ where $P = [F_o^2 + 2F_c^2]/3$). [b] $R_1 = \Sigma||F_o| - |F_c||/\Sigma|F_o|$; $wR_2 = [\Sigma w(F_o^2 - F_c^2)^2/\Sigma w(F_o^4)]^{1/2}$; $w = [\sigma^2(F_o^2) + (0.1002P)^2 + 4.1726P]^{-1}$ where $P = [\mathrm{Max}(F_o^2, 0) + 2F_c^2]/3$). [c] $R_1 = \Sigma||F_o| - |F_c|| / \Sigma|F_o|$. $wR_2 = [\Sigma(w(F_o^2 - F_c^2)^2) / \Sigma w(F_o^2)^2]^{1/2}$; $w = 1/[\sigma^2(F_o)^2 + (0.0334P)^2 + 0.5260P]$. [d] $R_1 = \Sigma||F_o| - |F_c|| / \Sigma|F_o|$. $wR_2 = [\Sigma(w(F_o^2 - F_c^2)^2) / \Sigma w(F_o^2)^2]^{1/2}$; $w = 1/[\sigma^2(F_o)^2 + (0.1643\mathrm{P})^2 + 71.9289\mathrm{P}]$.

Table B2. Bond lengths [Å] for APSO-PMC-I.

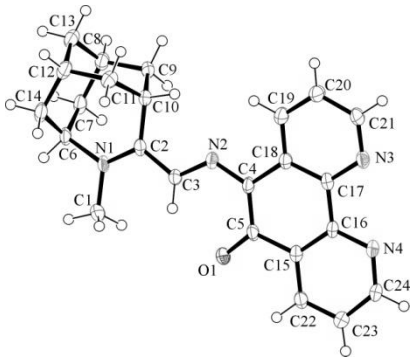

C(1)-N(1)	1.471(2)	C(7)–H(7B)	0.9900	C(15)–C(16)	1.410(2)
C(1)-H(1A)	0.9800	C(8)–C(9)	1.531(2)	C(16)–N(4)	1.363(2)
C(1)-H(1B)	0.9800	C(8)–C(13)	1.533(3)	C(16)–C(17)	1.460(2)
C(1)–H(1C)	0.9800	C(8)–H(8)	1.0000	C(17)–N(3)	1.356(2)
C(2)–N(1)	1.327(2)	C(9)–C(10)	1.541(2)	C(17)–C(18)	1.417(2)
C(2)–C(3)	1.427(2)	C(9)–H(9A)	0.9900	C(18)–C(19)	1.398(2)
C(2)–C(10)	1.505(2)	C(9)–H(9B)	0.9900	C(19)–C(20)	1.372(2)
C(3)–N(2)	1.326(2)	C(10)–C(11)	1.541(3)	C(19)–H(19)	0.9500
C(3)–H(3)	0.9500	C(10)–H(10)	1.0000	C(20)–C(21)	1.398(2)
C(4)–N(2)	1.346(2)	C(11)–C(12)	1.537(2)	C(20)–H(20)	0.9500
C(4)–C(5)	1.442(2)	C(11)–H(11A)	0.9900	C(21)–N(3)	1.324(2)
C(4)–C(18)	1.466(2)	C(11)–H(11B)	0.9900	C(21)–H(21)	0.9500
C(5)–O(1)	1.249(2)	C(12)–C(14)	1.532(3)	C(22)–C(23)	1.375(2)
C(5)–C(15)	1.483(2)	C(12)–C(13)	1.532(3)	C(22)–H(22)	0.9500
C(6)–N(1)	1.495(2)	C(12)–H(12)	1.0000	C(23)–C(24)	1.398(2)
C(6)–C(14)	1.523(3)	C(13)–H(13A)	0.9900	C(23)–H(23)	0.9500
C(6)–C(7)	1.532(2)	C(13)–H(13B)	0.9900	C(24)–N(4)	1.323(2)
C(6)–H(6)	1.0000	C(14)–H(14A)	0.9900	C(24)–H(24)	0.9500
C(7)–C(8)	1.527(3)	C(14)–H(14B)	0.9900		
C(7)–H(7A)	0.9900	C(15)–C(22)	1.396(2)		

Table B3. Bond angles [°] for APSO-PMC-I.

N(1)–C(1)–H(1A)	109.5	C(7)–C(8)–C(9)	112.24(14)
N(1)–C(1)–H(1B)	109.5	C(7)–C(8)–C(13)	109.68(14)
H(1A)–C(1)–H(1B)	109.5	C(9)–C(8)–C(13)	108.86(16)
N(1)–C(1)–H(1C)	109.5	C(7)–C(8)–H(8)	108.7
H(1A)–C(1)–H(1C)	109.5	C(9)–C(8)–H(8)	108.7
H(1B)–C(1)–H(1C)	109.5	C(13)–C(8)–H(8)	108.7
N(1)–C(2)–C(3)	118.72(15)	C(8)–C(9)–C(10)	113.32(14)
N(1)–C(2)–C(10)	121.38(14)	C(8)–C(9)–H(9A)	108.9
C(3)–C(2)–C(10)	119.89(14)	C(10)–C(9)–H(9A)	108.9
N(2)–C(3)–C(2)	118.82(15)	C(8)–C(9)–H(9B)	108.9
N(2)–C(3)–H(3)	120.6	C(10)–C(9)–H(9B)	108.9
C(2)–C(3)–H(3)	120.6	H(9A)–C(9)–H(9B)	107.7
N(2)–C(4)–C(5)	125.22(15)	C(2)–C(10)–C(9)	114.01(15)
N(2)–C(4)–C(18)	115.26(14)	C(2)–C(10)–C(11)	112.14(14)
C(5)–C(4)–C(18)	119.51(14)	C(9)–C(10)–C(11)	111.52(13)
O(1)–C(5)–C(4)	124.18(14)	C(2)–C(10)–H(10)	106.2
O(1)–C(5)–C(15)	118.41(15)	C(9)–C(10)–H(10)	106.2
C(4)–C(5)–C(15)	117.40(14)	C(11)–C(10)–H(10)	106.2
N(1)–C(6)–C(14)	111.70(14)	C(12)–C(11)–C(10)	113.75(16)
N(1)–C(6)–C(7)	112.58(13)	C(12)–C(11)–H(11A)	108.8
C(14)–C(6)–C(7)	112.47(14)	C(10)–C(11)–H(11A)	108.8
N(1)–C(6)–H(6)	106.5	C(12)–C(11)–H(11B)	108.8
C(14)–C(6)–H(6)	106.5	C(10)–C(11)–H(11B)	108.8
C(7)–C(6)–H(6)	106.5	H(11A)–C(11)–H(11B)	107.7
C(8)–C(7)–C(6)	114.30(16)	C(14)–C(12)–C(13)	109.12(16)
C(8)–C(7)–H(7A)	108.7	C(14)–C(12)–C(11)	112.51(14)
C(6)–C(7)–H(7A)	108.7	C(13)–C(12)–C(11)	109.20(14)
C(8)–C(7)–H(7B)	108.7	C(14)–C(12)–H(12)	108.6
C(6)–C(7)–H(7B)	108.7	C(13)–C(12)–H(12)	108.6
H(7A)–C(7)–H(7B)	107.6	C(11)–C(12)–H(12)	108.6

C(12)–C(13)–C(8)	109.87(14)	N(3)–C(21)–C(20)	123.71(15)
C(12)–C(13)–H(13A)	109.7	N(3)–C(21)–H(21)	118.1
C(8)–C(13)–H(13A)	109.7	C(20)–C(21)–H(21)	118.1
C(12)–C(13)–H(13B)	109.7	C(23)–C(22)–C(15)	119.86(15)
C(8)–C(13)–H(13B)	109.7	C(23)–C(22)–H(22)	120.1
H(13A)–C(13)–H(13B)	108.2	C(15)–C(22)–H(22)	120.1
C(6)–C(14)–C(12)	113.63(14)	C(22)–C(23)–C(24)	117.41(16)
C(6)–C(14)–H(14A)	108.8	C(22)–C(23)–H(23)	121.3
C(12)–C(14)–H(14A)	108.8	C(24)–C(23)–H(23)	121.3
C(6)–C(14)–H(14B)	108.8	N(4)–C(24)–C(23)	125.04(15)
C(12)–C(14)–H(14B)	108.8	N(4)–C(24)–H(24)	117.5
H(14A)–C(14)–H(14B)	107.7	C(23)–C(24)–H(24)	117.5
C(22)–C(15)–C(16)	118.46(14)	C(2)–N(1)–C(1)	120.02(13)
C(22)–C(15)–C(5)	119.29(14)	C(2)–N(1)–C(6)	124.18(14)
C(16)–C(15)–C(5)	122.25(14)	C(1)–N(1)–C(6)	115.79(13)
N(4)–C(16)–C(15)	121.74(15)	C(3)–N(2)–C(4)	123.36(14)
N(4)–C(16)–C(17)	118.58(14)	C(21)–N(3)–C(17)	117.65(14)
C(15)–C(16)–C(17)	119.66(14)	C(24)–N(4)–C(16)	117.42(14)
N(3)–C(17)–C(18)	123.00(15)		
N(3)–C(17)–C(16)	117.84(14)		
C(18)–C(17)–C(16)	119.15(14)		
C(19)–C(18)–C(17)	116.86(15)		
C(19)–C(18)–C(4)	121.33(14)		
C(17)–C(18)–C(4)	121.81(15)		
C(20)–C(19)–C(18)	120.19(15)		
C(20)–C(19)–H(19)	119.9		
C(18)–C(19)–H(19)	119.9		
C(19)–C(20)–C(21)	118.52(16)		
C(19)–C(20)–H(20)	120.7		
C(21)–C(20)–H(20)	120.7		

Table B4. Bond lengths [Å] for APSO-PMC-II.

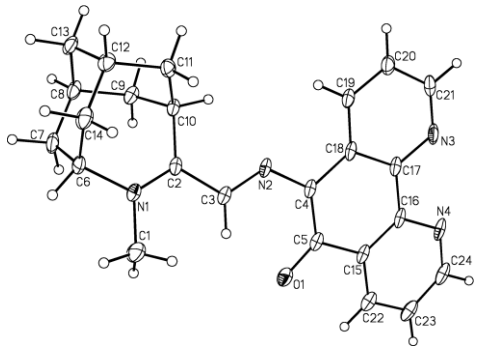

O(1)–C(5)	1.245(5)	C(7)–H(7A)	0.990(5)	C(15)–C(22)	1.387(6)
N(1)–C(1)	1.474(6)	C(7)–H(7B)	0.990(4)	C(16)–C(17)	1.445(6)
N(1)–C(2)	1.313(6)	C(7)–C(8)	1.507(7)	C(17)–C(18)	1.421(5)
N(1)–C(6)	1.505(5)	C(8)–H(8)	0.999(4)	C(18)–C(19)	1.397(6)
N(2)–C(3)	1.315(5)	C(8)–C(9)	1.537(6)	C(19)–H(19)	0.950(4)
C(2)–C(4)	1.359(5)	C(8)–C(13)	1.528(6)	C(19)–C(20)	1.364(6)
C(3)–C(17)	1.348(6)	C(9)–H(9A)	0.989(5)	C(20)–H(20)	0.949(5)
N(2)–C(21)	1.318(7)	C(9)–H(9B)	0.991(4)	C(20)–C(21)	1.393(7)
C(4)–C(16)	1.363(5)	C(9)–C(10)	1.551(5)	C(21)–H(21)	0.949(5)
C(4)–C(24)	1.320(6)	C(10)–H(10)	1.000(4)	C(22)–H(22)	0.949(5)
C(1)–H(1A)	0.980(6)	C(10)–C(11)	1.533(6)	C(22)–C(23)	1.382(6)
C(1)–H(1B)	0.980(6)	C(11)–H(11A)	0.990(4)	C(23)–H(23)	0.950(5)
C(1)–H(1C)	0.980(6)	C(11)–H(11B)	0.990(5)	C(23)–C(24)	1.386(6)
C(2)–C(3)	1.448(6)	C(11)–C(12)	1.529(6)	C(23)–H(24)	0.951(5)
C(2)–C(10)	1.498(7)	C(12)–H(12)	1.000(4)	C(24)–H(24)	0.85(3)
C(3)–H(3)	0.950(5)	C(12)–C(13)	1.528(6)	O(1S)–H(1SA)	0.85(3)
C(4)–C(5)	1.423(6)	C(12)–C(14)	1.510(7)	O(1S)–H(1SB)	0.85(3)
C(4)–C(18)	1.457(6)	C(13)–H(13A)	0.990(4)	O(2S)–H(2SA)	0.85(3)
C(5)–C(15)	1.494(6)	C(13)–H(13B)	0.991(5)	O(2S)–H(2SB)	0.85(3)
C(6)–H(6)	1.000(5)	C(14)–H(14A)	0.990(4)	O(3S)–H(3SA)	0.85(2)
C(6)–C(7)	1.524(6)	C(14)–H(14B)	0.989(4)	O(3S)–H(3SB)	0.85(3)
C(6)–C(14)	1.530(6)	C(15)–C(16)	1.400(6)		

Table B5. Bond angles [°] for APSO-PMC-II.

N(1)–C(1)–H(1A)	109.4(5)	C(7)–C(8)–C(9)	112.0(3)
N(1)–C(1)–H(1B)	109.5(5)	C(7)–C(8)–C(13)	110.0(4)
H(1A)–C(1)–H(1B)	109.5(5)	C(9)–C(8)–C(13)	109.0(3)
N(1)–C(1)–H(1C)	109.4(5)	C(7)–C(8)–H(8)	108.6(4)
H(1A)–C(1)–H(1C)	109.5(5)	C(9)–C(8)–H(8)	108.6(4)
H(1B)–C(1)–H(1C)	109.5(5)	C(13)–C(8)–H(8)	108.6(4)
N(1)–C(2)–C(3)	119.4(4)	C(8)–C(9)–C(10)	113.0(3)
N(1)–C(2)–C(10)	122.1(3)	C(8)–C(9)–H(9A)	109.0(4)
C(3)–C(2)–C(10)	118.5(3)	C(10)–C(9)–H(9A)	109.0(4)
N(2)–C(3)–C(2)	117.9(4)	C(8)–C(9)–H(9B)	109.0(4)
N(2)–C(3)–H(3)	121.0(4)	C(10)–C(9)–H(9B)	109.0(4)
C(2)–C(3)–H(3)	121.1(4)	H(9A)–C(9)–H(9B)	107.7(4)
N(2)–C(4)–C(5)	124.4(4)	C(2)–C(10)–C(9)	113.7(3)
N(2)–C(4)–C(18)	114.4(4)	C(2)–C(10)–C(11)	112.5(3)
C(5)–C(4)–C(18)	121.0(3)	C(9)–C(10)–C(11)	111.5(3)
O(1)–C(5)–C(4)	125.0(4)	C(2)–C(10)–H(10)	106.2(4)
O(1)–C(5)–C(15)	118.0(4)	C(9)–C(10)–H(10)	106.1(4)
C(4)–C(5)–C(15)	116.9(4)	C(11)–C(10)–H(10)	106.1(4)
N(1)–C(6)–C(14)	111.1(3)	C(12)–C(11)–C(10)	113.3(3)
N(1)–C(6)–C(7)	112.1(3)	C(12)–C(11)–H(11A)	108.9(4)
C(14)–C(6)–C(7)	112.6(4)	C(10)–C(11)–H(11A)	108.9(4)
N(1)–C(6)–H(6)	106.9(4)	C(12)–C(11)–H(11B)	108.9(4)
C(14)–C(6)–H(6)	106.9(4)	C(10)–C(11)–H(11B)	109.0(4)
C(7)–C(6)–H(6)	107.0(4)	H(11A)–C(11)–H(11B)	107.8(4)
C(8)–C(7)–C(6)	114.7(4)	C(14)–C(12)–C(13)	110.2(4)
C(8)–C(7)–H(7A)	108.6(4)	C(14)–C(12)–C(11)	111.8(4)
C(6)–C(7)–H(7A)	108.5(4)	C(13)–C(12)–C(11)	109.7(4)
C(8)–C(7)–H(7B)	108.6(4)	C(14)–C(12)–H(12)	108.4(4)
C(6)–C(7)–H(7B)	108.5(4)	C(13)–C(12)–H(12)	108.4(4)
H(7A)–C(7)–H(7B)	107.6(4)	C(11)–C(12)–H(12)	108.3(4)

C(12)–C(13)–C(8)	109.3(3)	N(3)–C(21)–C(20)	123.2(4)
C(12)–C(13)–H(13A)	109.8(4)	N(3)–C(21)–H(21)	118.4(5)
C(8)–C(13)–H(13A)	109.8(4)	C(20)–C(21)–H(21)	118.4(5)
C(12)–C(13)–H(13B)	109.9(4)	C(23)–C(22)–C(15)	119.2(5)
C(8)–C(13)–H(13B)	109.7(4)	C(23)–C(22)–H(22)	120.4(4)
H(13A)–C(13)–H(13B)	108.2(4)	C(15)–C(22)–H(22)	120.4(4)
C(6)–C(14)–C(12)	114.1(4)	C(22)–C(23)–C(24)	118.1(5)
C(6)–C(14)–H(14A)	108.7(4)	C(22)–C(23)–H(23)	120.9(4)
C(12)–C(14)–H(14A)	108.8(4)	C(24)–C(23)–H(23)	121.0(4)
C(6)–C(14)–H(14B)	108.7(4)	N(4)–C(24)–C(23)	124.4(4)
C(12)–C(14)–H(14B)	108.8(4)	N(4)–C(24)–H(24)	117.7(4)
H(14A)–C(14)–H(14B)	107.6(4)	C(23)–C(24)–H(24)	117.8(4)
C(22)–C(15)–C(16)	119.0(4)	C(2)–N(1)–C(1)	122.8(3)
C(22)–C(15)–C(5)	119.8(4)	C(2)–N(1)–C(6)	113.4(3)
C(16)–C(15)–C(5)	121.1(4)	C(1)–N(1)–C(6)	113.4(3)
N(4)–C(16)–C(15)	121.5(4)	C(3)–N(2)–C(4)	125.0(4)
N(4)–C(16)–C(17)	117.6(4)	C(21)–N(3)–C(17)	118.6(4)
C(15)–C(16)–C(17)	121.0(3)	C(24)–N(4)–C(16)	117.8(4)
N(3)–C(17)–C(18)	122.6(4)		
N(3)–C(17)–C(16)	118.4(4)		
C(18)–C(17)–C(16)	119.0(4)		
C(19)–C(18)–C(17)	116.3(4)		
C(19)–C(18)–C(4)	122.9(3)		
C(17)–C(18)–C(4)	120.7(4)		
C(20)–C(19)–C(18)	120.7(4)		
C(20)–C(19)–H(19)	119.6(4)		
C(18)–C(19)–H(19)	119.7(4)		
C(19)–C(20)–C(21)	118.6(4)		
C(19)–C(20)–H(20)	120.7(4)		
C(21)–C(20)–H(20)	120.7(4)		

Table B6. Bond lengths [Å] for $Mo(CO)_4$(APSO-PMC).

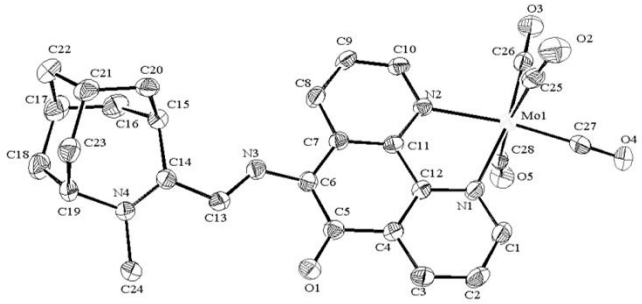

C(1)–N(1)	1.337(3)	C(13)–N(3)	1.315(3)	C(21)–C(22)	1.525(4)
C(1)–C(2)	1.381(3)	C(13)–C(14)	1.430(3)	C(21)–H(21)	1.0000
C(1)–H(1)	0.9500	C(13)–H(13)	0.9500	C(22)–H(22A)	0.9900
C(2)–C(3)	1.375(4)	C(14)–N(4)	1.324(3)	C(22)–H(22B)	0.9900
C(2)–H(2)	0.9500	C(14)–C(15)	1.502(3)	C(23)–H(23A)	0.9900
C(3)–C(4)	1.391(3)	C(15)–C(20)	1.535(3)	C(23)–H(23B)	0.9900
C(3)–H(3)	0.9500	C(15)–C(16)	1.538(4)	C(24)–N(4)	1.467(3)
C(4)–C(12)	1.397(3)	C(15)–H(15)	1.0000	C(24)–H(24A)	0.9800
C(4)–C(5)	1.485(3)	C(16)–C(17)	1.530(4)	C(24)–H(24B)	0.9800
C(5)–O(1)	1.236(3)	C(16)–H(16A)	0.9900	C(24)–H(24C)	0.9800
C(5)–C(6)	1.445(3)	C(16)–H(16B)	0.9900	C(25)–O(2)	1.153(3)
C(6)–N(3)	1.344(3)	C(17)–C(18)	1.520(4)	C(25)–Mo(1)	2.017(3)
C(6)–C(7)	1.452(3)	C(17)–C(22)	1.521(4)	C(26)–O(3)	1.166(3)
C(7)–C(11)	1.399(3)	C(17)–H(17)	1.0000	C(26)–Mo(1)	1.946(2)
C(7)–C(8)	1.400(3)	C(18)–C(19)	1.526(4)	C(27)–O(4)	1.167(3)
C(8)–C(9)	1.369(3)	C(18)–H(18A)	0.9900	C(27)–Mo(1)	1.944(3)
C(8)–H(8)	0.9500	C(18)–H(18B)	0.9900	C(28)–O(5)	1.140(3)
C(9)–C(10)	1.378(3)	C(19)–N(4)	1.496(3)	C(28)–Mo(1)	2.050(3)
C(9)–H(9)	0.9500	C(19)–C(23)	1.520(4)	N(1)–Mo(1)	2.2450(19)
C(10)–N(2)	1.333(3)	C(19)–H(19)	1.0000	N(2)–Mo(1)	2.2412(19)
C(10)–H(10)	0.9500	C(20)–C(21)	1.519(3)		
C(11)–N(2)	1.359(3)	C(20)–H(20A)	0.9900		
C(11)–C(12)	1.446(3)	C(20)–H(20B)	0.9900		
C(12)–N(1)	1.356(3)	C(21)–C(23)	1.525(3)		

Table B7. Bond angles [°] for $Mo(CO)_4$(APSO-PMC).

N(1)–C(1)–C(2)	123.2(2)	N(1)–C(12)–C(4)	123.1(2)
N(1)–C(1)–H(1)	118.4	N(1)–C(12)–C(11)	117.2(2)
C(2)–C(1)–H(1)	118.4	C(4)–C(12)–C(11)	119.7(2)
C(3)–C(2)–C(1)	119.2(2)	N(3)–C(13)–C(14)	117.9(2)
C(3)–C(2)–H(2)	120.4	N(3)–C(13)–H(13)	121.0
C(1)–C(2)–H(2)	120.4	C(14)–C(13)–H(13)	121.0
C(2)–C(3)–C(4)	119.4(2)	N(4)–C(14)–C(13)	120.1(2)
C(2)–C(3)–H(3)	120.3	N(4)–C(14)–C(15)	120.8(2)
C(4)–C(3)–H(3)	120.3	C(13)–C(14)–C(15)	119.06(19)
C(3)–C(4)–C(12)	117.7(2)	C(14)–C(15)–C(20)	112.1(2)
C(3)–C(4)–C(5)	120.3(2)	C(14)–C(15)–C(16)	114.3(2)
C(12)–C(4)–C(5)	122.0(2)	C(20)–C(15)–C(16)	111.2(2)
O(1)–C(5)–C(6)	124.1(2)	C(14)–C(15)–H(15)	106.2
O(1)–C(5)–C(4)	119.1(2)	C(20)–C(15)–H(15)	106.2
C(6)–C(5)–C(4)	116.7(2)	C(16)–C(15)–H(15)	106.2
N(3)–C(6)–C(5)	125.1(2)	C(17)–C(16)–C(15)	113.7(2)
N(3)–C(6)–C(7)	114.7(2)	C(17)–C(16)–H(16A)	108.8
C(5)–C(6)–C(7)	120.0(2)	C(15)–C(16)–H(16A)	108.8
C(11)–C(7)–C(8)	116.4(2)	C(17)–C(16)–H(16B)	108.8
C(11)–C(7)–C(6)	121.2(2)	C(15)–C(16)–H(16B)	108.8
C(8)–C(7)–C(6)	122.4(2)	H(16A)–C(16)–H(16B)	107.7
C(9)–C(8)–C(7)	119.9(2)	C(18)–C(17)–C(22)	109.7(2)
C(9)–C(8)–H(8)	120.0	C(18)–C(17)–C(16)	112.2(2)
C(7)–C(8)–H(8)	120.0	C(22)–C(17)–C(16)	109.6(2)
C(8)–C(9)–C(10)	119.7(2)	C(18)–C(17)–H(17)	108.4
C(8)–C(9)–H(9)	120.1	C(22)–C(17)–H(17)	108.4
C(10)–C(9)–H(9)	120.1	C(16)–C(17)–H(17)	108.4
N(2)–C(10)–C(9)	122.7(2)	C(17)–C(18)–C(19)	113.2(2)
N(2)–C(10)–H(10)	118.7	C(17)–C(18)–H(18A)	108.9
C(9)–C(10)–H(10)	118.7	C(19)–C(18)–H(18A)	108.9
N(2)–C(11)–C(7)	123.7(2)	C(17)–C(18)–H(18B)	108.9
N(2)–C(11)–C(12)	116.2(2)	C(19)–C(18)–H(18B)	108.9
C(7)–C(11)–C(12)	120.1(2)	H(18A)–C(18)–H(18B)	107.7

N(4)–C(19)–C(23)	112.8(2)	H(24A)–C(24)–H(24C)	109.5
N(4)–C(19)–C(18)	112.4(2)	H(24B)–C(24)–H(24C)	109.5
C(23)–C(19)–C(18)	112.3(2)	O(2)–C(25)–Mo(1)	170.2(2)
N(4)–C(19)–H(19)	106.3	O(3)–C(26)–Mo(1)	177.8(2)
C(23)–C(19)–H(19)	106.3	O(4)–C(27)–Mo(1)	179.2(2)
C(18)–C(19)–H(19)	106.3	O(5)–C(28)–Mo(1)	169.8(2)
C(21)–C(20)–C(15)	113.7(2)	C(1)–N(1)–C(12)	117.3(2)
C(21)–C(20)–H(20A)	108.8	C(1)–N(1)–Mo(1)	126.05(16)
C(15)–C(20)–H(20A)	108.8	C(12)–N(1)–Mo(1)	116.55(14)
C(21)–C(20)–H(20B)	108.8	C(10)–N(2)–C(11)	117.5(2)
C(15)–C(20)–H(20B)	108.8	C(10)–N(2)–Mo(1)	125.35(15)
H(20A)–C(20)–H(20B)	107.7	C(11)–N(2)–Mo(1)	117.07(14)
C(20)–C(21)–C(23)	112.4(2)	C(13)–N(3)–C(6)	125.3(2)
C(20)–C(21)–C(22)	109.7(2)	C(14)–N(4)–C(24)	122.11(19)
C(23)–C(21)–C(22)	109.1(2)	C(14)–N(4)–C(19)	123.99(19)
C(20)–C(21)–H(21)	108.5	C(24)–N(4)–C(19)	113.86(18)
C(23)–C(21)–H(21)	108.5	C(27)–Mo(1)–C(26)	90.41(10)
C(22)–C(21)–H(21)	108.5	C(27)–Mo(1)–C(25)	85.14(11)
C(17)–C(22)–C(21)	109.4(2)	C(26)–Mo(1)–C(25)	85.19(10)
C(17)–C(22)–H(22A)	109.8	C(27)–Mo(1)–C(28)	84.44(10)
C(21)–C(22)–H(22A)	109.8	C(26)–Mo(1)–C(28)	86.83(10)
C(17)–C(22)–H(22B)	109.8	C(25)–Mo(1)–C(28)	166.82(10)
C(21)–C(22)–H(22B)	109.8	C(27)–Mo(1)–N(2)	172.58(8)
H(22A)–C(22)–H(22B)	108.2	C(26)–Mo(1)–N(2)	96.91(8)
C(19)–C(23)–C(21)	113.9(2)	C(25)–Mo(1)–N(2)	96.65(9)
C(19)–C(23)–H(23A)	108.8	C(28)–Mo(1)–N(2)	94.71(8)
C(21)–C(23)–H(23A)	108.8	C(27)–Mo(1)–N(1)	99.75(9)
C(19)–C(23)–H(23B)	108.8	C(26)–Mo(1)–N(1)	169.74(8)
C(21)–C(23)–H(23B)	108.8	C(25)–Mo(1)–N(1)	97.08(9)
H(23A)–C(23)–H(23B)	107.7	C(28)–Mo(1)–N(1)	92.63(8)
N(4)–C(24)–H(24A)	109.5	N(2)–Mo(1)–N(1)	72.90(7)
N(4)–C(24)–H(24B)	109.5		
H(24A)–C(24)–H(24B)	109.5		
N(4)–C(24)–H(24C)	109.5		

Table B8. Bond lengths [Å] for **49**-PMC.

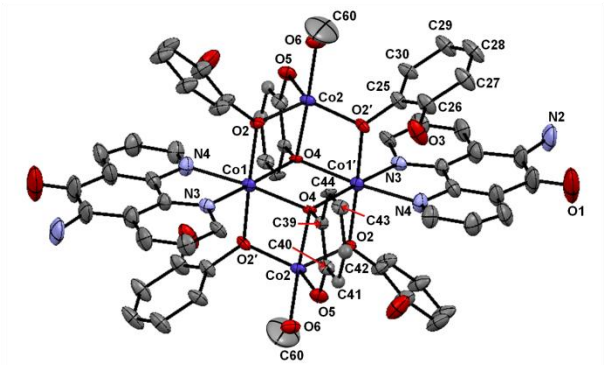

C(1)–N(1)	1.51(2)	C(9)–H(9A)	0.9900	C(21)–N(3)	1.338(17)
C(1)–H(1A)	0.9800	C(9)–H(9B)	0.9900	C(21)–H(21)	0.9500
C(1)–H(1B)	0.9800	C(10)–C(11)	1.64(4)	C(22)–C(23)	1.32(2)
C(1)–H(1C)	0.9800	C(10)–H(10)	1.0000	C(22)–H(22)	0.9500
C(2)–N(1)	1.22(3)	C(11)–C(12)	1.54(2)	C(23)–C(24)	1.39(2)
C(2)–C(3)	1.39(4)	C(11)–H(11A)	0.9900	C(23)–H(23)	0.9500
C(2)–C(10)	1.47(4)	C(11)–H(11B)	0.9900	C(24)–N(4)	1.332(18)
C(3)–N(2)	1.35(3)	C(12)–C(13)	1.52(3)	C(24)–H(24)	0.9500
C(3)–H(3)	0.9500	C(12)–C(14)	1.55(2)	C(25)–O(2)	1.354(7)
C(4)–N(2)	1.36(2)	C(12)–H(12)	1.0000	C(25)–C(26)	1.385(10)
C(4)–C(5)	1.41(3)	C(13)–H(13A)	0.9900	C(25)–C(30)	1.385(9)
C(4)–C(18)	1.45(2)	C(13)–H(13B)	0.9900	C(26)–O(3)	1.365(9)
C(5)–O(1)	1.28(2)	C(14)–H(14A)	0.9900	C(26)–C(27)	1.413(11)
C(5)–C(15)	1.49(2)	C(14)–H(14B)	0.9900	C(27)–C(28)	1.379(11)
C(6)–C(7)	1.42(3)	C(15)–C(16)	1.39(2)	C(27)–C(31)	1.546(12)
C(6)–C(14)	1.54(2)	C(15)–C(22)	1.39(2)	C(28)–C(29)	1.390(11)
C(6)–N(1)	1.60(4)	C(16)–N(4)	1.349(15)	C(28)–H(28)	0.9500
C(6)–H(6)	1.0000	C(16)–C(17)	1.429(18)	C(29)–C(30)	1.392(10)
C(7)–C(8)	1.42(3)	C(17)–N(3)	1.348(14)	C(29)–C(35)	1.541(11)
C(7)–H(7A)	0.9900	C(17)–C(18)	1.409(18)	C(30)–H(30)	0.9500
C(7)–H(7B)	0.9900	C(18)–C(19)	1.43(2)	C(31)–C(34)	1.47(2)
C(8)–C(13)	1.52(3)	C(19)–C(20)	1.34(2)	C(31)–C(33)	1.532(18)
C(8)–C(9)	1.57(4)	C(19)–H(19)	0.9500	C(31)–C(32)	1.539(13)
C(8)–H(8)	1.0000	C(20)–C(21)	1.431(18)	C(32)–H(32A)	0.9800
C(9)–C(10)	1.46(4)	C(20)–H(20)	0.9500	C(32)–H(32B)	0.9800

C(32)–H(32C)	0.9800	C(42)–C(41)	1.3900	C(48)–H(48A)	0.9800
C(33)–H(33A)	0.9800	C(42)–H(42)	0.9500	C(48)–H(48B)	0.9800
C(33)–H(33B)	0.9800	C(41)–C(40)	1.3900	C(48)–H(48C)	0.9800
C(33)–H(33C)	0.9800	C(41)–C(45)	1.555(14)	N(3)–Co(1)	2.128(7)
C(34)–H(34A)	0.9800	C(40)–O(5)	1.391(11)	N(4)–Co(1)	2.143(8)
C(34)–H(34B)	0.9800	C(49)–C(50)	1.514(17)	O(2)–Co(1)	2.070(4)
C(34)–H(34C)	0.9800	C(49)–C(52)	1.528(19)	O(3)–H(30)	1.03(9)
C(35)–C(36)	1.494(12)	C(49)–C(51)	1.533(19)	O(4)–Co(1)	2.158(7)
C(35)–C(37)	1.529(14)	C(50)–H(50A)	0.9800	O(4)–Co(2)	2.168(6)
C(35)–C(38)	1.540(13)	C(50)–H(50B)	0.9800	C(60)–O(6)	1.30(4)
C(36)–H(36A)	0.9800	C(50)–H(50C)	0.9800	C(60)–H(60A)	0.9800
C(36)–H(36B)	0.9800	C(51)–H(51A)	0.9800	C(60)–H(60B)	0.9800
C(36)–H(36C)	0.9800	C(51)–H(51B)	0.9800	C(60)–H(60C)	0.9800
C(37)–H(37A)	0.9800	C(51)–H(51C)	0.9800	O(6)–H(6A)	0.8400
C(37)–H(37B)	0.9800	C(52)–H(52A)	0.9800	O(5)–Co(2)	1.930(9)
C(37)–H(37C)	0.9800	C(52)–H(52B)	0.9800	O(7)–C(54)	1.29(4)
C(38)–H(38A)	0.9800	C(52)–H(52C)	0.9800	O(7)–H(7)	0.8400
C(38)–H(38B)	0.9800	C(45)–C(46)	1.513(15)	C(54)–H(54A)	0.9800
C(38)–H(38C)	0.9800	C(45)–C(48)	1.53(2)	C(54)–H(54B)	0.9800
C(39)–O(4)	1.376(9)	C(45)–C(47)	1.559(16)	C(54)–H(54C)	0.9800
C(39)–C(44)	1.3900	C(46)–H(46A)	0.9800	O(7B)–C(54B)	1.46(8)
C(39)–C(40)	1.3900	C(46)–H(46B)	0.9800	O(7B)–H(7B1)	0.84(7)
C(44)–C(43)	1.3900	C(46)–H(46C)	0.9800	C(54B)–H(54D)	0.9800
C(44)–H(44)	0.9500	C(47)–H(47A)	0.9800	C(54B)–H(54E)	0.9800
C(43)–C(42)	1.3900	C(47)–H(47B)	0.9800	C(54B)–H(54F)	0.9800
C(43)–C(49)	1.563(15)	C(47)–H(47C)	0.9800		

Table B9. Bond angles [°] for **49**-PMC.

N(1)–C(1)–H(1A)	109.5	C(7)–C(8)–C(9)	100(3)
N(1)–C(1)–H(1B)	109.5	C(13)–C(8)–C(9)	118(2)
H(1A)–C(1)–H(1B)	109.5	C(7)–C(8)–H(8)	108.3
N(1)–C(1)–H(1C)	109.5	C(13)–C(8)–H(8)	108.3
H(1A)–C(1)–H(1C)	109.5	C(9)–C(8)–H(8)	108.3
H(1B)–C(1)–H(1C)	109.5	C(10)–C(9)–C(8)	114(2)
N(1)–C(2)–C(3)	122(3)	C(10)–C(9)–H(9A)	108.7
N(1)–C(2)–C(10)	121(3)	C(8)–C(9)–H(9A)	108.7
C(3)–C(2)–C(10)	117(2)	C(10)–C(9)–H(9B)	108.7
N(2)–C(3)–C(2)	123(3)	C(8)–C(9)–H(9B)	108.7
N(2)–C(3)–H(3)	118.6	H(9A)–C(9)–H(9B)	107.6
C(2)–C(3)–H(3)	118.6	C(9)–C(10)–C(2)	111(3)
N(2)–C(4)–C(5)	125.9(15)	C(9)–C(10)–C(11)	113(2)
N(2)–C(4)–C(18)	114.9(16)	C(2)–C(10)–C(11)	112(3)
C(5)–C(4)–C(18)	119.2(14)	C(9)–C(10)–H(10)	107.0
O(1)–C(5)–C(4)	124.0(15)	C(2)–C(10)–H(10)	107.0
O(1)–C(5)–C(15)	117.5(18)	C(11)–C(10)–H(10)	107.0
C(4)–C(5)–C(15)	118.1(14)	C(12)–C(11)–C(10)	115(2)
C(7)–C(6)–C(14)	114(3)	C(12)–C(11)–H(11A)	108.6
C(7)–C(6)–N(1)	109(3)	C(10)–C(11)–H(11A)	108.6
C(14)–C(6)–N(1)	110(3)	C(12)–C(11)–H(11B)	108.6
C(7)–C(6)–H(6)	108.2	C(10)–C(11)–H(11B)	108.6
C(14)–C(6)–H(6)	108.2	H(11A)–C(11)–H(11B)	107.6
N(1)–C(6)–H(6)	108.2	C(13)–C(12)–C(11)	114(2)
C(8)–C(7)–C(6)	119(3)	C(13)–C(12)–C(14)	107(3)
C(8)–C(7)–H(7A)	107.6	C(11)–C(12)–C(14)	107(3)
C(6)–C(7)–H(7A)	107.6	C(13)–C(12)–H(12)	109.4
C(8)–C(7)–H(7B)	107.6	C(11)–C(12)–H(12)	109.4
C(6)–C(7)–H(7B)	107.6	C(14)–C(12)–H(12)	109.4
H(7A)–C(7)–H(7B)	107.0	C(12)–C(13)–C(8)	107(3)
C(7)–C(8)–C(13)	113(3)	C(12)–C(13)–H(13A)	110.4

C(8)–C(13)–H(13A)	110.4	C(15)–C(22)–H(22)	119.5
C(12)–C(13)–H(13B)	110.4	C(22)–C(23)-C(24)	119.0(15)
C(8)–C(13)–H(13B)	110.4	C(22)–C(23)–H(23)	120.5
H(13A)–C(13)–H(13B)	108.6	C(24)–C(23)–H(23)	120.5
C(6)–C(14)–C(12)	114(3)	N(4)–C(24)–C(23)	122.2(14)
C(6)–C(14)–H(14A)	108.9	N(4)–C(24)–H(24)	118.9
C(12)–C(14)–H(14A)	108.9	C(23)–C(24)–H(24)	118.9
C(6)–C(14)–H(14B)	108.9	O(2)–C(25)–C(26)	119.0(6)
C(12)–C(14)–H(14B)	108.9	O(2)–C(25)–C(30)	120.9(6)
H(14A)–C(14)–H(14B)	107.7	C(26)–C(25)–C(30)	120.1(6)
C(16)–C(15)–C(22)	117.3(14)	O(3)–C(26)–C(25)	121.0(6)
C(16)–C(15)–C(5)	120.9(15)	O(3)–C(26)–C(27)	118.5(7)
C(22)–C(15)–C(5)	121.6(15)	C(25)–C(26)–C(27)	120.5(6)
N(4)–C(16)–C(15)	121.8(13)	C(28)–C(27)–C(26)	117.2(7)
N(4)–C(16)–C(17)	117.7(11)	C(28)–C(27)–C(31)	121.8(7)
C(15)–C(16)–C(17)	120.4(12)	C(26)–C(27)–C(31)	121.0(7)
N(3)–C(17)–C(18)	123.1(12)	C(27)–C(28)–C(29)	123.7(7)
N(3)–C(17)–C(16)	117.4(10)	C(27)–C(28)–H(28)	118.2
C(18)–C(17)–C(16)	119.5(12)	C(29)–C(28)–H(28)	118.2
C(17)–C(18)–C(19)	117.1(13)	C(28)–C(29)–C(30)	117.4(7)
C(17)–C(18)–C(4)	121.6(15)	C(28)–C(29)–C(35)	120.6(7)
C(19)–C(18)–C(4)	121.2(13)	C(30)–C(29)–C(35)	122.0(7)
C(20)–C(19)–C(18)	119.6(12)	C(25)–C(30)–C(29)	121.1(7)
C(20)–C(19)–H(19)	120.2	C(25)–C(30)–H(30)	119.5
C(18)–C(19)–H(19)	120.2	C(29)–C(30)–H(30)	119.5
C(19)–C(20)–C(21)	119.8(14)	C(34)–C(31)–C(33)	107.7(11)
C(19)–C(20)–H(20)	120.1	C(34)–C(31)–C(32)	108.2(12)
C(21)–C(20)–H(20)	120.1	C(33)–C(31)–C(32)	106.6(10)
N(3)–C(21)–C(20)	121.6(12)	C(34)–C(31)–C(27)	112.3(11)
N(3)–C(21)–H(21)	119.2	C(33)–C(31)–C(27)	109.7(11)
C(20)–C(21)–H(21)	119.2	C(32)–C(31)–C(27)	112.0(8)
C(23)–C(22)–C(15)	121.0(15)	C(31)–C(32)–H(32A)	109.5
C(23)–C(22)–H(22)	119.5	C(31)–C(32)–H(32B)	109.5

H(32A)–C(32)–H(32B)	109.5	H(37B)–C(37)–H(37C)	109.5
C(31)–C(32)–H(32C)	109.5	C(35)–C(38)–H(38A)	109.5
H(32A)–C(32)–H(32C)	109.5	C(35)–C(38)–H(38B)	109.5
H(32B)–C(32)–H(32C)	109.5	H(38A)–C(38)–H(38B)	109.5
C(31)–C(33)–H(33A)	109.5	C(35)–C(38)–H(38C)	109.5
C(31)–C(33)–H(33B)	109.5	H(38A)–C(38)–H(38C)	109.5
H(33A)–C(33)–H(33B)	109.5	H(38B)–C(38)–H(38C)	109.5
C(31)–C(33)–H(33C)	109.5	O(4)–C(39)–C(44)	121.9(3)
H(33A)–C(33)–H(33C)	109.5	O(4)–C(39)–C(40)	118.1(3)
H(33B)–C(33)–H(33C)	109.5	C(44)–C(39)–C(40)	120.0
C(31)–C(34)–H(34A)	109.5	C(39)–C(44)–C(43)	120.0
C(31)–C(34)–H(34B)	109.5	C(39)–C(44)–H(44)	120.0
H(34A)–C(34)–H(34B)	109.5	C(43)–C(44)–H(44)	120.0
C(31)–C(34)–H(34C)	109.5	C(44)–C(43)–C(42)	120.0
H(34A)–C(34)–H(34C)	109.5	C(44)–C(43)–C(49)	121.0(6)
H(34B)–C(34)–H(34C)	109.5	C(42)–C(43)–C(49)	119.0(6)
C(36)–C(35)–C(37)	109.9(9)	C(41)–C(42)–C(43)	120.0
C(36)–C(35)–C(38)	108.1(10)	C(41)–C(42)–H(42)	120.0
C(37)–C(35)–C(38)	109.7(8)	C(43)–C(42)–H(42)	120.0
C(36)–C(35)–C(29)	112.5(7)	C(42)#1–C(41)–C(43)#1	159.8(9)
C(37)–C(35)–C(29)	108.0(9)	C(42)#1–C(41)–C(42)	25.5(7)
C(38)–C(35)–C(29)	108.7(8)	C(43)#1–C(41)–C(42)	167.7(3)
C(35)–C(36)–H(36A)	109.5	C(42)#1–C(41)–C(40)	145.3(7)
C(35)–C(36)–H(36B)	109.5	C(43)#1–C(41)–C(40)	51.9(3)
H(36A)–C(36)–H(36B)	109.5	C(42)–C(41)–C(40)	120.0
C(35)–C(36)–H(36C)	109.5	C(42)–C(41)–C(45)	118.6(6)
H(36A)–C(36)–H(36C)	109.5	C(40)–C(41)–C(45)	121.4(6)
H(36B)–C(36)–H(36C)	109.5	C(41)–C(40)–C(39)	120.0
C(35)–C(37)–H(37A)	109.5	C(41)–C(40)–O(5)	122.7(5)
C(35)–C(37)–H(37B)	109.5	C(39)–C(40)–O(5)	117.3(5)
H(37A)–C(37)–H(37B)	109.5	C(50)–C(49)–C(52)	108.0(17)
C(35)–C(37)–H(37C)	109.5	C(50)–C(49)–C(51)	107.7(19)
H(37A)–C(37)–H(37C)	109.5	C(52)–C(49)–C(51)	112(2)

C(50)–C(49)–C(43)	114.0(10)	N(3)–Co(1)–N(4)	77.6(3)
C(52)–C(49)–C(43)	104.4(19)	O(2)–Co(1)–O(4)	92.91(18)
C(51)–C(49)–C(43)	110(2)	N(3)–Co(1)–O(4)	172.0(2)
C(46)–C(45)–C(48)	108.0(16)	N(4)–Co(1)–O(4)	106.9(3)
C(46)–C(45)–C(41)	112.6(11)	O(5)–Co(2)–O(2)#1	108.7(3)
C(48)–C(45)–C(41)	111.4(16)	O(5)–Co(2)–O(4)	81.3(4)
C(46)–C(45)–C(47)	107.4(14)	C(54B)–O(7B)–H(7B1)	110(7)
C(48)–C(45)–C(47)	107.3(17)	O(7B)–C(54B)–H(54D)	109.5
C(41)–C(45)–C(47)	109.9(14)	O(7B)–C(54B)–H(54E)	109.5
C(2)–N(1)–C(1)	116(3)	H(54D)–C(54B)–H(54E)	109.5
C(2)–N(1)–C(6)	126(3)	O(7B)–C(54B)–H(54F)	109.5
C(1)–N(1)–C(6)	118(3)	H(54D)–C(54B)–H(54F)	109.5
C(3)–N(2)–C(4)	127(2)	H(54E)–C(54B)–H(54F)	109.5
C(21)–N(3)–Co(1)	126.7(8)		
C(17)–N(3)–Co(1)	113.7(7)		
C(24)–N(4)–C(16)	117.5(11)		
C(24)–N(4)–Co(1)	127.3(8)		
C(16)–N(4)–Co(1)	112.9(8)		
C(25)–O(2)–Co(1)	124.7(4)		
C(26)–O(3)–H(3O)	111(5)		
C(39)–O(4)–Co(1)	121.3(5)		
C(39)–O(4)–Co(2)	107.7(3)		
Co(1)–O(4)–Co(2)	94.1(2)		
O(6)–C(60)–H(60A)	109.5		
O(6)–C(60)–H(60B)	109.5		
H(60A)–C(60)–H(60B)	109.5		
O(6)–C(60)–H(60C)	109.5		
H(60A)–C(60)–H(60C)	109.5		
H(60B)–C(60)–H(60C)	109.5		
C(60)–O(6)–H(6A)	109.5		
C(40)–O(5)–Co(2)	115.2(6)		
O(2)–Co(1)–N(3)	93.79(11)		
O(2)–Co(1)–N(4)	89.53(12)		

Appendix C. Kinetic Fits for Determination of Rate Constants

Figure C1. First-order monoexponential fit (—) of the experimental absorbance (○) at 555 nm for a toluene solution (3×10^{-5} M) of APSO at 299 K upon thermal relaxation after generating a PSS with steady-state visible irradiation ($k_{vis}^{-1} = 0.19$ s^{-1}).

Figure C2. First-order monoexponential fit (—) of the experimental absorbance (○) at 555 nm for a toluene solution (3×10^{-5} M) of APSO at 299 K upon thermal relaxation after generating a PSS with steady-state UV irradiation ($k_{UV}^{-1} = 0.19$ s^{-1}).

Figure C3. First-order monoexponential fit (—) of the experimental absorbance (○) at 555 nm for a CH_2Cl_2 solution (3×10^{-5} M) of APSO at 301 K upon thermal relaxation after generating a PSS with steady-state visible irradiation ($k_{vis}^{-1} = 0.056$ s^{-1}).

Figure C4. First-order monoexponential fit (—) of the experimental absorbance (○) at 550 nm for an acetone solution (~2×10^{-5} M) of APSO at 299 K upon thermal relaxation after generating a PSS with steady-state visible irradiation ($k_{vis}^{-1} = 0.049$ s^{-1}).

Figure C5. First-order monoexponential fit (—) of the experimental absorbance (○) at 552 nm for a DMSO solution (~2×10^{-5} M) of APSO at 301 K upon thermal relaxation after generating a PSS with steady-state visible irradiation ($k_{vis}^{-1} = 0.077$ s^{-1}).

Figure C6. First-order monoexponential fit (—) of the experimental absorbance (○) at 582 nm for a toluene solution (2×10^{-3} M) of IPSO at 299 K upon thermal relaxation after generating a PSS with steady-state UV irradiation ($k_{UV}^{-1} = 0.23$ s^{-1}).

Figure C7. First-order monoexponential fit (—) of the experimental absorbance (○) at 591 nm for a CH_2Cl_2 solution of IPSO (3×10^{-4} M) at 299 K upon thermal relaxation after generating a PSS with steady-state UV irradiation ($k_{UV}^{-1} = 0.74$ s^{-1}).

Figure C8. First-order monoexponential fit (—) of the experimental absorbance (○) at 587 nm for an acetone solution (10^{-4} M) of IPSO at 299 K upon thermal relaxation after generating a PSS with steady-state UV irradiation ($k_{UV}^{-1} = 0.66$ s^{-1}).

Figure C9. First-order monoexponential fit (—) of the experimental absorbance (○) at 597 nm for a DMSO solution (10^{-4} M) of IPSO at 299 K upon thermal relaxation after generating a PSS with steady-state UV irradiation ($k_{UV}^{-1} = 0.66$ s^{-1}).

Figure C10. First-order monoexponential fit (—) of the experimental absorbance (○) at 546 nm for a toluene solution (1×10^{-4} M) of $Mo(CO)_4$(APSO) at 299 K upon thermal relaxation after generating a PSS with steady-state visible irradiation ($k_{vis}^{-1} = 0.0040$ s^{-1}).

Figure C11. First-order biexponential fit (—) of the experimental absorbance (○) at 546 nm for a toluene solution (1×10^{-4} M) of $Mo(CO)_4$(APSO) at 299 K upon thermal relaxation after generating a PSS with steady-state visible irradiation [$k_{vis}^{-1} = 0.0061$ s^{-1} (60%); 0.0027 s^{-1} (40%)].

Figure C12. First-order monoexponential fit (—) of the experimental absorbance (○) at 557 nm for a CH_2Cl_2 solution (3×10^{-4} M) of $Mo(CO)_4$(APSO) at 301 K upon thermal relaxation after generating a PSS with steady-state visible irradiation ($k_{vis}^{-1} = 0.0034$ s^{-1}).

Figure C13. First-order monoexponential fit (—) of the experimental absorbance (○) at 593 nm for a toluene solution (4×10^{-5} M) of $Mo(CO)_4$(IPSO) at 299 K upon PMC → SO isomerization immediately following dissolution of a solid sample ($k_{dis} = 0.023$ s^{-1}).

Figure C14. First-order monoexponential fit (—) of the experimental absorbance (○) at 585 nm for a toluene solution (3×10^{-5} M) of $Mo(CO)_4$(IPSO) at 299 K upon thermal relaxation after generating a PSS with steady-state visible irradiation ($k_{vis}^{-1} = 0.034$ s^{-1}).

Figure C15. First-order monoexponential fit (—) of the experimental absorbance (○) at 605 nm for a CH_2Cl_2 solution (2×10^{-5} M) of $Mo(CO)_4$(IPSO) at 301 K upon PMC → SO isomerization immediately following dissolution of a solid sample ($k_{dis} = 0.014$ s^{-1}).

Figure C16. First-order monoexponential fit (—) of the experimental absorbance (○) at 605 nm for a CH_2Cl_2 solution (2×10^{-5} M) of $Mo(CO)_4$(IPSO) at 301 K upon thermal relaxation after generating a PSS with steady-state visible irradiation ($k_{vis}^{-1} = 0.020$ s^{-1}).

Figure C17. First-order monoexponential fit (—) of the experimental absorbance (○) at 555 nm for a toluene solution (5×10^{-5} M) of Co(3,5-DTBQ)$_2$(APSO) at ~300 K upon thermal relaxation after generating a PSS with steady-state visible irradiation ($k_{vis}^{-1} = 0.016$ s^{-1}).

Figure C18. First-order biexponential fit (—) of the experimental absorbance (○) at 555 nm for a toluene solution (5×10^{-5} M) of Co(3,5-DTBQ)$_2$(APSO) at ~300 K upon thermal relaxation after generating a PSS with steady-state visible irradiation [$k_{vis}^{-1} = 0.021$ s^{-1} (80%); 0.0099 s^{-1} (20%)].

Figure C19. First-order monoexponential fit (—) of the experimental absorbance (○) at 590 nm for a toluene solution (2×10^{-4} M) of Co(3,5-DTBQ)$_2$(IPSO) at ~300 K upon thermal relaxation after generating a PSS with steady-state UV irradiation ($k_{UV}^{-1} = 0.14$ s^{-1}).

Figure C20. First-order biexponential fit (—) of the experimental absorbance (○) at 590 nm for a toluene solution (2×10^{-4} M) of Co(3,5-DTBQ)$_2$(IPSO) at ~300 K upon thermal relaxation after generating a PSS with steady-state UV irradiation [$k_{UV}^{-1} = 0.12$ s^{-1} (75%); 0.61 s^{-1} (25%)].

Figure C21. First-order monoexponential fit (—) of the experimental absorbance (○) at 555 nm for a toluene solution (2×10^{-5} M) of Co_4(3,5-DTBQ)$_6$(APSO)$_2$(MeO)$_2$ at 299 K upon thermal relaxation after generating a PSS with steady-state visible irradiation ($k_{vis}^{-1} = 0.017$ s^{-1}).

Figure C22. First-order biexponential fit (—) of the experimental absorbance (○) at 555 nm for a toluene solution (2×10^{-5} M) of Co_4(3,5-DTBQ)$_6$(APSO)$_2$(MeO)$_2$ at 299 K upon thermal relaxation after generating a PSS with steady-state visible irradiation [$k_{vis}^{-1} = 0.022$ s^{-1} (80%); 0.0077 (20%)].

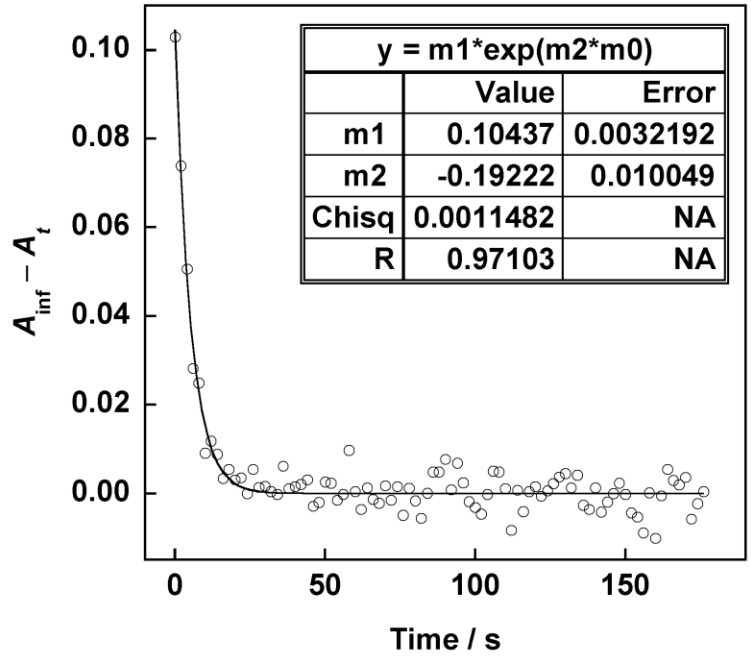

Figure C1. First-order monoexponential fit (—) of the experimental absorbance (○) at 555 nm for a toluene solution (3×10^{-5} M) of APSO at 299 K upon thermal relaxation after generating a PSS with steady-state visible irradiation (k_{vis}^{-1} = 0.19 s^{-1}).

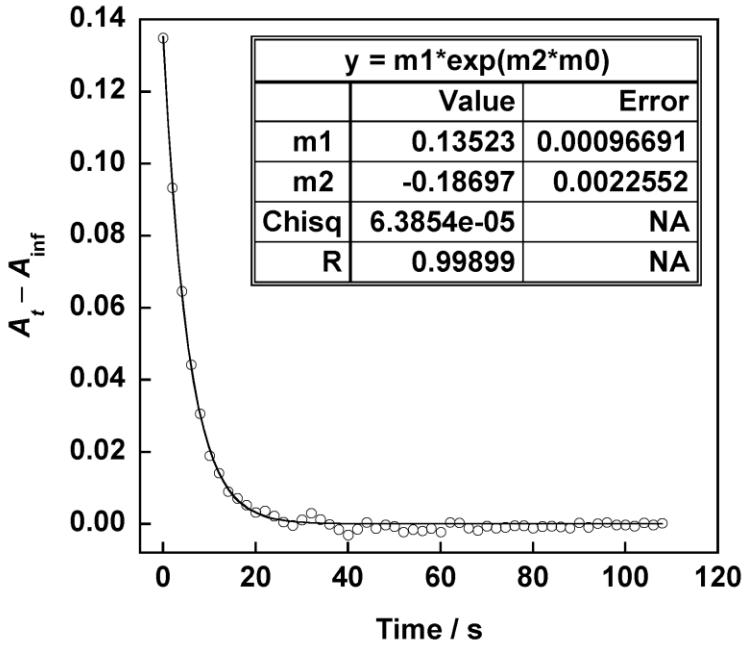

Figure C2. First-order monoexponential fit (—) of the experimental absorbance (○) at 555 nm for a toluene solution (3×10^{-5} M) of APSO at 299 K upon thermal relaxation after generating a PSS with steady-state UV irradiation (k_{UV}^{-1} = 0.19 s^{-1}).

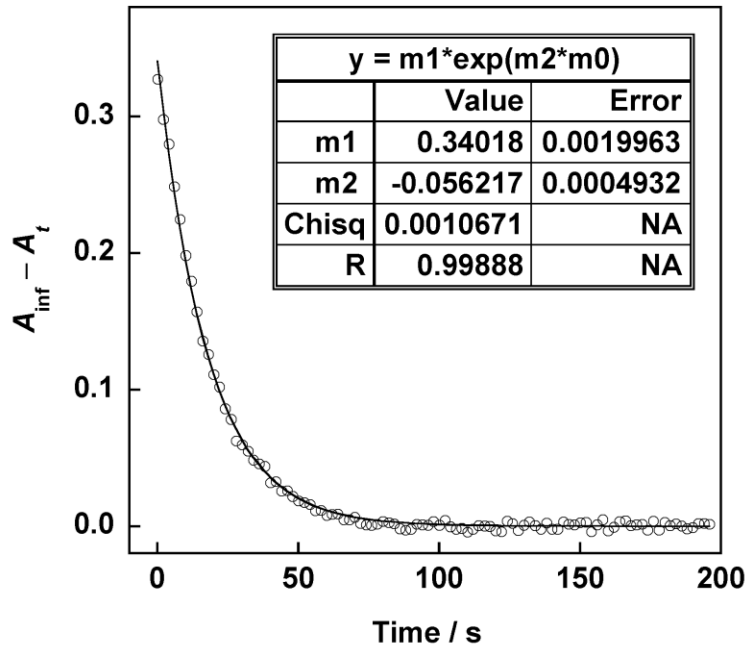

Figure C3. First-order monoexponential fit (—) of the experimental absorbance (○) at 555 nm for a CH_2Cl_2 solution (3×10^{-5} M) of APSO at 301 K upon thermal relaxation after generating a PSS with steady-state visible irradiation (k_{vis}^{-1} = 0.056 s^{-1}).

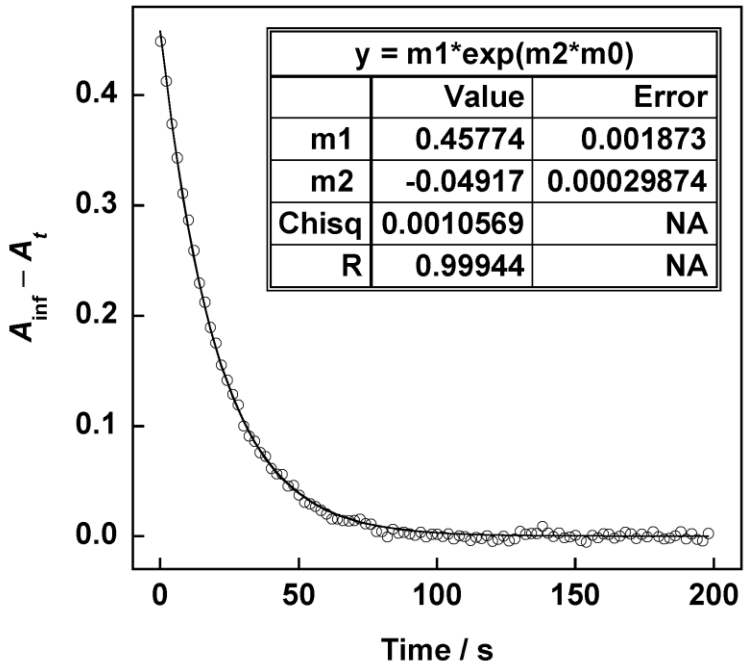

Figure C4. First-order monoexponential fit (—) of the experimental absorbance (○) at 550 nm for an acetone solution (~2×10^{-5} M) of APSO at 299 K upon thermal relaxation after generating a PSS with steady-state visible irradiation (k_{vis}^{-1} = 0.049 s^{-1}).

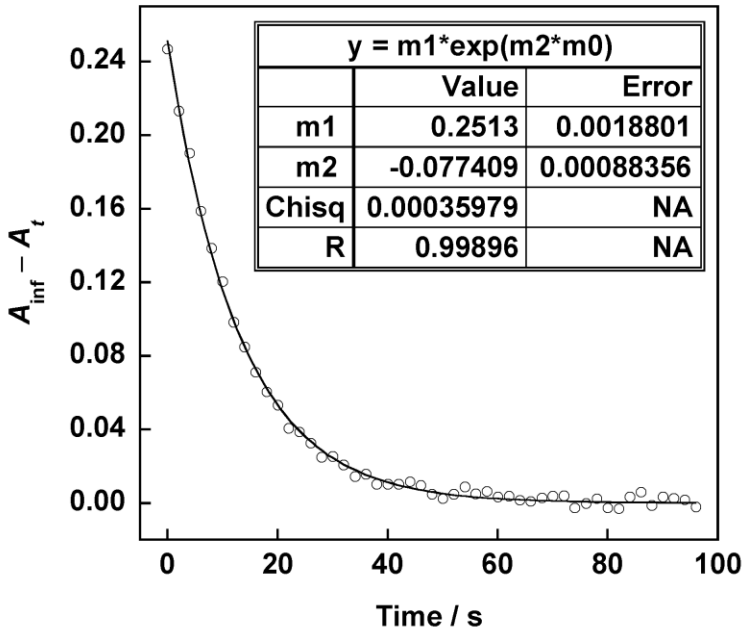

Figure C5. First-order monoexponential fit (—) of the experimental absorbance (○) at 552 nm for a DMSO solution (~2×10^{-5} M) of APSO at 301 K upon thermal relaxation after generating a PSS with steady-state visible irradiation (k_{vis}^{-1} = 0.077 s^{-1}).

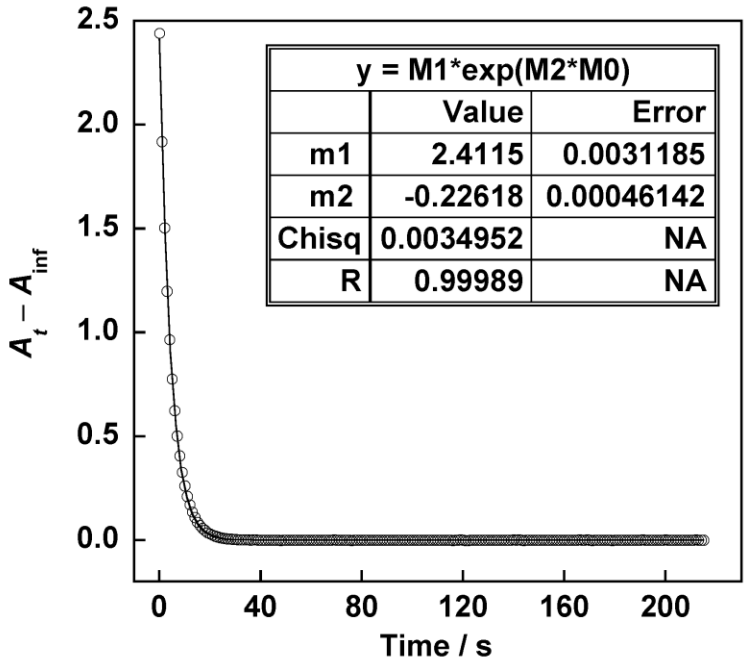

Figure C6. First-order monoexponential fit (—) of the experimental absorbance (○) at 582 nm for a toluene solution (2×10^{-3} M) of IPSO at 299 K upon thermal relaxation after generating a PSS with steady-state UV irradiation (k_{UV}^{-1} = 0.23 s^{-1}).

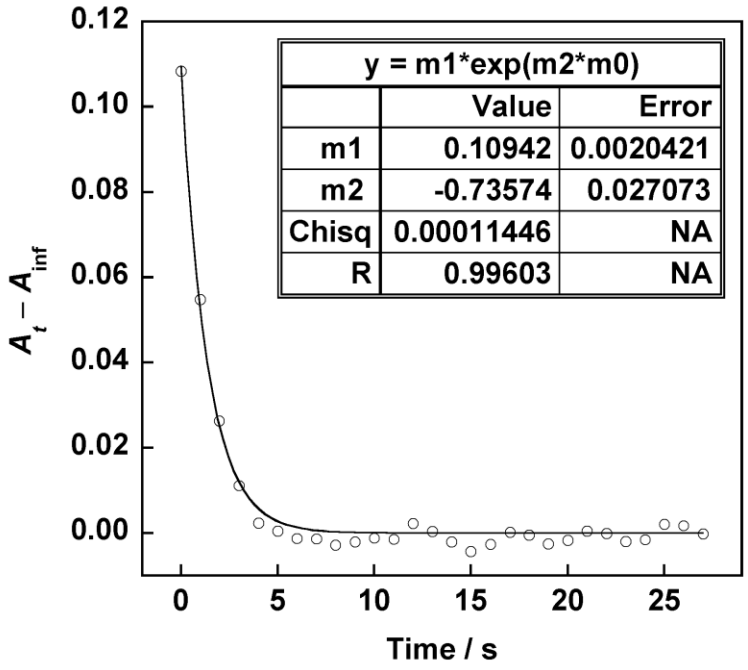

Figure C7. First-order monoexponential fit (—) of the experimental absorbance (○) at 591 nm for a CH_2Cl_2 solution of IPSO (3×10^{-4} M) at 299 K upon thermal relaxation after generating a PSS with steady-state UV irradiation (k_{UV}^{-1} = 0.74 s^{-1}).

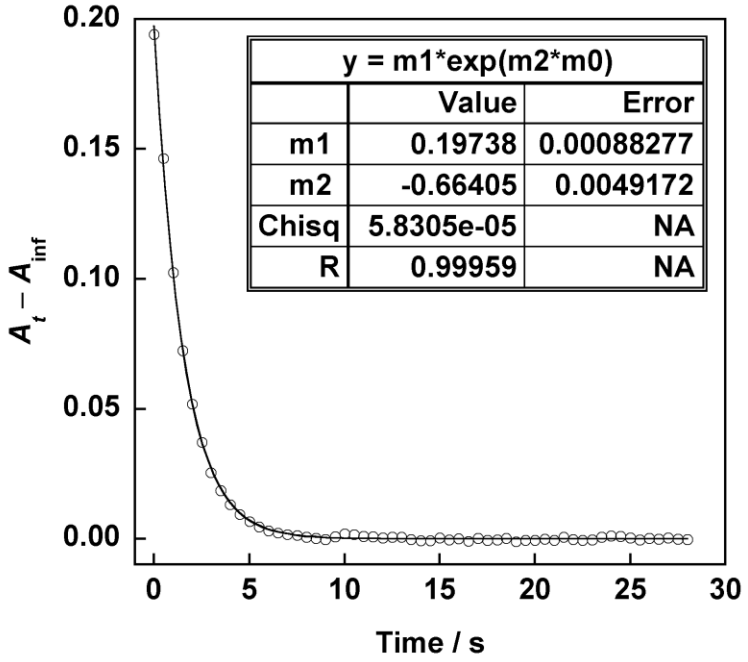

Figure C8. First-order monoexponential fit (—) of the experimental absorbance (○) at 587 nm for an acetone solution (10^{-4} M) of IPSO at 299 K upon thermal relaxation after generating a PSS with steady-state UV irradiation (k_{UV}^{-1} = 0.66 s^{-1}).

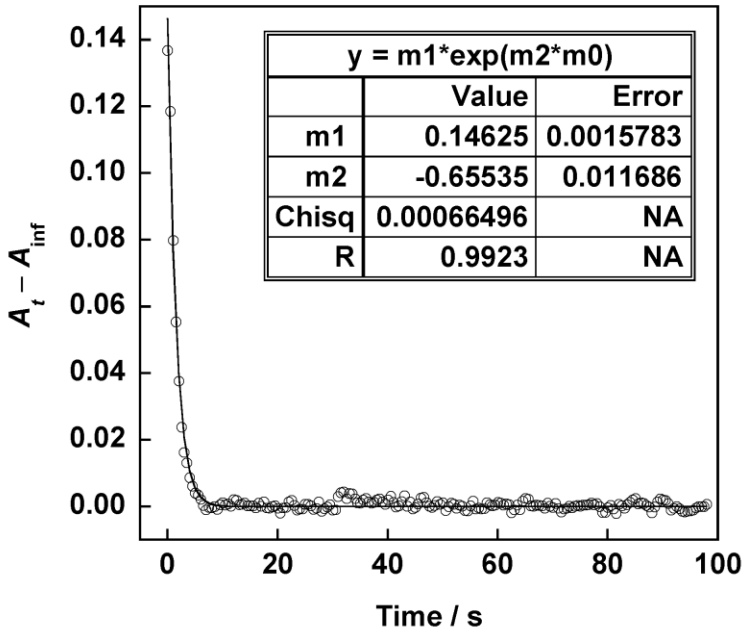

Figure C9. First-order monoexponential fit (—) of the experimental absorbance (○) at 597 nm for a DMSO solution (10^{-4} M) of IPSO at 299 K upon thermal relaxation after generating a PSS with steady-state UV irradiation (k_{UV}^{-1} = 0.66 s^{-1}).

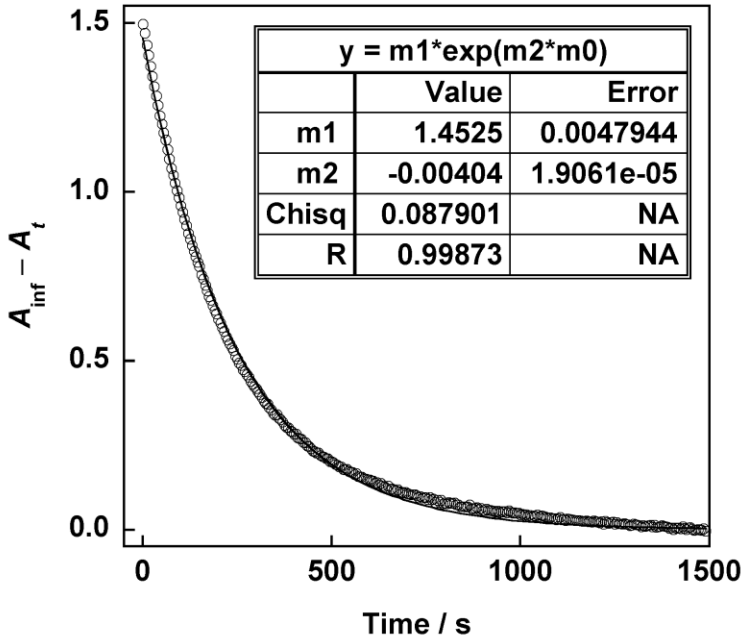

Figure C10. First-order monoexponential fit (—) of the experimental absorbance (○) at 546 nm for a toluene solution (1×10^{-4} M) of $Mo(CO)_4$(APSO) at 299 K upon thermal relaxation after generating a PSS with steady-state visible irradiation (k_{vis}^{-1} = 0.0040 s^{-1}).

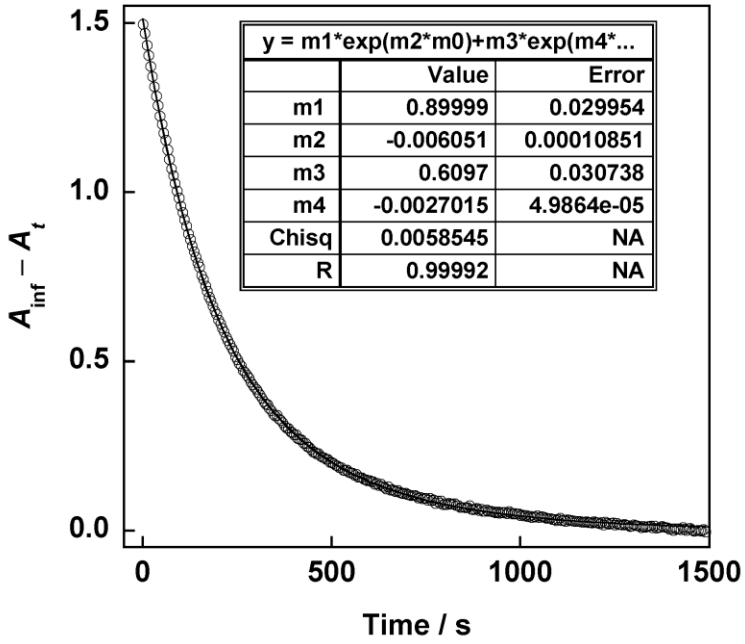

Figure C11. First-order biexponential fit (—) of the experimental absorbance (○) at 546 nm for a toluene solution (1×10^{-4} M) of $Mo(CO)_4$(APSO) at 299 K upon thermal relaxation after generating a PSS with steady-state visible irradiation [k_{vis}^{-1} = 0.0061 s^{-1} (60%); 0.0027 s^{-1} (40%)].

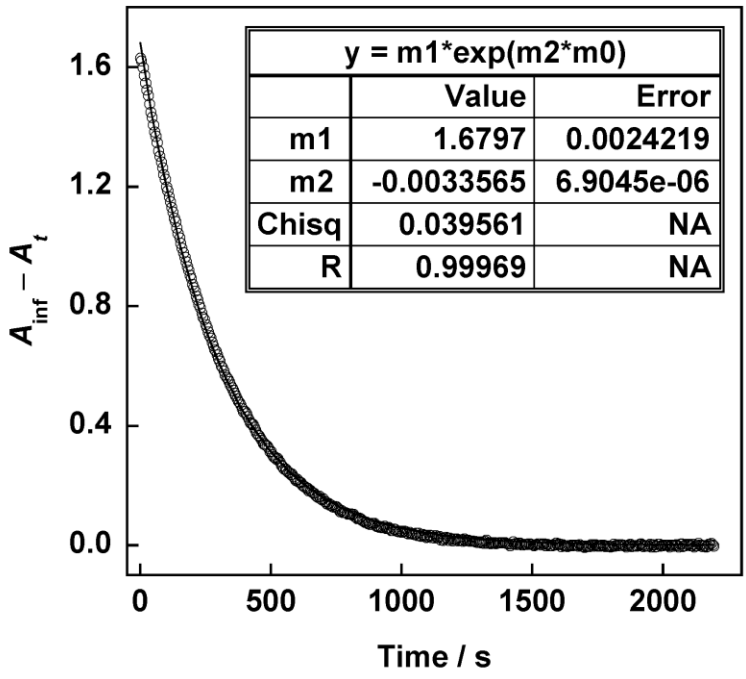

Figure C12. First-order monoexponential fit (—) of the experimental absorbance (○) at 557 nm for a CH_2Cl_2 solution (3×10^{-4} M) of $Mo(CO)_4$(APSO) at 301 K upon thermal relaxation after generating a PSS with steady-state visible irradiation (k_{vis}^{-1} = 0.0034 s^{-1}).

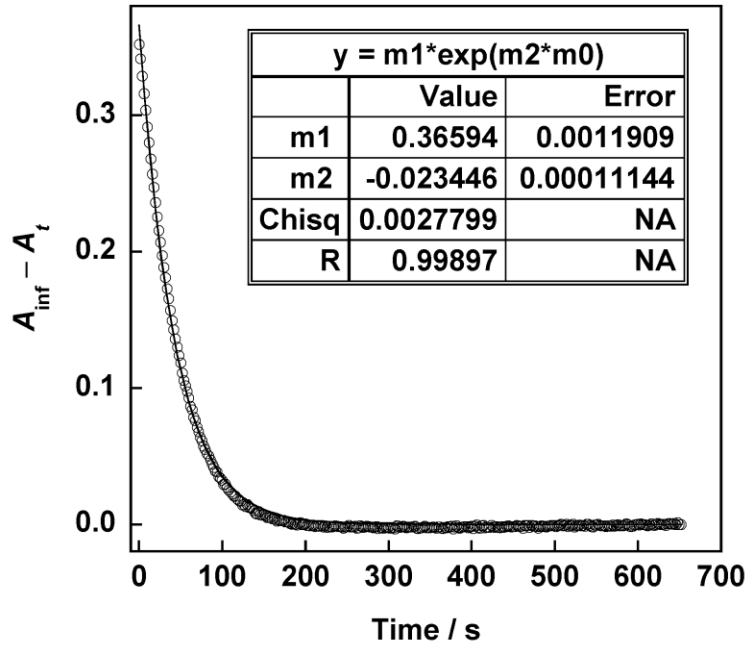

Figure C13. First-order monoexponential fit (—) of the experimental absorbance (○) at 593 nm for a toluene solution (4×10^{-5} M) of $Mo(CO)_4$(IPSO) at 299 K upon PMC → SO isomerization immediately following dissolution of a solid sample (k_{dis} = 0.023 s^{-1}).

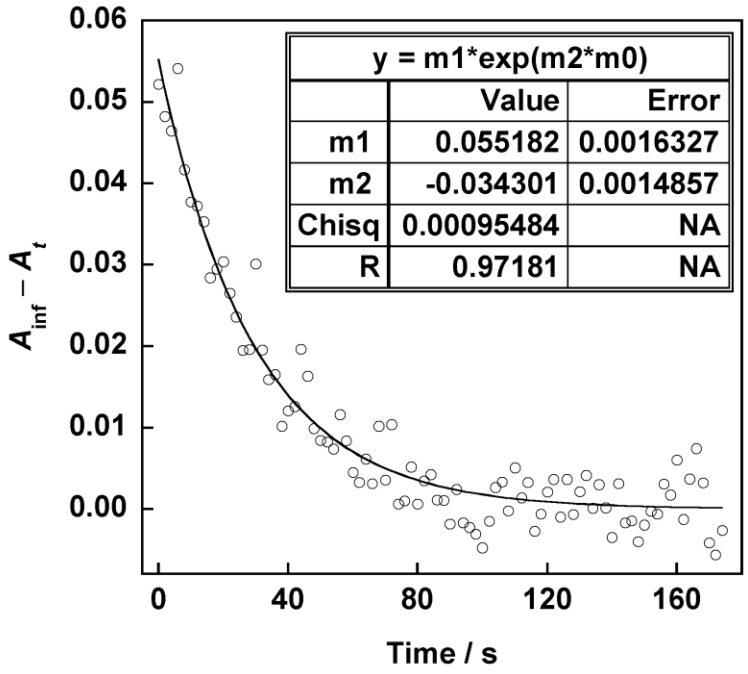

Figure C14. First-order monoexponential fit (—) of the experimental absorbance (○) at 585 nm for a toluene solution (3×10^{-5} M) of $Mo(CO)_4$(IPSO) at 299 K upon thermal relaxation after generating a PSS with steady-state visible irradiation (k_{vis}^{-1} = 0.034 s^{-1}).

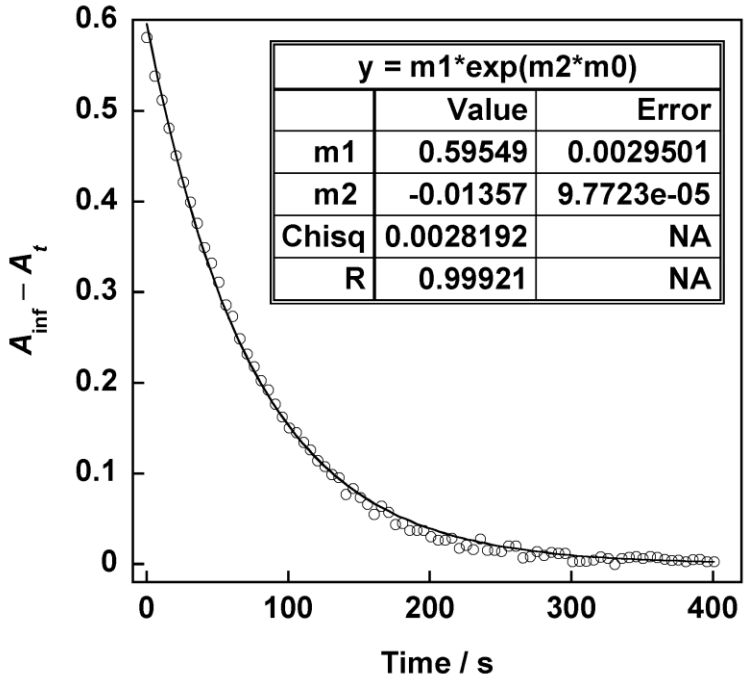

Figure C15. First-order monoexponential fit (—) of the experimental absorbance (○) at 605 nm for a CH_2Cl_2 solution (2×10^{-5} M) of $Mo(CO)_4$(IPSO) at 301 K upon PMC → SO isomerization immediately following dissolution of a solid sample (k_{dis} = 0.014 s^{-1}).

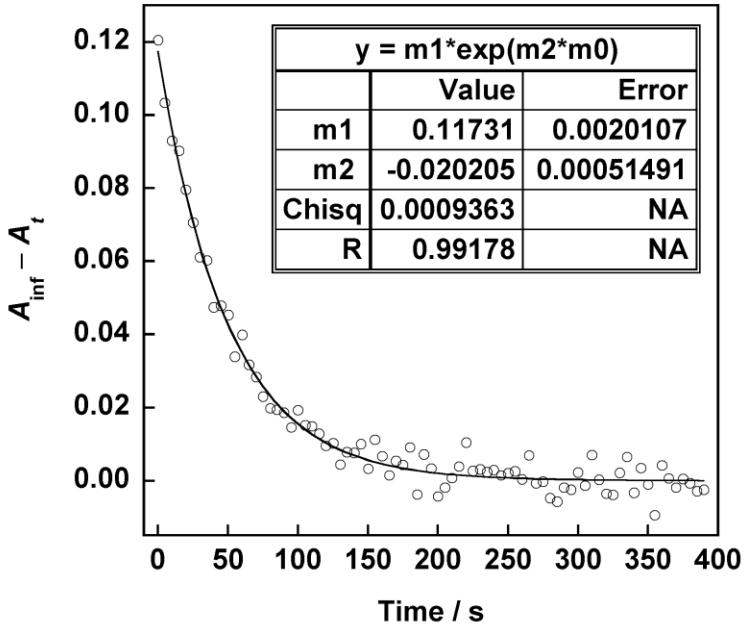

Figure C16. First-order monoexponential fit (—) of the experimental absorbance (○) at 605 nm for a CH_2Cl_2 solution (2×10^{-5} M) of $Mo(CO)_4$(IPSO) at 301 K upon thermal relaxation after generating a PSS with steady-state visible irradiation (k_{vis}^{-1} = 0.020 s^{-1}).

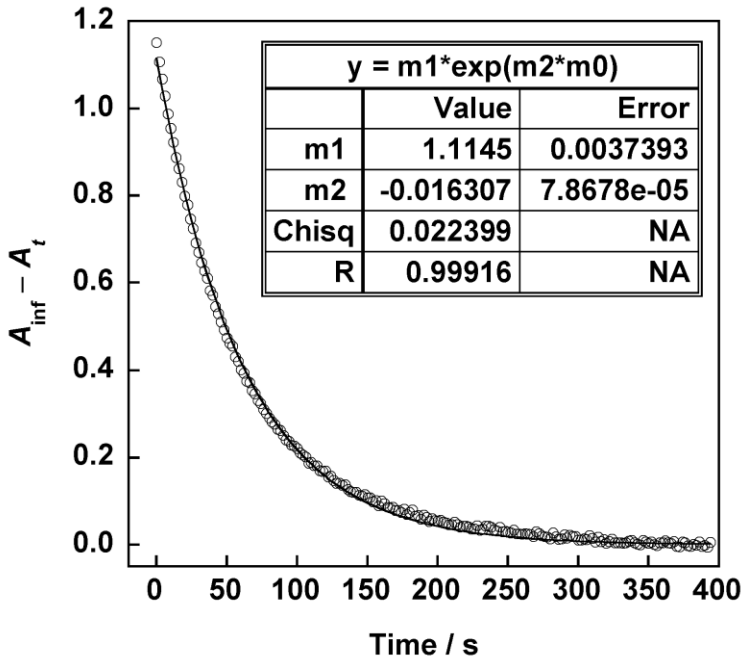

Figure C17. First-order monoexponential fit (—) of the experimental absorbance (○) at 555 nm for a toluene solution (5×10^{-5} M) of Co(3,5-DTBQ)$_2$(APSO) at ~300 K upon thermal relaxation after generating a PSS with steady-state visible irradiation (k_{vis}^{-1} = 0.016 s^{-1}).

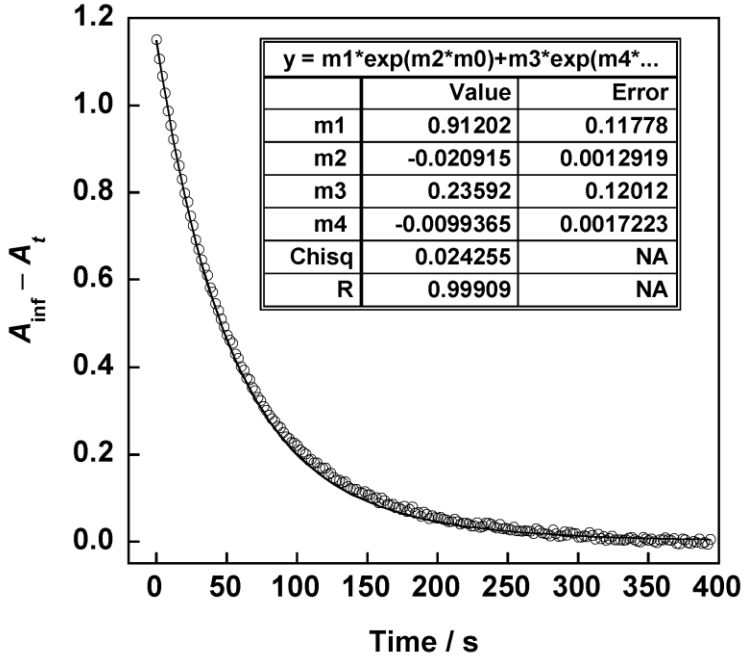

Figure C18. First-order biexponential fit (—) of the experimental absorbance (○) at 555 nm for a toluene solution (5×10^{-5} M) of Co(3,5-DTBQ)$_2$(APSO) at ~300 K upon thermal relaxation after generating a PSS with steady-state visible irradiation [k_{vis}^{-1} = 0.021 s^{-1} (80%); 0.0099 s^{-1} (20%)].

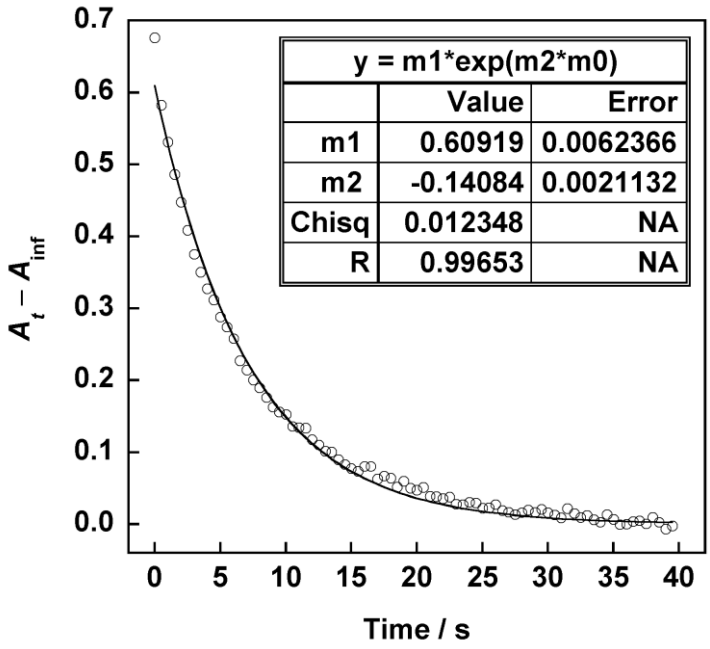

Figure C19. First-order monoexponential fit (—) of the experimental absorbance (○) at 590 nm for a toluene solution (2×10^{-4} M) of Co(3,5-DTBQ)$_2$(IPSO) at ~300 K upon thermal relaxation after generating a PSS with steady-state UV irradiation (k_{UV}^{-1} = 0.14 s^{-1}).

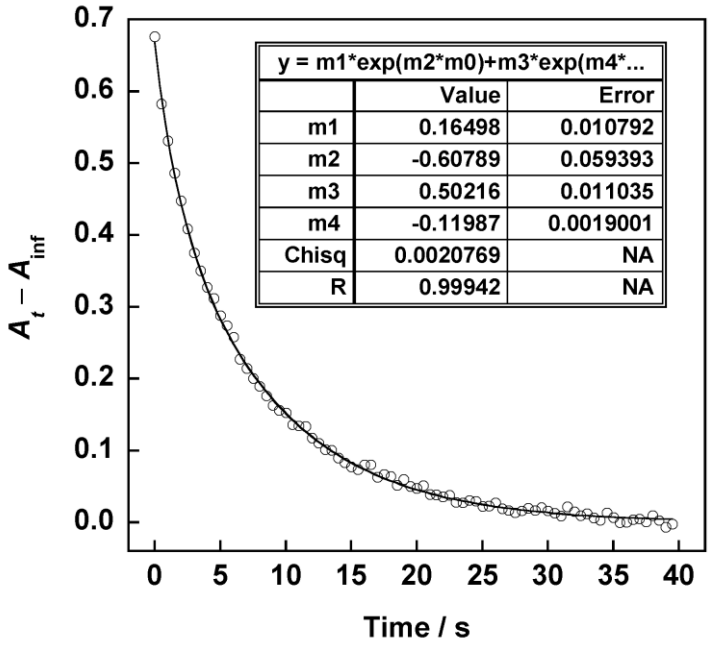

Figure C20. First-order biexponential fit (—) of the experimental absorbance (○) at 590 nm for a toluene solution (2×10^{-4} M) of Co(3,5-DTBQ)$_2$(IPSO) at ~300 K upon thermal relaxation after generating a PSS with steady-state UV irradiation [k_{UV}^{-1} = 0.12 s^{-1} (75%); 0.61 s^{-1} (25%)].

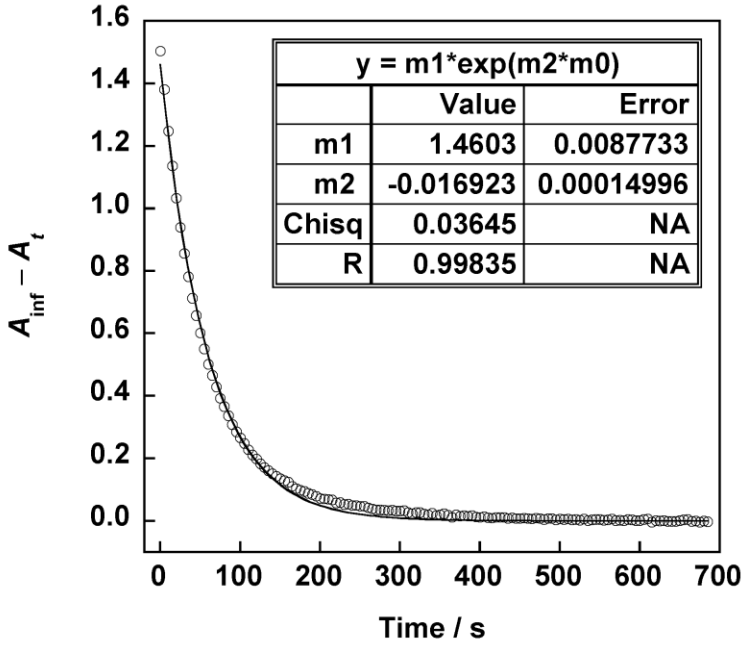

Figure C21. First-order monoexponential fit (—) of the experimental absorbance (○) at 555 nm for a toluene solution (2×10^{-5} M) of $Co_4(3,5\text{-DTBQ})_6(APSO)_2(MeO)_2$ at 299 K upon thermal relaxation after generating a PSS with steady-state visible irradiation (k_{vis}^{-1} = 0.017 s^{-1}).

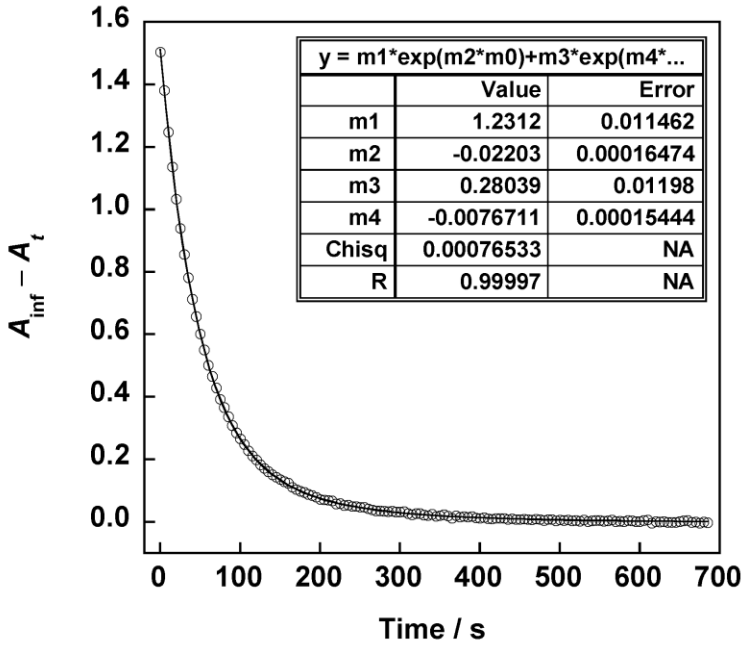

Figure C22. First-order biexponential fit (—) of the experimental absorbance (○) at 555 nm for a toluene solution (2×10^{-5} M) of $Co_4(3,5\text{-DTBQ})_6(APSO)_2(MeO)_2$ at 299 K upon thermal relaxation after generating a PSS with steady-state visible irradiation [k_{vis}^{-1} = 0.022 s^{-1} (80%); 0.0077 (20%)].

Appendix D. Gaussian Output

Table D1. APSO-SO, geometry optimization, B3LYP/6-31G(d,p).

FOpt\RB3LYP\6-31G(d,p)\C24H24N4O1\NLF\24-Jun-2009\0\\
opt rb3lyp/6-31g(d,p)\\APSO-SO form b3LYP/6-31G(d,p) added CH3\\0,1\
N,2.4989485663,-0.4417484213,-1.6087415653\C,0.7343821988,-1.951073347
7,-0.9557753538\H,1.3639337967,-2.7669894805,-1.3133442018\C,-1.320306
8193,-1.0779943131,-0.419129934\C,-0.8367661089,0.207068562,-0.4969245
277\N,-0.5157102331,-2.1641350089,-0.7952132796\C,-1.6929499614,1.3429
311319,-0.2926457334\C,-2.6983409867,-1.3124396857,-0.0662900138\C,-3.
0592485259,1.1414873165,0.0595924586\C,-3.5721697999,-0.2198065619,0.1
914090806\C,-1.2242514458,2.6677279374,-0.4228864233\H,-0.1888856768,2
.8398543757,-0.6947456263\C,-2.0986942816,3.7119430377,-0.205779853\H,
-1.7791221309,4.7450403243,-0.2981698856\C,-3.4288993231,3.4077437738,
0.1442345986\H,-4.1391255942,4.2138691861,0.3245802472\C,-3.2289692409
,-2.6166593939,0.0308921815\H,-2.5818742367,-3.4613444146,-0.177051006
3\C,-4.5530477526,-2.7773574863,0.382685279\H,-4.9963924333,-3.7646932
919,0.4679930045\N,-3.8998843527,2.1774340246,0.275053549\N,-4.8669886
872,-0.3917183583,0.5388851\C,-5.3293434631,-1.628283057,0.6316812873\
H,-6.3759983763,-1.7302762234,0.9157368044\C,1.4602892391,-0.635105546
2,-0.6570939001\C,4.491790291,-0.9548501876,0.8509186845\H,5.247361133
4,-1.6466849471,1.2450961615\C,4.6198801309,0.4032855261,1.56600345\H,
5.6158859779,0.8279603372,1.3854056105\H,4.518768027,0.2784991329,2.65
17633807\C,1.9061279401,-0.6351022005,0.8378264373\H,1.0362554813,-1.0
44471513,1.3651629688\C,4.7664081844,-0.7407260038,-0.6454697373\H,4.7
273822297,-1.6879209994,-1.194577218\H,5.7835035063,-0.3412654718,-0.7
586729493\C,3.7700234781,0.2429101778,-1.2926052614\H,4.1762653061,0.5
154092561,-2.2714197374\C,3.1034021558,-1.5744599806,1.1300504497\H,2.
9941640414,-2.5177395647,0.5826227559\H,3.0584470094,-1.8340850582,2.1
954958068\C,3.6702767493,1.555637545,-0.4759909268\H,2.846624097,2.165
632784,-0.8643634281\H,4.5941634295,2.1210328593,-0.6571857094\C,2.152
6023689,0.7710134188,1.4246718145\H,2.0983987648,0.6857480215,2.517937
8903\C,3.5225382877,1.3500743507,1.0454945014\H,3.6262999365,2.3289656
822,1.531372374\H,1.3491606136,1.4475039783,1.1242097517\C,2.054870309
7,-0.3026432719,-2.9943286363\H,1.7189615934,0.7146836307,-3.243158110
7\H,2.8692137169,-0.5769007513,-3.6717268527\H,1.2186261976,-0.9789283
43,-3.1903583091\O,0.4564876919,0.4593376334,-0.8262128778\\Version=Ma
c32-G03RevE.01\State=1-A\HF=-1223.2708289\RMSD=6.081e-09\RMSF=4.005e-0
5\Thermal=0.\Dipole=2.212378,0.0169678,-0.2065924\PG=C01 [X(C24H24N4O1
)]\\@

Table d2. IPSO-SO, geometry optimization, B3LYP/6-31G(d,p).

FOpt\RB3LYP\6-31G(d,p)\C24H20N4O1\NLF\24-Jun-2009\0\\
opt rb3lyp/6-31g(d,p)\\IPSO-SO form b3LYP/6-31G(d,p) added CH3\\0,1\
C,-3.8401104026,0.7678447149,2.1568433363\C,-3.1517426037,0.0148645861
,1.2084389652\C,-3.5994921436,-0.0729511002,-0.117814788\C,-4.75031514
79,0.590472639,-0.5113767072\C,-5.4579282875,1.3527149892,0.4313885394
\C,-5.0038113825,1.4330955138,1.7472395805\H,-3.4889176569,0.850788327
3,3.1798804429\H,-5.1018177722,0.5290114182,-1.537912684\H,-6.35776716
29,1.8817700229,0.1338624902\H,-5.5532336645,2.0286056922,2.4706610443
\C,-2.6763520694,-1.0066951803,-0.8877632675\C,-1.4123559433,-1.005508
7896,0.0658465681\N,-1.9805499363,-0.7439665422,1.3730462136\C,-0.5810
418113,-2.2708416983,0.0753357989\H,-1.1283567353,-3.2077608058,0.1510
672626\C,1.4170383427,-1.1266553114,-0.0208999349\C,0.7688747327,0.067
7233232,-0.2186686742\N,0.699348965,-2.3253614912,0.0611181137\O,-0.58
04344577,0.129144787,-0.3500128449\C,1.4852945475,1.3067053073,-0.3363
974161\C,2.8561696164,-1.1591091099,0.0766286582\C,2.9072321431,1.3044
003468,-0.2477430926\C,3.6110233218,0.0417525899,-0.0327147531\C,0.825
737547,2.538368489,-0.5352904648\H,-0.2566094919,2.558079548,-0.595784
3983\C,1.5794505366,3.688326162,-0.6418646052\H,1.1135180383,4.6564879
314,-0.7945809894\C,2.9809751845,3.5809836401,-0.545095867\H,3.5987844
957,4.4744903708,-0.6266515243\C,3.5614463753,-2.3646712957,0.27721760
65\H,3.0029524082,-3.2903457851,0.3576463659\C,4.9379816665,-2.3297901
619,0.3611635765\H,5.5149506702,-3.2366005967,0.5138894027\N,3.6284934
962,2.4420944765,-0.3540311014\N,4.9595601735,0.0614789643,0.053140217
7\C,5.5898941272,-1.0865463466,0.243695252\H,6.6759464558,-1.033749044
6,0.3080768827\C,-2.3446968507,-0.5430707244,-2.3119714199\H,-1.607058
6059,-1.2050310032,-2.777490375\H,-3.2494561641,-0.5734613284,-2.92738
7219\H,-1.9518841838,0.4737015884,-2.3272095821\C,-3.331790355,-2.4079
949523,-0.9436362927\H,-4.2915448531,-2.3312358131,-1.4617342964\H,-2.
7118414412,-3.1232565454,-1.4942906487\H,-3.5250008129,-2.8046506219,0
.0571108429\C,-1.123691966,-0.5504989285,2.5307647955\H,-0.3075000469,
-1.2748245193,2.5043250114\H,-0.6988919823,0.4621913615,2.5776942423\H
,-1.6976639527,-0.7294137437,3.4443822568\\Version=Mac32-G03RevE.01\St
ate=1-A\HF=-1220.8629936\RMSD=8.543e-09\RMSF=2.625e-06\Thermal=0.\Dipo
le=-1.5794071,-0.3582026,0.1892024\PG=C01 [X(C24H20N4O1)]\\@

Table D3. APSO-PMC, geometry optimization, B3LYP/6-31G(d,p).

FOpt\RB3LYP\6-31G(d,p)\C24H24N4O1\NLF\24-Jun-2009\0\\
opt rb3lyp/6-31g(d,p)\\APSO-PMC form b3LYP/6-31G (d,p) added CH3\\0,
1\C,0.8600708728,-0.9706076129,-0.2223639102\H,0.4911376641,-1.9829640
878,-0.2953415093\C,-1.3279962967,-0.0625274066,-0.1078386841\C,-2.063
0209154,-1.344697537,-0.1824043093\N,-0.0113821794,0.0503489789,-0.128
2426136\O,-1.4979499114,-2.4450342276,-0.2807353491\C,-3.5464579431,-1
.284252182,-0.1333026771\C,-2.0986428874,1.1895654809,-0.0008638992\C,
-4.2576982783,-0.070096347,-0.0255993756\C,-3.5157103311,1.2041464847,
0.0407999955\C,-4.2724302226,-2.482292802,-0.1960114365\H,-3.720581418
1,-3.4125836194,-0.2790311707\C,-5.6553869407,-2.4374133787,-0.1499707
922\H,-6.2562903359,-3.3401754036,-0.1952403717\C,-6.2668522732,-1.179
7354363,-0.0418286013\H,-7.3531315835,-1.1046387473,-0.0025957205\C,-1
.4494012756,2.4366825964,0.0651059986\H,-0.3669392041,2.4599604042,0.0
346285286\C,-2.1930951643,3.5989887177,0.1659680835\H,-1.7116120877,4.
5709463866,0.2177954248\N,-5.6040711865,-0.0288691318,0.0190060188\N,-
4.2365907431,2.3368265161,0.139152519\C,-3.5902856977,3.4949051062,0.1
996197835\H,-4.2085041952,4.3881403761,0.278511827\C,2.2386089298,-0.7
091472145,-0.2160164305\C,4.9618811235,0.5221199397,1.207463343\H,5.44
0723435,0.8272011673,2.1465236065\C,5.6838541035,1.1947525761,0.023693
5764\H,6.7465426769,0.919492696,0.0205014984\H,5.6380662816,2.28617327
06,0.1270137843\C,2.7332001885,0.7179049219,-0.0817852872\H,1.81131531
11,1.2984400519,-0.0463908715\C,5.0906371089,-1.0061558694,1.083039733
9\H,4.5627347347,-1.5120736098,1.8996935512\H,6.1506385974,-1.27683764
83,1.1751597759\C,4.59423474,-1.566597931,-0.268015581\H,4.9828422516,
-2.5832642489,-0.3527748819\C,3.4945028399,0.9808908884,1.2414484391\H
,2.9592101653,0.5108282079,2.0745851198\H,3.4722818587,2.062442291,1.4
277484929\C,5.1583084899,-0.762629456,-1.4597289484\H,4.6791361998,-1.
1046843536,-2.3842812798\H,6.2246862689,-1.0098099186,-1.54447814\C,3.
5471368111,1.2129479932,-1.3033658332\H,3.5227500352,2.3103139165,-1.2
921358767\C,5.0172271378,0.760304019,-1.2958949004\H,5.5300956615,1.24
13345078,-2.1383650683\H,3.0502799958,0.9012038267,-2.2295639808\N,3.1
202682543,-1.7362538012,-0.3271758535\C,2.6098810693,-3.102369668,-0.4
845075583\H,2.0381179712,-3.4196498746,0.3949950091\H,1.9523241196,-3.
1772541974,-1.3564735563\H,3.4468452933,-3.7857835606,-0.6217081518\\V
ersion=Mac32-G03RevE.01\State=1-A\HF=-1223.2768685\RMSD=5.336e-09\RMSF
=6.375e-06\Thermal=0.\Dipole=3.5426285,-0.7263462,-0.1039188\PG=C01 [X
(C24H24N4O1)]\\@

Table D4. APSO-PMC, volume, B3LYP/6-31G(d,p).


```
                    SP\RB3LYP\6-31G(d,p)\C24H24N4O1\NLF\09-Sep-2009\0\\#
 rb3lyp/6-31g(d,p) volume\\APSO-PMC-TTC B3LYP/6-31G(d,p) energy-volume\
 \0,1\C,0,0.75825898,-0.87862383,-0.04588827\H,0,0.4095213,-1.9007223,-
 0.0457879\C,0,-1.44792217,-0.00807348,-0.02941581\C,0,-2.15754976,-1.3
 0653424,-0.01491984\N,0,-0.13350754,0.1290344,-0.04149943\O,0,-1.57052
 584,-2.39972992,-0.02135644\C,0,-3.64241273,-1.2719813,0.01034716\C,0,
 -2.24344324,1.23298345,-0.02863391\C,0,-4.37784083,-0.06750789,0.01552
 62\C,0,-3.66098572,1.22256478,-0.00641427\C,0,-4.34474323,-2.48548954,
 0.03033199\H,0,-3.77435647,-3.40826274,0.02595677\C,0,-5.72881728,-2.4
 646927,0.05503092\H,0,-6.31191917,-3.38002798,0.07137584\C,0,-6.365323
 37,-1.21481832,0.05859311\H,0,-7.45327396,-1.15852777,0.07799924\C,0,-
 1.61879203,2.49414067,-0.05011463\H,0,-0.53663393,2.53651076,-0.068381
 13\C,0,-2.38559108,3.64575915,-0.04819872\H,0,-1.92327193,4.628204,-0.
 06484329\N,0,-5.725252,-0.0497351,0.03954404\N,0,-4.40438432,2.3449108
 6,-0.00443652\C,0,-3.78091482,3.51682867,-0.02461627\H,0,-4.4168964,4.
 40102879,-0.02236844\C,0,2.13140148,-0.59012245,-0.04189482\C,0,4.8103
 5436,0.80010954,1.31788202\H,0,5.26987016,1.1854775,2.23686823\C,0,5.5
 3642865,1.3945563,0.09540909\H,0,6.6040447,1.14101152,0.126974\H,0,5.4
 6863898,2.48955557,0.11417277\C,0,2.5970823,0.85255203,-0.01109883\H,0
 ,1.66402565,1.41567535,-0.03214928\C,0,4.96961048,-0.73034677,1.312628
 76\H,0,4.43967511,-1.18278764,2.15881023\H,0,6.03308864,-0.97210061,1.
 43883211\C,0,4.50324612,-1.40209817,0.00224111\H,0,4.91208725,-2.41435
 157,0.00065551\C,0,3.33426792,1.23090976,1.29775333\H,0,2.79603359,0.8
 1532442,2.15752465\H,0,3.28903547,2.32287692,1.40030505\C,0,5.06910809
 ,-0.6804672,-1.24024615\H,0,4.6097502,-1.10159186,-2.14193856\H,0,6.14
 105239,-0.91217669,-1.29209656\C,0,3.41897742,1.26890096,-1.25647502\H
 ,0,3.37379024,2.36321748,-1.32970389\C,0,4.89706598,0.8474291,-1.19545
 048\H,0,5.41280977,1.27278986,-2.06565573\H,0,2.94139325,0.87751565,-2
 .16235868\N,0,3.0337312,-1.6050103,-0.06266777\C,0,2.55144331,-2.98901
 677,-0.12136801\H,0,1.97321002,-3.24947867,0.77244997\H,0,1.90797064,-
 3.14332953,-0.99340253\H,0,3.40299711,-3.66416063,-0.19502102\\Version
 =Mac32-G03RevE.01\State=1-A\HF=-1223.2768175\RMSD=3.676e-06\Thermal=0.
 \Dipole=3.5551062,-0.6607266,-0.0023141\PG=C01 [X(C24H24N4O1)]\\@

Recommended a0 for SCRF calculation =  5.95 angstrom ( 11.25 bohr)
```

Table D5. APSO-PMC, geometry optimization, B3LYP/6-31G(d,p)/Onsager, toluene.

FOpt\RB3LYP\6-31G(d,p)\C24H24N4O1\NLF\15-Sep-2009\0\\
opt rb3lyp/6-31g(d,p) scrf=(solvent=toluene,dipole,a0=5.95)\\APSO-PM
C-TTC B3LYP/6-31G (d,p) opt toluene\\0,1\C,0.7543963556,-0.8767782947,
-0.0403920001\H,0.407544131,-1.8996814075,-0.038210773\C,-1.452481239,
-0.0112208678,-0.0264323234\C,-2.1579342021,-1.3054219761,-0.013129411
3\N,-0.133788505,0.1273650526,-0.0372873534\O,-1.5752622553,-2.4021569
037,-0.0187997849\C,-3.6445982459,-1.269858731,0.0090488925\C,-2.24596
32968,1.2290567335,-0.026668875\C,-4.3816255056,-0.0659333979,0.012798
9328\C,-3.6646707505,1.2224725585,-0.0073755392\C,-4.3448468532,-2.484
1639535,0.0275033491\H,-3.7709731144,-3.4048682833,0.0242506945\C,-5.7
291180572,-2.4661873309,0.0493452418\H,-6.3102714204,-3.3830426115,0.0
645093582\C,-6.3673464996,-1.2174152205,0.0516012789\H,-7.4560354239,-
1.1639212544,0.0687432886\C,-1.6192320611,2.4901784461,-0.0464009994\H
,-0.5370364701,2.5303472227,-0.0623041623\C,-2.3837360865,3.6427800409
,-0.045713125\H,-1.918676904,4.6240300911,-0.0609528398\N,-5.730715788
3,-0.0508812172,0.0339739479\N,-4.4064200142,2.3471936245,-0.006727247
3\C,-3.7796777305,3.5171180347,-0.0252166885\H,-4.4129063528,4.4036897
669,-0.024094392\C,2.1338289909,-0.5877289305,-0.0372861378\C,4.815654
8247,0.8008846466,1.3158488819\H,5.277716618,1.1860874468,2.2332434792
\C,5.538981293,1.3938976221,0.0911474284\H,6.6059406021,1.1395347878,0
.1200741392\H,5.4729374991,2.4889163738,0.1094490282\C,2.5987421586,0.
8551210013,-0.0075398084\H,1.6660307224,1.4186928428,-0.0265326318\C,4
.9728008018,-0.72964654,1.3115566694\H,4.4452180441,-1.1816716854,2.15
94768559\H,6.0357267044,-0.9731650843,1.4348029304\C,4.5046273203,-1.4
008479014,0.0025269571\H,4.9093503536,-2.4143247139,0.00031934\C,3.339
8246182,1.2325330126,1.299874507\H,2.8034284272,0.8179864364,2.1614849
624\H,3.2948926177,2.32454636,1.4010360452\C,5.0649952244,-0.681369506
4,-1.2427167619\H,4.6027548573,-1.1028026206,-2.1428316193\H,6.1357639
032,-0.915409118,-1.2977449991\C,3.418115185,1.2697373914,-1.255656109
6\H,3.3731002165,2.3640334693,-1.3279765878\C,4.8957683025,0.846753601
6,-1.1976987753\H,5.4096304888,1.2706120687,-2.0693232966\H,2.93768968
64,0.8789636204,-2.1604543995\N,3.0302498196,-1.6005643485,-0.05770801
75\C,2.5496540807,-2.9870664186,-0.117211179\H,1.9765891939,-3.2487011
53,0.7790582557\H,1.9044614737,-3.1401944601,-0.9876486833\H,3.4025152
02,-3.6594068024,-0.1948300432\\Version=Mac32-G03RevE.01\State=1-A\Die
lectric=2.379\A0=5.949\HF=-1223.2796778\RMSD=4.571e-09\RMSF=1.259e-05\
Thermal=0.\Dipole=4.5427443,-0.7755919,-0.0059607\PG=C01 [X(C24H24N4O1
)]\\@

Table D6. APSO-PMC, geometry optimization, B3LYP/6-31G(d,p)/Onsager, DMSO.

FOpt\RB3LYP\6-31G(d,p)\C24H24N4O1\NLF\16-Sep-2009\0\\
opt rb3lyp/6-31g(d,p) scrf=(solvent=dmso,dipole,a0=5.95)\\APSO-PMC-T
TC B3LYP/6-31G(d,p) opt Onsager DMSO\\0,1\C,0.7472538896,-0.8722380566
,-0.0279235059\H,0.4038332143,-1.8967983397,-0.0218073185\C,-1.4619115
079,-0.0161836617,-0.0188982178\C,-2.1600212714,-1.3034996691,-0.00866
11824\N,-0.1344813663,0.125544652,-0.0274815709\O,-1.5844501684,-2.406
3295649,-0.0107393844\C,-3.6495603721,-1.26606158,0.0054786341\C,-2.25
21875884,1.2215362788,-0.020579033\C,-4.3903424206,-0.0631116302,0.006
2861045\C,-3.6735526135,1.2219186398,-0.0082296088\C,-4.346234313,-2.4
819219049,0.0190383363\H,-3.7655977583,-3.3986002473,0.0181858942\C,-5
.7309224093,-2.4695438029,0.0330787616\H,-6.3084293819,-3.3893616201,0
.0441727339\C,-6.3727285347,-1.2228514575,0.0327738295\H,-7.4630541103
,-1.1747731181,0.0437521439\C,-1.6222563496,2.4834111625,-0.0347297959
\H,-0.5400162809,2.5200644669,-0.0449032892\C,-2.3829928791,3.63730845
2,-0.0357157295\H,-1.9133260013,4.6165482064,-0.0466230092\N,-5.742629
6527,-0.0535220447,0.0198668872\N,-4.4126538047,2.3508397972,-0.009223
9894\C,-3.7803105233,3.5172808264,-0.0224706989\H,-4.4087075762,4.4081
335937,-0.0228456544\C,2.1390581586,-0.5820925832,-0.027368315\C,4.828
285915,0.8035996119,1.3098610014\H,5.2959521674,1.189463826,2.22344032
76\C,5.5459986338,1.3919869207,0.0798493396\H,6.6117097686,1.135617698
3,0.1034582027\H,5.4839410964,2.4870611678,0.0959500064\C,2.6032204637
,0.8606025023,-0.0014538538\H,1.671308559,1.4255575549,-0.0166661318\C
,4.98071523,-0.7271577193,1.30922081\H,4.4579851846,-1.1771674882,2.16
13033778\H,6.0426552084,-0.9745095321,1.4263907777\C,4.5079453016,-1.3
991198938,0.0037779114\H,4.9047990516,-2.4149787115,0.0016566928\C,3.3
530804015,1.2375683029,1.3022009269\H,2.8206518664,0.8263291686,2.1682
182304\H,3.3092197303,2.3298206343,1.3992233681\C,5.0580057876,-0.6851
357688,-1.2477007833\H,4.5901101287,-1.1082677641,-2.1441567561\H,6.12
66146706,-0.9238682627,-1.3085758506\C,3.4175484057,1.2699998498,-1.25
58099409\H,3.3733639002,2.3641958529,-1.3275563184\C,4.8944185339,0.84
35317864,-1.2040176902\H,5.4043035416,1.2634575861,-2.0791239511\H,2.9
310318054,0.879556924,-2.1577855858\N,3.0243094871,-1.5920932714,-0.04
725678\C,2.5456065107,-2.9828421632,-0.1052024273\H,1.9831850054,-3.24
46727522,0.7968442155\H,1.8958534229,-3.1349671066,-0.9714866232\H,3.4
000147832,-3.6511642277,-0.1902256177\\Version=Mac32-G03RevE.01\State=
1-A\Dielectric=46.7\A0=5.949\HF=-1223.2847774\RMSD=4.030e-09\RMSF=1.88
0e-06\Thermal=0.\Dipole=6.3624688,-0.9523506,-0.0101818\PG=C01 [X(C24H
24N4O1)]\\@

Table D7. APSO-PMC, geometry optimization, B3LYP/6-31G(d,p)/Onsager, H_2O.


```
                    FOpt\RB3LYP\6-31G(d,p)\C24H24N4O1\NLF\16-Sep-2009\0\\
# opt rb3lyp/6-31g(d,p) scrf=(solvent=water,dipole,a0=5.95)\\APSO-PMC-
TTC B3LYP/6-31G(d,p) Onsager water\\0,1\C,0.7469773276,-0.8720229228,-
0.0275340547\H,0.4036824673,-1.896646335,-0.0212445291\C,-1.4623067351
,-0.0163403348,-0.0186550131\C,-2.1601513258,-1.3034296344,-0.00847147
62\N,-0.1345318535,0.1255221735,-0.027196423\O,-1.5848196675,-2.406473
3287,-0.0104152174\C,-3.649783184,-1.2659256729,0.005401134\C,-2.25247
10577,1.2212580706,-0.0203946326\C,-4.390718332,-0.0630092274,0.006102
6999\C,-3.673944854,1.2218897343,-0.0082486276\C,-4.3463305191,-2.4818
457177,0.0188102161\H,-3.7654388357,-3.3983721521,0.018044381\C,-5.731
0332675,-2.4696815512,0.0325958553\H,-6.308405376,-3.3896099629,0.0435
615865\C,-6.3729797855,-1.2230647916,0.0322007263\H,-7.4633703721,-1.1
751905915,0.0429786232\C,-1.6224362521,2.4831781671,-0.0343932784\H,-0
.5401951591,2.5197152252,-0.0444006342\C,-2.3830438316,3.6371100902,-0
.0354368318\H,-1.9132195257,4.6162799809,-0.0462266621\N,-5.7431241125
,-0.0536315461,0.0194384706\N,-4.4129547444,2.3509634306,-0.0092968381
\C,-3.7804178785,3.5172790537,-0.0223993475\H,-4.4086451228,4.40828501
61,-0.0228222279\C,2.1392692532,-0.5818530981,-0.0270846769\C,4.828741
0775,0.8036686883,1.3096892366\H,5.2965782659,1.1895340511,2.223156457
\C,5.5463181326,1.3918920667,0.0795269214\H,6.6119817158,1.1354335419,
0.1029893197\H,5.4844255279,2.4869686566,0.0955586646\C,2.6034314657,0
.8608220624,-0.0012828746\H,1.67155975,1.425848365,-0.016393609\C,4.98
09658592,-0.7271001407,1.3091697079\H,4.4583616668,-1.1770406258,2.161
3697874\H,6.0428622117,-0.974615775,1.4261711164\C,4.508090636,-1.3990
679425,0.0038199938\H,4.9046336907,-2.4150238638,0.0017139632\C,3.3535
672244,1.2377537422,1.302270571\H,2.8212374837,0.8266427363,2.16842304
64\H,3.3097660551,2.3300149789,1.3991431724\C,5.0578569084,-0.68527146
95,-1.2478442496\H,4.5898105102,-1.1084530801,-2.1442008988\H,6.126392
8741,-0.9241825817,-1.3088661554\C,3.417646942,1.2700258833,-1.2558273
562\H,3.3735117931,2.364219143,-1.3275467452\C,4.8944847679,0.84341578
14,-1.2041959759\H,5.4042695723,1.263207256,-2.0793993761\H,2.93094667
06,0.8796067425,-2.1577252839\N,3.0241087673,-1.5917713558,-0.04697459
21\C,2.5454806855,-2.982675841,-0.1049097601\H,1.9835394322,-3.2445834
601,0.797383684\H,1.8954868133,-3.1347168542,-0.9709931293\H,3.3999491
843,-3.6508332606,-0.1903289581\\Version=Mac32-G03RevE.01\State=1-A\Di
electric=78.39\A0=5.949\HF=-1223.2849653\RMSD=3.936e-09\RMSF=1.856e-06
\Thermal=0.\Dipole=6.4300639,-0.958276,-0.0103062\PG=C01 [X(C24H24N4O1
)]\\@
```

Table D8. APSO-PMC, geometry optimization, B3LYP/6-31+G(d,p).

FOpt\RB3LYP\6-31+G(d,p)\C24H24N4O1\NLF\07-Jul-2009\0\
\# opt rb3lyp/6-31+g(d,p)\\APSO-PMC form b3LYP/6-31G+(d,p)\\0,1\C,0.75
66982897,-0.8837714361,-0.0472011732\H,0.4102269196,-1.9070466539,-0.0
492074634\C,-1.4525137971,-0.0144746919,-0.0312125324\C,-2.1633118086,
-1.3094210488,-0.0174798778\N,-0.1356871274,0.1211036839,-0.0421847036
\O,-1.5728539171,-2.4044676327,-0.0258334594\C,-3.6481599336,-1.274457
8943,0.0094378677\C,-2.2444738009,1.2294053339,-0.0301905588\C,-4.3821
688342,-0.0670492018,0.0154527763\C,-3.6629926606,1.2224342225,-0.0073
868181\C,-4.3544962477,-2.4874105399,0.0301420923\H,-3.7897450489,-3.4
139012031,0.0252134097\C,-5.7398477327,-2.4636581342,0.0563482001\H,-6
.3245708232,-3.3781780633,0.0733023791\C,-6.3752788672,-1.2115898193,0
.0606692008\H,-7.4625289111,-1.1505212418,0.0812064904\C,-1.6158196682
,2.4900414997,-0.0523986346\H,-0.533566796,2.5314615702,-0.0709773419\
C,-2.3799364076,3.6451912011,-0.0505762251\H,-1.9147511796,4.626487601
9,-0.0677907347\N,-5.7300208811,-0.0488273281,0.0409280088\N,-4.401795
2063,2.348550305,-0.0056481239\C,-3.7772534492,3.5206396437,-0.0265219
87\H,-4.4126174408,4.4047609617,-0.0244253705\C,2.1341156123,-0.591775
131,-0.041393615\C,4.8132589949,0.8016785239,1.3188528104\H,5.27264071
01,1.1870117515,2.2382818089\C,5.5376842242,1.3985258905,0.0957230638\
H,6.6060839026,1.146132996,0.125990086\H,5.4683302496,2.4938650002,0.1
156801011\C,2.597691482,0.8519498104,-0.0088246966\H,1.6650000967,1.41
56537758,-0.0284319117\C,4.9739576459,-0.729187448,1.3121147033\H,4.44
45651954,-1.1822113968,2.158974589\H,6.0381218451,-0.9704036512,1.4371
540175\C,4.5074722342,-1.4000845164,0.0010485529\H,4.9159326136,-2.412
1954858,-0.0023110268\C,3.3356350062,1.2295640655,1.3006887051\H,2.799
4298001,0.8115600785,2.1611082786\H,3.2876696102,2.3217280708,1.403945
2493\C,5.0701044292,-0.6766273036,-1.2422332244\H,4.6088239723,-1.0963
452384,-2.144222679\H,6.1424142184,-0.9080971226,-1.2961623813\C,3.418
1002954,1.2709615467,-1.255153295\H,3.3703309791,2.3656902471,-1.32629
348\C,4.8974532681,0.8517488837,-1.1956640057\H,5.4116300262,1.2785730
735,-2.0664659503\H,2.9406862687,0.8795368193,-2.1616594434\N,3.035699
1166,-1.604682755,-0.0617252026\C,2.5582767808,-2.9927150339,-0.118595
7658\H,1.9801205344,-3.2521746672,0.7757943107\H,1.9181691636,-3.15144
97016,-0.9925466276\H,3.4136799941,-3.663430696,-0.1885284918\\Version
=Mac32-G03RevE.01\State=1-A\HF=-1223.3102557\RMSD=1.769e-09\RMSF=7.882
e-06\Thermal=0.\Dipole=3.8416167,-0.6391061,0.0003228\PG=C01 [X(C24H24
N4O1)]\\@

Table D9. APSO-PMC, geometry optimization, B3LYP/6-311G(d,p).

FOpt\RB3LYP\6-311G(d,p)\C24H24N4O1\NLF\04-Sep-2009\0\
\# opt rb3lyp/6-311g(d,p)\\APSO-TTC B3LYP/6311G(d,p) opt\\0,1\C,0.7577406459,-0.8802745832,-0.055606328\H,0.4136611095,-1.9022249302,-0.0610968447\C,-1.445753235,-0.0102263293,-0.0375189327\C,-2.1564298145,-1.3074865087,-0.0239151673\N,-0.1341303969,0.1236239517,-0.0487626294\O,-1.5740139544,-2.3959588186,-0.0365602889\C,-3.6413614418,-1.2687680667,0.0102406303\C,-2.2396574471,1.2312135363,-0.0347046507\C,-4.3730044574,-0.0650823432,0.0201561219\C,-3.6545791483,1.2232854466,-0.0063793613\C,-4.345699003,-2.4787156237,0.0340310494\H,-3.7796336012,-3.4021152634,0.0257888469\C,-5.7268959879,-2.4547415934,0.0673387697\H,-6.3110201979,-3.3672505663,0.0870528297\C,-6.360100311,-1.2057235681,0.0753122467\H,-7.4458052672,-1.1447101258,0.1015804363\C,-1.6145254914,2.4898611862,-0.0605610651\H,-0.5342827422,2.5313754606,-0.0838749672\C,-2.3784727505,3.6403819883,-0.0566722315\H,-1.9161917756,4.6208505276,-0.0767383429\N,-5.7172611636,-0.0457290055,0.0525074207\N,-4.3935586656,2.3448807219,-0.0024584055\C,-3.7716246073,3.5142357846,-0.0267252211\H,-4.407121889,4.3964903697,-0.0227537782\C,2.1304516648,-0.5922745718,-0.0462319401\C,4.8025289243,0.7950950432,1.3230123676\H,5.2589878356,1.1780586733,2.2421716991\C,5.5289823504,1.3945680177,0.1045369918\H,6.5953438116,1.1432585877,0.1369706197\H,5.4592649247,2.4876566501,0.127044145\C,2.5935958298,0.8493377536,-0.0091388565\H,1.6617130585,1.410297454,-0.0296667901\C,4.9640441638,-0.7340152956,1.3132303627\H,4.4324543868,-1.188205539,2.1552655249\H,6.0257929035,-0.9748977012,1.4418317588\C,4.5009641151,-1.4002297566,0.0002921132\H,4.9091343204,-2.4103774811,-0.004655106\C,3.3264685621,1.222396024,1.3022692064\H,2.7885605897,0.8011364136,2.1572927069\H,3.2779664202,2.3119507329,1.4108664073\C,5.0666915833,-0.6749765429,-1.2386932118\H,4.6074959228,-1.091582279,-2.140544095\H,6.1371533076,-0.9056756738,-1.2920014273\C,3.4157374932,1.2703284597,-1.2513229947\H,3.3680389529,2.3629955641,-1.3225465697\C,4.8933217373,0.8515314596,-1.1886315289\H,5.4092806096,1.2802253398,-2.0545797893\H,2.9412848272,0.8800840209,-2.1573081846\N,3.031139249,-1.6038479657,-0.0667251432\C,2.5541005763,-2.9901063212,-0.1272771554\H,1.9755089524,-3.2517952052,0.7640168123\H,1.9151446709,-3.1465354601,-1.0002367605\H,3.4084488495,-3.6592480484,-0.1981562992\\Version=Mac32-G03RevE.01\State=1-A\HF=-1223.5311372\RMSD=3.316e-09\RMSF=5.171e-06\Thermal=0.\Dipole=3.6038534,-0.6598341,0.0009428\PG=C01 [X(C24H24N4O1)]\\@

Table D10. APSO-PMC, geometry optimization, B3LYP/6-311+G(d,p).

FOpt\RB3LYP\6-311+G(d,p)\C24H24N4O1\NLF\21-Sep-2009\0
\\# opt rb3lyp/6-311+g(d,p)\\APSO-TTC B3LYP/6311+G(d,p) opt\\0,1\C,0.7
567215444,-0.8838263666,-0.0595762448\H,0.4150743523,-1.9067969803,-0.
0663217917\C,-1.4488515526,-0.0159557318,-0.0404920007\C,-2.1599783577
,-1.3102988171,-0.0255440867\N,-0.1357802285,0.1177519821,-0.052118053
2\O,-1.5751046963,-2.3999142326,-0.0391308207\C,-3.6442799601,-1.27134
93225,0.0115271921\C,-2.2402554235,1.2268849038,-0.038176947\C,-4.3754
413957,-0.0661513816,0.0214654318\C,-3.6555637596,1.2216832467,-0.0082
152816\C,-4.3509164411,-2.4807627059,0.0382465704\H,-3.7889278853,-3.4
06747777,0.0300968348\C,-5.7324207239,-2.455357673,0.0743546499\H,-6.3
172208208,-3.367416213,0.0964280762\C,-6.3650067081,-1.2055814012,0.08
20848459\H,-7.4505417034,-1.1438042559,0.1104812827\C,-1.6122457478,2.
4846186381,-0.0667257423\H,-0.5319303662,2.525050131,-0.0911630206\C,-
2.3736033401,3.6373704298,-0.0638677233\H,-1.9090942973,4.6167478981,-
0.086058417\N,-5.7196708244,-0.0471832231,0.05653214\N,-4.3907527192,2
.3459909804,-0.0054525634\C,-3.7675718204,3.514587886,-0.0323447422\H,
-4.4007637276,4.3983928125,-0.0293272792\C,2.1310634167,-0.592786389,-
0.0489752066\C,4.7990115626,0.7952522501,1.3279354071\H,5.2529482944,1
.1765205666,2.2491098544\C,5.526418463,1.3994078711,0.1123255145\H,6.5
933564367,1.1503825723,0.1460215456\H,5.4542767368,2.4923758937,0.1375
042369\C,2.5919223806,0.8495010031,-0.0078893323\H,1.6601061927,1.4107
49019,-0.0286300544\C,4.9630244955,-0.7335923485,1.3143676238\H,4.4319
417495,-1.190851418,2.1552360269\H,6.0250868526,-0.9733608517,1.443034
6412\C,4.5031314457,-1.3969321356,-0.0009102417\H,4.9116480323,-2.4068
969251,-0.0077510419\C,3.3221752349,1.2198277277,1.306000276\H,2.78398
12197,0.7952842794,2.1593365783\H,3.27133632,2.3090493046,1.4173993174
\C,5.0702557224,-0.6678418272,-1.2367377775\H,4.6149206564,-1.08294119
88,-2.1414040953\H,6.1412614703,-0.8969282007,-1.2872668687\C,3.415838
3066,1.2740769007,-1.2479096294\H,3.365914072,2.3668424045,-1.31696080
9\C,4.8941575153,0.8582410101,-1.1833214475\H,5.4106149926,1.289930760
5,-2.0475481606\H,2.9442019947,0.8847545944,-2.1558855915\N,3.03240352
,-1.6023828348,-0.071002382\C,2.5588822794,-2.9905940205,-0.1354057795
\H,1.9833413384,-3.2566342033,0.7564970744\H,1.919782929,-3.145849939,
-1.0083222412\H,3.4150434022,-3.6570588721,-0.2098472369\\Version=Mac3
2-G03RevE.01\State=1-A\HF=-1223.5443463\RMSD=7.957e-09\RMSF=9.791e-06\
Thermal=0.\Dipole=3.8073165,-0.6424733,0.0023725\PG=C01 [X(C24H24N4O1)
]\\@

Table D11. IPSO-PMC, geometry optimization, B3LYP/6-31G(d,p).


```
                    FOpt\RB3LYP\6-31G(d,p)\C24H20N4O1\NLF\26-Jun-2009\0\\
# opt rb3lyp/6-31g(d,p)\\IPSO-PMC form b3LYP/6-31G (d,p) added CH3 TTC
\\0,1\C,-5.1028369888,1.7808345886,-0.0028547376\C,-4.1798768765,0.737
8693974,-0.0014076815\C,-4.578815777,-0.605174512,-0.0004827481\C,-5.9
283499656,-0.9241518449,-0.0012228145\C,-6.8749169824,0.11003219,-0.00
28123506\C,-6.4609251907,1.443181665,-0.0035841113\H,-4.7984341019,2.8
217643929,-0.0032844414\H,-6.2524077571,-1.9611379385,-0.0005458387\H,
-7.9340106326,-0.1269979979,-0.0033831977\H,-7.2016015756,2.2370482974
,-0.0047121073\C,-3.3472295001,-1.4980981645,0.0013237906\C,-2.2215655
471,-0.4579211971,0.0013895663\N,-2.7727660794,0.795234525,-0.00061018
12\C,-0.8504619736,-0.6559917042,0.0031746919\H,-0.1822368629,0.196657
3933,0.0034580901\C,0.9185669291,-2.2368789897,0.0062348505\C,2.035260
5539,-1.2594396542,0.0065680133\N,-0.3611792854,-1.9148167573,0.004628
9596\O,1.8567034214,-0.0330519514,0.0052273202\C,3.417928245,-1.800640
3523,0.008421418\C,1.2418485317,-3.6758326061,0.0077227936\C,3.6947924
848,-3.1839938059,0.0098762504\C,2.5778205646,-4.1501914245,0.00950979
43\C,4.4941795207,-0.9016989709,0.0087682412\H,4.2763357692,0.16100586
82,0.0076444752\C,5.7870440986,-1.3970560531,0.0105269182\H,6.64920097
49,-0.7377983546,0.0108596254\C,5.9554347302,-2.7894047613,0.011889116
2\H,6.9578184311,-3.2161601556,0.0132951086\C,0.223697306,-4.647546607
,0.0074214795\H,-0.8084492642,-4.3200559718,0.0060602123\C,0.550599908
6,-5.9922978742,0.0088468718\H,-0.2197946816,-6.7573848268,0.008640800
5\N,4.9535235959,-3.6637688146,0.0115919182\N,2.8925079266,-5.45839280
21,0.0108916695\C,1.9059219727,-6.3472669642,0.0105673139\H,2.20215482
53,-7.3952474322,0.0117220971\C,-3.2935371046,-2.3771234486,-1.2701245
69\H,-2.3639813882,-2.9479184353,-1.2922732046\H,-4.1416859676,-3.0692
644717,-1.2786857315\H,-3.3476575443,-1.7640412844,-2.1742893736\C,-3.
2957549088,-2.3749790215,1.2743290089\H,-4.1438771111,-3.0671558355,1.
2825353104\H,-2.3662081028,-2.945677802,1.2991033853\H,-3.35152861,-1.
7603839767,2.1773648429\C,-1.9892421064,2.0197290933,-0.001455802\H,-1
.3544808855,2.0707774212,0.8888464526\H,-1.3474989936,2.0645409545,-0.
8870232285\H,-2.657503525,2.8790496979,-0.0072097075\\Version=Mac32-G0
3RevE.01\State=1-A\HF=-1220.8652237\RMSD=4.229e-09\RMSF=3.882e-06\Ther
mal=0.\Dipole=-2.3398035,1.5587926,-0.0039479\PG=C01 [X(C24H20N4O1)]\\
@
```

Table D12. IPSO-PMC, volume, B3LYP/6-31G(d,p).

```
                    SP\RB3LYP\6-31G(d,p)\C24H20N4O1\NLF\19-Sep-2009\0\\#
 rb3lyp/6-31g(d,p) volume\\IPSO-PMC-TTC B3LYP/6-31G (d,p) volume\\0,1\C
 ,0,-5.6960402,-1.47942488,-0.00030036\C,0,-4.44842088,-0.8604903,0.000
 06021\C,0,-4.31258082,0.53395145,-0.00008476\C,0,-5.44285138,1.3373680
 8,-0.00038285\C,0,-6.70903744,0.73545335,-0.00061632\C,0,-6.82720742,-
 0.65548644,-0.00060123\H,0,-5.80576627,-2.55838573,-0.00047985\H,0,-5.
 35281907,2.42007229,-0.00047323\H,0,-7.6010611,1.35364174,-0.00087177\
 H,0,-7.81219742,-1.11223784,-0.00088634\C,0,-2.83549272,0.89772574,0.0
 0008665\C,0,-2.18405371,-0.48961524,0.00021306\N,0,-3.16635037,-1.4431
 9728,0.0005847\C,0,-0.83921007,-0.82211478,-0.00006286\H,0,-0.54100315
 ,-1.86355995,-0.00043685\C,0,1.39472033,-0.02321987,-0.00002229\C,0,2.
 06145983,-1.34905968,-0.00011741\N,0,0.08785396,0.16002204,0.00005555\
 O,0,1.43448426,-2.41808405,-0.0000182\C,0,3.54615268,-1.36800823,-0.00
 015169\C,0,2.23577831,1.18827611,0.00005736\C,0,4.32328108,-0.19055571
 ,-0.00013257\C,0,3.65205295,1.1249736,-0.00001422\C,0,4.2049655,-2.605
 901,-0.00023158\H,0,3.60319314,-3.50849114,-0.00024514\C,0,5.58920455,
 -2.63352578,-0.00029859\H,0,6.13986703,-3.5687831,-0.00036449\C,0,6.26
 92196,-1.40691583,-0.00028476\H,0,7.35851594,-1.38877765,-0.00034201\C
 ,0,1.65818161,2.47172554,0.00021173\H,0,0.57866847,2.55675526,0.000281
 63\C,0,2.46714175,3.59458222,0.00027548\H,0,2.0413235,4.59335391,0.000
 39632\N,0,5.67003188,-0.219771,-0.00020341\N,0,4.43594051,2.21856468,0
 .00004933\C,0,3.85641202,3.41338525,0.00018541\H,0,4.52526882,4.272832
 19,0.00023157\C,0,-2.45649633,1.69135896,1.27235144\H,0,-1.3804941,1.8
 7034497,1.29590316\H,0,-2.98181538,2.65180654,1.28068807\H,0,-2.738480
 9,1.14332162,2.17592917\C,0,-2.45622625,1.69132497,-1.27210419\H,0,-2.
 98148649,2.65180305,-1.28053496\H,0,-1.38021072,1.87024582,-1.29547554
 \H,0,-2.73808748,1.14330232,-2.17572862\C,0,-2.90126493,-2.87254231,0.
 0011285\H,0,-2.33128792,-3.15833579,-0.8885986\H,0,-2.32465813,-3.1559
 6582,0.88728193\H,0,-3.84380291,-3.41719055,0.00548294\\Version=Mac32-
 G03RevE.01\State=1-A\HF=-1220.8652471\RMSD=6.502e-06\Thermal=0.\Dipole
 =-2.7597279,-0.561023,0.0003111\PG=C01 [X(C24H20N4O1)]\\@

Recommended a0 for SCRF calculation =  5.64 angstrom ( 10.66 bohr)
```

Table D13. IPSO-PMC, geometry optimization, B3LYP/6-31G(d,p)/Onsager, toluene.

FOpt\RB3LYP\6-31G(d,p)\C24H20N4O1\NLF\22-Sep-2009\0\\
opt rb3lyp/6-31g(d,p) scrf=(solvent=toluene,dipole,a0=5.64)\\IPSO-PM
C-TTC B3LYP/6-31G (d,p) opt toluene\\0,1\C,-5.6948236513,-1.4792988619
,-0.0002215154\C,-4.4496203275,-0.8568332258,0.0000847983\C,-4.3133915
299,0.5362693159,-0.0000594537\C,-5.4446126719,1.3393616322,-0.0003097
897\C,-6.7088631848,0.73480821,-0.0004950413\C,-6.8265426966,-0.656699
585,-0.0004779306\H,-5.8040833739,-2.5581756885,-0.000390954\H,-5.3572
869062,2.4221765226,-0.0003975204\H,-7.6019906941,1.3510547044,-0.0007
10064\H,-7.8111319117,-1.1134695684,-0.000720626\C,-2.8366138604,0.899
0736668,0.000056328\C,-2.1860555453,-0.4881391717,0.0001627676\N,-3.16
27192303,-1.4385636319,0.00054185\C,-0.835219535,-0.8212426882,-0.0001
399762\H,-0.5387221249,-1.863399429,-0.0005395812\C,1.3991848269,-0.02
73647357,-0.0000723842\C,2.061713594,-1.3479560415,-0.0001816335\N,0.0
878762272,0.1573012159,0.0000065125\O,1.4395078047,-2.4211976642,-0.00
02661215\C,3.548386639,-1.3655411994,-0.0001497332\C,2.2378353279,1.18
37065275,0.000038179\C,4.3270432671,-0.1886266302,-0.0000619371\C,3.65
54507805,1.1249601017,0.0000309928\C,4.2052018517,-2.6040448972,-0.000
2276398\H,3.6000108343,-3.5044384168,-0.0002977171\C,5.589492057,-2.63
44112999,-0.0002145206\H,6.1381475015,-3.5711148194,-0.0002714457\C,6.
2710980283,-1.4089292449,-0.0001275012\H,7.3610176475,-1.3936099732,-0
.0001176552\C,1.6577273622,2.4669706308,0.0001545614\H,0.5780745684,2.
5491364173,0.0001737675\C,2.46391656,3.5912790399,0.0002467962\H,2.034
8220634,4.5887590505,0.0003381237\N,5.6754481054,-0.2205027231,-0.0000
537328\N,4.4373466285,2.2214205853,0.0001170959\C,3.853940202,3.414053
9475,0.0002191684\H,4.5196910541,4.27635722,0.0002857437\C,-2.45695748
76,1.6916133344,1.2729805457\H,-1.3811518686,1.8722191588,1.2967898699
\H,-2.9841644634,2.6507982816,1.2816063277\H,-2.7390679883,1.143065362
7,2.1761289686\C,-2.4567895293,1.6915585993,-1.2728406417\H,-2.9839725
27,2.6507554738,-1.2815600205\H,-1.380978939,1.8721377318,-1.296537506
3\H,-2.7388085369,1.1429884504,-2.1760035225\C,-2.9007973727,-2.870180
9776,0.0010385933\H,-2.3325813055,-3.1562092349,-0.8893003478\H,-2.325
7650524,-3.1539220112,0.8876737944\H,-3.8449064573,-3.4114017117,0.005
4612488\\Version=Mac32-G03RevE.01\State=1-A\Dielectric=2.379\A0=5.639\
HF=-1220.8674412\RMSD=4.353e-09\RMSF=4.239e-06\Thermal=0.\Dipole=-3.93
75646,-0.6526906,0.0003523\PG=C01 [X(C24H20N4O1)]\\@

Table D14. IPSO-PMC, geometry optimization, B3LYP/6-31G(d,p)/Onsager, DMSO.

FOpt\RB3LYP\6-31G(d,p)\C24H20N4O1\NLF\22-Sep-2009\0\\
opt rb3lyp/6-31g(d,p) scrf=(solvent=dmso,dipole,a0=5.64)\\IPSO-PMC-T
TC B3LYP/6-31G (d,p) opt DMSO\\0,1\C,-5.6915811081,-1.485689072,-0.000
1179689\C,-4.4535720972,-0.8497202499,0.0001333189\C,-4.3213142692,0.5
417578381,-0.0001178141\C,-5.4578711892,1.3393624354,-0.0004282756\C,-
6.7156506971,0.7233895722,-0.000567031\C,-6.8272995047,-0.6704075945,-
0.0004426314\H,-5.7965954845,-2.5647639914,-0.0002084576\H,-5.38194371
66,2.4227228839,-0.0005920857\H,-7.6139234128,1.3315970097,-0.00082270
33\H,-7.8097852046,-1.1303969207,-0.0006482288\C,-2.8462533469,0.90689
55047,-0.0000061601\C,-2.1930185732,-0.4771322971,0.0001703185\N,-3.15
38549398,-1.4229946938,0.0005968184\C,-0.8240877039,-0.8101620503,-0.0
001341139\H,-0.5323528639,-1.8545944223,-0.0005360784\C,1.4150679591,-
0.0343275996,-0.000076448\C,2.0647397416,-1.3439890901,-0.0002482165\N
,0.0897870696,0.1577746158,0.0000347447\O,1.4519736312,-2.4271657366,-
0.0004022214\C,3.5554998408,-1.3601703414,-0.0001963241\C,2.249462516,
1.1718061248,0.0000892066\C,4.3415499457,-0.1857126351,-0.0000569404\C
,3.6716877542,1.1228563942,0.0000822434\C,4.2058068115,-2.6014749349,-
0.0003149345\H,3.5893826347,-3.4945899277,-0.0004253275\C,5.5901600446
,-2.6419792435,-0.0002908713\H,6.132065723,-3.583565452,-0.0003772063\
C,6.2787015683,-1.4205080361,-0.0001534411\H,7.3708013451,-1.414766186
8,-0.0001343065\C,1.6658298333,2.4571655592,0.0002648604\H,0.585979975
8,2.5344900937,0.0002902291\C,2.4671111542,3.5829139954,0.0004066344\H
,2.0317932256,4.5779441661,0.0005429927\N,5.6945057756,-0.2277331089,-
0.0000401288\N,4.4505480109,2.2255071519,0.0002158248\C,3.8595670487,3
.4134296442,0.0003692534\H,4.518810829,4.2820981089,0.0004735261\C,-2.
4672200567,1.698193239,1.274615968\H,-1.3922901702,1.8857170659,1.2991
004282\H,-3.0014843138,2.6528411978,1.2832042309\H,-2.7486998728,1.148
2401474,2.1769179569\C,-2.4670322634,1.6980601034,-1.2746443185\H,-3.0
013804619,2.6526590694,-1.2834678332\H,-1.3921179397,1.8856755012,-1.2
989453313\H,-2.748280059,1.1479651086,-2.1769316933\C,-2.896702553,-2.
8601754074,0.0011287745\H,-2.3326749928,-3.1451296388,-0.8910271456\H,
-2.3247730012,-3.142721139,0.8889542925\H,-3.8437584824,-3.3946410112,
0.0061521346\\Version=Mac32-G03RevE.01\State=1-A\Dielectric=46.7\A0=5.
639\HF=-1220.873235\RMSD=4.345e-09\RMSF=1.734e-06\Thermal=0.\Dipole=-7
.1859311,-0.7826845,0.0003646\PG=C01 [X(C24H20N4O1)]\\@

Table D15. IPSO-SO, NMR-GIAO, B3LYP/6-31G(d,p), IEFPCM, toluene.

SP|RB3LYP|6-31G(d,p)|C24H20N4O1|PCUSER|03-May-2010|0||# NMR=GIAO B3LYP/6-31G(D,P) SCRF=(IEFPCM,SOLVENT=TOLUENE,READ) GEOM=CONNECTIVITY||IPSO-SO, NMR-GIAO, IEFPCM-toluene, B3LYP/6-31G(d,p), may022010||0,1|C|C,1,1.39294663|C,2,1.40254801,1,121.3261351|C,3,1.38542967,2,120.25290586,1,-0.27377872,0|C,4,1.40375782,3,119.20668063,2,0.18650482,0|C,5,1.39432699,4,120.06153628,3,-0.18732431,0|H,1,1.08481318,2,121.56307714,3,-179.04697394,0|H,4,1.08678831,3,120.65749974,2,179.84405568,0|H,5,1.08541683,4,119.89918449,3,179.64464145,0|H,6,1.08620287,5,119.69553454,4,179.69715144,0|C,3,1.52213191,2,108.85149089,1,-177.66741913,0|C,11,1.58336991,3,100.31391707,2,-18.63584715,0|N,2,1.40520839,1,128.61167964,6,-179.39080505,0|C,12,1.514015,11,116.19807702,3,149.86670322,0|H,14,1.0877071,12,116.36175996,11,-46.20250756,0|C,14,2.30450582,12,93.48914343,11,135.65599567,0|C,16,1.37323328,14,91.63951797,12,-7.71567669,0|N,14,1.28162952,12,125.73453714,11,137.03425174,0|O,17,1.35707757,16,121.50678108,14,-3.64242236,0|C,17,1.43603352,16,121.78561253,14,178.23627199,0|C,16,1.44279711,14,148.30292607,12,169.1769785,0|C,20,1.42470105,17,119.4341301,16,0.05308534,0|C,21,1.42261357,16,120.33663302,14,-176.49036225,0|C,20,1.41122914,17,122.09955583,16,-179.78690446,0|H,24,1.08421571,20,119.35955062,17,0.39912905,0|C,24,1.37907395,20,118.8960432,17,-179.87771404,0|H,26,1.0852421,24,121.34093478,20,-179.96377613,0|C,26,1.40895625,24,118.34739874,20,-0.08154671,0|H,28,1.08935419,26,119.76942792,24,179.96125804,0|C,21,1.41103881,16,121.82897325,14,3.69810704,0|H,30,1.08409295,21,118.85389443,16,0.13314219,0|C,30,1.37953387,21,119.06421026,16,179.95890829,0|H,32,1.08559805,30,121.18215272,21,-179.93034903,0|N,28,1.32395395,26,124.19060956,24,-0.17038733,0|N,23,1.35141114,21,122.47426052,16,179.94662186,0|C,35,1.32347764,23,118.147528,21,0.12957373,0|H,36,1.0892391,35,116.18955043,23,-180.,0|C,11,1.53405081,3,114.54056639,2,-139.61694933,0|H,38,1.09499266,11,110.95467085,3,174.72768544,0|H,38,1.09464588,11,109.56443116,3,-66.70726382,0|H,38,1.09011981,11,111.88650509,3,53.5594634,0|C,11,1.54801807,3,108.46802915,2,97.91585729,0|H,42,1.09336501,11,108.97868261,3,60.71367188,0|H,42,1.09505924,11,111.69785273,3,179.62351545,0|H,42,1.09369161,11,111.72025324,3,-58.16897814,0|C,13,1.45325483,2,120.85389165,1,-16.5470229,0|H,46,1.09156538,13,109.46522437,2,176.38535782,0|H,46,1.09918011,13,112.61465191,2,-62.36168707,0|H,46,1.09368733,13,109.5279153,2,58.50919975,0||Version=x86-Win32-G03RevB.04|State=1-A|HF=-1220.8714154|RMSD=9.323e-009|Dipole=1.012041,-1.3971956,-0.8359836|PG=C01 [X(C24H20N4O1)]||

Table D16. IPSO-SO, NMR-GIAO, B3LYP/6-31G(d,p), IEFPCM, $CHCl_3$.

SP|RB3LYP|6-31G(d,p)|C24H20N4O1|PCUSER|05-May-2010|0||# NMR=GIAO B3LYP/6-31G(D,P) SCRF=(IEFPCM,SOLVENT=CHLOROFORM,READ) GEOM=CONNECTIVITY||IPSO-SO, NMR-GIAO, IEFPCM-CDCl3, B3LYP/6-31G(d,p), may052010||0,1|C|C,1,1.39294663|C,2,1.40254801,1,121.3261351|C,3,1.38542967,2,120.25290586,1,-0.27377872,0|C,4,1.40375715,3,119.20671009,2,0.186513,0|C,5,1.39432699,4,120.06150681,3,-0.18733238,0|H,1,1.08481318,2,121.56307714,3,-179.04697394,0|H,4,1.08678831,3,120.65749974,2,179.84405568,0|H,5,1.08541683,4,119.89921399,3,179.64464146,0|H,6,1.08620287,5,119.69553454,4,179.69715958,0|C,3,1.52213191,2,108.85149089,1,-177.66741913,0|C,11,1.58336991,3,100.31391707,2,-18.63584715,0|N,2,1.40520839,1,128.61167964,6,-179.39081325,0|C,12,1.514015,11,116.19807702,3,149.86670322,0|H,14,1.0877071,12,116.36175996,11,-46.20250756,0|C,14,2.30450582,12,93.48914343,11,135.65599567,0|C,16,1.37323328,14,91.63951797,12,-7.71567669,0|N,14,1.28162952,12,125.73453714,11,137.03425174,0|O,17,1.35707757,16,121.50678108,14,-3.64242236,0|C,17,1.43603352,16,121.78561253,14,178.23627199,0|C,16,1.44279722,14,148.30292046,12,169.1769042,0|C,20,1.42470105,17,119.4341301,16,0.05308534,0|C,21,1.42261357,16,120.33662981,14,-176.49032204,0|C,20,1.41122914,17,122.09955583,16,-179.78690446,0|H,24,1.08421571,20,119.35955062,17,0.39912905,0|C,24,1.37907395,20,118.8960432,17,-179.87771404,0|H,26,1.0852421,24,121.34093478,20,-179.96377613,0|C,26,1.40895625,24,118.34739874,20,-0.08154671,0|H,28,1.08935419,26,119.76942792,24,179.96125804,0|C,21,1.41103881,16,121.82897633,14,3.69819466,0|H,30,1.08409295,21,118.85389443,16,0.13309591,0|C,30,1.37953387,21,119.06421026,16,179.95886202,0|H,32,1.08559805,30,121.18215272,21,-179.93034903,0|N,28,1.32395395,26,124.19060956,24,-0.17038733,0|N,23,1.35141114,21,122.47426052,16,179.9466674,0|C,35,1.32347764,23,118.147528,21,0.12957373,0|H,36,1.08923913,35,116.18956001,23,-180.,0|C,11,1.53405081,3,114.54056639,2,-139.61694933,0|H,38,1.09499266,11,110.95467085,3,174.72768544,0|H,38,1.09464588,11,109.56443116,3,-66.70726382,0|H,38,1.09011981,11,111.88650509,3,53.5594634,0|C,11,1.54801807,3,108.46802915,2,97.91585729,0|H,42,1.09336501,11,108.97868261,3,60.71367188,0|H,42,1.09505924,11,111.69785273,3,179.62351545,0|H,42,1.09369161,11,111.72025324,3,-58.16897814,0|C,13,1.45325483,2,120.85389165,1,-16.5470229,0|H,46,1.09156538,13,109.46522437,2,176.38535782,0|H,46,1.09918011,13,112.61465191,2,-62.36168707,0|H,46,1.09368733,13,109.5279153,2,58.50919975,0||Version=x86-Win32-G03RevB.04|State=1-A|HF=-1220.8764909|RMSD=8.128e-009|Dipole=1.113964,-1.5210272,-0.9045926|PG=C01 [X(C24H20N4O1)]||@

Table D17. IPSO-SO, NMR-GIAO, B3LYP/6-31G(d,p), IEFPCM, DMSO.

SP|RB3LYP|6-31G(d,p)|C24H20N4O1|PCUSER|03-May-2010|0||# NMR=GIAO B3LYP/6-31G(D,P) SCRF=(IEFPCM,SOLVENT=DMSO,READ) GEOM=CONNECTIVITY||IPSO-SO, NMR-GIAO, IEFPCM-DMSO, B3LYP/6-31G(d,p), may032010||0,1|C|C,1,1.39294663|C,2,1.40254801,1,121.3261351|C,3,1.38542967,2,120.25290586,1,-0.27377872,0|C,4,1.40375715,3,119.20671009,2,0.186513,0|C,5,1.39432699,4,120.06150681,3,-0.18733238,0|H,1,1.08481318,2,121.56307714,3,-179.04697394,0|H,4,1.08678831,3,120.65749974,2,179.84405568,0|H,5,1.08541683,4,119.89921399,3,179.64464146,0|H,6,1.08620287,5,119.69553454,4,179.69715958,0|C,3,1.52213191,2,108.85149089,1,-177.66741913,0|C,11,1.58336991,3,100.31391707,2,-18.63584715,0|N,2,1.40520839,1,128.61167964,6,-179.39081325,0|C,12,1.514015,11,116.19807702,3,149.86670322,0|H,14,1.0877071,12,116.36175996,11,-46.20250756,0|C,14,2.30450582,12,93.48914343,11,135.65599567,0|C,16,1.37323328,14,91.63951797,12,-7.71567669,0|N,14,1.28162952,12,125.73453714,11,137.03425174,0|O,17,1.35707757,16,121.50678108,14,-3.64242236,0|C,17,1.43603352,16,121.78561253,14,178.23627199,0|C,16,1.44279722,14,148.30292046,12,169.1769042,0|C,20,1.42470105,17,119.4341301,16,0.05308534,0|C,21,1.42261357,16,120.33662981,14,-176.49032204,0|C,20,1.41122914,17,122.09955583,16,-179.78690446,0|H,24,1.08421571,20,119.35955062,17,0.39912905,0|C,24,1.37907395,20,118.8960432,17,-179.87771404,0|H,26,1.0852421,24,121.34093478,20,-179.96377613,0|C,26,1.40895625,24,118.34739874,20,-0.08154671,0|H,28,1.08935419,26,119.76942792,24,179.96125804,0|C,21,1.41103881,16,121.82897633,14,3.69819466,0|H,30,1.08409295,21,118.85389443,16,0.13309591,0|C,30,1.37953387,21,119.06421026,16,179.95886202,0|H,32,1.08559805,30,121.18215272,21,-179.93034903,0|N,28,1.32395395,26,124.19060956,24,-0.17038733,0|N,23,1.35141114,21,122.47426052,16,179.9466674,0|C,35,1.32347764,23,118.147528,21,0.12957373,0|H,36,1.08923913,35,116.18956001,23,-180.,0|C,11,1.53405081,3,114.54056639,2,-139.61694933,0|H,38,1.09499266,11,110.95467085,3,174.72768544,0|H,38,1.09464588,11,109.56443116,3,-66.70726382,0|H,38,1.09011981,11,111.88650509,3,53.5594634,0|C,11,1.54801807,3,108.46802915,2,97.91585729,0|H,42,1.09336501,11,108.97868261,3,60.71367188,0|H,42,1.09505924,11,111.69785273,3,179.62351545,0|H,42,1.09369161,11,111.72025324,3,-58.16897814,0|C,13,1.45325483,2,120.85389165,1,-16.5470229,0|H,46,1.09156538,13,109.46522437,2,176.38535782,0|H,46,1.09918011,13,112.61465191,2,-62.36168707,0|H,46,1.09368733,13,109.5279153,2,58.50919975,0||Version=x86-Win32-G03RevB.04|State=1-A|HF=-1220.8827244|RMSD=7.320e-009|Dipole=1.2381174,-1.6790811,-0.982745|PG=C01 [X(C24H20N4O1)]||@

Table D18. APSO-PMC (A), NMR-GIAO, B3LYP/6-31G(d,p), IEFPCM, toluene.

SP|RB3LYP|6-31G(d,p)|C24H24N4O1|PCUSER|01-May-2010|0||# NMR=GIAO B3LYP/6-31G(D,P) SCRF=(IEFPCM,SOLVENT=TOLUENE,READ) GEOM=CONNECTIVITY||APSO-TTC-QU, NMR-GIAO, IEFPCM-toluene, B3LYP/6-31G(d,p), may012010||0,1|C|H,1,1.07995487|C,1,2.3613265,2,93.50586899|C,3,1.484,1,96.31513232,2,0.49189063,0|N,3,1.279,1,28.29991837,4,179.85448471,0|O,4,1.221,3,123.10208412,1,-0.38778913,0|C,4,1.48451399,3,117.25710363,1,179.52591814,0|C,3,1.47312636,1,145.07577287,5,0.1320676,0|C,7,1.41125348,4,122.81129976,3,0.24871892,0|C,8,1.41775442,3,122.3068458,1,-179.5983761,0|C,7,1.40223746,4,118.66349735,3,-179.73135343,0|H,11,1.08483661,7,118.21115415,4,-0.03618432,0|C,11,1.38445056,7,119.20810609,4,179.949543,0|H,13,1.08540926,11,121.64627635,7,-179.98054714,0|C,13,1.40261901,11,117.84656673,7,0.01135405,0|H,15,1.08957806,13,119.94719239,11,-179.9852884,0|C,8,1.40753944,3,120.91442959,1,0.39681529,0|H,17,1.08314121,8,118.60015276,3,0.0637659,0|C,17,1.38355003,8,119.98807003,3,-179.96379511,0|H,19,1.08591623,17,121.13630373,8,-179.98143103,0|N,15,1.3294631,13,124.22219508,11,0.01264896,0|N,10,1.34621935,8,123.09483387,3,179.95393161,0|C,22,1.32759566,10,118.46263076,8,0.01920227,0|H,23,1.08916781,22,116.25490676,10,179.99359697,0|C,1,1.36,5,119.64212077,3,-179.19573065,0|C,25,3.31002171,1,151.56283723,5,58.72354096,0|H,26,1.09735989,25,146.14363367,1,22.07376294,0|C,26,1.54110056,25,102.55846171,1,-138.27896726,0|H,28,1.09776379,26,110.26130953,25,-133.14931875,0|H,28,1.09725578,26,110.01481407,25,109.23383748,0|C,25,1.51708829,1,119.70035153,5,0.93931614,0|H,31,1.09002024,25,103.24568986,1,-1.8874638,0|C,26,1.53872858,25,70.38039403,1,115.34772365,0|H,33,1.09615521,26,110.9689569,25,-81.67562127,0|H,33,1.09788781,26,108.59505556,25,161.25225661,0|C,33,1.54462342,26,113.84133942,25,42.03887317,0|H,36,1.09170033,33,106.94222834,26,164.51696679,0|C,26,1.53779861,25,48.38078406,1,-33.2368734,0|H,38,1.09618192,26,110.78304494,25,90.10455217,0|H,38,1.09770436,26,108.48204922,25,-153.36170621,0|C,36,1.5442555,33,111.63620012,26,47.6142893,0|H,41,1.09608599,36,109.1949354,33,-172.46970755,0|H,41,1.09792617,36,107.28561242,33,72.12063089,0|C,31,1.549135,25,113.6998411,1,-117.96999865,0|H,44,1.09769388,31,107.44111739,25,158.78526245,0|C,41,1.53820393,36,113.56277534,33,-47.98317581,0|H,46,1.09735195,41,108.02108011,36,174.55752143,0|H,44,1.0963095,31,109.70681103,25,43.47922902,0|N,25,1.355,1,119.76777635,5,-179.20493593,0|C,49,1.466807,25,119.15871939,1,1.44830529,0|H,50,1.09594888,49,111.41269214,25,-63.45775691,0|H,50,1.09467483,49,110.9875218,25,56.71007603,0|H,50,1.08921396,49,109.29923879,25,176.41738806,0||Version=x86-Win32-G03RevB.04|State=1-A|HF=-1223.2821669|RMSD=6.482e-009|Dipole=-3.8216581,-0.0240658,-0.4540361|PG=C01 [X(C24H24N4O1)]||@

Table D19. APSO-PMC (B), NMR-GIAO, B3LYP/6-31G(d,p), IEFPCM, toluene.

SP|RB3LYP|6-31G(d,p)|C24H24N4O1|PCUSER|30-Apr-2010|0||# NMR=GIAO B3LYP/6-31G(D,P) SCRF=(IEFPCM,SOLVENT=TOLUENE,READ) GEOM=CONNECTIVITY||APSO-TTC-ZW, NMR-GIAO, IEFPCM-toluene, B3LYP/6-31G(d,p), apr302010||0,1|C|H,1,1.07995487|C,1,2.3613265,2,91.35240923|C,3,1.397,1,98.46862437,2,0.4920501,0|N,3,1.376,1,26.14641932,4,179.85377335,0|O,4,1.362,3,123.10208412,1,-0.3933174,0|C,4,1.5049332,3,118.72950044,1,179.52038987,0|C,3,1.49444354,1,141.45798579,5,0.12636917,0|C,7,1.41125348,4,121.33891661,3,0.24474512,0|C,8,1.41775442,3,120.84258499,1,-179.59692699,0|C,7,1.40223746,4,120.13587774,3,-179.72743486,0|H,11,1.08483661,7,118.21115415,4,-0.0441661,0|C,11,1.38445056,7,119.20810609,4,179.94156122,0|H,13,1.08540926,11,121.64627635,7,-179.98054714,0|C,13,1.40261901,11,117.84656673,7,0.01135405,0|H,15,1.08957806,13,119.94719239,11,-179.9852884,0|C,8,1.40753944,3,122.37869019,1,0.4103451,0|H,17,1.08314121,8,118.60015276,3,0.05221971,0|C,17,1.38355003,8,119.98807003,3,-179.9753413,0|H,19,1.08591623,17,121.13630373,8,-179.98143103,0|N,15,1.3294631,13,124.22219508,11,0.01264896,0|N,10,1.34621935,8,123.09483387,3,179.96543195,0|C,22,1.32759566,10,118.46263076,8,0.01920227,0|H,23,1.08916781,22,116.25490676,10,179.99359697,0|C,1,1.46,5,119.64212077,3,-179.19573065,0|C,25,3.31036628,1,151.58044096,5,58.76595454,0|H,26,1.09735989,25,146.13489162,1,21.99872621,0|C,26,1.54110056,25,102.55817089,1,-138.31029936,0|H,28,1.09776379,26,110.26130953,25,-133.17676148,0|H,28,1.09725578,26,110.01481407,25,109.20639475,0|C,25,1.51628344,1,119.75195662,5,0.93946696,0|H,31,1.09002024,25,103.19410844,1,-1.88717008,0|C,26,1.53872858,25,70.40617566,1,115.31301521,0|H,33,1.09615521,26,110.9689569,25,-81.66790103,0|H,33,1.09788781,26,108.59505556,25,161.25997686,0|C,33,1.54462342,26,113.84133942,25,42.04659341,0|H,36,1.09170033,33,106.94222834,26,164.51696679,0|C,26,1.53779861,25,48.35499121,1,-33.26774368,0|H,38,1.09618192,26,110.78304494,25,90.11422903,0|H,38,1.09770436,26,108.48204922,25,-153.35202935,0|C,36,1.5442555,33,111.63620012,26,47.6142893,0|H,41,1.09608599,36,109.1949354,33,-172.46970755,0|H,41,1.09792617,36,107.28561242,33,72.12063089,0|C,31,1.549135,25,113.72392074,1,-117.95002631,0|H,44,1.09769388,31,107.44111739,25,158.73541105,0|C,41,1.53820393,36,113.56277534,33,-47.98317581,0|H,46,1.09735195,41,108.02108011,36,174.55752143,0|H,44,1.0963095,31,109.70681103,25,43.42937763,0|N,25,1.316,1,119.76777635,5,-179.20493593,0|C,49,1.466807,25,119.15871939,1,1.44830529,0|H,50,1.09594888,49,111.41269214,25,-63.45775691,0|H,50,1.09467483,49,110.9875218,25,56.71007603,0|H,50,1.08921396,49,109.29923879,25,176.41738806,0||Version=x86-Win32-G03RevB.04|State=1-A|HF=-1223.2672859|RMSD=6.759e-009|Dipole=-5.5077065,-0.0337774,-1.2750607|PG=C01 [X(C24H24N4O1)]||@

Table D20. APSO-PMC (A), NMR-GIAO, B3LYP/6-31G(d,p), IEFPCM, $CHCl_3$.

SP|RB3LYP|6-31G(d,p)|C24H24N4O1|PCUSER|05-May-2010|0||# NMR=GIAO B3LYP/6-31G(D,P) SCRF=(IEFPCM,SOLVENT=CHLOROFORM,READ) GEOM=CONNECTIVITY||APSO-TTC-QU, NMR-GIAO, IEFPCM-CHCl3, B3LYP/6-31G(d,p), may 012010||0,1|C|H,1,1.07995487|C,1,2.3613265,2,93.50586899|C,3,1.484,1,96.31513232,2,0.49189063,0|N,3,1.279,1,28.29991837,4,179.85448471,0|O,4,1.221,3,123.10208412,1,-0.38778913,0|C,4,1.48451399,3,117.25710363,1,179.52591814,0|C,3,1.47312636,1,145.07577287,5,0.1320676,0|C,7,1.41125348,4,122.81129976,3,0.24871892,0|C,8,1.41775442,3,122.3068458,1,-179.5983761,0|C,7,1.40223746,4,118.66349735,3,-179.73135343,0|H,11,1.08483661,7,118.21115415,4,-0.03618432,0|C,11,1.38445056,7,119.20810609,4,179.949543,0|H,13,1.08540926,11,121.64627635,7,-179.98054714,0|C,13,1.40261901,11,117.84656673,7,0.01135405,0|H,15,1.08957806,13,119.94719239,11,-179.9852884,0|C,8,1.40753944,3,120.91442959,1,0.39681529,0|H,17,1.08314121,8,118.60015276,3,0.0637659,0|C,17,1.38355003,8,119.98807003,3,-179.96379511,0|H,19,1.08591623,17,121.13630373,8,-179.98143103,0|N,15,1.3294631,13,124.22219508,11,0.01264896,0|N,10,1.34621935,8,123.09483387,3,179.95393161,0|C,22,1.32759566,10,118.46263076,8,0.01920227,0|H,23,1.08916781,22,116.25490676,10,179.99359697,0|C,1,1.36,5,119.64212077,3,-179.19573065,0|C,25,3.31002171,1,151.56283723,5,58.72354096,0|H,26,1.09735989,25,146.14363367,1,22.07376294,0|C,26,1.54110056,25,102.55846171,1,-138.27896726,0|H,28,1.09776379,26,110.26130953,25,-133.14931875,0|H,28,1.09725578,26,110.01481407,25,109.23383748,0|C,25,1.51708829,1,119.70035153,5,0.93931614,0|H,31,1.09002024,25,103.24568986,1,-1.8874638,0|C,26,1.53872858,25,70.38039403,1,115.34772365,0|H,33,1.09615521,26,110.9689569,25,-81.67562127,0|H,33,1.09788781,26,108.59505556,25,161.25225661,0|C,33,1.54462342,26,113.84133942,25,42.03887317,0|H,36,1.09170033,33,106.94222834,26,164.51696679,0|C,26,1.53779861,25,48.38078406,1,-33.2368734,0|H,38,1.09618192,26,110.78304494,25,90.10455217,0|H,38,1.09770436,26,108.48204922,25,-153.36170621,0|C,36,1.5442555,33,111.63620012,26,47.6142893,0|H,41,1.09608599,36,109.1949354,33,-172.46970755,0|H,41,1.09792617,36,107.28561242,33,72.12063089,0|C,31,1.549135,25,113.6998411,1,-117.96999865,0|H,44,1.09769388,31,107.44111739,25,158.78526245,0|C,41,1.53820393,36,113.56277534,33,-47.98317581,0|H,46,1.09735195,41,108.02108011,36,174.55752143,0|H,44,1.0963095,31,109.70681103,25,43.47922902,0|N,25,1.355,1,119.76777635,5,-179.20493593,0|C,49,1.466807,25,119.15871939,1,1.44830529,0|H,50,1.09594888,49,111.41269214,25,-63.45775691,0|H,50,1.09467483,49,110.9875218,25,56.71007603,0|H,50,1.08921396,49,109.29923879,25,176.41738806,0||Version=x86-Win32-G03RevB.04|State=1-A|HF=-1223.2880095|RMSD=5.281e-009|Dipole=-4.1924823,-0.0260371,-0.4985023|PG=C01 [X(C24H24N4O1)]||@

Table D21. APSO-PMC (B), NMR-GIAO, B3LYP/6-31G(d,p), IEFPCM, $CHCl_3$.

SP|RB3LYP|6-31G(d,p)|C24H24N4O1|PCUSER|06-May-2010|0||# NMR=GIAO B3LYP/6-31G(D,P) SCRF=(IEFPCM,SOLVENT=CHLOROFORM,READ) GEOM=CONNECTIVITY||APSO-TTC-ZW, NMR-GIAO, IEFPCM-CHCl3, B3LYP/6-31G(d,p), may 052010||0,1|C|H,1,1.07995487|C,1,2.3613265,2,91.35240923|C,3,1.397,1,98.46862437,2,0.4920501,0|N,3,1.376,1,26.14641932,4,179.85377335,0|O,4,1.362,3,123.10208412,1,-0.3933174,0|C,4,1.5049332,3,118.72950044,1,179.52038987,0|C,3,1.49444354,1,141.45798579,5,0.12636917,0|C,7,1.41125348,4,121.33891661,3,0.24474512,0|C,8,1.41775442,3,120.84258499,1,-179.59692699,0|C,7,1.40223746,4,120.13587774,3,-179.72743486,0|H,11,1.08483661,7,118.21115415,4,-0.0441661,0|C,11,1.38445056,7,119.20810609,4,179.94156122,0|H,13,1.08540926,11,121.64627635,7,-179.98054714,0|C,13,1.40261901,11,117.84656673,7,0.01135405,0|H,15,1.08957806,13,119.94719239,11,-179.9852884,0|C,8,1.40753944,3,122.37869019,1,0.4103451,0|H,17,1.08314121,8,118.60015276,3,0.05221971,0|C,17,1.38355003,8,119.98807003,3,-179.9753413,0|H,19,1.08591623,17,121.13630373,8,-179.98143103,0|N,15,1.3294631,13,124.22219508,11,0.01264896,0|N,10,1.34621935,8,123.09483387,3,179.96543195,0|C,22,1.32759566,10,118.46263076,8,0.01920227,0|H,23,1.08916781,22,116.25490676,10,179.99359697,0|C,1,1.46,5,119.64212077,3,-179.19573065,0|C,25,3.31036628,1,151.58044096,5,58.76595454,0|H,26,1.09735989,25,146.13489162,1,21.99872621,0|C,26,1.54110056,25,102.55817089,1,-138.31029936,0|H,28,1.09776379,26,110.26130953,25,-133.17676148,0|H,28,1.09725578,26,110.01481407,25,109.20639475,0|C,25,1.51628344,1,119.75195662,5,0.93946696,0|H,31,1.09002024,25,103.19410844,1,-1.88717008,0|C,26,1.53872858,25,70.40617566,1,115.31301521,0|H,33,1.09615521,26,110.9689569,25,-81.66790103,0|H,33,1.09788781,26,108.59505556,25,161.25997686,0|C,33,1.54462342,26,113.84133942,25,42.04659341,0|H,36,1.09170033,33,106.94222834,26,164.51696679,0|C,26,1.53779861,25,48.35499121,1,-33.26774368,0|H,38,1.09618192,26,110.78304494,25,90.11422903,0|H,38,1.09770436,26,108.48204922,25,-153.35202935,0|C,36,1.5442555,33,111.63620012,26,47.6142893,0|H,41,1.09608599,36,109.1949354,33,-172.46970755,0|H,41,1.09792617,36,107.28561242,33,72.12063089,0|C,31,1.549135,25,113.72392074,1,-117.95002631,0|H,44,1.09769388,31,107.44111739,25,158.73541105,0|C,41,1.53820393,36,113.56277534,33,-47.98317581,0|H,46,1.09735195,41,108.02108011,36,174.55752143,0|H,44,1.0963095,31,109.70681103,25,43.42937763,0|N,25,1.316,1,119.76777635,5,-179.20493593,0|C,49,1.466807,25,119.15871939,1,1.44830529,0|H,50,1.09594888,49,111.41269214,25,-63.45775691,0|H,50,1.09467483,49,110.9875218,25,56.71007603,0|H,50,1.08921396,49,109.29923879,25,176.41738806,0||Version=x86-Win32-G03RevB.04|State=1-A|HF=-1223.2752872|RMSD=3.083e-009|Dipole=-6.0260514,-0.0353341,-1.4169461|PG=C01 [X(C24H24N4O1)]||@

Table D22. APSO-PMC (A), NMR-GIAO, B3LYP/6-31G(d,p), IEFPCM, DMSO.

SP|RB3LYP|6-31G(d,p)|C24H24N4O1|PCUSER|01-May-2010|0||# NMR=GIAO B3LYP/6-31G(D,P) SCRF=(IEFPCM,SOLVENT=DMSO,READ) GEOM=CONNECTIVITY||APSO-TTC-QU, NMR-GIAO, IEFPCM-DMSO, B3LYP/6-31G(d,p), may012010||0,1|C|H,1,1.07995487|C,1,2.3613265,2,93.50586899|C,3,1.484,1,96.31513232,2,0.49189063,0|N,3,1.279,1,28.29991837,4,179.85448471,0|O,4,1.221,3,123.10208412,1,-0.38778913,0|C,4,1.48451399,3,117.25710363,1,179.52591814,0|C,3,1.47312636,1,145.07577287,5,0.1320676,0|C,7,1.41125348,4,122.81129976,3,0.24871892,0|C,8,1.41775442,3,122.3068458,1,-179.5983761,0|C,7,1.40223746,4,118.66349735,3,-179.73135343,0|H,11,1.08483661,7,118.21115415,4,-0.03618432,0|C,11,1.38445056,7,119.20810609,4,179.949543,0|H,13,1.08540926,11,121.64627635,7,-179.98054714,0|C,13,1.40261901,11,117.84656673,7,0.01135405,0|H,15,1.08957806,13,119.94719239,11,-179.9852884,0|C,8,1.40753944,3,120.91442959,1,0.39681529,0|H,17,1.08314121,8,118.60015276,3,0.0637659,0|C,17,1.38355003,8,119.98807003,3,-179.96379511,0|H,19,1.08591623,17,121.13630373,8,-179.98143103,0|N,15,1.3294631,13,124.22219508,11,0.01264896,0|N,10,1.34621935,8,123.09483387,3,179.95393161,0|C,22,1.32759566,10,118.46263076,8,0.01920227,0|H,23,1.08916781,22,116.25490676,10,179.99359697,0|C,1,1.36,5,119.64212077,3,-179.19573065,0|C,25,3.31002171,1,151.56283723,5,58.72354096,0|H,26,1.09735989,25,146.14363367,1,22.07376294,0|C,26,1.54110056,25,102.55846171,1,-138.27896726,0|H,28,1.09776379,26,110.26130953,25,-133.14931875,0|H,28,1.09725578,26,110.01481407,25,109.23383748,0|C,25,1.51708829,1,119.70035153,5,0.93931614,0|H,31,1.09002024,25,103.24568986,1,-1.8874638,0|C,26,1.53872858,25,70.38039403,1,115.34772365,0|H,33,1.09615521,26,110.9689569,25,-81.67562127,0|H,33,1.09788781,26,108.59505556,25,161.25225661,0|C,33,1.54462342,26,113.84133942,25,42.03887317,0|H,36,1.09170033,33,106.94222834,26,164.51696679,0|C,26,1.53779861,25,48.38078406,1,-33.2368734,0|H,38,1.09618192,26,110.78304494,25,90.10455217,0|H,38,1.09770436,26,108.48204922,25,-153.36170621,0|C,36,1.5442555,33,111.63620012,26,47.6142893,0|H,41,1.09608599,36,109.1949354,33,-172.46970755,0|H,41,1.09792617,36,107.28561242,33,72.12063089,0|C,31,1.549135,25,113.6998411,1,-117.96999865,0|H,44,1.09769388,31,107.44111739,25,158.78526245,0|C,41,1.53820393,36,113.56277534,33,-47.98317581,0|H,46,1.09735195,41,108.02108011,36,174.55752143,0|H,44,1.0963095,31,109.70681103,25,43.47922902,0|N,25,1.355,1,119.76777635,5,-179.20493593,0|C,49,1.466807,25,119.15871939,1,1.44830529,0|H,50,1.09594888,49,111.41269214,25,-63.45775691,0|H,50,1.09467483,49,110.9875218,25,56.71007603,0|H,50,1.08921396,49,109.29923879,25,176.41738806,0||Version=x86-Win32-G03RevB.04|State=1-A|HF=-1223.2948631|RMSD=9.045e-009|Dipole=-4.6280323,-0.0280178,-0.5479143|PG=C01 [X(C24H24N4O1)]||@

Table D23. APSO-PMC (B), NMR-GIAO, B3LYP/6-31G(d,p), IEFPCM, DMSO.

SP|RB3LYP|6-31G(d,p)|C24H24N4O1|PCUSER|30-Apr-2010|0||# NMR=GIAO B3LYP/6-31G(D,P) SCRF=(IEFPCM,SOLVENT=DMSO,READ) GEOM=CONNECTIVITY||APSO-TTC-ZW, NMR-GIAO, IEFPCM-DMSO, B3LYP/6-31G(d,p), apr302010||0,1|C|H,1,1.07995487|C,1,2.3613265,2,91.35240923|C,3,1.397,1,98.46862437,2,0.4920501,0|N,3,1.376,1,26.14641932,4,179.85377335,0|O,4,1.362,3,123.10208412,1,-0.3933174,0|C,4,1.5049332,3,118.72950044,1,179.52038987,0|C,3,1.49444354,1,141.45798579,5,0.12636917,0|C,7,1.41125348,4,121.33891661,3,0.24474512,0|C,8,1.41775442,3,120.84258499,1,-179.59692699,0|C,7,1.40223746,4,120.13587774,3,-179.72743486,0|H,11,1.08483661,7,118.21115415,4,-0.0441661,0|C,11,1.38445056,7,119.20810609,4,179.94156122,0|H,13,1.08540926,11,121.64627635,7,-179.98054714,0|C,13,1.40261901,11,117.84656673,7,0.01135405,0|H,15,1.08957806,13,119.94719239,11,-179.9852884,0|C,8,1.40753944,3,122.37869019,1,0.4103451,0|H,17,1.08314121,8,118.60015276,3,0.05221971,0|C,17,1.38355003,8,119.98807003,3,-179.9753413,0|H,19,1.08591623,17,121.13630373,8,-179.98143103,0|N,15,1.3294631,13,124.22219508,11,0.01264896,0|N,10,1.34621935,8,123.09483387,3,179.96543195,0|C,22,1.32759566,10,118.46263076,8,0.01920227,0|H,23,1.08916781,22,116.25490676,10,179.99359697,0|C,1,1.46,5,119.64212077,3,-179.19573065,0|C,25,3.31036628,1,151.58044096,5,58.76595454,0|H,26,1.09735989,25,146.13489162,1,21.99872621,0|C,26,1.54110056,25,102.55817089,1,-138.31029936,0|H,28,1.09776379,26,110.26130953,25,-133.17676148,0|H,28,1.09725578,26,110.01481407,25,109.20639475,0|C,25,1.51628344,1,119.75195662,5,0.93946696,0|H,31,1.09002024,25,103.19410844,1,-1.88717008,0|C,26,1.53872858,25,70.40617566,1,115.31301521,0|H,33,1.09615521,26,110.9689569,25,-81.66790103,0|H,33,1.09788781,26,108.59505556,25,161.25997686,0|C,33,1.54462342,26,113.84133942,25,42.04659341,0|H,36,1.09170033,33,106.94222834,26,164.51696679,0|C,26,1.53779861,25,48.35499121,1,-33.26774368,0|H,38,1.09618192,26,110.78304494,25,90.11422903,0|H,38,1.09770436,26,108.48204922,25,-153.35202935,0|C,36,1.5442555,33,111.63620012,26,47.6142893,0|H,41,1.09608599,36,109.1949354,33,-172.46970755,0|H,41,1.09792617,36,107.28561242,33,72.12063089,0|C,31,1.549135,25,113.72392074,1,-117.95002631,0|H,44,1.09769388,31,107.44111739,25,158.73541105,0|C,41,1.53820393,36,113.56277534,33,-47.98317581,0|H,46,1.09735195,41,108.02108011,36,174.55752143,0|H,44,1.0963095,31,109.70681103,25,43.42937763,0|N,25,1.316,1,119.76777635,5,-179.20493593,0|C,49,1.466807,25,119.15871939,1,1.44830529,0|H,50,1.09594888,49,111.41269214,25,-63.45775691,0|H,50,1.09467483,49,110.9875218,25,56.71007603,0|H,50,1.08921396,49,109.29923879,25,176.41738806,0||Version=x86-Win32-G03RevB.04|State=1-A|HF=-1223.2846516|RMSD=6.911e-009|Dipole=-6.6082285,-0.0363071,-1.5782137|PG=C01 [X(C24H24N4O1)]||@

Table D24. IPSO-PMC (A), NMR-GIAO, B3LYP/6-31G(d,p), IEFPCM, toluene.

SP|RB3LYP|6-31G(d,p)|C24H20N4O1|PCUSER|30-Apr-2010|0||# NMR=GIAO B3LYP/6-31G(D,P) SCRF=(IEFPCM,SOLVENT=TOLUENE,READ) GEOM=CONNECTIVITY||IPSO-TTC-QU, NMR-GIAO, IEFPCM-toluene, B3LYP/6-31G(d,p), apr302010||0,1|C|C,1,1.39270738|C,2,1.40104193,1,121.94965767|C,3,1.38671969,2,119.8419264,1,0.01035954,0|C,4,1.40197315,3,119.16878657,2,-0.00380546,0|C,5,1.39594966,4,120.28132979,3,0.,0|H,1,1.08452601,2,122.19247451,3,179.98186198,0|H,4,1.08644085,3,120.65242012,2,180.,0|H,5,1.08529467,4,119.85201802,3,-180.,0|H,6,1.08573835,5,119.73375126,4,-179.99371437,0|C,3,1.52122263,2,109.39936735,1,-179.98780376,0|C,11,1.53497018,3,101.06998558,2,0.00497062,0|N,12,1.355,11,109.24484217,3,-0.020490 5,0|C,12,1.36,11,128.79271989,3,179.9758498,0|H,14,1.08329832,12,119.86586281,11,-179.96844362,0|C,14,2.35933748,12,145.69625808,11,0.03399919,0|C,16,1.484,14,96.28056688,12,179.98193276,0|N,16,1.279,14,28.39807895,12,-0.01270827,0|O,17,1.221,16,122.91167565,14,-0.00934454,0|C,17,1.48482361,16,117.42894193,14,180.,0|C,16,1.4748335,14,145.18518034,12,-0.01809737,0|C,20,1.41078797,17,122.69319429,16,0.,0|C,21,1.41768897,16,122.20958817,14,-179.99714716,0|C,20,1.40228872,17,118.7541158,16,180.,0|H,24,1.08480332,20,118.28580332,17,0.,0|C,24,1.38451463,20,119.16542645,17,180.,0|H,26,1.08532732,24,121.63212374,20,-180.,0|C,26,1.4024951,24,117.86006826,20,0.,0|H,28,1.089447,26,119.95730851,24,-180.,0|C,21,1.40743016,16,121.00180181,14,0.00304532,0|H,30,1.0828566,21,118.7331322,16,0.,0|C,30,1.38391681,21,119.99976652,16,-180.,0|H,32,1.08575658,30,121.1385661,21,-180.,0|N,28,1.32978928,26,124.21518255,24,0.,0|N,23,1.34551853,21,123.07379165,16,180.,0|C,35,1.32794863,23,118.49206265,21,0.,0|H,36,1.0890443,35,116.23357063,23,-180.,0|C,11,1.54665696,3,111.14517091,2,-118.11540759,0|H,38,1.09104124,11,110.09641542,3,175.25831538,0|H,38,1.09475477,11,109.80721159,3,-64.45665716,0|H,38,1.09376108,11,111.05575637,3,54.96607225,0|C,11,1.54664565,3,111.14399607,2,118.12813004,0|H,42,1.09475437,11,109.80706287,3,64.46157758,0|H,42,1.09103951,11,110.09681152,3,-175.25322029,0|H,42,1.0937601,11,111.05569037,3,-54.96104246,0|C,13,1.4537185,12,123.64357431,11,-179.98422784,0|H,46,1.09460856,13,110.57067561,12,-60.26001017,0|H,46,1.09456472,13,110.54600282,12,59.82436339,0|H,46,1.08859464,13,109.51485835,12,179.76890084,0||Version=x86-Win32-G03RevB.04|State=1-A|HF=-1220.8714283|RMSD=3.356e-009|Dipole=0.7243073,0.0010551,-3.0230972|PG=C01 [X(C24H20N4O1)]||@

Table D25. IPSO-PMC (B), NMR-GIAO, B3LYP/6-31G(d,p), IEFPCM, toluene.

SP|RB3LYP|6-31G(d,p)|C24H20N4O1|PCUSER|30-Apr-2010|0||# NMR=GIAO B3LYP/6-31G(D,P) SCRF=(IEFPCM,SOLVENT=TOLUENE,READ) GEOM=CONNECTIVITY||IPSO-TTC-ZW, NMR-GIAO, IEFPCM-toluene, B3LYP/6-31G(d,p), apr302010||0,1|C|C,1,1.39270738|C,2,1.40104193,1,121.94965767|C,3,1.38671969,2,119.8419264,1,0.01035954,0|C,4,1.40197315,3,119.16878657,2,-0.00380546,0|C,5,1.39594966,4,120.28132979,3,0.,0|H,1,1.08452601,2,122.19247451,3,179.98186198,0|H,4,1.08644085,3,120.65242012,2,180.,0|H,5,1.08529467,4,119.85201802,3,-180.,0|H,6,1.08573835,5,119.73375126,4,-179.99371437,0|C,3,1.52122263,2,109.39936735,1,-179.98780376,0|C,11,1.54150743,3,100.38568247,2,0.00472182,0|N,12,1.316,11,109.92914533,3,-0.02044419,0|C,12,1.46,11,128.10841673,3,179.97593066,0|H,14,1.08329832,12,119.86586281,11,-179.96849917,0|C,14,2.35933748,12,147.8584313,11,0.03484486,0|C,16,1.397,14,98.44274014,12,179.98115252,0|N,16,1.376,14,26.23590568,12,-0.01346232,0|O,17,1.362,16,122.91167565,14,-0.00914014,0|C,17,1.4848129,16,117.42814604,14,180.,0|C,16,1.51832916,14,140.13676292,12,-0.01860141,0|C,20,1.41078797,17,122.69399019,16,0.,0|C,21,1.41768897,16,119.32334401,14,-180.,0|C,20,1.40228872,17,118.75331991,16,180.,0|H,24,1.08480332,20,118.28580332,17,0.,0|C,24,1.38451463,20,119.16542645,17,180.,0|H,26,1.08532732,24,121.63212374,20,-180.,0|C,26,1.40249051,24,117.86006826,20,0.,0|H,28,1.089447,26,119.95730851,24,-180.,0|C,21,1.40743016,16,123.88804596,14,0.00282403,0|H,30,1.0828566,21,118.7331322,16,0.,0|C,30,1.38391681,21,119.99976652,16,-180.,0|H,32,1.08575658,30,121.1385661,21,-180.,0|N,28,1.32978928,26,124.21518255,24,0.,0|N,23,1.34551853,21,123.07379165,16,180.,0|C,35,1.32794863,23,118.49206265,21,0.,0|H,36,1.0890443,35,116.23357063,23,-180.,0|C,11,1.54665696,3,111.14517091,2,-118.11540759,0|H,38,1.09104124,11,110.09641542,3,175.25831538,0|H,38,1.09475477,11,109.80721159,3,-64.45665716,0|H,38,1.09376108,11,111.05575637,3,54.96607225,0|C,11,1.54664565,3,111.14399607,2,118.12813004,0|H,42,1.09475437,11,109.80706287,3,64.46157758,0|H,42,1.09103951,11,110.09681152,3,-175.25322029,0|H,42,1.0937601,11,111.05569037,3,-54.96104246,0|C,13,1.4537185,12,123.64357431,11,-179.98422784,0|H,46,1.09460856,13,110.57067561,12,-60.26001017,0|H,46,1.09456472,13,110.54600282,12,59.82436339,0|H,46,1.08859464,13,109.51485835,12,179.76890084,0||Version=x86-Win32-G03RevB.04|State=1-A|HF=-1220.851158|RMSD=8.826e-009|Dipole=1.9524311,0.0020738,-4.6636953|PG=C01 [X(C24H20N4O1)]||@

Table D26. IPSO-PMC (A), NMR-GIAO, B3LYP/6-31G(d,p), IEFPCM, $CHCl_3$.

SP|RB3LYP|6-31G(d,p)|C24H20N4O1|PCUSER|06-May-2010|0||# NMR=GIAO B3LYP/6-31G(D,P) SCRF=(IEFPCM,SOLVENT=CHLOROFORM,READ) GEOM=CONNECTIVITY||IPSO-TTC-QU, NMR-GIAO, IEFPCM-CHCl3, B3LYP/6-31G(d,p), may 062010||0,1|C|C,1,1.39270738|C,2,1.40104193,1,121.94965767|C,3,1.38671969,2,119.8419264,1,0.01035954,0|C,4,1.40197315,3,119.16878657,2,-0.00380546,0|C,5,1.39594966,4,120.28132979,3,0.,0|H,1,1.08452601,2,122.19247451,3,179.98186198,0|H,4,1.08644085,3,120.65242012,2,180.,0|H,5,1.08529467,4,119.85201802,3,-180.,0|H,6,1.08573835,5,119.73375126,4,-179.99371437,0|C,3,1.52122263,2,109.39936735,1,-179.98780376,0|C,11,1.53497018,3,101.06998558,2,0.00497062,0|N,12,1.355,11,109.24484217,3,-0.0204905,0|C,12,1.36,11,128.79271989,3,179.9758498,0|H,14,1.08329832,12,119.86586281,11,-179.96844362,0|C,14,2.35933748,12,145.69625808,11,0.03399919,0|C,16,1.484,14,96.28056688,12,179.98193276,0|N,16,1.279,14,28.39807895,12,-0.01270827,0|O,17,1.221,16,122.91167565,14,-0.00934454,0|C,17,1.48482361,16,117.42894193,14,180.,0|C,16,1.4748335,14,145.18518034,12,-0.01809737,0|C,20,1.41078797,17,122.69319429,16,0.,0|C,21,1.41768897,16,122.20958817,14,-179.99714716,0|C,20,1.40228872,17,118.7541158,16,180.,0|H,24,1.08480332,20,118.28580332,17,0.,0|C,24,1.38451463,20,119.16542645,17,180.,0|H,26,1.08532732,24,121.63212374,20,-180.,0|C,26,1.4024951,24,117.86006826,20,0.,0|H,28,1.089447,26,119.95730851,24,-180.,0|C,21,1.40743016,16,121.00180181,14,0.00304532,0|H,30,1.0828566,21,118.7331322,16,0.,0|C,30,1.38391681,21,119.99976652,16,-180.,0|H,32,1.08575658,30,121.1385661,21,-180.,0|N,28,1.32978928,26,124.21518255,24,0.,0|N,23,1.34551853,21,123.07379165,16,180.,0|C,35,1.32794863,23,118.49206265,21,0.,0|H,36,1.0890443,35,116.23357063,23,-180.,0|C,11,1.54665696,3,111.14517091,2,-118.11540759,0|H,38,1.09104124,11,110.09641542,3,175.25831538,0|H,38,1.09475477,11,109.80721159,3,-64.45665716,0|H,38,1.09376108,11,111.05575637,3,54.96607225,0|C,11,1.54664565,3,111.14399607,2,118.12813004,0|H,42,1.09475437,11,109.80706287,3,64.46157758,0|H,42,1.09103951,11,110.09681152,3,-175.25322029,0|H,42,1.0937601,11,111.05569037,3,-54.96104246,0|C,13,1.4537185,12,123.64357431,11,-179.98422784,0|H,46,1.09460856,13,110.57067561,12,-60.26001017,0|H,46,1.09456472,13,110.54600282,12,59.82436339,0|H,46,1.08859464,13,109.51485835,12,179.76890084,0||Version=x86-Win32-G03RevB.04|State=1-A|HF=-1220.8772314|RMSD=7.965e-009|Dipole=0.8273593,0.0008858,-3.3431297|PG=C01 [X(C24H20N4O1)]||@

Table D27. IPSO-PMC (B), NMR-GIAO, B3LYP/6-31G(d,p), IEFPCM, $CHCl_3$.

SP|RB3LYP|6-31G(d,p)|C24H20N4O1|PCUSER|06-May-2010|0||# NMR=GIAO B3LYP/6-31G(D,P) SCRF=(IEFPCM,SOLVENT=CHLOROFORM,READ) GEOM=CONNECTIVITY||IPSO-TTC-ZW, NMR-GIAO, IEFPCM-CHCl3, B3LYP/6-31G(d,p), may062010||0,1|C|C,1,1.39270738|C,2,1.40104193,1,121.94965767|C,3,1.38671969,2,119.8419264,1,0.01035954,0|C,4,1.40197315,3,119.16878657,2,-0.00380546,0|C,5,1.39594966,4,120.28132979,3,0.,0|H,1,1.08452601,2,122.19247451,3,179.98186198,0|H,4,1.08644085,3,120.65242012,2,180.,0|H,5,1.08529467,4,119.85201802,3,-180.,0|H,6,1.08573835,5,119.73375126,4,-179.99371437,0|C,3,1.52122263,2,109.39936735,1,-179.98780376,0|C,11,1.54150743,3,100.38568247,2,0.00472182,0|N,12,1.316,11,109.92914533,3,-0.02044419,0|C,12,1.46,11,128.10841673,3,179.97593066,0|H,14,1.08329832,12,119.86586281,11,-179.96849917,0|C,14,2.35933748,12,147.8584313,11,0.03484486,0|C,16,1.397,14,98.44274014,12,179.98115252,0|N,16,1.376,14,26.23590568,12,-0.01346232,0|O,17,1.362,16,122.91167565,14,-0.00914014,0|C,17,1.4848129,16,117.42814604,14,180.,0|C,16,1.51832916,14,140.13676292,12,-0.01860141,0|C,20,1.41078797,17,122.69399019,16,0.,0|C,21,1.41768897,16,119.32334401,14,-180.,0|C,20,1.40228872,17,118.75331991,16,180.,0|H,24,1.08480332,20,118.28580332,17,0.,0|C,24,1.38451463,20,119.16542645,17,180.,0|H,26,1.08532732,24,121.63212374,20,-180.,0|C,26,1.4024951,24,117.86006826,20,0.,0|H,28,1.089447,26,119.95730851,24,-180.,0|C,21,1.40743016,16,123.88804596,14,0.00282403,0|H,30,1.0828566,21,118.7331322,16,0.,0|C,30,1.38391681,21,119.99976652,16,-180.,0|H,32,1.08575658,30,121.1385661,21,-180.,0|N,28,1.32978928,26,124.21518255,24,0.,0|N,23,1.34551853,21,123.07379165,16,180.,0|C,35,1.32794863,23,118.49206265,21,0.,0|H,36,1.0890443,35,116.23357063,23,-180.,0|C,11,1.54665696,3,111.14517091,2,-118.11540759,0|H,38,1.09104124,11,110.09641542,3,175.25831538,0|H,38,1.09475477,11,109.80721159,3,-64.45665716,0|H,38,1.09376108,11,111.05575637,3,54.96607225,0|C,11,1.54664565,3,111.14399607,2,118.12813004,0|H,42,1.09475437,11,109.80706287,3,64.46157758,0|H,42,1.09103951,11,110.09681152,3,-175.25322029,0|H,42,1.0937601,11,111.05569037,3,-54.96104246,0|C,13,1.4537185,12,123.64357431,11,-179.98422784,0|H,46,1.09460856,13,110.57067561,12,-60.26001017,0|H,46,1.09456472,13,110.54600282,12,59.82436339,0|H,46,1.08859464,13,109.51485835,12,179.76890084,0||Version=x86-Win32-G03RevB.04|State=1-A|HF=-1220.8590442|RMSD=6.295e-009|Dipole=2.2215939,0.0023928,-5.1761409|PG=C01 [X(C24H20N4O1)]||@

Table D28. IPSO-PMC (A), NMR-GIAO, B3LYP/6-31G(d,p), IEFPCM, DMSO.

SP|RB3LYP|6-31G(d,p)|C24H20N4O1|PCUSER|30-Apr-2010|0||# NMR=GIAO B3LYP/6-31G(D,P) SCRF=(IEFPCM,SOLVENT=DMSO,READ) GEOM=CONNECTIVITY||IPSO-TTC-QU, NMR-GIAO, IEFPCM-DMSO, B3LYP/6-31G(d,p), apr302010||0,1|C|C,1,1.39270738|C,2,1.40104193,1,121.94965767|C,3,1.38671969,2,119.8419264,1,0.01035954,0|C,4,1.40197315,3,119.16878657,2,-0.00380546,0|C,5,1.39594966,4,120.28132979,3,0.,0|H,1,1.08452601,2,122.19247451,3,179.98186198,0|H,4,1.08644085,3,120.65242012,2,180.,0|H,5,1.08529467,4,119.85201802,3,-180.,0|H,6,1.08573835,5,119.73375126,4,-179.99371437,0|C,3,1.52122263,2,109.39936735,1,-179.98780376,0|C,11,1.53497018,3,101.06998558,2,0.00497062,0|N,12,1.355,11,109.24484217,3,-0.0204905,0|C,12,1.36,11,128.79271989,3,179.9758498,0|H,14,1.08329832,12,119.86586281,11,-179.96844362,0|C,14,2.35933748,12,145.69625808,11,0.03399919,0|C,16,1.484,14,96.28056688,12,179.98193276,0|N,16,1.279,14,28.39807895,12,-0.01270827,0|O,17,1.221,16,122.91167565,14,-0.00934454,0|C,17,1.48482361,16,117.42894193,14,180.,0|C,16,1.4748335,14,145.18518034,12,-0.01809737,0|C,20,1.41078797,17,122.69319429,16,0.,0|C,21,1.41768897,16,122.20958817,14,-179.99714716,0|C,20,1.40228872,17,118.7541158,16,180.,0|H,24,1.08480332,20,118.28580332,17,0.,0|C,24,1.38451463,20,119.16542645,17,180.,0|H,26,1.08532732,24,121.63212374,20,-180.,0|C,26,1.4024951,24,117.86006826,20,0.,0|H,28,1.089447,26,119.95730851,24,-180.,0|C,21,1.40743016,16,121.00180181,14,0.00304532,0|H,30,1.0828566,21,118.7331322,16,0.,0|C,30,1.38391681,21,119.99976652,16,-180.,0|H,32,1.08575658,30,121.1385661,21,-180.,0|N,28,1.32978928,26,124.21518255,24,0.,0|N,23,1.34551853,21,123.07379165,16,180.,0|C,35,1.32794863,23,118.49206265,21,0.,0|H,36,1.0890443,35,116.23357063,23,-180.,0|C,11,1.54665696,3,111.14517091,2,-118.11540759,0|H,38,1.09104124,11,110.09641542,3,175.25831538,0|H,38,1.09475477,11,109.80721159,3,-64.45665716,0|H,38,1.09376108,11,111.05575637,3,54.96607225,0|C,11,1.54664565,3,111.14399607,2,118.12813004,0|H,42,1.09475437,11,109.80706287,3,64.46157758,0|H,42,1.09103951,11,110.09681152,3,-175.25322029,0|H,42,1.0937601,11,111.05569037,3,-54.96104246,0|C,13,1.4537185,12,123.64357431,11,-179.98422784,0|H,46,1.09460856,13,110.57067561,12,-60.26001017,0|H,46,1.09456472,13,110.54600282,12,59.82436339,0|H,46,1.08859464,13,109.51485835,12,179.76890084,0||Version=x86-Win32-G03RevB.04|State=1-A|HF=-1220.8841251|RMSD=7.013e-009|Dipole=0.9596401,0.0003476,-3.7209731|PG=C01 [X(C24H20N4O1)]||@

Table D29. IPSO-PMC (B), NMR-GIAO, B3LYP/6-31G(d,p), IEFPCM, DMSO.

SP|RB3LYP|6-31G(d,p)|C24H20N4O1|PCUSER|30-Apr-2010|0||# NMR=GIAO B3LYP/6-31G(D,P) SCRF=(IEFPCM,SOLVENT=DMSO,READ) GEOM=CONNECTIVITY||IPSO-TTC-ZW, NMR-GIAO, IEFPCM-DMSO, B3LYP/6-31G(d,p), apr302010||0,1|C|C,1,1.39270738|C,2,1.40104193,1,121.94965767|C,3,1.38671969,2,119.8419264,1,0.01035954,0|C,4,1.40197315,3,119.16878657,2,-0.00380546,0|C,5,1.39594966,4,120.28132979,3,0.,0|H,1,1.08452601,2,122.19247451,3,179.98186198,0|H,4,1.08644085,3,120.65242012,2,180.,0|H,5,1.08529467,4,119.85201802,3,-180.,0|H,6,1.08573835,5,119.73375126,4,-179.99371437,0|C,3,1.52122263,2,109.39936735,1,-179.98780376,0|C,11,1.54150743,3,100.38568247,2,0.00472182,0|N,12,1.316,11,109.92914533,3,-0.02044419,0|C,12,1.46,11,128.10841673,3,179.97593066,0|H,14,1.08329832,12,119.86586281,11,-179.96849917,0|C,14,2.35933748,12,147.8584313,11,0.03484486,0|C,16,1.397,14,98.44274014,12,179.98115252,0|N,16,1.376,14,26.23590568,12,-0.01346232,0|O,17,1.362,16,122.91167565,14,-0.00914014,0|C,17,1.4848129,16,117.42814604,14,180.,0|C,16,1.51832916,14,140.13676292,12,-0.01860141,0|C,20,1.41078797,17,122.69399019,16,0.,0|C,21,1.41768897,16,119.32334401,14,-180.,0|C,20,1.40228872,17,118.75331991,16,180.,0|H,24,1.08480332,20,118.28580332,17,0.,0|C,24,1.38451463,20,119.16542645,17,180.,0|H,26,1.08532732,24,121.63212374,20,-180.,0|C,26,1.4024951,24,117.86006826,20,0.,0|H,28,1.089447,26,119.95730851,24,-180.,0|C,21,1.40743016,16,123.88804596,14,0.00282403,0|H,30,1.0828566,21,118.7331322,16,0.,0|C,30,1.38391681,21,119.99976652,16,-180.,0|H,32,1.08575658,30,121.1385661,21,-180.,0|N,28,1.32978928,26,124.21518255,24,0.,0|N,23,1.34551853,21,123.07379165,16,180.,0|C,35,1.32794863,23,118.49206265,21,0.,0|H,36,1.0890443,35,116.23357063,23,-180.,0|C,11,1.54665696,3,111.14517091,2,-118.11540759,0|H,38,1.09104124,11,110.09641542,3,175.25831538,0|H,38,1.09475477,11,109.80721159,3,-64.45665716,0|H,38,1.09376108,11,111.05575637,3,54.96607225,0|C,11,1.54664565,3,111.14399607,2,118.12813004,0|H,42,1.09475437,11,109.80706287,3,64.46157758,0|H,42,1.09103951,11,110.09681152,3,-175.25322029,0|H,42,1.0937601,11,111.05569037,3,-54.96104246,0|C,13,1.4537185,12,123.64357431,11,-179.98422784,0|H,46,1.09460856,13,110.57067561,12,-60.26001017,0|H,46,1.09456472,13,110.54600282,12,59.82436339,0|H,46,1.08859464,13,109.51485835,12,179.76890084,0||Version=x86-Win32-G03RevB.04|State=1-A|HF=-1220.8682421|RMSD=8.537e-009|Dipole=2.5429501,0.0029355,-5.7562344|PG=C01 [X(C24H20N4O1)]||@

Table D30. TMS, geometry optimization, B3LYP/6-31G(d,p).


```
                FOpt|RB3LYP|6-31G(d,p)|C4H12Si1|PCUSER|29-Apr-2010|0||# O
PT B3LYP/6-31G(D,P) GEOM=CONNECTIVITY||TMS, opt, B3LYP/6-31G(d,p), apr
292010||0,1|Si,0.,0.,0.|C,0.,0.,1.8949860016|C,1.786609936,0.,-0.63166
20005|C,-0.893304968,-1.5472495912,-0.6316620005|C,-0.893304968,1.5472
495912,-0.6316620005|H,0.5104833785,-0.8841831479,2.2932685599|H,-1.02
09667569,0.,2.2932685599|H,0.5104833785,0.8841831479,2.2932685599|H,-0
.4004126619,-2.4619013702,-0.2831345085|H,-0.9108960404,-1.5777182223,
-1.7269995429|H,-1.9318627973,-1.5777182223,-0.2831345085|H,2.33227545
92,0.8841831479,-0.2831345085|H,1.8217920807,0.,-1.7269995429|H,2.3322
754592,-0.8841831479,-0.2831345085|H,-1.9318627973,1.5777182223,-0.283
1345085|H,-0.9108960404,1.5777182223,-1.7269995429|H,-0.4004126619,2.4
619013702,-0.2831345085||Version=x86-Win32-G03RevB.04|State=1-A1|HF=-4
49.2110017|RMSD=6.221e-010|RMSF=8.731e-005|Dipole=0.,0.,0.|PG=TD [O(Si
1),4C3(C1),6SGD(H2)]||@
```

Table D31. TMS, NMR-GIAO, B3LYP/6-31G(d,p), IEFPCM, toluene.

SP|RB3LYP|6-31G(d,p)|C4H12Si1|PCUSER|30-Apr-2010|0||# NMR
=GIAO B3LYP/6-31G(D,P) SCRF=(IEFPCM,SOLVENT=TOLUENE,READ) GEOM=CONNECT
IVITY||TMS, NMR-GIAO, IEFPCM-toluene, B3LYP/6-31G(d,p), apr302010||0,1
|Si|C,1,1.89498656|C,1,1.89498656,2,109.47122063|C,1,1.89498656,2,109.
47122063,3,120.,0|C,1,1.89498656,2,109.47122063,3,-120.,0|H,2,1.095902
23,1,111.31087464,3,-60.,0|H,2,1.09590223,1,111.31087464,3,180.,0|H,2,
1.09590223,1,111.31087464,3,60.,0|H,4,1.09590223,1,111.31087464,2,-60.
,0|H,4,1.09590223,1,111.31087464,2,180.,0|H,4,1.09590223,1,111.3108746
4,2,60.,0|H,3,1.09590223,1,111.31087464,2,-60.,0|H,3,1.09590223,1,111.
31087464,2,180.,0|H,3,1.09590223,1,111.31087464,2,60.,0|H,5,1.09590223
,1,111.31087464,2,-60.,0|H,5,1.09590223,1,111.31087464,2,180.,0|H,5,1.
09590223,1,111.31087464,2,60.,0||Version=x86-Win32-G03RevB.04|State=1-
A1|HF=-449.2112609|RMSD=3.265e-009|Dipole=0.,0.,0.|PG=TD [O(Si1),4C3(C
1),6SGD(H2)]||@

Table D32. TMS, NMR-GIAO, B3LYP/6-31G(d,p), IEFPCM, $CHCl_3$.

SP|RB3LYP|6-31G(d,p)|C4H12Si1|PCUSER|06-May-2010|0||# NMR
=GIAO B3LYP/6-31G(D,P) SCRF=(IEFPCM,SOLVENT=CHLOROFORM,READ) GEOM=CONN
ECTIVITY||TMS, NMR-GIAO, IEFPCM-CHCl3, B3LYP/6-31G(d,p), may062010||0,
1|Si|C,1,1.89498656|C,1,1.89498656,2,109.47122063|C,1,1.89498656,2,109
.47122063,3,120.,0|C,1,1.89498656,2,109.47122063,3,-120.,0|H,2,1.09590
223,1,111.31087464,3,-60.,0|H,2,1.09590223,1,111.31087464,3,180.,0|H,2
,1.09590223,1,111.31087464,3,60.,0|H,4,1.09590223,1,111.31087464,2,-60
.,0|H,4,1.09590223,1,111.31087464,2,180.,0|H,4,1.09590223,1,111.310874
64,2,60.,0|H,3,1.09590223,1,111.31087464,2,-60.,0|H,3,1.09590223,1,111
.31087464,2,180.,0|H,3,1.09590223,1,111.31087464,2,60.,0|H,5,1.0959022
3,1,111.31087464,2,-60.,0|H,5,1.09590223,1,111.31087464,2,180.,0|H,5,1
.09590223,1,111.31087464,2,60.,0||Version=x86-Win32-G03RevB.04|State=1
-A1|HF=-449.2114144|RMSD=2.987e-009|Dipole=0.,0.,0.|PG=TD [O(Si1),4C3(
C1),6SGD(H2)]||@

Table D33. TMS, NMR-GIAO, B3LYP/6-31G(d,p), IEFPCM, DMSO.

SP|RB3LYP|6-31G(d,p)|C4H12Si1|PCUSER|30-Apr-2010|0||# NMR
=GIAO B3LYP/6-31G(D,P) SCRF=(IEFPCM,SOLVENT=DMSO,READ) GEOM=CONNECTIVI
TY||TMS, NMR-GIAO, IEFPCM-DMSO, B3LYP/6-31G(d,p), apr302010||0,1|Si|C,
1,1.94|C,1,1.94,2,109.47122063|C,1,1.94,2,109.47122063,3,120.,0|C,1,1.
94,2,109.47122063,4,120.,0|H,2,1.07,1,109.47122063,3,-60.,0|H,2,1.07,1
,109.47122063,3,-180.,0|H,2,1.07,1,109.47122063,3,60.,0|H,4,1.07,1,109
.47122063,2,-60.,0|H,4,1.07,1,109.47122063,2,180.,0|H,4,1.07,1,109.471
22063,2,60.,0|H,3,1.07,1,109.47122063,2,-60.,0|H,3,1.07,1,109.47122063
,2,180.,0|H,3,1.07,1,109.47122063,2,60.,0|H,5,1.07,1,109.47122063,2,-6
0.,0|H,5,1.07,1,109.47122063,2,180.,0|H,5,1.07,1,109.47122063,2,60.,0|
|Version=x86-Win32-G03RevB.04|State=1-A1|HF=-449.2037757|RMSD=5.658e-0
09|Dipole=0.,0.,0.|PG=TD [O(Si1),4C3(C1),6SGD(H2)]||@

Table D34. Phenanthroline, geometry optimization, B3LYP/6-31G(d,p).

FOpt\RB3LYP\6-31G(d,p)\C12H8N2\NLF\16-Aug-2009\0\\# opt rb3lyp/6-31g(d,p)\\Phen B3LYP/6-31G(d,p)\\0,1\C,0.6802443451,2.1018792897,-0.0000000005\C,-0.6802443445,2.1018792899,-0.0000000005\C,-1.4167785674,0.8710582622,-0.0000000005\C,1.4167785676,0.8710582617,-0.0000000005\C,-0.7291866919,-0.3774521532,-0.0000000005\C,0.7291866918,-0.3774521535,-0.0000000005\C,-2.8285865239,0.8422362137,-0.0000000005\H,-3.3818800301,1.7779144223,-0.0000000005\C,-3.4817605069,-0.3716847044,-0.0000000005\H,-4.5654958517,-0.4320776578,-0.0000000005\C,-2.7042997489,-1.5472018922,-0.0000000005\H,-3.1944617589,-2.5200997785,-0.0000000005\C,2.8285865242,0.8422362129,-0.0000000005\H,3.3818800306,1.7779144213,-0.0000000005\C,3.4817605067,-0.3716847054,-0.0000000005\H,4.5654958516,-0.4320776592,-0.0000000005\N,-1.3812270768,-1.5632312731,-0.0000000005\N,1.3812270763,-1.5632312735,-0.0000000005\C,2.7042997484,-1.547201893,-0.0000000005\H,3.1944617581,-2.5200997795,-0.0000000005\H,-1.2340569734,3.0370325114,-0.0000000005\H,1.2340569743,3.037032511,-0.0000000005\\Version=Mac32-G03RevE.01\State=1-A1\HF=-571.6226722\RMSD=6.513e-09\RMSF=1.995e-04\Thermal=0.\Dipole=0.,1.267955,0.\PG=C02V [SGV(C12H8N2)]\\@

Table D35. $Mo(CO)_4$(IPSO-SO), geometry optimization, B3LYP/LANL2DZ.

FOpt\RB3LYP\LANL2DZ\C28H20Mo1N4O5\NLF\06-Oct-2009\0\\
opt rb3lyp/lanl2dz\\Mo-IPSO-SO B3LYP/LANL2DZ optimization\\0,1\C,-3.
9768598649,0.6516761713,1.945041292\C,-3.229941328,-0.0292002901,0.975
4874953\C,-3.6290838269,-0.0674598921,-0.3781032018\C,-4.7938641542,0.
5820584357,-0.7852391717\C,-5.5633402776,1.2800896712,0.1774488267\C,-
5.1568176049,1.3073692394,1.524464764\H,-3.6671094122,0.690324556,2.98
53064212\H,-5.1120965314,0.5612553349,-1.8252052544\H,-6.4704001291,1.
7967734788,-0.1245859097\H,-5.7543888518,1.8466001957,2.2557304582\C,-
2.6582581334,-0.9562124539,-1.1610973913\C,-1.4330505879,-1.0055836408
,-0.1551686254\N,-2.0243593489,-0.7606852876,1.1383897457\C,-0.5694836
954,-2.2562620193,-0.1774197575\H,-1.09502564,-3.206764363,-0.19090809
12\C,1.4551828428,-1.0734674204,-0.1027316089\C,0.8142584318,0.1414098
934,-0.3050311742\N,0.7288577449,-2.286845166,-0.1214604879\O,-0.54151
79425,0.2034307823,-0.5293963533\C,1.5433343942,1.3872862292,-0.335762
0972\C,2.8889753207,-1.11952262,0.0841771254\C,2.9543813442,1.34979741
99,-0.1504481579\C,3.6301901557,0.0947349761,0.0618567199\C,0.91783867
93,2.643819184,-0.539650182\H,-0.1566235412,2.6895086629,-0.6774650994
\C,1.7107854665,3.7924206927,-0.550961273\H,1.2757984201,4.7745672248,
-0.7024728181\C,3.1069221859,3.682042081,-0.359782492\H,3.7413370742,4
.5604468648,-0.3628450691\C,3.600165085,-2.3318054666,0.2856085127\H,3
.0517623683,-3.2667224932,0.2976802653\C,4.9838995013,-2.2799677211,0.
4563492654\H,5.5638843049,-3.1837895072,0.6115961841\N,3.7237629946,2.
4945347655,-0.1621294558\N,4.9983186197,0.1322775014,0.23381845\C,5.65
24260691,-1.0337733419,0.4271945875\H,6.7258829922,-0.9718182365,0.559
5673376\C,-2.2806964226,-0.420335915,-2.5558047056\H,-1.5111807329,-1.
0469533232,-3.0241718893\H,-3.1650043497,-0.4387031054,-3.2053670561\H
,-1.906168693,0.6043026196,-2.506528673\C,-3.2996417686,-2.3695944183,
-1.3044113468\H,-4.2442521484,-2.2757381832,-1.8515422938\H,-2.6521905
33,-3.0510118862,-1.8704191918\H,-3.5233278455,-2.8154734952,-0.327900
3249\C,-1.2513150944,-0.726653769,2.3813983489\H,-0.4357128868,-1.4540
670585,2.3339358203\H,-0.827155548,0.269834574,2.5797755478\H,-1.89299
98067,-1.004478483,3.2251727645\Mo,5.9330725865,2.1854743628,0.1652689
477\C,5.7532418692,2.4209631072,2.1860472129\O,5.7118664076,2.59187818
14,3.3585448269\C,7.8037220946,1.6161318571,0.4705335413\O,8.916239868
7,1.2244038202,0.6570482404\C,6.4616647204,4.0886902806,0.060575663\O,
6.7292948785,5.250793924,-0.01021848\C,6.2970890994,2.0495724966,-1.84
10056636\O,6.5714772293,2.0084138418,-2.9932703678\\Version=Mac32-G03R
evE.01\State=1-A\HF=-1741.5455768\RMSD=5.449e-09\RMSF=4.281e-06\Therma
l=0.\Dipole=-5.3578746,-2.3042995,-0.0449673\PG=C01 [X(C28H20Mo1N4O5)]
\\@

Table D36. $Mo(CO)_4$(IPSO-PMC), geometry optimization, B3LYP/LANL2DZ.


```
                    FOpt\RB3LYP\LANL2DZ\C28H20Mo1N4O5\NLF\05-Oct-2009\0\\
# opt rb3lyp/lanl2dz\\Mo-IPSO-PMC-TTC B3LYP/LANL2DZ optimization\\0,1\
C,-5.7605731262,-1.483748557,-0.0001011925\C,-4.5033977376,-0.86601867
24,0.0000301824\C,-4.3529276045,0.5363613835,-0.0001178799\C,-5.482811
263,1.3569120894,-0.0003339778\C,-6.7633094769,0.7578371628,-0.0004342
836\C,-6.8957983915,-0.6454106905,-0.0003327554\H,-5.8801651993,-2.562
7878961,-0.0000653431\H,-5.387509788,2.4398841434,-0.0004445526\H,-7.6
527154771,1.3819392345,-0.0006181496\H,-7.886567193,-1.0923176446,-0.0
004436298\C,-2.8662179275,0.8918518521,-0.0000291866\C,-2.220591643,-0
.5051735172,0.0001877453\N,-3.2059808211,-1.4621380315,0.000352018\C,-
0.8586634901,-0.8444693288,0.0001541194\H,-0.5647136883,-1.8888678256,
-0.000035409\C,1.4057618753,-0.041497819,0.0002038815\C,2.0708246361,-
1.3630869983,0.0002519813\N,0.0746120589,0.1386746311,0.0001901028\O,1
.423702872,-2.4625490139,0.0003448712\C,3.5588073897,-1.3918017097,0.0
001333611\C,2.2354693358,1.1769190191,0.0001523\C,4.3145308268,-0.1976
607879,0.0000262986\C,3.6526521315,1.0952503901,0.000102876\C,4.241890
059,-2.625947839,0.000120163\H,3.6610238385,-3.5422179493,0.0002143261
\C,5.6426292103,-2.6269927954,-0.0000139345\H,6.2075247936,-3.55306546
6,-0.0000233663\C,6.3310906221,-1.399599673,-0.0001513901\H,7.41394205
58,-1.3630619365,-0.0003006715\C,1.6646513344,2.4743267993,0.000165513
5\H,0.5858297708,2.5684772736,0.0001897982\C,2.4962573514,3.5982527291
,0.0001620433\H,2.0823220636,4.6014448045,0.000176833\N,5.6898697395,-
0.2027136548,-0.0001295218\N,4.4665992174,2.2036598956,0.0001110766\C,
3.8944548741,3.4314135558,0.0001524638\H,4.5665837252,4.2805652964,0.0
001911282\C,-2.4764094885,1.688822864,1.2795177542\H,-1.3958147661,1.8
534278372,1.3007711736\H,-2.9900082176,2.6581816034,1.2818289386\H,-2.
7657522809,1.1480360975,2.188326789\C,-2.4762108238,1.6886044288,-1.27
96495849\H,-2.989800223,2.6579653877,-1.2821954488\H,-1.3956111222,1.8
531769489,-1.300786874\H,-2.7654351627,1.1476643759,-2.188404393\C,-2.
9545572432,-2.9092181968,0.0006515143\H,-2.3864031777,-3.2017923446,-0
.8900172791\H,-2.382950806,-3.2006774161,0.8894497941\H,-3.9045236953,
-3.4453793721,0.0029022136\Mo,6.6908191163,1.8146520779,-0.0002037576\
C,6.785587259,1.8633704324,2.0397746495\O,6.9083761994,1.9263297878,3.
2173665535\C,7.281750331,3.7029040657,0.0001289445\O,7.5891030573,4.85
74704316,0.0004769216\C,8.5603332084,1.1693304527,-0.0008947797\O,9.67
1283136,0.7290146293,-0.0013881197\C,6.784554508,1.864115379,-2.040213
4777\O,6.9070502273,1.9269999654,-3.217839201\\Version=Mac32-G03RevE.0
1\State=1-A\HF=-1741.5536324\RMSD=6.021e-09\RMSF=5.113e-06\Thermal=0.\
Dipole=-7.4525625,-2.2281352,0.0002889\PG=C01 [X(C28H20Mo1N4O5)]\\@
```

Table D37. 42-SO, geometry optimization, B3LYP/6-31G(d).

FOpt|RB3LYP|3-21G|C24H20N4O1|PCUSER|20-Apr-2010|0||# OPT B3LYP/3-21G GEOM=CONNECTIVITY||2,3-IPSO, Opt, B3LYP, 3-21G, Apr202010||0,1|C,-1.0580760699,-0.6235878983,1.2554496701|C,-0.9121083202,-1.2327706332,2.4829808981|C,0.3695156559,-1.3610439145,3.0637610864|C,1.4763059203,-0.8334777639,2.3383126649|C,0.11466941,-0.1423063809,0.6180626933|C,0.5716292225,-1.9897329781,4.3364906464|C,2.8042926129,-0.9428211851,2.9071973412|C,2.9599462687,-1.5751731894,4.1742642809|C,1.8184849621,-2.0934911217,4.8718836251|C,4.2681079491,-1.6680810095,4.7053603541|H,4.4169100428,-2.1448978754,5.6680263994|C,5.3327884348,-1.1531850037,3.9938185381|C,5.0796441261,-0.5447938869,2.7465923861|H,-0.2927466998,-2.3805119805,4.8619513243|H,-1.7966372511,-1.6027056002,2.9873029019|H,1.971676566,-2.5693972043,5.8342715068|H,6.344452744,-1.2100953921,4.3752354337|H,5.9002680378,-0.1329267897,2.1682801145|C,-1.237186946,0.5427655878,-1.3453398131|C,-2.4003331739,0.0440465807,-0.5037690162|H,-3.3720368961,0.1843606732,-0.971819685|C,-1.1264792544,-0.2008024205,-2.7382467999|C,-1.9691531763,0.7164739337,-3.6240279178|C,-2.0931340825,1.9734008108,-2.9925657003|C,-2.7455427804,3.0271969382,-3.629709959|C,-2.4812342579,0.5141757962,-4.8911684336|C,-3.1465840436,1.569918406,-5.5422513294|H,-3.5647974439,1.4181380743,-6.5297878003|C,-3.2676427553,2.808364679,-4.9133851466|H,-3.7815650869,3.6191941367,-5.417296604|H,-2.8572571253,3.9906549718,-3.148653647|H,-2.3773256485,-0.4481059529,-5.3808020658|C,-1.525966989,3.0153888162,-0.7458232234|H,-0.747282169,2.8114303076,-0.0076457678|H,-1.2836979453,3.9603977153,-1.2417720921|H,-2.4966410954,3.1193721313,-0.2392537566|C,0.3431168594,-0.133180505,-3.2228214812|H,0.6938161057,0.9014577383,-3.2174009199|H,0.9925541451,-0.7236768238,-2.5719907822|H,0.3944914781,-0.5233731568,-4.244362242|C,-1.6097183554,-1.6595741483,-2.6749140629|H,-2.6654194289,-1.7276490944,-2.3974216888|H,-1.4831554438,-2.1281828562,-3.6570873497|H,-1.0135620129,-2.2263147432,-1.950511741|N,3.8619144237,-0.4393489762,2.2152440815|N,1.3185736896,-0.2330598916,1.1283912378|N,-1.5001968523,1.9377512488,-1.7313828265|N,-2.3421471824,-0.4730610803,0.6728786174|O,0.0323624095,0.4900756948,-0.6170108897||Version=x86-Win32-G03RevB.04|State=1-A|HF=-1214.1198355|RMSD=3.741e-009|RMSF=4.750e-006|Dipole=-0.2105114,-0.4326868,1.0013333|PG=C01 [X(C24H20N4O1)]||@

Table D38. 42-PMC, geometry optimization, B3LYP/6-31G(d).

FOpt|RB3LYP|6-31G(d)|C24H20N4O1|PCUSER|21-Apr-2010|0||# OPT B3LYP/6-31G(D) GEOM=CONNECTIVITY||2,3-IPSO-TTC, Opt, B3LYP, 6-31G, Apr212010||0,1|C,0.5928509591,0.0000854219,0.5376294967|C,0.5940302093,0.0000897888,1.9554825649|C,1.7704215663,0.00007789,2.6737983545|C,3.0172428913,0.0000328222,1.9104738791|C,1.921948891,0.0001383333,-0.1627709747|C,1.7949866601,0.0000766448,4.1134830411|C,4.2808248915,-0.000014474,2.6831684592|C,4.2307877513,-0.0000100921,4.1045651859|C,2.9635032524,0.0000374701,4.7995581404|C,5.4555140189,-0.0000555293,4.798895167|H,5.4532315848,-0.0000539738,5.8866539587|C,6.6431088853,-0.0001010352,4.0891294524|C,6.5775035095,-0.000100562,2.685936714|H,0.843000945,0.0001052064,4.6397074128|H,-0.3697292176,0.000090489,2.460200465|H,2.9721531001,0.0000362865,5.8867526589|H,7.6041924915,-0.0001363508,4.5952895974|H,7.4932331292,-0.0001354886,2.0957066032|C,-2.070440672,0.0000193791,-1.8977378463|C,-0.7768056916,0.0000468517,-1.3765601042|H,0.0837434773,0.000068543,-2.0382055839|C,-3.4052432469,-0.0000097822,-1.1500374567|C,-4.3919750351,-0.0000279856,-2.306478407|C,-3.688182789,-0.0000114899,-3.517652367|C,-4.3349492898,-0.0000233143,-4.7506774593|C,-5.7791244509,-0.0000567469,-2.3167532854|C,-6.4518762131,-0.0000690315,-3.5465740863|H,-7.537596791,-0.0000916636,-3.5675803066|C,-5.7341721322,-0.0000525132,-4.7448163657|H,-6.2660149678,-0.0000623689,-5.6918981606|H,-3.7914916228,-0.0000109224,-5.6897949309|H,-6.3409460178,-0.0000699432,-1.3863058582|C,-1.250520227,0.000044212,-4.2441088021|H,-0.6206602075,-0.8885374332,-4.1360125477|H,-1.6983290142,0.0000496308,-5.2369039071|H,-0.6206857584,0.8886412304,-4.1359916335|C,-3.5540020593,-1.2702242516,-0.2784621008|H,-3.4529487698,-2.178376622,-0.8815199693|H,-2.787503309,-1.2762131865,0.4992909547|H,-4.5442942522,-1.2816297687,0.190341852|C,-3.5540538524,1.2701951698,-0.2784570356|H,-3.4530391239,2.1783540126,-0.8815115892|H,-4.5443458802,1.28155756,0.1903482575|H,-2.7875542524,1.2762130938,0.4992950136|N,5.4410226043,-0.0000587254,2.0004152046|N,3.08063915,0.0000362773,0.6003835836|N,-2.3046963002,0.000018038,-3.2379182123|N,-0.6101922588,0.0000530744,-0.0482249249|O,2.0012381415,-0.0000827547,-1.3983321036||Version=x86-Win32-G03RevB.04|State=1-A|HF=-1220.8176824|RMSD=8.525e-009|RMSF=1.784e-005|Dipole=-2.9392159,0.0001162,-0.2721817|PG=C01 [X(C24H20N4O1)]||@

Table D39. 43-SO, geometry optimization, B3LYP/6-31G(d).

FOpt|RB3LYP|6-31G(d)|C36H32N6O2|PCUSER|05-Jun-2010|0||# OPT B3LYP/6-31G(D) GEOM=CONNECTIVITY||bis-2,3-IPSO, opt, B3LYP, 6-31G(d), June042010||0,1|C,-4.1527817698,-0.32294162,0.3559629648|C,-4.1574757159,-0.2743865207,1.7342385636|C,-2.9427726875,-0.1516066357,2.4438663417|C,-1.7423865299,-0.0805188615,1.6769473843|C,-2.8884742006,-0.2393341452,-0.2938046976|C,-2.8949228396,-0.0988872442,3.874349588|C,-0.4745629741,0.0424393961,2.3722455402|C,-0.4744291206,0.0925920581,3.7975986337|C,-1.7048264046,0.0192498272,4.527047067|C,0.7768449931,0.2160158646,4.4404270343|H,0.8477518193,0.2600323127,5.5238948384|C,1.9349865837,0.284848908,3.6947763096|C,1.80182496,0.2209583554,2.2784964403|H,-3.8288770121,-0.1552545817,4.4276184035|H,-5.1080408029,-0.3337301159,2.2574708296|H,-1.6681472576,0.0599697962,5.6126577464|C,-3.9823023498,-0.3754275631,-2.4662637038|C,-5.2488162941,-0.5064868952,-1.6370307962|H,-6.1679388544,-0.5917410268,-2.2188416292|C,-3.8195866693,-1.5306674168,-3.5349052493|C,-4.5721073783,-0.9234203298,-4.7114089696|C,-4.6694195989,0.4673952407,-4.5207218028|C,-5.2698538716,1.2861211917,-5.4764213958|C,-5.0574217249,-1.5028794457,-5.871828174|C,-5.6622231647,-0.6914834919,-6.8462652002|H,-6.0575406423,-1.1380903412,-7.7538885472|C,-5.7599660379,0.6844699014,-6.6440282596|H,-6.2327656561,1.3074382329,-7.3989218109|H,-5.3628436883,2.3573035578,-5.3266930796|H,-4.9807893884,-2.576500958,-6.0274237617|C,-4.3042701016,2.1338907656,-2.6999843078|H,-3.6793595362,2.2175206059,-1.8077114057|H,-3.980200104,2.9085184372,-3.4021088198|H,-5.352516561,2.329894289,-2.4242215576|C,-2.3286506863,-1.6889199862,-3.9142869435|H,-1.891766148,-0.7332908513,-4.2161335576|H,-1.7451520642,-2.0789834301,-3.0755673426|H,-2.2484276957,-2.3866789521,-4.7548311417|C,-4.3685455321,-2.8773620188,-3.0429772837|H,-5.4433713338,-2.8454237335,-2.8394736125|H,-4.197542283,-3.6504438303,-3.8001240176|H,-3.8532181577,-3.1952559581,-2.1290328718|N,0.6661309782,0.1056249568,1.6424673772|N,-1.7417091803,-0.1238005612,0.32200161|N,-4.0944431657,0.8306209335,-3.3002800051|N,-5.3513288544,-0.4472893915,-0.362753587|O,-2.8118618761,-0.2807810214,-1.6545642356|C,4.202953361,0.4887390364,3.5472452297|C,4.2201720937,0.3798199266,2.0317592496|O,2.9065172082,0.2830630336,1.4815934206|N,3.1851969374,0.4101345563,4.3191213281|C,5.023821262,1.5515246498,1.3358539014|C,6.3276049853,-0.4389871339,1.4917780676|C,6.4250600647,0.9551595385,1.3272874627|C,7.6596096224,1.5472649605,1.1195078307|C,7.4625314907,-1.2487417787,1.4709382446|C,8.812617162,0.7450724482,1.0923605382|C,8.7055499914,-0.6343832117,1.2636482071|N,4.992507851,-0.8150212698,1.6594965671|C,4.8947360588,2.8865652969,2.0828066488|H,3.8447026325,3.1954345057,2.1455941353|H,5.3026489399,2.8430757656,3.0973999739|H,5.4344265384,3.6717849636,1.5421284719|C,4.5389517456,1.7272065867,-0.1221951477|H,3.5150192778,2.1099160534,-0.1563397632|H,5.1984445661,2.4375506629,-0.6323892824|H,4.565238348,0.7795500918,-0.6666791558|H,7.7410947913,2.6235907327,0.9867357113|H,9.7867471958,1.20144435,0.9429984271|H,9.6010336333,-1.2502574257,1.2462894183|H,7.3947820786,-2.3226760994,1.6143693322|H,5.1875964669,0.5751495186,4.0093792957|C,4.6099256174,-2.1284191718,2.1406528349|H,4.9438012121,-2.3367862486,3.169434906|H,3.522230606,-2.2198317451,2.0935074318|H,5.0328884194,-2.8902521317,1.4782630179||Version=x86-Win32-G03RevB.04|State=1-A|HF=-1870.061511|RMSD=1.650e-009|RMSF=2.495e-006|Dipole=-0.2379021,-0.0042975,0.43448|PG=C01 [X(C36H32N6O2)]||@

Table D40. 43-PMC, geometry optimization, B3LYP/6-31G(d).

FOpt|RB3LYP|6-31G(d)|C36H32N6O2|PCUSER|06-Jun-2010|0||# OPT B3LYP/6-31G(D) GEOM=CONNECTIVITY||bis-2,3-IPSO-TTC, opt, B3LYP/6-31G(d), June052010||0,1|C,-3.1944961434,0.0000741514,-1.5580623666|C,-3.1987824703,0.0001075191,-0.1364317873|C,-2.0312262633,0.0000911497,0.5901905022|C,-0.7789290398,0.0000425284,-0.1638741945|C,-1.8625631062,0.0000232158,-2.2453292651|C,-2.0149822138,0.0001170021,2.0332722385|C,0.5091983627,0.000025098,0.6118025061|C,0.428501428,0.0000405342,2.0713743027|C,-0.8545668558,0.0000910145,2.7320440675|C,1.6168726978,0.0000067575,2.7634300259|H,1.6297328436,0.0000181691,3.8511853614|C,2.8713778728,-0.0000438133,2.0946485916|C,2.8557844359,-0.0000494627,0.5959364312|H,-2.9715909352,0.0001555843,2.5506375749|H,-4.1662121342,0.0001442087,0.3610186094|H,-0.8643702319,0.0001081102,3.8195508639|C,-5.837660951,0.0000787504,-4.0132742004|C,-4.5495307176,0.000056497,-3.4861908553|H,-3.6874981203,0.0000064273,-4.145295897|C,-7.176282407,0.0001240167,-3.2711382401|C,-8.1582558209,0.000103812,-4.4318025785|C,-7.4498574487,0.000058473,-5.6405519198|C,-8.0941351437,0.0000236932,-6.8751568279|C,-9.5451083902,0.0001223589,-4.4460857967|C,-10.2151110355,0.0000923972,-5.6776133457|H,-11.3008051667,0.0001059565,-5.7016595036|C,-9.4935432358,0.0000427346,-6.8733612733|H,-10.0223490458,0.0000163627,-7.8222566722|H,-7.5479234068,-0.0000208021,-7.8127541097|H,-10.1083807078,0.0001589035,-3.5164622107|C,-5.0107851946,0.0000193771,-6.3581636653|H,-4.3808211061,-0.8885167662,-6.2476361451|H,-5.4538127742,0.0001433454,-7.3532450303|H,-4.3806482396,0.8884140505,-6.2474995481|C,-7.3298256493,-1.2697773304,-2.400256082|H,-7.22440259,-2.1777546186,-3.0029048338|H,-6.567469471,-1.2754345884,-1.6183693206|H,-8.3227685223,-1.2827829742,-1.9366352243|C,-7.3297814847,1.2700844349,-2.4003342745|H,-7.2243319456,2.1780210364,-3.0030397235|H,-8.3227217059,1.2831510052,-1.9367092423|H,-6.5674213914,1.2757656661,-1.6184514284|N,1.6256684981,-0.0000103767,-0.0643067049|N,-0.7035976666,0.0000157219,-1.4669299868|N,-6.0684496169,0.0000562319,-5.3573576227|N,-4.3889872922,0.0000913934,-2.1539285894|O,-1.7610515374,0.0000155438,-3.4766250946|C,5.2093984487,-0.0001143518,2.3903814841|C,6.2778076004,-0.0000981195,3.2823446363|O,3.8965832001,-0.0000725425,-0.0697450615|N,3.9567795319,-0.000069586,2.8716742973|C,6.2480335928,-0.0002324633,4.8126343915|C,8.4702128259,-0.0000522344,3.9460988483|C,7.733223896,-0.0001797683,5.1376316879|C,8.3945730305,-0.0002584518,6.3567220772|C,9.8627924548,-0.0000468205,3.9380362415|C,9.7964660347,-0.0002267122,6.3728360062|C,10.5158034114,-0.0001287338,5.1757449796|N,7.5737331437,0.0000761161,2.8576087108|C,5.5502257865,-1.2702427753,5.355586055|H,4.5025474435,-1.2759491493,5.0475255401|H,6.0336309552,-2.1781431425,4.9804083292|H,5.6049320013,-1.2833599464,6.4500651664|C,5.5500741608,1.2696189938,5.3557671039|H,4.5023993904,1.2752510596,5.047686076|H,5.6047525465,1.2825741153,6.4502492961|H,6.0333835477,2.1776324963,4.9807388507|H,7.8364045235,-0.0003577326,7.2894190398|H,10.325571953,-0.0002953377,7.3211802934|H,11.6018442606,-0.0001285083,5.199268097|H,10.435988894,-0.0000104871,3.0166884429|H,5.3887182609,-0.0001185543,1.3201646481|C,7.9635559295,0.0003031302,1.454645812|H,7.5720012831,-0.8886047022,0.9495657143|H,7.5701762556,0.8883252132,0.9494499308|H,9.0502934623,0.0014454707,1.3807496784||Version=x86-Win32-G03RevB.04|State=1-A|HF=-1870.0271183|RMSD=8.735e-009|RMSF=3.951e-006|Dipole=-0.6110971,0.0001042,1.0148195|PG=C01 [X(C36H32N6O2)]||@

Table D41. 44-SO, geometry optimization, B3LYP/6-31G(d).

FOpt|RB3LYP|6-31G(d)|C24H20N4O1|PCUSER|24-Apr-2010|0||# OPT B3LYP/6-31G(D) GEOM=CONNECTIVITY||3,4-IPSO, opt, B3LYP/6-31G, Apr24 2010||0,1|C,-0.257387717,-0.1297469618,0.8793114423|C,-0.2627890011,0.0035936144,2.2934652307|C,0.9651149314,-0.2026829623,0.2295828358|C,-0.0997430059,-0.2470196093,-1.943985219|C,-1.3713420231,-0.2900392467,-1.110934693|H,-2.2971850176,-0.3239972565,-1.6872606763|C,-0.0543962636,-1.3428248505,-3.0805768352|C,-0.7291222092,-0.5887606652,-4.218302855|C,-0.681981273,0.789740104,-3.9422153124|C,-1.1869039056,1.7240479153,-4.845230395|C,-1.2643737606,-1.042072582,-5.4125424926|C,-1.7737673978,-0.113379011,-6.3351961454|H,-2.2072354019,-0.4595841844,-7.2688166502|C,-1.7288342446,1.2502365718,-6.048301973|H,-2.1289986458,1.9645174431,-6.7631265112|H,-1.1704532304,2.7876409643,-4.6288291029|H,-1.300517528,-2.1062129686,-5.6338335942|C,-0.1718947246,2.2957871877,-2.0205137245|H,0.451080957,2.2698650434,-1.1235915722|H,0.2266773892,3.0759521214,-2.67650372|H,-1.1982627505,2.572391939,-1.7336790296|C,1.4133640129,-1.6367789384,-3.4716336081|H,1.9540967628,-0.716912299,-3.7107525128|H,1.9440200285,-2.1463256186,-2.6620695961|H,1.4235112315,-2.2817293996,-4.3566786211|C,-0.7440906092,-2.6526329952,-2.6727443373|H,-1.8119793122,-2.5228858243,-2.4724967913|H,-0.6461753609,-3.392501233,-3.4746143269|H,-0.2740900776,-3.0752936521,-1.7771335355|N,-0.0822947614,1.0154658116,-2.6986363951|N,-1.4633223994,-0.1913135726,0.1625882042|O,1.0677073657,-0.3465204336,-1.1231373397|N,2.1734036177,-0.0232548234,2.2941345555|C,-1.4837037285,0.0840922764,3.0384815699|C,-1.4574271585,0.211489707,4.3941425774|C,0.9954843271,0.0540174492,2.9593748845|H,-2.3853646289,0.2712979723,4.958445089|C,1.0195358233,0.1929238366,4.4091941369|C,-0.2180895347,0.2701337151,5.1122429394|C,-0.1671098837,0.4038979567,6.5172186686|H,-1.0951868464,0.4649020167,7.081232996|C,1.0570665428,0.4550431711,7.1499869386|C,2.2203139672,0.3704256365,6.3573697474|C,2.1558539985,-0.1463538345,0.9807120717|N,2.2155361098,0.2442549986,5.0404519939|H,1.1349593683,0.5574619356,8.2282966816|H,3.2012967787,0.408323473,6.8306873265|H,-2.4188598033,0.0389651805,2.4916744782|H,3.1110862206,-0.2086039925,0.4609471608||Version=x86-Win32-G03RevB.04|State=1-A|HF=-1220.8281763|RMSD=3.486e-009|RMSF=4.395e-006|Dipole=-1.1486196,0.1378375,-0.4506589|PG=C01 [X(C24H20N4O1)]||@

Table D42. 44-PMC, geometry optimization, B3LYP/6-31G(d).

FOpt|RB3LYP|6-31G(d)|C24H20N4O1|PCUSER|28-Apr-2010|0||# OPT B3LYP/6-31G(D) GEOM=CONNECTIVITY||3,4-IPSO-TTC, opt, B3LYP/6-31G(d), Apr282010||0,1|C,1.479339769,0.0006481918,0.2227208007|C,1.484429227,0.0007350516,1.6866716582|C,2.7941883721,0.0009068832,-0.4556362768|C,-1.1183884939,-0.0014897708,-2.278868388|C,0.1579904832,0.0001875719,-1.7283998387|H,1.0267350081,0.0019193536,-2.3775781606|C,-2.4735922619,-0.0009030611,-1.5661896354|C,-3.4307793222,-0.0006742146,-2.7478196469|C,-2.6967435876,-0.0016020667,-3.9408675178|C,-3.3140194664,-0.0006049736,-5.1891087299|C,-4.8171811917,0.0004043059,-2.7921047149|C,-5.4602108298,0.0009046271,-4.0378441559|H,-6.5450957503,0.0018367577,-4.0852854925|C,-4.7130884993,0.0005197258,-5.2177290353|H,-5.2212797031,0.0013292402,-6.1777751285|H,-2.7478207832,-0.0001423854,-6.1147591028|H,-5.4014473292,0.0010109618,-1.8755333674|C,-0.244760221,-0.0058903687,-4.6076038642|H,0.3915484245,-0.8866415299,-4.4732777482|H,-0.6677459774,-0.0247526684,-5.6111776988|H,0.3747416774,0.8904572815,-4.498673725|C,-2.6503297615,-1.2729002099,-0.7028866891|H,-2.54318172,-2.1788027594,-1.3083231342|H,-1.9016993249,-1.2937890944,0.0918239759|H,-3.6505590885,-1.2800323593,-0.255412968|C,-2.6496510901,1.2713629685,-0.7032144451|H,-2.542095498,2.1770518265,-1.3088941979|H,-3.6498538104,1.2791013288,-0.2556964279|H,-1.9009846367,1.292128785,0.0914548405|N,-1.3216734583,-0.0035280502,-3.6282217434|N,0.3028428527,-0.0000180026,-0.3910447381|O,2.9587772258,0.0009874152,-1.6866288896|N,3.9384296582,0.0011738378,1.7300915071|C,0.2644546812,0.0005319604,2.4240699435|C,0.2610983024,0.0006699647,3.7926725594|C,2.7101047853,0.0010588035,2.3780094688|H,-0.6792259159,0.0005073292,4.3398253159|C,2.7244517795,0.0012370375,3.8209514065|C,1.4802444295,0.0010386481,4.5261476749|C,1.5214233162,0.0012169453,5.9405181087|H,0.5885833709,0.0010722845,6.5002592794|C,2.7390015975,0.0015721967,6.5814580179|C,3.9107209911,0.0017479039,5.7885671829|C,3.9670870858,0.0010239508,0.4399926173|N,3.9195686047,0.001590148,4.4696555|H,2.8121511688,0.0017192839,7.6650102864|H,4.8871696763,0.0020330244,6.2736346425|H,-0.6661687715,0.0002507845,1.8696983683|H,4.9370970088,0.0011052751,-0.0606911237||Version=x86-Win32-G03RevB.04|State=1-A|HF=-1220.8215604|RMSD=9.032e-009|RMSF=4.563e-006|Dipole=-3.0912065,-0.0025769,-1.3782964|PG=C01 [X(C24H20N4O1)]||@

Table D43. 45-SO, geometry optimization, B3LYP/6-31G(d).

FOpt|RB3LYP|6-31G(d)|C36H32N6O2|PCUSER|03-Jun-2010|0||# OPT B3LYP/6-31G(D) GEOM=CONNECTIVITY||bis-3,4-IPSO, opt, B3LYP/6-31G(d), june022010||0,1|C,-0.4508780176,-0.3168327138,-2.8064269857|C,-0.4508934387,-0.3169612114,-1.3861247684|C,0.7688908913,-0.3168786499,-3.4653557449|C,-0.3059522511,-0.1532663376,-5.6277651216|C,-1.5731268546,-0.2946658601,-4.7984695216|H,-2.502105743,-0.2845616406,-5.3707025923|C,-0.2577885242,-1.122488211,-6.8735760922|C,-0.9485144089,-0.2601876546,-7.9210862775|C,-0.9097338948,1.0824266245,-7.5030242896|C,-1.4292344531,2.1011207837,-8.3004126982|C,-1.4908372929,-0.5917470382,-9.1515446215|C,-2.0154231144,0.4233634976,-9.9686549155|H,-2.454460157,0.1724409061,-10.9297525186|C,-1.9779568656,1.7501111209,-9.5419388877|H,-2.3892707861,2.5314524056,-10.1757247192|H,-1.4182277691,3.1367387055,-7.9753220602|H,-1.5205246788,-1.627555306,-9.4816731155|C,-0.4043919088,2.3826810031,-5.4368632045|H,0.2147471795,2.2660209555,-4.5446600777|H,-0.0094118128,3.2316161108,-6.0036735941|H,-1.4342875997,2.6189605702,-5.1275483679|C,1.2101330739,-1.3573231394,-7.302279857|H,1.7398058531,-0.4111673631,-7.4432184116|H,1.7502118402,-1.9453524399,-6.5546084641|H,1.2212692588,-1.9032328301,-8.2516463762|C,-0.9304494822,-2.4757530942,-6.6029505361|H,-1.9979381834,-2.3802996962,-6.38263932|H,-0.8312769991,-3.1244011841,-7.4801854227|H,-0.4480631776,-2.9859642292,-5.7611282345|N,-0.3021793215,1.1822166379,-6.2468155496|N,-1.6595363315,-0.3229223292,-3.5210973602|O,0.8652516711,-0.3310855037,-4.8273396279|N,1.9852043942,-0.3263999402,-1.3971400574|C,-1.6656771138,-0.3162676695,-0.6286830165|C,-1.6391615756,-0.3140174315,0.7342168662|C,0.8097126074,-0.3213875451,-0.7229680605|H,-2.5564318495,-0.3153010388,1.3127536519|C,0.8377400962,-0.3223800857,0.7318880126|C,-0.3959072478,-0.3122732582,1.4439877984|C,-0.3378480518,-0.3041739947,2.8627981847|C,0.9055023757,-0.3042354786,3.4771337538|C,2.0677846036,-0.3355808489,2.6793982639|C,1.9619313929,-0.3231473045,-2.7167829251|N,2.0381426234,-0.339044944,1.3601986779|H,-2.6043724454,-0.3192626284,-1.1717054034|H,2.9155025885,-0.3277020121,-3.2433720648|C,-1.4010717238,-0.2735795536,4.8970101433|C,-0.1180393259,-0.1008137363,5.6901942413|C,0.7267022382,-0.5238728313,7.8050024232|C,0.8215404813,0.8677274664,7.6600269947|C,1.3326207685,-1.1834768918,8.8716877804|C,1.5235916904,1.6199817123,8.5882187784|H,1.6050131013,2.6990320425,8.4803546421|C,2.1396748412,0.9724283093,9.67059102|C,2.0389781085,-0.4120328235,9.804765686|N,-0.0427266537,-1.0693302233,6.7625453651|C,0.0195684374,1.292169113,6.438517841|N,-1.5161901473,-0.3500625953,3.6255170752|O,1.0486462146,-0.2975489947,4.828387055|C,0.7043123455,2.3571296399,5.5721912192|H,1.7108057433,2.0526162375,5.2792299853|H,0.1228903707,2.5640150782,4.6659894418|H,0.7795702445,3.295309102,6.1331629008|C,-1.3645535307,1.8098790224,6.898446675|H,-1.9940154305,2.0897890447,6.0453811627|H,-1.8967005942,1.0644031659,7.4979428473|H,-1.2267074648,2.7003895881,7.520071843|C,0.0379849508,-2.4862979093,6.4446379786|H,-0.6493106246,-2.7129376601,5.6250096035|H,1.0506963289,-2.7956109832,6.1502037893|H,-0.2728138002,-3.0737667811,7.3140905784|H,2.697768756,1.5508867918,10.4009975673|H,2.5230429013,-0.9089104877,10.6414605105|H,1.2742719441,-2.2620429686,8.9800374421|H,-2.3069147132,-0.3521161039,5.4980599918|H,3.0416737303,-0.3518677295,3.1671414929||Version=x86-Win32-G03RevB.04|State=1-A|HF=-1870.0484708|RMSD=7.832e-009|RMSF=1.472e-006|Dipole=-1.0271791,0.1764549,0.1437736|PG=C01 [X(C36H32N6O2)]||@

Table D44. 45-PMC, geometry optimization, B3LYP/6-31G(d).

FOpt|RB3LYP|6-31G(d)|C36H32N6O2|PCUSER|11-May-2010|0||# OPT B3LYP/6-31G(D) GEOM=CONNECTIVITY||bis-3,4-IPSO-TTC, opt, B3LYP/6-31G(d), may112010||0,1|C,2.1729056431,0.0124973693,-2.8972689036|C,2.1703743871,0.0107245896,-1.4326492165|C,3.4936106901,0.0137726312,-3.5641336289|C,-0.4040554018,0.0062471708,-5.418272267|C,0.8664831109,0.012015028,-4.8601554876|H,1.739863622,0.0183117934,-5.5030415168|C,-1.7638113251,0.0105151784,-4.7133766167|C,-2.7142402253,0.0120408253,-5.9004649536|C,-1.9736620336,0.0063740533,-7.0898837669|C,-2.5865772678,0.0102397254,-8.340678609|C,-4.1001679749,0.0182468969,-5.9509527165|C,-4.7384851468,0.0201003465,-7.1992903943|H,-5.8231693241,0.0253058399,-7.2515615545|C,-3.9856218763,0.0165687039,-8.3753945223|H,-4.489285586,0.0197418888,-9.3379252853|H,-2.0164668157,0.0107103,-9.2640668476|H,-4.6877491426,0.0222718629,-5.0364213915|C,0.4797409387,-0.0153197935,-7.7443728864|H,1.1412331696,-0.869045059,-7.5655646553|H,0.0633824866,-0.0962249074,-8.7478273953|H,1.0722947335,0.9035723913,-7.6760516878|C,-1.9477329994,-1.2600692481,-3.84967798|H,-1.8357966415,-2.1667575198,-4.4531884411|H,-1.2045471121,-1.2795078416,-3.0497834258|H,-2.9513689246,-1.26719374,-3.4094344565|C,-1.9418701529,1.2831639978,-3.851845971|H,-1.8262173137,2.1882881283,-4.456978128|H,-2.9452934512,1.2954287259,-3.4112545361|H,-1.1983511298,1.3008740408,-3.0522509895|N,-0.6014214118,-0.0030228036,-6.7714424597|N,1.0030592044,0.0109532519,-3.5195971269|O,3.6717099111,0.0154586516,-4.7923665115|N,4.6309173267,0.0109815744,-1.3703960826|C,0.9685404851,0.0093910921,-0.6927658151|C,0.9730841399,0.0063344797,0.6864509699|C,3.3973876373,0.0096154983,-0.7250364996|H,0.0376944998,0.0050328456,1.2339869393|C,3.4020912025,0.0064133929,0.7027196485|C,2.1797667089,0.0043845013,1.4183989823|C,2.1919482464,-0.0003436272,2.8829636358|C,3.5170171964,-0.0022087062,3.5411115833|C,4.6800820341,0.0007471431,2.6282346453|C,4.6626644878,0.0127332808,-2.658935013|N,4.639845913,0.0048307332,1.3399380157|H,5.6551119397,-0.000493759,3.1196082686|H,0.0295640847,0.0105025962,-1.2341283852|H,5.6344356491,0.0138041351,-3.1567226826|N,1.026226736,-0.0044350203,3.5129726549|C,0.8984782194,-0.0092988891,4.8543924599|C,-0.3683685598,-0.0171511379,5.4208158737|C,-1.7327129031,-0.0087872865,4.7248674828|C,-2.6753513277,-0.0119063669,5.9181473203|C,-1.9270054914,-0.0235471386,7.1026476159|C,-4.0609126566,-0.0048171622,5.9777484899|C,-2.5317004921,-0.0247135225,8.3574420322|C,-4.6910317895,-0.0080468376,7.230242733|C,-3.930482499,-0.0174173662,8.4013591019|N,-0.5568883163,-0.0327366485,6.7751913379|C,0.5305357318,-0.0504763536,7.7410310551|C,-1.9231838575,-1.2753849327,3.8567362909|C,-1.9155135978,1.267812015,3.8702096274|H,-4.6544722425,0.0038103485,5.0671179779|H,-5.7753454175,-0.0021897401,7.289647562|H,-4.4278262359,-0.0180831385,9.3671755446|H,-1.9555378136,-0.0286807436,9.2770572002|H,0.1207219009,-0.1388665182,8.7465526955|H,1.1916601347,-0.9022647103,7.5520408954|H,1.1217545595,0.8694821776,7.6753160426|H,-1.8079229498,-2.1848347619,4.4554476426|H,-2.9296928868,-1.279871619,3.4230660079|H,-1.1852807613,-1.2917507838,3.0518958801|H,-1.7952784238,2.1701426836,4.4786110008|H,-1.1772218138,1.2886006688,3.0658618183|H,-2.9217867073,1.2827150046,3.4362492721|H,1.776076706,-0.0060195985,5.4915312843|O,3.7032027584,-0.0061468895,4.768139658||Version=x86-Win32-G03RevB.04|State=1-A|HF=-1870.0343364|RMSD=1.078e-009|RMSF=3.537e-006|Dipole=-4.297718,-0.0257402,0.0141015|PG=C01 [X(C36H32N6O2)]||@

Appendix E. Calculated and Experimental NMR Shift Correlations

Figure E1. Calculated [GIAO, B3LYP/6-31G(d,p), IEFPCM, toluene] and experimental [toluene-d_8, 300 K] ^{1}H NMR chemical shifts, δ, of IPSO-SO.

Figure E2. Calculated [GIAO, B3LYP/6-31G(d,p), IEFPCM, $CHCl_3$] and experimental [$CDCl_3$, 300 K] ^{1}H NMR chemical shifts, δ, of IPSO-SO.

Figure E3. Calculated [GIAO, B3LYP/6-31G(d,p), IEFPCM, $CHCl_3$] and experimental [$CDCl_3$, 300 K] ^{13}C NMR chemical shifts, δ, of IPSO-SO.

Figure E4. Calculated [GIAO, B3LYP/6-31G(d,p), IEFPCM, DMSO] and experimental [DMSO-d_6, 300 K] ^{1}H NMR chemical shifts, δ, of IPSO-SO.

Figure E5. Calculated [GIAO, B3LYP/6-31G(d,p), IEFPCM, DMSO] and experimental [DMSO-d_6, 300 K] ^{13}C NMR chemical shifts, δ, of IPSO-SO.

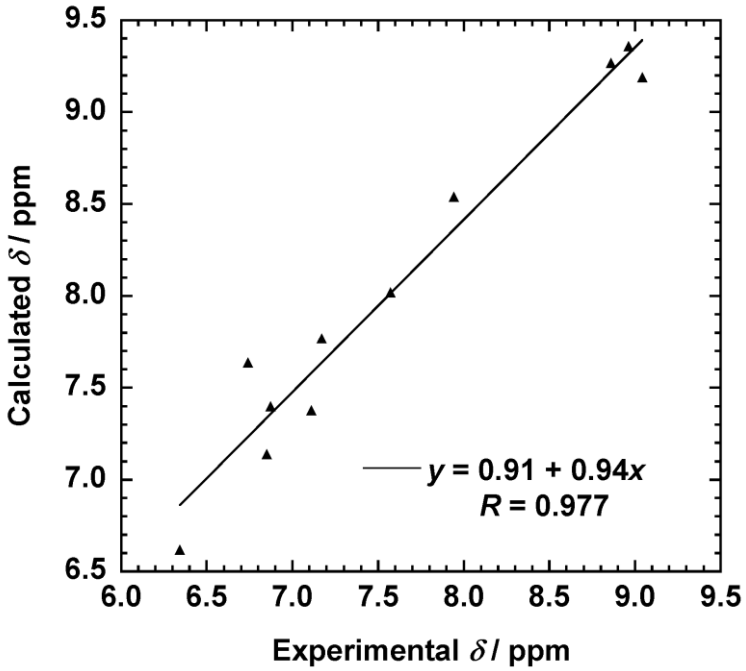

Figure E1. Calculated [GIAO, B3LYP/6-31G(d,p), IEFPCM, toluene] and experimental [toluene-d_8, 300 K] ^{1}H NMR chemical shifts, δ, of IPSO-SO.

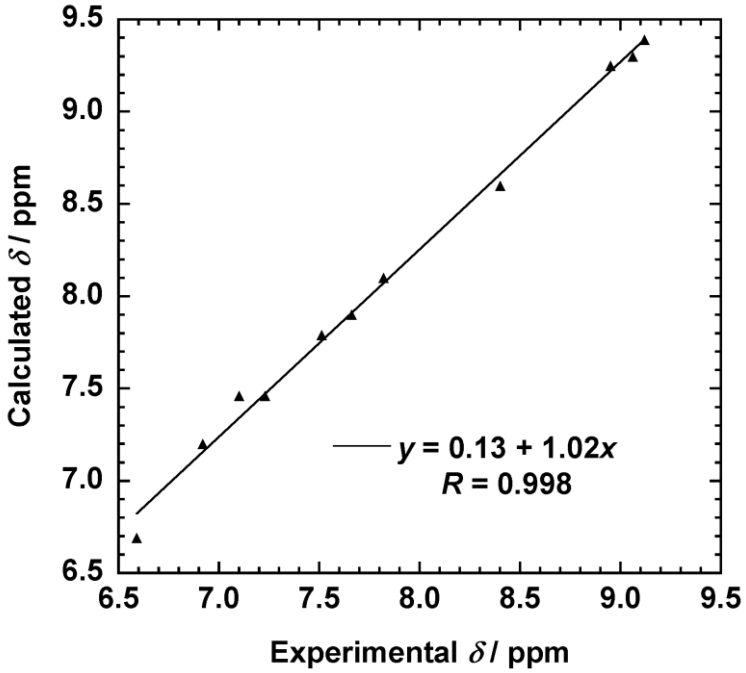

Figure E2. Calculated [GIAO, B3LYP/6-31G(d,p), IEFPCM, $CHCl_3$] and experimental [$CDCl_3$, 300 K] ^{1}H NMR chemical shifts, δ, of IPSO-SO.

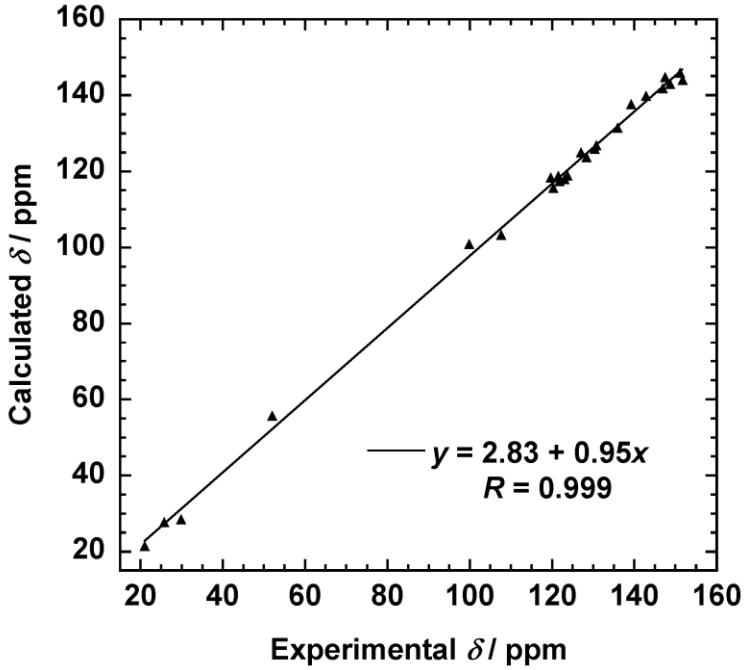

Figure E3. Calculated [GIAO, B3LYP/6-31G(d,p), IEFPCM, $CHCl_3$] and experimental [$CDCl_3$, 300 K] ^{13}C NMR chemical shifts, δ, of IPSO-SO.

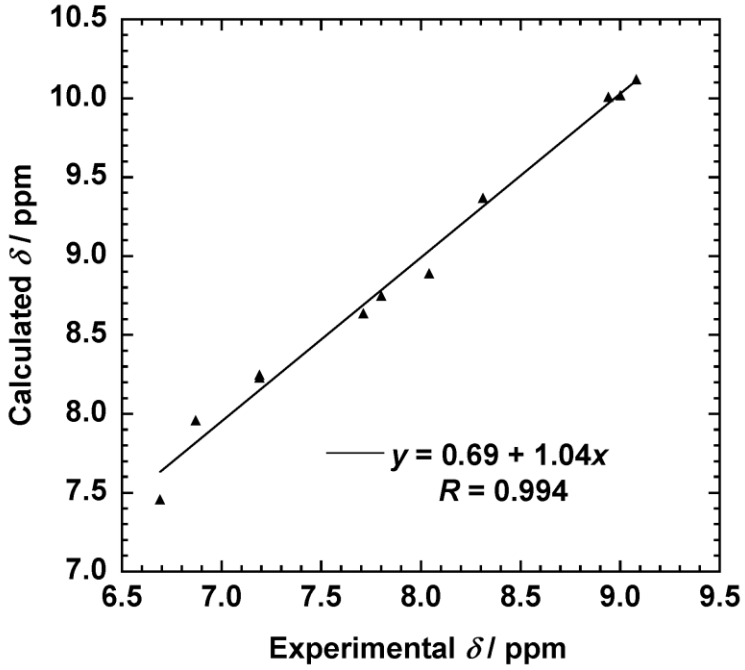

Figure E4. Calculated [GIAO, B3LYP/6-31G(d,p), IEFPCM, DMSO] and experimental [DMSO-d_6, 300 K] ^{1}H NMR chemical shifts, δ, of IPSO-SO.

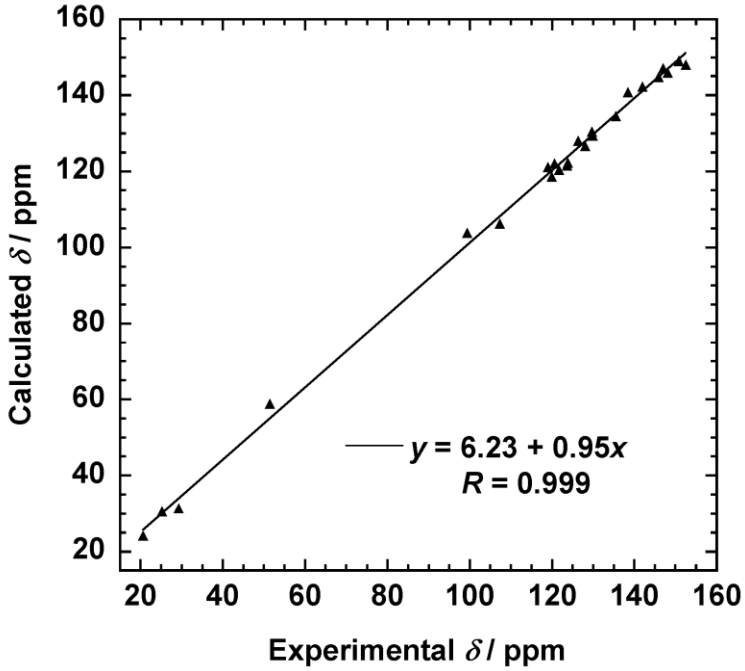

Figure E5. Calculated [GIAO, B3LYP/6-31G(d,p), IEFPCM, DMSO] and experimental [DMSO-d_6, 300 K] ^{13}C NMR chemical shifts, δ, of IPSO-SO.

Appendix F. Copyright Licenses

License Number	2499070660099
License date	Aug 30, 2010
Licensed content publisher	American Chemical Society
Licensed content publication	Journal of the American Chemical Society
Licensed content title	A Solution- and Solid-State Investigation of Medium Effects on Charge Separation in Metastable Photomerocyanines
Licensed content author	Dinesh G. Patel et al.
Licensed content date	Aug 1, 2010
Volume number	0
Issue number	0
Type of Use	Thesis/Dissertation
Are you the Author of original article?	Yes
Format	Electronic
Portion	50% or more of original article
Order reference number	
Title of the thesis / dissertation	Designing Optically Switchable Multifunctional Materials Using Photochromic Spirooxazine Ligands
Expected completion date	Dec 2010
Estimated size(pages)	350
Billing type	Invoice
Billing address	409-1066 Foul Bay Rd. Victoria, BC V8S4J2 Canada
Customer reference info	
Permissions price	0.00 USD

License Number	2527490963891
License date	Oct 14, 2010
Licensed content publisher	Elsevier
Licensed content publication	Inorganica Chimica Acta
Licensed content title	Intramolecular electron transfer in the mixed-valence [Co(3,5-DTBCat)(3,5-DTBSQ)(bpy)] complex: Beyond valence tautomerism
Licensed content author	Emi Evangelio, David N. Hendrickson, Daniel Ruiz-Molina
Licensed content date	1 September 2008
Licensed content volume number	361
Licensed content issue number	12-13
Number of pages	7
Type of Use	reuse in a thesis/dissertation
Intended publisher of new work	other
Portion	figures/tables/illustrations
Number of figures/tables/illustrations	1
Format	both print and electronic
Are you the author of this Elsevier article?	No
Will you be translating?	No
Order reference number	
Title of your thesis/dissertation	Designing Optically Switchable Multifunctional Materials Using Photochromic Spirooxazine Ligands
Expected completion date	Dec 2010
Estimated size (number of pages)	350
Elsevier VAT number	GB 494 6272 12
Permissions price	0.00 USD
Value added tax 0.0%	0.0 USD / 0.0 GBP
Total	0.00 USD

License Number	2527500246708
License date	Oct 14, 2010
Licensed content publisher	American Chemical Society
Licensed content publication	Journal of the American Chemical Society
Licensed content title	Bistability in the [CoII(semiquinonate)2] to [CoIII(catecholate)(semiquinonate)] valence-tautomeric conversion
Licensed content author	David M. Adams et al.
Licensed content date	Sep 1, 1993
Volume number	115
Issue number	18
Type of Use	Thesis/Dissertation
Are you the Author of original article?	No
Format	Print and Electronic
Portion	Table/Figure/Micrograph
Number of Tables/Figures/Micrographs	1
Order reference number	
Title of the thesis / dissertation	Designing Optically Switchable Multifunctional Materials Using Photochromic Spirooxazine Ligands
Expected completion date	Dec 2010
Estimated size(pages)	350
Billing type	Invoice
Billing address	409-1066 Foul Bay Rd. Victoria, BC V8S4J2 Canada
Customer reference info	
Permissions price	0.00 USD

License Number	2531810092364
License date	Oct 18, 2010
Licensed content publisher	Elsevier
Licensed content publication	Coordination Chemistry Reviews
Licensed content title	Control of magnetism by isomerization of intercalated molecules in organic–inorganic hybrid systems
Licensed content author	N. Kojima, M. Okubo, H. Shimizu, M. Enomoto
Licensed content date	November 2007
Licensed content volume number	251
Licensed content issue number	21-24
Number of pages	9
Type of Use	reuse in a thesis/dissertation
Intended publisher of new work	other
Portion	figures/tables/illustrations
Number of figures/tables/illustrations	1
Format	both print and electronic
Are you the author of this Elsevier article?	No
Will you be translating?	No
Order reference number	
Title of your thesis/dissertation	Designing Optically Switchable Multifunctional Materials Using Photochromic Spirooxazine Ligands
Expected completion date	Dec 2010
Estimated size (number of pages)	350
Elsevier VAT number	GB 494 6272 12
Permissions price	0.00 USD
Value added tax 0.0%	0.0 USD / 0.0 GBP
Total	0.00 USD

October 19, 2010

Dear Customer,

Thank you for your email.

- We hereby grant permission for the requested use expected that due credit is given to the original source.

If material appears within our work with credit to another source, authorization from that source must be obtained.

Credit must include the following components:

- Books: Author(s)/ Editor(s) Name(s): Title of the Book. Page(s). Publication year. Copyright Wiley-VCH Verlag GmbH & Co. KGaA. Reproduced with permission.
- Journals: Author(s) Name(s): Title of the Article. Name of the Journal. Publication year. Volume. Page(s). Copyright Wiley-VCH Verlag GmbH & Co. KGaA. Reproduced with permission.

With kind regards

Bettina Loycke
****
Bettina Loycke
Senior Rights Manager
Wiley-VCH Verlag GmbH & Co. KGaA
Boschstr. 12
69469 Weinheim
Germany

Phone: +49 (0) 62 01- 606 - 280
Fax: +49 (0) 62 01 - 606 - 332
Email: rights@wiley-vch.de

A01_First_Name: Michelle
A02_Last_Name: Paquette
A03_Company: Department of Chemistry, University of Victoria
A04_Address: PO Box 3065
A05_City: Victoria
A06_Province: BC
A07_Zip: V8W 3V6
A08_Country: Canada
A09_Phone: 1-250-721-8838
A10_Fax: 1-250-721-7147
A11_Email: paquettm@uvic.ca
A16_Product_Title: Magnetism: Molecules to Materials II: Models and Experiments
A17_ISBN: 9783527303014
A18_Author_Name: David A. Shultz (chapter author), Joel S. Miller and Marc Drillon (book editors),
A19_Page_Number: Ch. 8, p. 294, Figure 15
A24_Organization_Name: University of Victoria
A25_Purpose_Reproduction: Thesis
A26_Title_Your_Work: Designing Optically Switchable Multifunctional Materials Using Photochromic Spirooxazine Ligands
A26A_Resale: No
A27_Print_Run: 5
A28_Publication_Date: December 2010

COPYRIGHT PERMISSION REQUEST FORM

Date: Oct 14, 2010

To: The Chemical Society of Japan
1-5,Kanda-Surugadai,Chiyoda-ku,
Tokyo 101-8307, Japan

Fax: +81-3-3292-6318
E-mail: info@chemistry.or.jp

From: Michelle Paquette
Dept. of Chemistry, Univ. Victoria
PO Box 3065, Victoria, BC, V8W 3V6
Phone: 1-250-721-8838
Fax: 1-250-721-7147
E-mail: paquettm@uvic.ca

I am preparing a thesis entitled:

Designing Optically Switchable Multifunctional Materials Using Photochromic Spirooxazine Ligands

which is published by

The University of Victoria

Expected publication date: December 2010

I request your permission to include the following material in this and in all subsequent editions of this work to be published by the University of Victoria or its licensees for distribution throughout the world, in all media including electronic/online and microfilm.

Title of Publication: Chemistry Letters

Author(s)/Editor(s): Sato, O.; Hayami, S.; Gu, Z.; Seki, K.; Nakajima, R.; Fujishima, A.

Title of Selection: Photo-Induced Long-Lived Intramolecular Electron Transfer in a Co Valence Tautomeric Complex

Year: 2001 Vol.: 30 No.: 9

Figure(s)/Table(s): Figure 3 Page(s): 875

We hereby grant permission for the use of the material requested above.

Nobuyuki Kawashima
Executive Director
The Chemical Society of Japan

Date: Oct. 15, 2010

Our Ref. No. CY-RT 10-114